Pseudo Direct Drives for Safety Critical Applications

Radu – Stefan Dragan

A thesis submitted for the degree of

Doctor of Philosophy

Department of Electronic and Electrical Engineering

November 2018

Abstract

Electro-mechanical actuators are currently being developed to replace hydraulic actuation solutions previously used on existing and new aircraft platforms. The replacement of hydraulic actuators constitutes an important step towards realising the More/All Electric Aircraft concept, where all the different power sources used for non-propulsive systems, are substituted with an electrical power source and distribution network. This new system architecture is aimed at optimising aircraft performance by reducing weight, decreasing operational and maintenance costs, improving reliability and efficiency, while reducing emissions. Conventionally, all the non-propulsive aircraft systems are driven by different secondary power sources such as pneumatic, hydraulic, and electrical. Advancements in the field of electrical machines and power electronics are enabling the feasibility of the More/All Electric Aircraft concept.

The proposed electro-mechanical magnetically geared actuator aims to eliminate the mechanical gear stages from the actuator drive train by directly connecting a fault tolerant Pseudo Direct Drive motor to the mechanical drive train. The key advantages in adopting a magnetically geared motor are reductions of drive train complexity, resulting in reduced mass and improved reliability, while introducing a compliant transmission acting as a passive anti-jamming overload protection, which isolates the high kinetic energy components, i.e. high-speed rotor, from the mechanical drivetrain.

This thesis presents all the stages of the electromagnetic design and manufacture of the fault-tolerant Pseudo Direct Drive motor for primary flight control actuation. The design of the magnetically geared electrical machine is centred around achieving a lightweight fault tolerant machine with a high torque density and reduced output rotor inertia. It is shown that several PDD topologies exist for which a duplex 3-phase fault tolerant configuration can be implemented. It is also shown that adopting a fault-tolerant PDD results in a considerably lower mass and rotor inertia referred to the mechanical drivetrain of the actuator, while achieving and exceeding the dynamic requirements of the actuator. The findings are validated on magnetic gear and fault tolerant PDD demonstrators, which have been designed and built to meet the requirements of a rudder primary control surface.

List of Publications

- E. K. Hussain, K. Atallah, M. Odavic, R. S. Dragan, and R. E. Clark, “Pseudo Direct Drive electrical machines for flight control surface actuation,” in 8th IET International Conference on Power Electronics, Machines and Drives (PEMD 2016), 2016, pp. 1–6.

- R. S. Dragan, R. E. Clark, E. K. Hussain, K. Atallah, and M. Odavic, “Magnetically geared pseudo direct drive for safety critical applications,” in 2017 IEEE International Electric Machines and Drives Conference (IEMDC), 2017, pp. 1–8.

- R. S. Dragan, R. E. Clark, E. K. Hussain, M. Odavic, and K. Atallah, “Pseudo Direct Drive Electrical Machine for Primary Flight Control Surface Actuation,” in Recent Advances in Aerospace Actuation Systems and Components, 2018, pp. 24–33.

- R. S. Dragan, R. Clark, E. K. Hussain, K. Atallah, and M. Odavic, “Magnetically Geared Pseudo Direct Drive for Safety Critical Applications,” *IEEE Trans. Ind. Appl.*, pp. 1–1, 2018.

Acknowledgements

I would like to thank everyone who has helped me with the research and write-up of this thesis.

Firstly, I wish to express my sincere gratitude to my supervisor, Professor Kais Atallah, for his motivation, patience and immense knowledge. His guidance and support helped me in completing the research and writing this thesis. I also thank Dr Milijana Odavic for her suggestions and advice.

My sincere thanks also go to Dr Richard Clark, Dr David Powell and Dr Stuart Calverley, for their constructive feedback and suggestions. I thank my fellow work colleagues at Magnomatics Ltd. for their continuous encouragement. Additionally, I am thankful to Robert Barret, Ferran Garcia and Dr Glynn Cooke for their help during the manufacture of the prototype electrical machine and continuous friendship.

I gratefully acknowledge the financial support provided by Royal Commission for the Exhibition of 1851 under their Industrial Fellowship programme.

Last but not the least, I would like to thank my family for their continuous love, encouragement and support they have given me throughout this incredible journey.

Table of Contents

Figure and Table List

Nomenclature

Symbol	Description	Units
$\boldsymbol{\sigma_w}$	Target pre-stress applied to banding	Pa
$\boldsymbol{\varnothing_M}$	Average diameter of pole piece rotor	m
$\boldsymbol{\varnothing_{pp}}$	Pole piece diameter	m
$\boldsymbol{\Omega_{HSR}}$	Mechanical rotational velocity of HSR	rpm
$\boldsymbol{\Omega_{PPR}}$	Mechanical rotational velocity of PRR	rpm
$\boldsymbol{A_{copper}}$	Copper area	m^2
$\boldsymbol{A_{slot}}$	Slot area	m^2
$\boldsymbol{B_h}$	Viscous damping of HSR	$Nm/rads^{-1}$
$\boldsymbol{B_{PPR}}$	Viscous damping of PPR	$Nm/rads^{-1}$
$\boldsymbol{B_r}$	Magnetic remanence	T
$\boldsymbol{C_{T_{in}}}$	Cogging torque factor HSR – PPR	-
$\boldsymbol{C_{T_{out}}}$	Cogging torque factor PPR – stator PMs	-
$\boldsymbol{C_T}$	Cogging torque factor HSR – stator	-
$\boldsymbol{D_{r_{DD}}}$	Diameter of rotor of direct drive SPM	m
$\boldsymbol{D_{r_{MG}}}$	Diameter of rotor of mechanically geared SPM	m
$\boldsymbol{D_{PPRi}}$	Pole piece rotor inner diameter	m
$\boldsymbol{D_{PPRo}}$	Pole piece rotor outer diameter	m
$\boldsymbol{D_r}$	Electrical machine rotor outer diameter	m
$\boldsymbol{E_{DD}}$	Kinetic energy of direct drive SPM	J
$\boldsymbol{E_{MG}}$	Kinetic energy of mechanically geared SPM	J
$\boldsymbol{E_{PDD}}$	Kinetic energy of PDD output rotor	J
$\boldsymbol{F_C}$	Centrifugal / Centripetal force	N
$\boldsymbol{F_t}$	Tensile force	N
$\boldsymbol{G_r}$	Magnetic gear ratio	-
$\boldsymbol{G_{rm}}$	Mechanical gear ratio	-
$\boldsymbol{H_c}$	Coercivity	kA/m
$\boldsymbol{H_{ci}}$	Intrinsic coercivity	kA/m
$\boldsymbol{I_{d_{SS}}}$	d-axis steady stator short circuit current	A
$\boldsymbol{I_{q_{ss}}}$	q-axis steady stator short circuit current	A
$\boldsymbol{I_d}$	d-axis current	A
$\boldsymbol{I_q}$	q-axis current	A
$\boldsymbol{I_{rms}}$	RMS phase current	A
$\boldsymbol{I_{sc_{ss}}}$	Total steady state short circuit current	A
$\boldsymbol{J_h}$	Inertia of HSR	kgm^2
$\boldsymbol{J_{GF}}$	Inertia of PPR support structure	kgm^2
$\boldsymbol{J_L}$	Inertia of load	kgm^2
$\boldsymbol{J_{PDD}}$	PDD output rotor inertia	kgm^2

J_{PP}	Inertia of pole pieces	kgm^2
J_{PPR}	Inertia of PPR	kgm^2
J_{SPM}	Inertia SPM rotor	kgm^2
J_T	Total system inertia	kgm^2
J_{eddy}	Eddy current density	A/mm^2
J_{endp}	Inertia of rotor endplate	kgm^2
J_{screw}	Inertia of screw	kgm^2
J_x, J_y, J_z	X, Y, Z – axis current density	A/mm^2
K_d	Damping due to EM PDD losses	Nm/rads^{-1}
K_{es}	Stiffness of magnetic gear element	N/m
L_{PDD}	PDD active length	m
L_{act}	Active length	m
L_d	d-axis inductance	H
L_{endp}	Endplate axial thickness	m
L_{ph}	Phase inductance	H
L_q	q-axis inductance	H
L_w	Copper wire total length	m
M_{12}	Mutual inductance	H
M_{pole}	Mass of PM pole block	kg
M_r	SPM rotor mass	kg
N_f	Number of filaments of tow	-
N_{pp}	Number of pole pieces of PPR	-
N_s	Number of slots	-
N_t	Number of healthy turns	-
P_{hyst}	Hysteresis loss	W
P_{cl}	Classical eddy current loss	W
P_{cu}	Copper loss	W
P_{eddy}	Eddy current power loss	W
P_{ex}	Excess eddy current loss	W
R_{hlb}	Halbach ratio	-
R_{PPRi}	Pole piece rotor inner radius	m
R_{PPRo}	Pole piece rotor outer radius	m
R_{cog}	Radius of centre of gravity	m
R_i	Inner radius of PM cylinder	m
R_o	Outer radius of PM cylinder	m
R_{ph}	Phase resistance	Ω
T_{DD}	Torque of direct drive electrical machine	Nm
$T_{HSR\ drag}$	HSR drag torque	Nm
T_{HSR}	High speed rotor torque	Nm
T_L	Load torque	Nm

T_{L_MAX}	Absolute maximum load torque	Nm
T_{MG}	Torque of mech. geared electrical machine	Nm
$T_{PPR\,drag}$	PPR drag torque	Nm
T_{PPR}	Pole piece rotor torque	Nm
T_e	HSR electromagnetic torque	Nm
T_m	PPR pull-out torque	Nm
T_r	HSR rated torque	Nm
T_{rated}	Rated output torque	Nm
V_{DC}	DC voltage	V
V_d	d-axis voltage	V
V_{ph}	Phase voltage	V
V_q	q-axis voltage	V
X_m	Maximum linear displacement of screw slide	m
d_f	Filament diameter	m
d_m	Mean screw diameter	m
d_o	Outer screw diameter	m
f_{hsr}	Electrical frequency of HSR	Hz
f_{PPR}	Electrical frequency of PPR	Hz
f_l	Actuator bandwidth	Hz
k_h	Hysteresis loss material constant	-
k_d	Distribution factor	-
k_e	Classical eddy current loss material constant	-
k_{ex}	Excess eddy current loss constant	-
k_p	Pitch factor	-
k_{skw}	Skew factor	-
k_w	Winding factor	-
l_{im}	Inner magnet radial thickness	m
l_{om}	Stator PM radial thickness	m
l_{pp}	Pole piece radial thickness	m
l_{stat}	Stator radial thickness	m
n_f	Number of faulty turns	-
p_h	Number of pole pairs of HSR	-
p_{fact}	Packing factor	-
p_l	Number of pole pairs of stator PM array	-
q_{spk}	Number of spokes per phase	-
s_p	Stator slot pitch	deg.
t_e	Electrical time constant	s
t_l	Thickness of electrical steel laminations	m
w_m	Stator magnetic loading	Wb
α_c	Coil span angle	rad

$\boldsymbol{\alpha_{ph}}$	Electrical angle between phasors	rad
$\boldsymbol{\alpha_{pp}}$	Nominal pole piece pitch	rad
$\boldsymbol{\alpha_{spk}}$	Mechanical angle between adjacent spokes	rad
$\boldsymbol{\beta_{pp}}$	Actual pole piece pitch	deg.
$\boldsymbol{\gamma_{PM}}$	Electrical conductivity of PM	S/m
$\boldsymbol{\gamma_{TTN}}$	Electrical conductivity of Titanium	S/m
$\boldsymbol{\gamma_{cu}}$	Copper conductivity	S/m
$\boldsymbol{\gamma_{fe}}$	Electrical steel conductivity	S/m
$\boldsymbol{\delta_{pp}}$	Pole piece pitch ratio	-
$\boldsymbol{\zeta_{DD}}$	Aspect ratio of direct drive SPM	-
$\boldsymbol{\zeta_{MG}}$	Aspect ratio of mechanically geared SPM	-
$\boldsymbol{\theta_{h}}$	Angular displacement of HSR	rad
$\boldsymbol{\theta_{hH}}$	Solution to homogeneous ODE	rad
$\boldsymbol{\theta_{hP}}$	Function for non-homogeneous eqn.	-
$\boldsymbol{\theta_{Circ}}$	Arc of circumferentially magnetised HSR PM	deg.
$\boldsymbol{\theta_{Rad}}$	Arc of radially magnetised HSR PM	deg.
$\boldsymbol{\theta_{e}}$	Magnetic gear load angle	elect. deg.
$\boldsymbol{\theta_{in}}$	Pole piece inner angle	deg.
$\boldsymbol{\theta_{m}}$	Maximum angular position of PPR	deg.
$\boldsymbol{\theta_{out}}$	Pole piece outer angle	deg.
$\boldsymbol{\theta_{ppr}}$	Angular displacement of PPR	deg.
$\boldsymbol{\nu_{scr}}$	Linear rate of screw	m/s
$\boldsymbol{\rho_{DD}}$	Density of rotor of direct drive SPM	kg/m^3
$\boldsymbol{\rho_{GF}}$	Density of glass fibre PPR support structure	kg/m^3
$\boldsymbol{\rho_{MG}}$	Density of rotor of mechanically geared SPM	kg/m^3
$\boldsymbol{\rho_{PDD}}$	Density of PDD output rotor	kg/m^3
$\boldsymbol{\rho_{PM}}$	Density of PM material	kg/m^3
$\boldsymbol{\rho_{PP}}$	Density of ferromagnetic pole pieces	kg/m^3
$\boldsymbol{\rho_{SPM}}$	Density of SPM rotor	kg/m^3
$\boldsymbol{\rho_{al}}$	Density of aluminium	kg/m^3
$\boldsymbol{\rho_{fe}}$	Density of electrical steel	kg/m^3
$\boldsymbol{\sigma_{DD}}$	Airgap shear stress of direct drive electrical machine	Pa
$\boldsymbol{\sigma_{MG}}$	Airgap shear stress of mechanically geared electrical machine	Pa
$\boldsymbol{\sigma_{PPR}}$	PDD output rotor airgap shear stress	Pa
$\boldsymbol{\sigma_{r}}$	Resultant stress in banding layer	Pa
$\boldsymbol{\tau_{HSR}}$	Electrical period of HSR	s
$\boldsymbol{\tau_{e}}$	Time length of electrical cycle	s
$\boldsymbol{\psi_{PM}}$	PM flux linkage	Wb
$\boldsymbol{\psi_{d}}$	d-axis flux linkage	Wb

$\boldsymbol{\psi_q}$	q-axis flux linkage	Wb
$\boldsymbol{\omega_h}$	Rotational velocity of HSR	rads^{-1}
$\boldsymbol{\omega_{h\_MAX}}$	Limit of HSR frequency	rads^{-1}
$\boldsymbol{\omega_L}$	Rotational velocity of load	rads^{-1}
$\boldsymbol{\omega_e}$	Electrical frequency of HSR	rads^{-1}
$\boldsymbol{\omega_l}$	Electrical frequency of PPR	rads^{-1}
$\boldsymbol{\omega_{ppr}}$	Rotational velocity of PPR	rads^{-1}
$\boldsymbol{\omega_{scr}}$	Mechanical rotational velocity	rads^{-1}
FT	Fault tolerant	
HSR	High speed rotor	-
MG	Magnetic gear	-
ODE	Ordinary differential equation	-
PDD	Pseudo Direct Drive	-
PM	Permanent magnet	-
PPR	Pole piece rotor	-
SPM	Surface permanent magnet	-
$\boldsymbol{Z}$	Machine periodicity	-
$\boldsymbol{E}$	Back-EMF voltage	V
$\boldsymbol{F}$	Axial force / load of screw	N
$\boldsymbol{H(t)}$	Hazard rate	h^{-1}
$\boldsymbol{J}$	Intrinsic polarisation	T
$\boldsymbol{K}$	Knock-down factor	-
$\boldsymbol{M}$	Number of channels for normal operation	-
$\boldsymbol{N}$	Number of total independent channels	-
$\boldsymbol{P}$	Pre-tension applied to the tow	N
$\boldsymbol{R(t)}$	Reliability function	-
$\boldsymbol{T}$	Torque required for screw	Nm
$\boldsymbol{X}$	Number of failures accepted	-
$\boldsymbol{k}$	Number of 3-phase lanes	-
$\boldsymbol{l}$	Screw lead	m
$\boldsymbol{m}$	Number of phases per lane	-
$\boldsymbol{rt_{in}}$	Pole piece inner pitch ratio	-
$\boldsymbol{rt_{out}}$	Pole piece outer pitch ratio	-
$\boldsymbol{t}$	Time	s
$\boldsymbol{x}$	Banding radial thickness	m
$\boldsymbol{y, C, C_1, C_2, C_3}$	Constants	-
$\boldsymbol{\gamma}$	Post cure fill factor of banding	-
$\boldsymbol{\zeta}$	Aspect ratio	-
$\boldsymbol{\eta}$	Screw efficiency	%
$\boldsymbol{\lambda}$	Screw lead angle	deg.
$\boldsymbol{\xi}$	Failure rate of each lane	h^{-1}

$\boldsymbol{\sigma}$	Airgap shear stress	Pa
$\boldsymbol{\phi}$	Screw friction angle	deg.

Chapter 1: Introduction

1.1 The More Electric Aircraft

The concept of the More Electric Aircraft represents the electrification of all or a majority of the aircraft secondary systems, such that electrical power is generated and consumed on board. The adoption of electrical power in aircraft can be traced back to the 1950s, when, due to the increase in size and speed, the need for power surface control systems was introduced. Military British bombers such as the Valiant, Victor and Vulcan utilised electrical power for primary flight control and engine-drive starter-generators [1], [2].

The 1980's mark the beginning of large-scale aircraft electrification, with the 'Fly-By-Wire' system being integrated on board commercial aircraft the Airbus A320 and Boeing 777. In this topology, the mechanical control inputs of the pilot were converted into electrical signals. The on-board flight computers would respond to these inputs by controlling each flight control surface of the aircraft and obtain the desired response. This meant an increase in reliability and safety as the pilots have reduced workload and increased precision of controls, which are also checked against the aircraft flight protection envelope. The weight and fuel consumption of the aircraft have also been reduced, as the heavy mechanical controls have been replaced with electrical signal wires.

Aircraft electrical power distribution systems have been developed to replace other hydraulic and mechanical aircraft systems such as landing gear deployment and taxing, wing de-icing and jet engine starter/generator. Named "Power-By-Wire", this technology replaced heavy hydraulic power distribution systems with electrical power networks. The reported advantages are reduced weight associated with electrical distribution power cables, improved reliability and reduced maintenance costs as well as power generation at variable frequencies [3]. It is reported in [4] that the electric power generation capacity of the Boeing B787 and Airbus A380 is approximately 1.4MW and 850kW respectively.

The majority of commercial aircraft use the gas turbine jet engines, which also produce thrust, as the main source of power for the aircraft subsystems. The main engines are used to drive mechanically geared generators to produce electrical power, while providing pneumatic, hydraulic and mechanical power for cabin pressurisation, air-conditioning, wing ice protection, hydraulic systems, fuel and oil pumps. The total secondary power supplied by the engines of a large civil aircraft can be between 1.3-1.7 MW [5]. In comparison the More Electric Aircraft concept aims convert these four types of auxiliary power to electrical power systems in order to increase global system efficiency, reduce aircraft mass and fuel consumption, with the absolute goal of reducing the cost and environmental impact of air travel [6].

Power generation in electrified aircrafts is focus around three main voltage standards which include $28V_{DC}$ for load power loads, $270V_{DC}$ for surface control systems and $115V_{AC}$ at 400Hz for large loads on civil aircrafts. Recently, with the increase on-board electrical loads, the voltage has been increased to $540V_{DC}$ and $230V_{AC}$ with a variable frequency between 320-800Hz, in order to reduce cable weight [7], [8]. Furthermore, by adopting high voltage, the conduction losses in the distribution network can be reduced, increasing system efficiency. It is reported that the $270\ V_{DC}$ power distribution system is desirable since the large DC link capacitors can provide stable voltage output during system transients. In contrast AC distribution systems require larger wires to accommodate the reactive power flow [4].

The main areas of research and development related to the More Electric Aircraft platform include electrical engine starter/generators, primary and secondary flight control surface actuation, auxiliary and emergency power units and fault-tolerant power management and motor drive systems [9].

The electrical engine starter/generator is used to start the main engines without the need of a pneumatic air starter system. Variable frequency AC systems are preferred over the conventional integrated drive generators, which required complex hydraulic systems to be able to produce a fixed frequency AC voltage for a variable engine speed. In comparison, AC generators can be directly coupled to the engine shaft, with a simplified mechanical drive train, such that efficiency and reliability are increased, while overall weight is reduced [10], [11].

Control surface actuation is traditionally achieved using hydraulic actuators. In the More Electric Aircraft concept these can be replaced with electro-hydraulic and electro-mechanical actuators, which take advantage of the advancements in high power density, fault-tolerant electrical machines. Electric actuation can improve system reliability and reduce mass due to the lack of seals, hydraulic distribution system and hydraulic fluid [12]–[15].

The emergency power generation can be provided, from the wind-milling effect of the engine fan, during engine shutdown, by fan powered generators. These generators could be used during normal engine operation to supplement the main generation system [16].

1.2 Electro-hydrostatic actuators – EHA

In conventional large aircraft, the control surface actuation is supplied by a centralised hydraulic system consisting of a hydraulic pump and electric motor which deliver pressurised hydraulic fluid to the hydraulic actuators which are connected to the control surfaces. This actuation strategy is control using the “fly-by-wire” concept, where the control signals from the pilot travel via wires to the control unit, rather than mechanical linkages. The main disadvantages of this architecture are represented by the high complexity and additional weight of the hydraulic lines and fluid which span across the aircraft to reach the different control surfaces [17].

As part of the More Electric Aircraft concept, the centralised hydraulic actuation network is replaced with electro-hydrostatic actuators, EHA, and electro-mechanical actuators, EMA. It is reported in [18] that several tier 1 aerospace manufacturers prefer the use of EHAs for primary surface control actuation due to the reliability issues of EMAs, which include jamming of the mechanical drive train of the EMA due to the high number of mechanical contacts associated with the mechanical gearbox and linear screw.

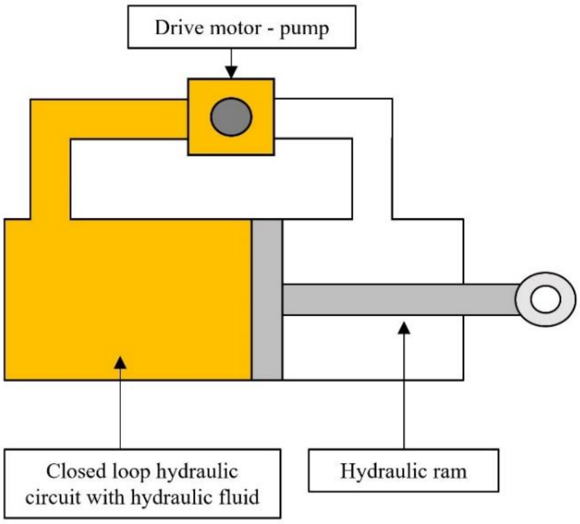

Figure 1.1. Schematic of EHA

The EHA system architecture, shown in Figure 1.1, is composed out of a closed loop hydraulic circuit and electric motor pump assembly which controls the flow of hydraulic fluid in the hydraulic cylinder in order to displace the hydraulic ram connected to the control surface. EHAs are attractive since they can be controlled as conventional hydraulic actuators, and provide passive damping of the control surface due to the hydraulic fluid and piston. Moreover, since the EHA is an isolated system, it can introduce weight savings associated with the lack of hydraulic pipelines and fluid of a conventional centralised hydraulic actuation system. The main drawback is associated with the reliability of the hydraulic seals which need to be inspected periodically for any leaks [19]. EHAs have been used for primary control surface actuation in aircraft as the Vulcan bomber, Boeing 787 and Airbus A380 [20].

1.3 Electro-mechanical actuators – EMA

Advancements in permanent magnet materials capable of high temperature operation, electromagnetic design and control power electronics as well as power by wire implementation have made the electromechanical actuator (EMA) topology desirable for flight actuation of the 'More Electric' aircraft platform. The EMA actuator can be implemented in the rotary or linear topology.

The rotary EMA, Figure 1.2, consists of a fault tolerant high-speed electrical motor and fault tolerant power electronics drive. The output shaft of the electrical machine is connected to the input (high) side of a mechanical gearbox in order to match the motor torque to the control surface requirement. The mechanical gearbox is typically a high ratio planetary gear set or harmonic drive. It is common for rotary EMAs to have a large gearbox outer diameter which means that the actuator cannot be directly connected to the control surface in the slim part of the wing due to the limited envelope available.

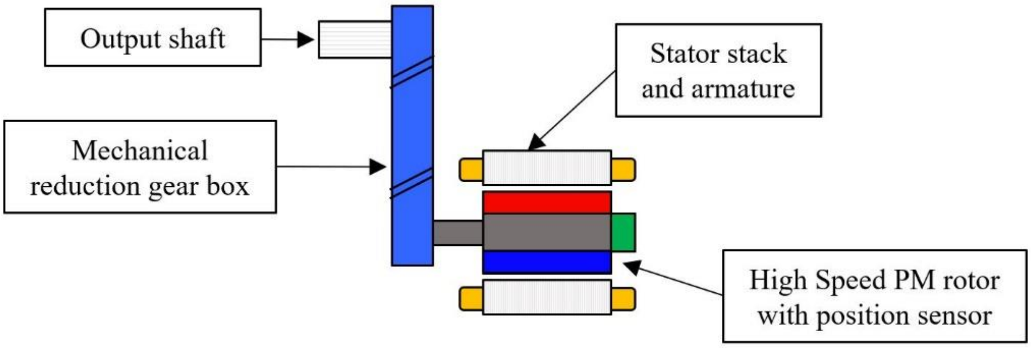

Figure 1.2. Rotary EMA topology

The authors of [21] have successfully implemented and demonstrated the concept of a rotary landing gear actuator for helicopters. This rotary EMA has an electrical machine, typically a brushless DC or PM synchronous motor, connected to a high ratio (30-320:1) single stage harmonic drive. The high-power conversion density of this type of mechanical gearbox allows for a small actuator package and reduced weight.

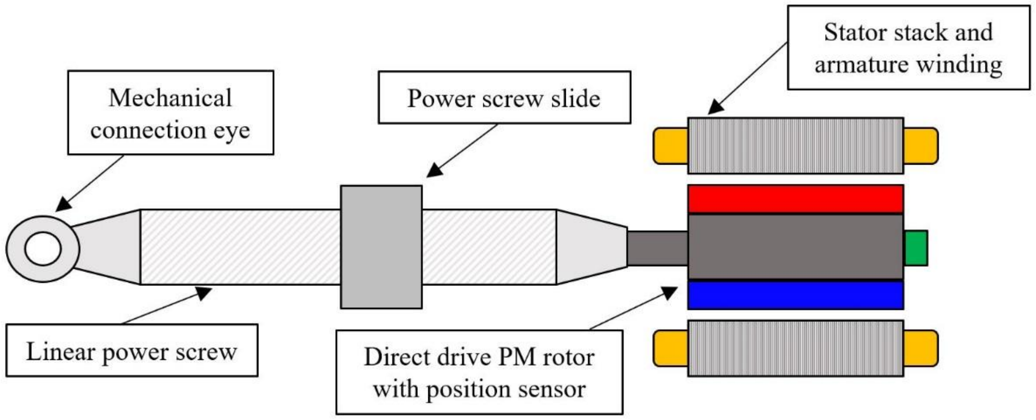

Figure 1.3. Linear direct drive EMA topology

The linear actuator topology can be divided into direct drive and geared EMAs. The direct drive topology, Figure 1.3, consists of a high torque density fault tolerant electrical machine with rotor position feedback sensor and fault tolerant control power electronics. The output shaft of the electrical motor is connected to the linear power screw, typically with the help of a spline interface. The power screw, which can be a ball screw, lead screw or planetary roller screw, converts the rotary motion of the motor into linear actuation of the slide. Typically, for a direct drive EMA, a planetary roller screw is preferred due to its high forward and reverse efficiency and conversion ratio which help reduce the torque, size and weight requirement on the electrical machine side [22]. The linear position of the slide is monitored using linear variable differential transformer (LVDT). The reading from this sensor can also be used to check the position of the direct drive rotor. The main advantage of the direct drive linear topology lies in its simple drive train with a reduced number of components and mechanical contacts which improve the overall failure rate of the system [23].

In contrast, the linear geared EMA drive train, Figure 1.4, is comprised of a fault tolerant permanent magnet motor connected to the linear power screw via a mechanical reduction gearbox. The angular position of the motor is given by the rotor feedback sensor while the linear position of the nut/slide is obtained from the output of the LVDT. Similarly to the rotary EMA topology, the mechanical gearbox does reduce the electric motor torque requirement and weight, but increases the number of mechanical contacts and failure rate of the actuator drive train. The mechanical gearbox can be a multi stage planetary gear set or a high ratio harmonic drive.

The main concern of aerospace manufacturers for the usage of EMAs for primary and secondary flight control actuation is related to jamming of the actuator mechanical drive train which would result in permanent loss of actuation capability. This is regarded as a critical failure mode of the actuation system as it can lead to reduced or complete loss of aircraft control. Actuator jamming is mainly caused by mechanical faults of the actuator drive train. Electrical faults caused by a fault of the motor controller or loss of EMA power supply in combination with a non-back-drivable power screw design can also cause jamming of the actuator.

The mechanical jamming faults of conventional EMAs are related to the high number of mechanical contacts of the gearbox, linear screw-nut assembly and thrust bearings [22], [23], [24]. The degradation of mechanical gearboxes used in EMAs can be caused by overload conditions, excessive axial and radial loads combined with a loss of lubrication of the meshing teeth.

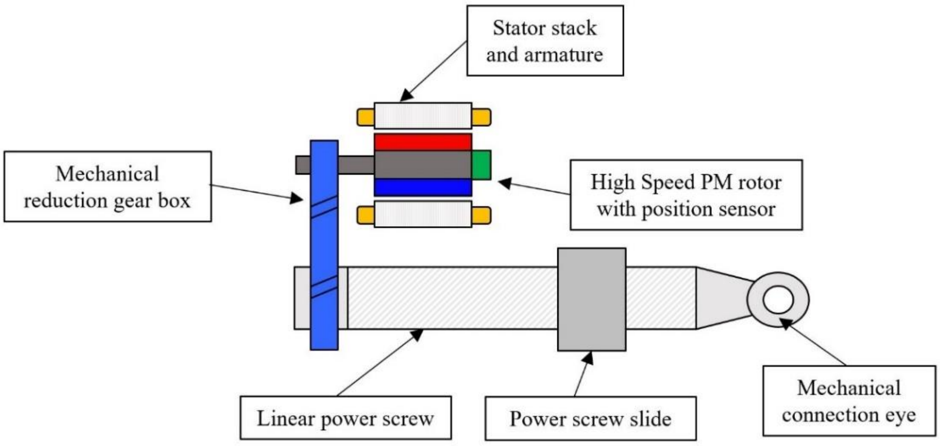

Figure 1.4. Linear geared EMA topology

This would result in cracks or plastic deformation of the gear teeth, which can lead to teeth shearing off and causing a permanent jam of the actuator load path [24], [25]. Figure 1.5 and 1.6 show examples of tooth root cracks and broken gear tooth from a mechanical gearbox used in an EMA drive train.

Ball screw faults can be caused by deformation of the ball screw channel or metal flaking from the ball screw race which would result in an increase in the load on the circulating balls. This can increase the friction between the balls and race, cause vibration and eventually jamming of the actuator [26]. Flaking of material from the ball race or balls, Figure 1.7, occurs due to poor lubrication, corrosion, indentations and contamination of the ball race.

Figure 1.5. Gear wheel with tooth root crack [25]

Figure 1.6. Gear wheel with broken tooth [25]

Figure 1.7. Flaking of material off the ball screw race [27]

Linear power screws are also affected by wear caused by high friction between the screw race and rolling elements due to loss of lubrication or contamination with foreign residue. Figure 1.8 shows an example of wear on the nut of a ball screw due to high friction between the race and balls caused by loss of lubrication. Eventually, this condition can aggravate and lead to a jamming condition of the actuator.

Figure 1.8. Wear of ball screw nut race [28]

Ball screws are also affected by indentations in the ball race due to high impact loads or contamination with metal debris. Figure 1.9, shows an example of indentations on the ball screw race caused by the high loading of the balls as a result of impact loading.

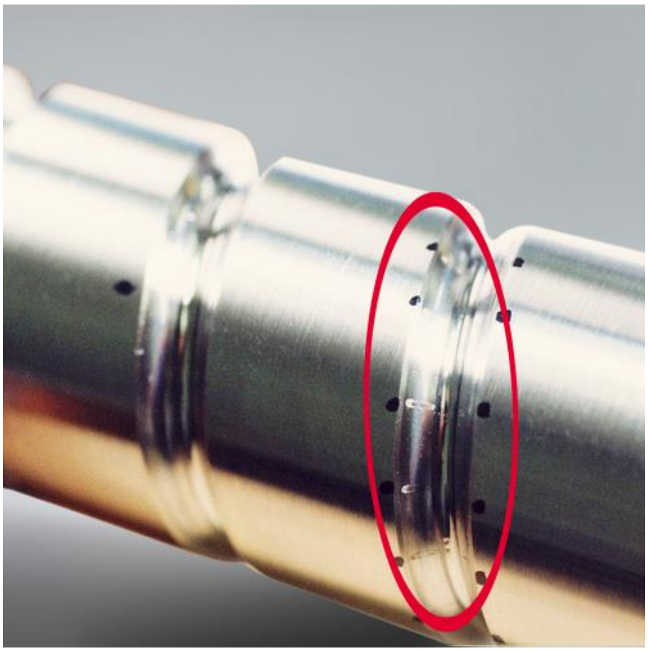

Figure 1.9. Indentation on ball screw race [29]

Roller and lead screws can also seize due to different impurities (metal particles or sand) contaminating the meshing teeth. This can be due to the operation of the EMA is harsh environments combined with poor or loss of lubrication [22]. Axial and radial loads which are higher that the static and dynamic capability of the screw, can degrade the performance of power screw due to plastic deformation of the screw shaft, ball races or planetary rollers. This would result in increased friction between the balls/rollers and ball races/teeth of the linear power screw.

Bearings are regarded as the third mechanism of actuator jamming. The bearings used in the actuator drive train and in the electrical machine are typically cylindrical/tapered roller bearings and deep grove angular contact ball bearings respectively. However, the bearing selection is based on the specific actuator application, duty cycle profiles, operating conditions, axial and radial cyclic loads as well as lifetime and lubrication requirements. Bearing faults like flaking, Figure 1.10, create a rough surface on the inner and outer bearing race. This is caused by excessive loads during bearing insertion or operation, contamination with foreign particles and fatigue of the rolling elements [30].

Figure 1.10. Flaking of ball bearings races [30]

Bearing spalling and peeling, shown in Figure 1.11 and 1.12, are represented by small scratches and scores on the bearing race and rolling elements. This is cause due to poor mounting procedure, poor lubrication of the rolling elements or contamination with foreign particles.

Figure 1.11. Bearing race spalling [30]

Figure 1.12. Bearing roller elements peeling [30]

Bearing wear, Figure 1.13, is characterised by rough and scared bearing race surface with uneven indentations. This occurs due to ingress of dirt and sand or other foreign contaminants combined with poor or loss of lubrication. Chipping and cracking in a bearing can affect the inner and outer bearing race as well as the rolling elements due to overload or contamination. Figure 1.14 shows an example of chipping on the inner and outer guide rings of a roller bearing due to high impact load, which can occur in an EMA application.

Figure 1.13. Roller bearing wear of inner race [30]

Figure 1.14. Roller bearing chipping of inner and outer guide rings [30]

Bearing fretting, Figure 1.15, manifests itself as dents in the bearing race caused by the rolling elements. In an actuator this can be caused by high load and bandwidth cycles with short actuator strokes. Bearing seizure can be recognized due to discoloration and loss of hardness of the bearing races and rolling elements as shown in Figure 1.16. This is mainly due to poor lubrication and axial or radial overload which would increase the bearing frictional load, losses and heat generation. This would translate in a reduction of system efficiency and could result in a jam of the mechanical drive train [25].

Figure 1.15. Bearing fretting caused by roller elements [30]

Figure 1.16. Bearing rollers removed from seized bearing [30]

Jamming of the actuator can also occur due to shock loads of the control surface caused by sudden wind gusts or foreign object impact. In this case the high stored kinetic energy of the rotor of the electrical machine is dissipated through the mechanical contacts of the gearbox and power screw resulting in damage of the meshing teeth or balls and races. This can be aggravated in highly geared actuators where the inertia of the electrical machine rotor referred to the output side of the gearbox is increased by the square of the gear ratio. Thus, the referred stored energy of the rotor is significantly increased, causing a high likelihood of actuator jam during sudden surface overload conditions. The authors of [31] have investigated EMA jamming of ball screws by increasing the pressure between the ball the race. This was achieved by reducing the number of ball circuits and increasing the axial and radial load on the screw. An actuator jamming hazard rate of $3.6 \cdot 10^{-8}$ per flight hour was predicted, which is higher than the actuator-disconnect and runaway failure rates of $6 \cdot 10^{-9}$and $2 \cdot 10^{-12}$, respectively.

1.4 Jam-tolerant electromechanical actuators

Since the major concern with EMAs is related to their susceptibility towards mechanical jamming of the load path, research efforts have targeted different concepts of disconnect devices. Such devices for EMAs can be classified based on their ability to reverse the disconnect procedure and re-engage operation using the primary load path. Another aspect is related to the ability to test the disconnect device before flight, as part of pre-flight checks.

The authors of [32] have developed, as part of the European funded Clean-Sky project, jam-tolerant actuators for landing gear door, landing gear retraction and rudder control surface. The anti-jamming system is based on an auxiliary BLDC electrical motor that would disengage a piston located inside the shaft of the ball screw [32]. This will allow the landing gear or control surface to free fall under gravity or return to its neutral position under aerodynamic drag. The system is capable of re-engaging the piston, allowing for the load to be transmitted through the ball-screw after the jam condition has been removed. This anti-jamming device does not have a limit number of cycles and can be fully tested in pre-flight checks. Figure 1.17 and 1.18 show the EMA operating under normal and emergency extension conditions.

Figure 1.17. EMA extension under normal operating conditions [32]

Figure 1.18. EMA extension under emergency conditions – free fall operation [32]

Another jam-tolerant EMA design is presented in [33], which has the capability to be fully testable during pre-flight tests. A schematic of the actuator and built-in disconnect device is shown in Figure 1.19.

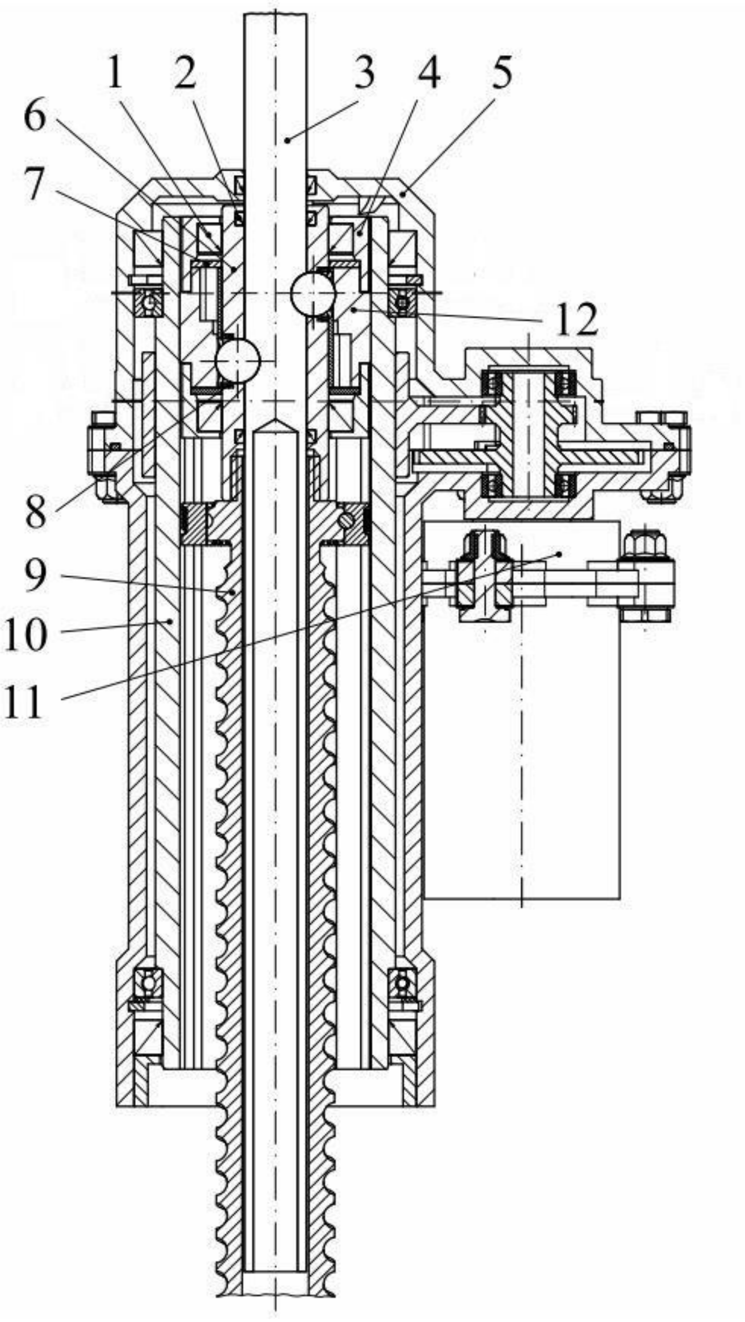

1 – shaft seals
2 – rod seals
3 – output shaft
4 – caps
5 – EMA housing
6 – adapter
7 – discs
8 – retaining element
9 – ball screw shaft
10 – shifting sleeve
11 – geared motor
12 – locking sleeve

Figure 1.19. Built-in testable jam-tolerant EMA [33]

The device is able to transfer loads and decouple the load path between the ball screw and output shaft. This is achieved by using locking balls situated between a shifting and a locking sleeve. The latter is connected to a secondary electrical machine through a mechanical gear stage. When the secondary BLDC motor is enabled, the locking balls disengage the main load path from the output and fall in the recesses of the locking sleeve. This main load path can be re-engaged by driving the disconnect motor in the opposite direction. The geared connection between the secondary electrical motor and locking sleeve is shown in Figure 1.20.

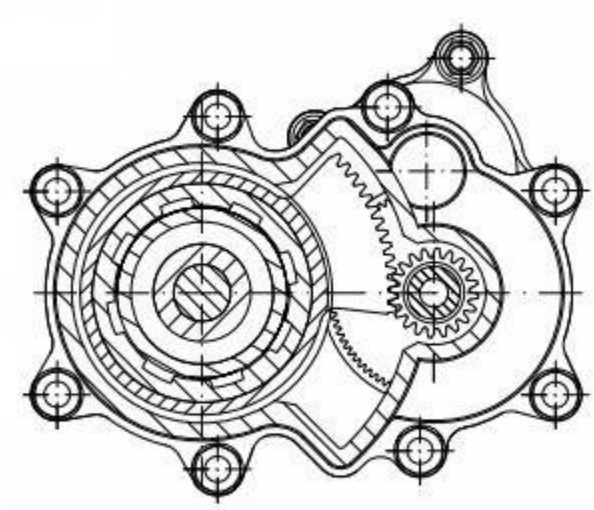

Figure 1.20. Geared connection between disconnect device and secondary BLDC motor [33]

The authors of [34] present a testable jam-tolerant EMA shown in Figure 1.21. The disengage mechanism is based on two sets of balls, a locking sleeve and two sets of springs. The first ball set is locked in position radially by the locking sleeve. The second ball set controls the position of the locking sleeve. An electromagnet within the actuator together with the inner set of springs are used to change the position of the second ball set in the radial direction. The locking sleeve and the first set of balls are then moved outward in the radial direction by the outer set of springs. In this position, the disconnect device is engaged, breaking the load path between the nut of the actuator and output shaft. In order to re-engage the main load path, a secondary EMA is required to drive the locking sleeve, and sets of balls into position.

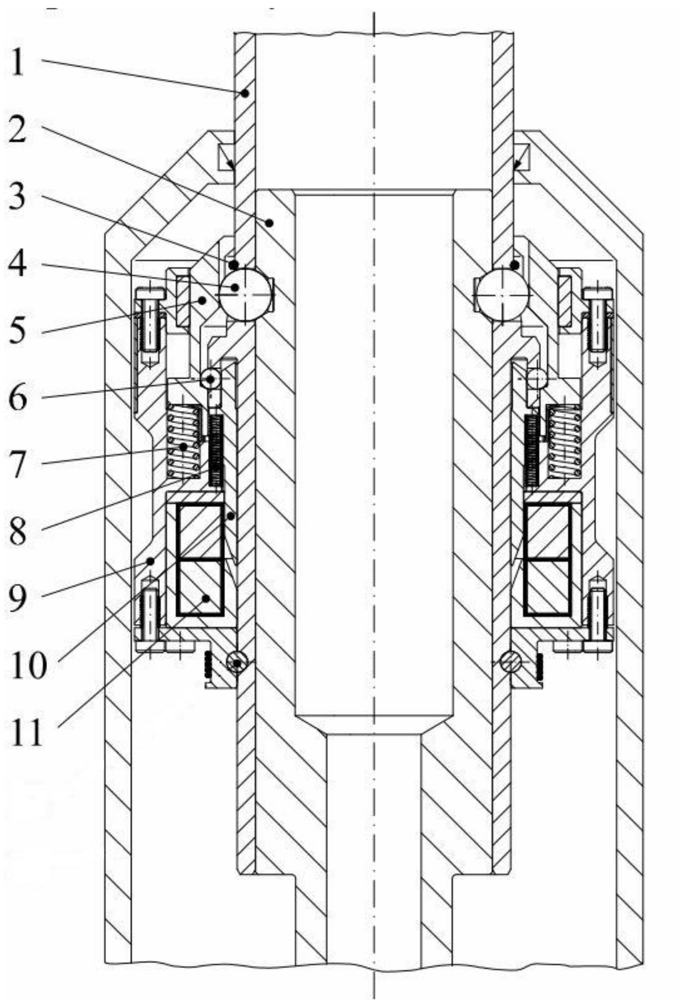

1 – output shaft

2 – ball nut

3 – elastic ring

4 – first ball set

5 – locking sleeve

6 – second ball set

7 – outer spring set

8 – inner spring set

9 – disconnect device housing

10 – armature

11 - electromagnet

Figure 1.21. Jam-tolerant testable EMA [34]

Another disconnect device, Figure 1.22, presented in [34], is based on a single shot pyrotechnical trigger used to disengage the main load path. During normal operation, the locking balls enable the transmission of axial load from the nut of the EMA to the output shaft. The sleeve assembly which consists of the locking sleeve, pulling sleeve and disk is held in position on top of the locking balls by a set of shear pins. In order to enable the disconnect device, a pyrotechnic combustion is triggered in two gas combustion chambers. This will shear the pins and cause the sleeve assembly to move releasing the locking balls radially. From this point, the load path is permanently disconnected with the control surface being in free-fall operation under aerodynamic load. This type of device does not allow for re-engagement of normal operation.

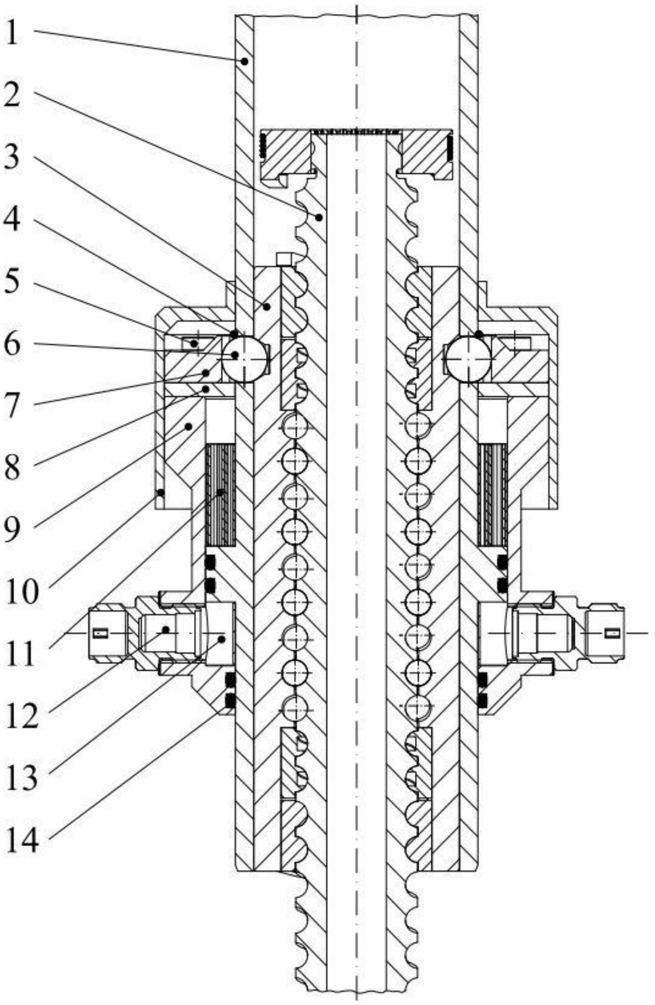

1 – output shaft

2 – ball screw shaft

3 – nut

4 – positioning ring

5 – shear pins

6 – locking balls

7 – locking sleeve

8 – disc

9 – pulling sleeve

10 – housing

11 – end stop

12 – gas generator

13 – combustion chamber

14 - seals

Figure 1.22. Single use non-testable jam-tolerant EMA [34]

The aerospace manufacturer Airbus has patented multiple embodiments of a jam-tolerant EMA in [35]. The drive train of the actuator is based on two linear motion screw-nut assemblies, each connected directly or via a mechanical gear stage to separate electrical motors. In order to reduce the overall size of the EMA, the first linear screw has a larger diameter and houses the second screw within its bore, as shown in Figure 1.23. The actuator extension is given either due to the relative axial displacement between the first screw and first nut or due to the axial movement of the second screw and its nut. When a mechanical jam occurs on any one of the linear screws, the secondary screw can be used in conjunction with its electrical motor to retract or extend the load. In this configuration the second linear screw can be considered as back-up. A non-back-drivable screw could be used for the secondary load path in order to hold a static load without requesting a holding torque from the motor. This would result in a reduced size and mass of the secondary electrical machine without the need for a mechanical brake. Another option would be to use mechanical brakes on both load paths in conjunction with back-drivable linear screws having high forward efficiencies.

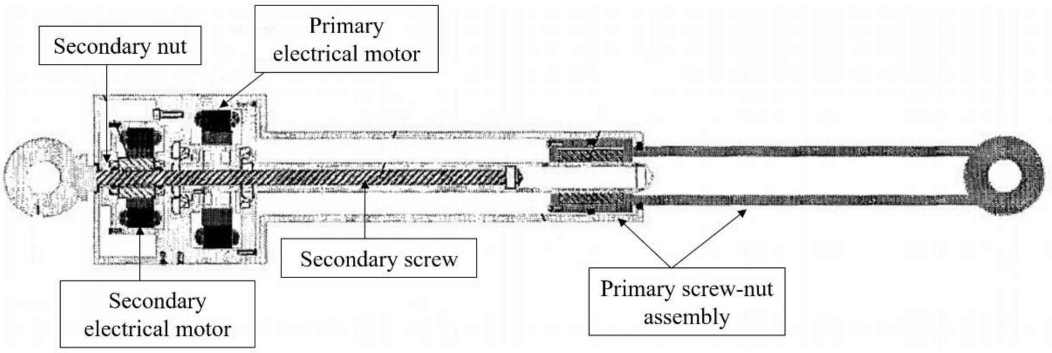

Figure 1.23. Airbus jam-tolerant EMA [35]

Parker-Hannifin have also patented a fully reversible and testable jam-tolerant EMA in [36]. The proposed topology, Figure 1.24, can disconnect the output of the EMA from the load using a pair of locking plates connected through a mechanical gear set to a secondary electrical motor. The decoupling mechanism can be driven clockwise or anti-clockwise by the secondary motor in order to engage or disengage the locking plate which would couple or decouple the load from the actuator assembly.

BAE Systems Plc. have also patented in [37] an EMA with a mechanical or electromechanical disconnect clutch device placed between the output of the electrical motor and lead screw. The engagement and disengagement of the mechanical clutch is done by a secondary electrical machine.

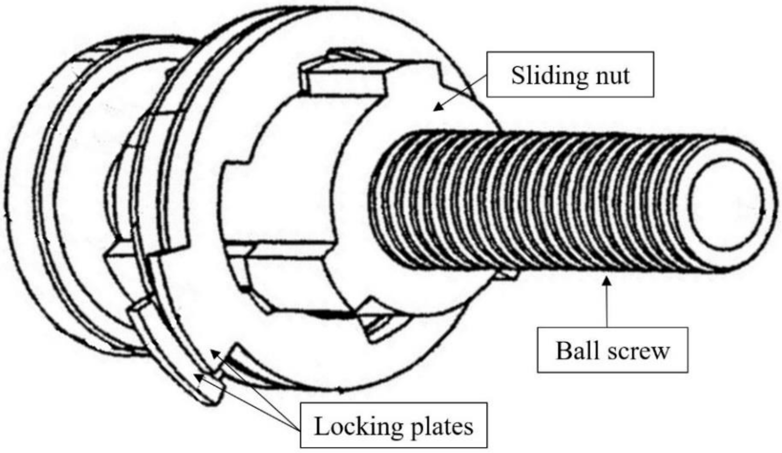

Figure 1.24. Jam tolerant EMA with locking plate decoupling device [36]

The jam-tolerant EMA designs discussed, do provide multiple solutions to avoid mechanical jamming of the actuator load path, but also introduce a large number of additional components. This can include secondary electrical motors in combination with extension/retraction pistons, secondary power screw driver or mechanical and electromagnetic clutches. Other designs include ball sets, locking plates and springs required to engage and disengage the main load path. Non-testable jam-tolerant designs are based on shear pins and pyrotechnical triggers. Thus, adding jam-tolerant functionality comes at the cost of a high number of additional components when compared to the standard EMA drive train shown in Figure 1.3 and 1.4. This increases the total mass and space envelope of the EMA and as a consequence reduces the power density of the actuator making it less attractive for primary and secondary actuation when compared to an EHA platform.

The proposed novel actuator platform, Figure 1.25, is based on a direct drive configuration that combines a high efficiency linear screw with a magnetically geared synchronous permanent magnet motor. The EMMAS actuator was designed to actuate a primary flight control surface, the rudder of a small jet aircraft with a MTOW between 7-10 tonnes.

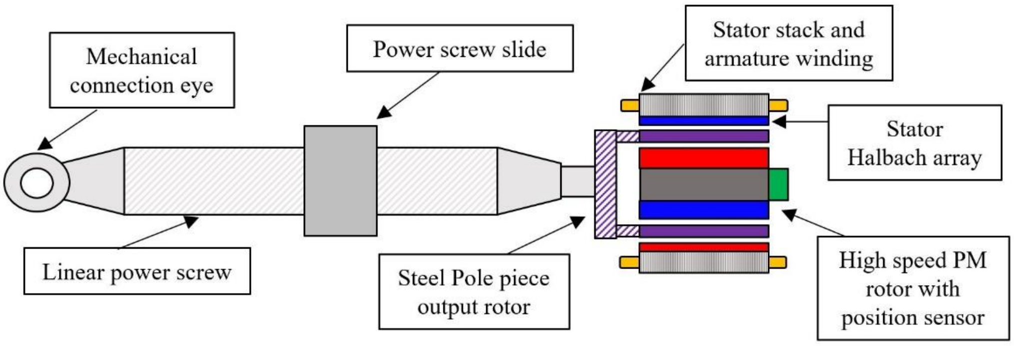

Figure 1.25. Electromagnetic mechanical actuator system - EMMAS

The fault tolerant magnetically geared motor or Pseudo Direct Drive (PDD), shown in Figure 1.26, consists of a mechanically and magnetically integrated magnetic gear and brushless permanent magnet motor. The components of the magnetic gear are represented by the inner permanent magnet high speed rotor (PM HSR), outer output pole piece rotor (PPR) and stationary Halbach magnet array. The components of the core brushless electrical machine are the inner HSR PM rotor which is synchronously coupled to the stator winding. Thus, by combining the core components of the two electrical machine topologies, a PDD unit is obtained, where the inner HSR couples with the stator armature to produce electromagnetic torque. This is transmitted to the output PPR through the interaction between the stationary permanent magnets on the stator bore and the asynchronous space harmonic produced by the modulation of the fields of the permanent magnets on the HSR by the ferromagnetic pole pieces of the output rotor.

Due to the embedded magnetic gear element, the mechanical gear states typically present in an EMA are completely removed and the HSR is directly connected through the magnetic gear to the linear screw. This increases the overall reliability of the actuator system by removing a large number of mechanical contacts while reducing the likelihood of jamming the mechanical drive train. The inherent compliance and torque limiting characteristics of the magnetic gear element isolate the mechanical drive train of the actuator from the negative effects of the stored kinetic energy in the HSR. The inertia of the hollow output rotor of the PDD is reduced due to its light construction and small wall thickness which further helps to minimise the risk of mechanically jamming the linear screw.

The magnetic gear element also enables the PDD to achieve a high torque density while having an embedded passive, non-contact torque fuse mechanism. This passive anti-jamming mechanism is related to the maximum torque transmission capability of the magnetic gear element. It is inherently triggered when the load torque on the output rotor of the PDD exceeds the maximum pull-out torque that the magnetic gear can transmit. In this scenario, as long as the overload condition is present, the output rotor of the PDD will be disengaged from the inner HSR which will rotate freely. The re-engagement of the magnetic transmission will occur when the overload condition is removed and the output torque requirement of the PDD is lower than the maximum torque transmission capability of the magnetic gear.

Through its embedded magnetic transmission, the PDD motor achieves a compact design with a reduced weight and size while being controlled using standard existing power electronic converters just like conventional PM synchronous motors. In comparison, the conventional PM motor can only output between 10-30 Nm/L with natural or liquid cooling while the PDD can achieve a substantially higher 60 to 90 Nm/L with natural air cooling. Thus, it can be concluded that through its high torque density, reduced mass, simplified and reduced component count together with the torque fuse capability, the PDD motor is a worthy option for the EMMAS actuator platform.

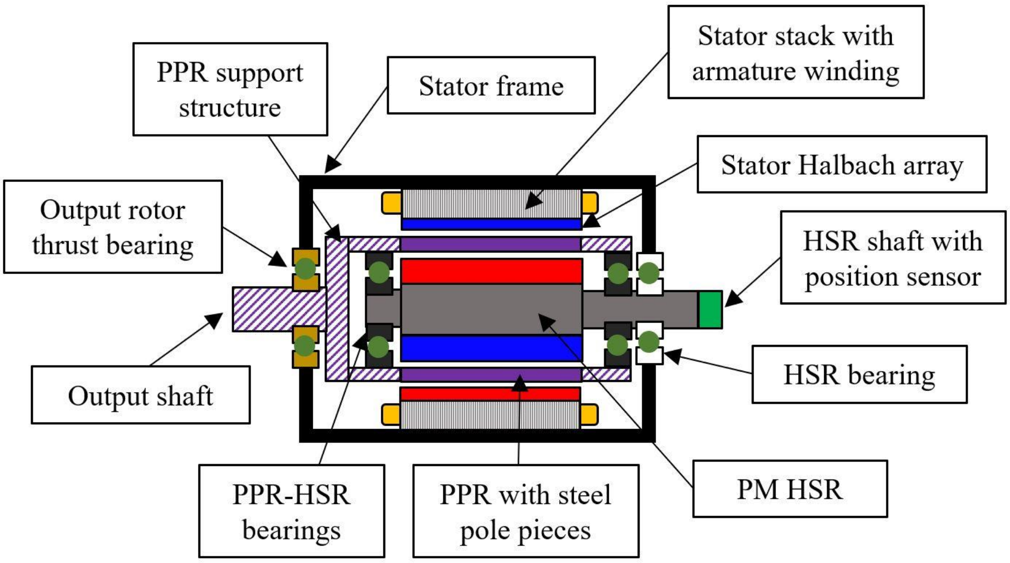

Figure 1.26. Pseudo Direct Drive motor topology

1.5 Fault-tolerant electrical machines used in aerospace

- Switched reluctance (SR) electrical machines

Switched reluctance electrical machines have been proposed for safety critical applications, such as aerospace actuation, due to their robust design and inherent fault tolerant capability [38], [39]. The SR electrical machine represents a doubly salient topology due to the structure of the rotor and stator iron cores. The salient rotor of the SR machine does not utilise PM material or windings, and is manufactured from steel laminations, which makes it robust for high speed applications. The stator is represented by a laminated stack, with stator teeth that support the concentrated coils. The principle of operation of SR machines is based on reluctance torque which is produced due to the tendency of the rotor to align with the energised stator teeth [40].

The fault tolerance requirements of electrical, magnetic, and physical isolation between phases are inherently met in SR machines. The stator coils are concentrated around a single tooth and separate half H-bridge rectifiers can be used to control each phase, achieving electrical isolation [41]. Moreover, the SR electrical machine is characterised by reduced mutual magnetic coupling between phases. The inherent fault tolerance of SR machines is given by the non-exited rotor. For example, if a fault occurs on one of the phases, the fault current will cease to exist once the power supply of that phase is switched off [42]. In this case, no braking torque will exist due to the faulted phase.

An issue with SR machines is given by the fact that two sides of different coils share the same stator slot. Thus, thermal isolation of different phases can be problematic. Due to the single excitation topology, SR machines have a reduced torque density when compared to PM machines. In contrast, SR machine have a high overload factor and can operate at high temperatures due to the absence of permanent magnets. The overload factor in an SR machine is limited by the insulation class of the copper winding which would dictate the maximum temperature that the winding can operate at, without degrading the copper insulation. The downside of SR machines is represented by the reduced efficiency of SR machines over the PM machines, as well as more expensive semiconductor switches required to drive the high stator excitation currents [43]. SR machine have been proposed for use in aircraft fuel pumps [4], turbine engine starter/generator [44], [45], and secondary control surface actuation [46], [47].

- Permanent magnet (PM) electrical machines

Advancements in permanent magnet (PM) materials and manufacturing technologies have enabled permanent magnet electrical machines to achieve high torque density, improved efficiency and high reliability, which makes them attractive for aerospace safety critical applications. PM machines can be categorised, based on the stator excitation, into synchronous AC PM machines with sinusoidal excitation, and DC PM machines with rectangular excitation. PM electrical machines with high torque densities typically consist of a surface mount PM rotor and stator stack with teeth and copper coil which form the stator winding. Torque production is given by the synchronous coupling between the fundamental PM magnetic field component and stator MMF.

A multitude of slot-pole combinations and winding topologies can be adopted in order to produce PM electrical machine designs which are fault tolerant and provide a certain degree of redundancy [48], [49]. Fault tolerant PM electrical machines characterised by a multi-lane 3-phase arrangement, with electrical, magnetic, thermal and physical isolation between lanes, have presented in literature and validated for safety critical applications such as aerospace actuators [49]–[51], green taxiing of aircraft on landing [52], [53] and high power density aircraft generators [54]. Alternatively, fault tolerant PM machine with multi-phase stator topologies, where each phase is independently controlled from a separate H-bridge power inverter have been presented in [42], [55]–[57].

The main advantages introduced by such PM electrical machines are represented by increased torque density and higher efficiency when compared to the switched reluctance topology. Due to the constant presence of the PM rotor field, PM machines need to be designed with 1 p.u phase inductance, such that in the event of single phase short-circuit, phase to phase short-circuit or symmetrical 3-phase short-circuit, the fault current is limited to the value of the rated machine current. In comparison to SR machine, the high inductance of fault tolerant PM machines can slightly increase the size of the power inverter [58]. In comparison with SR machine, the speed capability of PM machine is lower due to the mechanical limits related to the high-speed operation of the PM rotor. Adequate banding or interior PM rotor designs need to be considered for high speed operation, together with the voltage limit of the power inverter. This makes PM machine slightly more complex and expensive to manufacture when compared to the SR topology.

1.6 Magnetically geared electrical machines

The magnetically geared electrical machines investigated in the presented research are represented by co-axial magnetic gears and Pseudo Direct Drive electric motors

1.6.1 Magnetic gears

Geared and mechanically geared machines are extensively used in a wide range of applications in order for the prime mover to satisfy the rotational velocity requirement of the output load. Mechanical gears transmit power through the meshing of mechanical teeth of two or more rotors in a well lubricated environment. Capable of high torque densities and gear ratios, mechanical gears are susceptible to wear of the meshing elements, excess noise, vibrations, poor overload characteristics and reduced reliability.

Magnetic gears have been developed for more than a century with the initial designs being based on the topologies of mechanical counterparts, as shown in Figure 1.27. The meshing teeth have been replaced by magnetised rotors separated by an airgap with the gear ratio being related to the diameter ratio and pole number of the rotors. Although the initial designs were characterised by low torque densities, advancements in permanent magnet materials and development of electromagnetic finite element software have made magnetic gears competitive with the mechanical variants, developing in excess of 100kNm/m^3. The benefits of magnetic gears are related to the high contactless transmission efficiency, absence of lubrication and improved reliability. Magnetic gears can operate with low noise and vibrations while filtering the torque pulsations of the input source. The inherent torque overload protection allows the magnetic gear transmission to maintain structural integrity and re-engage normal operation once the excess load is removed. These performance characteristics are desired by industrial system manufacturers in applications with a high reliability requirement and safety critical operation such as wind and marine power, artificial oil lifts and aerospace.

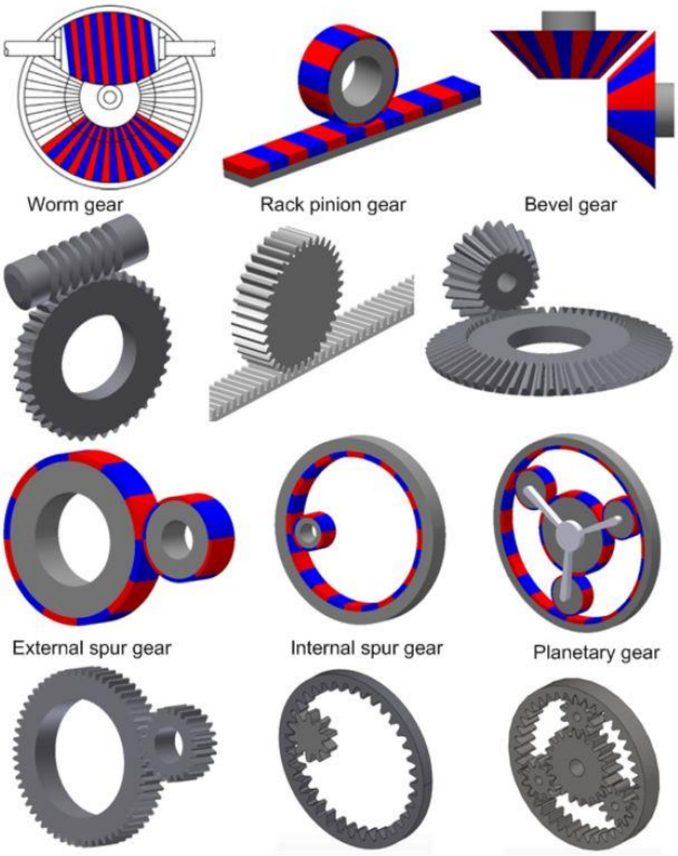

Figure 1.27. Mechanical and magnetic gear topologies [59]

The first patent regarding an early concept of magnetic gear transmission was awarded to Charles G. Armstrong [60] on the 26th of November 1901. This describes a novel contactless power transmission device composed out of primary and secondary movers, as shown in Figure 1.28. The prime mover is a wheel with coils wound onto equally spaced teeth. The coils are connected to a commutator which is powered from a battery pack. The commutator controls the direction of current within the coils creating a magnetic field. A secondary, much larger, mover is represented by a ferromagnetic wheel with teeth placed in close proximity to the prime mover. The electromagnetic field produced by the prime mover interacts with the magnetic teeth of the secondary mover. If a torque and speed were imposed to the prime mover the secondary would rotate due to the magnetic attraction forces between the two wheels. Thus, power is transmitted from the input side of the gear to the output. This device was said to be quiet, efficient with no mechanical contacts between the two movers and easily controller.

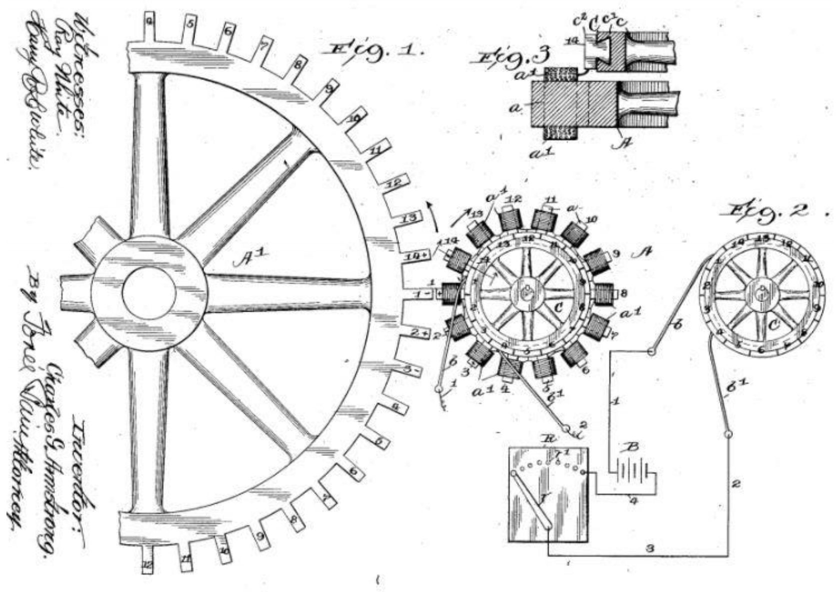

Figure 1.28. Wound field magnetic gear [60]

A second patent application was submitted by Harold T. Faus in 1940 for a magnetic gear with permanent magnet intermeshing teeth [61]. As shown in Figure 1.29, the magnetic gear is represented by two wheels with permanent magnet teeth having the same polarity. This device was quoted to have a gear ratio of 2:1. The strong magnetic repulsion tangential forces between the permanent magnets of each wheel ensure mechanical separation of the teeth of both wheels. At low loads the magnetic gear transmits power from the input to the output shaft solely due to the magnetic interaction of the two magnet arrays. When the load is increased beyond the maximum magnetic force transmission capability, the teeth of the two gears would make contact. Thus, in this case the gear would act as a conventional mechanical gear and would not slip at high loads. This invention was characterised by low wear, noise and friction and with no backlash when operating as purely a magnetic gear.

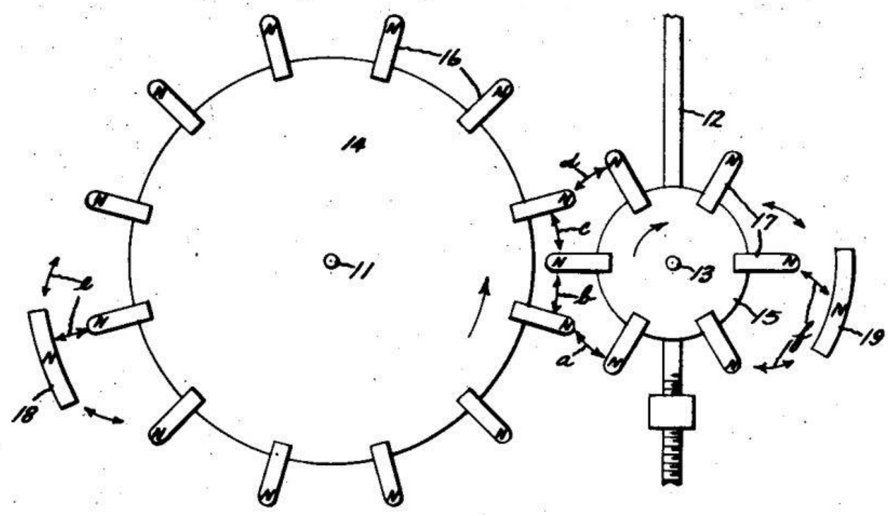

Figure 1.29. Permanent magnet magnetic gear [61]

Patents for radial field magnetic gears, [62]–[64] have been awarded in 1964, 1968 and 1974. The magnetic transmission topologies shown in Figure 1.30-33, are based on the architecture of planetary gearboxes with three concentric rings representing the sun gear, ring gear and planet carrier. The author of [63] and [64] present magnetic gear topologies where in inner rotor is composed out of a permanent magnet array and represents the sun gear of the magnetic transmission. The outer magnet array, ring gear, is concentric with the inner ring, but on a larger diameter. The middle ring is composed of ferromagnetic equally spaced pole pieces and is stationary. The authors also describe a novel permanent magnet material used in the design of the magnetic gear. The “Cera Magnet” manufactured from barium carbonate in combination with ferric oxide was produced at that time by the Stockpole Carbon Company [63]. These permanent magnets were regarded as resistant to demagnetisation and with high electrical resistivity resulting in low Eddy current losses when used in a magnetic gear assembly. Due to its different number of magnetic poles on the two rotors, the magnetic gear shown in Figure 1.33 was regarded as a speed multiplier or reducer. This invention was designed to be used in conjunction with fixed speed alternate current induction motors in order to match the speed and torque of the load to the motor side in belt drives and centrifugal pumps.

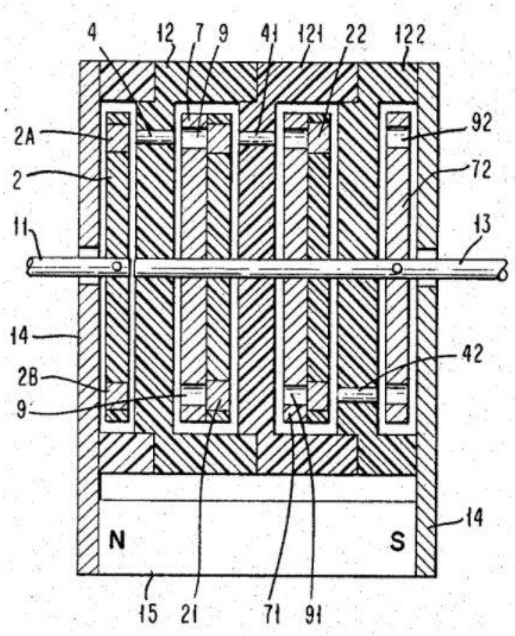

Figure 1.30. Multi-stage magnetic gear [62]

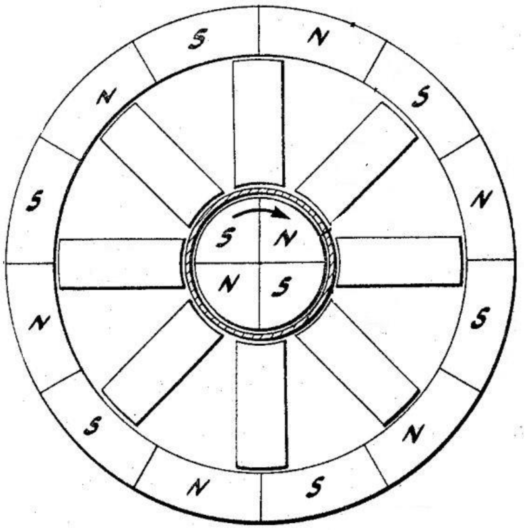

Figure 1.31. Radial magnetic gear with pole piece rotor [63]

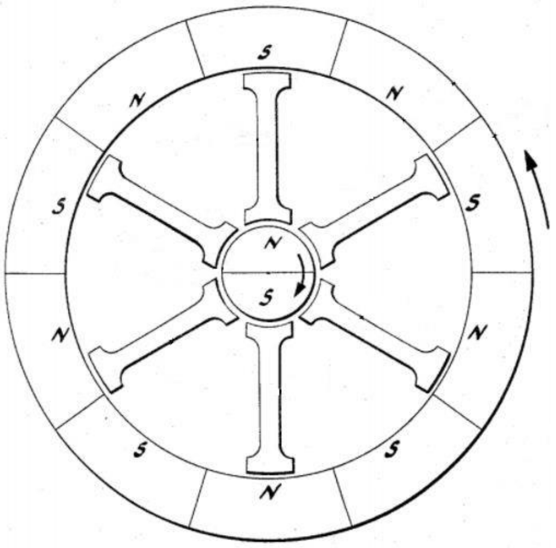

Figure 1.32. Radial magnetic gear with pole piece rotor [63]

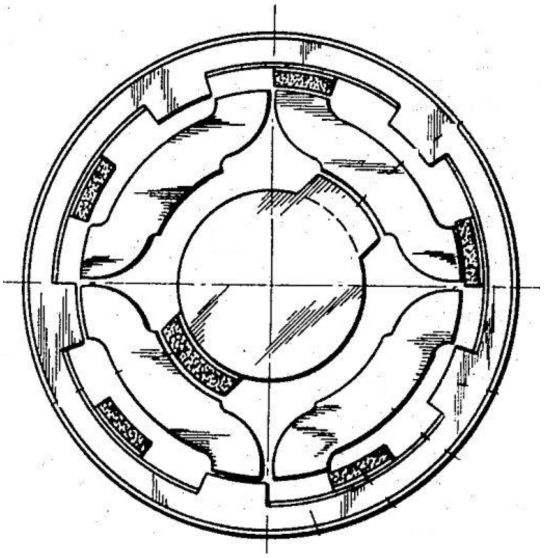

Figure 1.33. Radial magnetic gear with wound stator teeth and pm [64]

A rotary axial field permanent magnet based magnetic gear, Figure 1.34, was presented in 1987 by the authors of [65]. The gear ratio was fixed to 3:1 and the peak torque transmission capability was measured at 5.5Nm. The magnetic gear topology, shown in Figure 1.35, is based on an involute steel gear design with an 80mm pinion gear and 160mm gear disk. The meshing teeth were replaced with $SmCo_5$ permanent magnets in an NS alternating pattern on the two rotors. The axial airgap was set at 1mm and a peak flux density of 0.2T was measured in the airgap between the two rotors. This gear was characterized by low operation noise and vibrations, reduced wear due to the absence of meshing teeth and with a high enough torque transmission capability for industrial applications.

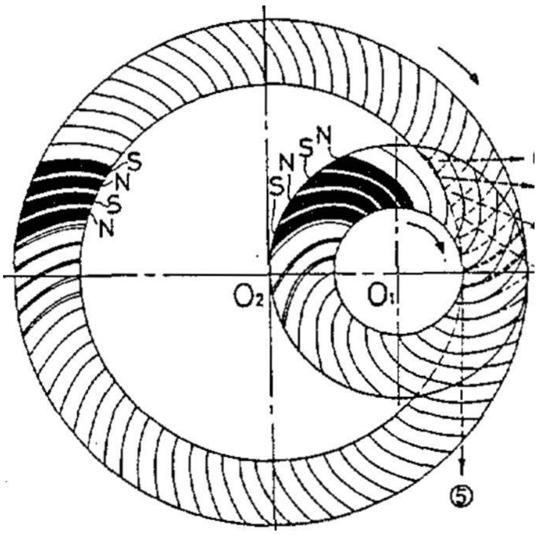

Figure 1.34. Concept of axial field magnetic gear [65]

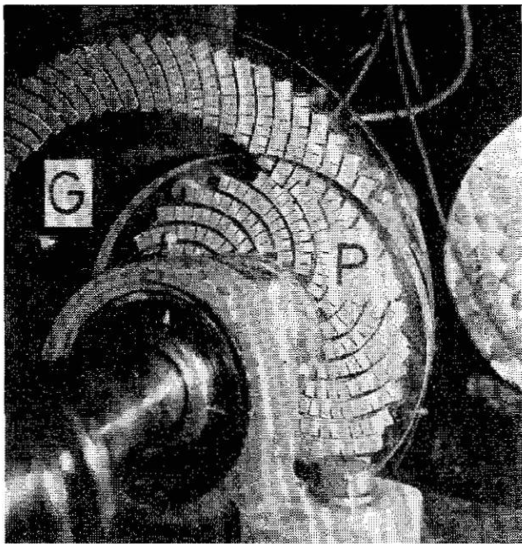

Figure 1.35. Axial field magnetic gear prototype [65]

An axial field magnetic gear with a 50:1 gear ratio is presented in [66]. This designed is based on five stator disks with 200 radial lines, Figure 1.36, and five rotor disks with 196 radial lines, Figure 1.37. The ferromagnetic disks are stacked alternatively in the axial direction, creating four disk sectors with low reluctance where the lines of the ten disks are aligned, as shown in Figure 1.38. In the rest of the disk areas where the lines are not aligned, a high reluctance path is created. In this configuration the stator disks are fixed while the rotor disks are free to rotate. A four pole magnet disk, Figure 1.39, is then stacked at one side of the stator-rotor disk assembly. The complete axial magnetic gear stack assembly is shown in Figure 1.40. The high reluctance difference between the areas where the lines are aligned and not aligned causes the rotor disks to be coupled to the field of the permanent magnet disk. When the permanent magnet disk is rotated by one pole pitch, the rotor disks would rotate by one radial line pitch. Thus, the magnet disk can be regarded as the input rotor while the rotor disks represent the output side of the magnetic gear. The magnetic field passing through the stator and rotor disks can cause mutual attracting between the disks, resulting in a loss of airgap, increased wear and friction. This behaviour is aggravated by the small airgaps of the device ($40\ \mu m$) and thin radial lines of each disk. The authors of [66] state that the efficiency and controllability of the device are also affected by contaminants in the airgap. Mechanical backlash is introduced by the high tolerance indentations used to fix the stator and rotor disks to the case and output shaft, respectively.

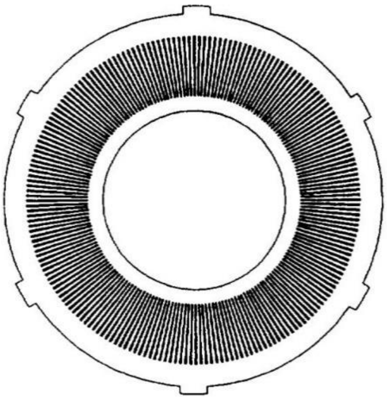

Figure 1.36. Stator disk with 200 radial lines [66]

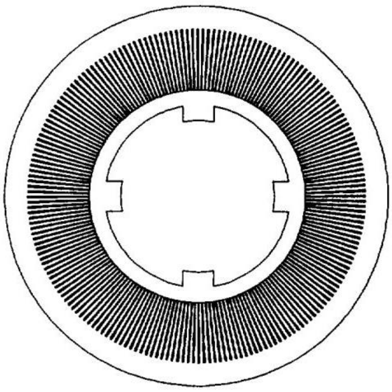

Figure 1.37. Rotor disk with 196 radial lines [66]

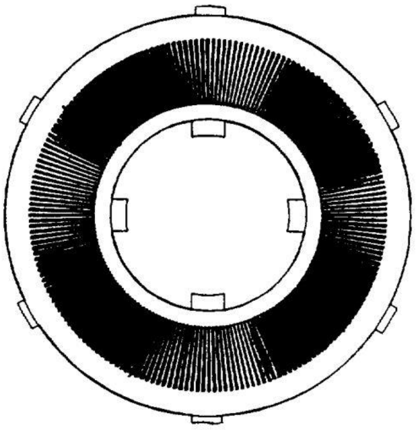

Figure 1.38. Aligned and un-aligned line areas of stator and rotor disks [66]

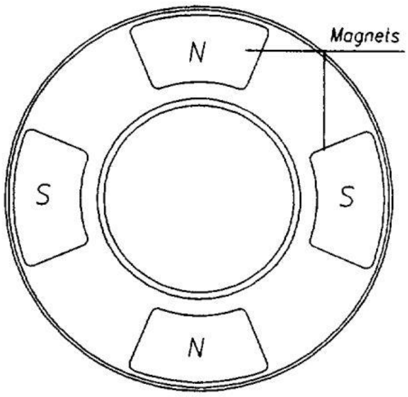

Figure 1.39. Permanent magnet rotor [66]

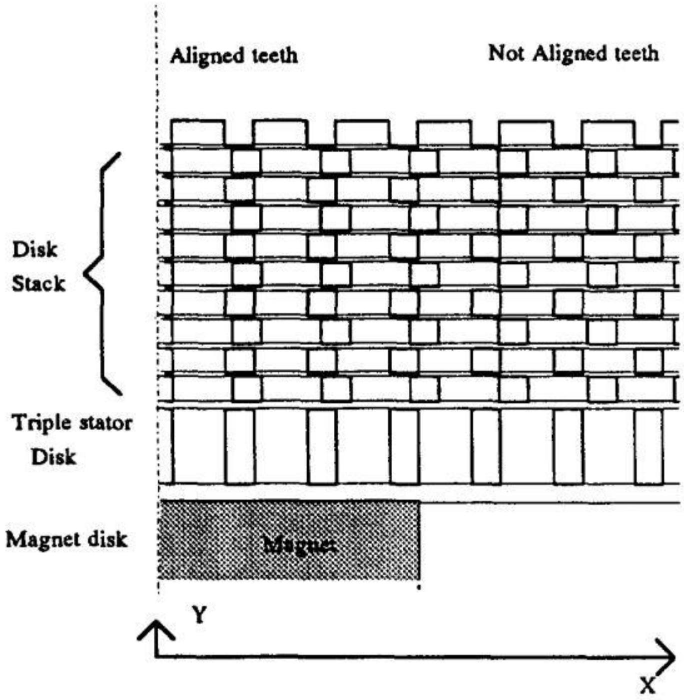

Figure 1.40. Axial stacking of stator, rotor and magnet disks [66]

A concentric radial field magnetic gear, shown in Figure 1.41, with a contemporary design was patented in 1997 [67]. This topology is based on two concentric permanent magnet rotors of different pole numbers. The rotors are separated by a ferromagnetic ring with a smooth inner bore and teeth on the outer diameter. This ring modulates both magnetic fields created by the two rotors which results in a magnetic coupling effect between the two rotors. The authors have identified two configurations in which this magnetic gear can be operated. In the first one, the middle ferromagnetic modulator ring is held stationary while in input and output shafts are connected to the inner and outer permanent magnet rotors, respectively. In the second configuration, the outer magnet rotor is held stationary while the input shaft is connected to the inner most rotor and the output shaft is connected to the modulator ring. Similarly to the designs patented in [63], [64], this magnetic gear has a high magnet utilisation factor since all the PMs are used to transmit torque at any instance of operation.

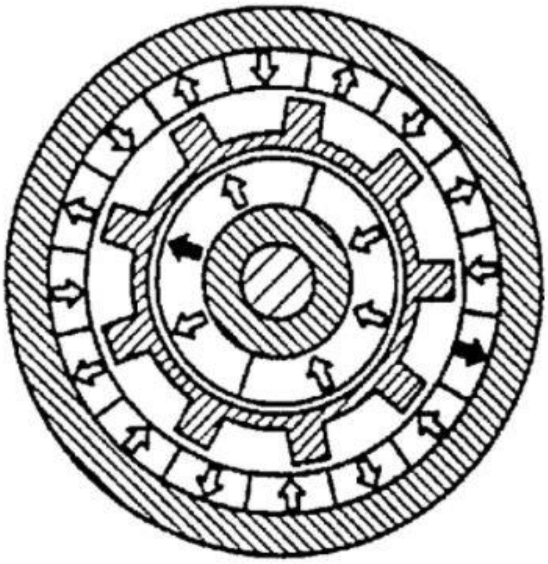

Figure 1.41. Radial field concentric rotor magnetic gear [67]

An axial field magnetic gear was developed in 2001 by Charpentier and presented in [68]. The magnetic gear shown in Figure 1.42, is based on two ironless rotors with square permanent magnets which are magnetised along the z-axis of rotation of the gear. The radii of the rotors were fixed at 90mm with 10mm thick PMs and a 2mm airgap between the two rotors. Due to the fact that both rotors have equal outer radii and the same number of magnetic pole pairs, the resultant gear ratio was fixed at 1:1. Compared to modern PM grades, the permanent magnets used in this magnet gear were only magnetised to a field of 1T. This, combined with the fact that only a third of the total magnet material is used to transmit torque results in a low torque transmission capability of only 6 Nm.

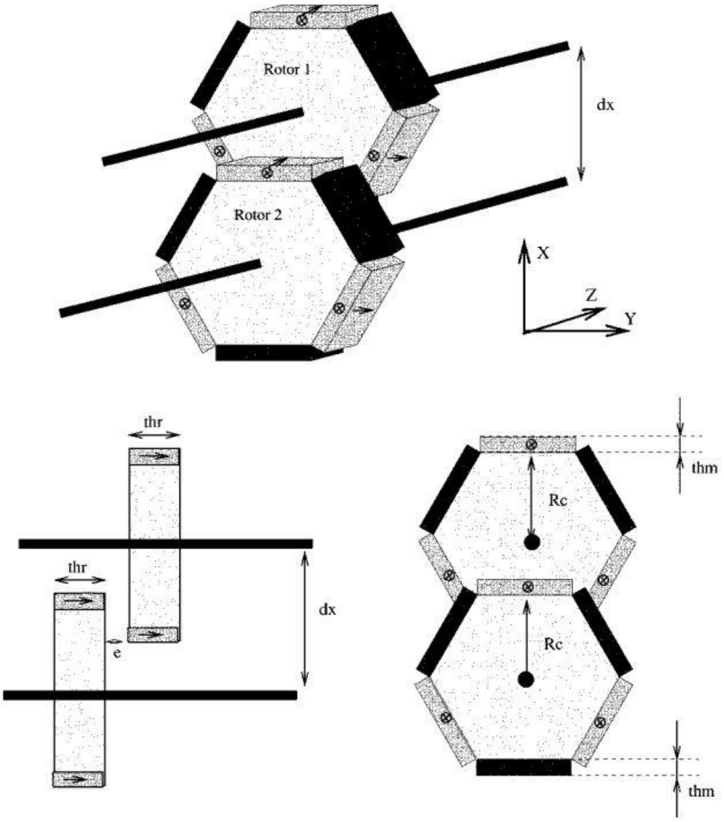

Figure 1.42. Axial field magnetic gear [68]

The first high torque density magnetic gear, comparable with two and three stage helical gearboxes was developed in 2001 by K. Atallah et al [69] with the prototype being tested in [70]. The magnetic gear topology Figure 1.43 is based on two permanent magnet rotors with stationary pole pieces acting as a modulating ring. The outer diameter of the magnetic gear was fixed at 140mm with a 50mm axial length. The remanence of the permanent magnets was 1.25T. The finite element (FE) was 100kNm/m^3 while the measured value was lower by ≈30% at 72kNm/m^3 due to 3D flux leakage effects and twist of the stationary pole piece rotor. The maximum torque transmission capability was measured at 60Nm. This magnetic gear topology represents the foundation for the magnetic geared PDD electrical machine designed and investigated in this industrial research thesis.

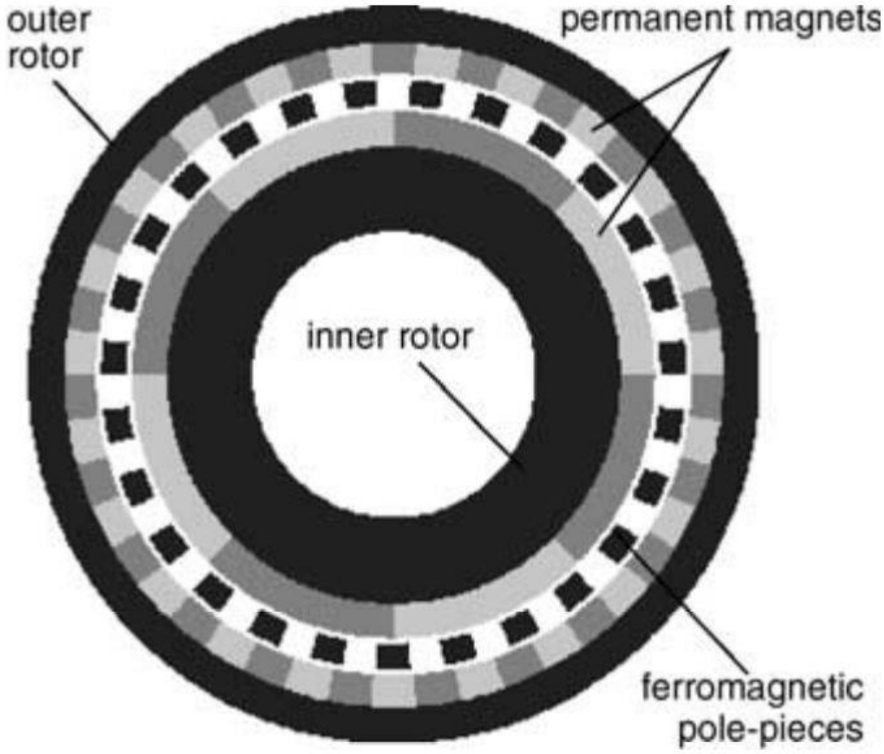

Figure 1.43. High torque density coaxial magnetic gear [69]

The magnetic gear design from [69] and [70] was modified by P.O. Rasmussen in [71]. The surface mount PM arrangement from the high-speed rotor of the magnetic gear was replaced with rectangular buried magnets, as shown in Figure 1.44. This simplified and reduced the cost of manufacture for the high-speed rotor. The outer diameter of the magnetic gear, including the case, was set at 160mm, the total axial length of the prototype was 90mm and the gear ratio was 5.5:1. The 2D FE analysis predicted a pull-out torque of 27Nm with a torque density of 92kNm/m^3. The measured maximum transmission torque was 16Nm with a 40% reduction in torque density. The reduction in torque density was attributed by the authors to inter-magnet flux leakage of the buried high-speed rotor PM, leakage flux in the stationary pole piece structure and low stiffness of the pole piece holder. The magnetic gear FE predicted efficiency was 92% while the measured efficiency was 81%. The poor efficiency is attributed to the losses in the high-speed rotor bearings caused by the leakage flux from the high-speed rotor PMs.

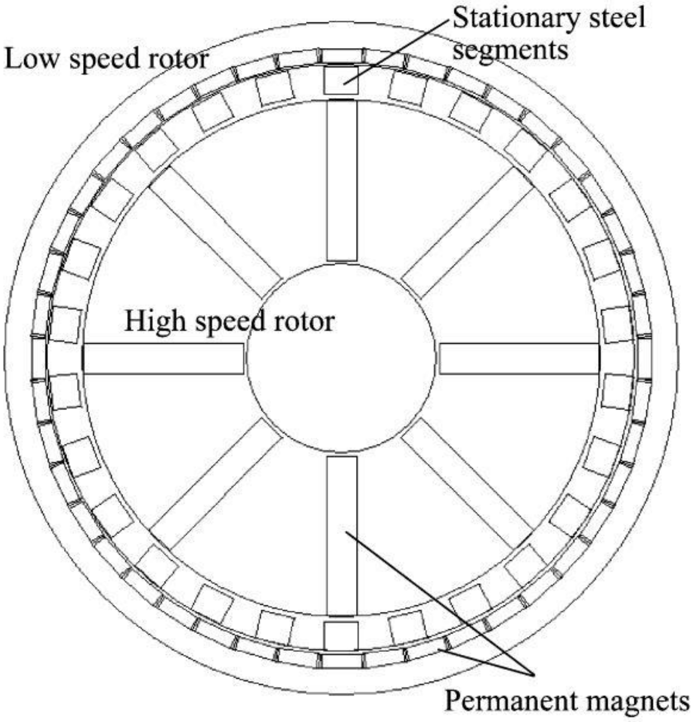

Figure 1.44. Concentric magnetic gear with buried rectangular PMs [71]

Another coaxial magnetic gear was designed and manufactured by L. Shah et al. in [72] for a contra-rotating tidal turbine. The magnetic gear is based on two surface mount radially magnetised permanent magnet rotors separated by a pole piece rotor. The gear outer diameter and axial length were fixed to 120mm and 15mm, respectively. The magnetic gear was designed to operate either with the pole piece rotor or outer magnet array static, achieving a gear ratio of 5.5:1 and 6.5:1, respectively. The 2D FE predicted torque densities for the two operation modes were 62kNm/m^3 and 74kNm/m^3. The authors acknowledged that the measured torque densities were 25% less than the predicted values. The efficiency of the magnetic gear was measured between 50-75% based on the operating speed and output torque.

A comparison between radially and Halbach magnetised magnetic gears was conducted in 2009 by L. Jian et al. in [73]. The outer diameters and axial length for both gears was set to 214mm and 40mm, respectively. The gear ratio was designed at 4.25:1. The magnetic gears shown in Figure 1.45, were designed by the authors using 2D and 3D analysis in order to fully capture the effect of flux leakage on the pull-out torque. It was shown that the radially magnetised magnet gear had a 2D FE pull-out torque of 195.2Nm while the 3D and measured values were 139.7Nm and 137.2Nm, respectively. The Halbach magnetised magnetic gear was found to have a 14% higher pull-out torque with a 2D FE value of 221.1Nm and 3D and measured amplitudes of 159.2Nm and 155.8Nm, respectively. The Halbach magnetic gear was also characterised by a lower output torque ripple and a 25% reduction in the FE predicted iron loss, with 40.4W compared to the 54.2W of loss for the radially magnetised design. The benefits of the Halbach magnetic gear were attributed by the authors to the nearly sinusoidal flux distribution of the Halbach array. In comparison, the radially magnetised gear had high frequency components in the harmonic analysis of the airgap magnetic flux distribution. The measured no load losses for the radially and Halbach magnetised magnetic gear were measured at 196W and 173W, respectively. The extra loss from the measured values was attributed to a poor bearing arrangement which generated excess mechanical losses. The Halbach magnetic gear efficiency was measured at 91-97% while the radially magnetised gear had an efficiency between 88-94% depending on the operating speed and transmitted torque.

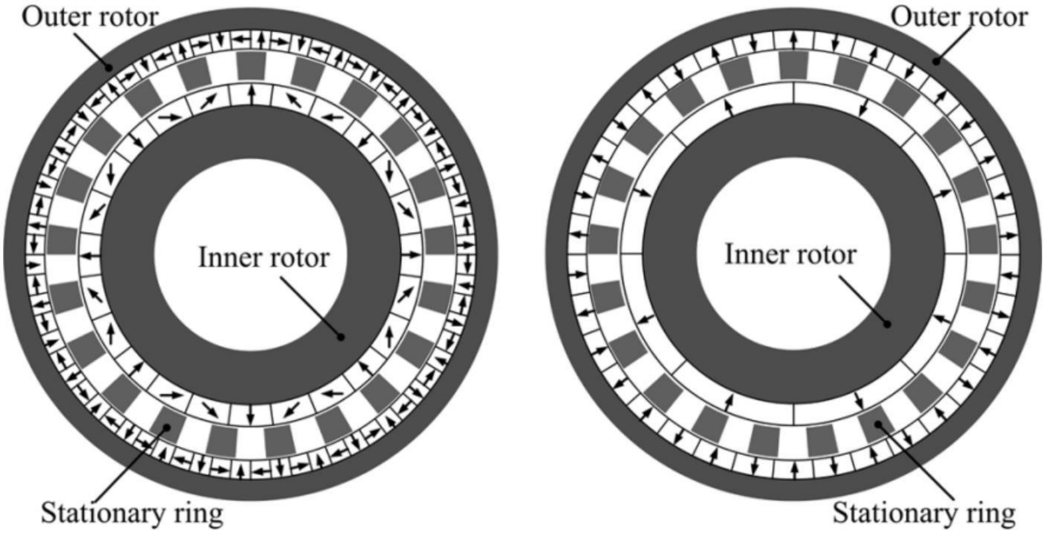

Figure 1.45. Halbach (left) and radially (right) magnetised concentric magnetic gears [73]

N.W. Frank et al. investigated coaxial magnetic gears with conventional surface mount (SPM) and interior permanent magnet (IPM) inner high speed rotors having the same geometrical dimensions and gear ratios [74]. The torque transmission capability of the SPM gear was compared with two IPM high speed rotor designs having a salient design with flux barriers, Figure 1.46, and an IPM type design with integrated flux barriers,

Figure 1.47. The magnetic gear outer diameter was set to 260mm with an active stack length of 50mm. The predicted torque density of the conventional SPM gear was 130 kNm/m^3 while the salient and IPM designs had reduced torque densities of 110kNm/m^3 and 107kNm/m^3, respectively. The torque ripple of the inner high-speed rotor was also predicted to be 1.97% and 2.58% of the rated inner rotor torque, for the salient and IPM designs while the control SPM design had a value of 3.37%. The authors conclude that the torque ripple can be reduced by using buried PM high speed rotor, but with a decrease of the maximum torque transmission capability of the resulting magnetic gear.

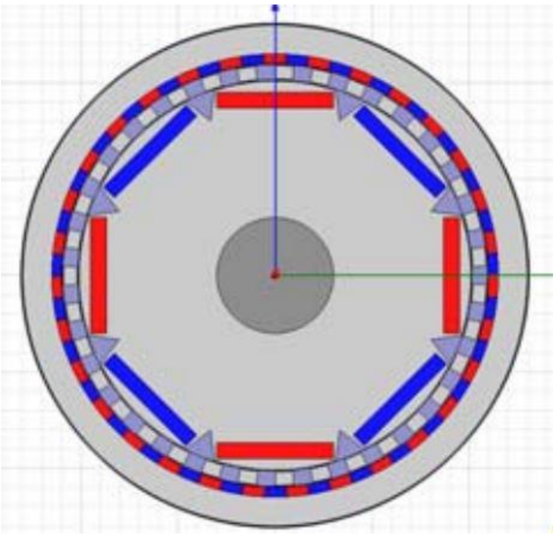

Figure 1.46. Salient high speed rotor with flux barriers [74]

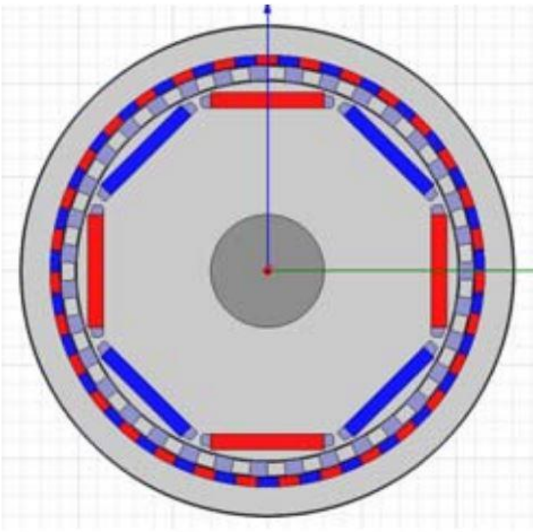

Figure 1.47. IPM high speed rotor with integrated flux barriers [74]

Different pole piece rotor designs, shown in Figure 1.48, have been investigated in [75] by N.W. Frank et al. as part of a concentric magnetic gear. Two designs have been implemented for the high-speed rotor with either a SPM or IPM permanent magnet arrays. The pole piece rotor designs are characterised by equally spaced square pole pieces with thin bridges linking the pole pieces on the inner and outer diameters. This is done in order to increase the stiffness and manufacturability of the pole piece assembly structure.

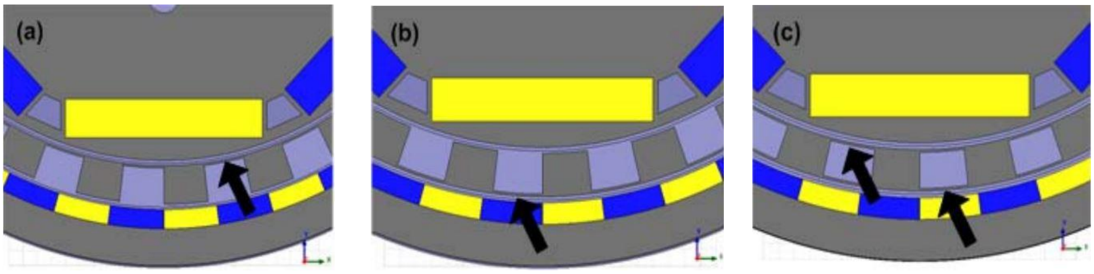

Figure 1.48. IPM inner rotor magnetic gears with (a) inner bridged, (b) outer bridged and (c) inner-outer bridged pole pieces [75]

By holding the pole piece structure stationary, a gear ratio of 5.5:1 was achieved. The gear outer diameter was fixed at 120mm and the axial length was 25mm. The 2D FE predicted torque densities of the different magnetic gear designs are shown in Table 1.1.

Table 1.1. Torque density of magnetic gear designs [75]

Magnetic gear design	**Torque density (kNm/m^3)**
SPM inner rotor with non-bridged pole pieces	115.5
IPM inner rotor with non-bridged pole pieces	86.6
IPM inner rotor with inner bridged pole pieces	85.2
IPM inner rotor with outer bridged pole pieces	68.0
IPM inner rotor with inner and outer bridged pole pieces	66.7

It can be observed that the magnetic gear having the SPM rotor with a non-bridged pole piece structure exhibits the highest torque density. It is also shown that the IPM design without pole pieces bridges and the design having inner bridged pole pieces have a similar torque density. However, the outer and outer and inner bridged pole piece structures have the lowest torque densities with a 42% reduction when compared to the conventional SPM design. The authors concluded that bridged pole pieces represent an option to increase the stiffness of the pole piece assembly structure, but reduce the maximum stall torque of the magnetic gear.

A novel design for a concentric, high gear ratio magnetic gear was presented by Y. Man et al. in [76]. The magnetic gear shown in Figure 1.49, has a ratio of 50:1, and employs an inner permanent magnet rotor with surface mount radially magnetised PMs. The pole piece rotor has equally spaced pole pieces with a comb tooth structure on the outer diameter. The ferromagnetic stator has a similar small teeth arrangement on the inner diameter. The main advantages of this magnetic gear design are the high gear ratio and reduced PM mass. However, the torque density of the design cannot be assessed from [76], since the authors do not present any simulation data on the torque transmission capability of the proposed magnetic gear.

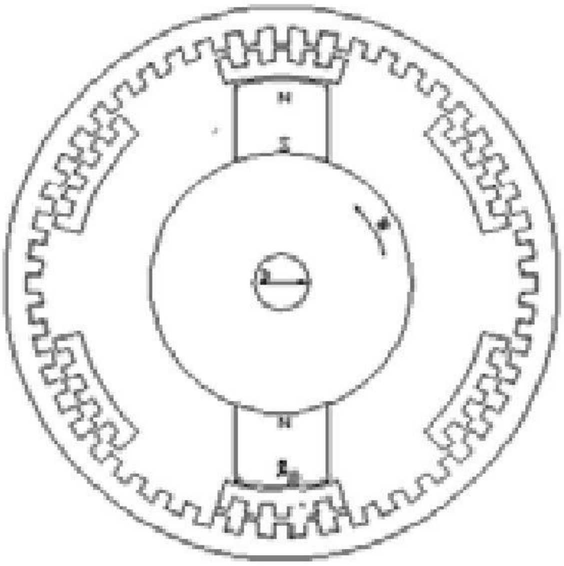

Figure 1.49. Concept of high gear ratio magnetic gear [76]

A novel magnetic gear topology was presented by L. Yong et al. in [77]. The input high speed rotor and output low speed rotor have different pole pair numbers, but the same outer diameter. The two rotors are displaced axially and surrounded on the outer diameter by the static pole piece structure, as shown in Figure 1.50. The input and output rotors are magnetically coupled axially due to the magnetic field which is transmitted axially through the pole pieces. The gear ratio of the prototype was set at 6.5:1. The 3D FE pull-out torque was predicted at 7.1Nm with 6Nm measured amplitude. Although this topology does simplify the construction of the magnetic gear when compared to a coaxial design, the torque density is very low at only 8kNm/m^3.

K.K. Uppalapati et al. present in [78] a coaxial magnetic gear with flux focusing ferrite magnet arrays, Figure 1.51. The inner high-speed rotor consists of rectangular ferrite magnets arranged in a flux focussing spoke-type array, and represents the input rotor of the magnetic gear. In this particular design the output rotor is the pole piece rotor which consists of equally spaced ferromagnetic pole pieces. The stator is represented by the outer spoke-type flux focusing ferrite magnet array.

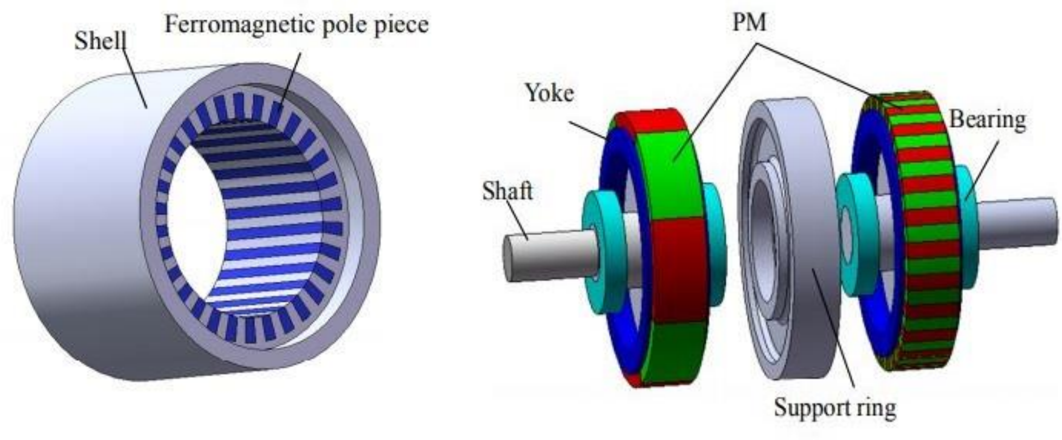

Figure 1.50. Novel axially displaced magnetic gear topology [77]

The ferrite magnet used, Hitachi NMF-12F, had a magnetic remanence field of 0.46 T. The gear ratio was set to 4.25:1. The inner and outer magnet arrays and steel pole pieces were optimised in 2D FE to increase the maximum torque transmission capability of the magnetic gear. An impressive predicted value of 65.5 kNm/m^3 was obtained.

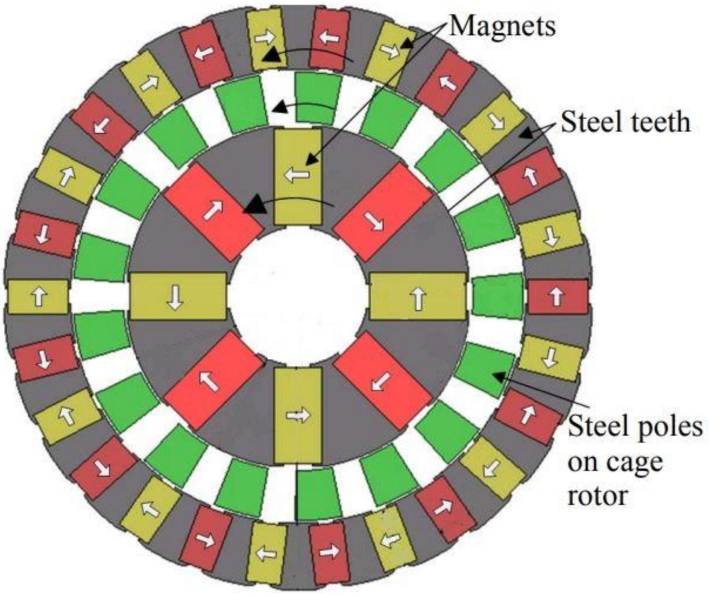

Figure 1.51. Coaxial flux focusing magnetic gear topology [78]

The magnetic gear designed in [78] was manufactured in two variants and tested in [79]. The first variant had both magnet arrays manufactured from ferrite magnets while the second variant had the inner PM array made from N40H-NdFeB permanent magnet and the outer PM array from Ferrite magnet. The Ferrite magnetic gear had a measured pull-out torque of 24Nm, resulting in a torque density of 33kNm/m^3. This 50% reduction from the design value was attributed by the authors to discrepancies in the ferrite magnet and steel magnetic properties. In contrast the hybrid flux focusing magnetic gear had a 2D FE predicted and measured pull-out torque of 61Nm and 48Nm, respectively. This translated into a measured torque density of 66.3kNm/m^3. The efficiency of both gears was found to decrease with pole piece rotor output speed, from 98% at 10 rpm down to 94% at 100rpm. The drop in efficiency with the increase of output speed was related to large eddy currents of the ferromagnetic pole piece rotor.

K.K. Uppalapati et al. presented in [80] another design and implementation of the flux focusing magnetic gear with high torque density characteristic. The magnetic gear was designed from the topology presented in [78], [79] by doubling the number of pole pairs of each rotor and keeping the gear ratio to 4.25:1. The outer diameter of the gear was set to 220mm while the axial length was fixed at 75mm. Full Ferrite and NdFeB designs were optimised in 2D FE for maximum torque density with values of 84.4kNm/m^3 and 244.4kNm/m^3, respectively. The efficiency for both gears was similar and decreased with output speed from 98.5% at 10RPM to 93% at 100RPM. It was found that the predicted efficiency of the Ferrite gear was higher than the NdFeB variant by 1% on average throughout the speed range. The manufactured NdFeB gear had a pull-out torque of 731Nm and a torque density of 238.7 kNm/m^3. The magnetic gear also showed a low torque ripple on the inner and output rotor with measured values of 2.0 Nm and 1.6Nm, respectively.

The coaxial concentric radial magnetic gears presented in [69] and [70] are capable of achieving high torque densities (>100kNm/m^3) comparable to mechanical gears and high transmission efficiency. However, it was acknowledged in [81] that using the concentric magnetic gear for a gear ratio higher than 20:1 would result in a reduction in the achievable torque density.

J. Rens at al. propose a novel harmonic magnetic gear in [81] and [82] which is capable of high gear ratios and torque density. This type of magnetic gear operates based on a sinusoidal variation of the airgap length with time between two PM arrays. The first PM array is mounted on a flexible low speed rotor, as shown in Figure 1.52. This represents the output rotor of the harmonic magnetic gear. The other magnet array is mounted on the inner diameter of a cylindrical outer stator. The wave generator of the harmonic gear is represented by an oval inner high-speed rotor which rotates independently to the low speed rotor due to a sliding contact interface. This inner rotor deforms the flexible low speed rotor and creates a sinusoidal variable airgap length between the low speed rotor and stator. The variable airgap modulates both magnetic fields produced by each magnet array and enables the asynchronous fundamental space harmonic field given by one magnet array to have the same pole pair number as the neighbouring PM array. The authors of [82] present several harmonic gear designs capable of a maximum torque density of 150 kNm/m^3.

The major drawbacks of harmonic magnetic gears are related to the manufacturability and reliability of the flexible low speed rotor and the required flexible connection between the output shaft of the gear and load. A solution to replace the flexible rotor is given by a harmonic gear with one sinusoidal airgap cycle per rotation. In this novel topology, Figure 1.53, the flexible low speed rotor is replaced with a cylindrical conventional surface mount PM rotor.

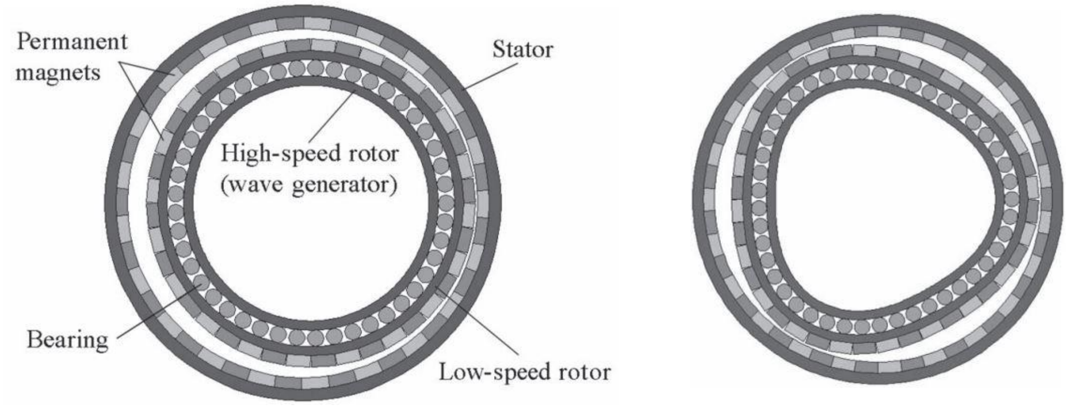

Figure 1.52. Harmonic magnetic gear [81]

An excentric high speed rotor is used to impose an excentric motion on the low speed rotor. This rotation pattern creates a sinusoidal varying airgap profile between the low speed output rotor and stator. The drawbacks for this topology are related to the high radial forces on the bearings, acoustic noise and vibrations, and the need for a flexible coupling between the output rotor and load.

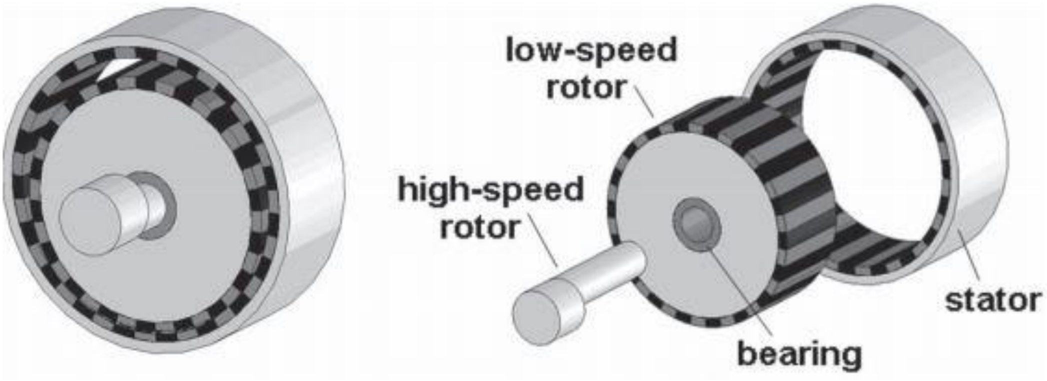

Figure 1.53. Harmonic magnetic gear with rigid low speed rotor and eccentric high speed rotor [81]-[82]

The authors suggest a two-stage harmonic magnetic gear, Figure 1.54, in order to remove the need for a flexible output coupling. The first stage operates as the harmonic gear described above, with a flexible low speed rotor shaft. In the second stage of the gear, the stator is allowed to rotate and represents the output rotor of the two-stage harmonic gear.

The flexible intermediate rotors of each stage are part of the same mechanical assembly, but have a different number of pole pairs.

During operation, the rotation imposed on the input high speed rotor would create a geared rotation of the flexible rotor of the first stage. Thus, the flexible rotor of the second stage would rotate and generate a geared rotation of the output rotor of the gear. Since the output rotor of the two-stage harmonic gear is cylindrical, a torsionally rigid coupling can be used to connect it to the load. The authors present a prototype of a two-stage harmonic gear with a 360:1 gear ratio capable of a torque density of 75 kNm/m^3.

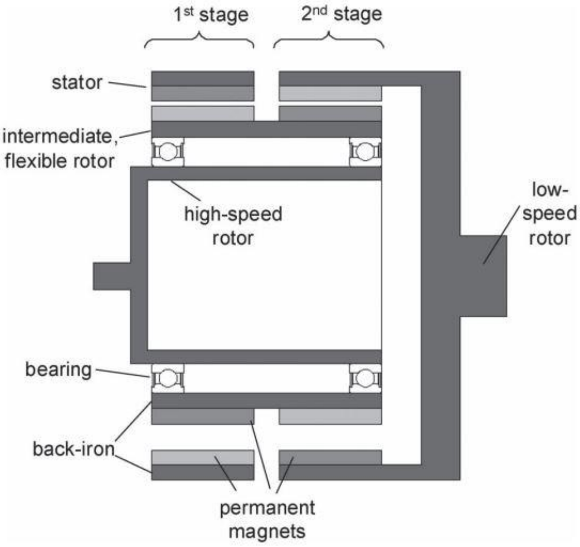

Figure 1.54. Rotor layout of 2 stage harmonic gear [81]-[82]

1.6.2 Magnetic gears – Principle of operation

The principle of operation of coaxial magnetic gears is based on the modulation of the magnetic fields produced by the inner high-speed rotor (HSR) and stator PM arrays, by the ferromagnetic pole pieces of the pole piece output rotor (PPR) which is connected to the load. The base magnetic gear topology researched and implemented in this industrial research project is shown in Figure 1.55. The inner PM arrays represents the input HSR while the outer PM arrays is stationary and fixed on to the bore of the stator. The ferromagnetic pole pieces form the output PPR and act to modulate both magnetic fields such that the resultant modulated field distribution of the HSR in the outer airgap has an asynchronous space harmonic component with the same number of poles as the stator PM array. The same modulation occurs for the PM field distribution of the stator PMs, which create in the inner airgap an asynchronous space harmonic with the same number of poles as the fundamental component of the HSR magnetic field.

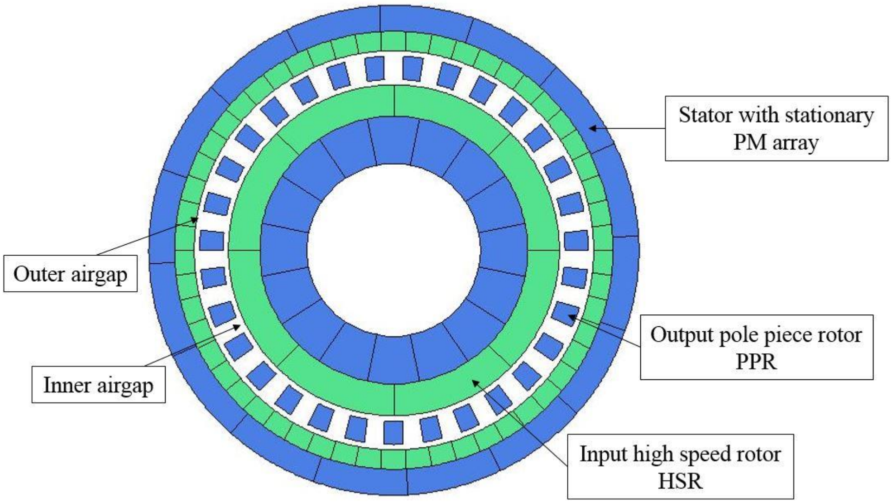

Figure 1.55. Magnetic gear topology

The equations which describe the radial and tangential magnetic flux density distribution in the airgaps of the magnetic gear, due to the modulation of the PPR are presented and discussed in [69], [81], [83].

The magnetic gear can be operated by keeping either the PPR or stator stationary. For the case of a stationary PPR, the input shaft is connected to the HSR and the output is represented by the rotating outer magnet array, with the gear ratio being expressed as:

$$G_r = -\frac{p_l}{p_h} = \frac{p_h - N_{pp}}{p_h} \tag{1.1}$$

where p_h, p_l and N_{pp} are the number of pole pairs on the HSR and stator, and number of ferromagnetic pole piece, respectively.

In the case of a stationary stator and outer PM array, as the magnetic gear topology implemented in this research project, the gear ratio, G_r, between the input HSR and output PPR is given by:

$$G_r = \frac{N_{pp}}{p_h} \tag{1.2}$$

In order to illustrate the modulation of the HSR and stator PM magnetic field by the PPR, a 7.75:1 magnetic gear with 4 pole pairs on the HSR, 27 pole pairs on the stator and 31 ferromagnetic pole pieces was modelled using 2D FE electromagnetic software. Table 1.2 presents the geometric and material characteristics of the modelled magnetic gear.

Table 1.2. Parameters of 7.75:1 magnetic gear

Parameter	**Value**
Stator outer diameter	63.0 mm
Stator back iron radial thickness	3.3 mm
Stator magnet radial thickness	2.5 mm
PPR outer diameter	50.0 mm
Pole piece radial thickness	3.0 mm
HSR outer diameter	42.6 mm
HSR PM radial thickness	4.0 mm
HSR hub radial thickness	6.1 mm
Inner airgap length	0.7 mm
Outer airgap length	0.7 mm
Active axial length	50.0 mm
PM remanence at 20°C	1.10 T

Figure 1.56 shows the variation of the radial flux density component in the outer airgap adjacent to the outer stator PMs created by the 4 pole pair high speed PM rotor without

and with the modulating pole pieces. Figure 1.57 shows the harmonic content of the radial flux density waveform created by the HSR without and with the addition of the PPR. It can be observed that without the modulating pole pieces, the HSR produces a sinusoidal magnetic flux distribution with a 4 pole pair fundamental component in the outer airgap. The addition of PPR increases the 4 pole pair fundamental component of the HSR magnetic field due to the low reluctance path created by the 31 ferromagnetic pole pieces, but also creates asynchronous space harmonic in the outer airgap. The largest asynchronous harmonic, in the outer airgap adjacent to the stator PMs, is the 27-pole pair space harmonic which magnetically couples with the 27 pole pairs of the stationary stator magnet array.

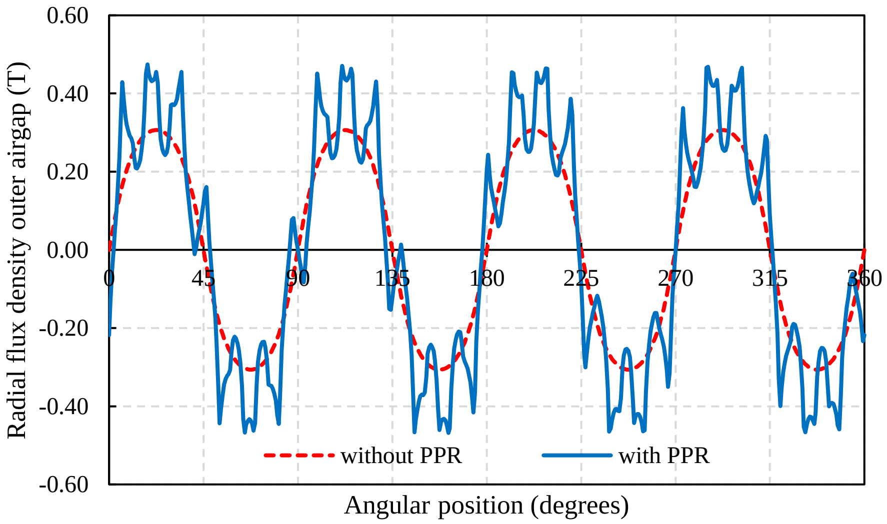

Figure 1.56. Variation of the radial flux density in the outer airgap due to the HSR PM

Similarly, Figure 1.58 shows the tangential component of the flux density in the outer airgap due to the HSR without and with the addition of the modulating pole pieces. Figure 1.59 shows the harmonic spectrum of the tangential magnetic flux distribution created by the HSR in the outer airgap adjacent to the stator magnets. It can be observed that similarly to the radial field component, the PPR modulation of the tangential field component results in a slightly increased synchronous 4 pole pair fundamental and 27 pole pair asynchronous harmonic which couples to the 27 pole pairs of the outer magnet array.

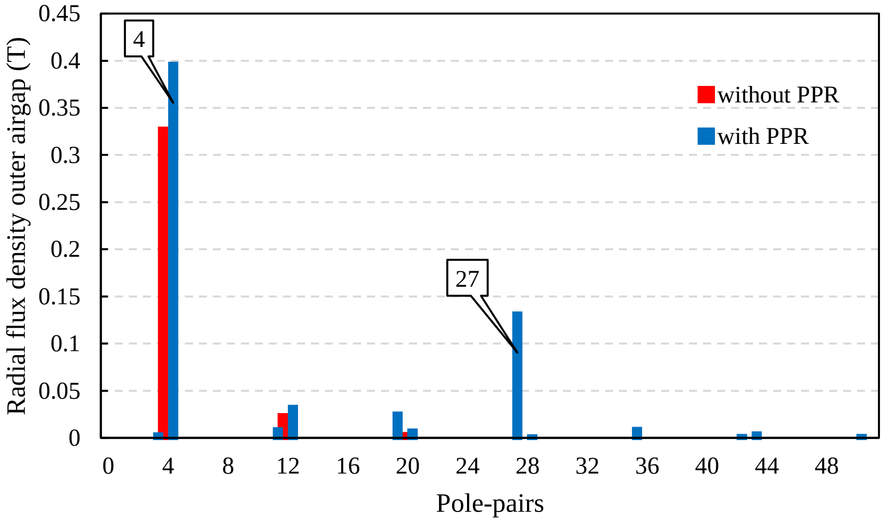

Figure 1.57. Harmonic spectrum of the radial flux density in the outer airgap due to the HSR PM

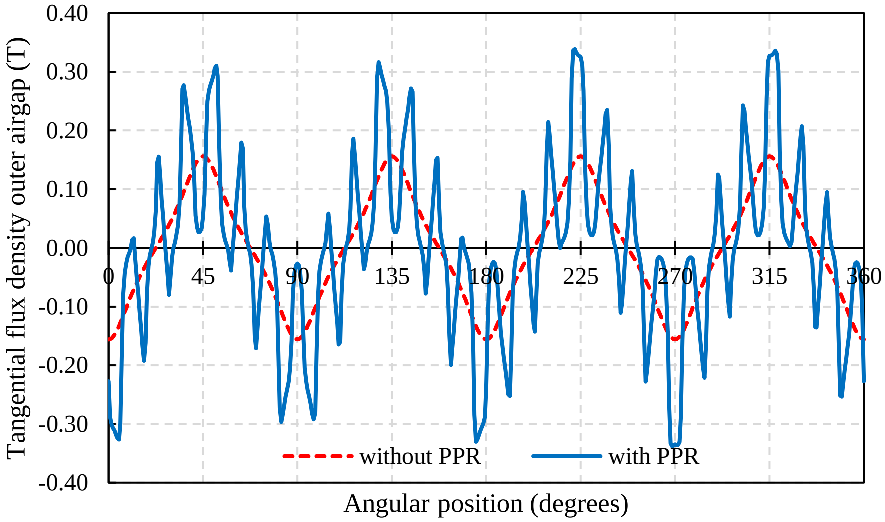

Figure 1.58. Variation of the tangential flux density in the outer airgap due to the HSR PM

The same modulation process is true with respect to the stator PM magnetic field. Figure 1.60 shows the radial flux distribution in the inner airgap adjacent to the HSR created by the stator PM array without and with the modulating ferromagnetic pole pieces. Figure 1.61 shows the harmonic spectrum of the radial flux density. It can be observed that without the pole pieces, the stator magnet array creates in the inner airgap a magnetic field distribution having a 27-pole pair harmonic. The addition of the modulating PPR, results in an asynchronous 4 pole pair space harmonic in the inner airgap which couples with the 4-pole pair fundamental components of the HSR PM field.

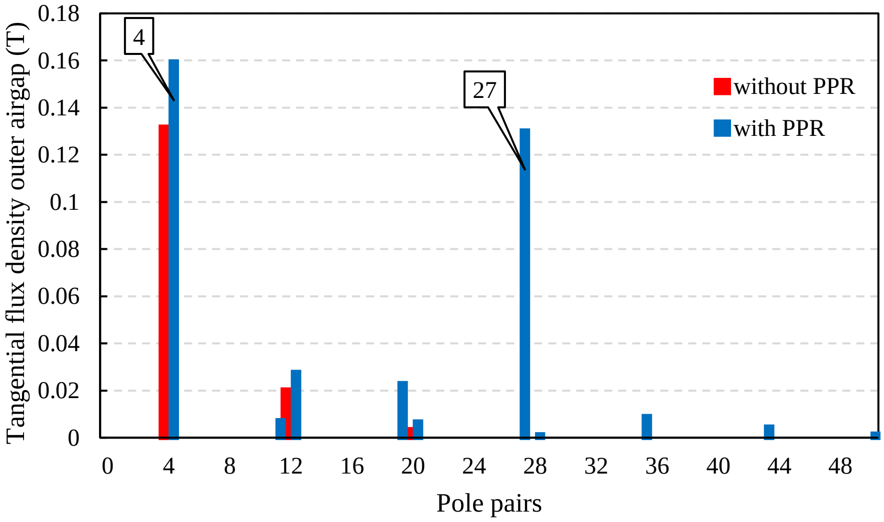

Figure 1.59. Harmonic spectrum of tangential airgap flux density in the outer airgap due to the HSR PM

The tangential component of the flux density created the by stator magnets in the inner airgap is shown in Figure 1.62 with its harmonic spectrum being illustrated in Figure 1.63. It can be observed that by introducing the 31 ferromagnetic pole pieces, the tangential flux distribution of the stator PMs in the inner airgap has apart from the 27 pole pair fundamental, a 4 pole pair asynchronous space harmonic which magnetically couples to the HSR fundamental in order to transmit torque.

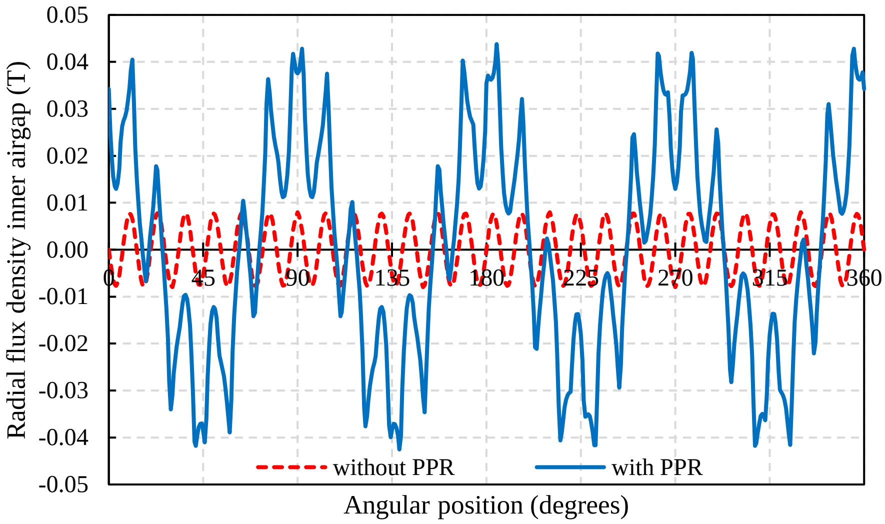

Figure 1.60. Variation of the radial flux density in the inner airgap due to the stator PM array

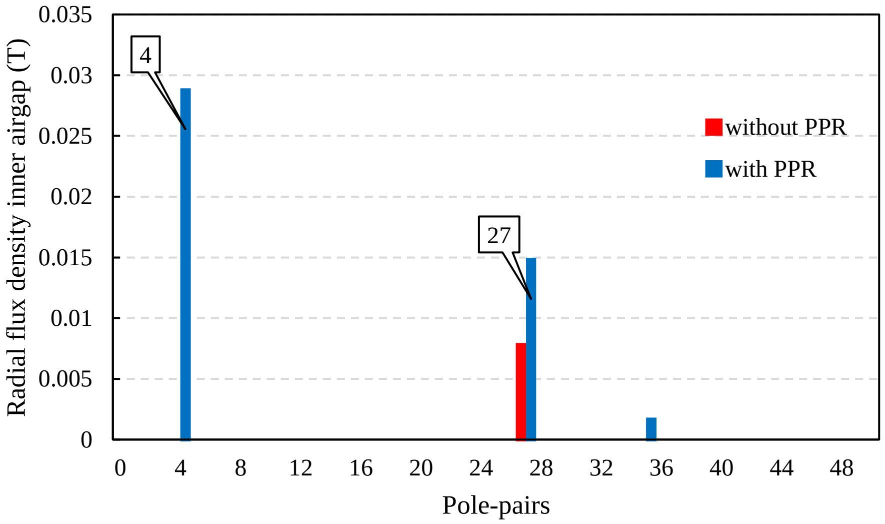

Figure 1.61. Harmonic spectrum of the radial flux density in the inner airgap due to the stator PM array

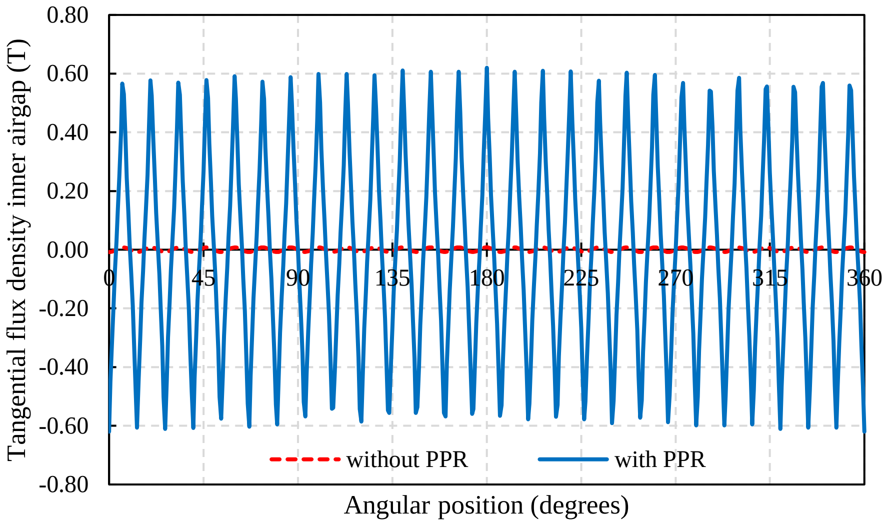

Figure 1.62. Variation of the tangential flux density in the inner airgap due to the stator PM array

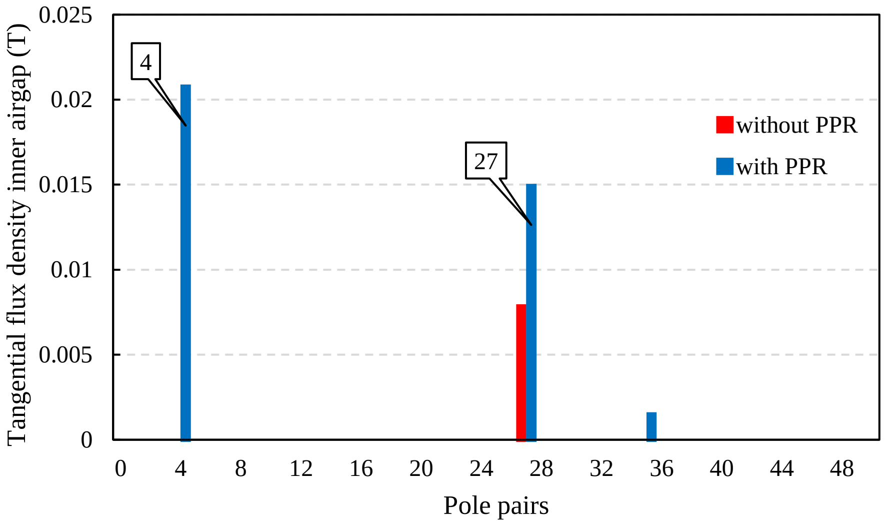

Figure 1.63. Harmonic spectrum of the tangential flux density in the inner airgap due to the stator PM array

In order to illustrate the modulation process of the PPR for a different pole pair number, an additional 7:1 magnetic gear was modelled having a 3 pole pair HSR, 21 pole pieces and 18 pole pairs for the stator magnet array. The design was based on the same geometric dimensions as presented in Table 1.2.

Figure 1.64 and 1.65 show that the 3 pole pair HSR of the 7:1 magnetic gear produces with the addiction of the 21 pole pieces, an asynchronous harmonic component in the outer airgap having the same number of pole pairs as the stationary stator PM array.

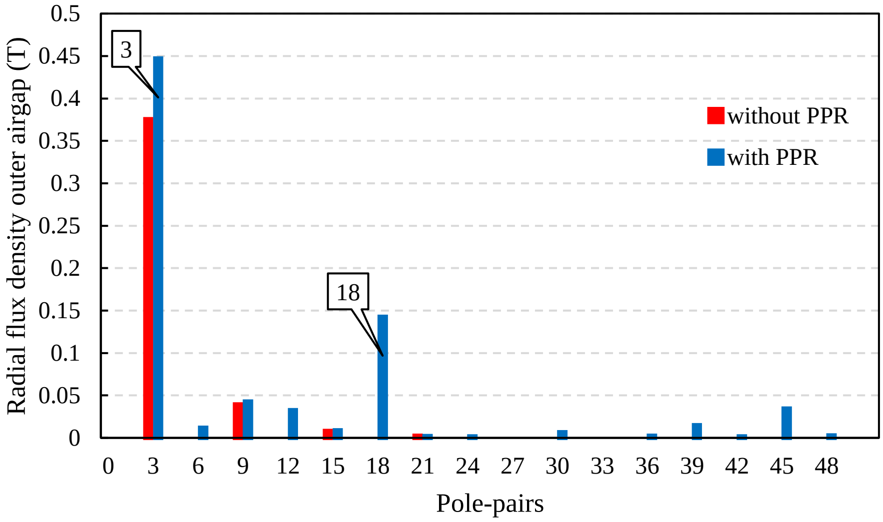

Figure 1.64. Harmonic spectrum of radial flux density in the outer airgap due to the HSR PM

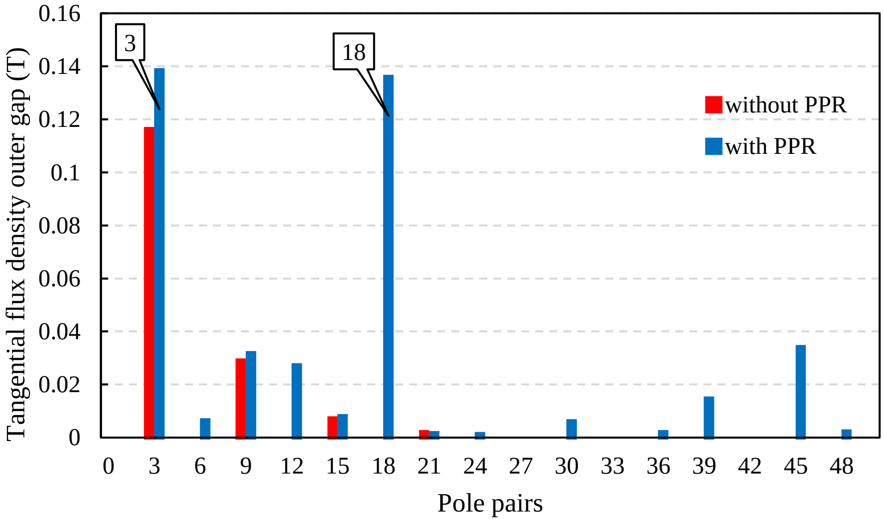

Figure 1.65. Harmonic spectrum of the tangential flux density in the outer airgap due to the HSR PM

Similarly, from Figure 1.66 and 1.67, it can be seen that the 18 pole pair magnetic field produced by the stator magnets is modulated by the PPR, such that a 3 pole pair asynchronous harmonic is created in the inner airgap adjacent to the 3 pole pair HSR.

The magnetic gear is characterised by a maximum torque transmission capability, T_m given by the load angle between the HSR and PPR, such that:

$$T_{PPR} = T_m \cdot \sin(\theta_e) \tag{1.3}$$

where T_{PPR} is the torque on the PPR and θ_e is the relative angular displacement between the HSR and PPR in electrical degrees. The angular displacement can be defined based on the absolute displacement angles of the HSR and PPR, θ_h and θ_{ppr} such that:

$$\theta_e = p_h\theta_h - N_{pp}\theta_{ppr} \tag{1.4}$$

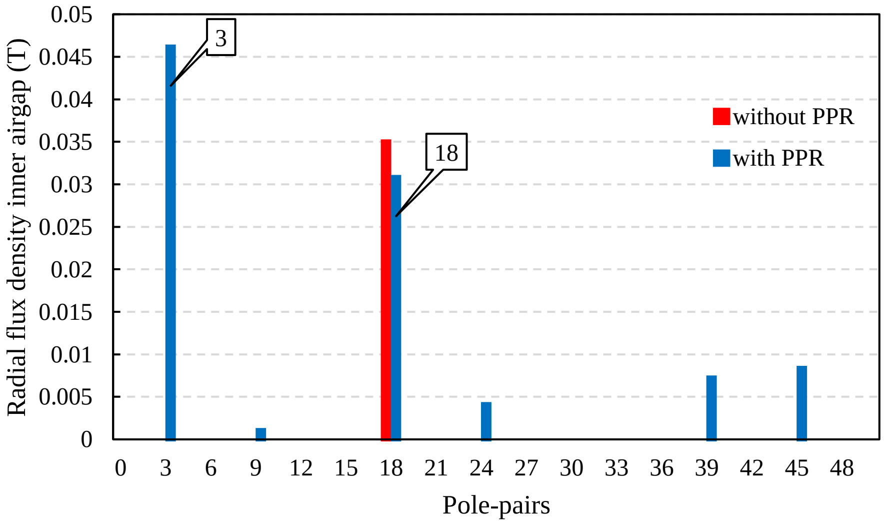

Figure 1.66. Harmonic spectrum of the radial flux density in the inner airgap due to the stator PM array

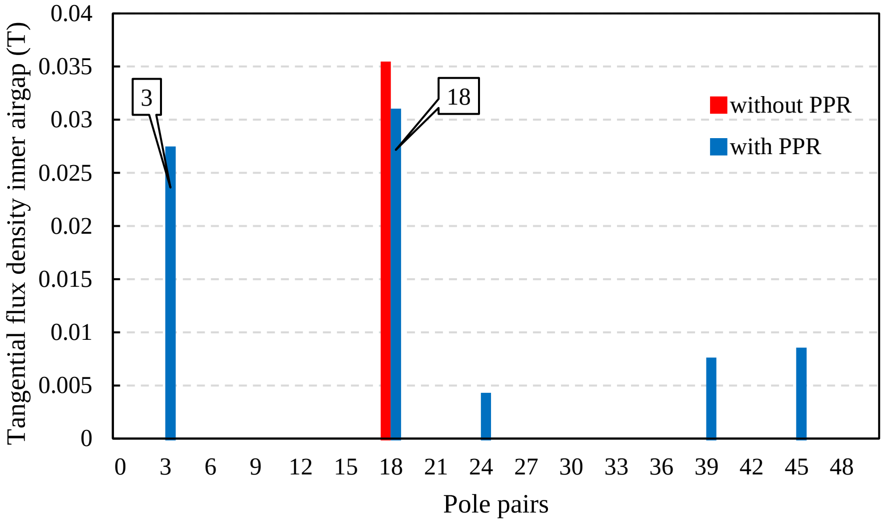

Figure 1.67. Harmonic spectrum of tangential flux density in the inner airgap due to the stator PM array

The torque transmission characteristic of the 7.75:1 magnetic gear is shown in Figure 1.68. It can be observed that both the HSR and PPR torque follow a sinusoidal profile with the ratio between them being equal to the gear ratio. The maximum value of the HSR and PPR torque represents the maximum torque transmission capability of the magnetic gear.

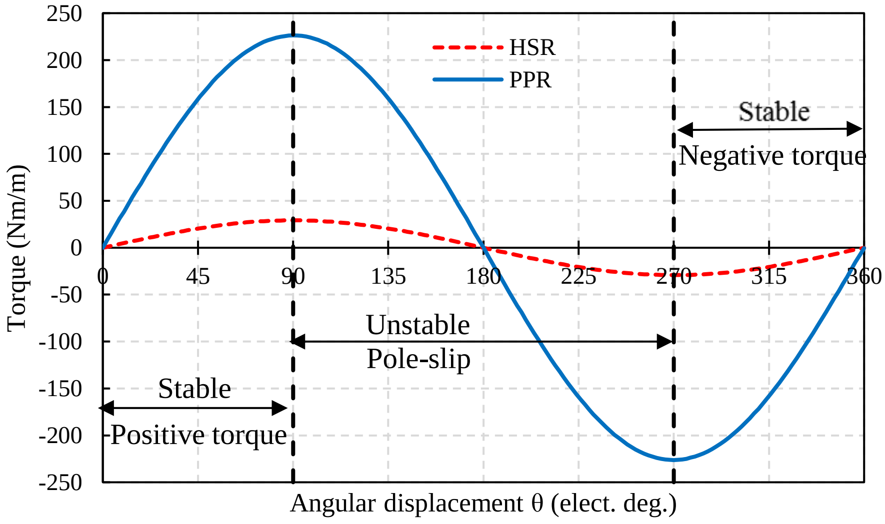

Figure 1.68. Magnetic gear torque transmission capability

The torque transmission profile can be divided in two operating regions. The magnetic gear would operate in the 'Stable' region as long as the load torque applied by the load to the PPR is lower than the maximum torque transmission capability of the gear. Figure 1.69 shows the radial magnetic field distribution in the inner airgap due to the HSR PMs and the modulated field of the stator PMs at zero angular displacement between the HSR and PPR. It can be observed that the flux density distribution of the HSR is 180° out of phase when compared to the modulated field of the stator PMs. In this position the magnetic gear is in a 'Stable', un-loaded state.

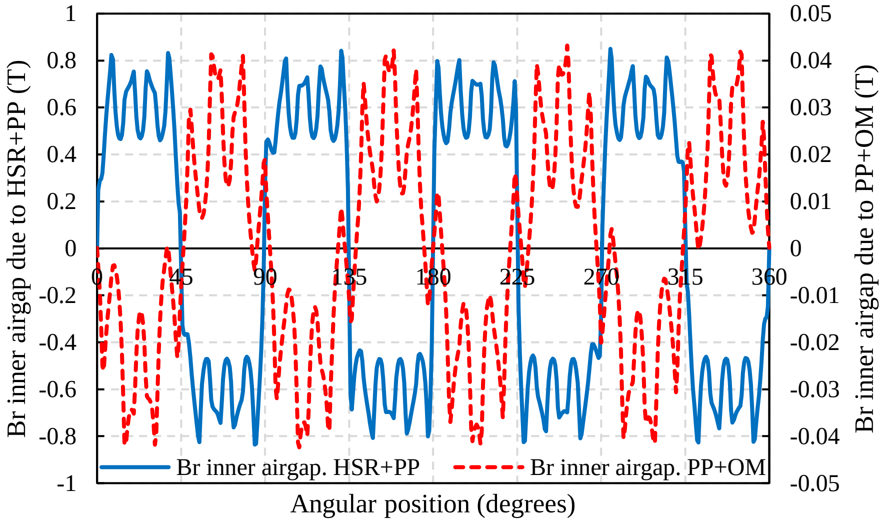

Figure 1.69. Radial magnetic field in the inner airgap at $\theta_e=0^o$

As the load on the PPR is increased, the load angle between the HSR and PPR increases. At $\theta_e = 90^o$ the magnetic gear has reached it maximum torque transmission capability. Figure 1.70 shows the radial magnetic field distribution in the inner airgap due to the HSR PMs and the modulated field of the stator PMs at the peak torque transmission position. It can be observed that HSR PM field and modulated stator PM field are 22.5° or half of HSR PM pole pitch out of phase.

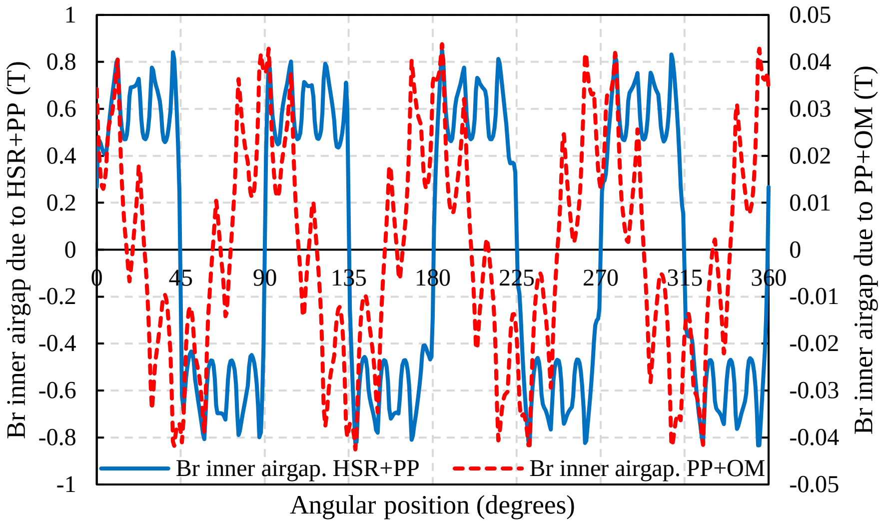

Figure 1.70. Radial magnetic field in the inner airgap at $\theta_e=90^o$

If the load torque is further increased past the maximum torque transmission capability, the magnetic gear would be unable to transmit the required torque and would pole slip, disengaging normal operation. This is marked in Figure 1.68 as the ‘Unstable – Pole slip region’ and represents the passive torque fuse behaviour of the magnetic gear where the transmitted torque of the gear is decreased as the load angle, θ_e, is increased. During pole-slipping, the input HSR would be driven by the input prime mover and would rotate independently of the PPR. Thus, the magnetic gear would go through several sinusoidal torque profiles until the excess output torque is removed from the PPR output shaft.

Figure 1.71 shows the HSR and modulated stator PM fields in the inner airgap when $\theta_e = 180^0$. It can be observed that this is not a stable zero torque position for the magnetic gear since the HSR and modulated stator PM fields are in phase and would repel each other.

Thus, if the excess load torque is removed from the output PPR, the gear would go back to a ‘Stable’ loaded position (i.e $0^o < \theta_e \leq 90^o or\ 270^o \leq \theta_e < 360^o$) depending on the direction of the load torque and re-engage normal operation. If the output torque is completely removed (i.e $T_{PPR} = 0\ Nm$), the magnetic gear would only be able to settle into a ‘Stable’ unloaded position at $\theta_e = 0^o$ or $\theta_e = 360^0$ and not $\theta_e = 180^0$.

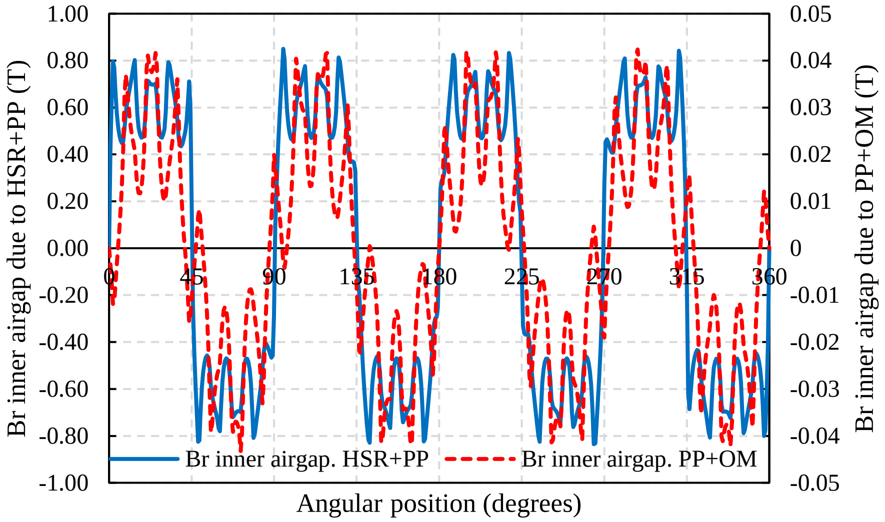

Figure 1.71. Radial magnetic field in the inner airgap at θ_e=180°

1.6.3 Magnetically geared electrical machine – Pseudo Direct Drive

There are several ways in which the benefits of the magnetic gear transmission can be incorporated in an electrical machine drive. The simplest arrangement would be to mechanically couple the output of the electrical machine to the input high-speed rotor of the magnetic gear. This configuration is characterised by a high active volume, and utilises a large amount of permanent magnet material for the input high-speed rotor of the magnetic gear and rotor of the electrical machine. The authors of [84] have proposed an improved electrical machine topology, shown in Figure 1.72, where the magnetic gear is mechanically integrated and magnetically coupled with a brushless PM electrical machine, creating the Pseudo Direct Drive (PDD).

This PDD topology is characterised by two airgaps, between the high HSR and PPR, and between the PPR and stator assembly. The HSR and PPR represent the input and output rotors of the PDD magnetic gear element. For the topology shown in Figure 1.72, the 4 pole pair magnetic flux density waveform of the HSR is modulated, by the 31 ferromagnetic pole pieces, to produce a 27 pole pair asynchronous space harmonic field, in the outer airgap, which couples to the stationary stator PM array.

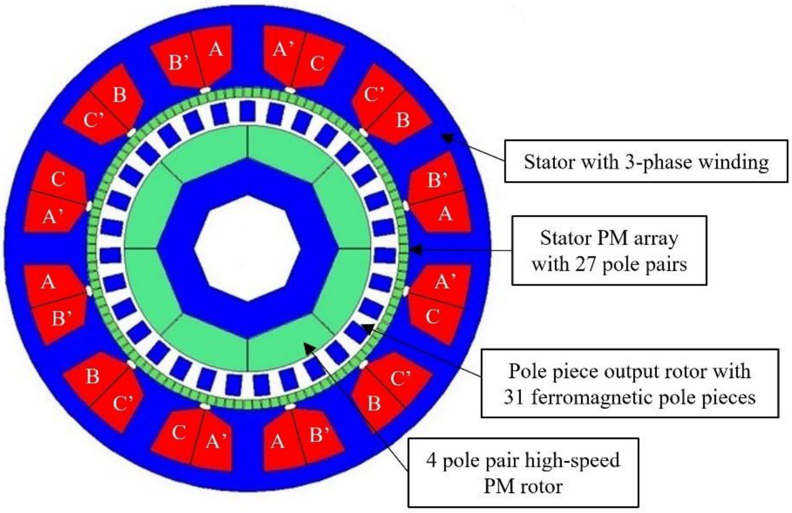

Figure 1.72. Pseudo Direct Drive electrical machine topology

The same is true for the 27 pole pair magnetic flux density of the stator PM array which is modulated by the PPR to produce a 4 pole pair asynchronous space harmonic field, in the inner airgap, which couples to the HSR. As a result, torque is transmitted from the HSR to the PPR, with a gear ratio given by:

$$G_r = \frac{N_{pp}}{p_h} \tag{1.5}$$

The electromagnetic torque of the PDD, T_e, or input torque of the magnetic gear element is produced by the synchronous coupling of the HSR fundamental magnetic field component with the fundamental component of the stator MMF. By considering that the HSR of the PDD is a non-salient structure, the electromagnetic torque can be expressed as a function of the d-axis PM flux linkage, ψ_{PM}, and q-axis current, I_q, such that:

$$T_e = \frac{3}{2} p_h \psi_{PM} I_q \tag{1.6}$$

The magnetically transmitted torque to the output rotor, T_{PPR}, is given by:

$$T_{PPR} = G_r \left(T_e - J_h \frac{d^2\theta_h}{dt^2} \right) = G_r \left(\frac{3}{2} p_h \psi_{PM} I_q - J_h \frac{d^2\theta_h}{dt^2} \right) \tag{1.7}$$

where J_h and θ_h are the inertia and angular position of the HSR, respectively.

The equations which govern the motion of the PDD rotors have been presented in [85], [86] and are given by:

$$J_h \frac{d^2\theta_h}{dt^2} = T_e - \frac{T_m}{G_r} \sin(\theta_e) - B_h \omega_h - K_d (p_h \omega_h - N_{pp} \omega_{ppr}) \tag{1.8}$$

$$J_{PPR} \frac{d^2\theta_{ppr}}{dt^2} = T_m \cdot \sin(\theta_e) - T_L - B_{PPR} \omega_{ppr} - K_d G_r (p_h \omega_h - N_{pp} \omega_{ppr}) \tag{1.9}$$

where ω_h, J_h, B_h represent the angular velocity, inertia and viscous damping of the HSR while $\omega_{ppr}, J_{PPR}, B_{PPR}$ are the angular velocity, combined inertia and viscous damping of the PPR and load. The number of pole pairs of the HSR and the number of ferromagnetic pole pieces are represented by p_h, N_{pp}. The angular displacement of the HSR and PPR are represented by θ_h and θ_{ppr}. The load torque applied to the output shaft of the PDD is given by T_L, while the maximum torque that the magnetic gear element can transmit is represented by T_m. The factor K_d represent the damping associated with the electromagnetic iron losses of the PDD electrical machine.

For the magnetic gear element of the PDD, the electromagnetic torque is transmitted from the input HSR to the output PPR through an equivalent magnetic spring, for which the stiffness, K_{es}, is given as a function of the magnetic load angle between the HSR and PPR, such that:

$$K_{es} = T_m cos(\theta_e) \tag{1.10}$$

It is reported in [87] that the magnetic gear operates in its stable torque transmission region shown in Figure 1.68, when the stiffness K_{es} is positive and the referred angle, θ_e, is within the range given by:

$$2\pi n - \frac{\pi}{2} > \theta_e > 2\pi n + \frac{\pi}{2} \tag{1.11}$$

where n is an integer number.

It has to be considered that due to the embedded magnetic geared transmission, which has a limited torque transmission capability, the PDD motor cannot be overloaded to produce a higher torque than the pull-out torque rating of the magnetic gear element.

Since its introduction in 2008, the PDD has received increasing attention in research and literature. The control and pull-out prevention and recovery have been extensively investigated and implemented by the authors of [85]–[90]. Due to its advantages over conventional direct drive PM electrical machines, such as high torque density, improved efficiency, high power factor, reduced cooling requirements, low cogging torque and reduced torsional vibrations of the output shaft, the PDD was proposed as a propulsion motor for naval application in [91]. In wind power generation, the PDD can be used to remove the complex mechanical gear states from the drive train and improve reliability and cost. The analytical modelling and optimisation of PDDs for wind power application has been presented in [92] and [93], with the scaling of such electrical machines power outputs between 5 - 20MW being investigated in [94]. Efforts have been made in [95]–[97] in order to reduce the amount of PM material utilised and adopt stator winding configurations which can be implemented in high volume manufacturing.

1.7 Fault-tolerant electrical machine design

All safety critical aerospace applications which employ electrical machine to convert electrical to mechanical energy require high system reliability and power density. The main electrical faults with can occur in electrical machine are represented by winding open-circuit and winding short circuit which includes phase to ground, phase to phase, 3-phase symmetrical short circuit and inter-turn short circuit [42]. Several PM electrical machines that have a modular stator and winding design, where each module operates independently from the others, have been proposed in literature [58], [98]–[100]. Such a configuration can be achieved by employing multiphase independent winding configurations [55], where each phase is independently controlled by a H-bridge, or 3-phase multilane configurations, where each 3-phase lane is independently controlled by independent 3-phase drives [101]. This results in a PM machine design with electrical isolation between lanes such that the electromagnetic coupling is reduced and each lane can provide rated power. Magnetic isolation is also required such that the mutual coupling between adjacent phases is reduced and the fault current in one phase will not induce large voltages in the adjacent phases. This is typically achieved by opting for a single layer winding design, such that each slot only contains the conductors of one phase, with any two adjacent phases being separated by a stator tooth, as proposed in [102]–[105]. For such a winding design, thermal and physical isolation between phases is also achieved, since the tooth acts as a solid barrier between adjacent phases, reducing thermal interaction and eliminating the likelihood of phase to phase faults.

For a fault tolerant PM machine, it is also important to limit the amplitude of the winding short circuit current such that the copper loss of the faulted lane is limited to the rated value. Typically, in a fault tolerant PM electrical machine, the amplitude of the short circuit current for a 3-phase symmetrical short circuit is limited to the value of the rated phase current by employing a machine design with 1 p.u. armature d-axis inductance. Such designs are presented in [49], [50], [54], where the authors show the inductive reactance limited short circuit characteristic and corresponding drag torque of the short circuited 3-phase lane.

1.8 Inter-turn short circuit

An inter-turn short circuit fault represents a short circuit between a reduced number of turns from the coil bundle [106]. Compared to the 3-phase symmetrical short circuit fault, where the short circuit current can be limited to the value of the rated current by the 1 p.u. phase inductance, the fault current which results from turn to turn faults is several times higher than the rated machine current. Although inter-turn fault can occur between multiple turns from the total number of turns, N_t , the most severe case is a 1 turn short-circuit. In the case of a shorted turn, the EMF seen by the shorted turn and its phase resistance are reduced by N_t, when compared to the total phase EMF and resistance, while the inductance of the shorted turn is reduced by N_t^2 when compared to the total phase inductance. Thus, the 1 turn short circuit current would be substantially higher than the 1 p.u 3-phase fault current due to the greatly reduced inductance of the shorted turn. In this case the MMF of the shorted turn is creating a flux component which opposes the PM flux linkage. As presented in [42], for a 1p.u. 3-phase fault current design, if the inductive reactance of the shorted turn is greater than its resistance, the fault current in the shorted turn would be N_t times greater than the symmetrical 3-phase short circuit current.

Several stator turn fault detection techniques have been presented in literature. The authors of [107]–[109] based the turn fault detection algorithm on motor current signal analysis. This non-evasive method is based on detecting the second harmonic components in the dq-axis motor currents which are caused by the fault current in the faulted turn. A similar technique is shown in [110], [111] where the second harmonic component of the dq-axis voltages are used to detect stator turn faults during the operation of induction machines. It is reported that such methods can be affected by pre-existing imbalance in the motor drive and stator windings which would cause second harmonic components in the dq-axis current and voltages and trigger false detections. The authors of [112], [113] have presented detection methods where the presence of second harmonic components in the instantaneous active and reactive powers is used to indicate inter-turn faults. It is acknowledged that these methods are not accurate during low speed operation.

In order to limit the high turn to turn short circuit current for a fault tolerant 1 p.u. machine design, assuming this fault is detected quickly, certain remedial actions have been proposed in [114] and [115]. These include turning the inter-turn short circuit into a 3-phase symmetrical short circuit by shorting the machine terminals via the converter switches. In this case, all the shorted turns would equally share the total MMF, reducing the high inter-turn short circuit current to the 1.p.u 3-phase fault current.

The authors in [116] proposed a vertical winding topology in order to limit the change in turn to turn short circuit current with the position in the slot of the shorted turn. It was shown that for a stranded coil topology, the position of the shorted turn within the slot can influence the inductance of the shorted turn and amplitude of the fault current. In comparison, for the vertical winding topology, it was shown that the position within the slot of the shorted turn has a minimal effect on the amplitude of the short circuit current. The amplitude of the short circuit current was reduced by a factor of 2.5 when adopting the vertical winding topology.

A different inter-turn short circuit current minimisation technique was presented in [117], which is based on reducing the flux linkage of the faulty turn in order to reduce the amplitude of the turn to turn short circuit current. It order to achieve this, a current that is equal to the ratio of no-load flux linkage, in the shorted turn, to the mutual inductance, between the healthy and faulty turns, has to be injected in the remaining healthy turns. The phase of the injected current is at 90^o lagging the phase EMF. This was shown to limit the fault current in the shorted turns to 1.42 p .u.

The authors of [118] proposed a spring actuated mechanical shunt which operates in the slot opening and can decouple the rotor PM flux from the stator. Thus, under faulty conditions the magnetic wedge slides in the slot opening and the coupling between the PM flux and stator winding is reduced as the PM flux is now short circuited through the magnetic wedge. Hence, in this condition due to the low flux linkage associated with the shorted turn, the fault current is substantially reduced. The drawbacks of this mechanism are represented by the reliability and size of the mechanical shunt mechanism which can also reduce the copper fill factor. Moreover, due to size restrictions, this mechanism cannot be implemented in small actuator motors such as the proposed fault tolerant PDD. A similar approach was implemented in [119] where an electrical shunt triggered by an auxiliary winding was placed in the slot opening. During normal operation, the auxiliary winding is energised and the slot opening wedge is saturated allowing for coupling between the rotor PM flux and stator winding. Under faulty conditions the auxiliary winding is turned off and the PM flux is short circuited by the non-saturated slot wedge. Similarly to the mechanical shunt, the auxiliary winding does reduce the copper fill factor in the slot and needs to be continuously energised on during normal operation such that the slot opening wedge is saturated and the stator flux linkage is not reduced.

1.9 Demagnetisation in PM electrical machines

The effect of partial and global reversible and irreversible demagnetisation in permanent magnet electrical machines has been extensively studied in literature. The demagnetisation phenomenon of high grade rare-earth neodymium and samarium based permanent magnets as well as low grade ferrite and Alnico permanent magnets has been presented in [120] and [121]. The authors have also tested the demagnetisation characteristics using iron core fixtures that subject the PMs to demagnetising magnetic fields. The previous FE demagnetisation analysis has been accurately validated by the demagnetisation experiments.

The authors of [122] present a dovetail rotor designs which utilises two grades of PMs, one with high intrinsic coercivity, for use in rotor regions with high demagnetisation potential, and the other with high remanence for regions that have a low demagnetisation risk. In the proposed experiment, the rotor with buried PMs is demagnetised during a locked rotor test, where the machine temperature is artificially raised while the inverter supplies sinusoidal currents of fixed frequency. The authors conclude that after the demagnetisation tests, the rotor with a single high remanence PM grade showed a larger degree of demagnetisation than the mixed grade rotor. Thus, a moderate cost saving can be achieved in such a design by utilising the cheaper magnet with a lower intrinsic coercivity in the rotor regions that have a lower demagnetisation risk.

In [123] the authors present the demagnetisation effect in a fractional slot concentrated winding generator under 3-phase symmetrical short circuit. It is concluded that due to the high negative d-axis short circuit transient current, irreversible local demagnetisation is achieved. However, this can be avoided by designing a PM machine with a thicker permanent magnet, which would increase the cost of the generator, or increase the phase resistance and reactance to reduce the negative peak of the demagnetising current, which during normal operation would result in lower efficiency and power factor. The authors of [124] present the demagnetisation of an IPM machine under asymmetrical single phase short circuit and symmetrical 3-phase short circuit. For the particular machine design, it is shown that the single phase short circuit current results in a 10.3 p.u. negative d-axis current, while the 3-phase short circuit current generates a 5p.u negative d-axis current. As a result, the demagnetisation of the PM rotor is more severe during the single phase short circuit. During the 3-phase symmetrical short circuit, only the corners of each PM segment are affected, with the remanent magnet flux density in such regions being reduced to 50%. In contrast, during the asymmetrical single phase short circuit, most of the PM material has its remanent magnet flux density reduced by 20% - 40%, with 100% reduction in the corners of the PM blocks.

In [125] and [126], the authors present the effect of PM eddy current losses, magnet temperature and segmentation on the demagnetisation of an IPM machine. It is shown that due to the high transient induced PM eddy currents, the PMs are temporarily shielded from the demagnetizing stator MMF generated by the negative d-axis current. As time progresses and the amplitude of the eddy currents has stabilised to a lower value, the shielding effect is reduced and significant irreversible demagnetisation is seen in the PMs of the rotor. Thus, it is concluded that the eddy currents induced in the PMs have a very short duration shielding effect and irreversible demagnetisation is still being achieved. In comparison, the effect of PM temperature is concluded to have the most significant influence on the irreversible PM demagnetisation. It is shown that irreversible demagnetisation is avoided if the PM temperature is reduced from 180^{o}C to 140^{o}C. Finally, the authors conclude that the degree and type of segmentation has no significant effect on the demagnetization behavior of the IPM rotor for a given operation temperature and demagnetizing negative d-axis field.

Permanent magnet demagnetization in a 6-phase IPM fractional slot electrical machine with distributed winding under 3 and 6-phase short circuit faults has been presented in [127]. The authors conclude that the 6-phase short circuit has a higher risk of irreversible demagnetization since, during this fault, the flux density on the surface of the PMs is lower than in the case of a 3-phase short circuit fault.

The authors of [128]–[130] present FE studies and experimental validation of rotor demagnetization in a fractional slot concentrated winding IPM electrical machine during symmetrical 3-phase short circuit and asymmetrical single phase short circuit. For the particular machine design, it is concluded that under a 3-phase short circuit fault, at 3000 rpm and for a PM temperature of 80°C, irreversible demagnetization is avoided due to the low amplitude of the transient fault current. During the single phase short circuit fault, at 10000 rpm and 120°C, irreversible demagnetization is seen at several locations within the PM blocks, due to the high fault current which is approximatively double in amplitude when compared to the 3-phase short circuit case. The demagnetization shielding effect of the PM eddy currents is also presented. The findings are validated with experimental tests, which show a good agreement between measured and predicted results.

At the time this research was conducted, the topic of demagnetization in magnetic gears did not receive a great deal of attention in the existing research literature. Moreover, research in PM demagnetization in pseudo-direct drive electrical machines could not be found.

The authors of [131] investigate the effect of several geometric parameters on the performance of coaxial magnetic gears. In such electrical machines, the demagnetization of either of the PM arrays is due to the opposing field created by the opposing PM array. It is observed that, due to the reduced radial thickness of the outer PM array required to obtain a torque dense gear design, the outer magnet array is highly susceptible to demagnetization caused by the opposing magnetic field created by the inner rotor PMs, which are generally thicker. It is shown that at low gear ratios achieved with reduced number of pole pairs and high PM volume, the optimal thickness ratio, between the inner and outer PMs, required to avoid demagnetization, results in a suboptimal design in terms of the maximum torque capability of the magnetic gear.

In [132] the authors use 2D FE to shown PM irreversible demagnetization in a coaxial magnetic gear for different PM temperature. It is concluded that demagnetization of the outer PM array is aggravated in extreme operating conditions due to the high operating temperature.

The authors of [133] present a trans-rotary magnetic gear design which converts the linear motion of the translator into rotary motion of the output rotor. The rotor PM array is radial magnetisation pattern while the translator utilises a helix PM array. The PM demagnetisation effect is purely based on the interaction of the two opposing fields created by the two PM arrays. The worst demagnetisation position is achieved when two PMs with identical magnetisation direction are opposing each other. It is shown that at room temperature, for equal PM thicknesses on the rotor and translator, irreversible demagnetisation is avoided. However, at higher temperatures, the area of the PMs, where the magnetic flux density is below the knee point of the particular PM grade, is increased. It is concluded that in order to avoid irreversible local demagnetisation in such a magnetic gear design, the ratio of the thicknesses of the two PM arrays should be selected close to one. Moreover, a high coercivity PM grade can also be used to alleviate irreversible demagnetisation at high operating temperatures.

1.10 Finite element electromagnetic design software

The electromagnetic analysis, undertaken in this research project and presented in this thesis, was conducted using the Opera finite element analysis electromagnetic design software. The Opera FEA software is divided into two design and post-processing environments for 2D and 3D FEA, which solve partial differential and integral equations used for describing the behaviour of electric and magnetic fields in time and space. The main Opera 2D and 3D modules used in this research project include static and transient electromagnetic analysis [134].

All the electromagnetic simulations conducted under this research project were implemented and solved on an Intel-Xeon E5-2640 v3 3.2 GHz with 32GB of 3000 MHz RAM and 500 Gb SSD storage. Due to the multi-core CPU, large memory and fast storage, a total of 12 Opera 2D simulations were solved in parallel.

The magnetic gears and PDD electrical machines studied under this research were modelled in Opera 2D without the use of symmetry, due to the different numbers of pole pairs and pole pieces which, for several selected gear ratios, could not be divided by a common integer number. On average the 2D mesh of the PDD model, shown in Figure 1.73 (a), contained 120000 elements for 604 regions and 2 airgaps. The outer boundaries of the model were set such that the magnetic field is tangential to the outer limit of the design space. Due to the large number of elements required for a PDD design, in comparison with a conventional PM machine, the solving time for a static solution was approximatively 1.5 minutes, while a transient simulation with 180 steps took approximatively 4.5 hours to complete. The large solving time of the transient simulation can be reduced by reducing the number of steps or disabling the calculation of eddy currents. For both types of analyses with non-linear material characteristics, the solution convergence tolerance was set to $1 \cdot 10^{-6}$.

Static Opera 3D FEA was mainly used to approximate the end flux leakage effects and obtain a better prediction of the MG and PDD active length. Transient 3D electromagnetic FE analysis was used to simulate the eddy current losses in the non-laminated PDD components, while taking into account the flux end leakage effects. Due to the large active component count and double airgap topology of the PDD, 3D FE simulations can take a substantial amount of time to solve. A static simulation was timed at 22 hours, while a transient model 3D simulation took between 14-25 days to solve. The non-linear solution convergence of the 3D FEA was set to $1 \cdot 10^{-6}$ for all the conducted simulations.

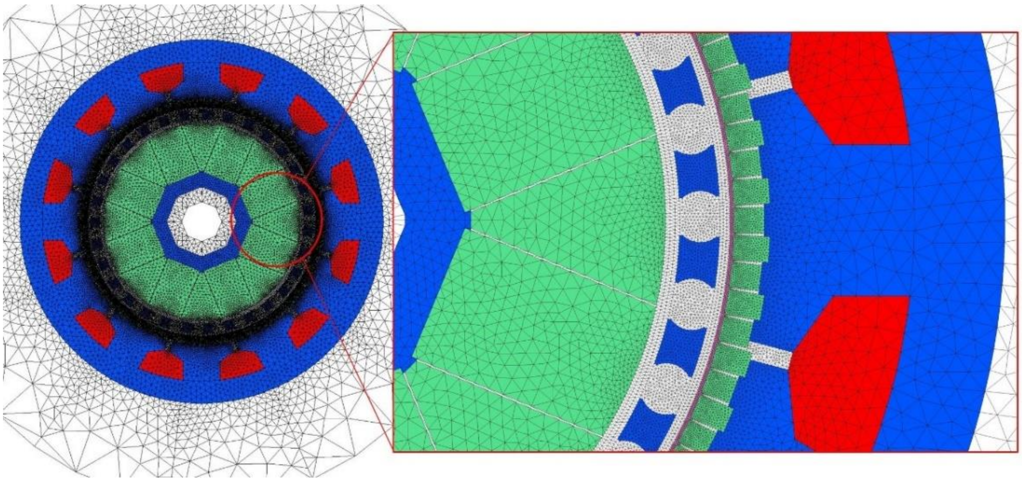

(a)

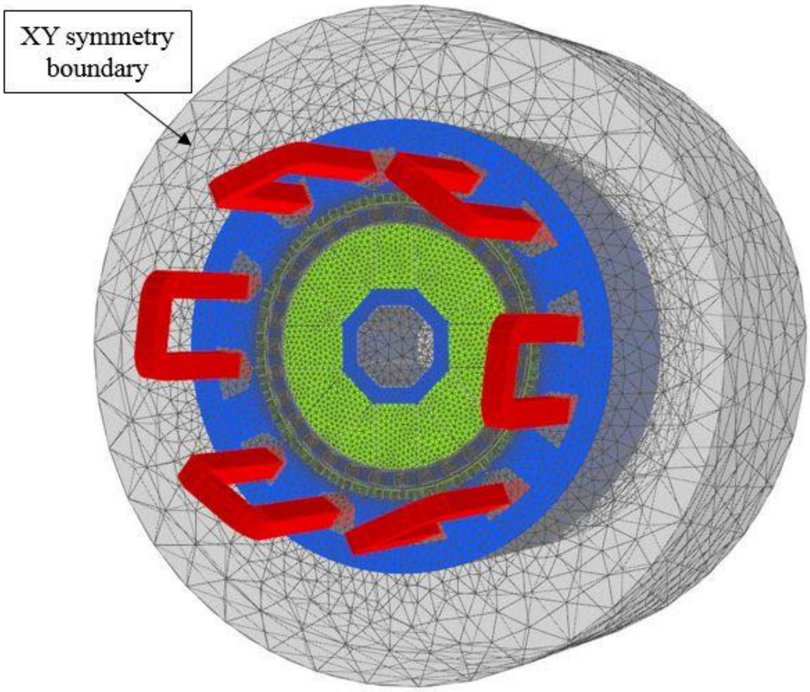

(b)

Figure 1.73. PDD model with mesh (a) 2D (b) 3D

The 3D FE PDD model was meshed to approximatively 6 million elements. Since an XY-plane tangential symmetry boundary was used to be able to model only half the PDD, along the Z-axis, this number of elements is concentrated only in the modelled half. An example of the mesh used in 3D FEA is shown in Figure 1.73 (b). As for the 2D model, the outer boundary of the 3D design space was set to tangential magnetic.

1.11 Thesis Outline

The research presented in this thesis was conducted in line with the Electro-Mechanical Magnetic Actuator Systems (EMMAS) project, funded by Innovate UK. The main objective of the EMMAS project is to develop an innovative electro-mechanical actuator that showcases the core benefits of the PDD electrical machine topology.

The project partners of the EMMAS project, and their areas of research, are as follows:

- Triumph Group – Project lead in charge of actuator mechanical and electrical integration
- Magnomatics Ltd. – Responsible of complete design, manufacturing and experimental validation of FT PDD prototype motors.
- Romax Technology – Responsible of mechanical analysis of the mechanical components of the actuator drive train.
- University of Sheffield – Responsible of fault-tolerant control system design with fault detection and pull-out recovery of FT PDD motor.

The research undertaken in this thesis is as follows:

Chapter 2 – The linear and rotary actuator drive train topologies are presented together with the specifications for primary and secondary control surfaces. The targeted control surface for the magnetically geared electro-mechanical actuator is selected based on severity of the operational conditions, nature of duty cycle and flight usage. Analytical models are used to compare three main linear power screw topologies in terms of efficiency and overall mass. Based on this, the actuator specifications are converted to reflect the PDD operational requirements. From an analytical comparison with conventional geared and direct drive actuator drive trains, it is shown that the PDD presents a significantly lower inertia and stored kinetic energy of the output pole piece rotor connected to the mechanical drive train.

Chapter 3 – A hazard rate analysis is conducted on several fault tolerant winding configurations. The winding topology with the lowest hazard rate was selected for the fault-tolerant PDD. Different fractional and integer slot-pole configurations, capable of accommodating the proposed winding arrangement, are presented and discussed, and magnetic gear ratios suitable for the identified slot-pole combinations are selected. An initial sizing of the magnetic gear element is conducted considering a range of output rotor diameters and achievable airgap shear stress. Furthermore, the influence of the magnetic gear ratio on the active components of the magnetic gear element, is presented.

Chapter 4 – An investigation into the effects of the key design parameters on torque density and inertia of the output rotor of the PDD is undertaken. The electromagnetic analysis is focused on the performance gains that can be obtained from Halbach PM arrays versus the conventional radial configuration, for the HSR and stator PMs. The pole piece rotor design is investigated by comparing the electromagnetic performance capabilities of three different pole piece topologies.

Chapter 5 – A 2D FE parametric scan is conducted on the optimal PDD topology identified in the previous chapter. The results for several magnetic gear ratios for the 12s8p and 12s10p PDD topologies are compared. It is shown that a trade-off exists between achieving a low mass PDD design and minimising the output rotor inertia.

Analytical models are developed to estimate the magnetic gear response time and actuator bandwidth for the aforementioned slot-pole combinations and corresponding gear ratios that meet the actuator motor mass requirement.

Chapter 6 – The manufacturing considerations behind the proposed PDD are presented and discussed. The stator cross-section is modified in order to obtain 1p.u. inductance such that under symmetrical 3-phase short circuit of one lane, the short circuit current is limited to the rated value. The transient and steady state short circuit current was predicted using analytical and FE models. Furthermore, the inter-turn short circuit current is predicted for different shorted turns. A fault mitigation technique, which reduces the amplitude of the inter-turn short circuit current, is implemented in 2D FE and discussed.

Chapter 7 – The demagnetisation behaviour of the FT PDD PM arrays under healthy and faulty operating conditions is investigated for several PM operating temperature. The degree of PM demagnetisation of the HSR and stator PM arrays is presented and discussed.

Chapter 8 – The electromagnetic losses of the FT PDD are predicted in 2D and 3D FEA, for healthy and faulty operation modes, by considering the copper loss, iron loss and eddy current losses of the non-laminated components. A comparison is made between the 2D and 3D FEA predicted eddy current losses of the non-segmented PMs, pole pieces and Titanium stator PM retention sleeve. It is shown that a good agreement exists for the PM losses in 2D and 3D FEA. The additional eddy current loss mechanism of the solid pole piece due to the end flux leakage effect is investigated using 3D FEA. Furthermore, the reduction in eddy current loss of the Titanium sleeve through axial segmentation is investigated and discussed. The efficiency of the FT PDD is predicted for healthy and faulty operation modes, while considering laminated and non-laminated PDD components.

Chapter 9 – The manufacturing of the main components of the magnetic gear prototype is presented in detail. Two pole piece rotor topologies, with different non-magnetic support structures, are manufactured and presented. The results of the experimental validation of the magnetic gear demonstrator are presented, and include the measurement of the HSR PM flux density distribution, power loss during no-load and on-load operation, together with static and dynamic pull-out tests.

Chapter 10 – Based on the lessons learned from the manufacturing and experimental validation of the magnetic gear demonstrator, the design and manufacturing of the FT PDD is presented. The tests conducted on the FT PDD prototype include healthy no-load and on-load operation, power loss measurements, terminal 3-phase short circuit operation, static and dynamic pull-out torque measurements, thermal performance during actuation drive cycles. The FT PDD bandwidth capability was experimentally validated on a bespoke dynamometer setup, where the load machine has a similar inertia to the combined inertia of the actuator drive train, and applied a position dependent load torque, in order to represent the aerodynamic load.

Chapter 11 – Conclusions are drawn from the presented theoretical and experimental work conducted on the FT PDD actuator motor. A comparison between an off-the-shelf actuator PM motor and the FT PDD illustrates the weight and inertia reduction introduced by the proposed motor topology. Areas of future work are proposed.

Chapter 2: Electro-Mechanical actuation

Electro-mechanical actuation of primary and secondary aircraft flight controls continues to progress in research and development as new aircraft platforms are being developed in line with the More Electric Aircraft concept.

2.1 Actuation drive train topology

Electro-mechanical aerospace control surface actuators can be divided into two main architectures. The rotary actuator topology, Figure 2.1, consists of an electrical machine with position and current sensors for position and torque control. The output shaft of the electrical machine is connected to a multi stage mechanical gearbox. The first stage is represented by the Spur gear set with typical gear ratios in the range of 4:1 to 8:1. A planetary or harmonic drive is typically selected for the second stage of the mechanical gear box with gear ratios between 30:1 and 160:1. Thus, the total gear ratio achieved within a rotary actuator is typically in the range of 120:1 to 1280:1. The high gear ratio between the motor and load reduces the torque demand and size of the motor allowing for a high speed compact machine. Although beneficial in reducing the size and mass of the electrical machine, the gear stages increase the referred inertia of the output rotor of the motor by the square of the combined gear ratio. This translates to an increase in the stored kinetic energy of the rotor when referred to the output side of each gear stage, which can be detrimental to the structural integrity of the mechanical drive train, which can occur during control surface overload caused by sudden wind gusts or shock loads due to impact with a foreign object.

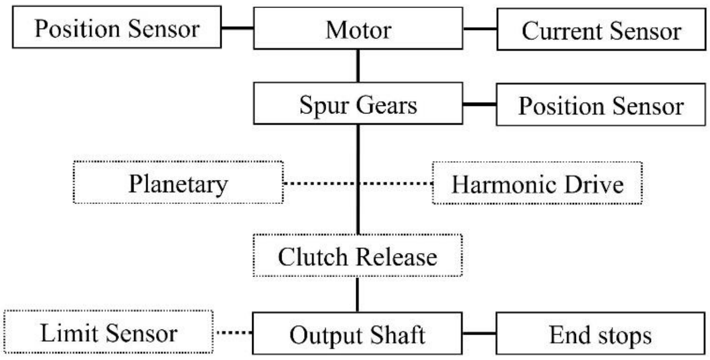

Figure 2.1 Rotary actuator topology

The clutch is used as a mechanical disconnect between the output of the mechanical gear stage and output shaft. It allows for freewheeling operation in the event of jamming of the mechanical gear stages or loss of control of the electrical machine. Spring or rubber based end stops are incorporated in the drive train of the EMA in order define the mechanical limits of rotation / stroke and add mechanical damping to the system or to protect from actuator runaway in the event of loss of motor control.

The linear actuator drive train, Figure 2.2, has the same electrical architecture as the rotary topology. The Spur gear stage has a similar gear ratio and it is used as a speed reduction stage. The linear power screw converts the rotational motion and torque produced by the electrical motor into a linear motion and force applied to the control surface actuated. Linear position sensors, typically in the form of linear variable differential transformers or LVDTs are used for position feedback of the actuated surface. End stops are incorporated to introduce a mechanical defined stroke range and protect against loss of actuator control. Additional damping can also be introduced in the actuator systems with the help of end stops and, similarly to the rotary topology, they should be sized to absorb the kinetic energy stored in the mechanical drive train.

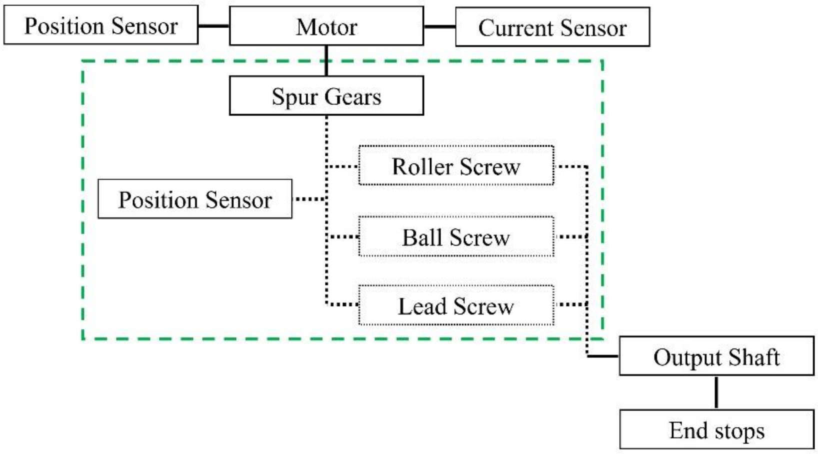

Figure 2.2 Linear actuator topology

The weight breakdown based on the total actuator weight of the rotary and linear actuator topologies is presented in Figure 2.3. The two examples are based on single drive electrical motors with high ratios gearboxes and single linear power screw. In the rotary topology, 25% of the total actuator weight is taken up by the electrical machine and mechanical gear stages. In comparison, in the linear topology, the motor and gears take up 18% with 10% being allocated to the linear power screw and nut/slide. The PDD actuator platform aims to replace the electrical motor and mechanical gearbox stages with a single magnetically geared electrical machine with the same maximum allowable total weight.

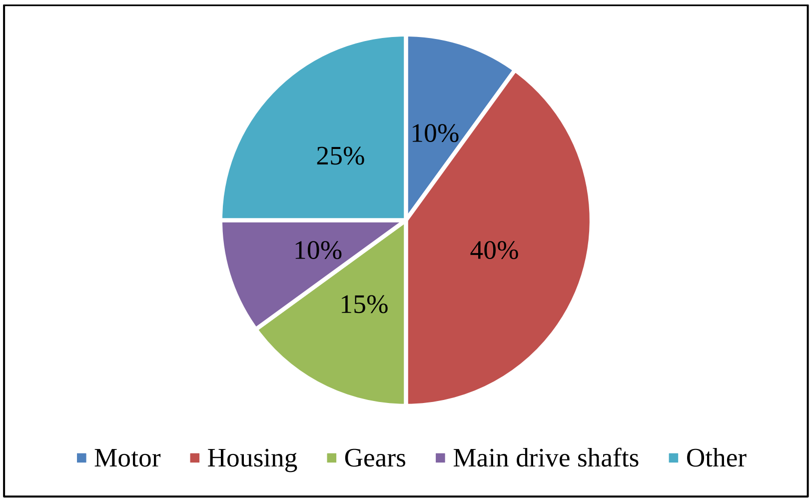

(a)

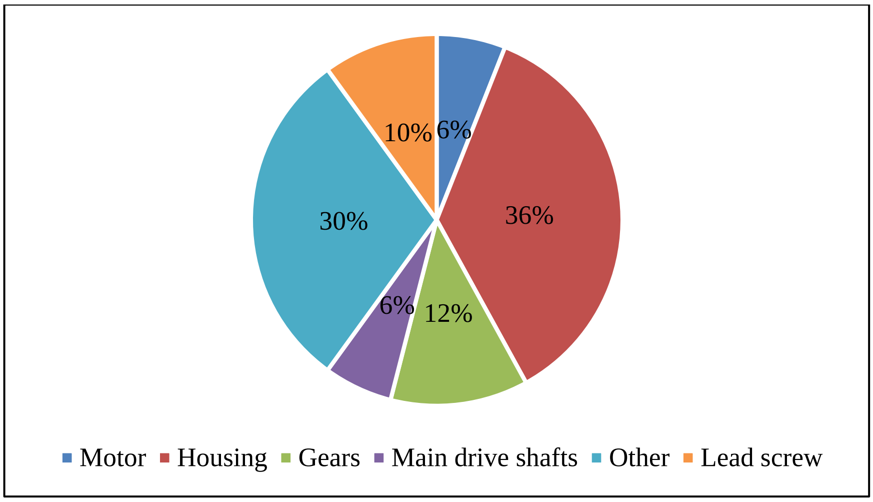

(b)

Figure 2.3 Actuator weight breakdown (a) rotary (b) linear [135]

2.2 Control surface specification

The specifications for the novel PDD based actuator drive train were obtained from a Tier 1 aerospace equipment manufacturer. All the requirements are representative of a light to medium aircraft platform with a maximum take-off weight (MTOW) in the range of 7,000 to 10,000 kg. The specifications were studied in order to select an actuation surface which was going to showcase the magnetically geared actuator drive train platform. Primary and secondary flight control surfaces, presented in Table 2.1, were considered during the surface selection process.

Table 2.1 Aircraft flight control surfaces

	Primary			**Secondary**	
	Rudder	**Aileron**	**THSA**	**Flap**	**Spoiler**
EMA topology	Linear	Linear	Linear	Linear	Linear
	Rotary	Rotary	X	Rotary	Rotary

All the EMA specifications are presented in this chapter, from the point of view of the electromagnetic design of the novel fault tolerant Pseudo Direct Drive motor. Other details such as actuator control unit architecture and power distribution system were investigated by the Tier 1 and the University of Sheffield project partners.

The axial force or torque that the linear or rotary actuator drive trains need to supply at the hinge of the control surface are presented in Figure 2.4 and Figure 2.5. The Operational load is the rated load that the electrical machine must supply. The Stall load is the maximum load reacted by the electrical motor, but only for 10 seconds in a 10 minute time interval. The Limit load represents the maximum load that the structure can withstand without causing plastic deformation. The Ultimate load is the load that will cause the mechanical structure to yield and can be applied for a limited amount of time before mechanical failure occurs. The structure is allowed to buckle and deform at this load but should not affect the normal operation of nearby aircraft systems. The Limit and Ultimate load are not required to be reacted by the actuator electrical motor.

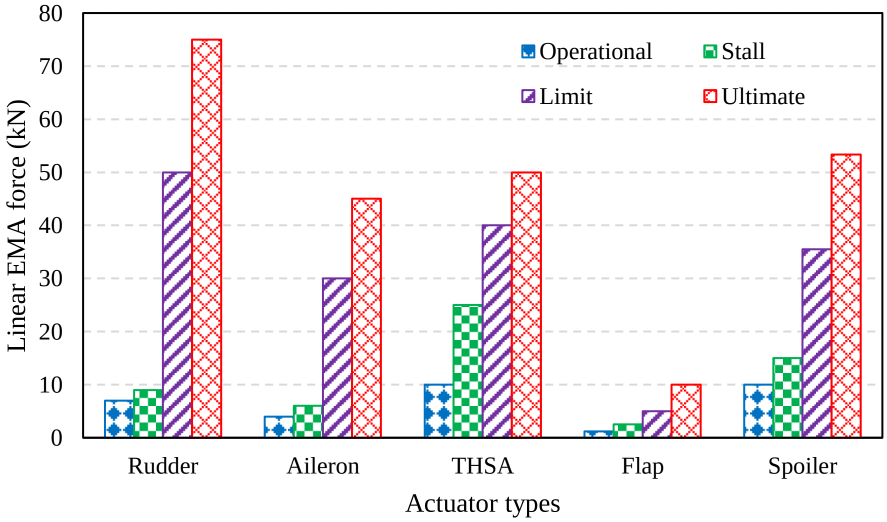

Figure 2.4. Linear actuator loads

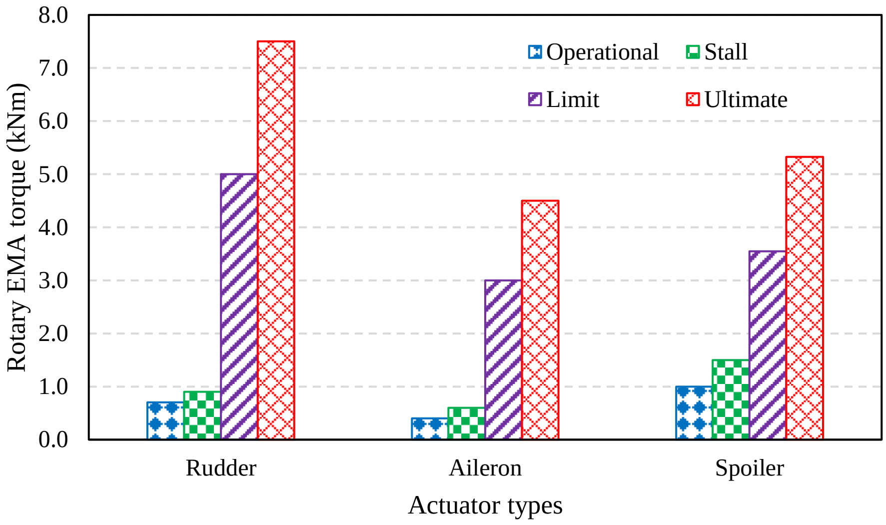

Figure 2.5. Rotary actuator torque

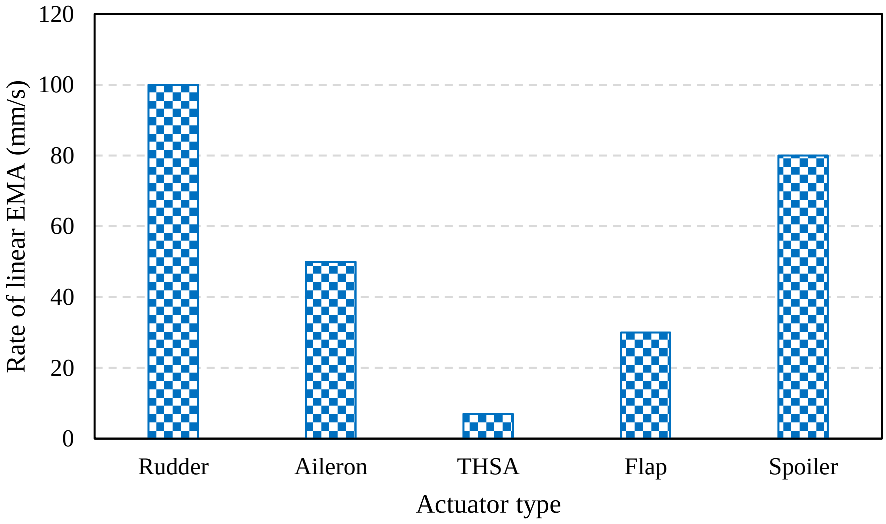

Figure 2.6. Rate of linear actuator

The linear/rotary rate requirements, for the control surfaces, are shown in Figure 2.6 and Figure 2.7. The highest linear/rotary rate is required by the rudder actuator while the THSA, being only an angle trimmable control surface which is set to hold a certain position, requires a very low linear rate for deployment and retraction. The load and rate actuator demands were used to calculate the rated torque and speed of the electrical machine once the linear power screw or rotary gearbox (if required to meet the motor mass and space envelope limits) were selected.

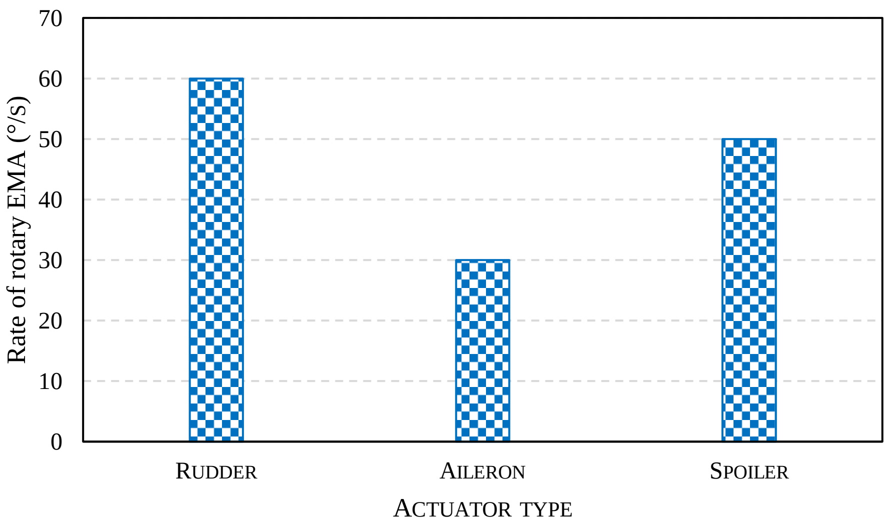

Figure 2.7. Rate of rotary actuator

The stroke requirement of the linear actuators is shown in Figure 2.8. This dimension represents the length of the linear power screw and the maximum travel range of the screw nut which is connected to the control surface of the aircraft.

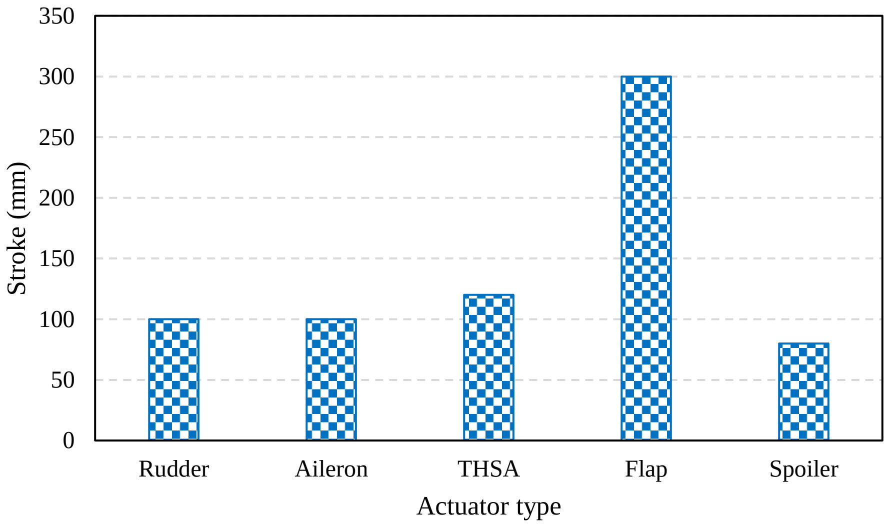

Figure 2.8. Actuator stroke requirement

The electrical system of the actuator was required to have redundancies incorporated in the motor and power controller architecture. These would act as a back-up capable of producing rated power. In order to achieve this, several EMA units having a nonredundant nature could be used to actuate the same surface. This option does introduce additional weight into the actuator system, as in order to achieve a redundant path, all the actuator components would have to be duplicated. A more weight effective option was selected, which requires the implementation of fault tolerant motor power converters and windings of the electrical machine. The electrical DC power supply was limited to a maximum of 2kW per EMA depending on the control surface actuated, as shown in Figure 2.9. The nominal DC bus voltage was set at a nominal value of 270VDC with the minimum and maximum values at 235 and 285 VDC, respectably. The actuator is required to operate normally and achieve its maximum linear rate with the minimum DC supply voltage. This minimum supply voltage was used during the motor winding design process to ensure the correct number of turns is selected.

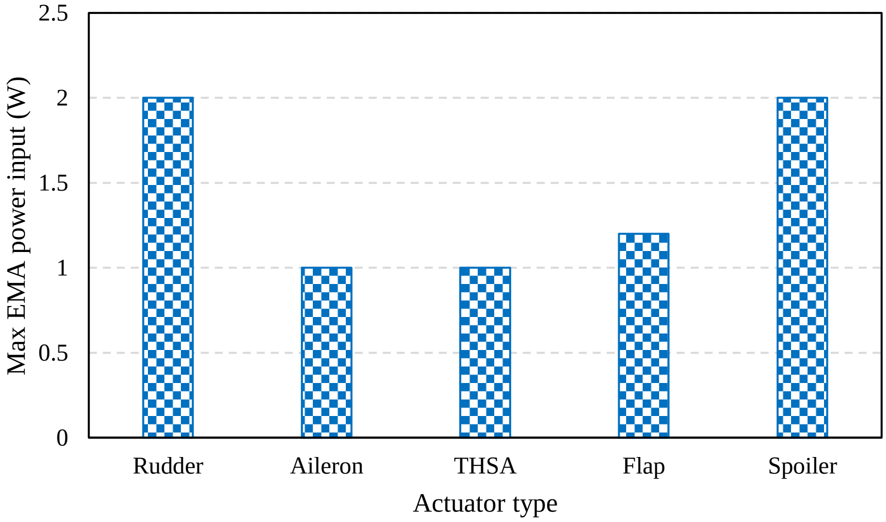

Figure 2.9. Maximum allowable power draw

The available DC current from the supply is shown in Figure 2.10. The current ratings are based on a nominal 270 VDC supply with minimum and maximum values of 235VDC and 285V, respectively.

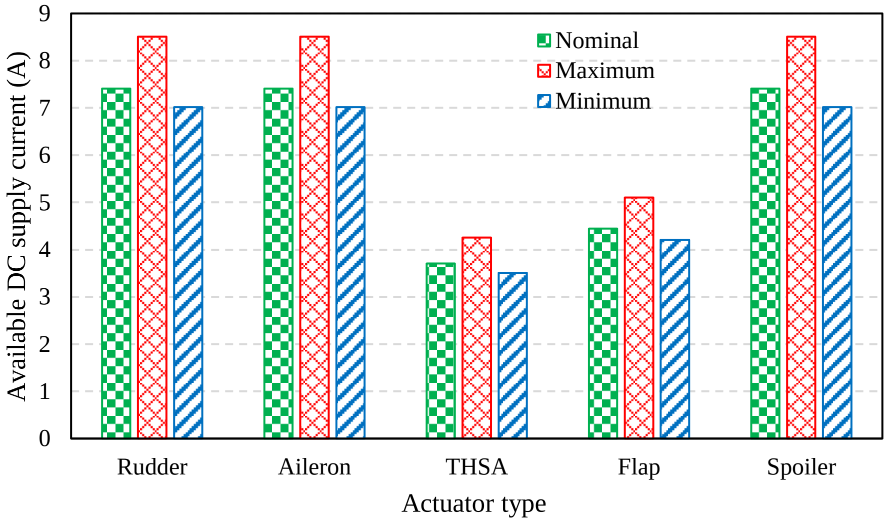

Figure 2.10. Maximum DC supply current

The bandwidth requirement as a function displacement is presented in Figure 2.11. For the non-dynamic control surfaces, such as THSA and flaps, a fixed nominal bandwidth of 1Hz was defined. In comparison, the rudder, ailerons and spoilers are characterised by a dynamic operation cycle with a bandwidth ranging from 1.5Hz at small displacements down to 0.2Hz for a full 100mm stroke.

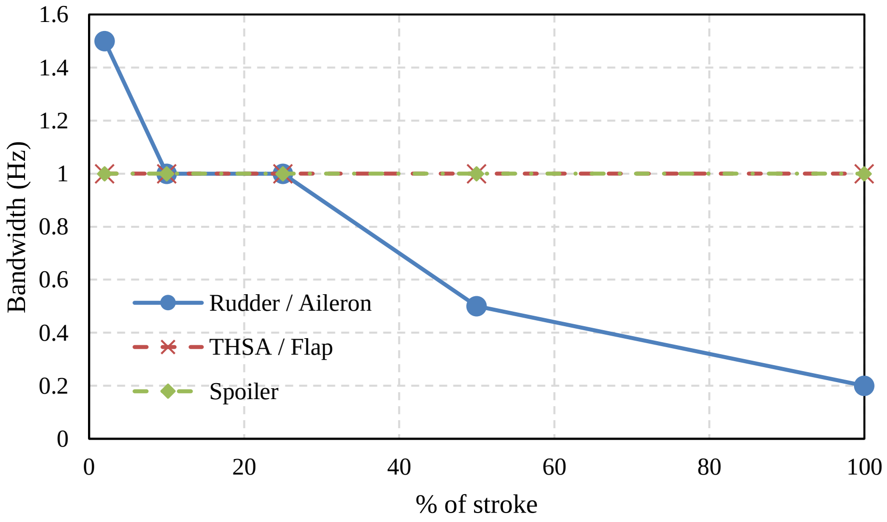

Figure 2.11. Actuator bandwidth requirement

The available actuator envelope is shown in Figure 2.12. It can be observed that the rudder control surface can accept a larger volume actuator unit than the rest of the actuator types.

Considering the linear/rotary loads required by the actuation surface from Figure 2.4 and Figure 2.5, the rudder actuator is characterised by a lowest force/torque density when compared to the other control surfaces, as shown in Figure 2.13. The maximum actuator weight is shown in Figure 2.14, with the rudder having the highest allowable EMA mass of 12kg. Figure 2.15 shows the torque/force of the EMA per total mass, with the THSA and Spoiler being load dense actuator platforms in contrast to the reduced load per mass of the flap rudder and aileron actuators.

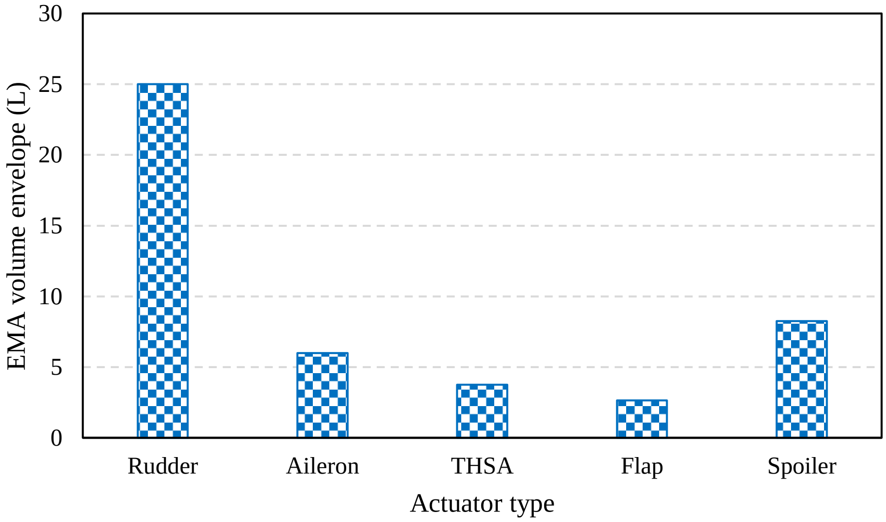

Figure 2.12. Actuator volume envelope

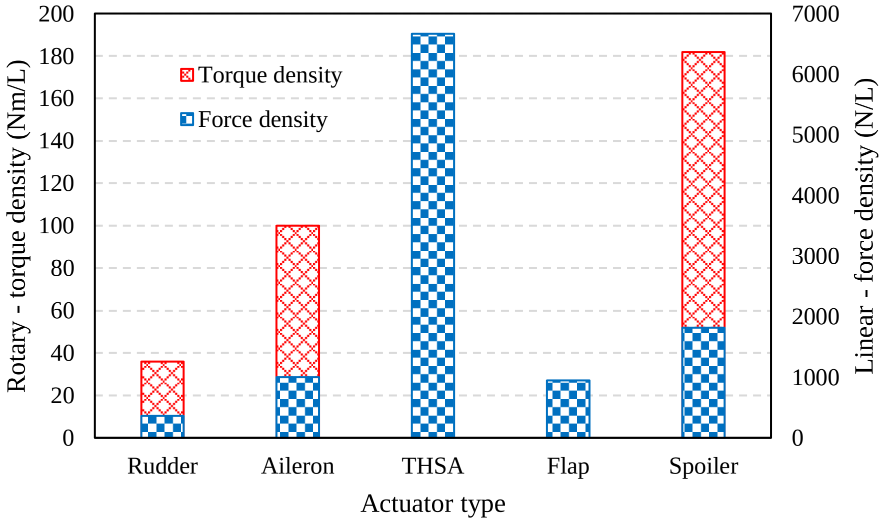

Figure 2.13. Actuator torque/force volumetric density

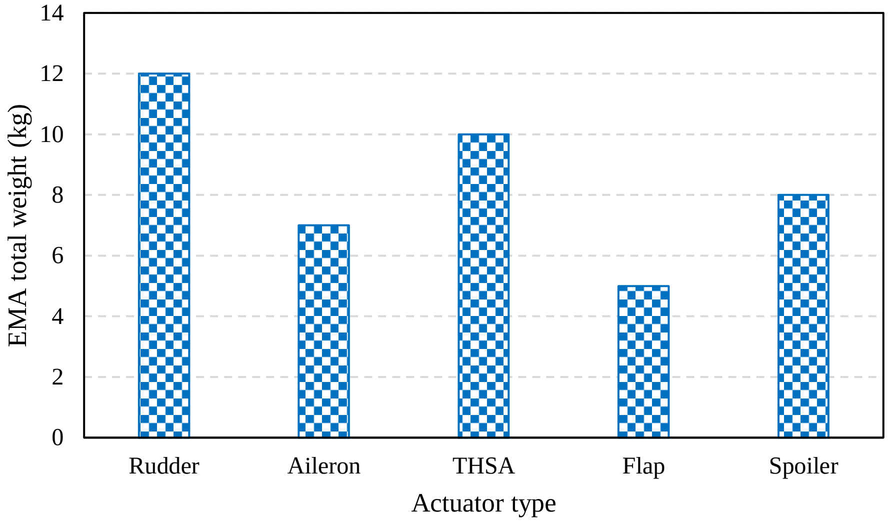

Figure 2.14. Actuator total weight

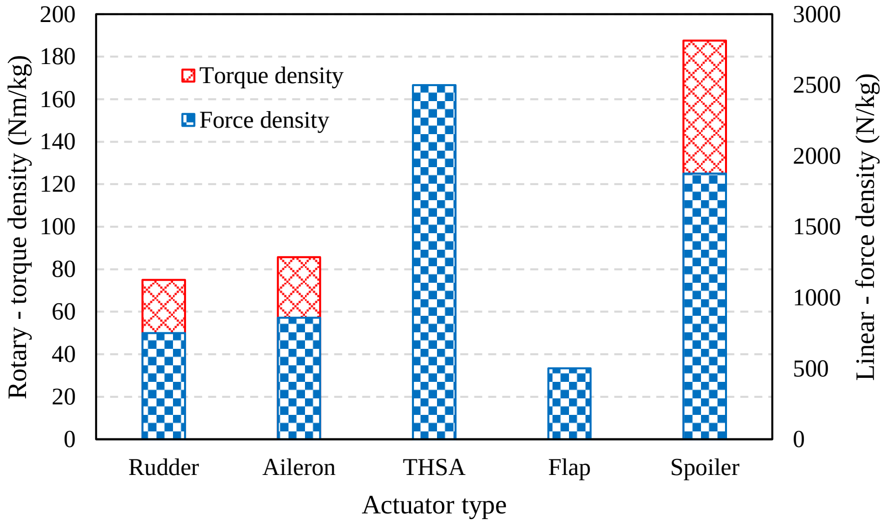

Figure 2.15. Actuator torque/force mass density

2.3 Control surface selection

The electro-mechanical magnetic actuator system (EMMAS) demonstrator research project was undertaken in order to implement and evaluate the performance of a PDD fault tolerant electrical machine as part of a mechanical actuator drive train. This novel actuator platform is intended as a possible replacement of conventional EMAs used on aircraft with a MTOW of 7-10 tonnes. Primary actuator control surfaces were preferred, in order to increase the impact of the research project and evaluate the capability of the compliant magnetically geared actuator to satisfy stringent dynamic duty cycles with high bandwidth requirements.

In order to down-select a control surface actuator platform for the EMMAS demonstrator, a selection matrix, shown in Table 2.2, was created, which scores each actuator surface in terms of experienced operational conditions, nature of duty cycle and in-flight usage. Several secondary non-flight critical actuators have been included for comparison.

Table 2.2. Control surface selection matrix

Key	1-Safe				2-Moderate				3-Critical						
Aircraft Actuator	**Heat experienced**	**Vibration experienced**	**Shock loads**	**Lightning Strike**	**Pressure Variation**	**Fluid Damage**	**Sand/Dust ingress**	**Salt ingress**	**Icing Experienced**	**Emergency duty cycle**	**Ease of maintenance**	**Required for flight**	**Impact possibility**	**Usage during flight**	**Overall Score**
Main Landing Gear	2	2	3	1	1	1	2	2	2	2	2	3	3	1	27
Nose Landing Gear	2	2	3	1	1	1	2	2	2	2	2	3	2	1	26
Flap/Slat Actuator	1	2	1	3	2	1	3	3	2	2	3	3	3	2	31
Landing Gear Door	1	2	2	1	2	1	1	1	2	2	1	2	1	1	20
Aileron Actuator	1	3	1	3	2	1	3	3	3	1	3	3	3	3	33
THSA (Elevator) Actuator	1	3	1	3	2	1	3	3	3	1	3	3	3	3	33
Rudder Actuator	1	3	1	3	2	1	2	3	3	3	3	3	3	2	33
Internal Utility Actuator	1	1	1	1	1	1	2	1	1	1	1	1	1	1	15
Spoiler	1	3	2	2	2	1	2	3	2	3	3	2	3	2	31

The operational conditions in which the actuated surfaces/platforms have to operate include hot environments with pressure variations, sand dust and salt ingress. A safe score in the ‘heat experienced’ category indicates an actuator control surface that is normally placed in a controlled environment which will not experience an increase of temperature outside its normal operations range or is within forced air flow. Such examples include most of the surface controls which, during flight, are in direct contact with the air flow or have additional cooling heat sinks. In contrast the electric brake actuator can experience high temperature operation during landing cycles. Vibration and shock loads are typically experienced by control surfaces located on the wings and tail of the aircraft which are constantly under aerodynamic loads and sudden wind gusts or object strikes. The 'Lightning strike' category has a critical rating for actuator surfaces that are likely to be struck by lightning and which could cause critical aircraft instabilities if their operation is stopped as a result.

Control surfaces on the wings and tail of the aircraft can also be subjected to changes in air pressure during aircraft flight adjustments. 'Safe' and 'Moderate' scores were assigned in this category due to the commercial nature of the aircraft targeted by the PDD actuator platform. A critical rating in the 'Pressure variation' category would indicate rapid changes in pressure during ascent and descent manoeuvres which are typical for military platforms.

The majority of the aircraft control actuators are shielded from fluid exposure scoring 'Safe' in the 'Fluid damage' category, but did receive moderate and critical scores with respect to 'Sand, dust and salt ingress' which can produce additional loading on the control surface and actuator motor. In the 'Icing experienced' category, the wing and tail control surfaces received a critical score to indicate the high possibility of icing on the control surface or the actuator. This can increase the force/torque demand leading to high motor currents or partial loss in actuator performance. Control surfaces can also be used in an emergency duty cycle. For example, the primary and secondary flight control surfaces can be used to stabilise and control the aircraft during an engine failure on one side of the aircraft.

The ‘Ease of maintenance’ category describes actuator placement locations in relation to how easily they can be replaced or maintained during planned maintenance intervals. In contrast, a critical rating means that the actuator location is difficult to access or fault finding process is complex. An example would be replacing seals in a hydraulic system.

Control surfaces on the wings and rudder of the aircraft have been scored as ‘Critical’ in the ‘Impact possibility’ category in order to highlight their exposure during flight to object strikes or repeatable wind gust. These factors can overload the control surface together with the actuator mechanical drive train. The ‘Usage during flight’ is also regarded as critical for the flight control surfaces present on the wings and tail of the aircraft in contrast to the landing gear or parking brake which are passive during flight.

Based on the presented scoring categories and reasoning, the overall scores for the selection matrix were calculated. The primary control surfaces rudder, THSA and ailerons received the highest scores based on the operational conditions, duty cycles and usage during flight.

The second stage of the selection was conducted between the linear and rotary actuator topology for the control surfaces highlighted red in Table 2.2. The rudder and aileron can both accept a rotary topology, but a harmonic drive would be required to meet the torque requirement for the given space envelope. This would also add weight to the drive train and required a redesign of the actuator attachments points for fitting on existing aircrafts. A linear topology was selected which would allow retro-fitting of the novel actuator while achieving the required target mass and size limit.

The trimmable horizontal stabilizer with the attached elevator actuator requires the highest force within a small space envelope, resulting in a high force per litre specification. This actuator application is usually targeted by hydraulic or electro-hydrostatic actuators capable of reacting high axial loads. In this respect, it was considered that the magnetically geared actuator would have difficulties in meeting the load requirement without an increase in available space and weight. This would significantly reduce the possibility of retro-fitting existing aircraft platforms.

The primary rudder and aileron control surfaces have similar force, torque and bandwidths requirements, but the aileron actuator requires a 5 times smaller space envelope weighing only 60% of the mass of the rudder actuator. Thus, in order not to increase the overall project risk and ensure the proposed novel actuator topology would meet the requirements, the rudder linear actuator was selected as target for implementing the EMMAS actuator platform.

2.4 Linear power screws

An analysis was conducted on linear drive screws suitable for aerospace actuation in order to select the diameter and lead of the screw and convert the control surface load and linear rate into the torque and speed requirement of the PDD motor. Trapezoidal lead, ball and planetary roller screws were evaluated in terms of driving efficiency and total weight.

Trapezoidal lead screws, Figure 2.16, also known as Acme screws are characterised by a thread with equal leading and trailing angles. The nut has a simple construction with no additional moving parts and a similar thread profile. These types of linear screws represent a low-cost alternative to ball or planetary roller screws. Trapezoidal lead screws with a lead angle smaller than 5^{o} will not back-drive and in certain applications they negate the need for a brake to hold the load. Such screws are also quieter than ball and planetary roller screws due to the absence of the recirculating balls or rollers. Lead screws with very fine threads are ideal for applications where positional accuracy is paramount. The main disadvantage of this power screw topology is related to its low efficiency between 20-40% [136]. In aerospace actuation applications this would result in an increase in the torque requirement of the electrical machine. Thus, the weight and size of the motor and actuator would increase.

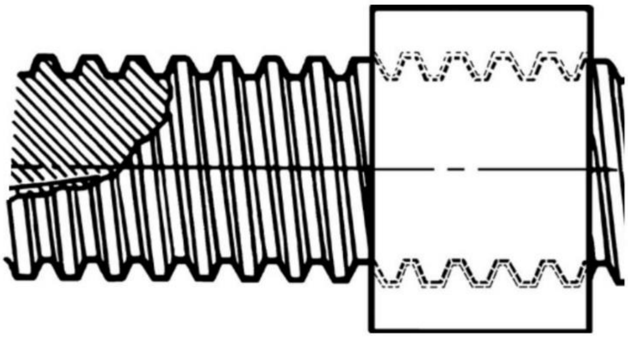

Figure 2.16. Trapezoidal lead screw [136]

Ball screws, Figure 2.17, have a main screw shaft with ball grooves. The nut has a closed channel circuit with recirculating ball bearings which represent the load transfer path. As the nut is displaced axially with respect to the screw shaft, the balls are recirculated within the closed circuit of the nut. Such power screws have high driving efficiency between 75-90% and back-drivable requiring a brake or motor holding torque in order to hold a static load [136].

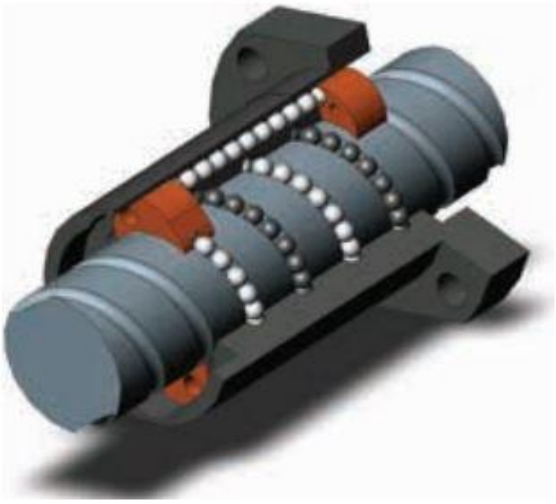

Figure 2.17. Ballscrew [137]

Planetary roller screws, Figure 2.18, have a threaded shaft while the nut is composed of a series of threaded rollers that represent the contact surface between the screw shaft and the nut. The rollers rotate around the main screw shaft as the nut translates axially.

This screw topology has a high number of mechanical contacts between the nut and the main shaft, making it ideal to actuate heavy loads while achieving long service life [138]. A sealed nut assembly with integrated brushes enable the planetary rollers to operate in contaminated environments without a decrease in efficiency. This type of screw can also be selected with small thread lead, as low as 2mm to provide high axial stiffness, accuracy and speed capability. Roller screws can achieve a high driving efficiency, >90%, and long service life, but they represent a heavier and costly alternative to ball screws [139].

Figure 2.18. Planetary roller screw [137]

The torque, T, required to rotate a power screw with a thread lead l and producing an axial load F is given by:

$$T = \frac{Fl}{2\pi\eta} \tag{2.1}$$

The efficiency, η, of the screw is predicted using:

$$\eta = \frac{\tan(\lambda)}{\tan(\lambda + \phi)} \tag{2.2}$$

$$\lambda = \operatorname{atan}\left(\frac{l}{\pi d_m}\right) \tag{2.3}$$

where λ is the screw lead angle and ϕ represents the friction angle. The friction angle values used in the screw calculation are shown in Table 2.3. It can be observed that the trapezoidal lead screw has a much higher friction angle then the ball/planetary roller screws which negatively affects the driving efficiency.

Table 2.3. Friction angle of power screw topologies

Screw Type	**Friction angle ($\boldsymbol{\phi}$)**
Trapezoidal lead screw	$6^0 - 9^0$ [140]
Ball screw	$0.25^0 - 0.35^0$ [137]
Planetary roller screw	$0.20^0 - 0.30^0$ [138]

The screw mean diameter, d_m, is a function of the outer screw diameter, d_o, and lead, such that:

$$d_m = d_o - \frac{l}{2} \tag{2.4}$$

The rotational velocity of the screw driver, ω_{scr}, and the linear rate, ν_{scr}, of the screw are proportional to the lead such that:

$$\omega_{scr} = \frac{2\pi \nu_{scr}}{l} \tag{2.5}$$

In order to minimise size and mass of the EMA drive train, it is important to select a screw topology with a high driving efficiency. This will ensure that the torque requirement of the electrical machine is reduced, as resulting from (2.1), enabling a compact and light machine design. The predicted efficiency for the three major screw topologies is shown in Figure 2.19. It can be observed that the trapezoidal lead screws have the lowest efficiency between 20-35% depending on the lead and screw diameter selection. In contrast, the ball and planetary roller screws have a high efficiency, between 60-90%, which translates in a smaller PDD torque demand for a given axial force.

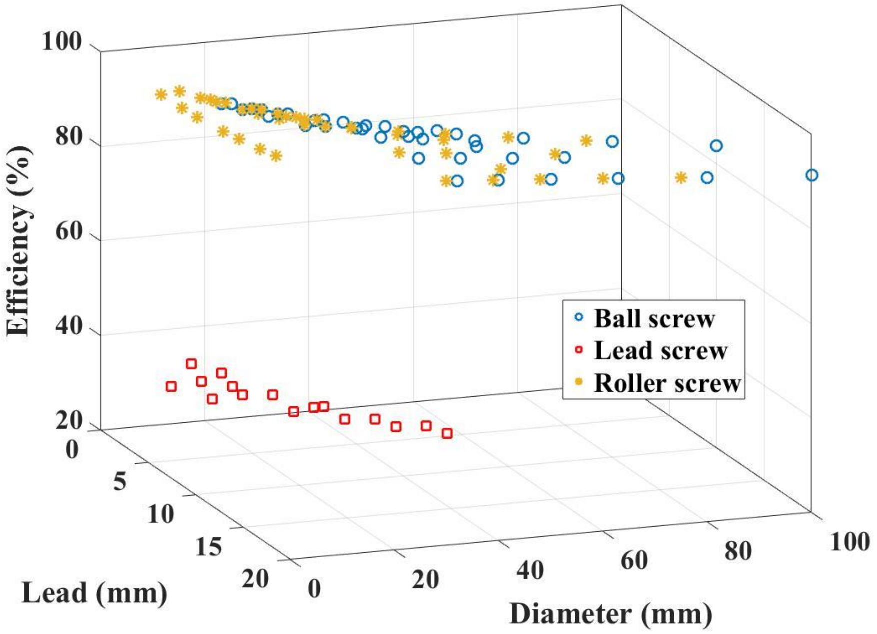

Figure 2.19. Power screw predicted efficiency

The total mass, screw and nut, of the linear screws is shown in Figure 2.20. Due to their simply construction, the trapezoidal screws have the smallest mass. The ball and planetary roller screws have a similar mass at low shaft diameters, but at high diameters the weight is increased due to the additional weight associated with the balls and rollers.

Figure 2.21 and 2.22 show the resultant PDD torque and speed requirement based on the three screw topologies. As a result of having a high efficiency, the ball and planetary roller screws drastically reduce the PDD torque requirement when compared to the trapezoidal lead screws.

The PDD speed requirement is purely based on the lead of the screw such that a smaller lead would result in a high output speed. As a result, in order to achieve a lightweight actuator drive train, an efficient linear screw having a shaft diameter between 15-30 mm with a small lead between 2-8 mm should be selected. This would enable the design of a compact PDD with a low torque requirement and copper loss, but high output speed.

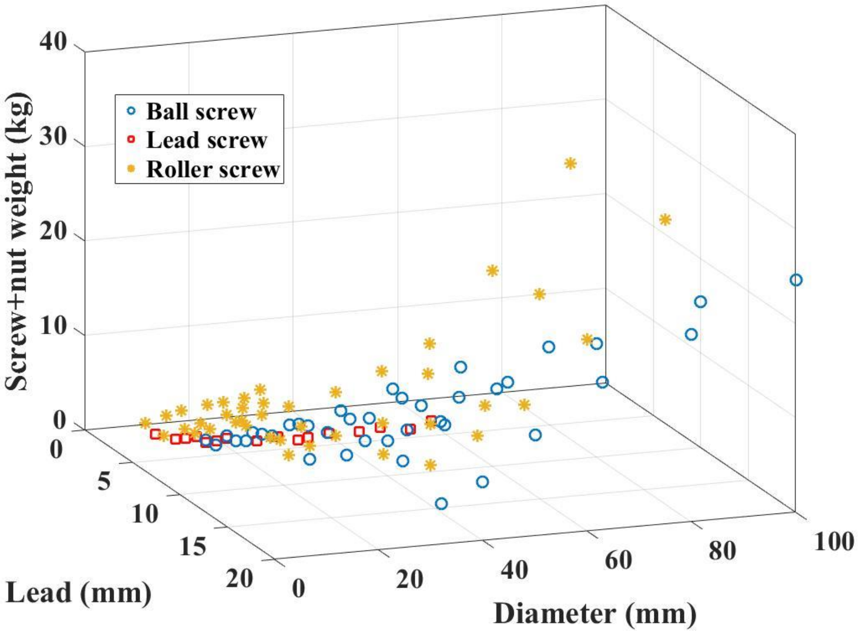

Figure 2.20. Power screw total mass

Other aspects of selecting a suitable power screw include dynamic and static loading capabilities which should be higher than the stall load of the control surface. The buckling load of the screw is also required to be higher than the limit load of the actuator in order to avoid plastic deformation of the screw. Thus, by considering the efficiency and torque trends presented, a ball screw topology was selected with the geometric and operational parameters shown in Table 2.4

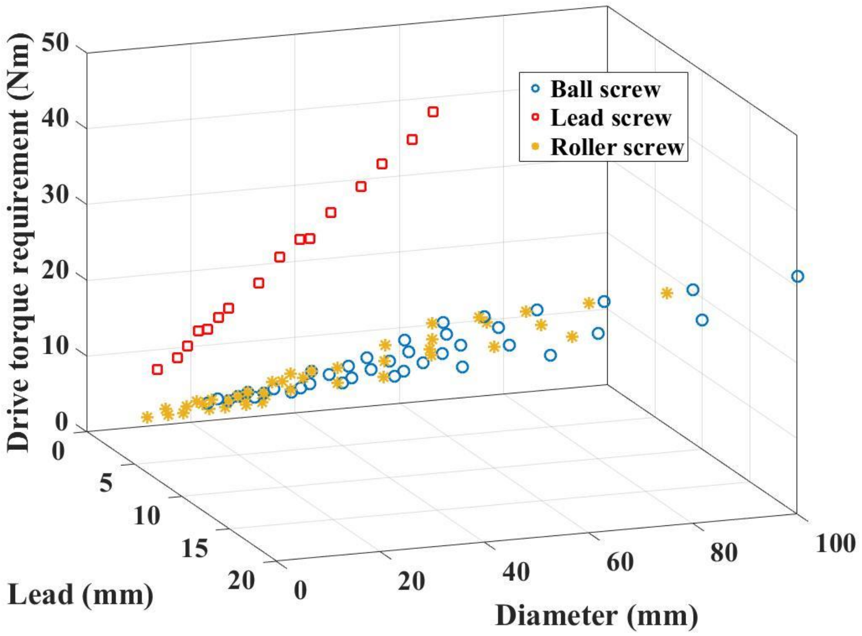

Figure 2.21. PDD torque requirement

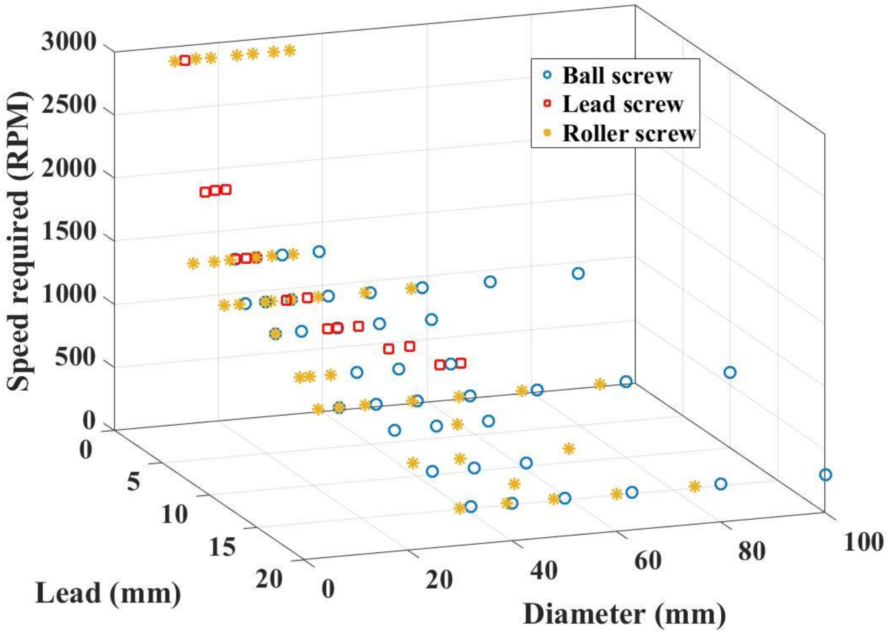

Figure 2.22. PDD speed requirement

.

Table 2.4. Ball screw parameters

Diameter	25	mm
Lead	5	mm
Efficiency	89%	
Linear rate	100	mm/s
Stroke	100	mm
Static / Dynamic loading	16.7 / 44.0	kN
Buckling load	173.0	kN
Total mass	1.7	kg

2.5 Fault-tolerant PDD motor specifications

The parameters of the selected screw were used to obtain the PDD specification, Table 2.5, based on the axial force and linear rate of the rudder control surface. The rated and peak torque are required from the PDD in order to produce the rudder operational and stall loads, respectively. The slip torque represents the maximum torque transmission of the magnetic gear element of the PDD and was set 20% higher than the peak torque of the machine.

Table 2.5. PDD specification

Rated torque	7.2	Nm
Peak torque	8.6	Nm
Slip torque	10.3	Nm
Output speed	1200	RPM
Max bandwidth	1.5	Hz
DC bus voltage	270	Vdc
Max power supply	2	kW
Operating temperature	-55 / +75	^{o}C

The duty cycle of the actuator was specified based on the load, position and frequency of the screw nut during Take-off, Cruise and Landing. The rudder actuator axial loads during Take-off and Landing are considered directly proportional to the position of the slide, while during Cruise the factor of proportionality is 2.5, as shown in Figure 2.23.

The complete actuator duty cycles were divided in smaller sinusoidal load and position profiles of different amplitudes and frequencies. Figure 2.24 shows an example of a load and position cycles from the Take-off complete drive cycle. In this scenario, the maximum load is ±700 N with a ±5 mm displacement of the screw slide and a frequency of 0.1 Hz.

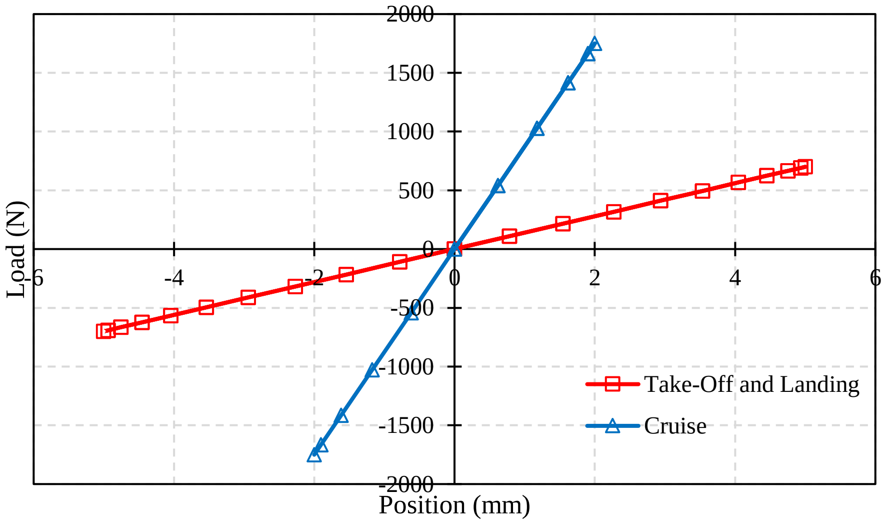

Figure 2.23. Duty cycle load variation with slide position

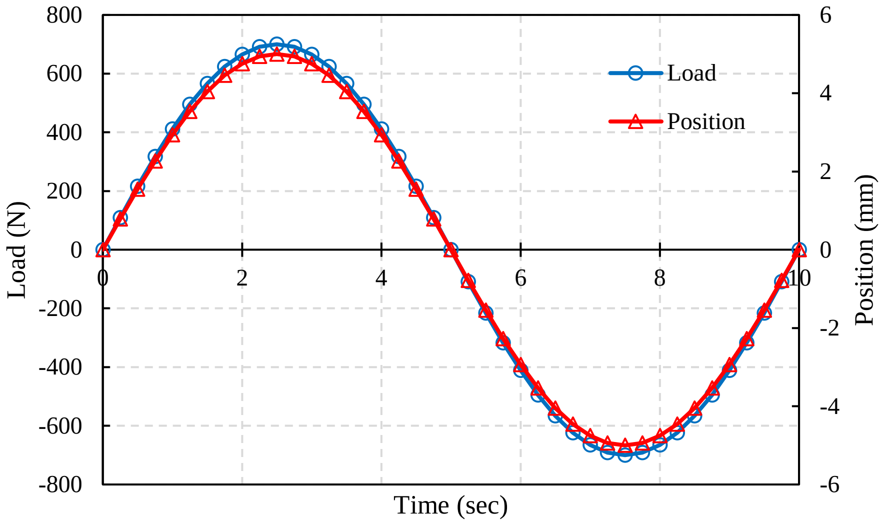

Figure 2.24. Example of initial cycle during Take-off

The linear rate of the slide was obtained as the ratio of change in position, Δx, to the change in time, Δt, of the particular cycle such that:

$$v_{scr} = \frac{\Delta x}{\Delta t} \tag{2.6}$$

As shown in Figure 2.25, a sinusoidal position cycle would result in a cosine linear rate profile. The resultant variation of load and linear rate are shown in Figure 2.26. It can be observed that in order to achieve ±5 mm slide displacement with a frequency of 0.1 Hz, a ±3.1 mm/s linear rate is required.

The frequencies of the sinusoidal load profiles for the entirety of three actuator duty cycles is shown in Figure 2.27.

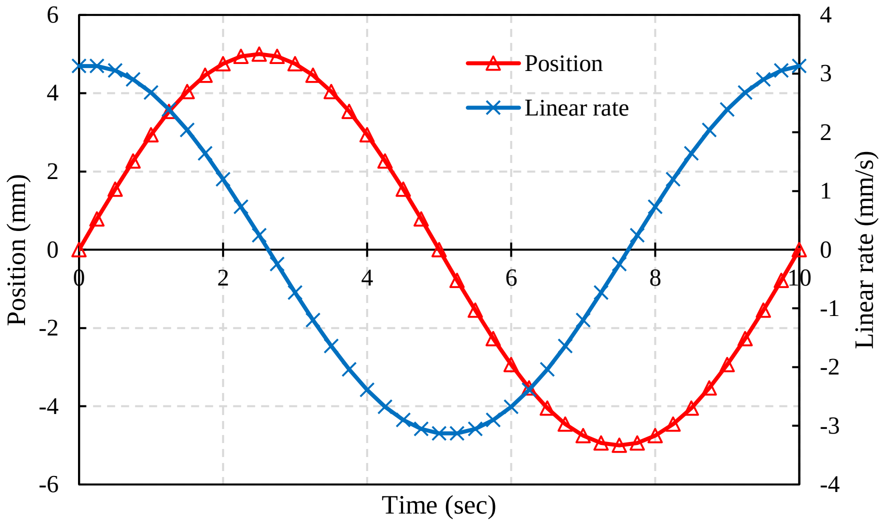

Figure 2.25. Variation of slide position and linear rate

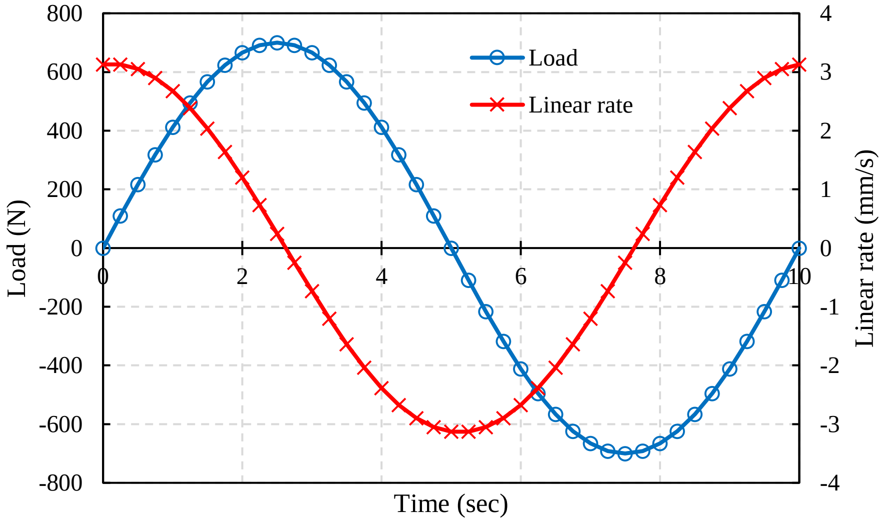

Figure 2.26. Variation of load and linear rate

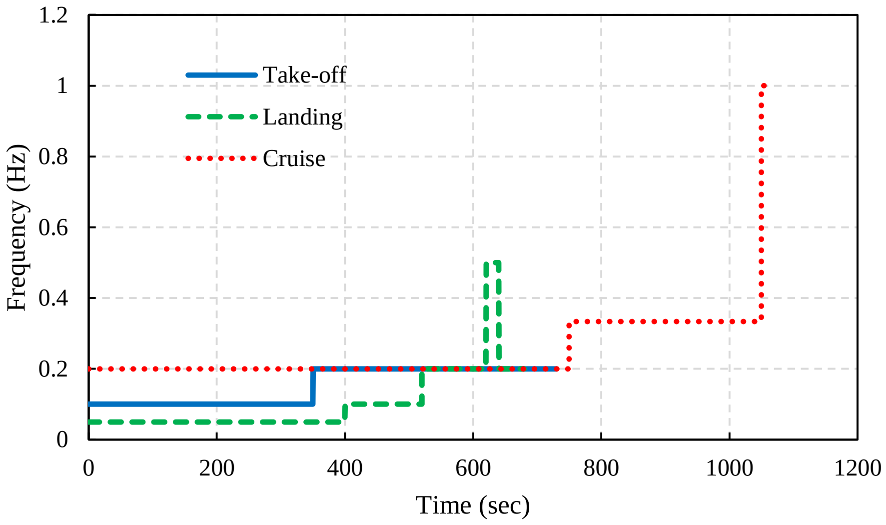

Figure 2.27. Frequency requirement during Take-off, Cruse and Landing duty cycles

The load and position requirement of the rudder control surface during Take-off, Cruise, Landing and emergency Cruise are shown in Figure 2.28, 2.30, 2.32 and 2.34 respectively. The load and position profiles were transformed into a torque and speed requirement of the PDD actuator motor, as shown in Figure 2.29, 2.31, 2.33 and 2.35 respectively. The emergency Cruise cycle symbolises a failure of one of the two engines of the aircraft platform. In this scenario the rudder would be offset to one side in order to keep the aircraft flying straight. This excess load on the rudder surface was specified as an offset which was added to the normal Cruise cycle. The offset in load represents 30% of the rated actuator load.

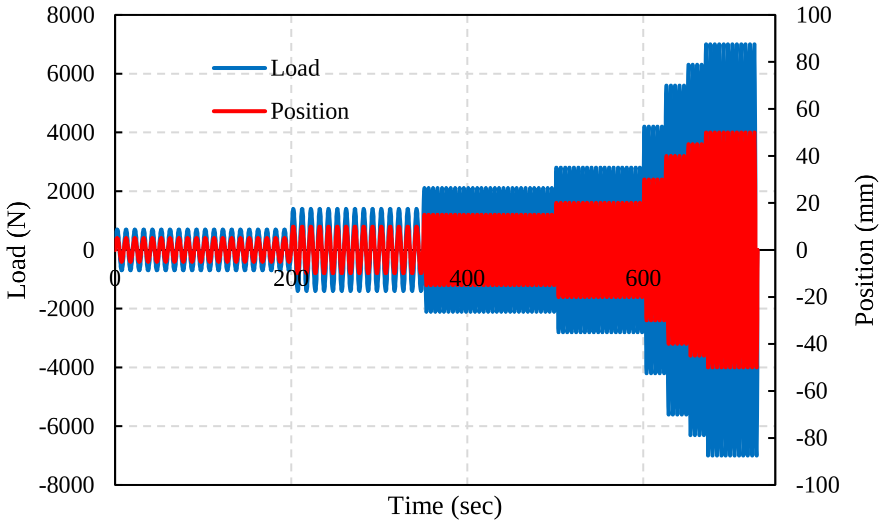

Figure 2.28. Take-off load and position duty cycle

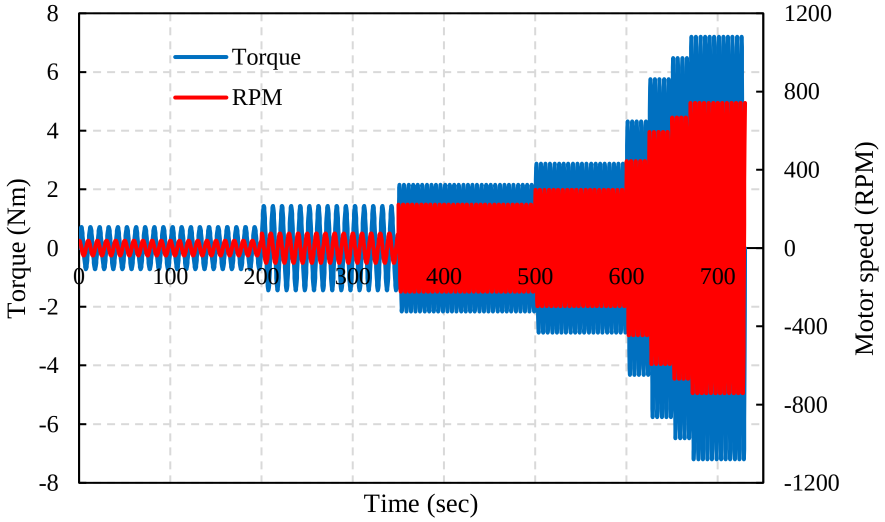

Figure 2.29. Take-off motor load and speed duty cycle

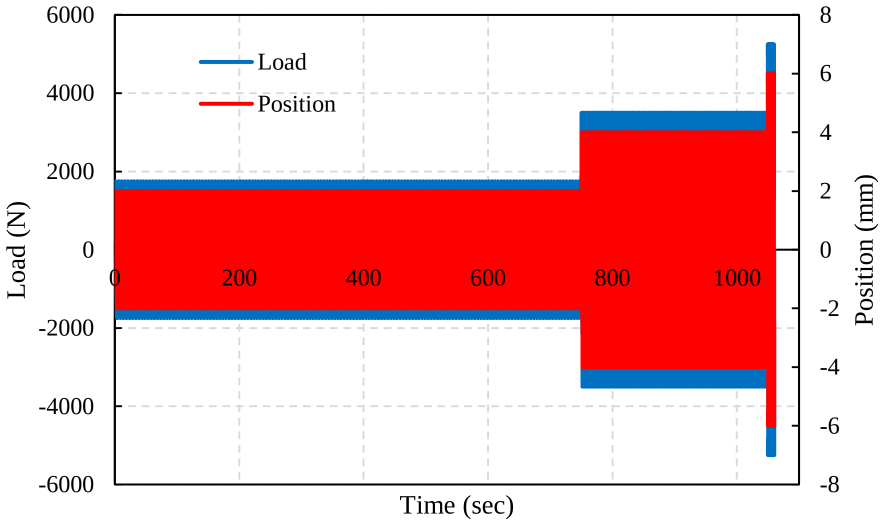

Figure 2.30. Cruise load and position duty cycle

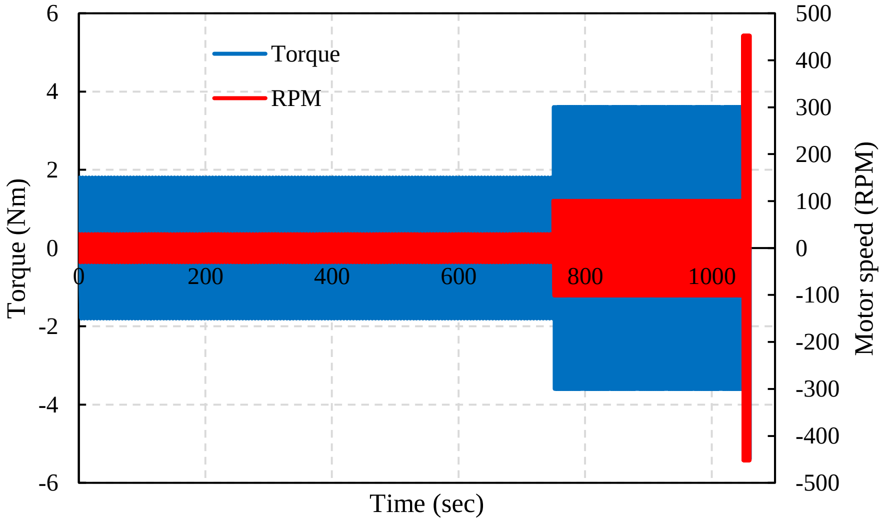

Figure 2.31. Cruise motor load and speed duty cycle

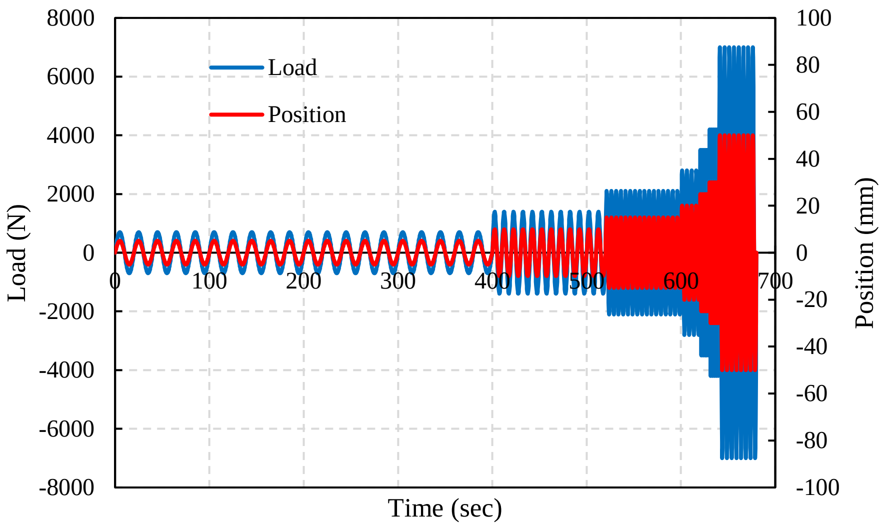

Figure 2.32. Landing load and position duty cycle

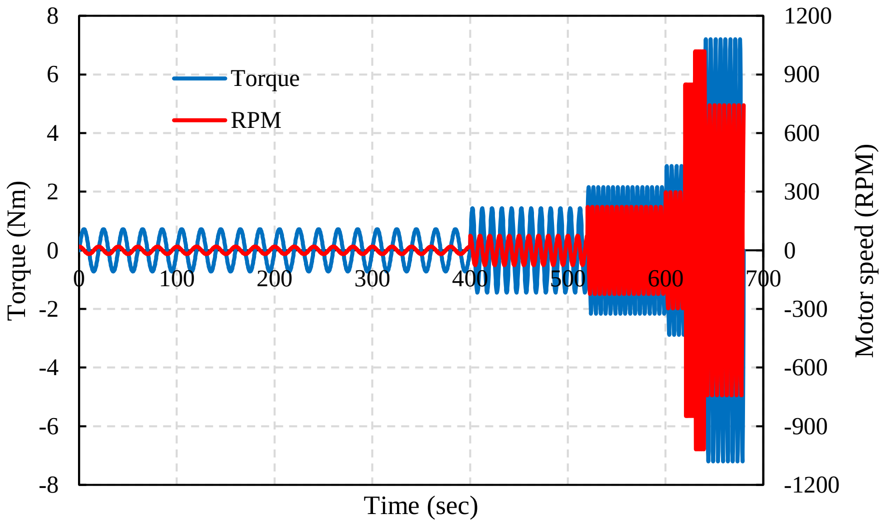

Figure 2.33. Landing motor load and speed duty cycle

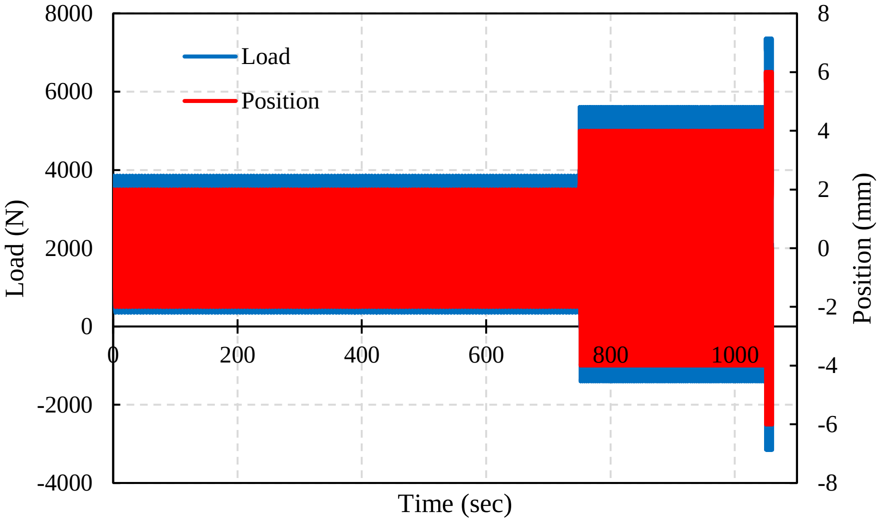

Figure 2.34. Emergency cruise load and position duty cycle

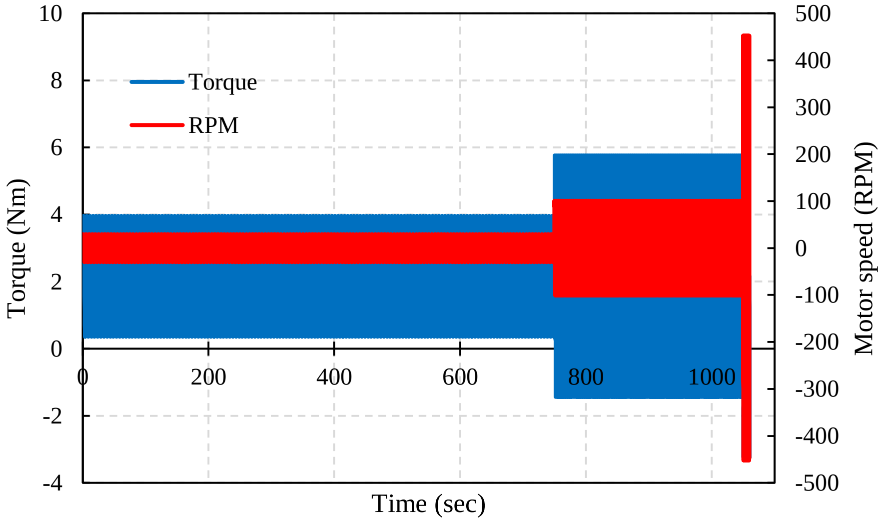

Figure 2.35. Emergency cruise motor load and speed duty cycle

2.6 Output rotor stored kinetic energy

A large percentage of existing EMA topologies use a permanent magnet electrical motor connected to the input side of the mechanical power screw through a reduction mechanical gear box. This is done in order to reduce the torque demanded from the electric motor and as a result reduce the size and mass of the electrical machine. The mechanical gearbox however increases the probability of mechanical jamming of the actuator load path during an overload condition on the control surface which could be caused by a sudden wind gust or object strike. This is due to the high number of mechanical contacts related to the meshing teeth of the mechanical gearbox, but it is also related to the mechanical energy stored in the gear actuator drive train. Thus, in a geared system as shown in Figure 1.4, the inertia of the output rotor of the electrical machine, when referred to the output side of the gearbox or input side of the linear power screw is increased by the square of the gear ratio [24]. As a consequence, the referred rotational kinetic energy stored due to the output rotor of the electrical motor is increased which can raise the jamming probability during a sudden overload of the control surface.

An analytical comparison was conducted in order to show that the stored kinetic mechanical energy in a PM motor mechanically geared actuation system is several times higher than in a PDD actuation drive train. For ease of comparison, both the conventional PM and magnetically geared PDD electrical machines, shown in Figure 2.36 and 2.37, are assumed to be mechanically geared to the input of the linear screw. Both topologies were compared against a PM direct drive actuator drive train as shown in Figure 2.38.

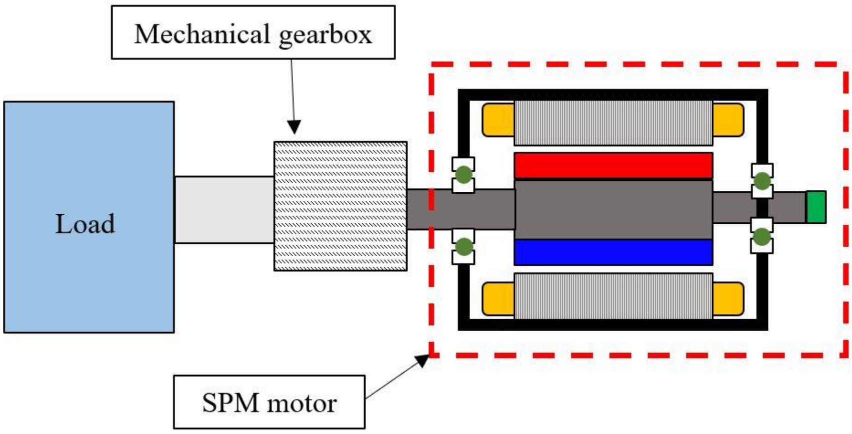

Figure 2.36. Mechanically geared SPM topology

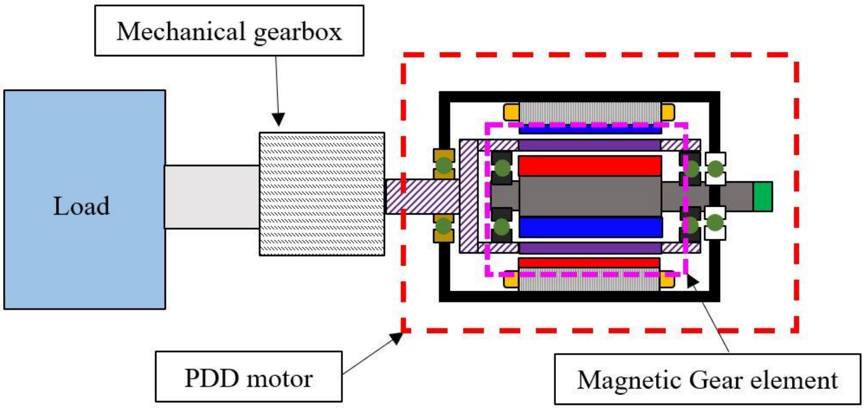

Figure 2.37. Mechanically geared PDD topology

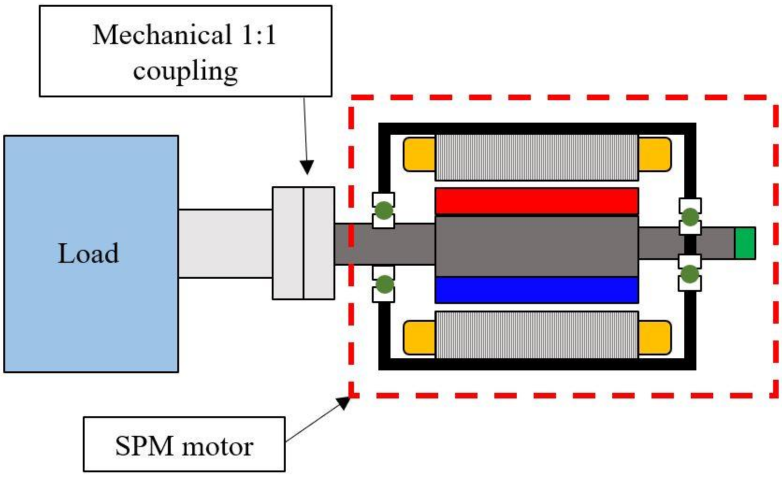

Figure 2.38. Direct Drive SPM topology

The inertia, J_{SPM}, of the rotor of a conventional SPM machine can be defined as a function of the rotor mass and outer diameter, M_r and D_r respectively.

$$J_{SPM} = \frac{M_r}{2} \cdot \frac{D_r^2}{4} \tag{2.7}$$

The mass of the rotor can be expressed as a function of its active length, L_{act} and density ρ_{SPM}, such that:

$$J_{SPM} = \frac{1}{32} \pi \rho_{SPM} D_r^4 L_{act} \tag{2.8}$$

The aspect ratio, ζ, of an electrical machine can be expressed as a ratio between its length, L_{act}, and rotor diameter, D_r, such that:

$$\zeta = L_{act}/D_r \tag{2.9}$$

Thus, by combining equations (2.8) and (2.9) the inertia of the rotor is given by:

$$J_{SPM} = \frac{1}{32}\pi\zeta\rho_{SPM}D_r^5 \tag{2.10}$$

The kinetic store energy of the output rotor of an electrical machine can be expressed as a function of the rotor inertia and rotational velocity. Thus, for the direct drive configuration, the speed of the output rotor is equal to the speed of the load, ω_L. The kinetic energy of the direct drive, E_{DD}, and mechanically geared, E_{MG}, SPM machine rotors can be expressed as:

$$E_{DD} = \frac{1}{2}\cdot\frac{\pi\zeta_{DD}\rho_{DD}D_{r_{DD}}^5}{32}\cdot\omega_L^2 \tag{2.11}$$

$$E_{MG} = \frac{1}{2}\cdot\frac{\pi\zeta_{MG}\rho_{MG}D_{rMG}^5}{32}\cdot\omega_L^2 G_{rm}^2 \tag{2.12}$$

where G_{rm} is the gear ratio of the mechanical gearbox.

Thus, the ratio between the kinetic energy in a geared and direct drive SPM is given by:

$$\frac{E_{MG}}{E_{DD}} = \frac{\rho_{MG}\zeta_{MG}D_{rMG}^5}{\rho_{DD}\zeta_{DD}D_{rDD}^5}G_{rm}^2 \tag{2.13}$$

In order to further simplify (2.13), it has to be considered that both direct drive and geared SPM drive train configurations produce the same load torque, such that:

$$T_{MG} = \frac{T_{DD}}{G_{rm}} \tag{2.14}$$

The torque produced by both drive train configurations can be expressed as a function of the rotor diameter, D, aspect ratio of the machine, ζ and airgap shear stress, σ, such that:

$$T_{MG} = \frac{\pi \zeta_{MG} \sigma_{MG} D_{rMG}^3}{2} \tag{2.15}$$

$$T_{DD} = \frac{\pi \zeta_{DD} \sigma_{DD} D_{rDD}^3}{2} \tag{2.16}$$

From (2.14), (2.15) and (2.16), a ratio between the outer diameters of the direct drive and geared SPM can be obtained, such that:

$$\frac{D_{rMG}}{D_{rDD}} = \sqrt[3]{\frac{\sigma_{DD} \zeta_{DD}}{\sigma_{MG} \zeta_{MG} G_{rm}}} \tag{2.17}$$

From (2.13) and (2.17), the energy ratio between the mechanically geared and direct drive SPM machine can be expressed as:

$$\frac{E_{MG}}{E_{DD}} = \frac{\rho_{MG}}{\rho_{DD}} \left(\frac{\sigma_{DD}}{\sigma_{MG}}\right)^{\frac{5}{3}} \left(\frac{\zeta_{DD}}{\zeta_{MG}}\right)^{2/3} G_{rm}^{1/3} \tag{2.18}$$

In order to further simplify the energy ratio relation (2.18), it is assumed that the electrical SPM motors used in the mechanically geared and direct drive topologies have the same rotor density, ρ_{SPM}, airgap shear stress, σ_{SPM}, and aspect ratio, ζ_{SPM}.

$$\frac{E_{MG}}{E_{DD}} = G_{rm}^{1/3} \tag{2.19}$$

The inertia of the PDD output pole piece rotor is simplified by considering the PPR as a solid cylinder such that:

$$J_{PDD} = \frac{\pi \rho_{PDD}}{32} L_{act} D_{PPRo}^4 \tag{2.20}$$

This is done since no information regarding the PPR inner diameter is available at this point. Hence, this represents a worst case, since in reality the PPR is a hollow cylinder, with a smaller inertia than the one given by (2.20). Thus, the energy ratio between the mechanically geared PDD and direct drive topology is given by:

$$\frac{E_{PDD}}{E_{DD}} = \frac{\rho_{PDD}}{\rho_{DD}} \left(\frac{\sigma_{DD}}{\sigma_{PDD}}\right)^{5/3} \left(\frac{\zeta_{DD}}{\zeta_{PDD}}\right)^{2/3} G_{rm}^{1/3} \tag{2.21}$$

In order to evaluate (2.18) and (2.21) the parameters in Table 2.6 were used. Since the output rotor of the SPM machine is mainly composed out of permanent magnet and electrical steel, an average density of 7575 kg/m^3 was used. Similarly, the output rotor of the PDD is typically composed of equally spaced steel pole pieces surrounded by a non-magnetic reinforced plastic or glass fibre support structure. Thus, the average density used for the PDD pole piece output rotor was 4725 kg/m^3. Since the actuation profiles used in aerospace are transient, it was assumed that the conventional SPM electrical machine can produce an airgap shear stress of 60kPa. The airgap shear stress of the PDD was varied from 60kPa to 100kPa.

Table 2.6. Machine parameters used in energy ratio comparison

Parameter	**Value**	**Units**
ρ_{MG}/ρ_{DD}	7575	kg/m^3
ρ_{PDD}	4725	kg/m^3
σ_{MG} ; σ_{DD}	60	kPa
σ_{PDD}	60 – 100	kPa
ζ_{MG}; ζ_{DD} ; ξ_{PDD}	1	

The comparison of the stored kinetic energy of the mechanically geared conventional SPM and PDD is shown in Figure 2.39. All the values are normalised to the kinetic energy of a direct drive topology. The airgap shear stress of the PDD was varied from 60kPa to

100kPa. It can be observed that the kinetic energy stored in the geared SPM drive train is higher than in a PDD system by a factor of ≈ 1.7 when the airgap shear stress of the PDD is set low at 60kPa. At higher values of airgap shear stress (100kPa) the energy of the PDD output rotor is fairly flat with the mechanical gear ratio and lower than the SPM drive train by a factor of ≈ 3.75. Based on the presented results, it can be concluded that the PDD has a significantly lower kinetic stored energy on the output rotor due to its high achievable airgap shear stress and light construction, low inertia pole piece output rotor. This makes it an ideal candidate for an anti-jamming EMA drive train.

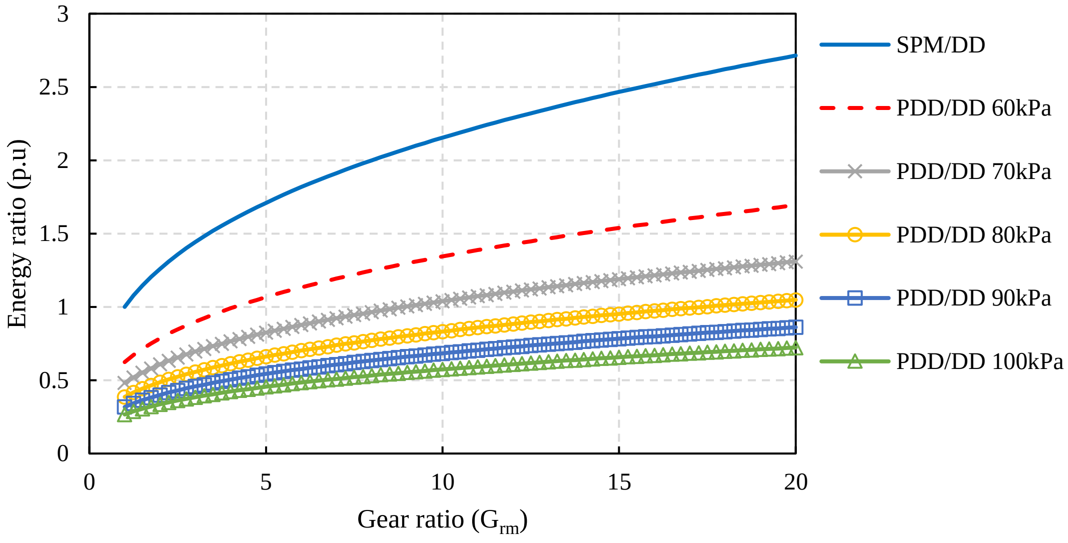

Figure 2.39. Kinetic energy ratio comparison (aspect ratio 1)

2.7 Conclusions

The linear and rotary actuator drive topologies were presented together with the weight breakdown. The specifications of the different primary and secondary control surface actuators were obtained from a Tier 1 aerospace manufacturer were compared in terms of linear force, torque, rate of actuation, stroke and bandwidth. Furthermore, the available DC supply current and power, for each actuator, are presented. The torque or force densities, of the two actuator topologies, were approximated based on the total allowed EMA envelope and load requirement. It has been shown that the THSA requires the highest force density, for the linear topology, while the spoiler requires the highest torque density, for the rotary topology. The rudder primary flight control surface actuator was selected as a target safety-critical application for the magnetically geared actuator platform. This was done in order to explore the applicability of the PDD and resultant EMA for a primary and dynamic control surface.

The main linear power screw topologies, which include lead, ball and planetary roller screws, have been presented in terms of efficiency and total weight. It has been shown that the trapezoidal lead screws have a poor efficiency, of approximatively 20-35%, which would substantially increase the motor torque requirement, size and weight. In comparison, the ball and planetary roller screws have a high efficiency, between 60-90%, depending of the screw diameter. From the two topologies, the planetary roller screws have the highest efficiency, but also achieve the highest weight due to the additional weight introduced by the rollers of the nut.

A ball screw topology was selected for the proposed PDD based EMA, with an efficiency of 89% and total mass of 1.7kg. The PDD motor specifications were derived from the specifications of the rudder actuator by considering the parameters of the selected linear screw.

An analytical comparison was conducted in order to show that the stored kinetic energy of a PDD based actuation drive train is several times smaller than that of a PM motor mechanically geared actuation system. It can be concluded that the PDD presents a significantly lower inertia referred to the screw, with a substantially lower kinetic energy of the output rotor, when compared to the direct-drive or mechanically geared motor solutions. The low referred inertia and associated kinetic energy of the PDD output rotor, together with its torque limiting characteristics, can reduce the probability of jamming of the mechanical drive train of the EMA when shock loads are applied to the control surface.

Chapter 3: Fault-tolerant PDD topology for aerospace actuation

Pseudo Direct Drive (PDD) electrical machines are currently being designed and manufactured for several applications such as EV traction, marine propulsion, wind and marine energy generation. Such applications do not require a high level of fault tolerance for the inverter, associated control and phase windings of the electrical machine, and as a result are designed with conventional double or single layer concentrated or distributed winding topologies. Having short end windings and extensively used in three phase PDD electrical machines, as presented in [84] and [141] , the double layer concentrated winding topology assumes that every slot is filled by two half coils of two different phases with each stator tooth supporting one coil. In contrast the distributed winding configurations can be automated during manufacture and result in each stator slot being filled with the conductors of one or two phases as presented in [142]. These types of windings usually result in large overlapping end windings due to the distributed nature of the phase start and end positions within the stator slots, which can increase copper loss and reduce efficiency. The double layer winding topology is deemed not to be suitable for fault tolerant electrical machines as it does not respect the basic principles of physical, electrical, magnetic and thermal isolation between phases. For such a winding configuration, a failure on any one of the phases could potentially affect the normal operation of the remaining healthy phases.

3.1 Selection of fault-tolerant winding configuration

In order to select a suitable winding configuration for the fault tolerant PDD which would introduce a certain degree of fault tolerance, a hazard rate analysis was conducted by the authors of [143], in order to evaluate the reliability of different winding topologies and associated power stage and control electronics. The redundant winding topologies considered can be separated into 3-phase windings topologies with duplex, triplex or quadruple configurations with each 3-phase lane supplied from independent 6-switch inverters, and configurations with 3, 4, 5 and 6 independent phases with each phase supplied from independent H bridge inverter. Figure 3.1 shows a single power inverter and control lane connected to one 3-phase winding lane of the PDD electrical machine which represents a single building block of the duplex, triplex or quadruple configurations. The architecture of such a lane consists of a μ-Processor which controls the gate signals of the 6-switches that dictate the phase current amplitude and phase angle for the 3-phase winding lane of the fault tolerant PDD electrical motor. The current control loop is defined by the 6-switches which control the phase currents in the windings and three current sensors, one for each phase, which produce a current measurement feedback signal for the field orientated control (FOC) in the μ-Processor. The gate control signals of the 6 switches are generated by the μ-Processor based on the feedback signal from inner HSR position sensor (resolver), such that the phase current is in phase with the back-EMF of the PDD. For redundancy reasons, one position sensor is assumed per lane.

The independent lane of the independent multi-phase topologies is shown in Figure 3.2 and consists of the power inverter, associated control and phase winding. For the independent winding topologies, an H-bridge, with 4 switches, is used to control the phase current in a single PDD motor winding. Similarly to the multiple 3-phase topologies, a current transducer is used to generate the current feedback for the current control loop and a HSR resolver is used for the position feedback required for correct phase commutation.

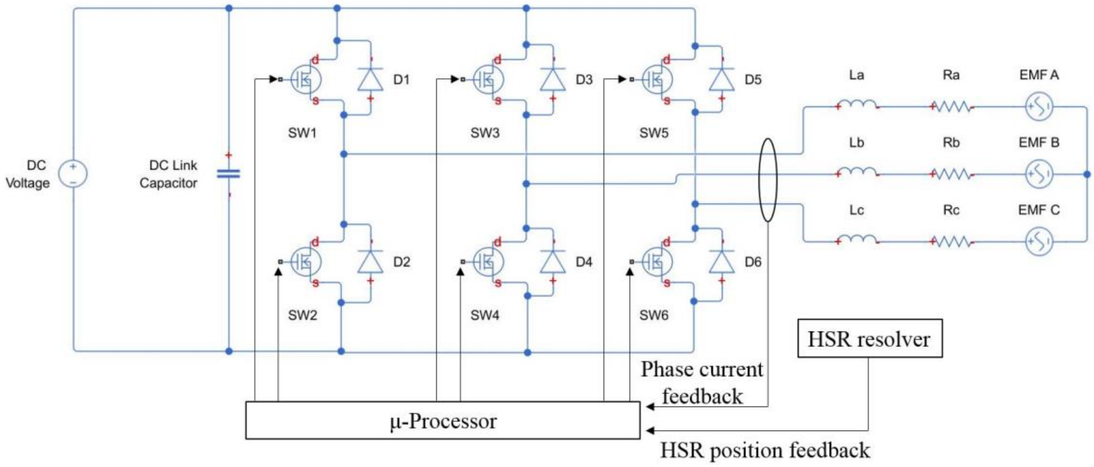

Figure 3.1. Power inverter and control module for three phase lane

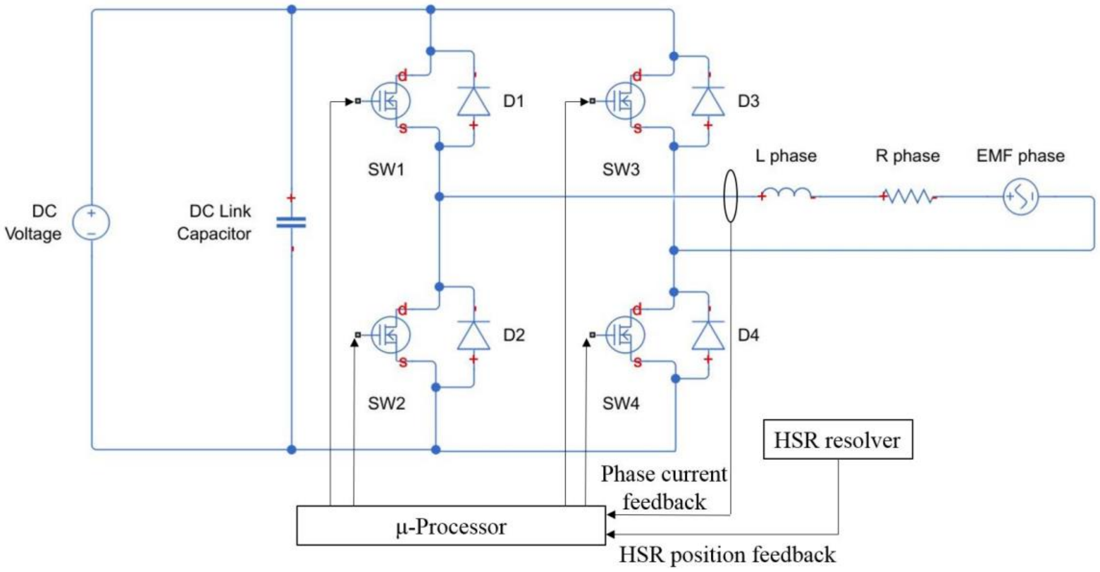

Figure 3.2. Power inverter and control module for independent phase

In order to estimate the hazard rate of the fault tolerant PDD winding topologies and associated power electronics, it was assumed in [143] that out of the total N independent channels of each winding topology, only M are required for normal operation of the fault tolerant PDD. This implies that the number of failures which can be tolerated by each topology is given by:

$$X = N - M \tag{3.1}$$

For all the described fault tolerant configurations, the hazard rate, $H(t)$, is a function of the reliability function, $R(t)$, of each lane [144], such that:

$$H(t) = \frac{1}{R(t)} \cdot \frac{dR(t)}{dt} \tag{3.2}$$

The reliability function, $R(t)$, of the M-out-of-N channels required for normal PDD operation is given by [144] :

$$R(t) = \sum_{i=M}^{N} \binom{N}{i} \left(e^{-\xi i t}\right)\left(1 - e^{-\xi t}\right)^{N-i} \tag{3.3}$$

where ξ is the failure rate of each lane and is given by the sum of the failure rates of all the components which constitute the lane. The time, t, represents the flight time for which the hazard rate was calculated. An average flight time of 8 hours was assumed for the particular medium sized aircraft platform targeted under this research project.

The component count for the 3-phase and independent lanes as well as the failure rate per hour for each component are presented in Table 3.1. The total failure rate per module was calculated as the sum of failure rates of all its components. It can be observed that at a lane level, a single 3-phase lane has a higher failure rate per flight hour than the independent lane. This is due to the reduced component count of the independent lane when compared to the 3-phase lane.

The relative hazard rates of the selected PDD winding and inverter configurations are compared in Figure 3.3. Although the 3-phase lane of the duplex configuration has a larger failure rate than the independent lane, only two 3-phase lanes are required to achieve a duplex 3-phase configuration. In contrast, three independent phase lanes are required for a 3-phase independent topology which results in a higher total failure rate when compared to the duplex 3-phase configuration.

Table 3.1. Failure rate for 3-phase and independent topologies [145], [146]

Component	**Component count**		**Failure rate per hour**	**Operating temperature**
	3-phase lane	**Independent lane**		
IGBT	6	4	5.00×10^{-7}	90°C
Diode	6	4	1.20×10^{-6}	75°C
DC link capacitor	1	1	2.00×10^{-6}	75°C
Winding	3	1	1.14×10^{-5}	150°C
Current transducer	3	1	2.00×10^{-6}	60°C
Signal connector	9	6	6.00×10^{-10}	45°C
μ-Processor	1	1	1.45×10^{-5}	75°C
Position Sensor	1	1	2.00×10^{-6}	60°C
Fuses	2	2	1.50×10^{-7}	75°C
Power connector	4	5	8.50×10^{-7}	45 °C
Total failure rate/module	7.26×10^{-5}	4.33×10^{-5}		

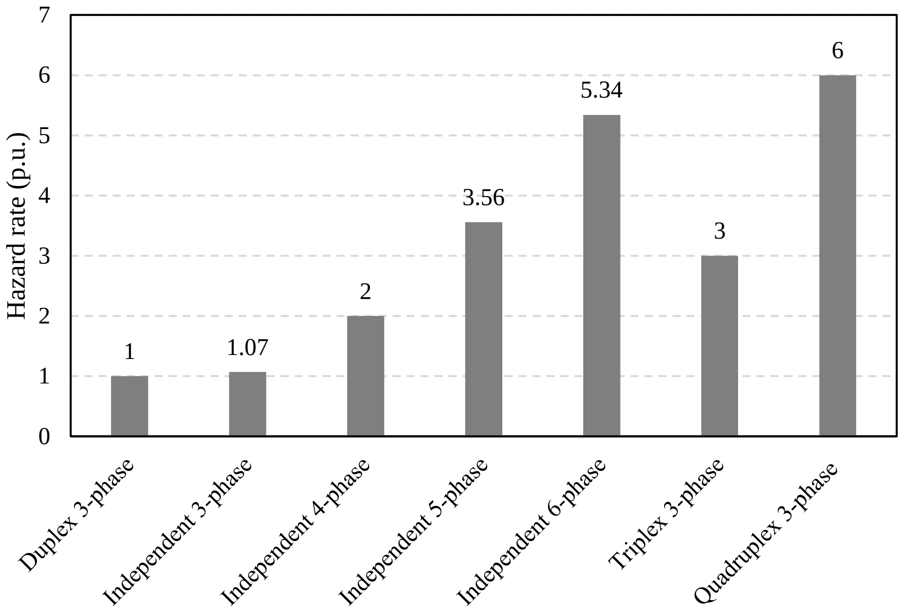

Figure 3.3. Hazard rate of fault tolerant PDD winding configurations

It can be observed that duplex 3-phase winding configuration, supplied from a duplex 3-phase conventional 6-switch converters, exhibits the lower hazard rate when compared to the other fault tolerant topologies investigated under this research project. The independent 3-phase topology exhibits a slightly higher failure rate than the duplex 3-phase by 7%. On the basis of this reliability investigation for the converter and PDD winding topology, the duplex 3-phase configuration was selected for implementation in the fault tolerant PDD actuator motor.

3.2 Viable fault-tolerant PDD slot-pole combinations

In order to achieve a fault-tolerant PDD design, the principles of magnetic, electrical, physical and thermal isolation must be respected [42], [51]. This is enabled by selecting a single layer concentrated machine winding topology which can be arranged in a duplex 3-phase configuration. The single layer concentrated winding assumes that each slot only contains the conductors of one coil side and the stator has coils wound on only half of the total number of teeth, with adjacent coils being separated by one empty tooth. The alternate winding pattern and concentrated coils provide effective physical isolation between coils/phases and highly reduce the probability of phase to phase faults.

In an electrical machine using this winding scheme, the highest temperature rise usually occurs within the slot area of the active coils. Thus, the empty teeth minimise the thermal interaction between two adjacent coils by providing a high thermal conductivity path to the outer surface of the stator.

The single layer winding topology does also reduce the mutual coupling between phases by reducing the cross-slot leakage. In conventional SPM electrical machines, the armature reaction airgap flux is small, with a large percentage of the phase inductance being given by the cross-slot leakage. Thus, by implementing a single layer winding in contrast to a double layer topology, the phase inductance is mostly influenced by the self-inductance component and the mutual component is minimised. A low mutual coupling component between phases would also ensure that the armature reaction of the healthy coils does not increase the short circuit current in the faulty phases. Moreover, the voltage induced in the healthy phases by the fault current flowing in the faulty coils would also be limited, ensuring the controllability of the healthy lane is not affected.

Electrical isolation for the proposed PDD duplex 3-phase topology is implemented at both the machine and power inverter level by having two independent 3-phase windings and converter lanes, each capable of supplying rated power and overcoming the losses of the faulty lane. Based on this duplex winding topology, two modes of operation can be defined for the fault tolerant PDD actuator motor, assuming both winding lanes are healthy. In the Active-Passive operation mode, only one lane, winding and corresponding converter, is used to supply rated power. The passive lane is switched off and kept as a back-up in case a fault arises in the active lane. In comparison, in the Active-Active mode of operation both winding lanes are used, each contributing to half of the rated power of the electrical machine. This operation mode can have certain advantages such as reduced total copper loss by half due to the fact that each lane is only supplied with half the rated current. This can also improve the thermal performance of the electrical machine, resulting in a lower steady state temperature and potentially longer life and improved reliability. In order for a stator to have the correct number of teeth (or slots), N_s, to accept a duplex 3-phase single layer winding configuration, the following equation must be satisfied such that:

$$\frac{N_s}{2} = m * k \tag{3.4}$$

where m is the number of phases per lane and k is the number of 3-phase lanes.

3.2.1 Fractional slot-pole combinations

Due to the small torque requirement and high torque density capability of the PDD electrical machine which would result in a small diameter motor, a stator having 12 slots was selected for the fault tolerant fractional slot PDD electrical actuator motor. It can be observed that from equation (3.4), that for a 12-slot stator, the number of phases per lane $m = 3$, the number of lanes is $k = 2$. Thus, two 3-phase lanes can be implemented in a 12-slot stator, resulting in a duplex 3-phase winding topology. Based on equation (3.4) it can also be observed that 12 stator slots represent the smallest number of slots for which a duplex 3-phase configuration is possible. Table 3.2 shows the integer slot-pole combinations targeted during the electro-magnetic design of the fault tolerant PDD actuator motor.

Table 3.2. Selected fault tolerant PDD fractional slot-pole combinations

Stator slots (N_s)	12			
HSR poles ($2p_h$)	8	10	14	16

The star of slots was used to represent the EMF phasor diagrams for the main harmonic for the PDD slot-pole combinations presented in Table 3.2 in order to obtain the coil slot distribution for the duplex 3-phase single layer fault tolerant winding topology. The method used to obtain the star of slots phasor representation was outlined in [147]. In order to check the winding feasibility, the following equation must be satisfied:

$$\frac{N_s}{m\,\mathrm{Z}} = integer \tag{3.5}$$

where Z is the machine periodicity and is given by:

$$\mathrm{Z} = GCD\{N_s/p_h\} \tag{3.6}$$

where p_h is the number of pole pairs of the HSR.

The star of slots is composed of N_s/Z spokes, with each spoke containing Z phasors. The mechanical angle in radians between two adjacent spokes of the star of slots, α_{spk} is given by:

$$\alpha_{spk} = \frac{2\pi}{(N_s/\mathrm{Z})} \tag{3.7}$$

The electrical angle in radians between the phasors of adjacent stator slots, α_{ph} is obtained from:

$$\alpha_{ph} = \frac{2\pi}{N_s} p_h \tag{3.8}$$

For the PDD slot-pole combinations presented in Table 3.2, the star of slots was initially used to obtain the main harmonic EMF phasor representation for a double layer concentrated winding configuration, with each coil EMF phasor being numbered with the number of the slot in which its return path was placed. This double layer configuration was converted to a single layer by removing the even phasors such that only the odd phasors are left. The transformation from double to single layer is only achievable if the machine periodicity, Z, is even. Thus, the stator coil distribution for a single layer is characterised by each slot being filled only by one coil side. Table 3.3 shows the calculated parameters for the star of slot conversion from double layer concentrated to single layer winding topology.

Figure 3.4 to 3.11 show the star of slot phasor representation for the double layer and the corresponding conversion to a single layer winding topology for each of the slot pole combinations from Table 3.2.

Table 3.3. Parameters for double layer star of slots phasor representation

Stator slots (N_s)	12			
HSR poles ($2p_h$)	8	10	14	16
No. of phases (m)	3			
No. of spokes	3	12	12	3
Periodicity (Z)	4	1	1	4
α_{spk}	120^o	30^o	30^o	120^o
α_{ph}	120^o	150^o	210^o	240^o

It can be observed that the single layer phasor representation has half the number of EMF phasors when compared to the corresponding double layer topology. The number of each phasor represent the number of the slots onto which the phase coil is wound. The phasors which have negative identifiers have been shifted by 180° in order to simplify the phasor diagram. These phasors represent coils which are wound with a reverse polarity when compared to the coils whose phasors have positive identifiers.

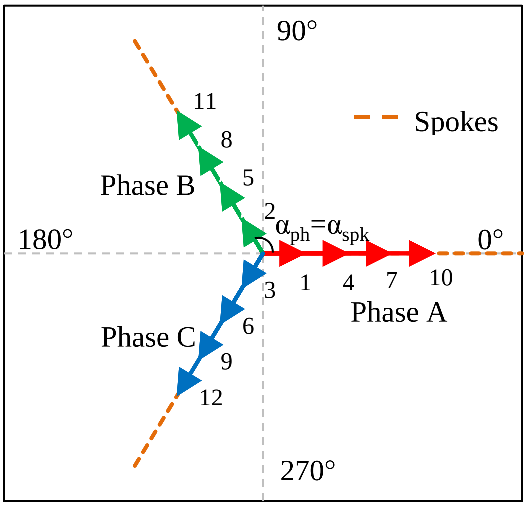

Figure 3.4. Star of slots 12S8P double layer

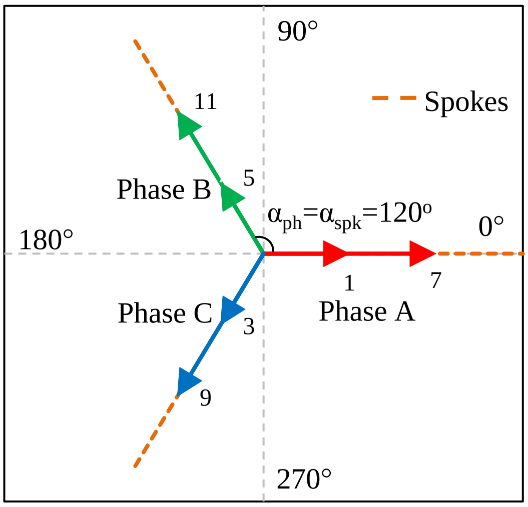

Figure 3.5. Star of slots 12S8P single layer

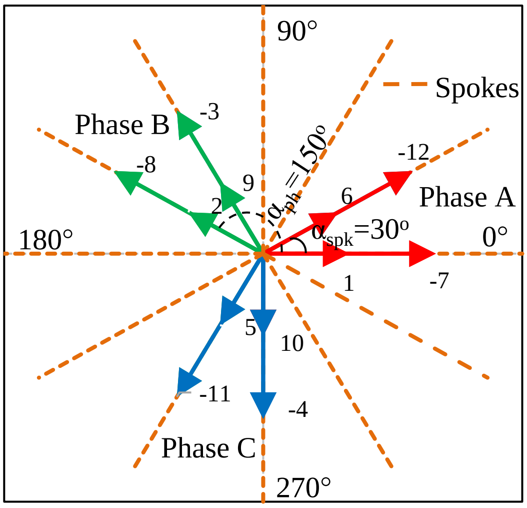

Figure 3.6. Star of slots 12S10P double layer

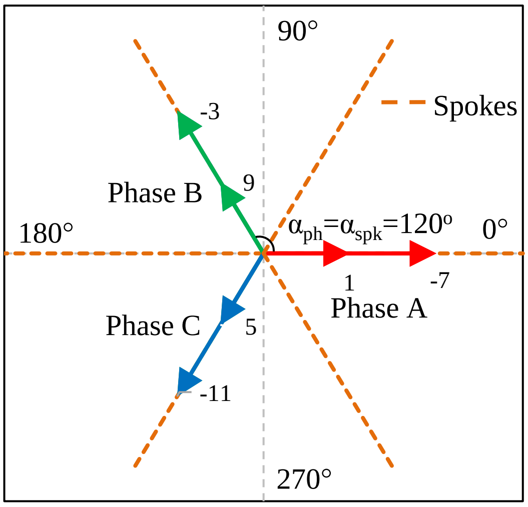

Figure 3.7. Star of slots 12S10P single layer

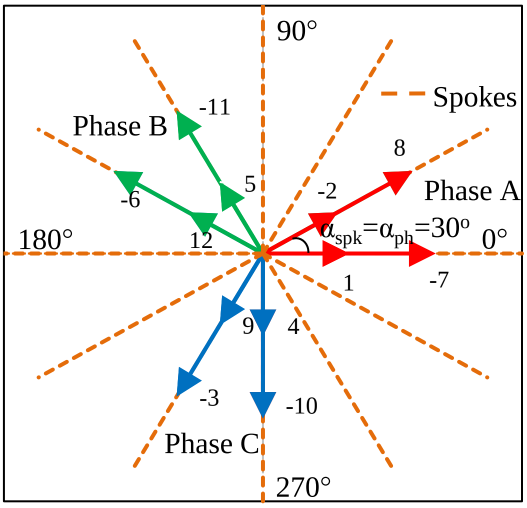

Figure 3.8. Star of slots 12S14P double layer

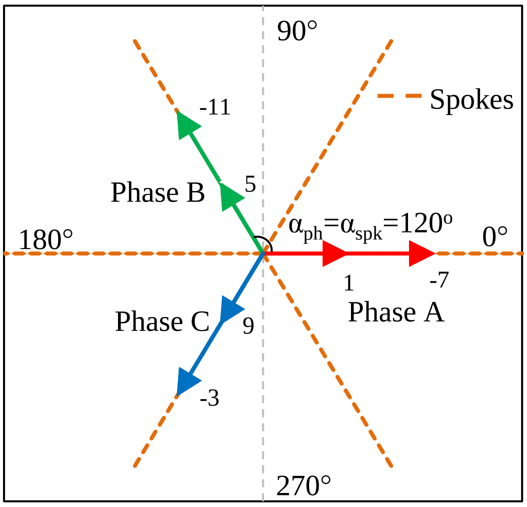

Figure 3.9. Star of slots 12S14P single layer

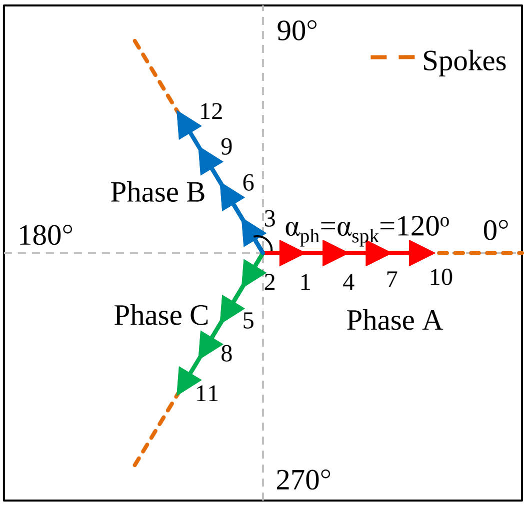

Figure 3.10. Star of slots 12S16P double layer

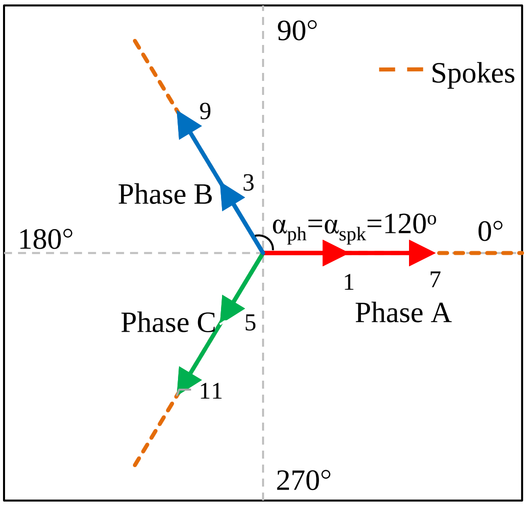

Figure 3.11. Star of slots 12S16P single layer

Figure 3.12 to 3.15 show the coil placement which resulted from the star of slots phasor diagrams for the single layer concentrated 3-phase winding topology. It can be observed that the negative phasor identifiers result in the coil being wound with a reverse polarity. In order to obtain the 3-phase duplex winding topology, coils A_1, B_1 and C_1 have been grouped to form Lane 1 and coils A_2, B_2 and C_2 are part of Lane 2.

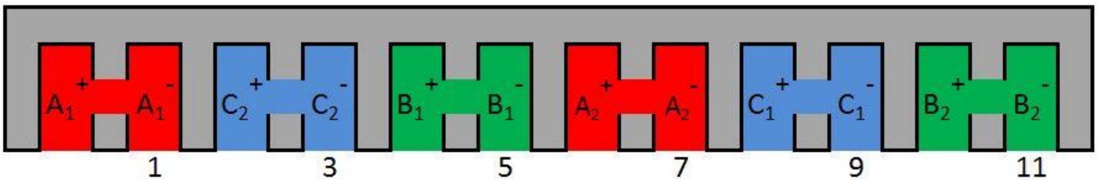

Figure 3.12. 12S8P single layer coil placement

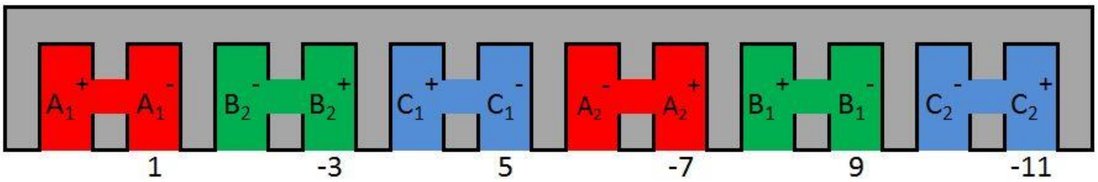

Figure 3.13. 12S10P single layer coil placement

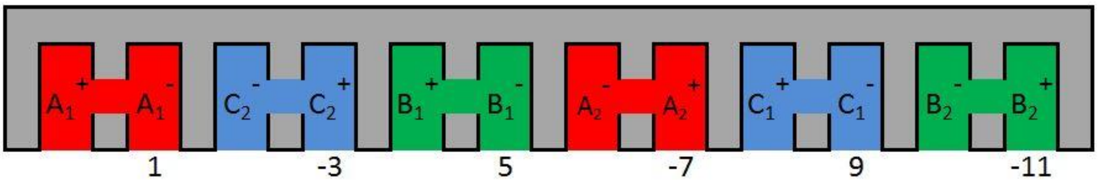

Figure 3.14. 12S14P single layer coil placement

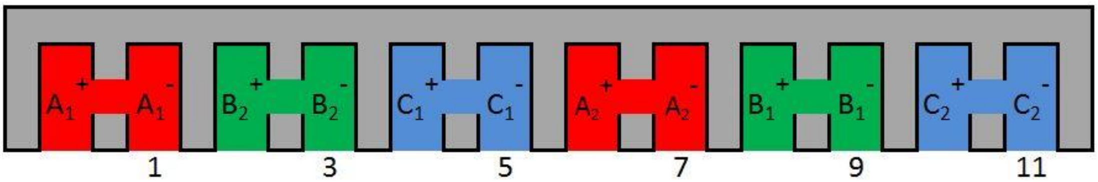

Figure 3.15. 12S16P single layer coil placement

The winding factor, k_w, can be calculated by considering the distribution factor, k_d, pitch factor, k_p, and skew factor k_{skw}, such that:

$$k_w = k_d k_p k_{skw} \tag{3.9}$$

For the selected slot-pole combinations shown in Table 3.2, no skewing was implemented on the inner high-speed rotor or stator such that:

$$k_{skw} = 1 \tag{3.10}$$

The distribution factor for the main EMF harmonic can be calculated based on the number of spoke per phase, q_{spk}, from the star of slots representation, such that:

$$k_d = \frac{\sin\left(\frac{q_{spk}\alpha_{spk}}{4}\right)}{\frac{q_{spk}}{2} sin\left(\frac{\alpha_{spk}}{2}\right)} \; for\; q_{spk} = even \tag{3.11}$$

$$k_d = \frac{sin\left(q_{spk}\frac{\alpha_{spk}}{4}\right)}{q_{spk} sin\left(\frac{\alpha_{spk}}{4}\right)} \; for\; q_{spk} = odd \tag{3.12}$$

where q_{spk} is the number of spokes per phase of the star of slots given by the phasor diagrams. The pitch factor, k_p, is calculated based on the slot pitch, s_p, and coil span angle, α_c, such that:

$$s_p = round\left\{\frac{N_s}{2p_h}\right\} \tag{3.13}$$

$$\alpha_c = \frac{2\pi p_h s_p}{N_s} \tag{3.14}$$

$$k_p = sin\left(\frac{\alpha_c}{2}\right) \tag{3.15}$$

where s_p lowest value is rounded to unity.

The distribution, pitch and winding factors for the selected fractional slot double and single layer winding topologies are shown in Table 3.4. It can be observed that the spokes of the double layer star of slots of the 12S8P and 12S16P topologies have both even and odd phasors. When the star of slots is converted to a single layer layout, the even phasors are removed and the spokes have only odd phasors. Thus, the number of spokes of the star of slots, and implicitly the distribution factor, does not change from double to single layer. In contrast, for the 12S10P and 12S14P the double layer star of slots has one phasor per spoke. When the single layer transformation is conducted, the spokes with even phasors are removed. Thus, the single layer star of slots has only half the number of phasors and spokes, and the distribution factor is increased. For all the factional slot-pole combinations, the pitch factor is only a function of the coil span angle and does not change from double to single layer. Hence the 12S10P and 12S14P have a 3.5% increase in the winding factor from double to single layer while the 12S8P and 12S16P have a constant winding factor.

Table 3.4. Winding factor for selected fractional slot pole combinations

Slot – pole	**Double layer**			**Single layer**		
	k_d	k_p	k_w	k_d	k_p	k_w
12S8P	1	0.866	0.866	1	0.866	0.866
12S10P	0.966	0.966	0.933	1	0.966	0.966
12S14P	0.966	0.966	0.933	1	0.966	0.966
12S16P	1	0.866	0.866	1	0.866	0.866

3.2.2 Integer slot-pole combinations

The integer slot-pole combinations which were identified as suitable for the duplex 3-phase winding configuration are shown in Table 3.5. Although such slot-pole combinations result in winding topologies with high winding factors, the distributed winding arrangement can result in large end winding lengths which would increase the phase resistance, motor active mass and manufacturing complexity and cost.

Table 3.5. Selected fault tolerant PDD integer slot-pole combinations

Stator slots (N_s)	12	24
HSR poles ($2p_h$)	4	8

Equation (3.4) was used to identify how many 3-phase lanes can be achieved using the integer slot-pole combinations from Table 3.5. Thus, the 12S4P can have two 3-phase lanes while the 24S8P can accommodate four 3-phase lanes. The latter slot-pole combination can be utilised with a duplex 3-phase winding topology by grouping the four lanes in pairs such that each 3-phase lane has two coils per phase in comparison to just one coil per phase on the 12S4P combination.

Figure 3.16 and 3.17 show the star of slots for the 12S4P and 24S8P single layer winding configurations. It can be observed that the two phasor representations have the same number of spokes but the number of phasors is doubled by doubling the number of stator slots and HSR poles.

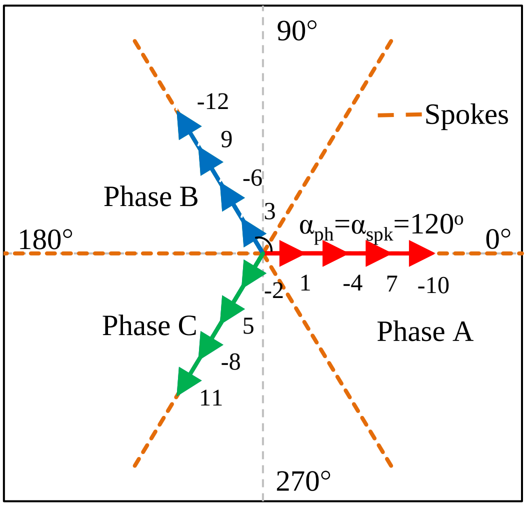

Figure 3.16. Star of slots 12S4P single layer

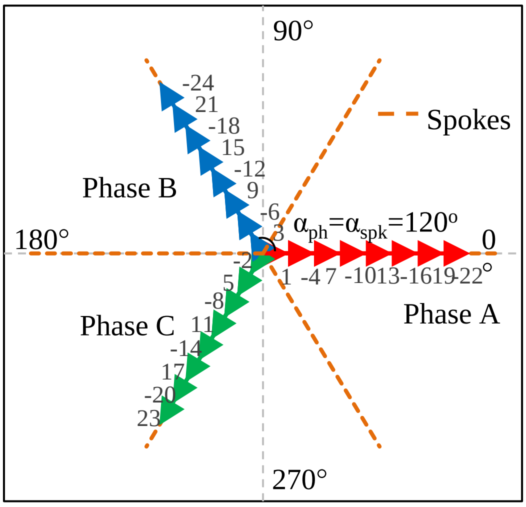

Figure 3.17. Star of slots 24S8P single layer

Figure 3.18 and 3.19 show the coil placement for the 12S4P and 24S8P 3-phase duplex winding topology. It can be seen that although the selected integer winding topologies have overlapping end-windings, the principle of physical, magnetic, electrical and thermal isolation are respected by grouping the coils into individual lanes. This ensures that the end-windings of Lane 1 are isolated from those of Lane 2. The main disadvantage of the 12S4P integer topology is represented by the fact that all the coils of Lane 1 are grouped together and occupy six consecutive slots with Lane 2 being housed in the remaining six slots. This configuration would have an increased unbalanced magnetic pull when operating in the Active-Passive mode due to the fact that only 1 lane is energised, creating an uneven magnetic flux distribution in the airgap. This issue is eliminated in the 24S8P topology as the two lanes are evenly distributed within the 24 slots.

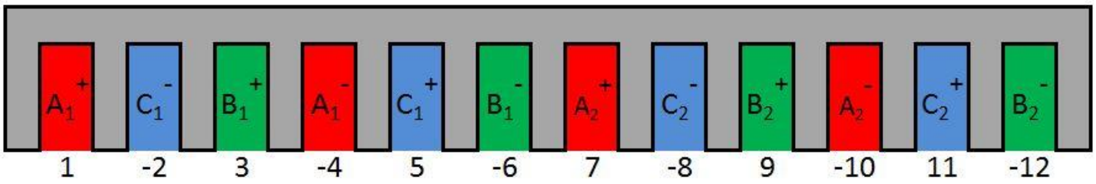

Figure 3.18. 12S4P single layer coil placement

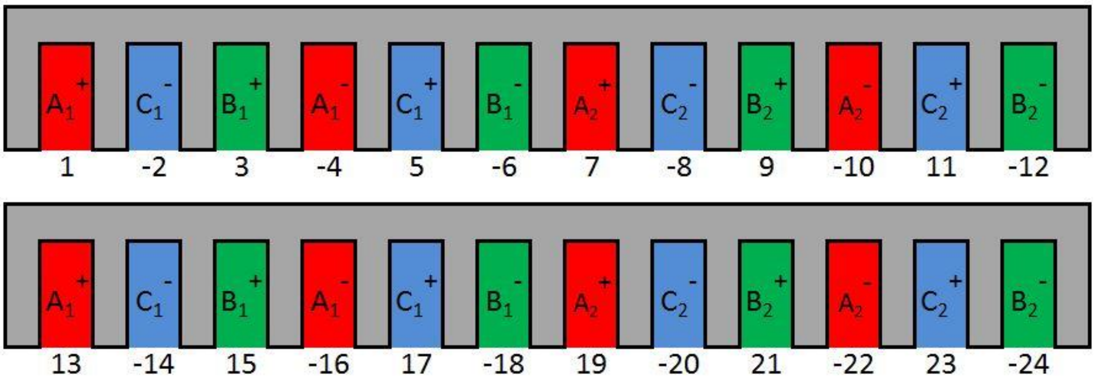

Figure 3.19. 24S8P single layer coil placement

Table 3.6 shows the distribution, pitch and winding factor of the integer slot winding topologies. It can be observed that the maximum possible winding factor is achieved.

Table 3.6. Winding factor for selected integer slot pole combinations

Slot-pole	**Single layer**		
	k_d	k_p	k_w
12S4P	1	1	1
24S8P	1	1	1

In conventional surface permanent magnet electrical machines, a high winding factor is beneficial as it can be used to either reduce the permanent magnet mass used to achieve a fixed flux linkage by reducing the radial magnet thickness or to reduce the active length of the machine and achieve a lighter design for the same copper loss as a longer, heavier design with a lower winding factor. Ultimately, by keeping the same magnet mass, a high winding factor can be used to reduce the copper loss and increase the efficiency of the conventional PM machine. In contrast, in a PDD motor the length is given by the maximum torque transmission capability of the magnetic gear element and changing the winding to achieve a higher winding factor does not bring similar PM or overall mass savings as in the case of conventional PM motors. In a PDD, a high winding factor would only bring efficiency and cooling benefits by increasing the winding flux linkage and reducing the copper loss. Hence, in the case of the PDD winding design, careful consideration must be given when selecting an integer versus a fractional slot winding. The integer slot would have a slightly higher winding factor by 3.5% -15.5% which would result in the phase current being reduced by 3.4% - 13.4%, when compared to a fractional slot topology. If the end-winding length is ignored, and the same phase resistance is assumed for both integer and fractional slot-pole topologies, the copper loss of the integer slot is reduced by 6.7% when compared to the copper loss of a single layer fractional slot with $k_w = 0.966$ and 25% when compared to the copper loss of a single layer fractional slot with $k_w = 0.866$. However, these benefits in copper loss over the fractional slot topology can be considerably reduced due to the larger coil span of 3 slots for the integer slot winding when compared to the 1 slot coil span of the fractional slot winding. Thus, the end-winding length and implicitly the phase resistance of the integer slot winding would be increased when comparing to the fractional slot topology.

3.3 Viable fault-tolerant PDD magnetic gear ratios

The PDD gear ratio selection was based on gear ratios which are compatible with the slot-pole combinations capable of accepting a duplex 3-phase winding topology.

3.3.1 Magnetic gear ratios and cogging torque factor

Having identified the viable slot-pole combinations in section 3.2, the number of high-speed rotor poles was fixed to either 8, 10, 14 or 16 poles. The gear ratio of the magnetic gear element integrated in the fault-tolerant PDD is dependent on the number of high-speed rotor pole pairs, p_h, number of ferromagnetic pole pieces, N_{pp}, and the number of pole pairs of the stator permanent magnet array, p_l. The selected PDD topology, Figure 3.20, assumes that the stator PM array is fixed to the stator teeth and acts as the earth for the magnetic gear transmission. In this configuration, the input rotor of the magnetic gear transmission is the inner HSR and the output rotor of the PDD is represented by the PPR, with both rotors rotating in the same direction. The gear ratio in this configuration is given by:

$$G_r = \frac{N_{pp}}{p_h} \tag{3.16}$$

where the number of ferromagnetic pole pieces is given by:

$$N_{pp} = p_h + p_l \tag{3.17}$$

Since the outer magnet array is fixed to the stator only two airgaps are required, between the HSR and PPR and between the PPR and stator magnets.

A large number of magnetic gear ratios, which are compatible with the fractional slot-pole combinations presented in Table 3.3, can be accommodated within the PDD architecture. Table 3.7 shows the multitude of viable PDD gear ratios based on the number of HSR pole pairs, stator PM pole pairs and number of pole pieces.

The cogging torque factor was introduced in [70] and [148] as a “goodness” factor with respect to the cogging torque and torque ripple of different slot – pole combinations for conventional PM machines and of different gear ratios of the PDD magnetic gear element.

The cogging torque between the HSR pole and stator slots is caused by the interaction between the HSR inter-pole region and the stator slot openings. The maximum amplitude of cogging torque occurs when the HSR inter-pole axis is aligned with the edges of the slot openings.

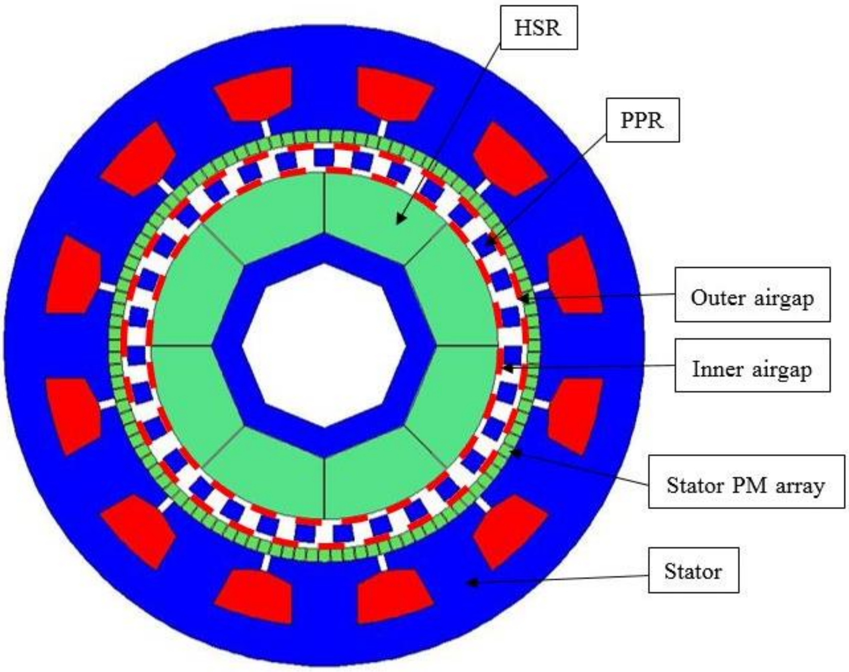

Figure 3.20. PDD with stationary stator PM array

The cogging torque factor between the HSR rotor and PDD stator is influenced by the number of poles of the rotor and number of stator slots, and given by:

$$C_T = \frac{2p_h N_s}{LCM(2p_h, N_s)} \tag{3.18}$$

Table 3.8 shows the cogging torque factor of the selected PDD slot-pole combinations. It can be observed that the fractional slot-pole combinations exhibit a lower cogging torque factor than the integer topology. Additionally, the slot-pole combinations which have a larger LCM are characterised by a reduced cogging torque factor.

Table 3.7. Viable magnetic gear ratios for fault tolerant PDD

HSR p_h	**Stator PM p_l**	**Pole pieces N_{pp}**	**Gear ratio G_r**
4	21	25	6.25
	24	28	7.00
	27	31	7.75
	30	34	8.50
	31	35	8.75
	35	39	9.75
	36	40	10.00
	39	43	10.75
5	27	32	6.40
	30	35	7.00
	33	38	7.60
	39	44	8.80
	45	50	10.00
	47	52	10.40
7	27	34	4.86
	41	48	6.86
	42	49	7.00
	55	62	8.86
8	31	39	4.88
	47	55	6.88
	48	56	7.00
	55	63	7.88

Table 3.8. Cogging torque factor of PDD slot-pole combinations

Stator slots N_s	HSR p_h	LCM $(2p_h, N_s)$	C_t
12	4	24	4
	5	60	2
	7	84	2
	8	48	4
24	4	24	8

The magnetic gear within the PDD is characterised by cogging torque between the HSR and PPR and cogging torque between the stator PM array and PPR. This is mainly due to the change in reluctance introduced by the modulating alternating magnetic and non-magnetic PPR structure. The cogging torque factors between the HSR-PPR, $C_{T_{in}}$ and PPR and stator PMs, $C_{T_{out}}$, are given by:

$$C_{T_{in}} = \frac{2p_h N_{pp}}{LCM\left(2p_h, N_{pp}\right)} \tag{3.19}$$

$$C_{T_{out}} = \frac{2p_l N_{pp}}{LCM\left(2p_l, N_{pp}\right)} \tag{3.20}$$

The cogging torque factors of the magnetic gear listed in Table 3.7, are shown in Table 3.9. For the selected HSR pole pairs, a large range of possible magnetic gear ratios exist. It can be seen that the cogging torque factors are equal and, compared to the non-integer gear ratios, the integer gear ratios have higher cogging torque factors. Thus, in order to effectively minimise the PDD output rotor cogging torque and torque ripple, only gear ratios having a cogging torque factor of 1 were considered during the optimisation of the fault tolerant PDD motor.

Table 3.9. Cogging torque factors of selected gear ratios

p_h	p_l	N_{pp}	G_r	$LCM\ (2p_h, N_{pp})$	$LCM\ (2p_l, N_{pp})$	$C_{T\,in}$	$C_{T\,out}$
4	21	25	6.25	100	525	1	1
	24	28	7.00	28	168	4	4
	27	31	7.75	124	837	1	1
	30	34	8.50	68	510	2	2
	31	35	8.75	140	1085	1	1
	35	39	9.75	156	1365	1	1
	36	40	10.00	40	360	4	4
	39	43	10.75	172	1677	1	1
5	27	32	6.40	160	864	1	1
	30	35	7.00	35	210	5	5
	33	38	7.60	190	1254	1	1
	39	44	8.80	220	1716	1	1
	45	50	10.00	50	450	5	5
	47	52	10.40	260	2444	1	1
7	27	34	4.86	238	918	1	1
	41	48	6.86	336	1968	1	1
	42	49	7.00	49	94	7	7
	55	62	8.86	434	3410	1	1
8	31	39	4.88	312	1209	1	1
	47	55	6.88	440	2585	1	1
	48	56	7.00	56	336	8	8
	55	63	7.88	504	3465	1	1

3.3.2 Initial sizing of PDD magnetic gear element

The fault tolerant PDD has to satisfy a total mass requirement while minimising the inertia of the output PPR. The embedded magnetic gear element of the PDD is characterised by a passive 'torque fuse' capability which causes the inner HSR to slip and effectively disengage from the remaining stages of the actuator drive train when an overload occurs on the control surface. This overload can be caused by sudden shock loads such as wind gusts or object strikes. Assuming an overload scenario, where the PDD actuator is in position control, and following a ramp position demand, an overload on the control surface would cause the integrated magnetic gear to reach its maximum torque transmission capability and harmlessly pole slip. Thus, the kinetic energy stored in the inner HSR is effectively isolated from the rest of the mechanical actuator drive train. In comparison, the output PPR is directly connected to the linear actuator screw. Hence, it is important to consider and minimise the inertia of the PDD output rotor in order to further ensure that the probability of mechanical jamming is reduced.

Figure 3.21 and 3.22 show a pultruded glass fibre beam PPR design typically employed in PDD motor. The ferromagnetic pole pieces are supported on either side by glass fibre rods which are connected to the castellated PPR endplates.

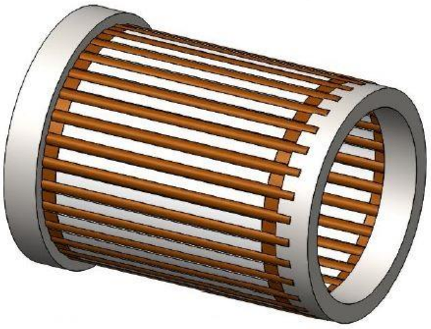

Figure 3.21. Pultruded beam PPR concept

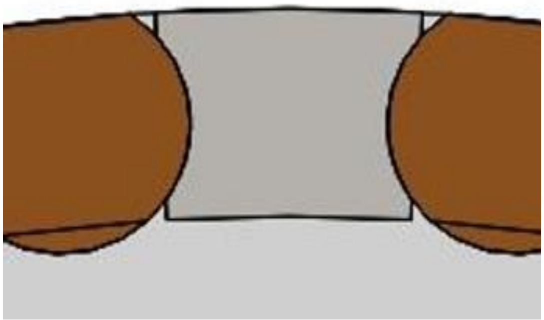

Figure 3.22. Cross-section of PPR concept

Assuming a 50/50 split between the ferromagnetic pole pieces and glass fibre support rods, the total inertia of the PPR can be calculated by considering the inertia of a hollow cylinder which is half made of pole pieces and the other half is represented by the glass fibre rods. Thus, the inertial components of the pole pieces, J_{PP}, and glass fibre support rods, J_{GF}, are given by:

$$J_{PP} = \frac{\pi}{4} \rho_{PP} L_{PDD} (R_{PPRo}^4 - R_{PPRi}^4) \tag{3.21}$$

$$J_{GF} = \frac{\pi}{4} \rho_{GF} L_{PDD} (R_{PPRo}^4 - R_{PPRi}^4) \tag{3.22}$$

where R_{PPRo} and R_{PPRi} are the outer and inner PPR radii, ρ_{PP} and ρ_{GF} are the densities of the pole piece M270-35A steel and glass fibre composite rods and L_{PDD} is the active length of the electrical machine.

The inertia of both PPR endplates, drive and non-drive end, J_{endp}, was calculated by assuming an endplate thickness of 5mm and is given by:

$$J_{endp} = \pi \rho_{al} L_{endp} R_{PPRo}^4 \tag{3.23}$$

where ρ_{al} and L_{endp} are the density of aluminium and thickness of the PPR endplate respectively. From (3.21) and (3.22) it can be observed that the inertia of the PPR is mainly influenced by the inner and outer radius of the PPR and active length of the machine, while the inertia of the rotor endplates is influenced by the outer radius of the PPR endplate and thickness of the endplate. In order to obtain an estimation of the PDD active length and calculate the corresponding PPR inertias, a range of PPR outer diameters were considered together with typical airgap shear stress values obtained from PDD machines presented in literature [83]. The active length L_{PDD} can be expressed as a function of the rated machine output torque, T_{rated}, PPR outer diameter, D_{PPRo}, and PPR airgap shear stress, σ_{PPR} such that:

$$L_{PDD} = \frac{2T_{rated}}{\pi \sigma_{PPR} D_{PPRo}^2} \tag{3.24}$$

For a fixed PDD maximum slip PPR torque of 10.3Nm, Figure 3.23 shows the variation of PDD active length with PPR outer diameter and outer airgap shear stress. It can be observed that for a fixed PPR diameter, a design with a low airgap shear stress would produce an increase in the active length of the PDD motor. For a fixed achievable airgap shear stress, the active length is reduced as the PPR outer diameter is increased.

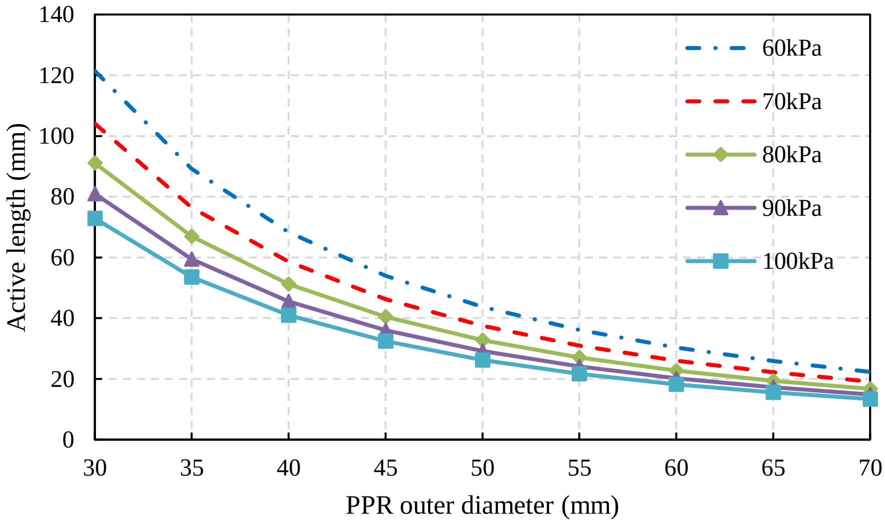

Figure 3.23. Variation of PDD active length and PPR outer diameter with airgap shear stress

Figure 3.24 shows the variation of the PPR inertia with the PPR airgap shear stress and outer diameter for a range of pole piece radial lengths. It can be seen that for a fixed airgap shear stress and pole piece radial length, the inertia of the output PDD rotor is rapidly increased by an increase of the PPR outer diameter. For example, for an airgap shear stress of 80kPa with a 2mm radially thick pole piece, the inertia of the PPR is increased by a factor of 6 from 30mm to 70mm outer rotor diameter. If the PPR outer diameter and pole piece radial thickness are fixed, the inertia of the output rotor is only slightly increased when the PPR airgap shear stress is reduced. Thus, motor designs which are characterised by a low airgap shear stress for a fixed rotor diameter would have an increased active length and thus increase the inertia of the PPR. For example, for a PPR diameter of 50mm and radial pole piece thickness of 2mm, the inertia of the output rotor is only increased by a factor of 1.38 when the PPR airgap shear stress is reduced from 100kPa to 60kPa. In addition, an increase in the pole piece radial length, assuming a fixed airgap shear stress and PPR outer diameter, would also bring an increase in the PPR inertia. As an example, for a PPR outer diameter of 50mm and 80kPa airgap shear stress, the inertia is increased by a factor of 2.1 when the pole piece radial thickness is increased from 2mm to 8mm.

Thus, it can be concluded that, for a fixed pole piece thickness, the increase in PPR inertia is mainly dominated by the increase in rotor outer diameter, which is expected since in (3.21) and (3.22) the inertia is proportional to the rotor radius term to the power of four. In comparison, achieving a high airgap shear stress would minimise the active length of the machine for a fixed output torque, reducing the PPR inertia by the same percentage, since the inertia and machine active length are proportional.

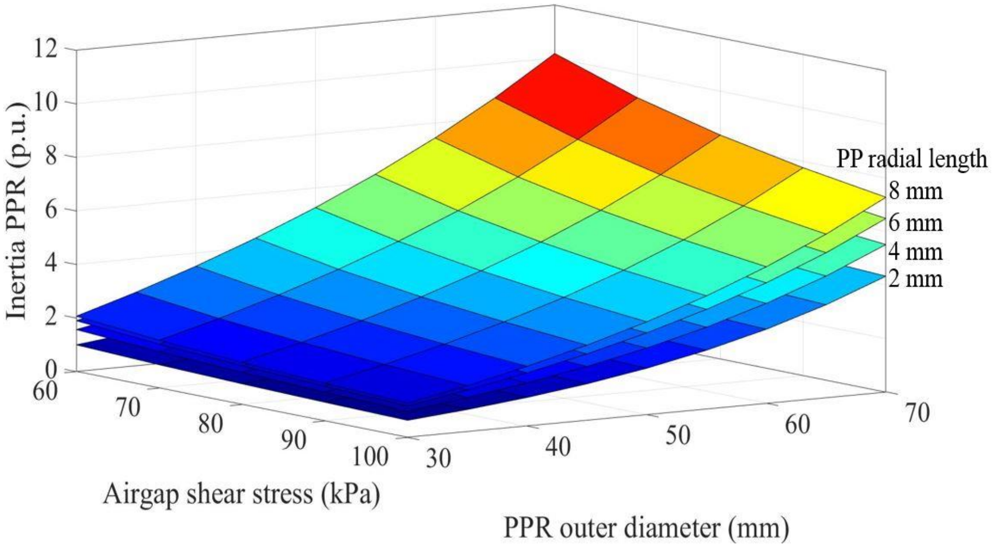

Figure 3.24. Variation of PPR inertia with PPR airgap shear stress and outer diameter

3.3.3 Influence of gear ratio on pole piece and outer magnet design

From the initial sizing of the magnetic gear element presented in Figure 3.23, it can be observed that a relatively small PPR diameter is required to produce a machine design capable of achieving the required pull-out torque. For the selected HSR pole numbers, it can be observed in Table 3.7 that increasing the gear ratio means increasing the number of pole pieces and outer magnets. This means that for a fixed diameter of the PPR and outer magnet array, a design with a higher gear ratio would require an increasingly small pole piece and outer magnet width. Hence, careful consideration needs to be given when selecting the gear ratio such that the resulting machine design can be successfully manufactured.

For the selected PDD gear ratios, Figure 3.25 to 3.28 show the variation of the pole piece width for a range of PPR outer diameters.

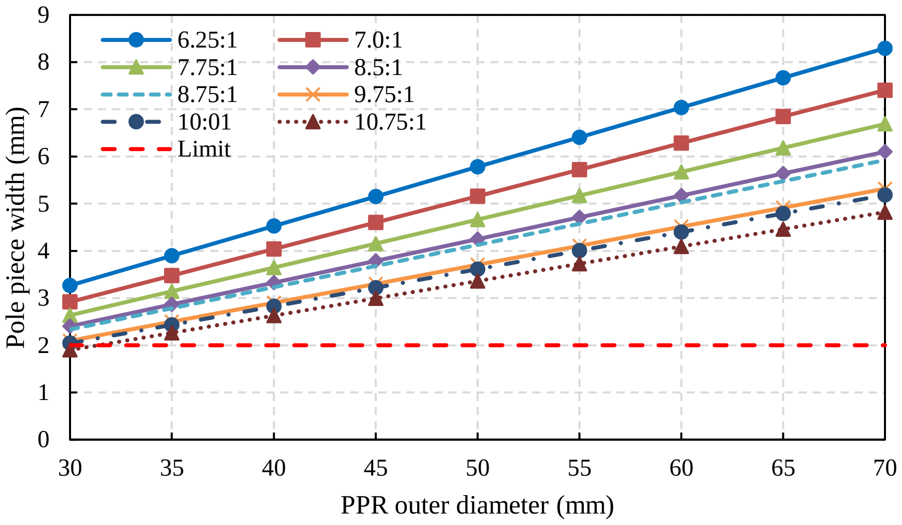

Figure 3.25. Variation of pole piece width for $p_h = 4$

As the number of pole pairs on the HSR is increased, the number of pole pieces required to achieve a similar gear ratio, as for a lower number of HSR pole pairs, is increased. For a 2mm pole piece width limit, for 7 pole pairs of the HSR, an 8.86:1 gear ratio can be implemented only if the PPR outer diameter is larger than 45mm. In comparison, for $p_h = 8$, an even larger number of pole pieces is required in order to achieve similar gear ratio and the PPR outer diameter has to be increased even further.

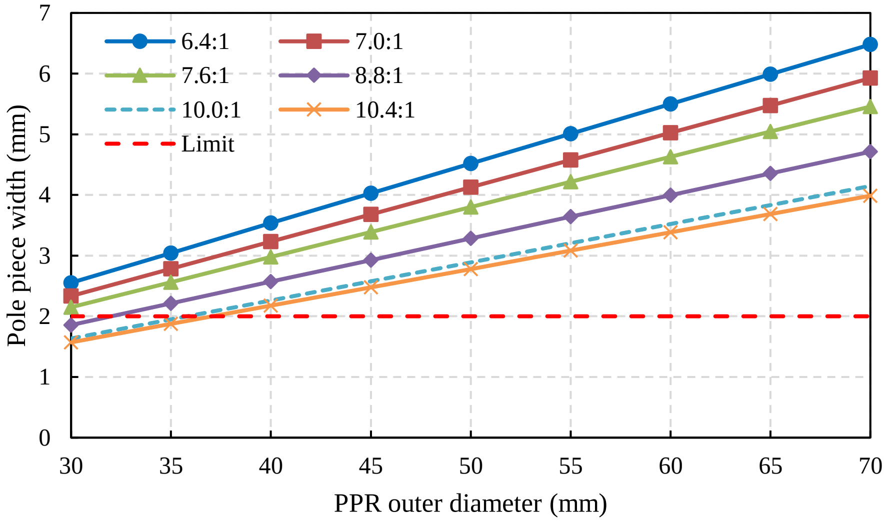

Figure 3.26. Variation of pole piece width for $p_h = 5$

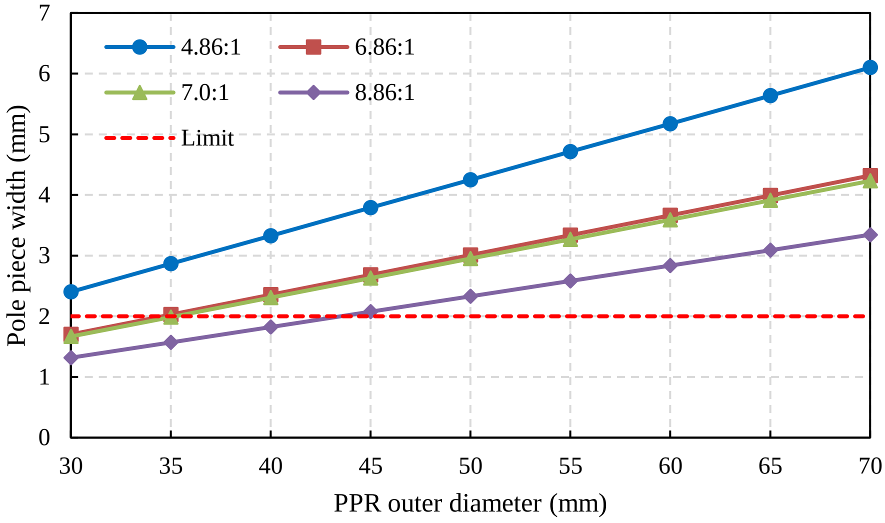

Figure 3.27. Variation of pole piece width for $p_h = 7$

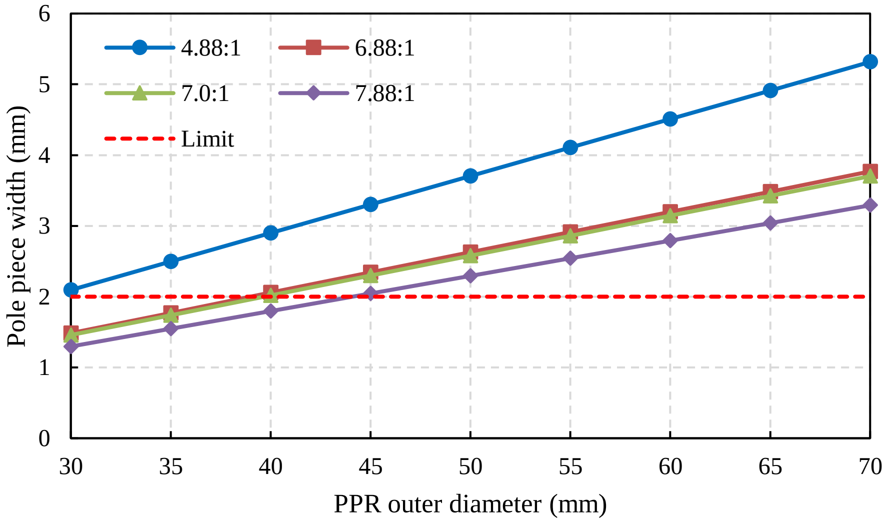

Figure 3.28. Variation of pole piece width for $p_h = 8$

The stator outer magnet array can be implemented as a conventional radial or a Halbach array. For the magnetic gear ratios presented in Table 3.7, it can be observed that the number of individual outer magnets is rapidly increased when the gear ratio and pole pair number of the HSR are increased.

Figure 3.29 to 3.32 show the variation of the width of a single stator magnet for different number of HSR pole pairs and different gear ratios, while considering a Halbach stator

PM array with four individual PM blocks per pole pair. Since the outer magnet array is fixed to the stator teeth and is not required to transmit torque, the limit for the magnet width was set to 1mm. The outer magnet array inner diameter was derived from the PPR outer diameter assuming a 0.5mm airgap. For four HSR pole pairs, the outer magnet width drops below 1mm for gear ratios ranging from 7.75 to 10.75:1 when the inner diameter of the outer magnet array is between 30 to 45mm. By increasing the number of HSR pole pairs while achieving similar gear ratios, a larger number of possible designs fall below the limit. For 8 pole pairs of the HSR, the gear ratios above 4.88:1 do not meet the limit of outer magnet width, even at large outer magnet array diameters.

In conclusion, the limiting factor to achieving a high gear ratio from a manufacturing point of view is represented by the number of pole pieces and stator permanent magnets. Increasing the HSR pole pairs while achieving a high gear ratio aggravates the issue of thin pole pieces and outer magnets for small PDD motors.

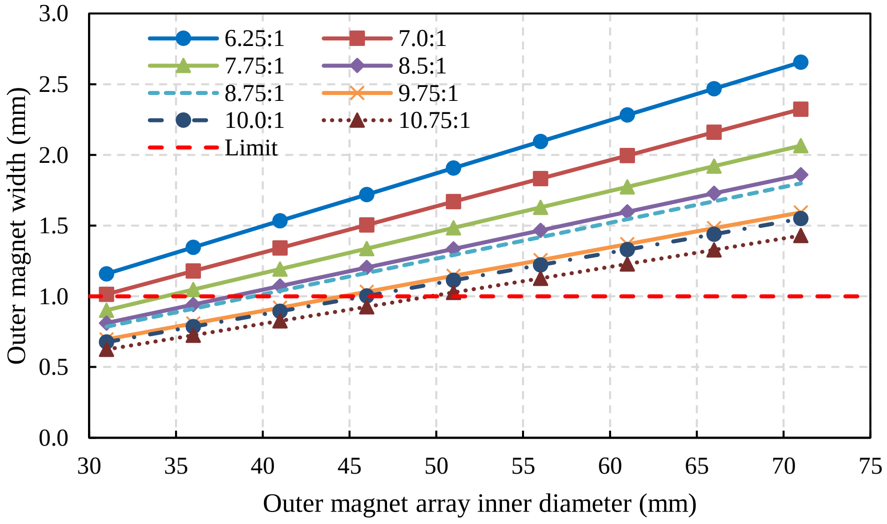

Figure 3.29. Variation of outer magnet width for $p_h = 4$

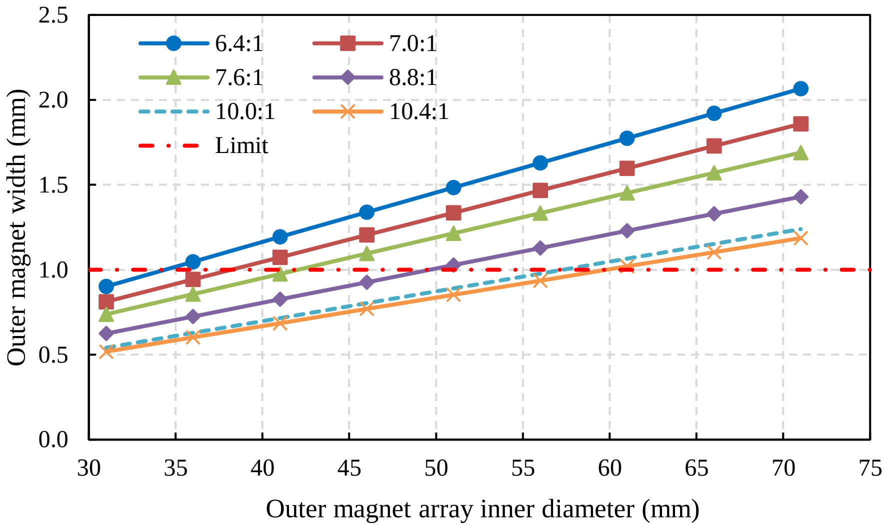

Figure 3.30. Variation of outer magnet width for $p_h = 5$

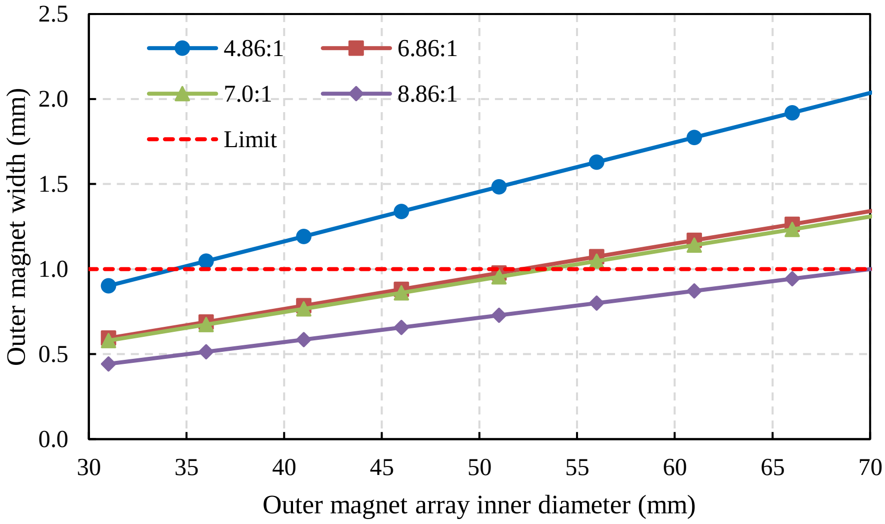

Figure 3.31. Variation of outer magnet width for $p_h = 7$

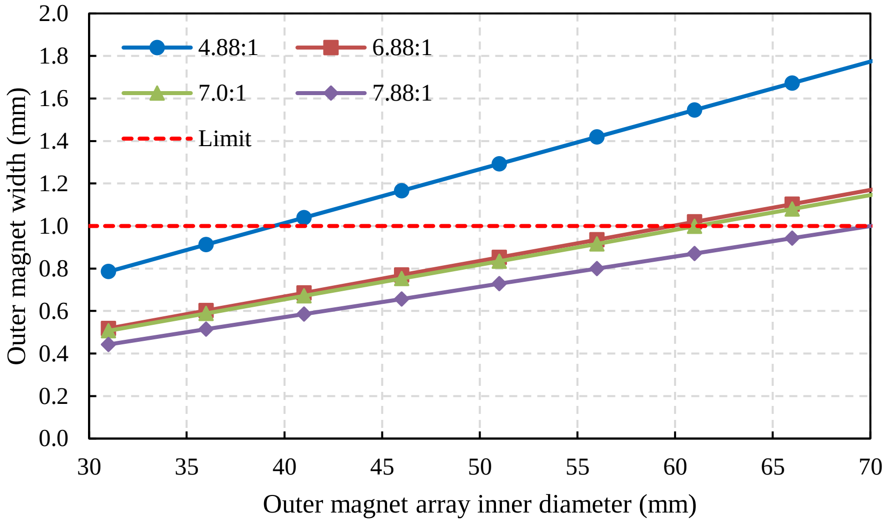

Figure 3.32. Variation of outer magnet width for $p_h = 8$

3.3.4 Influence of gear ratio on HSR PM retention sleeve

In a PDD motor, due to the embedded magnetic gear transmission, the inner HSR can rotate with an angular velocity several times higher than the output rotor. For example, in the case of a PDD that meets the actuator motor output speed requirement of 1200rpm, having a magnetic gear ratio of 10:1, the inner HSR would reach 12000rpm. Due to the geared high rotational velocity of the HSR, a high centrifugal force is developed which acts on the HSR permanent magnets, tending to move them away from the steel hub. This centrifugal force is a reaction force which is opposed to the centripetal force that pulls the rotating body towards the centre of the circle described by the rotating pattern.

For a conventional surface permanent magnet rotor, the first magnet retention mechanism is given by the adhesive holding the permanent magnets onto the surface of the rotor hub. However, in order to ensure the PMs are not allowed to move and lift away from the hub in the case of glue bond failure, a secondary retention system is often employed for high speed machines. The proposed magnet retention system for the PDD actuator motor consists of a composite over-banding magnet retention system designed to provide a force onto the magnets, acting towards the centre of rotation. This force should have a sufficient amplitude in order to prevent the magnet from lifting away from the surface of the HSR hub throughout the speed operating range of the electrical machine. In order to create this force, a pre-stress is applied to the composite fibres as they are wound on the outer surface of the HSR PMs. This pre-stress must always be greater than the centrifugal force developed during rotor rotation at maximum angular velocity. If this condition is not met, the HSR magnets could lift away from the HSR hub surface and create an uneven stress distribution in the composite sleeve. Depending on the rotating velocity, immediate failure might not occur, but the HSR PMs could become free to move on the surface of the HSR hub which could result in a premature failure.

The thickness of the HSR banding can be calculated based on the target pre-stress applied to the composite banding during winding onto the surface of the HSR PMs.

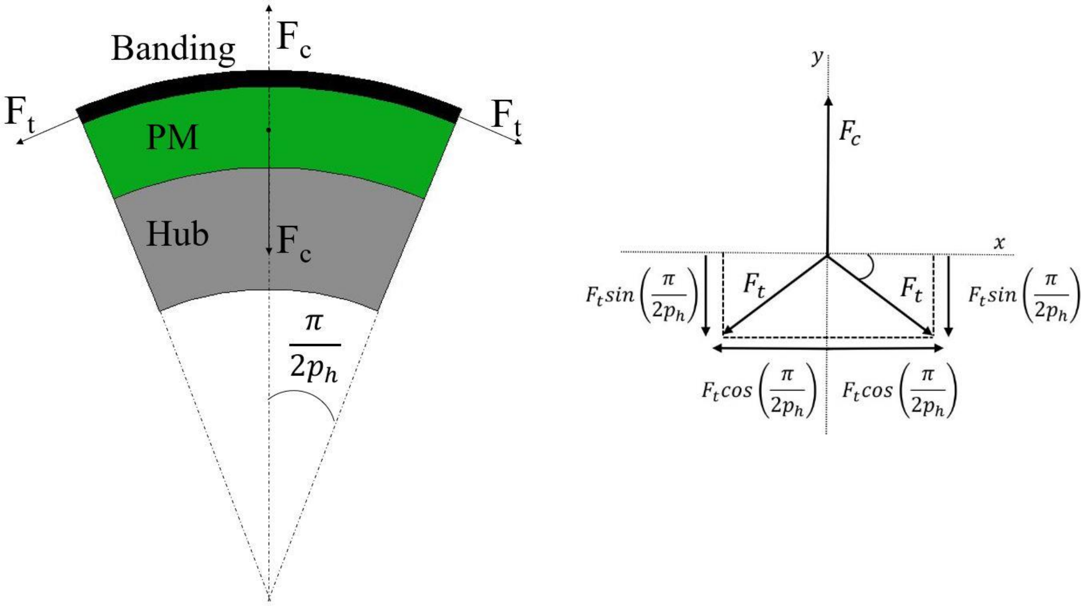

(a) (b)

Figure 3.33. HSR pole section (a) topology (b) resolved forces

Figure 3.33 shows one pole of the HSR hub-magnet assembly with the resultant centrifugal and banding tension forces. It is assumed that the magnet section has no magnetic attraction to the HSR hub or other components. The outer PM surface is assumed to be smooth, cylindrical such that no uneven high stress concentration is induced in the banding layer. The banding layer is assumed to have zero density since the mass of the banding is considerably smaller than the mass of the PM block. In order to calculate the thickness of the banding layer, the forces acting on the PM block and banding layer need to be resolved on the X and Y axes.

Thus, the sum of forces on the X-axis, for a tensile force, F_t, developed in the banding layer as a result of the centrifugal force, F_C, can be resolved such that:

$$\sum F_x = 0 \tag{3.25}$$

The sum of forces on the Y-axis can be resolved such that:

$$\sum F_y = 0 \tag{3.26}$$

$$F_c = 2F_t sin\left(\frac{\pi}{2p_h}\right) = M_{pole}R_{cog}\omega_h^2 \tag{3.27}$$

where M_{pole}, R_{cog} and ω_h are the mass of the PM block, radius of the centre of gravity of the PM block and rotational velocity of the HSR, respectively.

The mass of the cylindrical PM block can be calculated based on the mass of a hollow cylinder segment such that:

$$M_{pole} = \frac{\rho_{PM}\pi L_{PDD}(R_o^2 - R_i^2)}{2p_h} \tag{3.28}$$

where ρ_{PM}, R_o and R_i are the density of the permanent magnet material, outer and inner radius of the magnet cylindrical segment, respectively.

The radius of the centre of gravity of the permanent magnet segment is given by:

$$R_{cog} = \frac{2}{3}\frac{(R_o^3 - R_i^3)}{(R_o^2 - R_i^2)}\frac{sin\left(\frac{\pi}{2p_h}\right)}{\left(\pi/_{2p_h}\right)} \tag{3.29}$$

From (3.27), (3.28) and (3.29) the tensile force in the HSR banding layer can be calculated as:

$$F_t = \frac{\rho_{PM} L_{PDD} (R_o^3 - R_i^3)\omega_h^2}{3} \tag{3.30}$$

From (3.30) it can be observed that the tensile force is heavily influenced by the outer and inner radii of the HSR PMs, as well as the rotational velocity of the HSR.

The resultant stress in the banding layer, σ_r, can be calculated as the ratio between the tensile force and cross-section area of the banding layer, such that:

$$\sigma_r = \frac{\rho_{PM}(R_o^3 - R_i^3)\omega_h^2}{3x} \tag{3.31}$$

Thus, the radial thickness, x, of the banding layer is given by:

$$x = \frac{\rho_{PM}(R_o^3 - R_i^3)\omega_h^2}{3\sigma_r} \tag{3.32}$$

The resultant stress in the banding layer, σ_r, can be expressed as a function of the target pre-stress, σ_w, applied to the composite during the winding operation, such that:

$$\sigma_r = K\sigma_w = K\frac{P\gamma}{N_f \pi \left(^{d_f}/_2\right)^2} \tag{3.33}$$

where K is the knock-down factor representing the fibres that are lost during winding/curing, P is the pre-tension applied to the tow of the banding fibre during winding, N_f is the fibre count of the tow, γ is the fill factor of the fibre in the composite banding layer and d_f is the individual fibre diameter.

By substituting (3.33) in (3.32), the thickness of the banding layer required to achieve the target pre-stress σ_w is given by:

$$x = \frac{\pi \rho_{PM} (R_o^3 - R_i^3) \omega_h^2 N_f \left({}^{d_f}/_{2} \right)^2}{3KP\gamma} \tag{3.34}$$

It can be observed that the thickness of the banding layer is highly influenced by the outer diameter and thickness of the HSR PMs as well as the rotational velocity of the HSR. Thus, in a PDD it can be said that a high magnetic gear ratio will increase the thickness of the banding layer for a fixed output PPR velocity. The tension, P, applied to the tow is limited by the pull force supplied by the banding rig used to feed the tow of the surface of the HSR. A high tension can be used to minimise the thickness of the PM retention layer, as long as it is within the tensile strength limit of the banding material

For the fault tolerant PDD actuator motor, an aerospace approved carbon fibre, designed for filament winding, was identified as suitable for banding the HSR. Table 3.10 shows the physical properties of the carbon fibre tow used in the banding thickness calculation.

Due to the prototype nature of the fault-tolerant PDD combined with manufacturing tolerances during banding and grinding operations, a high safety factor of 5 was used to calculate the banding thickness values [149]. For a prototype demonstrator, a high safety factor is recommended in order protect against unforeseen shock or cyclic loads during final assembly and testing under abnormal conditions.

Table 3.10. Hextow AS4C carbon fibre properties

Fibre property	**Value**	**Units**
No. of filaments – N_f	6000	-
Tensile strength	4447	MPa
Ultimate elongation at failure	1.7%	-
Density	1.78	g/cm^3
Weight/Length	0.4	g/m
Filament diameter - d_f	6.9	μm
Tow cross-sectional area	0.22	mm^2
Knock down factor – K	0.9	-
Tension applied to tow – P	177 (18)	N (kg)
Fill factor of banding layer post cure - γ	0.7	-

Figure 3.34 shows the variation of the carbon fibre banding thickness with the HSR outer diameter for a range of magnetic gear ratios for a fixed PM radial thickness of 10mm. As expected, an increase in the rotor outer diameter would increase the centripetal load acting on the PM blocks, increasing the thickness of the banding for a fixed tension of 177 N applied during winding. The high magnetic gear ratios also cause an increase in the banding thickness due to the high resulting HSR rotational velocity for a fixed PPR output speed requirement. Figure 3.35 shows the variation of the HSR banding thickness with HSR outer diameter for a range of PM radial thicknesses for a fixed gear ratio of 7.75:1. As the magnet thickness is increased for a fixed rotor outer diameter, the tension required to counteract the centrifugal force is increased. Thus, even for medium rotor diameters between 40 to 50 mm, a banding thickness between 0.1 – 0.3 mm is required in order to safely meet the output velocity requirements of the actuator PDD motor. This represents an important proportion of a typical physical airgap of 0.5 mm and needs to be considered during the electromagnetic design of the PDD motor.

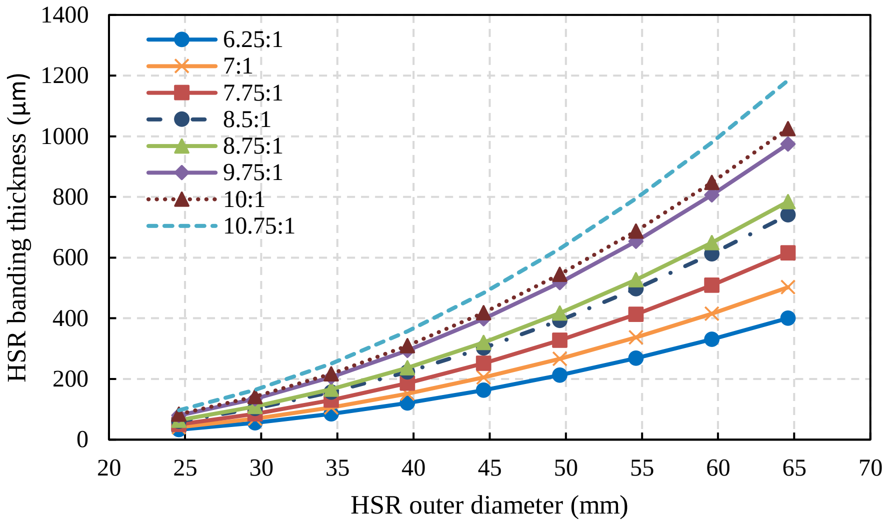

Figure 3.34. Variation of HSR banding thickness with rotor outer diameter and gear ratio

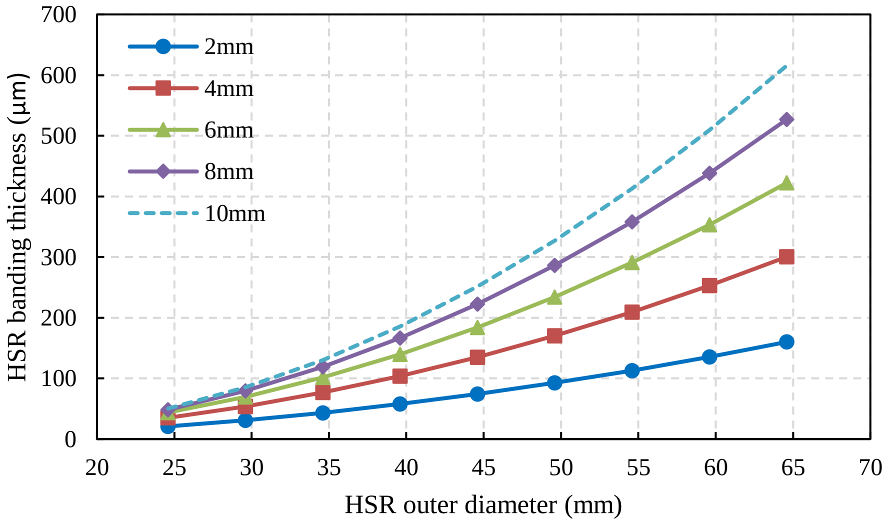

Figure 3.35. Variation of HSR banding thickness with rotor outer diameter and magnet thickness

3.4 Conclusions

The reliability of different winding topologies, with the associated power stage and control electronics, was evaluated based on the failure rate of each component. It was shown that the duplex 3-phase winding topology, controlled by two independent 3-phase power inverters, achieves the lowest hazard rate.

Several fractional and integer slot-pole combinations, capable of accepting the duplex 3-phase winding topology, while respecting the principles of electrical, magnetic, physical and thermal isolation, have been identified as suitable for the proposed PDD actuator motor. Based on the selected high-speed rotor pole count, different magnetic gear ratios, characterised by low cogging torque factors, can be implemented. It is shown that, for a fixed number of HSR poles, increasing the magnetic gear ratio results in an increase in the number of pole pieces and stator permanent magnets. Furthermore, for a fixed magnetic gear ratio, the number of pole pieces and stator permanent magnets is increased with the HSR pole number. Thus, PDD designs with high magnetic gear ratios can results in narrow pole piece and stator PM cross-sections, which can increase the manufacturing and assembly complexity.

The initial sizing of the PDD motor was based on a range of output rotor diameters and values of outer airgap shear stress. It is shown that, for a fixed value of airgap shear stress, increasing the PPR outer diameter results in a decrease in the active length of the machine. The inertia of the PDD output rotor was analytically predicted as a function of outer airgap shear stress and PPR outer diameter, for a range of pole piece thicknesses. It is concluded that, for a fixed pole piece thickness, the increase in PPR inertia is dominated by the rotor outer diameter. Moreover, for a fixed output torque requirement, achieving a high airgap shear stress would minimise the machine active length, mass and output rotor inertia.

An analytical procedure was proposed for approximating the thickness of the banding layer required to secure the HSR PMs. It is shown that, for a fixed banding tension applied to the overwrapping filament, the thickness of the retention layer is increased with the magnetic gear ratio and thickness of the HSR PMs.

Chapter 4: Electromagnetic design of PDD for high torque density and low output inertia

The electromagnetic design of the PDD was focused on achieving a high torque transmission capability of the magnetic gear element with a low output rotor inertia, while maximising the stator flux linkage. In order to achieve this, several PM topologies for the HSR and stator PM arrays, together with different pole piece cross-sections have been investigated and compared.

4.1 Comparison of radial and Halbach magnetised PM arrays for PDD motor

The torque density and mass of a PDD motor is mainly influenced by the torque transmission capability of the magnetic gear element. For a fixed output motor rated torque requirement and a fixed machine outer diameter, the active length of the PDD motor is calculated based on the peak transmission torque of the embedded magnetic gear.

In literature, several magnetic gear and PDD motor designs having radially magnetised PM arrays capable of high torque densities, between 60-240 kNm/m^3 have been proposed [69], [71], [73], [80], [81], [84], [142]. The electrical machine designs achieve the high torque density due to the relatively large PPR diameter, which would not satisfy the inertia and mass requirements of the aerospace actuator. Thus, at low PPR and HSR diameters it is important to consider employing Halbach PM arrays on the HSR and stator magnets in order to increase the torque density, reduce rotor inertia and obtain a satisfactory amplitude of the stator winding flux linkage fundamental field component.

The Halbach permanent magnet array was first introduced in 1980 by K. Halbach in [150], where a design was presented for a 4 pole discrete Halbach rotor capable of achieving a high sinusoidal flux distribution.

A review of electrical machines with Halbach PM array was conducted by the authors of [151]. It was established that employing such an array would result in a near sinusoidal airgap flux distribution and EMF and reduced cogging torque. The self-shielding magnetisation pattern of the Halbach PM array was also found to reduce the magnetic flux density in the rotor steel hub, thus allowing for a thinner rotor base, reducing the mass and inertia of the rotor.

Several high speed SPM electrical machines have been presented in literature with Halbach PM rotors which are used for achieving a strong multi-pole near sinusoidal field distribution in the airgap of electrical machines while reducing cogging torque and torque ripple as the airgap field harmonics which produce torque ripple are reduced and the main harmonic used for torque production is increased [152]–[155]. Several authors have employed the Halbach PM array in magnetic gears, achieving an increase in the maximum torque transmission capability and torque density while reducing the torque ripple of the output rotor [156]–[160]. The authors of [161] have compared a radial field magnetic gear design employing radial and Halbach magnetisation. It was concluded that, for the same volume of permanent magnet material, the torque density of the Halbach variant was higher by 13% while the combined iron losses in the HSR hub, ferromagnetic pole pieces and stator laminations were reduced by 28% and cogging torque on the output rotor was reduced by 67%.

Due to the near sinusoidal airgap field distribution, the Halbach array can be employed in high speed electrical machines to reduce the overall loss and increase torque density. The authors of [162] have shown that for a rotor stainless steel sleeve designed to secure the PM blocks during high speed operation, the Halbach array can reduce the eddy current losses in the sleeve by 24% for the same PM volume when compared to a radially magnetised rotor. The authors also presented the demagnetisation behaviour of the radial and Halbach rotor under 3-phase symmetrical short circuit. It was concluded that the Halbach array has a reduced demagnetisation susceptibility due to the self-shielding magnetisation and a significantly higher working point than a radially magnetised PM rotor array.

The manufacturability of Halbach PM arrays has also been considered by the authors of [163] and [164]. It was concluded that although an ideal Halbach array has a perfect sinusoidal flux distribution, it is difficult and expensive to manufacture. Thus, discrete Halbach PM arrays, with multiple PM blocks per pole with radial and circumferential magnetisation directions, are considered to be a compromise between reducing the manufacturing costs and slightly increasing THD of the airgap field distribution and torque ripple when compared to an ideal Halbach PM array [165]–[167].

In order to study the effect implementing different permanent magnet topologies for the PM arrays of the PDD actuator motor, four slot-pole combinations compatible with the duplex 3-phase fault tolerant winding have been selected. Due to the large number of possible combinations of ferromagnetic pole pieces and stator PM poles, the magnetic gear ratio was limited to one value for each slot pole combination. Table 4.1 shows the selected slot pole combinations and corresponding magnetic gear ratios.

Table 4.1. PDD topologies selected for PM topology investigation

Slot-pole	**HSR p_h**	**PPR N_{pp}**	**Stator PM p_l**	**Gear ratio G_r**
12S8P	4	31	27	7.75 : 1
12S10P	5	38	33	7.60 : 1
12S14P	7	49	42	7.00 : 1
12S16P	8	63	55	7.88 : 1

For each of the slot pole and gear ratio combinations in Table 4.1, four different PM arrays combinations have been considered, with Halbach on the HSR and Halbach on the stator PMs, Halbach on the HSR – radially magnetised PMs on the stator, radially magnetised PMs on the HSR – Halbach on the stator PMs and both HSR and stator PM arrays with radial magnetisation. The Halbach PM arrays for the HSR and stator PMs were limited to two PM blocks per pole. The magnetisation angle difference between the radial and circumferential PMs was fixed at 90 degrees. The PM material used throughout this investigation was Recoma 28 with the magnetic remanence, B_r, set to 1.10 for an operating temperature of 20^{o}C and a maximum energy product of 225 kJ/m^3. Table 4.2 shows the PDD parameters used in the PM array topology investigation. In order to achieve a fair comparison of the electromagnetic performance, the outer diameter of the PPR was fixed to 45mm with a radial thickness of the ferromagnetic pole pieces of 2mm. The ratio between the ferromagnetic pole piece arc and neighbouring non-magnetic support was fixed to 1.

The 2D electromagnetic finite element software, Opera from Cobham, was used to simulate the PDD in its various configuration, using the transient electromagnetic analysis solver. The outputs compared in this PM array topology investigation are represented by the average PPR pull-out torque and peak stator flux linkage.

The average PPR pull-out torque represents the maximum torque transmission capability of the embedded magnetic gear element of the PDD. Achieving an electromagnetic design of the magnetic gear components such that the PPR pull-out torque is maximized is a key aspect in ensuring a low mass and high torque density design with a reduced output rotor inertia. In contrast, in order to maximise the stator flux linkage and improve efficiency, the overall airgap between the HSR PMs and stator teeth needs to be minimised. Thus, a trade-off can be obtained between maximising the pull-out torque of the magnetic gear element and increasing the flux linkage of the PM motor element.

Table 4.2. PDD parameters

PDD parameter	Range	Increment
HSR PM radial thickness (mm)	4 – 12	+1
HSR Halbach ratio	0.5 – 5	+0.5
Pole piece radial thickness (mm)	2	-
PPR outer diameter (mm)	45	-
Stator PM thickness (mm)	1 – 3	+0.5
Stator Halbach ratio	1	-
Inner airgap (mm)	0.7	-
Outer airgap (mm)	0.7	-
Slot depth (mm)	6.5	-
Stator back iron thickness (mm)	3.5	-
Tooth tip thickness (mm)	1.8	-
Tooth width (mm)	7.0	-
PM remanence B_r (T)	1.10	-
PM coercivity H_c (kA/m)	800	-

The no load stator magnetic loading per unit length is given by the product of pole pairs of the HSR and d-axis flux linkage component, such that:

$$w_m = p_h \psi_d \tag{4.1}$$

The Halbach ratio, R_{hlb} was defined as the ratio between the arc lengths of the radial and circumferential PM blocks such that:

$$R_{hlb} = \frac{\theta_{Rad}}{\theta_{Circ}} \tag{4.2}$$

4.1.1 Halbach PM topology for HSR and stator PM arrays

For the PDD parameters shown in Table 4.2, and for a fixed radial thickness of the stator PMs of 1.5mm, Figure 4.1 shows the variation of the maximum PDD output pull-out torque for the 12 slot 8 pole configuration with Halbach PM arrays on both the HSR and stator bore. Figure 4.2 shows the corresponding peak stator magnetic flux linking the windings. It can be observed that for a fixed Halbach ratio, both the pull-out torque and peak stator magnetic loading are increased with the HSR PM radial thickness. Increasing the HSR PM thickness over 10mm does not bring substantial benefits in terms of pull-out torque capability of the magnetic gear element. The optimal Halbach ratio for maximum pull-out torque and magnetic loading was identified as being 1 for all the HSR and stator PM thicknesses. Figure 4.3 and 4.4 show the variation of the PPR pull-out torque and peak stator magnetic loading with the stator PM radial thickness, for a unity Halbach ratio of the HSR PM array. It can be observed that increasing the stator PM thickness increases the torque transmission capability of the magnetic gear element, reducing the overall length and mass of the machine for a fixed output torque. In contrast, this increase in stator PM thickness acts to increase the overall airgap between that HSR PMs and stator teeth, which reduces the HSR flux linking the stator winding, reducing the stator magnetic loading and increasing the electrical loading and copper loss at the cost of reducing the overall motor efficiency. Thus, for the fault tolerant actuator PDD motor, a compromise has to be made between achieving a torque dense machine which satisfies the total mass and output rotor inertia requirements and keeping the copper loss within a safe thermal limit.

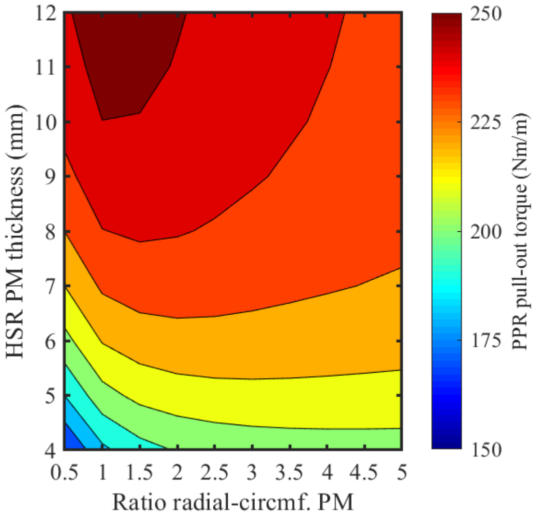

Figure 4.1. Variation of PDD pull-out torque for Halbach HSR PM – Halbach stator PM – 12S8P

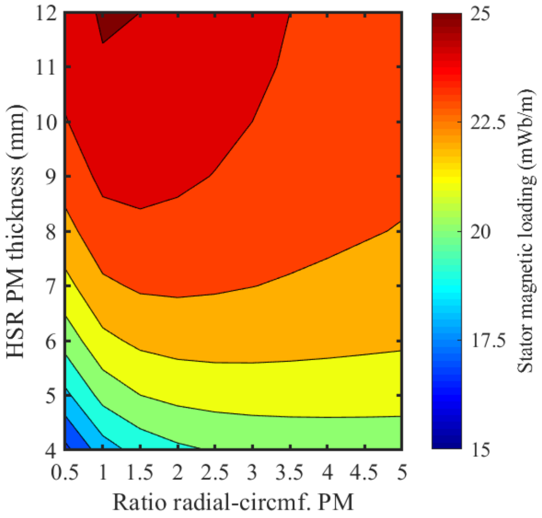

Figure 4.2.Variation of stator magnetic loading for Halbach HSR PM – Halbach stator PM – 12S8P

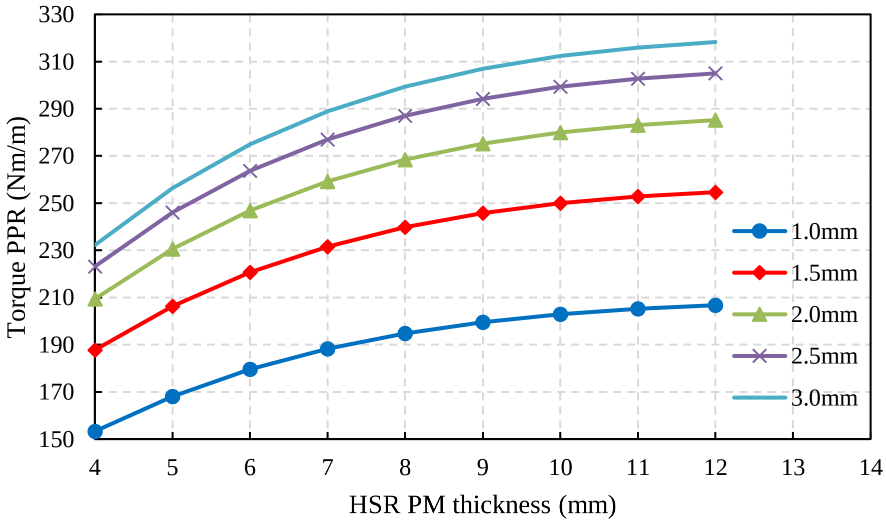

Figure 4.3. Variation of PDD output torque with HSR PM thickness for $R_{hlb} = 1$ and different stator PM thicknesses (Halbach HSR PM – Halbach stator PM – 12S8P)

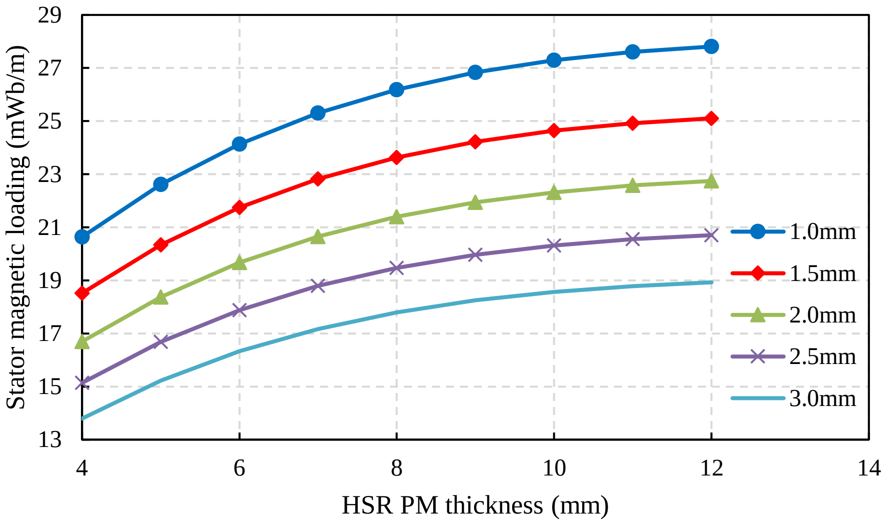

Figure 4.4. Variation of stator magnetic loading with HSR PM thickness for $R_{hlb} = 1$ and for different stator PM thicknesses (Halbach HSR PM– Halbach stator PM – 12S8P)

4.1.2 Halbach HSR PM and radial stator PM array topologies

The variations of PPR pull-out torque and peak stator magnetic loading for a 12s8p 7.75:1 PDD topology with HSR Halbach PM array and stator radial PM array, as a function of PM thickness and Halbach ratio, is shown in Figure 4.5 and 4.6. It can be observed that the maximum achievable PPR pull-out torque for the Halbach HSR – radial stator PM combination is reduced by 11% when compared to a Halbach HSR – Halbach stator PM topology. In contrast the peak stator magnetic loading is not affected by the change to a radial magnetisation pattern of the stator PM array, since it is mainly given by the HSR PM flux, airgap thickness between the HSR and stator and winding factor of the winding topology. The optimum Halbach ratio for both maximum PPR pull-out torque and stator magnetic loading was identified as 1, for a two segment per pole HSR Halbach array.

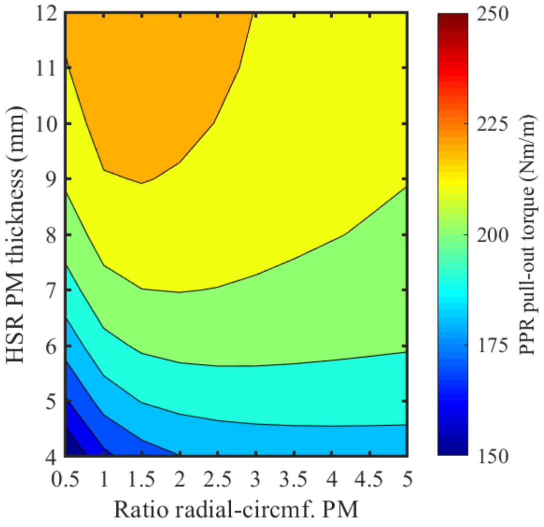

Figure 4.5. Variation of PDD pull-out torque for Halbach HSR PM – Radial stator PM – 12S8P

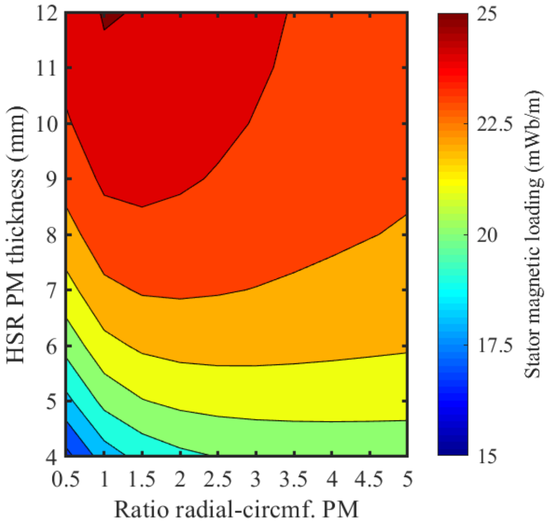

Figure 4.6. Variation of stator magnetic loading for Halbach HSR PM – Radial stator PM – 12S8P

Figure 4.7 and 4.8 show the variation of the PPR pull-out torque and peak stator magnetic loading for the optimum HSR Halbach ratio of 1, with the increase of the HSR and stator PM thickness. It can be observed that for a fixed HSR PM thickness, increasing the stator PM thickness increases the torque transmission capability of the magnetic gear element but reduces the magnetic loading of the brushless PM machine element with in the PDD. This trade-off between PPR pull-out torque and stator magnetic loading is similar to the one resulting from the Halbach HSR – Halbach stator PM arrangement, but the amplitude of the PPR pull-out torque is reduced due to the lower airgap flux created by the radial magnetisation of the stator PMs for the same amount of magnet material.

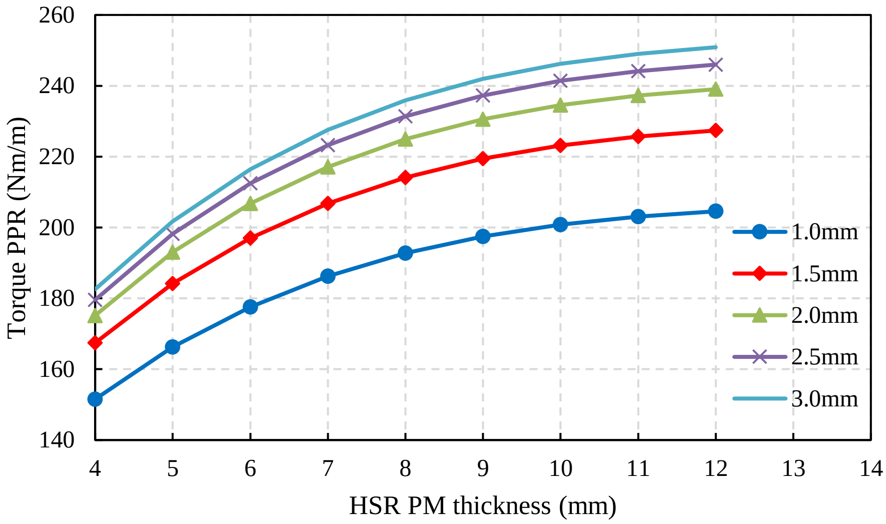

Figure 4.7. Variation of PDD output torque with HSR PM thickness for R_{hlb}=1 and for different stator PM thicknesses (Halbach HSR PM – Radial stator PM – 12S8P)

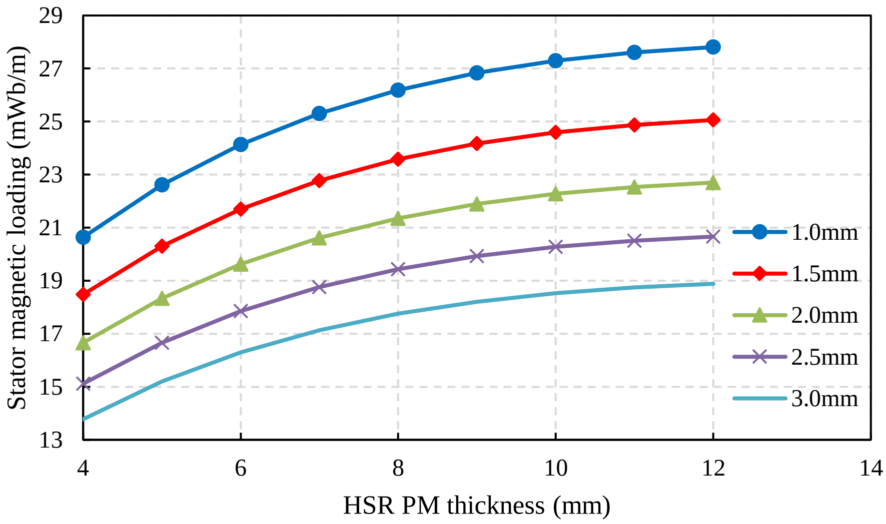

Figure 4.8. Variation a stator magnetic loading with HSR PM thickness for R_{hlb}=1 and for different stator PM thicknesses (Halbach HSR PM – Radial stator PM – 12S8P)

4.1.3 Radial HSR PM and Halbach stator PM array topologies

The variation of the PPR pull-out torque and peak stator magnetic loading, for radial HSR magnetisation and Halbach stator PM topology, are shown in Figure 4.9 and 4.10. The Halbach stator PM ratio was fixed at 1 throughout this investigation. Due to the large number of stator PM poles, reducing or increasing the Halbach ratio would increase the manufacturing cost and complicate the manufacturing process and could also result in stator PM blocks which have a very thin cross-section, which can become very difficult to handle during assembly. For a fixed stator PM thickness of 1.5mm the maximum achievable PPR pull-out torque is reduced by 15% and 5% when compared to the Halbach HSR with Halbach stator PM and Halbach HSR with radial stator PM topologies, respectively. For the same stator PM thickness, the peak stator magnetic loading is reduced by 15% when compared to a Halbach HSR PM array.

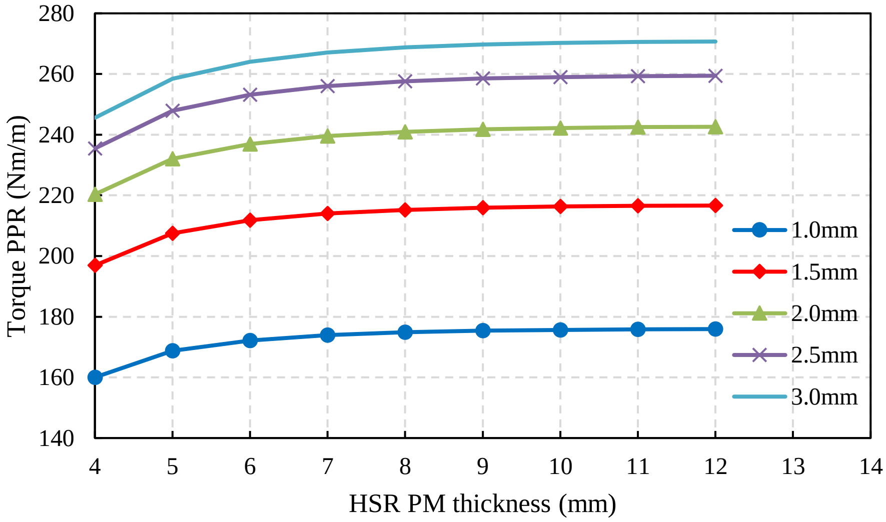

Figure 4.9. Variation of PDD pull-out torque with HSR PM thickness for different stator PM thicknesses (Radial HSR PM – Halbach stator PM – 12S8P)

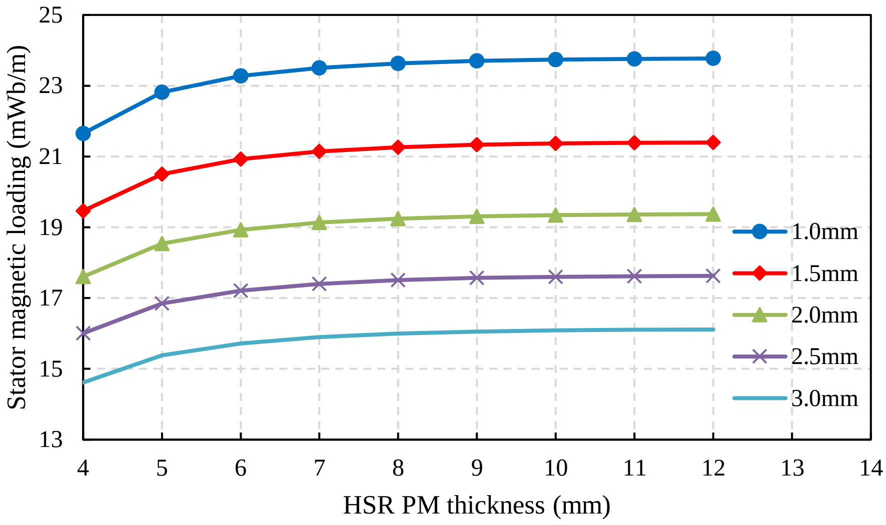

Figure 4.10. Variation of stator magnetic loading with HSR PM thickness for different stator PM thicknesses (Radial HSR PM – Halbach stator PM – 12S8P)

4.1.4 Radial HSR PM and stator PM array topologies

Figure 4.11 and 4.12 show the PPR pull-out torque and peak stator flux for a radial HSR and stator PM topologies. For a fixed stator PM radial thickness of 1.5mm, the PPR pull-out torque is reduced by 24%, 15% and 10% when compared with Halbach HSR – Halbach stator PM, Halbach HSR – radial stator PM and radial HSR – Halbach stator PM topologies, respectively. The peak stator magnetic loading is reduced by 15% when compared to the results obtained by utilising a Halbach PM array on the HSR for the same radial stator PM thickness.

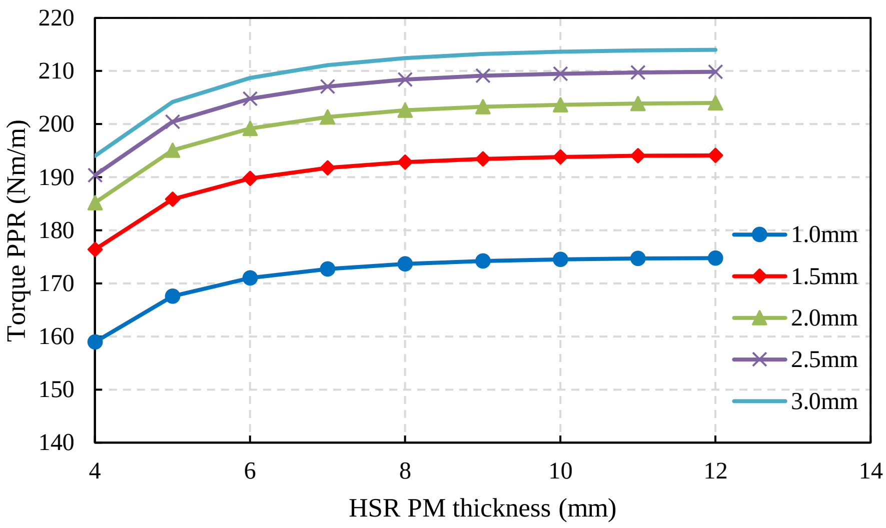

Figure 4.11. Variation of PDD pull-out torque with HSR PM thickness for different stator PM thicknesses (Radial HSR PM – Radial stator PM – 12S8P)

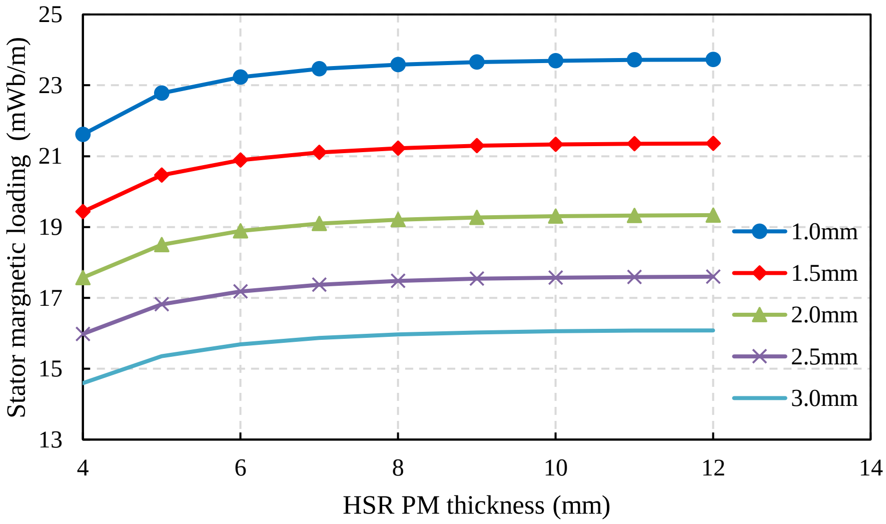

Figure 4.12. Variation of stator magnetic loading with HSR PM thickness for different stator PM thicknesses (Radial HSR – Radial stator PM – 12S8P)

4.1.5 Comparison of PM topologies for different slot-pole combinations

Figure 4.13 shows the comparison of the maximum achievable PPR pull-out torque for the selected 3-phase duplex compatible slot-pole combinations and corresponding gear ratios, for HSR PM radial thickness of 10mm, stator PM radial thickness of 1.5mm and

HSR Halbach ratio of 1. The PPR outer diameter was fixed at 45mm and the radial thickness of the pole pieces was set at 2mm. It can be observed that the Halbach HSR – Halbach stator PM topology achieves the highest torque transmission capability for all the considered slot pole combinations and corresponding gear ratios. Furthermore, the 12 slot 8 pole 7.75:1 PDD topology has the highest PPR pull-out torque when compared to the other slot-pole combinations for the same PM array topology and mass. The ability of the Halbach PM array of producing the highest PPR pull-out torque is due to its flux focusing capability which increases the magnetic flux density in both airgaps of the PDD. Thus, for high values of the radial and tangential flux density components, the torque developed in the airgap is increased.

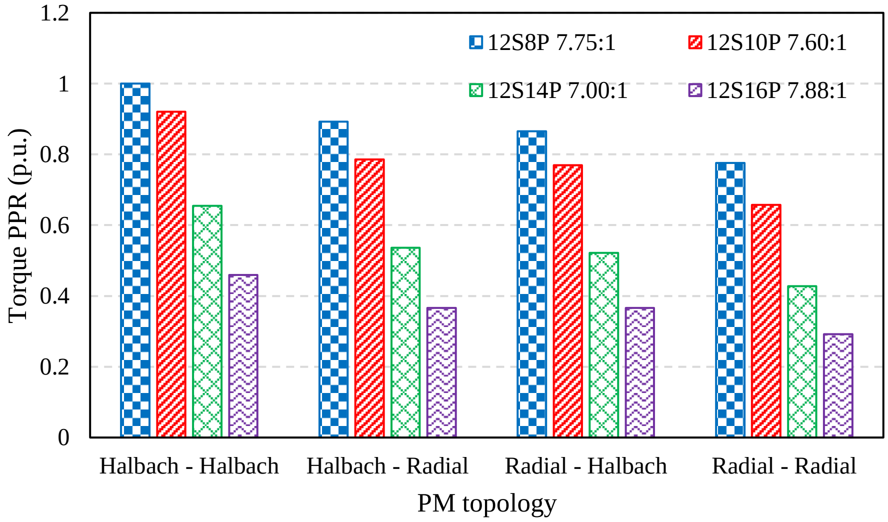

Figure 4.13. Comparison of PPR pull-out torque for different slot pole combinations and corresponding gear ratios

The contribution of each PM array to the airgap magnetic field density in both airgaps can be considered in the FE software by magnetising only one PM array at a time and interrogating the magnetic field density in the airgap.

In the inner airgap, the magnetic coupling is realised between the fundamental magnetic field component produced by the HSR and the asynchronous magnetic field component produced due to the modulation of the stator PM field by the ferromagnetic pole pieces. Hence, the HSR fundamental and resulting asynchronous harmonic of the stator PM – PPR assembly have the same harmonic order.

For the fixed parameters shown in Table 4.2, and for a fixed radial thickness of the HSR PM array of 10mm, Figure 4.14 shows the contribution of the HSR PM array in the inner airgap, adjacent to the HSR. This is shown in terms of the radial and tangential fundamental components of the magnetic field density for the different PM topologies and selected fractional slot-pole combinations.

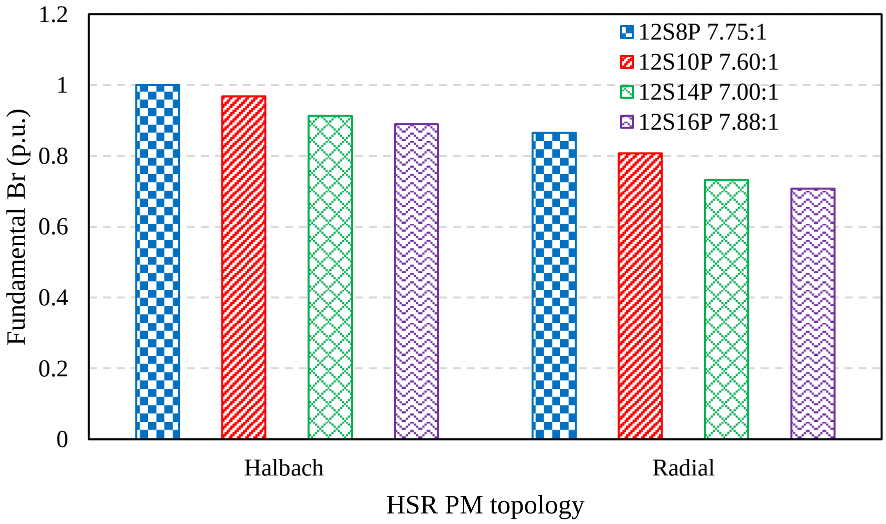

(a)

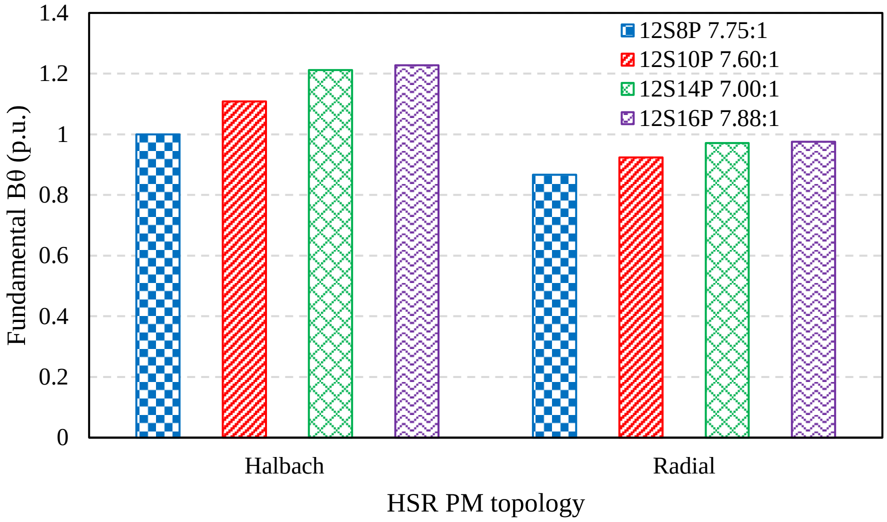

(b)

Figure 4.14. Fundamental component of (a). B_r and (b). B_θ in the inner airgap due to the HSR PM array

It can be observed that the Halbach array, irrespective of pole number, produces a higher magnetic flux density in the inner airgap, when compared to the radial PM array. Furthermore, for a fixed magnetisation pattern and rotor diameter, increasing the number of poles reduces the radial component and increases the tangential component of the fundamental flux density distribution due to the HSR in the inner airgap. This is related to the small HSR outer diameter and PM pole arc which is reduced as the pole number is increased. Thus, at high pole counts, the magnetic field has a larger tangential component, with respect to the outer circumference of the rotor, which reduces the radial component.

Figure 4.15 compares the amplitudes of the radial and tangential components of the asynchronous harmonic, in the inner airgap, produced by the modulation of the stator PM magnetic field by the ferromagnetic pole pieces. This asynchronous harmonic magnetically couples to the fundamental component of the HSR PM magnetic field. It can be observed that, irrespective of gear ratio and pole count of the stator PM array, the

Halbach PM topology produces a higher amplitude for the asynchronous harmonic than the radial magnetisation pattern.

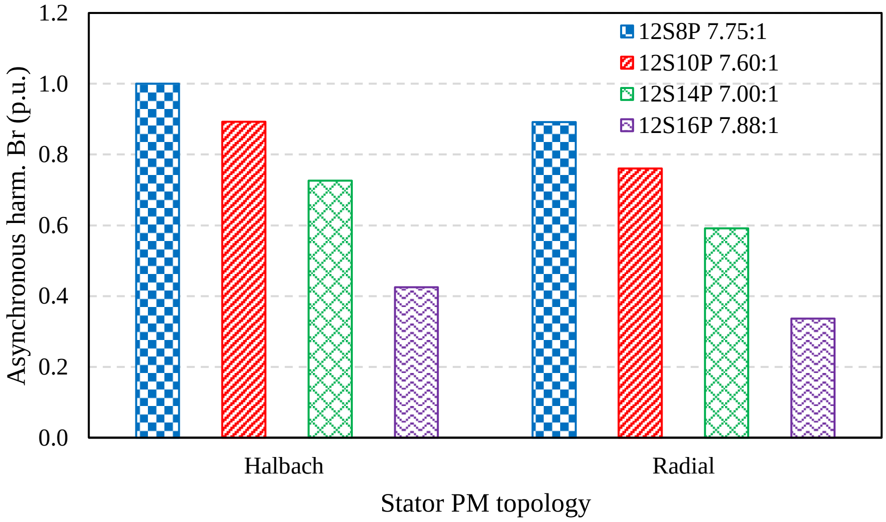

(a)

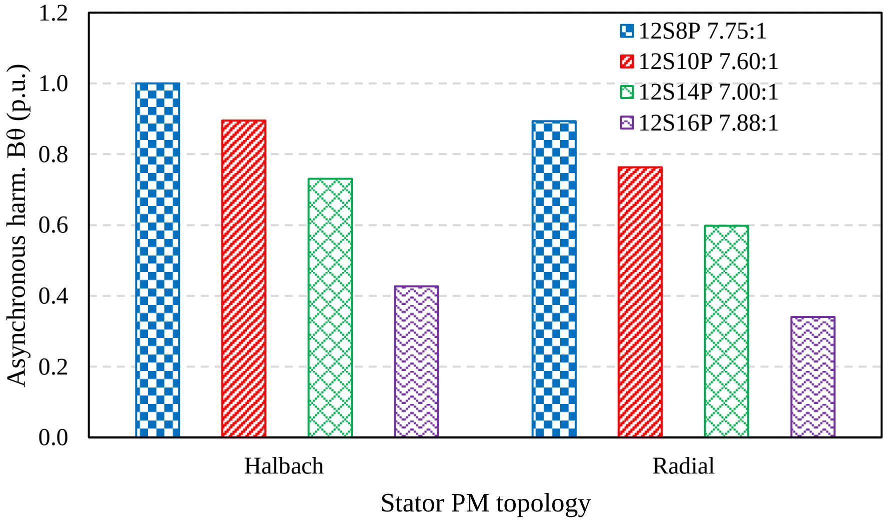

(b)

Figure 4.15. Asynchronous harmonic component of (a). B_r and (b). B_θ in the inner airgap due to the PPR - stator PM assembly

In the outer airgap, the magnetic coupling is established between the fundamental components of the stator PM field distribution and the asynchronous harmonic component due to the PPR modulation of the HSR magnetic field distribution. Hence, the fundamental stator PM field and asynchronous HSR-PPR harmonic field components have the same harmonic order number.

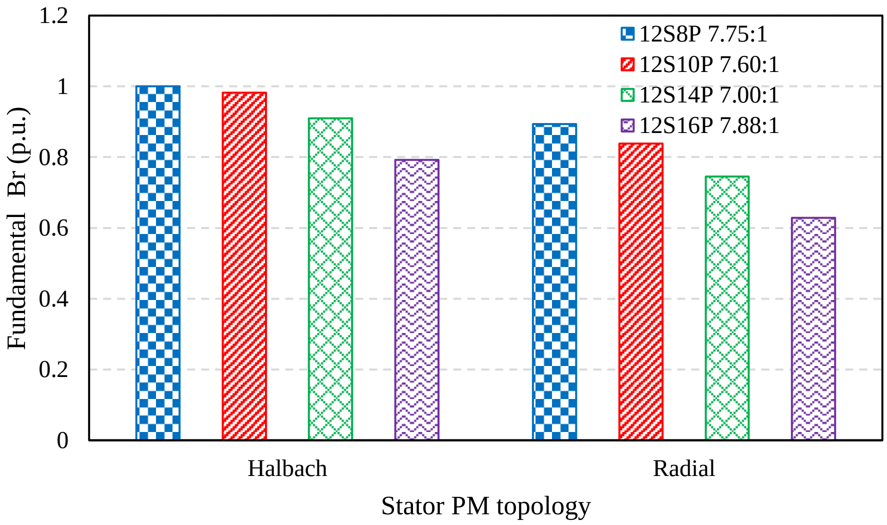

(a)

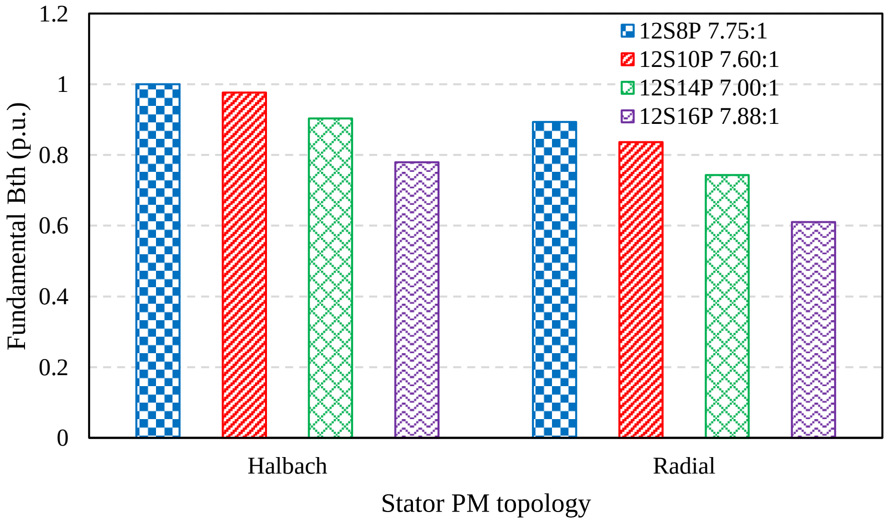

(b)

Figure 4.16. Fundamental harmonic component of (a). B_r and (b). B_θ in the outer airgap due to the stator PMs

Figure 4.16 compares the amplitudes of the radial and tangential fundamental components of the stator PM magnetic field distribution in the outer airgap for the investigated PM array topologies. It can be observed that for all the selected gear ratios and slot-pole combinations, the Halbach PM array produces a higher amplitude fundamental field component than the radial PM topology.

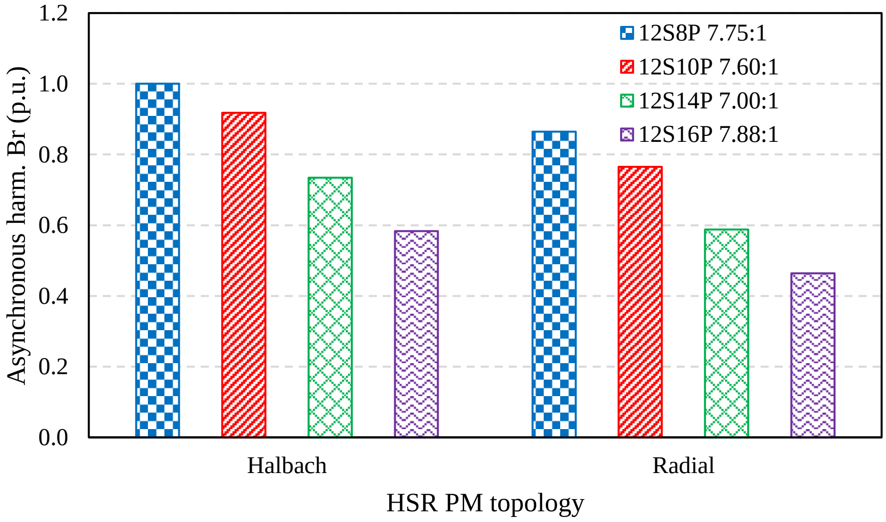

(a)

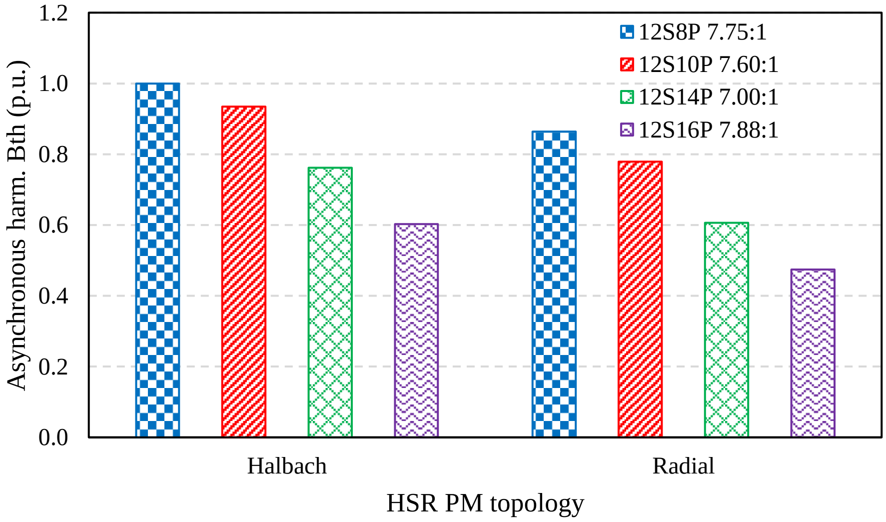

(b)

Figure 4.17. Asynchronous harmonic component of (a). B_r and (b). B_θ in the outer airgap due to the HSR-PPR assembly

Figure 4.17 shows the asynchronous harmonic radial and tangential components of the modulated HSR magnetic field distribution in the outer airgap. It can be observed that in the inner and outer airgaps, the Halbach HSR – Halbach stator PM topology produces the highest amplitudes for the fundamentals and asynchronous harmonics of the magnetic field distributions in both the radial and tangential direction. Thus, this PM arrangement produces the highest PPR pull-out torque in the outer airgap and equivalent HSR magnetic gear input torque in the inner airgap, increasing the PM utilisation and reducing the length, inertia and mass of the resulting PDD electrical machine.

Figure 4.18 shows the maximum achievable stator magnetic flux for the selected fractional slot-pole combinations with the different HSR and stator PM topologies for the same geometrical dimensions used in the PPR pull-out comparison from Figure 4.13. Since the effective airgap length between the HSR and stator bore is the same for all the designs, the stator magnetic loading per unit length is mainly influenced by the HSR PM topology and winding function, k_w,of the selected fractional slot-pole combinations and is not dependent on the stator PM topology.

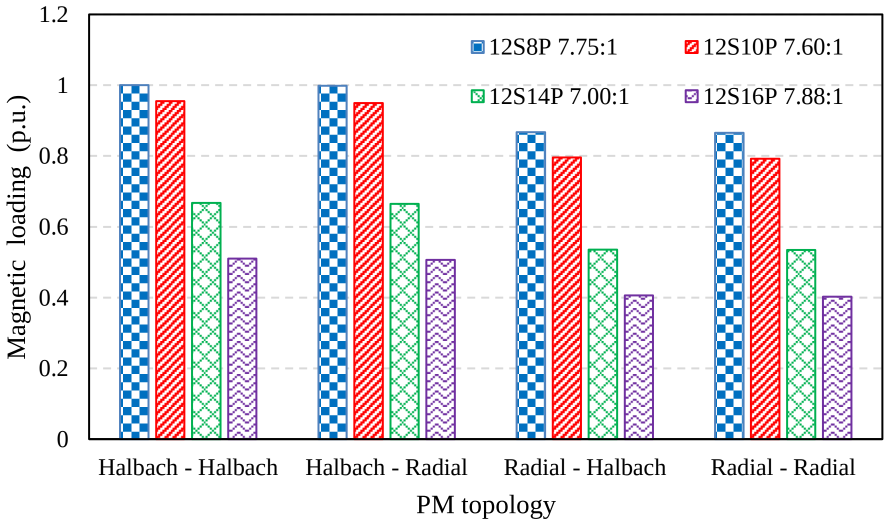

Figure 4.18. Comparison of peak stator flux linkage for different slot pole combinations and corresponding gear ratios

Thus, the Halbach HSR PM arrangement produced the highest stator magnetic flux irrespective of the slot-pole combination. It can also be observed that, although the 12s8p duplex 3-phase winding topology has an 11% lower winding factor than the 12s10p topology, it achieves a 5% higher magnetic loading for the Halbach HSR PM topology. In comparison, for Halbach HSR PM arrays, the magnetic loading of the 12s14p and 12s16p topologies are 33.3% and 49% lower when compared to the 12s8p variant.

The reduction in flux linkage with the increase in number of HSR poles is due to the reduced pole arc of the HSR PMs combined with the characteristically large airgap of the PDD. The thickness of the airgap, with respect to the PMs of the inner HSR, is given by the radial thicknesses of the inner airgap, PPR, outer airgap and stator PM array. Thus, by increasing the number of HSR poles, the pole arc is reduced and becomes comparable or less than the total PDD airgap, increasing the HSR PM flux leakage and reducing the PM flux linking with the stator windings. In this case, the magnetic flux from a HSR ‘north’ pole would short circuit through the pole pieces, flowing circumferentially from one pole piece to the neighbouring one towards a HSR ‘south’ pole and would not cross the outer airgap to reach that stator teeth and link with the stator windings.

Figure 4.19 shows the flux line plots, at no load, for the selected slot pole topologies with Halbach PM arrays. It can be observed that increasing the number of HSR poles, together with increasing the number of pole pieces required to achieve a similar gear ratio between the selected slot-pole combinations at a fixed PPR outer diameter, causes an increasing amount of flux to flow from the extremities of the radially magnetised HSR PMs, through the pole pieces and back towards the adjacent HSR poles. Thus, this flux does not cross the airgaps and does not return through the stator teeth, effectively reducing the flux linking with the stator coils.

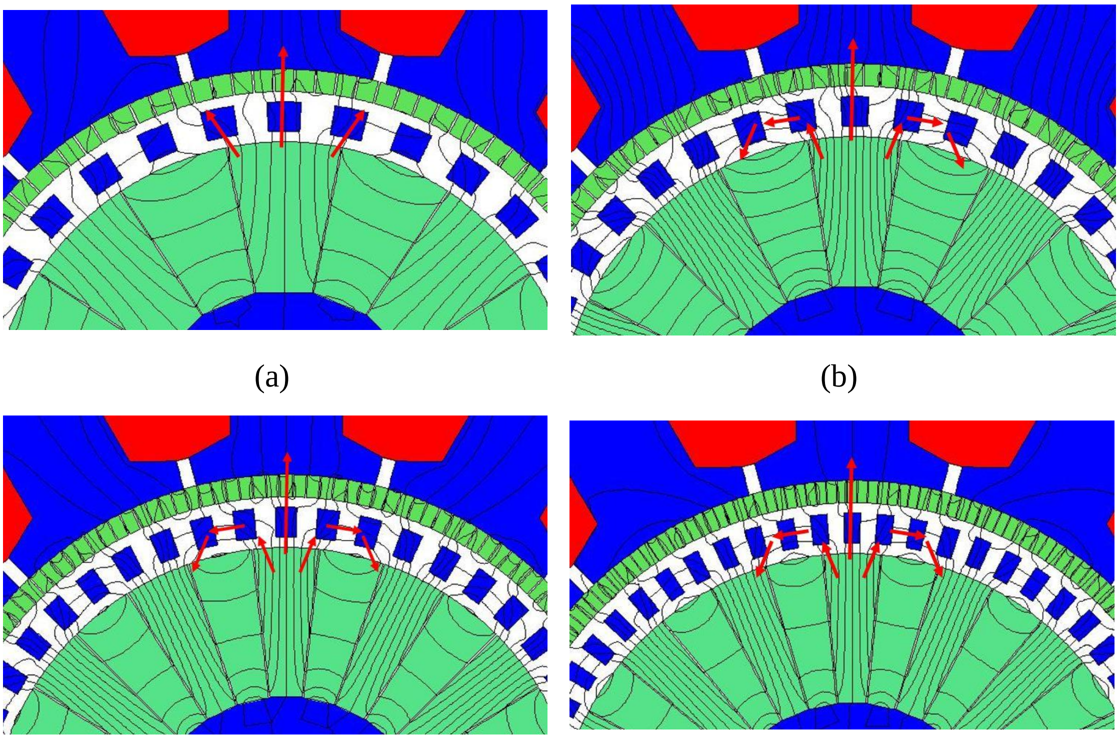

(a) (b)

(c) (d)

Figure 4.19. No-load magnetic flux line plot for (a)12s8p (b)12s10p (c)12s14p (d)12s16p with Halbach PM arrays

The rated copper loss of the PDD actuator motor operated in the constant torque region under FOC, with $I_d = 0$, can be calculated by considering the RMS phase current and phase resistance. The RMS phase current for the rated PPR torque, T_{PPR}, is given by:

$$I_{rms} = \frac{2T_{PPR}}{3\sqrt{2}\, p_h \psi_d G_r} \tag{4.3}$$

where ψ_d is d-axis HSR PM flux linking with the stator windings.

The phase resistance was calculated for a single turn winding with the wire having a cross section given by:

$$A_{copper} = A_{slot}\, p_{fact} \tag{4.4}$$

where A_{slot} is the slot cross-section area, which is constant for all the designs studied in this investigation, and p_{fact} is the packing factor of the copper wire in the slot. A copper fill factor of 40% was assumed. The phase resistance, for one coil per phase of the investigated fractional slot topologies, is given by:

$$R_{ph} = \frac{L_w}{\gamma_{cu} \cdot A_{copper}} \tag{4.5}$$

where γ_{cu} and L_w are the copper conductivity and total copper wire length, respectively.

Thus, the copper loss considering the rated torque of the actuator motor is given by:

$$P_{cu} = 3\left(\frac{2T_{PPR}}{3\sqrt{2}\, p_h \psi_d G_r}\right)^2 \frac{L_w}{A_{slot}\, p_{fact} \gamma_{cu}} \tag{4.6}$$

Figure 4.20 compares the resultant copper loss at the rated operating point of the actuator motor, for the different slot-pole combinations and gear ratios. The active length of all the different PM arrangements has been calculated based on the PPR pull-out torque capability shown in Figure 4.13. It can be observed that the 12s8p and 12s10p PDD topologies show a substantially reduced copper loss with the Halbach HSR PM array combined with either Halbach or radially magnetised stator PMs. In comparison, the 12s14p and 12s16p have a high copper loss due to the reduced magnetic loading caused by the HSR flux leakage irrespective of PM topology.

The resultant active mass of the PDD designs compared in Figure 4.20, is shown in Figure 4.21. It can be observed that the 12s14p and 12s16p topologies are characterised by a high active mass due to their poor torque transmission capability of the magnetic gear element. This implies that the active length of the 14 and 16 pole topologies has to be increased in order to meet the PDD pull-out torque requirement. In comparison the 12s8p and 12s10p topologies, due to their high PPR pull-out torque capability per unit length, have resulted in lightweight PDD designs with low and comparable copper losses.

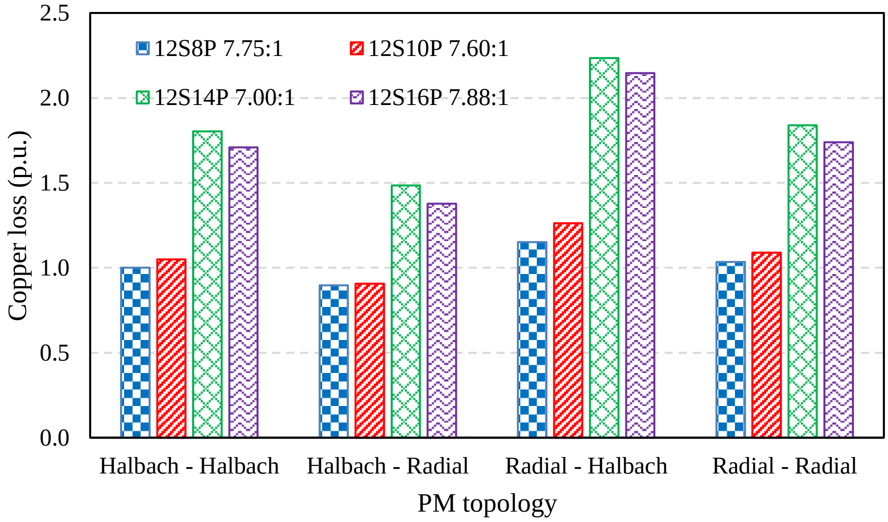

Figure 4.20. Comparison of copper loss for different slot-pole combinations and corresponding gear ratios

The cogging and ripple torque in PDD electrical machines are substantially more difficult to define than in conventional PM machines due to the two degrees of freedom of the magnetic gear element, represented by the HSR and PPR. The two rotors of the PDD can rotate independently with a varying load angle, during start up and transient events, or at different constant velocities with a constant load angle during steady state operation. In this investigation, the torque ripple of the HSR and PPR was predicted from 2D FE simulations, for a constant load angle between the two rotors.

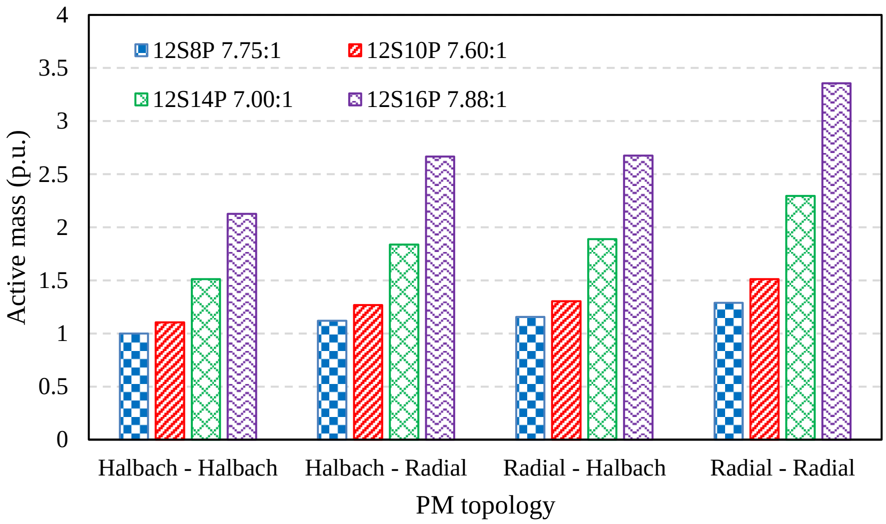

Figure 4.21. Comparison of active mass for the different slot-pole combinations and corresponding gear ratios

Figure 4.22 and 4.23 show the variation of the torque ripple as a percentage of the rated torque for the HSR and PPR, respectively. It can be observed that for the non-integer magnetic gear ratios, implementing a Halbach on the HSR does slightly reduce the torque ripple when compared to a radial PM topology on both the HSR and stator bore. The integer gear ratio, as expected due to its higher cogging torque factor, has a higher torque ripple for any of the PM topologies. Implementing Halbach HSR and Halbach stator PM arrays does reduce the torque ripple of this gear ratio by 50% when compared to a purely radial PM arrangement.

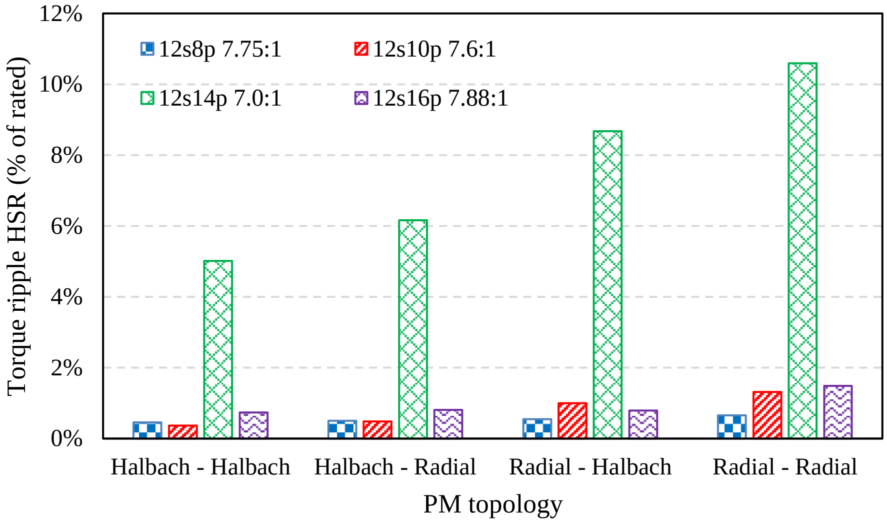

Figure 4.22. Comparison of HSR torque ripple with HSR and stator PM topology

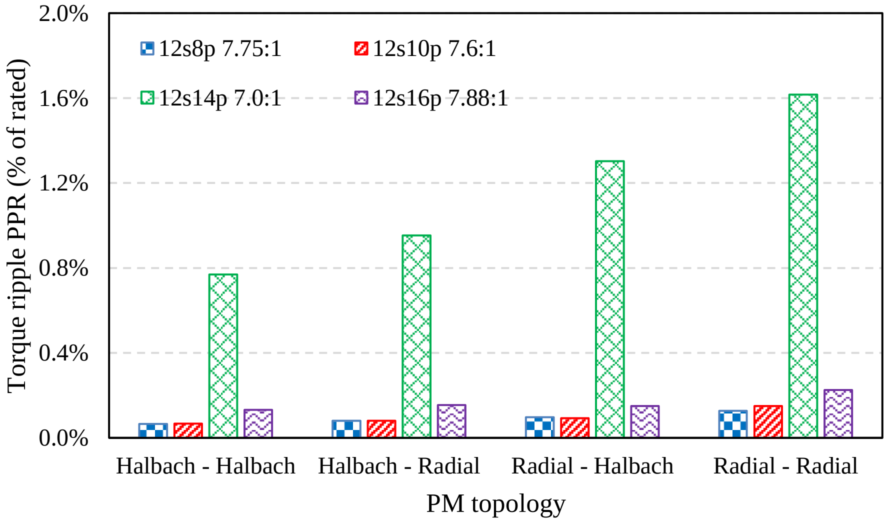

Figure 4.23. Comparison of PPR torque ripple with HSR and stator PM topology

4.1.6 Conclusions

The PDD electromagnetic performance for different PM array topologies, on the HSR and stator bore, was investigated for a fixed PPR outer diameter and pole piece radial thickness. It was shown that for a Halbach HSR PM array, the PPR pull-out torque capability is maximised by increasing the HSR PM radial thickness for a fixed stator PM thickness. For the HSR Halbach PM array, a pole pitch ratio of 1, between the radially and circumferentially magnetised PMs, was identified as being an optimum in terms of maximising the PPR pull-out torque and peak stator magnetic loading. Increasing the stator PM thickness can be beneficial to maximising the torque transmission capability of the magnetic gear, but does increase the effective airgap between the HSR PMs and stator bore, reducing the flux linkage of the stator windings. Hence, selecting the stator PM radial thickness would bring a compromise between achieving a torque dense PDD design, which meets the mass and inertia targets while accepting a certain decrease in efficiency.

The four PM topology combinations were implemented on four different slot-pole combinations with similar gear ratios and compared in terms of PPR pull-out torque, copper loss, active mass and torque ripple. It was shown that utilising Halbach PM arrays on both the HSR and stator of a PDD, does increase the PPR pull-out torque and reduces the PDD active mass for all the considered slot pole combinations, when compared to the other PM topologies. Moreover, the 12s8p and 12s10p topologies, with Halbach PMs, achieved lower copper losses and active masses when compared to the 12s14p and 12s16p variants, which were characterized by high flux leakage from the HSR and poor pull-out torque capability.

The torque ripple of the different slot-pole combinations was investigated, showing that the PDD designs with non-integer gear ratios have a small torque ripple when compared with integer gear ratios. It was also shown that the Halbach PM array can be used to reduce the torque ripple of integer gear ratios by a factor of 50%.

4.2 Design of output pole piece rotor

The pole piece output rotor (PPR) represents an integral part of the magnetic gear element and PDD electrical machine. The PPR rotor is composed of equally spaced ferromagnetic pole pieces which act to modulate the PM field distribution from the HSR and stator PMs. The structure of the PPR is representative of a hollow cylinder with a reduced wall thickness, with the ferromagnetic pole pieces being circumferentially separated by non-magnetic spacers. Endplates are mechanically attached to both ends of the PPR structure which also act as a bearing support for the HSR bearings. The output shaft of the PDD is usually machined as part of the drive-end PPR endplate. In order to reinforce the PPR assembly, a torque tube can be applied on the inner diameter. This would increase the stiffness to torsional loads allowing for a greater torque to be transmitted to the load. An overwrap can be implemented along the outer circumference of the PPR in order to provide radial stiffness and act as a retention mechanism for the pole pieces.

The electromagnetic design of the PPR is of prime importance when considering the PDD performance parameters such as torque density, torque ripple, loss and active mass. The mechanical design and manufacturability of the PDD is also affected by the selected optimum pole piece shape since the PPR has to transmit the rated torque to the load while constantly being subjected to radial and tangential loads. Thus, minimum radial and tangential thickness limits are imposed on the pole piece cross-section by the mechanical engineers based on rated torque, pole piece loads and length of the machine in order to avoid excessive bending or twist of the PPR structure. For a fixed outer stator diameter of the PDD and split ratio between the PPR outer diameter and stator outer diameter, the selected gear ratio can also influence the PPR design with high magnetic gear ratios being characterised by a high number of ferromagnetic pole pieces. The authors of [131] have shown that for a fixed outer magnetic gear diameter and fixed length, the PPR maximum torque transmission capability or pull-out torque is reduced when the gear ratio is increased for a fixed HSR pole pair number. The influence of the pole piece geometry on the PPR pull-out torque is studied by varying the ferromagnetic opening (width of pole piece) to pole piece pitch ratio and radial pole piece thickness to pole piece pitch ratio. The pole piece pitch is the circumferential distance between the centres of neighbouring pole pieces. The authors conclude that for a fixed number of outer PM poles, increasing the inner PM pole pair number results in a radially thinner pole piece for optimal PPR pull-out torque capability. It is acknowledged that thin pole pieces required for peak electromagnetic performance are not always practical or achievable due to mechanical stress limits and manufacturability/cost constraints.

The authors of [77] show the PPR pull-out torque variation as a function of PPR radial thickness and width. Increasing the radial pole piece thickness, sharply increases the PPR pull-out torque until an optimum is reached. Increasing the pole piece radial thickness further causes the maximum PPR torque to only gradually reduce. A similar behaviour of the PPR pull-out torque with respect to the pole piece radial thickness has been presented in [70]. Thus, if tight tolerances cannot be achieved during manufacturing, it could be beneficial to select a pole piece radial thickness value which is higher than the optimum such that the PPR pull-out torque is only slightly reduced and the design does not fall on the first steep side of the trend. The variation of PPR pull-out torque with the width of the pole pieces is also presented for a fixed radial pole piece thickness. A similar PPR design approach is presented in [168]. The authors propose a pole piece cross section with circular cut-outs on both right and left sides of each pole piece designed to increase the maximum torque transmission capability and reduce the torque ripple by increasing the radial flux and reducing the tangential flux components in each pole piece. For the same pole piece radial thickness and fixed PM mass utilised in the magnetic gear, the pull-out torque was increased by 1.8% and torque ripple reduced by 1% when compared to a square pole piece shape.

Another PPR design, with ferromagnetic bridges on the inner diameter of each pole piece is presented by the authors of [169]–[171], in order to ease the manufacturing process and improve the stiffness of the PPR. The first PPR design is characterised by a relatively thick magnetic pole piece bridge and was supported by steel bolts and epoxy resin. This introduced additional losses in the pole pieces and supporting bolts. The ferromagnetic pole pieces bridges accounted for a 4% reduction in the pull-out torque of the proposed PDD electrical machine. For the second PPR design, the thickness of the pole piece bridges are reduced in order to reduce the iron losses and the flux leakage from the HSR PMs. A slot was machined on the inner diameter of each pole piece in order to reduce the HSR PM eddy current loss by reducing the variation in PM working point as the HSR PMs pass by each pole piece. At 11 krpm, the HSR PM loss was reduced by 30% due to the machined pole piece slots.

In order to investigate the effect of the leading pole piece design parameters on the electromagnetic performance of the actuator PDD motor, two slot-pole combinations have been selected, based on the results presented in subchapter 4.1, with Halbach PM arrays on both the HSR and stator bore. These are represented by the 12s8p and 12s10p topologies. The other slot pole combinations, 12s14p and 12s16p, have been discarded due to the poor pull-out torque capability and reduced stator magnetic flux. For the selected slot pole combinations, the PPR outer diameter was fixed at 45mm based on the rotor inertia trend shown in Figure 3.24. In the presented literature review, the pole piece design parameters were varied for a fixed outer PPR diameter and fixed HSR PM thickness. Thus, as the radial pole piece thickness was increased, the mass of the HSR PM per meter length was also increased.

In this investigation, the HSR PM mass per meter was fixed, and since the PPR outer diameter was fixed, the HSR PM radial thickness was recalculated for each radial thickness of the pole pieces. This ensures that for any change in the PPR cross-section, the mass of HSR PM per meter length, or cross-section area of the HSR PM, is kept constant. Moreover, the mass of PM on the stator bore was also fixed by setting the PM radial thickness to 1.5mm, since the PPR outer diameter and stator teeth bore diameter do not change. The effects of changing the PM thickness for a fixed PPR design have already been presented in subchapter 4.1. Based on the results from subchapter 4.1, the Halbach ratio of the HSR PMs was fixed at 1, which implies that the radial and circumferential PMs have an equal pitch angle. Table 4.3 shows the selected slot pole combinations, corresponding gear ratios and the fixed PDD parameters which were used to investigate the two preliminary PPR designs. The resultant PDD outer diameter was constant at 73.8mm.

Table 4.3. Fixed PDD parameters

Slot - pole	**Gear ratio**	**HSR PM area (mm^2)**	**Stator PM thickness (mm)**	**Stator / back-iron thickness (mm)**
12S8P	6.25	727	1.5	12/4.4
	7.75			
	10.0			
12S10P	6.4			
	7.6			
	10.0			

The electromagnetic airgaps between the HSR-PPR and PPR-stator PMs were fixed at 0.7mm. This allowed for a 0.2 mm carbon fibre overwrap to be applied to the HSR PMs and for a 0.2 mm sleeve to be applied to the inner diameter of the stator PMs as a secondary retention method for the stator PM array. Thus, the mechanical airgaps of the PDD electrical machine were reduced to 0.5 mm.

4.2.1 Trapezoidal pole piece cross-section

The proposed trapezoidal pole piece cross section is shown in Figure 4.24. The parameters used to define it are represented by the radial thickness, l_{pp}, outer angle, θ_{out}, and inner angle, θ_{in}, of the pole piece. The inner and outer pole piece angles are given by:

$$\theta_{out} = \frac{2\pi}{N_{pp}} rt_{out} \tag{4.7}$$

$$\theta_{in} = \frac{2\pi}{N_{pp}} rt_{in} \tag{4.8}$$

where rt_{out} and rt_{in} are the outer and inner pole piece pitch ratios.

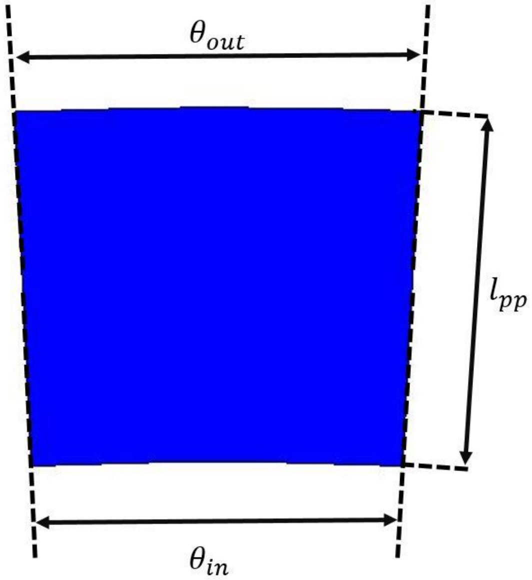

Figure 4.24. Trapezoidal pole piece cross-section

The ranges of the pole piece parameters used in the FE electromagnetic analysis are shown in Table 4.4. A pole piece having an outer and inner pitch ratio of 0.1 represents a narrow ferromagnetic cross-section, while a high pitch ratio of 0.9 represents a wide cross-section.

Table 4.4. Ranges of pole piece parameters

Parameter	Lower limit	Upper limit
l_{pp}	1.5 mm	4 mm
rt_{in}	0.1	0.9
rt_{out}	0.1	0.9

Figure 4.25 (a)-(d) show the variation of the PPR pull-out torque as a function of inner and outer pole piece pitch ratios and pole piece thickness. It can be observed that, as the pole piece radial thickness is increased, the maximum torque transmission capability of the PDD magnetic gear element is substantially reduced. For a fixed output torque requirement, this would increase the active length of the machine together with the active mass and rotor inertia. Thus, it is important to select the smallest possible pole piece thickness such that the PPR withstands the torsional loads without deforming while allowing the design to meet the mass limit for the actuator motor. It can also be observed that as the pole piece thickness is increased, a different optimum in pole piece inner and outer pitch exists for maximum PPR pull-out torque.

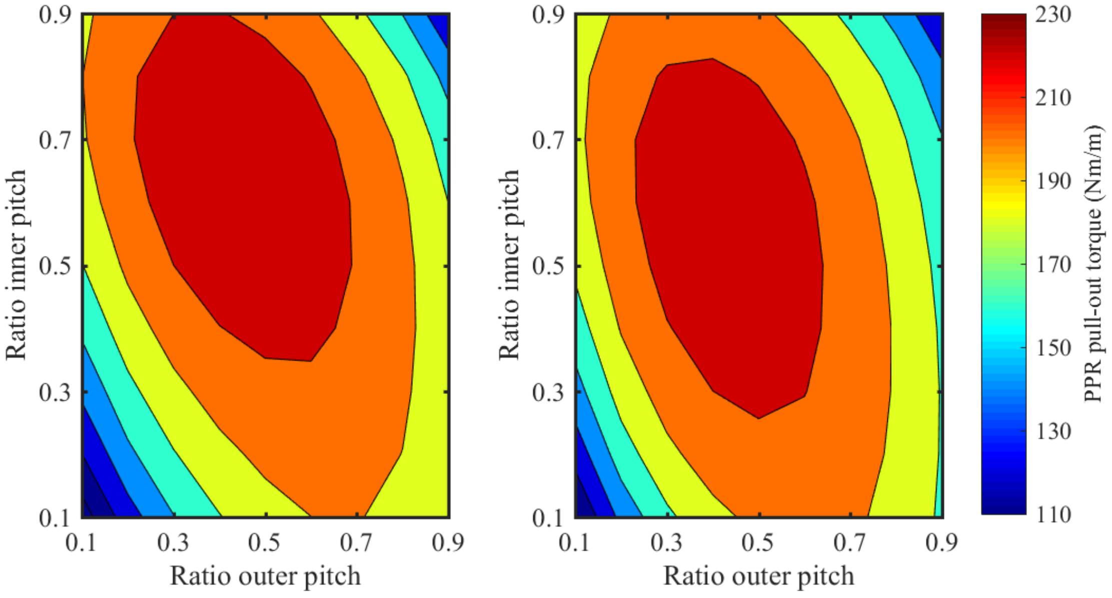

(a) (b)

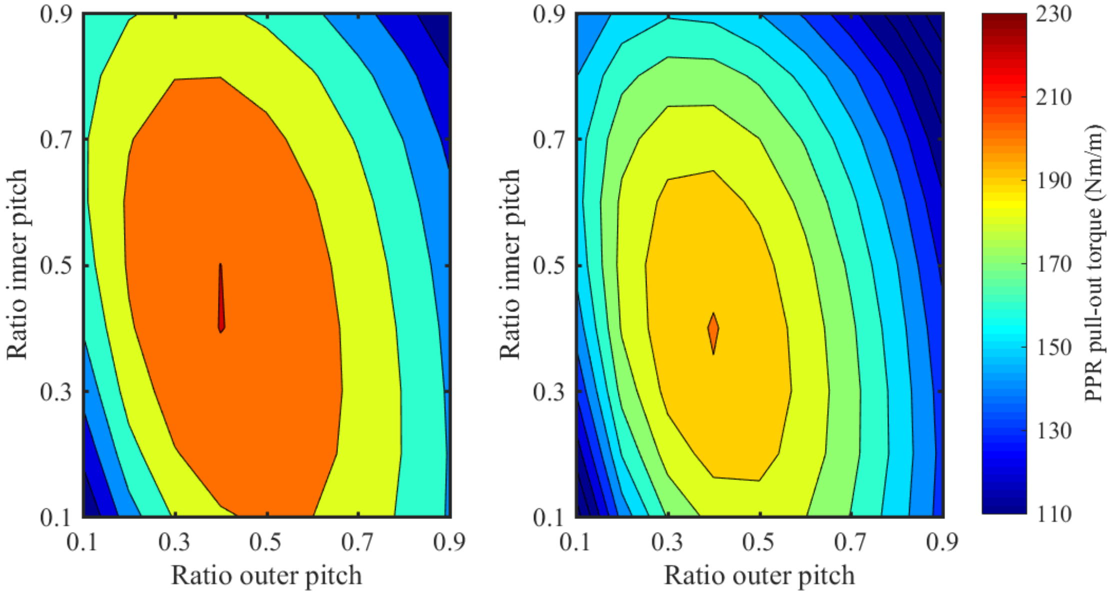

(c) (d)

Figure 4.25. PPR pull-out torque variation with inner/outer pole piece pitch ratio and l_{pp} (a) 1.5mm (b) 2mm (c) 3mm (d) 4mm for 12S8P 7.75:1

Figure 4.26 (a)-(d) show the variation of the PDD active mass as a function of inner and outer pole piece pitch ratios and pole piece thickness. It can be observed that at low (0.1) and high (0.9) pole piece pitch ratios, the active mass is significantly increased as the machine has to be longer for a fixed output PPR pull-out torque. Moreover, increasing the radial thickness of the pole piece also increases the active mass of the machine. It can also be observed that the optimum pole piece ratios for PPR pull-out torque and active mass are fairly equal.

Figure 4.27 (a)-(d) shows the variation of the PPR rotor inertia with the change in the inner and outer pole piece pitch ratios and pole piece radial thickness. The additional inertia of the endplates and shaft was not considered, as it would be constant for a fixed PPR outer diameter and fixed endplate thickness. It can be observed that the PPR inertia is increased with the increase in pole piece radial thickness and pitch ratios. This is due to the low torque transmission capability of the magnetic gear element which, for a fixed torque output requirement, results in a PDD design with a larger active length. In Figure 4.25, it can be observed that although at low pole piece pitch ratios the PPR pull-out torque capability is heavily reduced, the resulting inertia of the PPR, shown in Figure 4.27, is within the optimum low region. This is due to the fact that the pole pieces are narrow and their total mass is now reduced and comparable with the mass of the PPR support structure which is made from a much lesser dense material, such as G11 reinforced fibre glass. The density ratio between ferromagnetic steel and G11 fibre glass is approximatively 7:1.

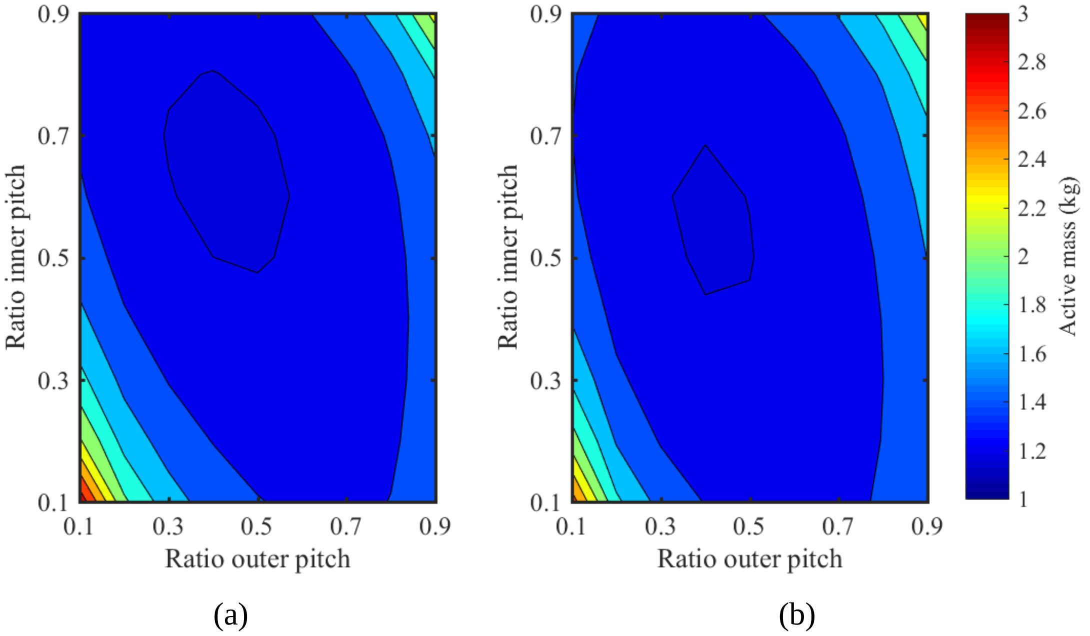

(a) (b)

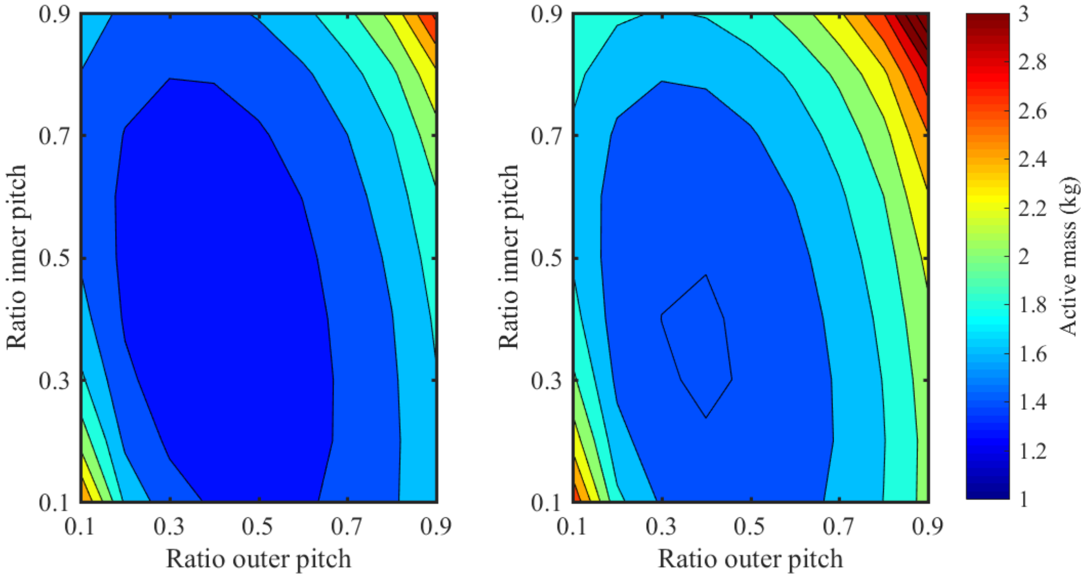

(c) (d)

Figure 4.26. PDD active mass variation with inner/outer pole piece pitch ratio and l_{pp}(a) 1.5mm (b) 2mm (c) 3mm (d) 4mm for 12S8P 7.75:1

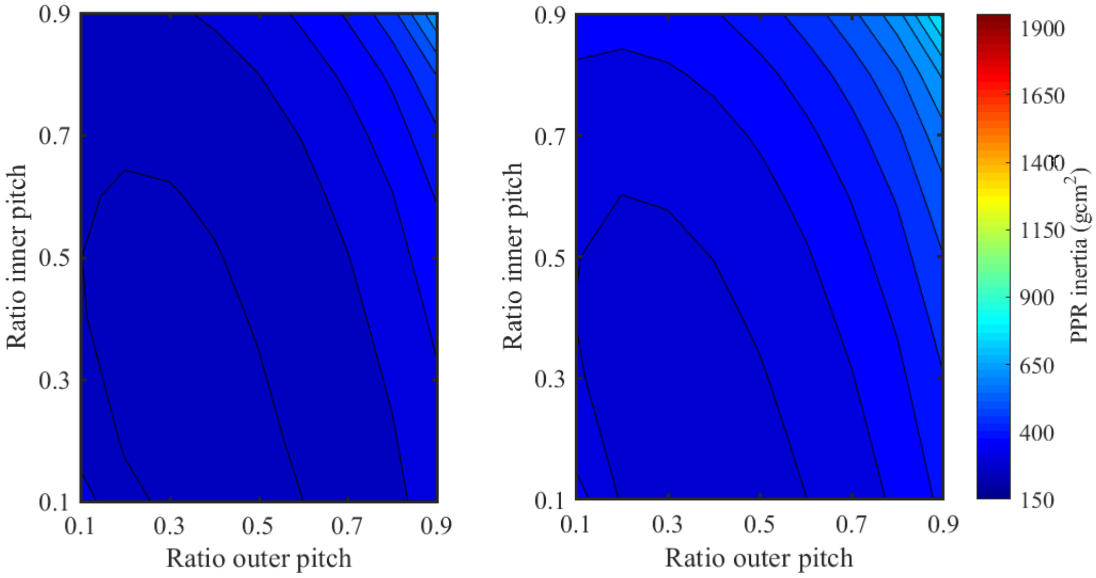

(a) (b)

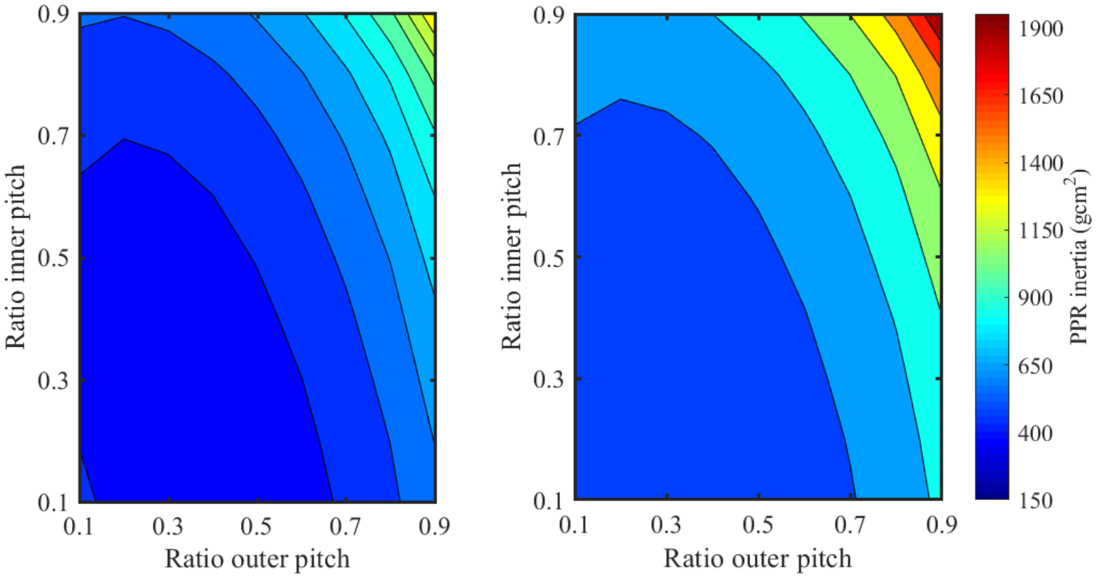

(c) (d)

Figure 4.27. PPR rotor inertia variation with inner/outer pole piece pitch ratio and l_{pp} (a) 1.5mm (b) 2mm (c) 3mm (d) 4mm for 12S8P 7.75:1

Figure 4.28 (a)-(d) shows the resultant rated copper loss as a function of pole piece inner and outer pitch and pole piece radial thickness. It can be observed that the copper loss increases with pole piece radial thickness. This is due to the fact that when the PPR thickness is increased, the effective airgap between the HSR PMs and stator bore is increased, which reduces the stator PM flux linkage, ψ_d, and increases the phase current required for rated torque production. Moreover, as the PPR radial thickness is increased, the pull-out torque capability of the magnetic gear element within the PDD is reduced, which increases the active length of the machine for a fixed rated torque.

For a fixed pole piece radial thickness, the copper loss is reduced at low pole piece pitch and increased at high pole pitch ratios. This is due to the fact that, at low pole piece pitch ratios, the HSR PM flux leaking from one pole piece to the next one is reduced as greater separation exists between neighbouring pole pieces. The reverse is true at high pole piece ratios, where a greater proportion of the HSR PM flux is short circuited through the PPR and does not cross the outer airgap to couple with the stator windings, increasing the current demand and implicitly the copper loss.

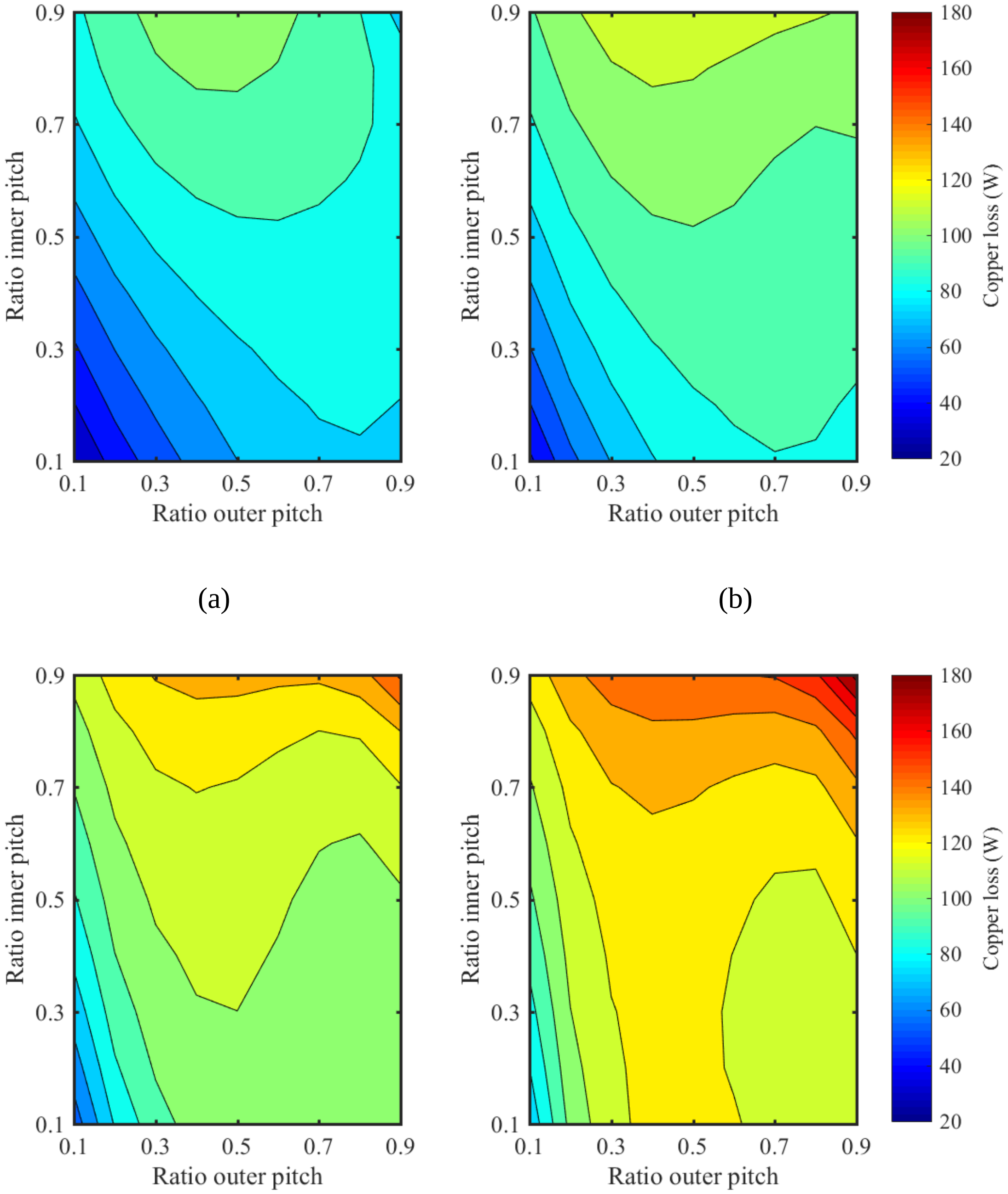

(a) (b)

(c) (d)

Figure 4.28. Copper loss variation with inner/outer pole piece pitch ratio and l_{pp} (a) 1.5mm (b) 2mm (c) 3mm (d) 4mm for 12S8P 7.75:1

From the presented results with respect to the cross-section design of the trapezoidal pole piece, it can be observed that a trade-off exists between the maximum torque capability of the magnetic gear element, PDD output rotor inertia, active mass and copper loss. Thus, in order to obtain a design with a reduced active mass and output rotor inertia, an increase in copper loss has to be accepted.

The 1.5 mm radial pole piece thickness showed the best performance characteristics, but was regarded as not a sufficiently thick PPR cross-section to withstand the radial and torsional loads during operation. Moreover, the current manufacturing processes would make it significantly difficult and risky to produce a PDD prototype having a 1.5mm thick pole piece rotor. Thus, the optimum minimum acceptable pole piece thickness was fixed at 2mm.

Figure 4.29 shows the PPR pull-out torque variation for the 12s8p and 12s10p designs and corresponding gear ratios for a fixed 2mm pole piece radial thickness and equal inner and outer pole piece angles, such that $\theta_{in} = \theta_{out}$. It can be observed that for a similar gear ratio and the same PDD cross section, the 12s8p designs have a higher PPR pull-out torque than the 12s10p topologies. For a fixed slot pole combination, it can be observed that the PPR pull-out torque is reduced as the gear ratio is increased. Moreover, a pole piece pitch ratio of 0.5 represents the optimum for maximum torque transmission capability, for all the slot-pole combinations and corresponding gear ratios. Figure 4.30 and 4.31 show the variation of active mass and PDD output rotor inertia for the designs presented in Figure 4.29. It can be observed that for a fixed output torque requirement, the high gear ratios which have a poor PPR pull-out torque capability, resulting in an increased machine active length, are also characterised by an increased active mass and output rotor inertia. Figure 4.32 shows the PDD copper loss at the rated operating point for the selected slot-pole combinations and corresponding gear ratios. It can be observed that the copper loss is increased with the reduction of the PDD magnetic gear ratio. This is due to the fact that, for a fixed output PPR torque, at low gear ratios, the input torque of the magnetic gear element or the electromagnetic HSR torque, T_{HSR}, developed by the PDD is increased and given by:

$$T_{HSR} = \frac{T_{PPR}}{G_r} \tag{4.9}$$

Thus, as the gear ratio is reduced, the PDD phase current demand is increased for a fixed PPR torque output, resulting in an increased copper loss. Hence, for the PDD actuator motor, selecting a PDD gear ratio in the range of 7.5:1 to 8.0:1 represents a good compromise between active mass, PPR inertia and resulting copper loss.

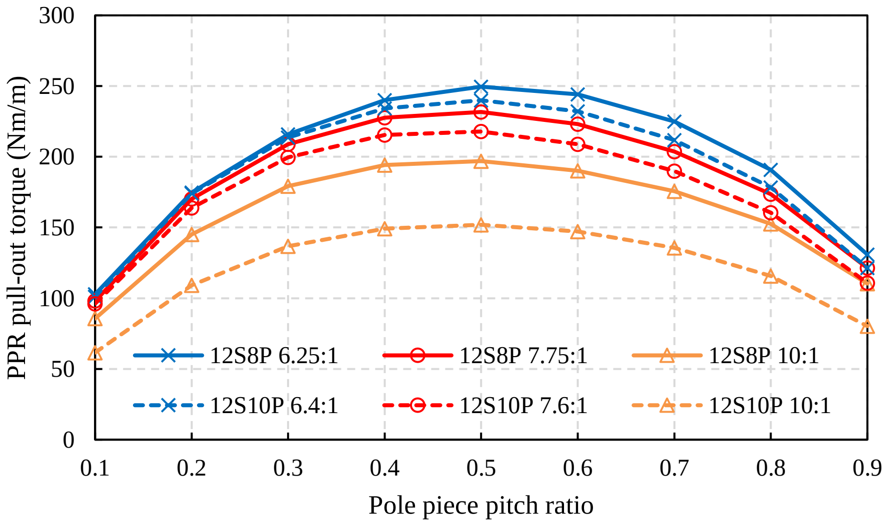

Figure 4.29. PPR pull-out torque variation with slot-pole and gear ratio for $l_{pp} = 2\ mm$ and $\theta_{in} = \theta_{out}$

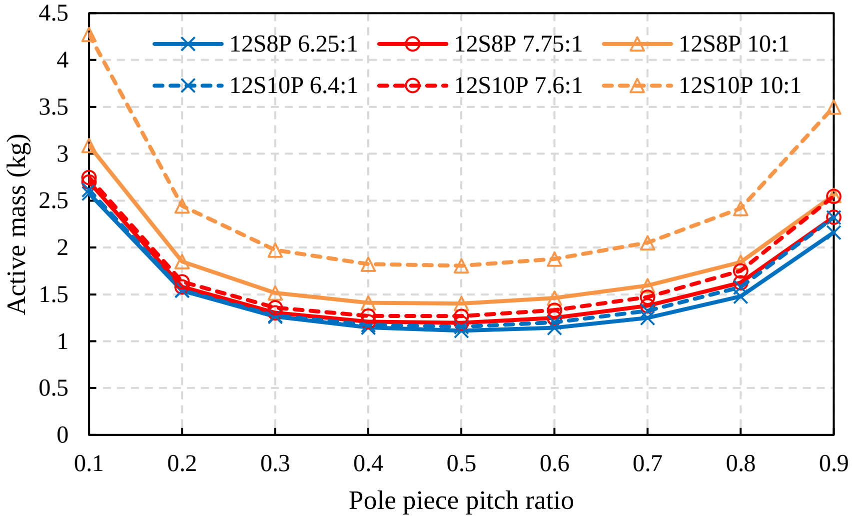

Figure 4.30. PDD active mass variation with slot-pole and gear ratio for $l_{pp} = 2\ mm$ and $\theta_{in} = \theta_{out}$

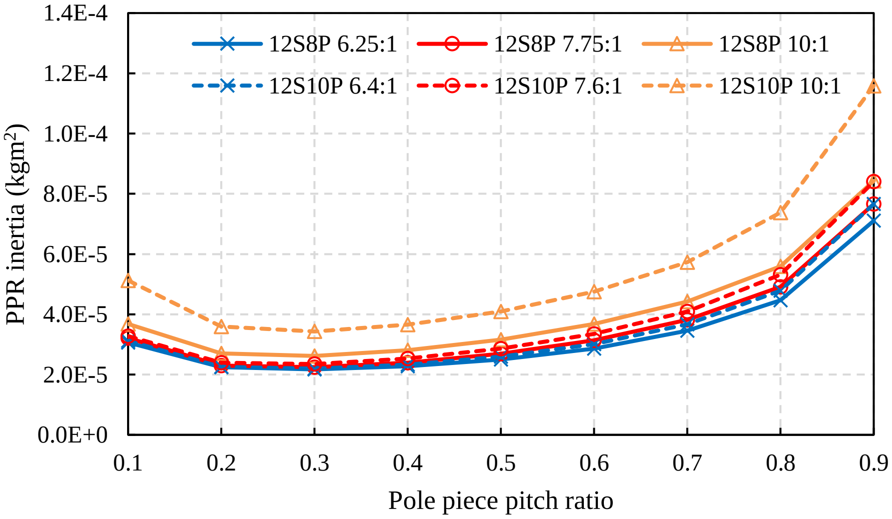

Figure 4.31. PPR inertia variation with slot-pole and gear ratio for $l_{pp} = 2\ mm$ and $\theta_{in} = \theta_{out}$

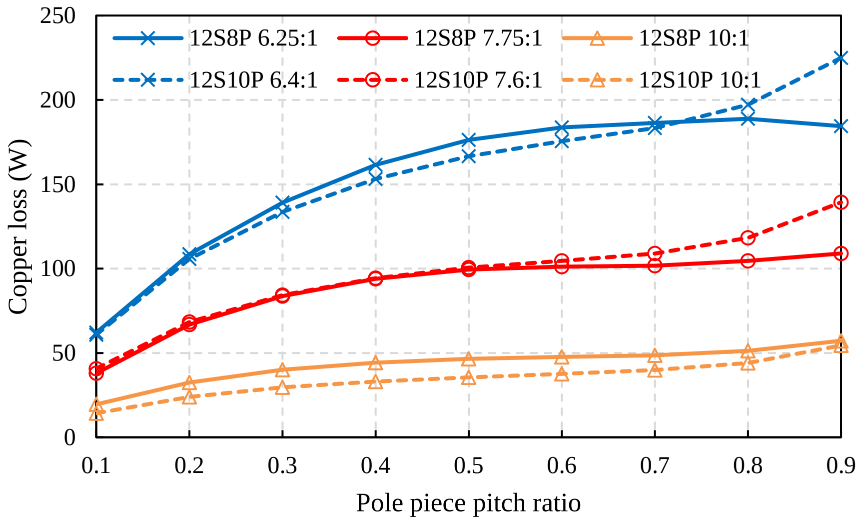

Figure 4.32. Copper loss variation with slot-pole and gear ratio for $l_{pp} = 2\ mm$ and $\theta_{in} = \theta_{out}$

A concept PPR design for a 12s8p 7.75:1 PDD topology with trapezoidal pole pieces having a pole piece pitch ratio of 0.5 and a pole piece radial thickness of 2 mm is shown in Figure 4.33 (a). The pole pieces are bonded within the slots of the monocoque PPR non-magnetic support structure. The axial extensions of the PPR support structure represent the electrical insulator regions and act to electrically insulate the pole piece from each other and from the endplates of the PPR. This is done in order to greatly reduce the eddy current path and to stop the eddy current from flowing between the pole pieces and into the PPR endplates.

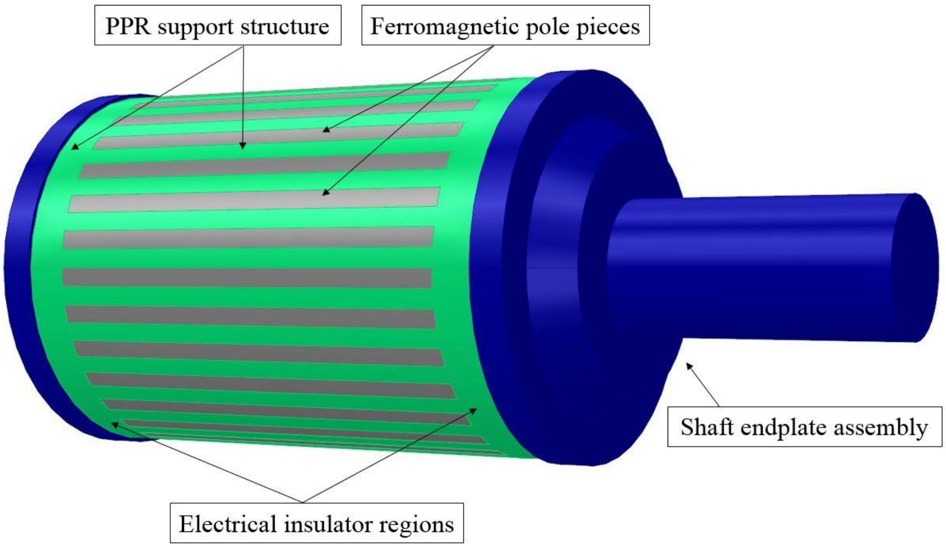

(a)

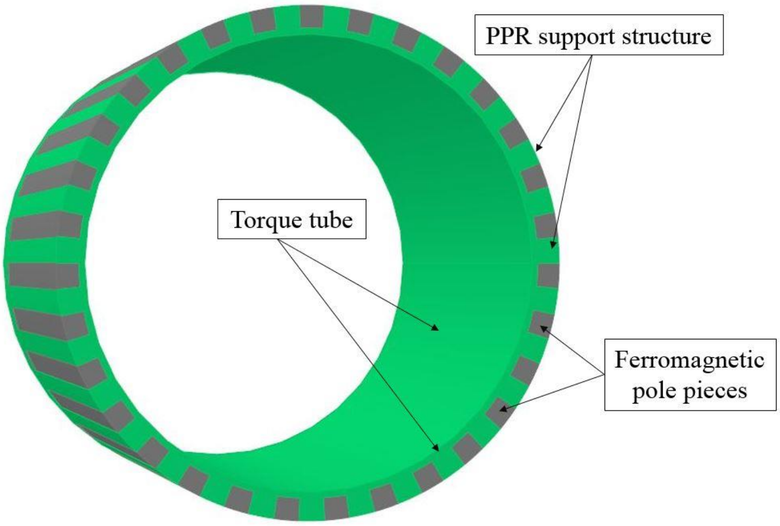

(b)

Figure 4.33. PPR concept design with $l_{pp} = 2\ mm$ and $rt_{in} = rt_{out} = 0.5$ (a) side view (b) cross-section

Ideally the PPR endplates should be manufactured from a non-magnetic alloy having a permeability of approximatively 1, such as aluminium or Inconel, in order to prevent the HSR and stator PM flux from leaking into the PPR endplates and induce loss of power and a decrease in efficiency.

Figure 4.33 (b) shows the cross section of the PPR. The primary pole piece retention method is represented by the adhesive applied on the three pole piece faces that are in contact with the composite PPR slot. Due to the trapezoidal shape of the pole pieces, a secondary retention method, in the form of an inner torque tube, is required to restrict the pole pieces from being displaced towards the inner airgap of the PDD. It can be observed that for fixed PPR outer diameter pole piece radial thickness and mechanical airgap thickness, the inner electromagnetic airgap of the PDD is increased by the radial thickness of the torque tube. This would result in an increase in the magnetic gear element active length and implicitly the PDD active mass and PPR inertia. Moreover, for a fixed slot-pole combination increasing the PDD effective airgap between the HSR and stator bore would increase copper loss, reducing motor efficiency. A composite overwrap can be applied to the surface of the PPR as a secondary retention mechanism to restrict the pole pieces from moving in the radial outward direction during rotation. This type of overwrap is similar to the one used in banding of surface PM rotor for conventional SPM 3-phase electrical machines. The PPR overwrap can be applied on the full surface of the PPR, increasing the thickness of the outer airgap. Another option would be to machine slots on the surface of the PPR and apply the composite overwrap in axially displaced concentric rings, as shown in Figure 4.34. Typical composite fibres used can be Carbon or Kevlar based.

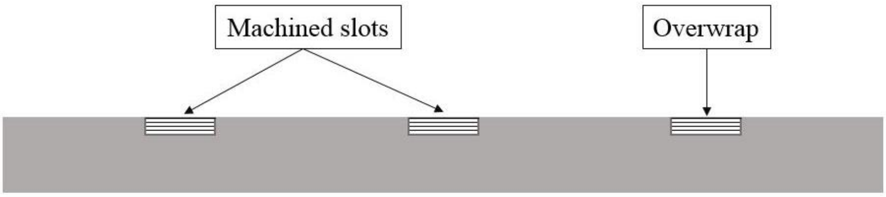

Figure 4.34. Pole piece side view with composite overwrap

By implementing this pole piece retention method, the outer airgap of the PDD is not increased and the increase in machine length and mass is affected by the ratio between the depth and thickness of the overwrap slots. The dimensions of the slots is mainly affected by the PPR outer diameter, pole piece thickness, rated speed and radial electromagnetic forces between the stator PM and pole pieces. Increasing the wrapping tension within the material limits during application, can also reduce the required size of the overwrap slots. The overwrap process can be removed by tapering the pole pieces such that only a torque tube composite layer is required which is part of the PPR monocoque structure. Figure 4.35 shows the two tapered pole piece designs. The PPR support structure only requires a torque tube on the inner or outer diameter based on the taper orientation. This design concept removes the need for an additional overwrap, reducing the resultant inner or outer airgap for fewer manufacturing steps.

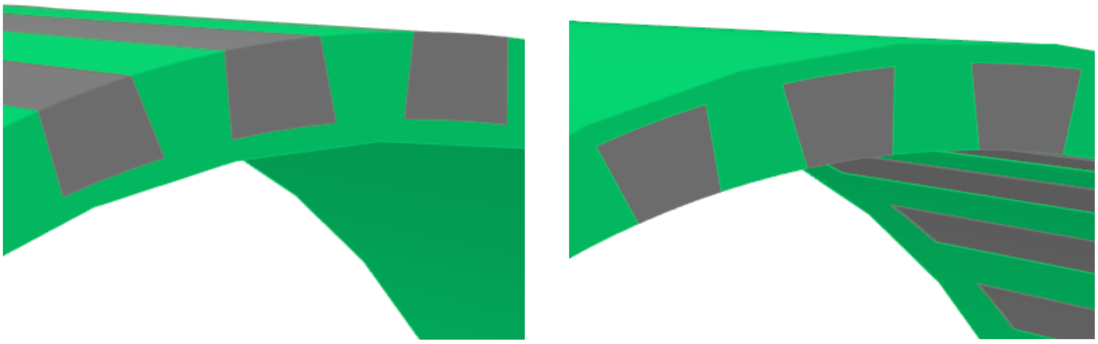

(a) 0.5 / 0.6 taper ratios

(b) 0.6/ 0.5 taper ratios

Figure 4.35. PPR cross-section (a) outer (b) inner pole piece taper

4.2.2 Circular pole piece cross-section

The proposed circular pole piece cross section is shown in Figure 4.36. This particular pole piece shape was parametrised based on the nominal pole piece pitch, α_{pp}, and the actual pole piece pitch of the circular ferromagnetic rod, β_{pp}. For simplicity, the pole piece pitch was approximated to be equal to the pole piece diameter, $\O_{pp}$.

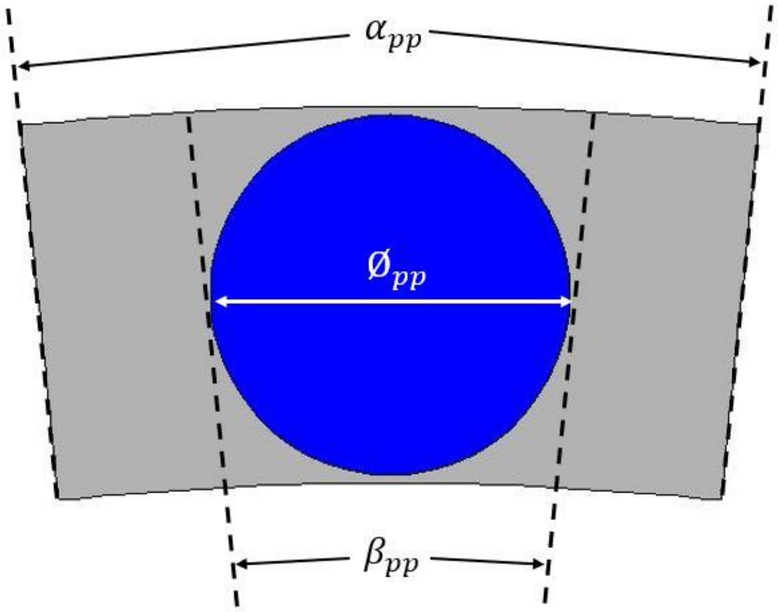

Figure 4.36. Circular pole piece cross-section

The pole piece pitch ratio, δ_{pp}, between the actual and nominal pole piece pitch is given by:

$$\delta_{pp} = \frac{\beta_{pp}}{\alpha_{pp}} = \frac{\emptyset_{pp}}{\frac{\pi\emptyset_M}{N_{pp}}} \tag{4.10}$$

where $\emptyset_M$ is the average diameter of the pole piece rotor given by:

$$\emptyset_M = D_{PPRo} - \emptyset_{pp}/2 \tag{4.11}$$

where D_{PPRo} is the PPR outer diameter.

From (4.10) and (4.11), the pole piece diameter, $\emptyset_{pp}$, can be expressed as a function of the pole piece pitch ratio, number of pole pieces and PPR outer diameter, such that:

$$\emptyset_{pp} = \frac{\delta_{pp}\pi D_{PPRo}}{N_{pp} + \frac{\delta_{pp}\pi}{2}} \tag{4.12}$$

Figure 4.37 shows the variation of the maximum torque transmission capability of the magnetic gear element for the selected slot-pole combinations and corresponding gear ratios as a function of the pole piece pitch ratio. It can be observed that the 8 pole topologies have a higher PPR pull-out torque than the 10 pole designs. For a fixed slot-pole combination, the maximum PPR pull-out torque is reduced by increasing the PDD gear ratio. It can also be observed that each of the selected slot-pole combinations and corresponding gear ratios have the same optimum pole piece pitch at 0.5. This corresponds to different optimum pole piece diameters based on the number of pole pieces required to achieve each gear ratio and is related to the optimum separation between adjacent pole pieces, which causes the HSR/stator PM flux that short circuits through the PPR to be minimised.

Figure 4.38 and 4.39 show the variation in PDD active mass and PPR inertia as a function of pole piece pitch ratio. It can be observed that the 0.5 pole piece pitch ratio, which produce the lightest PDD designs, may not result in minimum PPR inertia. For the presented PDD slot-pole combinations, the optimum pole piece pitch ratio, in terms of low PPR inertia, is at 0.25, with the output rotor inertia being increased by approximatively 45% when the pole piece pitch ratio is 0.5. It can also be observed that, for a fix PPR pull-out torque requirement, the low gear ratio PDD designs have the lowest mass since the torque transmission capability of the magnetic gear is maximised and the active length of the PDD is reduced.

The corresponding PDD copper loss at the rated torque value is shown in Figure 4.40. As for the trapezoidal pole piece cross-section, increasing the PDD gear ratio reduces the copper loss for a fixed output PPR torque. It can also be observed that at low pole piece pitch ratios the copper loss is low. This is due to the increase in machine length caused by the low PPR pull-out torque capability combined with a large separation between adjacent pole pieces which reduced the HSR PM flux leakage and increases the fundamental flux linking with the stator coils. In contrast, at high pole piece pitch ratios, the separation between adjacent pole pieces is heavily reduced, which causes an increase in the HSR PM flux leakage and greatly reduces the stator magnetic flux which increases the electric loading and the copper loss. In order to obtain a PDD design with circular pole pieces and reduced copper loss, the pole piece pitch ratio cannot be set low as it would greatly increase the active mass of the motor. Hence, the copper loss can be effectively reduced without affecting the PDD mass by increasing the gear ratio, such that the electromagnetic torque requirement for a fixed output torque is reduced. For example, for a 12s8p design with a pole piece pitch ratio of 0.5, the copper loss can be reduced by 54.3% by increasing the gear ratio from 6.25 to 7.75. In this case, the PDD active mass would be increased by only 5.3% while the inertia of the PPR would actually be reduced by 11.6%. This decrease in the PPR inertia between the two gear ratios for a fixed pole piece pitch ratio is given by the higher number of pole pieces required by the 7.75:1 design which results in a smaller pole piece diameter and reduced mass of the PPR.

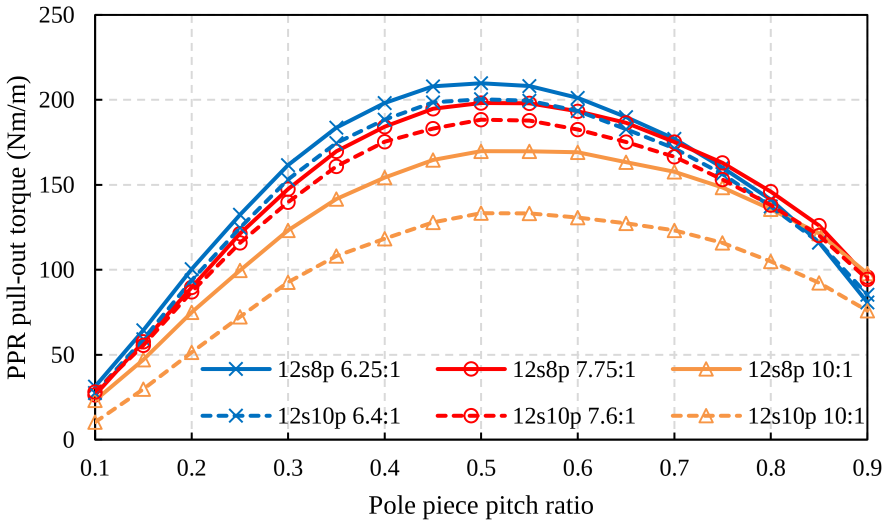

Figure 4.37. PPR pull-out torque variation with pole piece pitch ratio δ_{pp}

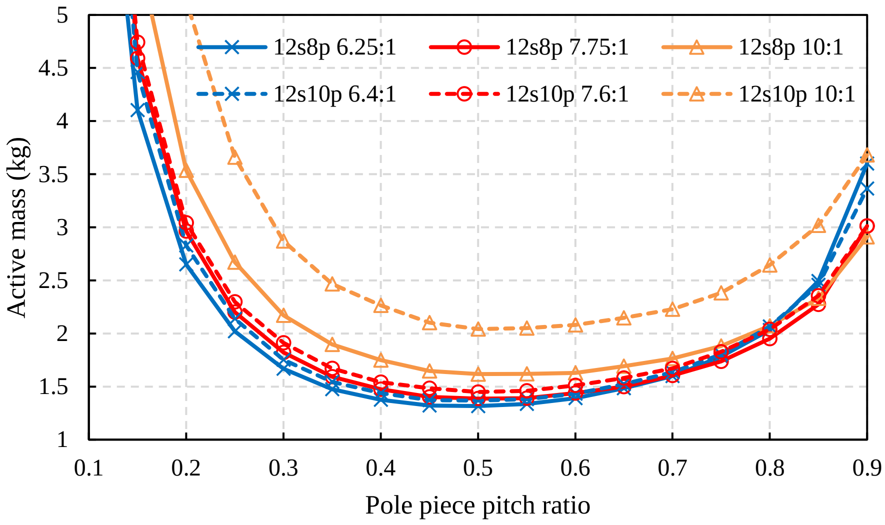

Figure 4.38. PDD active mass variation with pole piece pitch ratio δ_{pp}

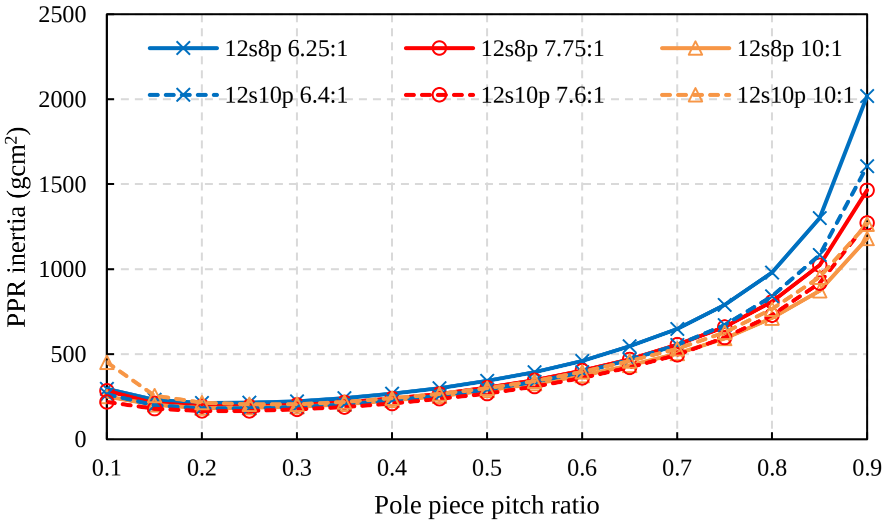

Figure 4.39. PPR inertia variation with pole piece pitch ratio δ_{pp}

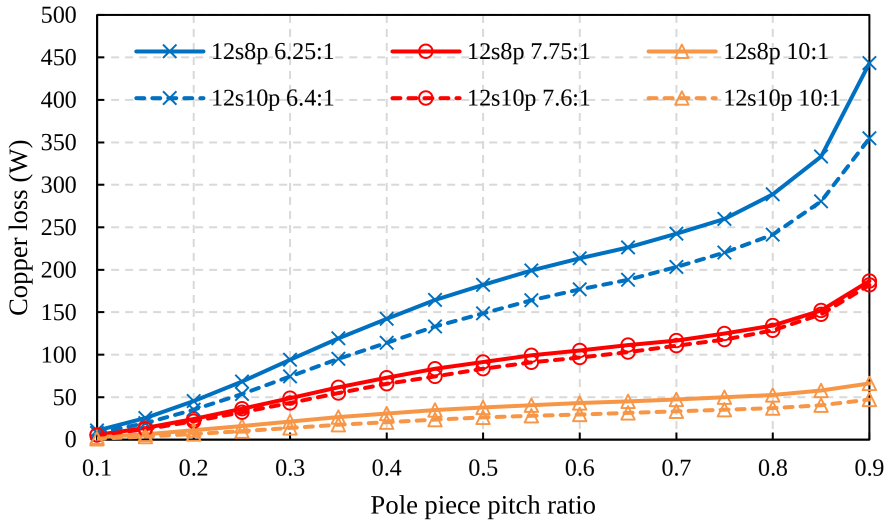

Figure 4.40. Copper loss variation with pole piece pitch ratio δ_{pp}

From the presented results, it can be observed that in order to obtain a low mass PDD design, the pole piece pitch ratio has to be fixed at 0.5 for a circular pole piece cross section. At this pole piece pitch ratio, the PPR inertia is increased with an average of 45% from its lowest value. If this increase in PDD active mass would be tolerated, the decrease in PPR inertia would reduce the mass of the actuator end stops. These are sized based on the kinetic energy, stored in the mechanical drive train of the actuator, which gets absorbed by the end stops during loss of control or actuator run-away.

For a low mass solution, some of the selected gear ratios would result in designs with a low pole piece diameter and are not regarded mechanically reliable at withstanding the torsional and radial loads applied to the PPR during operation. Thus, as for the trapezoidal pole piece cross section, a lower limit of 2 mm was applied to the minimum allowable thickness of the circular pole pieces. For a minimum mass PDD solution, Table 4.5 shows the optimum and achievable pole piece pitch ratios and corresponding diameters for the selected slot-pole combinations and gear ratios. The percentage increase in mass and output rotor inertia is also presented, showing that for the high gear ratio of 10:1 a substantial penalty in mass and PPR inertia has to be incurred in order to obtain a mechanically achievable and reliable design.

Table 4.5. Comparison of optimum FE and manufacturable circular pole piece cross-section parameters

Slot - pole	**Gear ratio**	**Optimum δ_{pp} / Pole piece diam. (mm)**	**Achievable δ_{pp} / Pole piece diam. (mm)**	**% mass increase from optimum**	**% J_{PPR} increase from optimum**
12s8p	6.25:1	0.5 / 2.76	0.5 / 2.76	-	-
	7.75:1	0.5 / 2.24	0.5 / 2.24	-	-
	10.0:1	0.5 / 1.75	0.6 / 2.1	0.6%	30%
12s10p	6.4:1	0.5 / 2.17	0.5 / 2.17	-	-
	7.6:1	0.5 / 1.84	0.55 / 2.02	0.7%	15%
	10.0:1	0.5 / 1.40	0.75 / 2.1	17%	110%

A concept PPR design for a 12s8p 7.75:1 PDD topology with circular pole pieces is shown in Figure 4.41. This design has the benefit of being simple to manufacture and cost effective as it does not require a PPR monocoque and uses the solid pole pieces which are fastened in the PPR endplates. The non-laminated pole pieces can be coated with an electrical insulator such that they are isolated from each other and the PPR endplates. This would act to reduce the induced eddy current loss in the pole pieces, although this would still be considerably higher than an axially laminated pole piece structure. The pole pieces can be threaded in the end plates or secured with radial grub screws displaced through the endplate which engage with a flat face on the pole piece. Thus, the dependence on composites and adhesives is removed by this PPR concept. By removing the composite support structure the resultant PPR cage acts as a fan, increasing the cooling of the steel pole pieces and promoting air flow between the two airgaps.

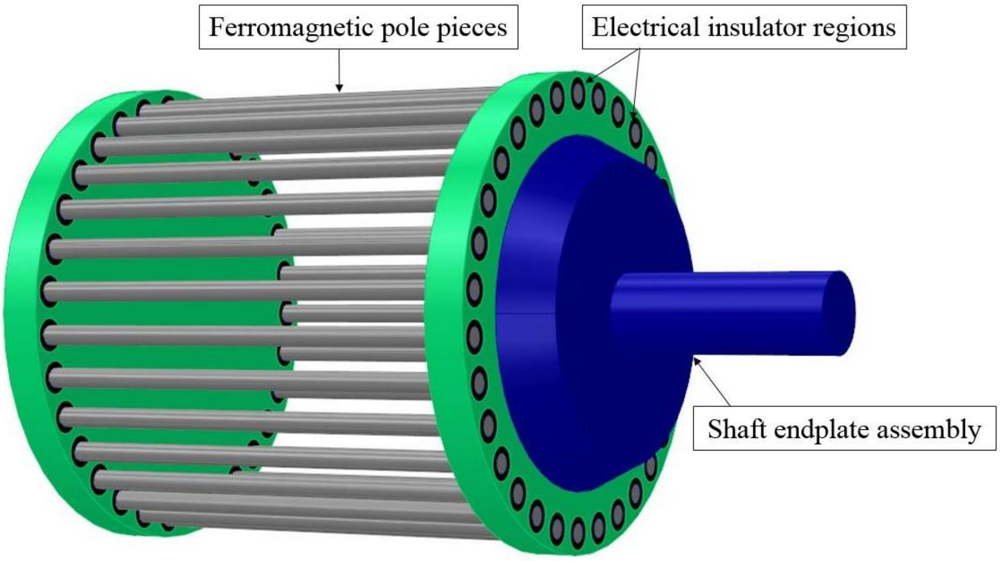

Figure 4.41. PPR concept design with circular pole pieces $\O_{pp} = 2mm$

4.2.3 Proposed pole piece cross-section

The proposed pole piece cross section for the PDD prototype was based on the electromagnetic FE results presented for the standard trapezoidal and circular pole piece cross sections. A trapezoidal pole piece cross section was preferred over the circular one since, for the same machine cross section design, it provides a higher output rotor pull-out torque, effectively reducing the mass and inertia of the PDD actuator motor.

Figure 4.42 shows the proposed pole piece cross section with circular cut-outs on both sides of the ferromagnetic pole piece. The circular cut-outs were used in conjunction with non-magnetic glass fibre support rods designed to engage with the pole piece and secure it in the PPR assembly. Based on the trapezoidal pole piece FE results, the radial length of the pole piece was fixed at 2mm with a 0.5 inner and outer pitch ratio. The curvature for both sides of the pole piece was set such that a 2.5mm grass fibre rod can fit between two adjacent pole pieces. The excess glass fibre material pultruding into the inner and outer airgaps of the PDD motor would be ground off during the post PPR assembly operations. This would ensure that the cross section of the PPR is exactly 2mm thick without increasing the mechanical airgaps of the PDD above the fixed 0.5mm.

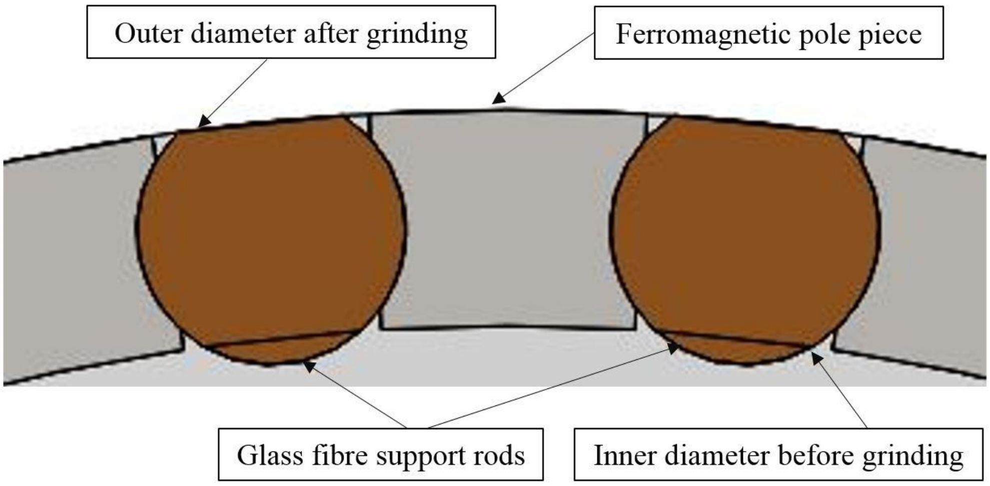

Figure 4.42. Proposed pole piece cross section with non-magnetic support rods

For the trapezoidal, circular and proposed pole piece cross sections with the optimum selected pole piece design parameters for low active mass, Figure 4.43 compares the average PPR pull-out torque of the different slot-pole combinations and corresponding gear ratios. It can be observed that, for all the slot-pole combinations and gear ratios, the circular pole piece design has the lowest average pull-out torque, with the trapezoidal and proposed pole piece designs being evenly matched. Figure 4.44 compares the active mass of the PDD designs shown in Figure 4.43. Since all the presented PDD designs have the same rotor and stator diameters, the active mass is heavily influenced by the active length which results from the average PPR pull-out torque capability. Thus, design which have a higher PPR pull-out torque capability per meter length are also characterised by a shorter active length for a given pull-out torque requirement. Thus, the poor PPR pull-out torque capability of the circular pole pieces results in PDD designs with an increased active mass for all the slot pole combinations and gear ratios over the trapezoidal and proposed pole piece designs.

Figure 4.45 compares the PPR inertia of the selected slot-pole combinations and gear ratios for the three pole piece designs under investigation. For fixed inner and outer rotor diameters, the inertia is influenced by the total active length of the rotor. Thus, as the PPR based on circular pole pieces is longer and implicitly heavier, the rotor inertia is also increased compared to the PPRs based on the trapezoidal and proposed pole piece designs. It can also be observed that the proposed PPR design has a slightly lower inertia when compared to the trapezoidal variant. This is due to the side cut-outs of the proposed pole pieces which results in high density lamination steel material being replaced by low density glass fibre, effectively reducing the mass of the PPR. On average, the inertia of the proposed PPR design is reduced by 10-15% when compared with the trapezoidal pole piece design.

Figure 4.46 shows the copper loss at the rated operating point for the investigated PPR designs, with the different slot-pole combinations and corresponding gear ratios. From (4.6), it can be observed that the copper loss for a fixed output torque is influenced by the gear ratio, stator magnetic loading and active length of the machine. Thus, in Figure 4.46 it can be observed that as the gear ratio is increased, the copper loss is substantially reduced. For a fixed slot-pole combination and gear ratio, the circular pole pieces help to reduce the PDD copper loss when compared to the trapezoidal and proposed designs. This is due to the fact that the circular pole pieces limit the amount of HSR PM flux leakage that short circuits through the PPR and increases the radial field component which links with the stator winding. Thus, the fundamental flux linkage component linking with the stator winding is increased and acts to reduce the copper loss in spite of a longer active length of the PDD stator winding given by the poor pull-out torque capability.

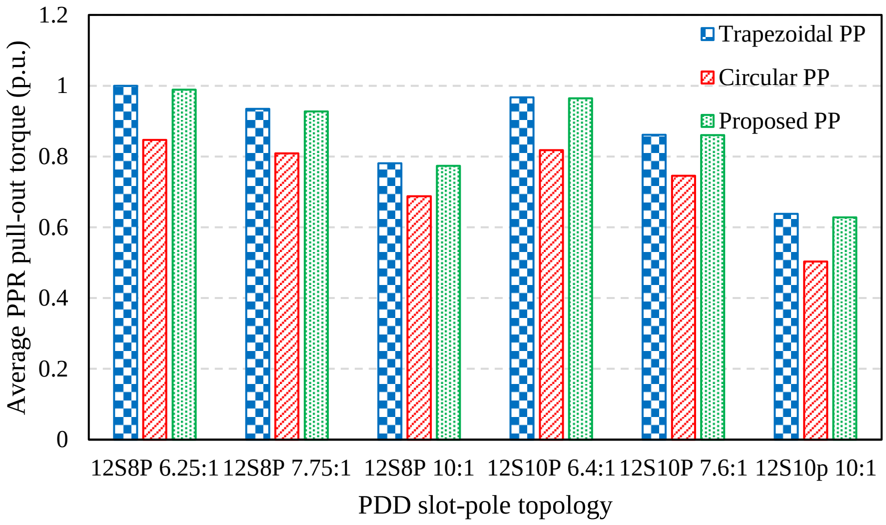

Figure 4.43. Comparison of PPR pull-out torque for different slot-pole, gear ratio and pole piece topologies

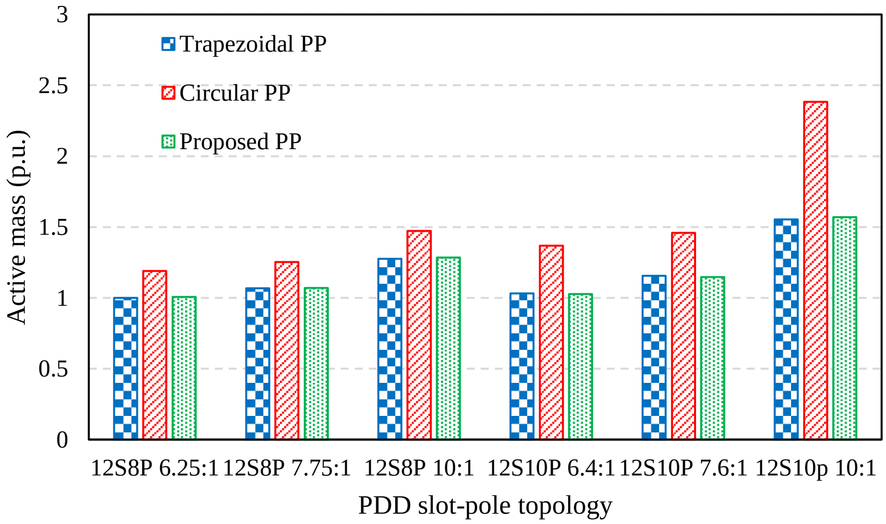

Figure 4.44. Comparison of PDD active mass for different slot-pole, gear ratio and pole piece topologies

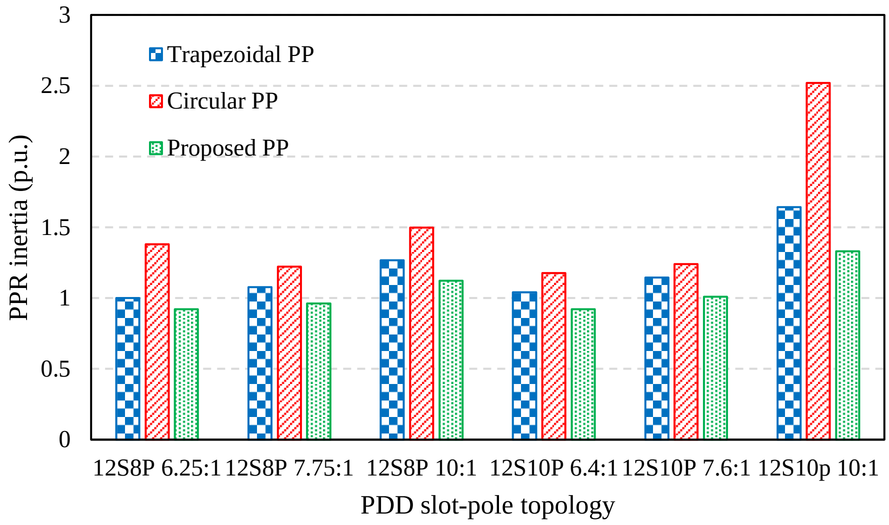

Figure 4.45. Comparison of PPR inertia for different slot-pole, gear ratio and pole piece topologies

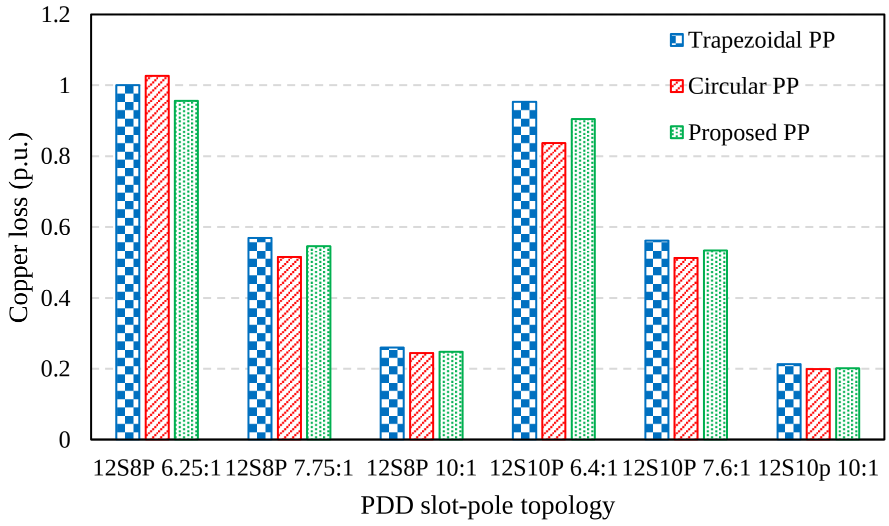

Figure 4.46. Comparison of PDD copper loss for different slot-pole, gear ratio and pole piece topologies

The PDD designs in this investigation were simulated in the electromagnetic FE software with a constant load angle such that the PPR produced the rated torque required for the actuator application. As discussed, the integer gear ratios are characterised by a high cogging torque factor and produce a large torque ripple on the HSR and PPR. Figure 4.47

and 4.48 show the peak to peak torque ripple as a percentage of the rated torque on the HSR and PPR for the both non-integer and integer gear ratios. The non-integer gear ratios have a cogging factor of 1, while the 8 and 10 pole integer gear ratios have a cogging torque factor of 4 and 5 respectively. Thus, it can be observed that the integer gear ratios have a considerably higher torque ripple than the non-integer topologies. Moreover, for the integer gear ratios, the circular and proposed pole piece cross-sections greatly increase the torque ripple on both the HSR and PPR. For the non-integer gear ratios and for the three pole piece cross-sections, the torque ripple of the HSR and PPR was predicted to be below 0.5% and 0.1% respectively.

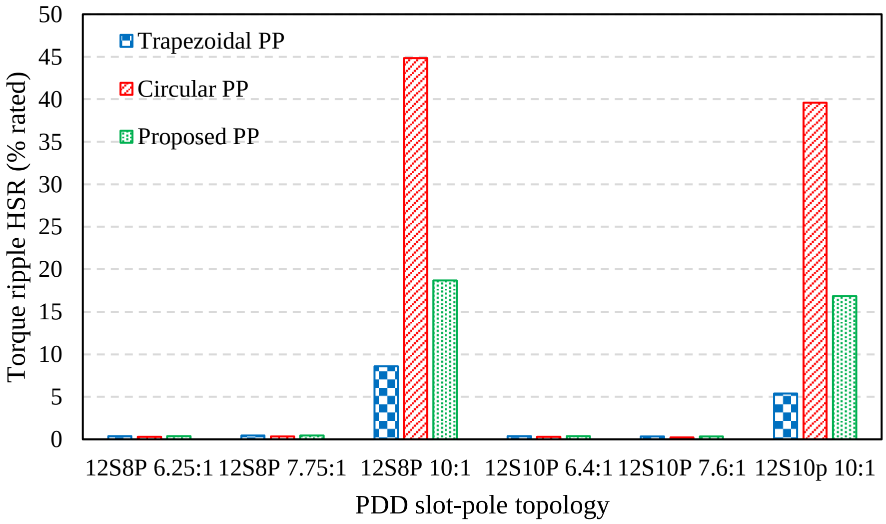

Figure 4.47. Comparison of HSR torque ripple for different slot-pole, gear ratio and pole piece topologies

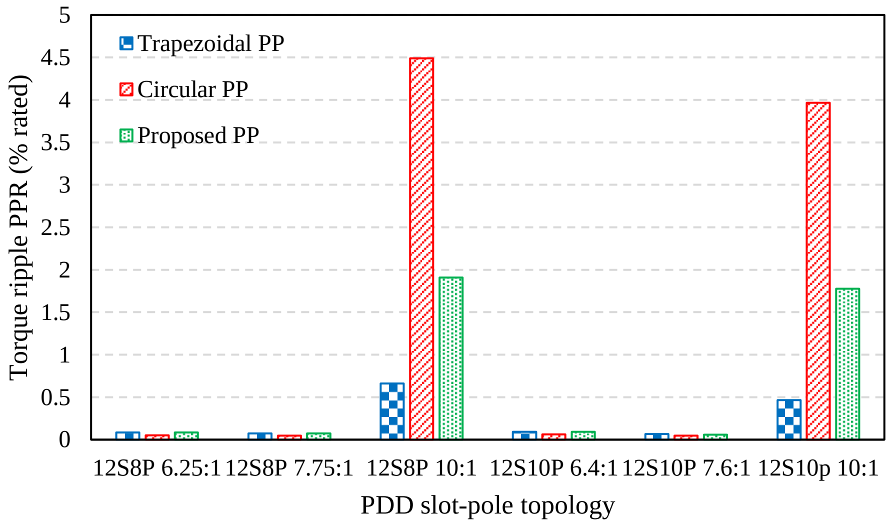

Figure 4.48. Comparison of PPR torque ripple for different slot-pole, gear ratio and pole piece topologies

4.2.4 Conclusions

An investigation into the pole piece cross section design was conducted for two slot-pole combinations, each with three distinct magnetic gear ratios. The trapezoidal, circular and proposed pole piece cross sections were parametrised in terms of radial thickness and inner and outer angular width. The outer diameter of the PPR was fixed and for each pole piece radial thickness, the total PM mass per unit length of each PDD design was kept constant.

For the trapezoidal pole piece cross-section, reducing the pole piece radial thickness acts to increase the PPR pull-out torque amplitude, reducing the active mass, PPR inertia and copper loss of the resulting PDD designs. It was shown that the optimum values for the inner and outer pole piece pitch change based on the pole piece thickness. The low mass PDD designs with the circular pole piece cross section showed an optimum pole piece pitch ratio of 0.5. The proposed pole piece cross section is based on a glass fibre rod design which interlocks with the ferromagnetic pole pieces. Thus, this design is based on the trapezoidal pole piece shape and does not require an inner or outer torque tube to retain the pole pieces during rotation.

The comparison of the three pole piece shapes showed that the circular pole piece cross section achieves an inferior PPR-pull out torque characteristic, with the trapezoidal and proposed topologies being evenly matched. As a result, the active mass and PPR inertia for all the PDD designs irrespective of slot-pole combination and gear ratios is increased if the circular pole piece design is selected. The proposed PPR cross section design showed a slightly reduced inertia when compared to the trapezoidal topology due to a lower rotor active mass. The circular pole piece cross section did achieve a slightly reduced copper loss when compared with the other two pole piece designs, but at the expense of longer and heavier PDD designs.

It was also shown that irrespective of the pole piece topology or slot-pole combination, increasing the magnetic gear ratio results in the decrease of the PPR pull-out torque and increase in active mass and output rotor inertia. In contrast, increasing the gear ratio does reduce the copper loss of the PDD, as the electromagnetic torque requirement is reduced for a fixed output torque.

In terms of HSR and PPR torque ripple, it was shown that the fractional gear ratios with a cogging torque factor of 1 have a substantially lower torque ripple than the integer gear ratios with higher cogging torque factors. It was also established that, for integer gear ratios, the circular pole piece design can greatly increase the torque ripple.

Chapter 5: Investigation of leading PDD design parameters

The fault tolerant PDD design for the actuator drive train has been based around a low mass and low PPR inertia solution. Based on the linear actuator weight breakdown and rudder actuator total mass, the fault tolerant PDD total mass was limited to 3.6 kg. Due to the nature of the PDD actuator motor, it was decided to produce a standalone PDD design capable of being tested independently of the actuator platform. Moreover, the PDD would then be inserted in the actuator frame and connected to the mechanical drive train without modifications to the PDD structural elements such as outer case and endplates. Thus, the additional weight introduced by the structural PDD components enabling the standalone testing of the prototype, was considered. Typically, the total PDD mass is larger than the active mass by a factor of 2 – 2.5 due to the additional weight introduced by structural components such as frame, endplates, shafts, bearings and fault tolerant position sensors. It is also important to consider the fact that the 2D active length would have to be increased by a 3D factor in order to compensate for the 3D end flux leakage. In a PDD, the end flux leakage can introduce a reduction in PPR pull-out torque capability and increase in copper loss when compared to the 2D FE predictions. This is influenced by the machine aspect ratio, slot-pole combination and pole piece radial thickness. A PDD with a large diameter but reduced active length (aspect ratio < 1) would have a higher 3D factor than a design having an aspect ratio of 1, for example. Moreover, the large effective PDD airgap between the HSR and stator can increase the end leakage effects in a PDD when compared to a conventional SPM. This 3D factor is typically predicted with 3D FE electromagnetic analysis in the detail design stage, after the 2D design has been selected. For simplicity, at this stage, a 3D factor of 15% was assumed. Thus, based on the presented assumptions, the targeted 2D PDD active mass was fixed at 1.5 kg.

5.1 PDD parametric scan

In order to investigate the effects of the leading PDD design parameters, 2D parametric scans were implemented on the slot pole combinations and gear ratios shown in Table 5.1.

Table 5.1. Selected PDD slot-pole combinations

No. slots	**Gear ratio**	**HSR pole pairs ($2p_h$)**	**Stator pole pairs (p_l)**	**Pole pieces (N_{pp})**
12	6.25:1	8	21	25
	7.75:1		27	31
	9.25:1		33	37
	10:1		36	40
	6.4:1	10	27	32
	7.6:1		33	38
	9.2:1		41	46
	10:1		45	50

The 12s14p and 12s16p topologies were not considered in this investigation due to the increased HSR PM flux leakage effects which lead to poor pull-out torque capability and high PDD active mass, as shown Chapter 4. Due to the reduced PDD torque requirement and constrained mass, these high pole count topologies are characterized by a high degree of flux leakage in the airgaps caused by the small pole pitch relative to the total airgap. Thus, this would result in an increased active length, mass and rotor inertia combined with poor stator magnetic loading which would reduce machine efficiency.

As well as satisfying the active mass requirement, the PDD design is required to have a low output rotor inertia. It is important to consider that a high PPR inertia would increase the kinetic energy stored in the rotor during operation. Thus, at actuator level, all the mechanical components connected to the PDD output rotor such as couplings, linear screw and end stops would have to be sized to handle the excess load during shock loading of the control surface, which can be caused by object strikes or sudden wind gusts. Hence, it is important to have a low output rotor inertia in order to reduce mass from the mechanical drive train components.

Since the PPR inertia is mainly influenced by rotor diameter and scales linearly with PDD active length, the parametric scans were conducted for a range of output rotor diameters as shown in Table 5.2.

Table 5.2. Ranges of PDD parametric scan parameters

D_{PPRo} (mm)	l_{stat} (mm)	l_{im} (mm)	l_{pp} (mm)	l_{om} (mm)
30	10 - 13	5 - 7	2 - 3	1.5 - 3
35 - 40		5 - 9		
45		5 - 11		
50 - 70		5 - 12		

The additional 2D FE scan variables include the stator, inner/outer magnet and pole piece radial thicknesses. The length of the inner and outer airgap was fixed to 0.7 mm which includes a mechanical separation of 0.5 mm and a 0.2mm HSR carbon fibre wrap in the inner airgap and a 0.2 mm inner sleeve for the retention of the stator PMs for the outer airgap. Halbach PM arrays have been used for the HSR and stator bore. In order to minimise the number of design of the parametric scans the pole pitch ratio of the HSR Halbach PMs was fixed to 1 based on the results presented in Chapter 4, section 4.1. For simplicity the PPR design was based on the trapezoidal cross-section with the pole piece inner and outer pitch ratio fixed at 0.5. Based on the results presented in Chapter 4, section 4.2, this pole piece pitch ratio maximised the PPR pull-out torque reducing the length and active mass of the PDD with only a moderate increase in the PPR inertia. The Recoma 28

Samarium Cobalt PM grade was selected for both PM arrays. For the parametric scan the PM temperature of the HSR and stator arrays was fixed at 80°C and 100°C, respectively. The copper temperature used to predict the phase resistance and the copper loss was assumed to be 100°C. The lamination material was selected as M270-35A. The magnetic properties of the PMs and laminated electrical steel are presented in Appendix 1.

The variation of PPR inertia with the PDD active mass for a range of PPR outer diameters, for the 12s8p 7.75:1 designs that have an RMS slot current density lower or equal to 10 A/mm^2, is shown in Figure 5.1. It can be seen that as the PPR outer diameter is increased the mass of the PDD is reduced, but the PPR inertia is increased. The increase in PPR outer diameter increases the pull-out torque capability of the magnetic gear element and reduces the active length of the PDD for a fixed slip torque requirement. Thus, the decrease in length reduces the active mass. In contrast, the PPR inertia is proportional with the outer radii at the power of four and is rapidly increased by increasing the outer diameter of the rotor. Increasing the PPR outer diameter beyond 45mm results in a large increase in rotor inertia with only a moderate decrease in machine mass. For example, increasing the PPR outer diameter from 45mm to 50mm brings an increase of 20% for the output rotor inertia, but only a 7% reduction in active mass. The PDD designs with the lowest active mass and output rotor inertia, for each PPR outer diameter design family, have been selected and are highlighted in Figure 5.1. It can be observed that the selected 45mm PPR outer diameter design qualifies for the minimum mass requirement with the lowest output rotor inertia. Similar trends in inertia and mass have been observed for all the other slot-pole combinations and corresponding gear ratios shown in Table 5.1.

Figure 5.2 shows the variation of the HSR inertia with PDD active mass. It can be observed that, for the selected designs from each of the PPR design families, the HSR inertia is maximised. This is due to the fact that the HSR PM mass is increased by increasing the HSR PM radial thickness, in order to generate PDD designs having a reduced mass, current density and PPR inertia. Thus, for the actuator PDD motor, the mass and inertia of the HSR are higher than that of the PPR. It is important to consider that the inertia of the HSR and implicitly the kinetic energy stored in the rotor during operation are isolated from the actuator mechanical drive train due to the contactless compliant magnetic gear transmission. Thus, in the case of control surface overload, the magnetic gear element of the PDD will pole-slip, with zero average power transmitted to the static PPR from the HSR. During this overload condition, only the low energy PPR is directly connected to the linear screw and control surface. Thus, since the energy stored in the PPR during operation is low, mass can be reduced from the mechanical drive train of the actuator without affecting the structural integrity during overload conditions. However, it is important to point out that the inertia of the HSR has a significant effect on the dynamics of the actuator.

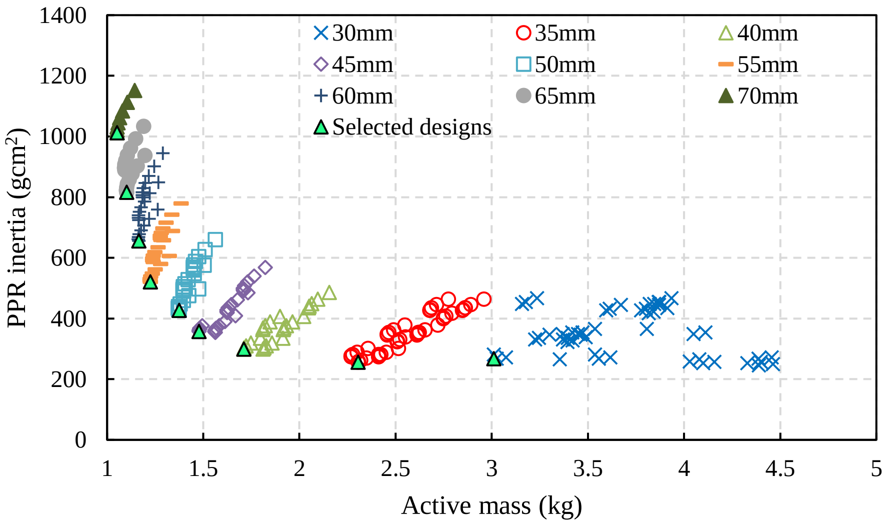

Figure 5.1. Variation of PPR inertia with PDD active mass for 12s8p 7.75:1 designs

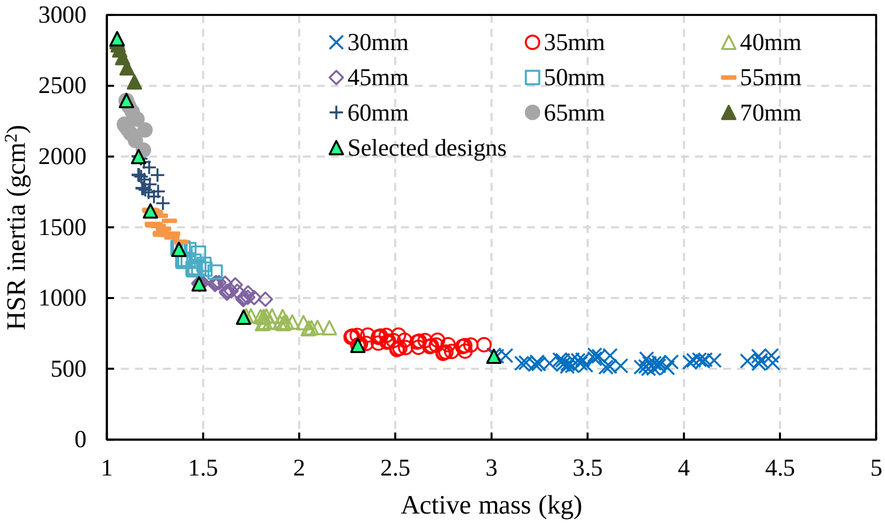

Figure 5.2. Variation of HSR inertia with PDD active mass for 12s8p 7.75:1 designs

The variation of the HSR and stator PM mass with PDD active mass is shown in Figure 5.3. It can be observed that the HSR PM mass is maximised for the selected designs in order to increase the stator magnetic loading, PPR pull-out torque and while reducing the PDD active mass and current density. In contrast the stator PM mass is reduced due to the minimised active length of the PDD and reduced stator PM thickness required to increase the stator magnetic loading from the HSR.

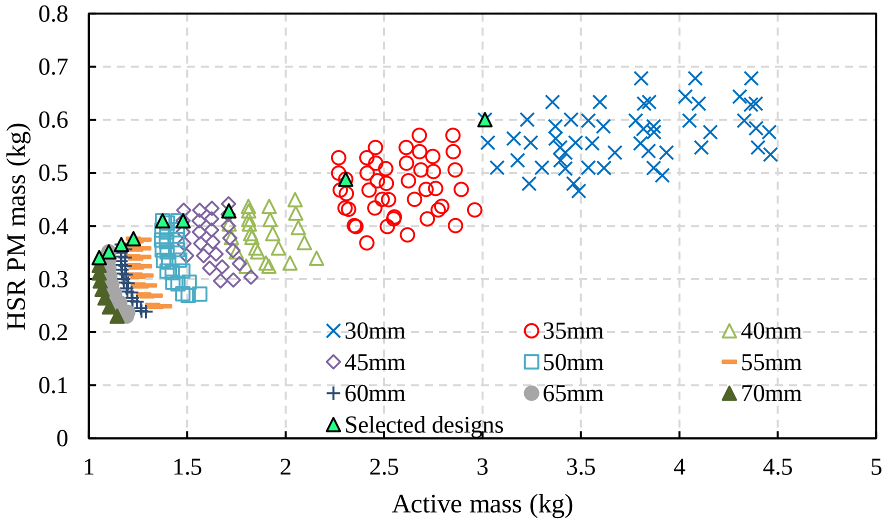

(a)

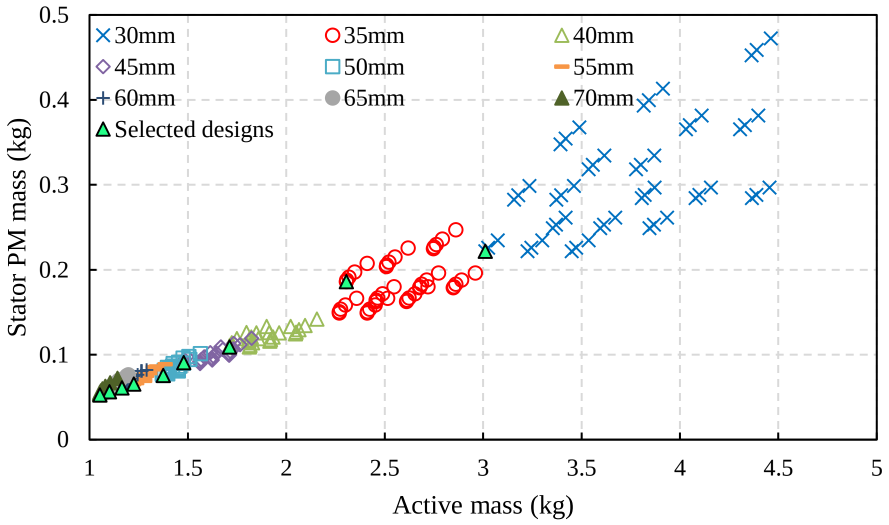

(b)

Figure 5.3. Variation of (a) HSR (b)stator PM mass with PDD active mass for 12s8p 7.75:1 designs

The variation of PPR pull-out torque capability with PDD active mass for the 12s8p 7.75:1 designs, is shown in Figure 5.4. It can be observed that the PPR pull-out torque is maximised by increasing the PPR outer diameter. As the PPR pull-out torque is increased, the active length of the PDD magnetic gear element is reduced for a fixed output torque requirement. As a result, the active mass of the PDD is reduced by an increase in PPR diameter. However, at high PPR diameters, diminishing returns are gained in terms of active mass. Figure 5.5 shows the variation of the PPR outer airgap shear stress pull-out torque with PDD active mass. It can be observed that, for the selected design from each PPR diameter family, the airgap shear stress is maximised. The highest outer airgap shear stress is achieved by the 55mm PPR diameter design, at 81kPa.

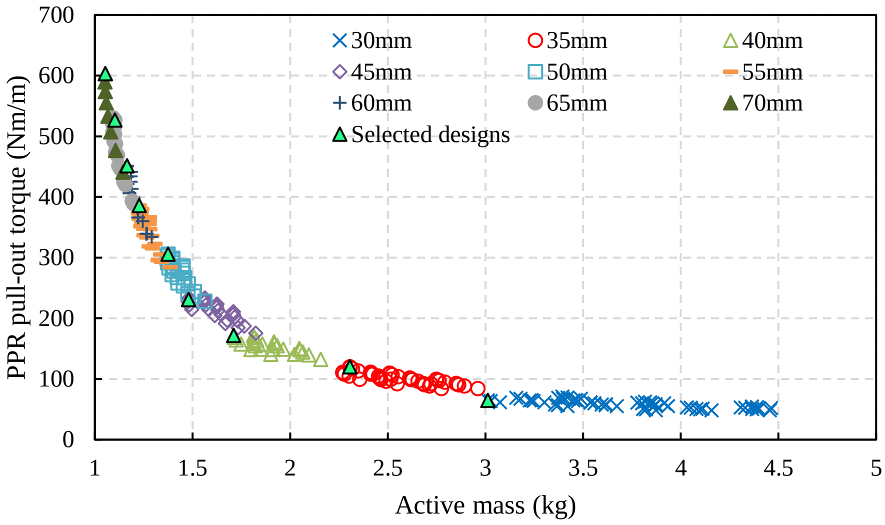

Figure 5.4. Variation of PPR pull-out torque capability with PDD active mass for 12s8p 7.75:1 designs

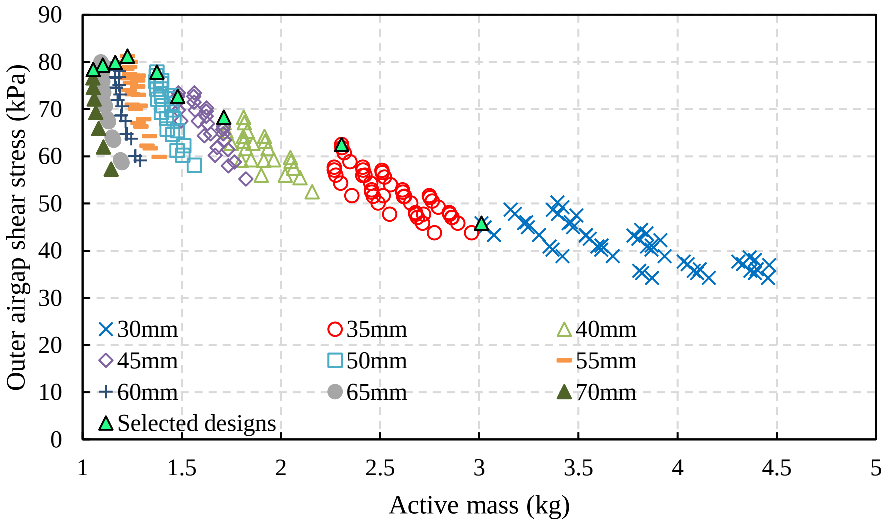

Figure 5.5. Variation of peak PPR airgap shear stress with PDD active mass for 12s8p 7.75:1 designs

The variation of the rated copper loss with PDD active mass is shown in Figure 5.6. The copper loss was predicted with the PDD operating in Active-Passive mode, with only one lane of the duplex 3-phase winding producing rated torque. It can be seen that the copper loss and active mass are reduced by increasing the PPR outer diameters. For a fixed PPR diameter, the copper loss is reduced by increasing the PM mass of the HSR while minimising the stator PM thickness in order to reduce the effective HSR-stator airgap and increase the stator magnetic loading. This reduced the amplitude of the current demand for a fixed output torque and minimised copper loss. Figure 5.7 shows the variation of the corresponding PDD efficiency for the selected designs. The efficiency at the rated operation point was estimated by considering the iron loss in the lamination steel of the PPR and stator as well as the copper loss in one lane of the duplex 3-phase winding. The PM and stator PM sleeve eddy current loss will be predicted by 3D FE analysis and has been ignored for this efficiency prediction. Since for this PDD design the copper loss is dominant, the designs with the lowest copper loss have the highest efficiency. Thus, as the PPR and implicitly HSR diameters are increased, the motor efficiency is increased. For the selected designs predicted efficiency varies from 84% to 91%.

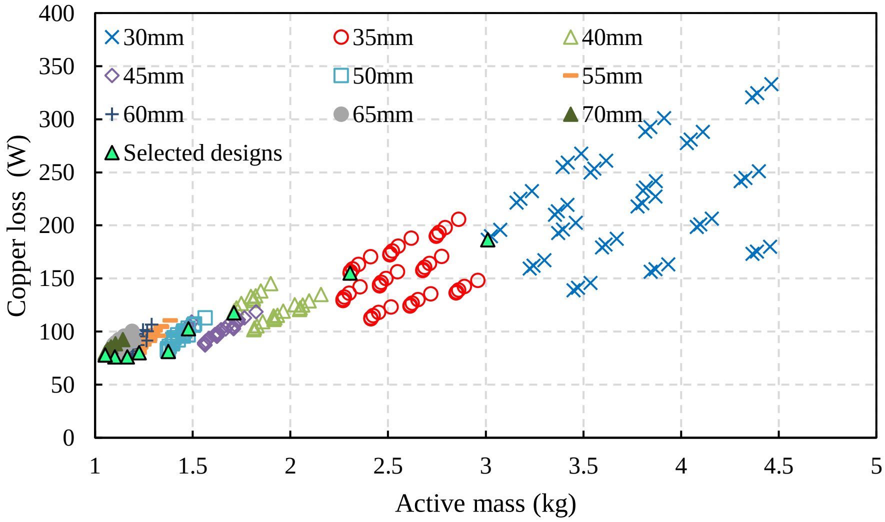

Figure 5.6. Variation of rated copper loss with PDD active mass for 12s8p 7.75:1 designs

.

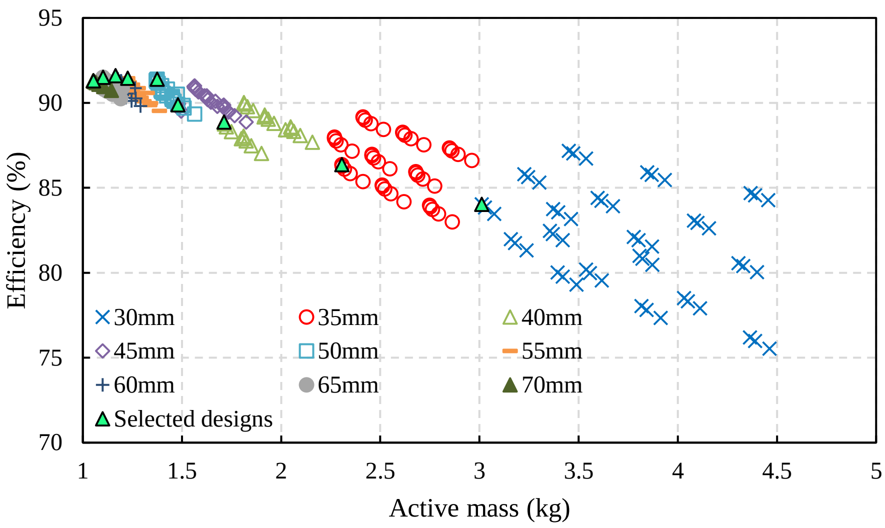

Figure 5.7. Variation of efficiency with PDD active mass for 12s8p 7.75:1 designs

From the results of the 2D parametric scans for the PDD slot-pole combinations and corresponding gear ratios show in Table 5.1, PDD designs which have the lowest active mass and PPR inertia have been selected for a range of PPR outer diameters

Figure 5.8 shows the variation of the PPR inertia and PDD active mass with the PPR outer diameter for the 12s8p PDD designs and corresponding gear ratios. For all the selected gear ratios, increasing the PPR diameters increases the PPR inertia while reducing the PDD active mass.

It can be observed that increasing the PPR outer diameter beyond 45mm brings diminishing returns in terms of PDD active mass while the PPR inertia is rapidly increased for all the gear ratios. Moreover, the smallest PPR outer diameter that allows for the PDD target active mass requirement to be satisfied is 45mm for the 12s8p 6.25:1 and 7.75:1 topologies. In contrast, the other gear ratios of the 12s8p design require a minimum PPR outer diameter of 50mm, which reduces the active mass by 5.4%, but increases the inertia by 17% when compared with the 7.75:1 selected design.

Figure 5.9 shows variation of PPR inertia and PDD active mass for the selected gear ratios of the 12s10p designs. As for the 12s8p designs, the 12s10p topologies show diminishing returns in terms of PDD active mass if the PPR diameter is increased beyond 45mm while the PPR inertia is rapidly increased. For comparison, at an equal PPR diameter of 45mm, the 12s10p 7.6:1 design is characterised by a 12% increase in PDD active mass and 3% increase in output rotor inertia when compared to the 12s8p 7.75:1 topology. From Figure 5.9 (b) is can be observed that the minimum PPR outer diameter for which the PDD active mass limit is satisfied is 47.5mm for the 12s10p 6.4:1 topology, which results in a design having 3% reduction in active mass and an 8.5% increase in output rotor inertia when compared to the 12s8p 7.75:1 design with a 45mm diameter PPR. Moreover, for the 12s10p 7.6:1 topology, the PPR diameter has be increased to 50mm in order to satisfy the active weight limit, which results in a design having a 1.7% reduction in active mass and a 25% increase in PPR inertia when compared to the 12s8p 7.75 topology with a 45mm diameter PPR.

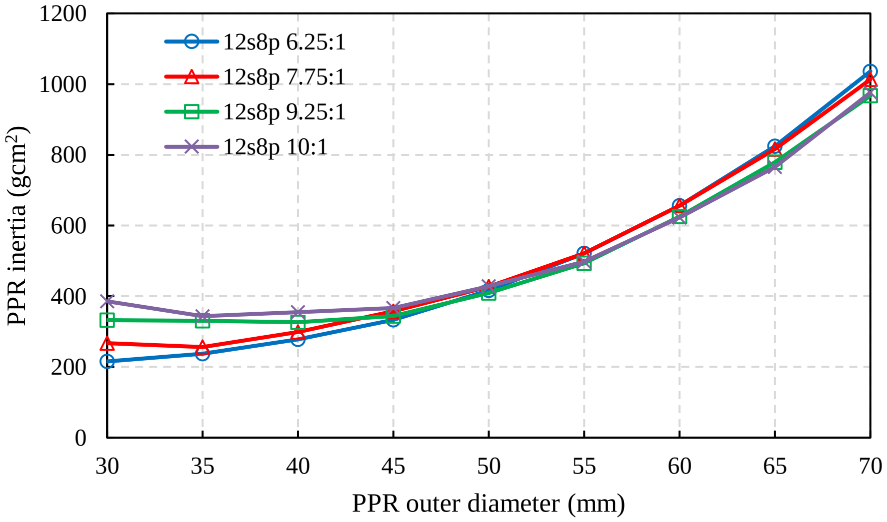

(a)

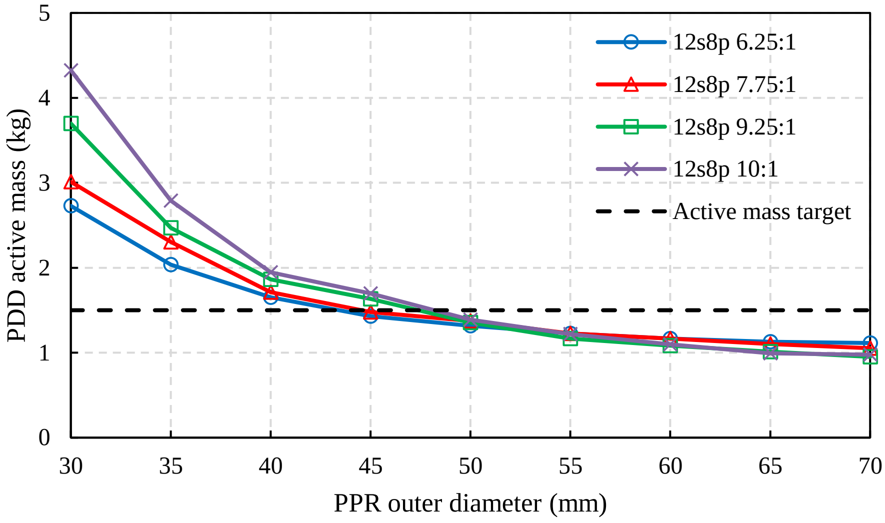

(b)

Figure 5.8. Variation of (a) PPR inertia (b) PDD active mass with PPR outer diameter for 12s8p PDD topology

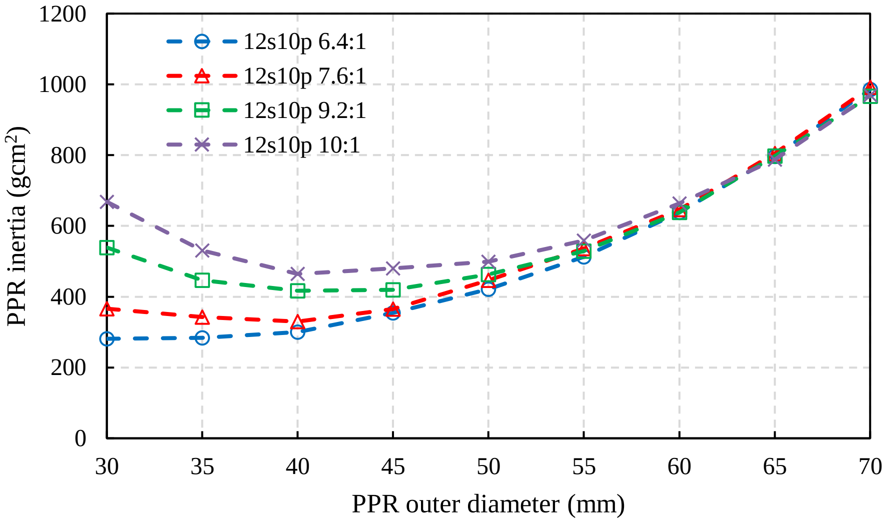

(a)

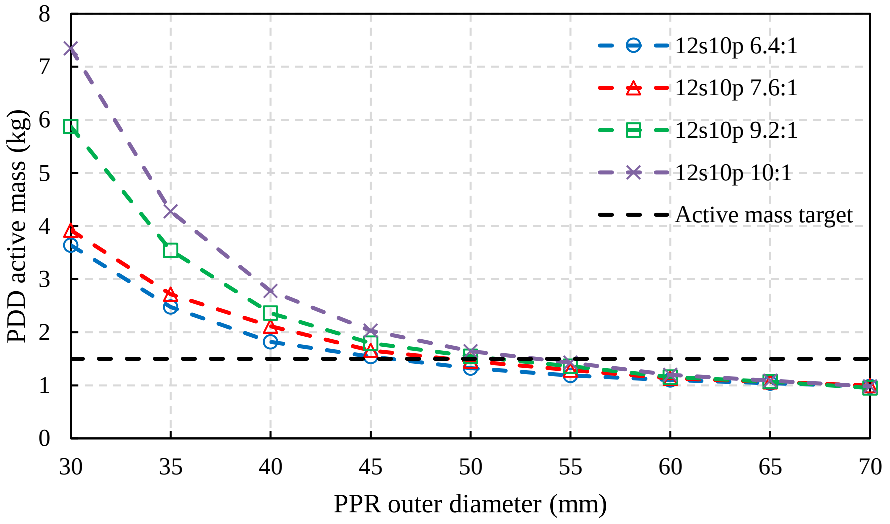

(b)

Figure 5.9. Variation of (a) PPR inertia (b) PDD active mass with PPR outer diameter for 12s10p PDD topology

The variation of total PM mass for the selected 12s8p and 12s10p PDD designs is shown in Figure 5.10. It can be observed that, for all the selected gear ratios, the selected designs of the 12s8p topology have a lower PM mass than the 12s10p designs. For both slot-pole combinations, increasing the PPR diameter reduces the PM mass required to achieve a fixed output torque. At larger PPR diameters, between 50-70mm the reduction in PM mass due to the increase in PPR diameter is negligible.

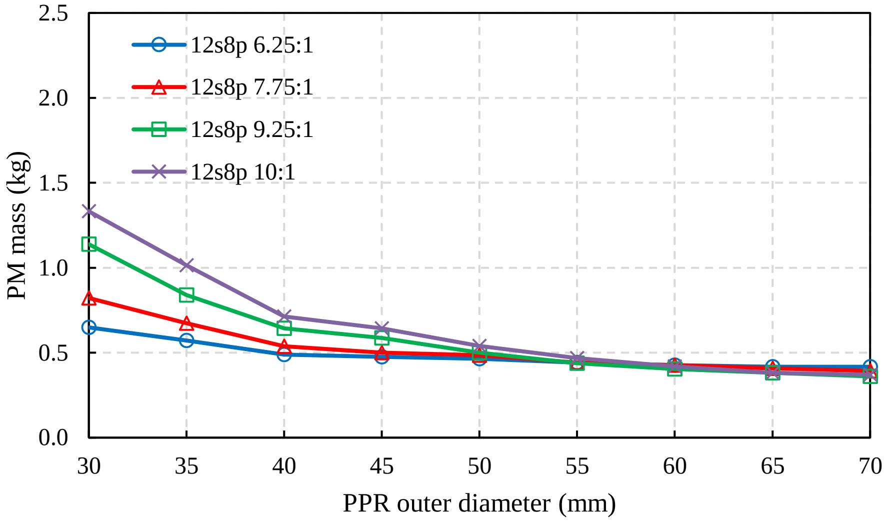

(a)

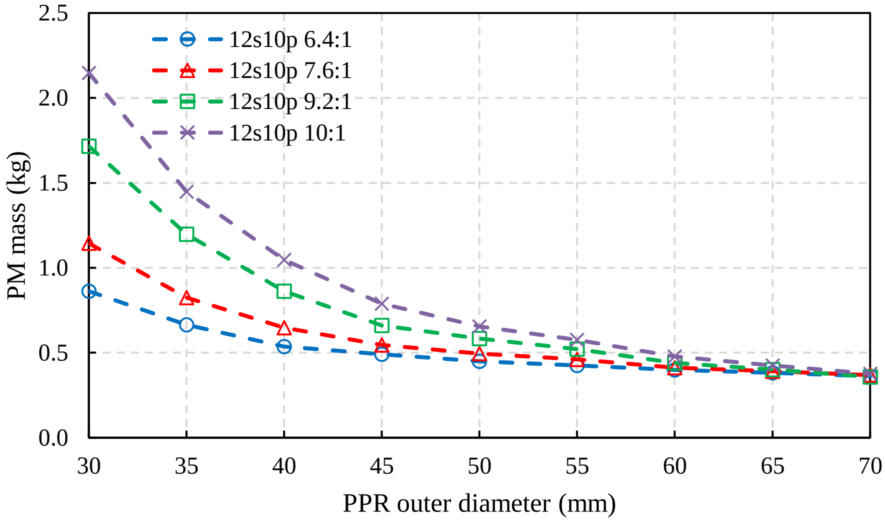

(b)

Figure 5.10. Variation of PM mass for (a) 12s8p (b) 12s10p selected PDD designs

Figure 5.11 shows the variation in motor efficiency, predicted in the Active-Passive operation mode of the selected PDD designs. It can be observed that increasing the PPR outer diameter brings an increase, between 3-7%, in efficiency. For both slot pole combinations, the selected PDD designs with low gear ratios of 6.25:1 and 6.4:1 have the lowest motor efficiency, due to the increased electromagnetic torque required to achieve a fixed PPR output torque. For example, for a fixed 45mm PPR diameter, the 12s8p 6.25:1

design has the active mass and PPR inertia reduced by 3.2% and 6.7%, respectively, while the copper loss is increased by 53.5% and iron loss is reduced by 33.3% when compared to the 12s8p 7.75:1 design. This translates to a 3.6% reduction in efficiency of the 12s8p 6.25:1 design when compared to the 12s8p 7.75:1 variant. Thus, as the gear ratio is increased, the electromagnetic torque requirement is linearly reduced, which reduces the electric loading requirements and copper loss. However, due to the small diameter range, increasing the gear ratio causes a significant increase in the HSR PM flux leakage. In PDDs with high gear ratios and reduced PPR diameters, this is due to the high number of narrow pole pieces which allow the HSR PM flux to short circuit without linking with the stator windings. Thus, the high PDD gear ratios in the range of 9-10:1 allow for a linear reduction in the HSR electromagnetic torque for a fixed PPR output torque, but are also affected by HSR PM flux leakage which reduces the stator magnetic loading, increasing the copper loss and reducing efficiency. Hence, it can be observed in Figure 5.11, that this trade-off between low HSR torque and increased HSR PM flux leakage results in a similar efficiency for all the selected gear ratios in the range of 7.5-10:1.

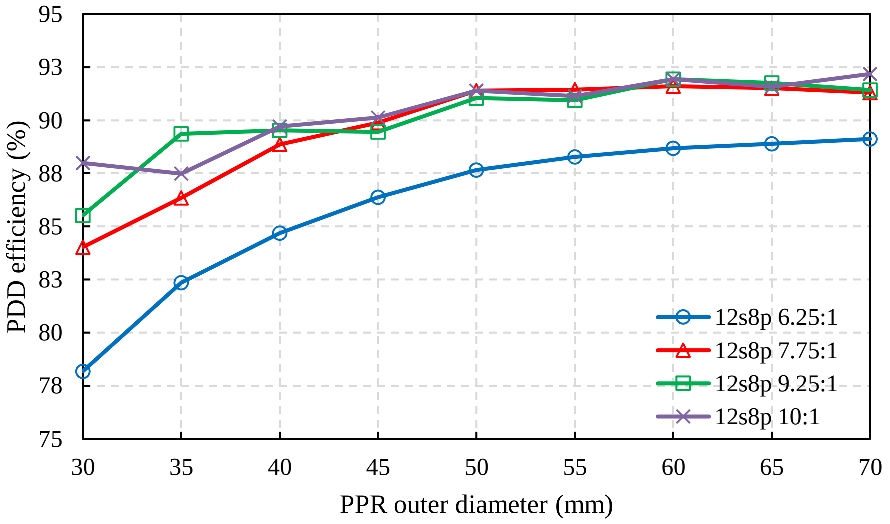

(a)

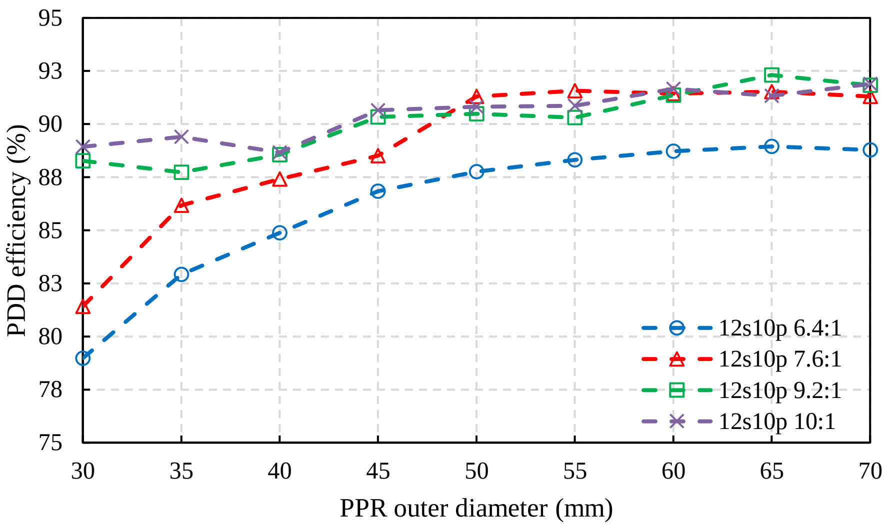

(b)

Figure 5.11. Variation of PDD efficiency for (a) 12s8p (b) 12s10p selected PDD designs

5.2 Magnetic gear torque response time

The proposed PDD electrical motor represents an improved electrical machine topology where the magnetic gear element is mechanically and magnetically integrated with a conventional 3-phase brushless AC PM electrical machine. The PDD torque response time is given by electrical time constant of the electrical machine as well as the magnetic gear element torque transmission response time. The electrical time constant, t_e, of the brushless PM machine element, represents the time required for the current in the windings to rise to the demanded value in order to produce the required torque on the HSR of the PDD and is given by:

$$t_e = \frac{L_{ph}}{R_{ph}} \tag{5.1}$$

where L_{ph} and R_{ph} are the phase inductance and resistance.

The MG element torque response time represents the time delay required to transmit the electromagnetic torque from the HSR to the output PPR, through the compliant magnetic transmission. The torque transmission capability of a 12s8p 7.75:1 PDD design as a function of the of the load angle, θ_e, between the HSR and PPR is shown in Figure 5.12.

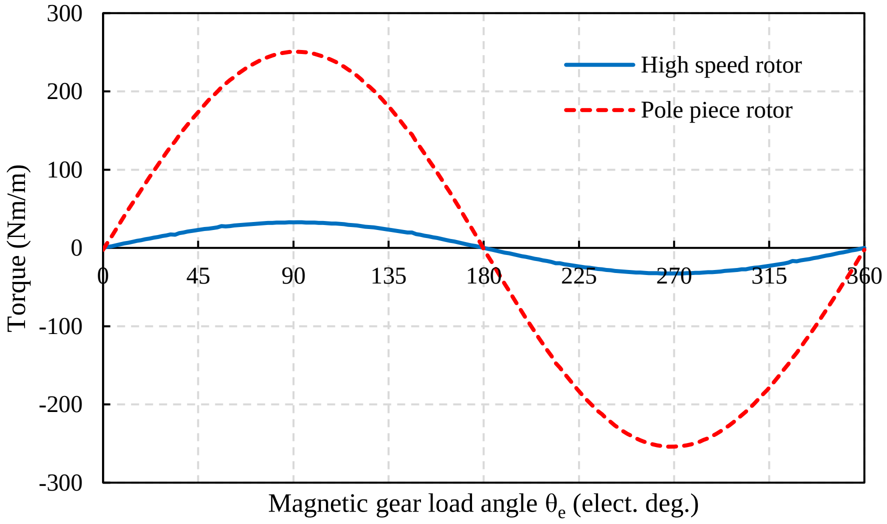

Figure 5.12. Variation of HSR and PPR torque with magnetic gear load angle

It can be observed that the transmitted torque is determined by the relative positions of the HSR and PPR. The peak torque transmission capability of the magnetic gear element is achieved when a relative displacement of 90° electrical exists between the HSR and PPR. Thus, the HSR must move in order to transmit the geared electromagnetic torque to the PPR, with the relative load angle between the two rotors, θ_e, being given by:

$$\theta_e = p_h\theta_h - N_{pp}\theta_{ppr} \tag{5.2}$$

where p_h and θ_h are the number of pole pairs and displacement of the HSR while N_{pp} and θ_{ppr} represent the number of pole pieces and displacement of the PPR.

Furthermore, when the rated torque, T_r, of the HSR is applied, the equation governing the motion of the HSR is given by:

$$J_h \frac{d\omega_h}{dt} = T_r - \frac{T_m}{G_r} \sin(p_h\theta_h - N_{pp}\theta_{ppr}) \tag{5.3}$$

where J_h and ω_h are the inertia and angular velocity of the HSR, and T_m represents the PPR pull-out torque.

Assuming the PPR remains static, i.e. $\theta_{ppr} = 0$, equation (5.3) becomes:

$$\frac{d^2\theta_h}{dt^2} = \frac{T_r}{J_h} - \frac{T_m}{J_h G_r} \sin(p_h\theta_h) \tag{5.4}$$

For simplicity, it was assumed that when, $0 \leq \theta_h \leq \frac{1}{p_h} \sin^{-1}\left(\frac{G_r T_r}{T_m}\right)$, the transmitted torque varies linearly with the load angle, i.e.:

$$T_r = \frac{y}{p_h} \sin^{-1}\left(G_r \frac{T_r}{T_m}\right) \tag{5.5}$$

where y is a constant given by:

$$y = \frac{T_r p_h}{\sin^{-1}\left(\frac{T_r G_r}{T_m}\right)} \tag{5.6}$$

By substituting (5.5) in (5.4), a second order linear non-homogeneous differential equation is obtained such that:

$$\frac{d^2\theta_h}{dt^2} + \frac{y}{J_h}\theta_h = \frac{T_r}{J_h} \tag{5.7}$$

The general solution of (5.7) can be expressed as:

$$\theta_h(t) = \theta_{hH} + \theta_{hP} \tag{5.8}$$

where θ_{hH} is the solution to the homogenous ordinary differential equation given by (5.9) and θ_{hP} represents any function that satisfies the non-homogeneous equation given by (5.7).

$$\frac{d^2\theta_h}{dt^2} + \frac{y}{J_h}\theta_h = 0 \tag{5.9}$$

Thus, the solution, θ_{hH}, for (5.9) is given by:

$$\theta_{hH} = C_1 \cos\left(\sqrt{\frac{y}{J_h}}t\right) + C_2 \sin\left(\sqrt{\frac{y}{J_h}}t\right) \tag{5.10}$$

where C_1 and C_2 are constants.

The particular solution θ_{hP} can be found by considering $\theta_h = C_3$ in (5.7) such that:

$$C_3 = \frac{T_r}{y} \tag{5.11}$$

Thus, the solution for the variation of the HSR displacement with time is given by:

$$\theta_h(t) = C_1 \cos\left(\sqrt{\frac{y}{J_h}}t\right) + C_2 \sin\left(\sqrt{\frac{y}{J_h}}t\right) + \frac{T_r}{y} \tag{5.12}$$

The constant C_1 and C_2 can be found by applying two boundary conditions to equation (5.12). Thus, a $\mathrm{t} = 0$, the HSR displacement is $\theta_h(t) = 0$ and the HSR angular velocity is $\omega_h(t) = 0$, such that:

$$C_1 = -\frac{T_r}{y} \tag{5.13}$$

$$C_2 = 0 \tag{5.14}$$

Thus, by considering (5.12), (5.14) and (5.15), the solution to equation (5.7) is given by:

$$\theta_h(t) = \frac{T_r}{y}\left(1 - \cos\left(\sqrt{\frac{y}{J_h}}t\right)\right) \tag{5.15}$$

Thus, assuming the transmitted torque varies linearly with load angle for $0 \leq \theta_h \leq \frac{1}{p_h}\sin^{-1}\left(\frac{G_r T_r}{T_m}\right)$, equation (5.15) becomes:

$$\theta_h(t) = \frac{T_r}{y}\left(1 - \cos\left(\sqrt{\frac{y}{J_h}}t\right)\right) = \frac{1}{p_h}\sin^{-1}\left(\frac{G_r T_r}{T_m}\right) \tag{5.16}$$

From (5.6) and (5.16), the time taken to transmit the electromagnetic torque from the HSR to the PPR is given by:

$$t = \frac{\pi}{2}\sqrt{\frac{J_h \sin^{-1}\left(\frac{T_r G_r}{T_m}\right)}{T_r p_h}} \tag{5.17}$$

For the PDD selected designs from Figure 5.8 and 5.9, the time taken for the magnetic gear element to transmit the rated torque from the HSR to the PPR, which is connected to the load, is shown in Figure 5.13. For a fixed slot-pole combination, the torque transmission delay is increased since the HSR inertia is increased with the increase in PPR outer diameter for a fixed inner airgap length. For a PDD, increasing the magnetic gear ratio results in the reduction of the HSR rated torque. Thus, by reducing the rated electromagnetic torque, the transmission time delay is increased. For the selected PDD designs, this effect is more apparent at high PPR diameters (>50mm) where the inertia of the HSR is constant for an increase in gear ratio.

For fixed PPR diameter and comparable gear ratio, increasing the number of HSR poles reduces the magnetic torque transmission delay, due to the smaller angle that the HSR has to rotate in order to transmit rated torque to the PPR. For example, for the selected PDD designs having 45mm PPR outer diameter, the time delay is reduced by 10% when the number of HSR poles is increased from 8 to 10 poles.

It is important to note that the time amplitude associated with the actuator bandwidth requirement are much greater than the maximum time delay of the selected PDD designs. Thus, the bandwidth of the actuator is mainly dependant on the required displacement, inertia of the drive train, and particularly, the inertia of the HSR and load torque.

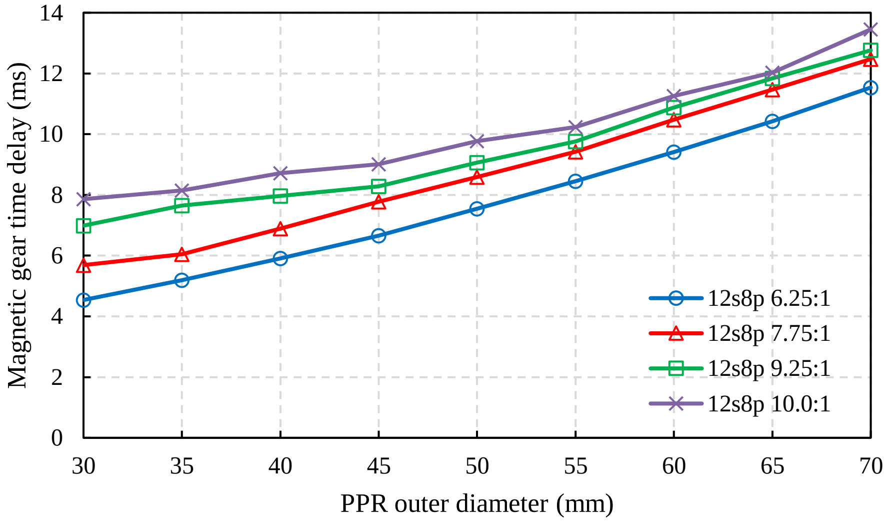

(a)

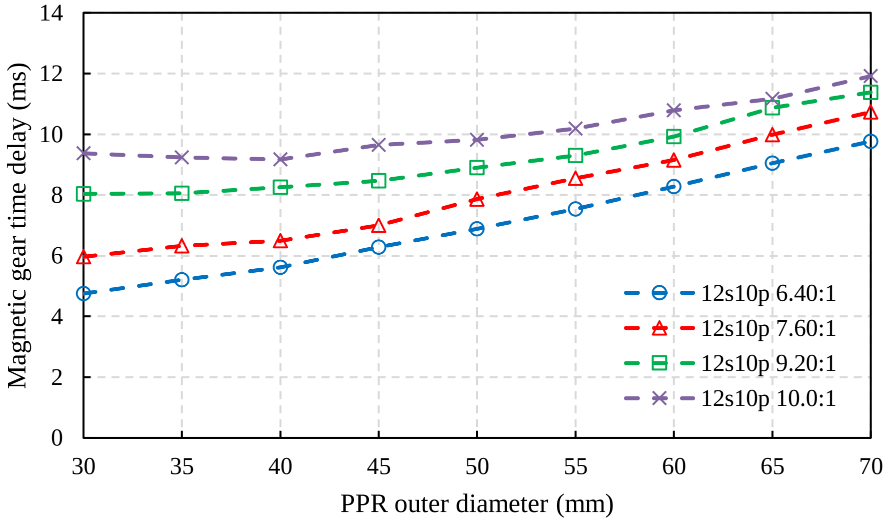

(b)

Figure 5.13. Variation of magnetic gear torque transmission delay time with PPR diameter for (a) 12s8p (b)12s10p selected PDD designs

5.3 Actuator bandwidth

The actuator drivetrain comprises the fault tolerant PDD which drives the ball screw, connected to the rudder control surface. The bandwidth of the actuator can be analytically predicted by considering the PDD output torque, load torque on the control surface as well as the equivalent inertias of the PDD rotors, linear screw and control surface. The nominal actuator bandwidth requirement is dependent on the actuator position as shown in Figure 2.11 in Chapter 2. For this actuator specification, the control surface load was set proportional to the angular displacement of the rudder, as shown in Figure 2.23 in Chapter 2. For a sinusoidal displacement the angular position of the PPR, θ_{ppr}, is given by:

$$\theta_{ppr} = \theta_m \sin(\omega_l t) \tag{5.18}$$

where ω_l and θ_m represent the PPR frequency and maximum angular position at the particular frequency.

The required PPR acceleration for the fixed maximum displacement is given by:

$$\frac{d^2\theta_{ppr}(t)}{dt^2} = -\theta_m \omega_l^2 \sin(\omega_l t) \tag{5.19}$$

Due to the very short time it takes for the torque to be transmitted to the PPR, as shown in Figure 5.13, compared to the required bandwidth, Figure 2.11, magnetic gear torque transmission transients are neglected and the PDD output torque is approximated by $T_e G_r$. The electromagnetic torque of the PDD, T_e, or input torque of the magnetic gear element is produced by the synchronous coupling of the HSR fundamental field component with the fundamental magnetic field component of the stator MMF and can be expressed as:

$$T_e = \frac{3}{2} p_h \psi_d I_q \tag{5.20}$$

where ψ_d and I_q are the fundamental flux linkage and q-axis current, respectively.

The equation governing the motion of the PPR is given by:

$$-J_T \theta_m \omega_l^2 \sin(\omega_l t) = G_r T_e(t) - T_L \tag{5.21}$$

where T_L is the load torque given by the aerodynamic loading of the control surface and J_T is the total system inertia. Since the aerodynamic load torque for this specific actuator is proportional to the angular position, a ratio between the absolute maximum load torque, T_{L_MAX}, and angular position, θ_m, can be defined by:

$$C = \frac{T_{L\_MAX}}{\theta_m} \tag{5.22}$$

where θ_m is related to the maximum linear displacement of the slide, X_m, of the linear screw such that:

$$\theta_m = \frac{2\pi X_m}{l} \tag{5.23}$$

Thus, equation (5.21) becomes:

$$-J_T \theta_m \omega_l^2 \sin(\omega_l t) = G_r T_e(t) - C\theta_m \sin(\omega_l t) \tag{5.24}$$

Therefore, at maximum displacement, θ_m:

$$(C - J_T \omega_l^2)\theta_m = G_r T_x \tag{5.25}$$

From equations (5.23) and (5.25), the variation of the bandwidth of the actuator with the maximum displacement, X_m, is given by:

$$f_l = \frac{1}{2\pi} \sqrt{\frac{\left(C - \frac{G_r T_x l}{2\pi X_m}\right)}{J_T}} \tag{5.26}$$

where $T_x = T_r$, when $\left(C - G_r \frac{T_r}{\theta_m}\right) \geq 0$, and $T_x = -T_r$ when $\left(C - G_r \frac{T_r}{\theta_m}\right) < 0$.

In order to calculate the total system inertia, J_T, the HSR inertia has to be referred through the magnetic gear to the output side and added to the load, screw and PPR inertias, J_L, J_{screw} and J_{PPR}, respectively, such that:

$$J_T = J_L + J_{screw} + J_{PPR} + J_h G_r^2 \tag{5.27}$$

However, the speed of the HSR is limited to ω_{h_MAX} and f_l must also satisfy:

$$\omega_{h\_MAX} \geq \frac{4\pi^2 X_m f_l}{l} G_r \tag{5.28}$$

The variation of the PDD bandwidth with screw slide displacement for a range of PPR outer diameters for the 12s8p 7.75:1 selected PDD designs is shown in Figure 5.14. It can be observed that as the HSR and PPR inertias are increased by increasing the PPR diameter, the achievable bandwidth of the PDD is reduced. For all the PPR diameters, the achievable bandwidth for a given screw slide displacement is higher than the actuator requirement.

The variation of the PDD bandwidth with the screw slide displacement for the 12s8p and 12s10p selected designs, with a PPR diameter of 45mm, is shown in Figure 5.15. It can be observed that the maximum achievable bandwidth at low displacements is reduced as the magnetic gear ratio is increased. This is due to the high PPR and HSR inertia of the high gear ratio PDD designs which results from the reduced PPR pull-out torque capability and increased active length when compared with the low gear ratio designs.

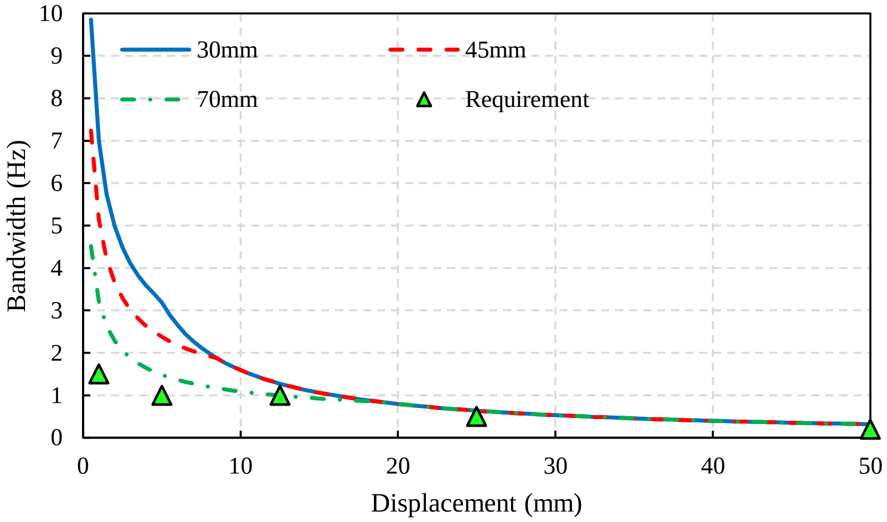

Figure 5.14. Variation of the PDD bandwidth with screw slide displacement for 12s8p 7.75:1 topology

At small displacements, the 6.25:1 PPD designs achieves a higher bandwidth than the 6.4:1 designs by 7%. The PDD designs with gear ratios of 7.75:1 and 7.6:1 have the same maximum bandwidth capability. In contrast, at low displacements, the 9.25:1 PDD designs achieves a 14% higher bandwidth than the 9.2:1 designs, while the 12s8p 10:1 design has a 20% higher bandwidth than the 12s10p 10:1 variant.

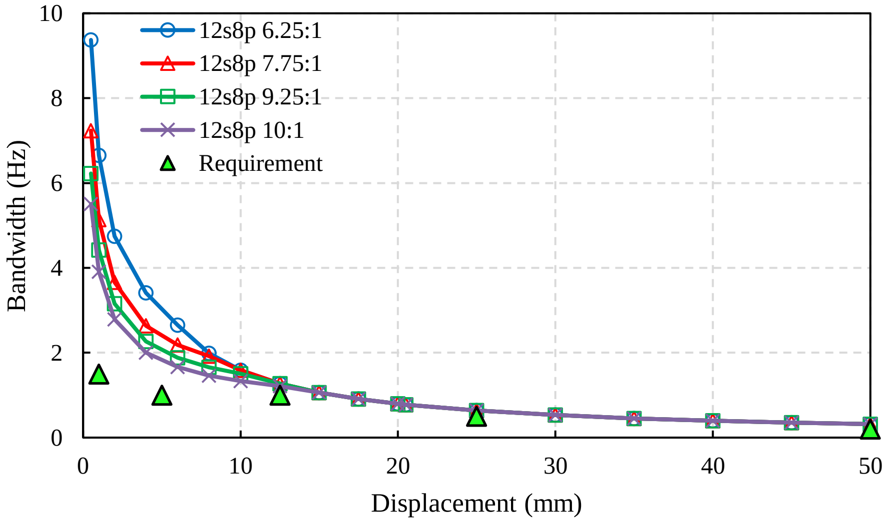

(a)

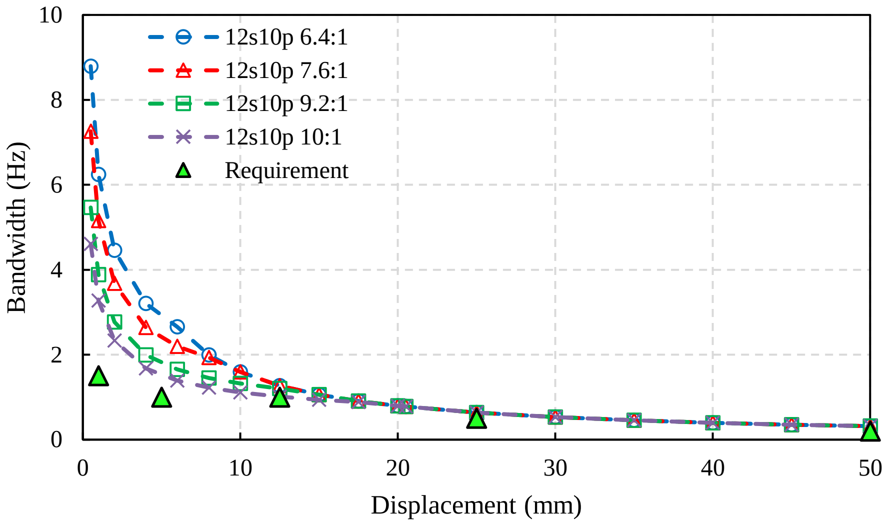

(b)

Figure 5.15. Variation of PDD bandwidth with screw slide displacement for (a) 12s8p (b) 12s10p PDD selected designs

For a displacement higher than 12.5mm the bandwidth for all the designs is limited by the maximum allowable PPR speed, which is fixed at 1200 rpm for all the selected PDD designs. Thus, in this case, the bandwidth which results from equation (5.28) is equal for all the slot-pole combinations and corresponding gear ratios.

5.4 Conclusions

The 2D FE electromagnetic parametric scans have been conducted for the 12s8p and 12s10p topologies with different magnetic gear ratios in the range of 6 – 10:1. The parameters varied during the parametric scan are shown in Table 5.2. It is shown, in Figure 5.1, that by increasing the PPR outer diameter, the PDD active mass is reduced and PPR inertia is increased. Increasing the PPR outer diameter beyond 45mm results in a large increase in the output rotor inertia while the PDD active mass is only moderately reduced. In contrast, the resultant HSR inertia is maximised for the PDD designs that have minimum PPR inertia, as shown in Figure 5.2. This is due to the fact that the HSR PM mass is increased in order to increase the PPR pull-out torque capability and reduce the active length and mass of the PDD. It is important to consider that the kinetic energy associated with the inertia of the HSR is isolated from the actuator mechanical drive train due to the torque fuse characteristic of the contactless magnetic gear transmission. Thus, during actuator operation, in case of control surface overload, the magnetic gear element within the PDD will pole slip and the HSR will rotate independently from the PPR, with zero average power being transmitted from the HSR to the PPR. During the overload condition, only the low inertia PPR is connected to the mechanical drive train of the actuator. Thus, due to the low PPR inertia, the rotor stored kinetic energy is minimised and additional mass can be removed from the actuator mechanical drive train and end stops.

The results of the parametric scans showed that, for the selected designs with low PPR inertia and active mass, the HSR PM mass is maximised in order to increase the stator magnetic loading for reduced current density. Moreover, such designs have the PPR pull-out torque capability maximised together with the PPR outer airgap shear stress, as shown in Figure 5.4. The corresponding efficiency of the designs studied in the parametric scans was predicted by considering the copper and iron losses in the stator laminations and pole pieces when the fault tolerant PDD actuator motor delivers rated power in an Active-Passive operation mode. For the investigated designs the efficiency is increased with PPR outer diameter as shown in Figure 5.7.

The preferred 12s8p and 12s10p PDD designs have been selected based on the criteria of lowest mass and PPR inertia for each PPR outer diameter design family. It is shown in Figure 5.8 (b) and 5.9 (b) that the 12s8p topologies achieve designs that satisfy the maximum allowable active mass requirement of 1.5 kg at lower PPR outer diameters than the 12s10 variants. Thus, the PPR inertia of the 12s8p designs is reduced when compared to the 12s10p variants.

For the selected PDD designs, the magnetic gear torque response time which represents the duration taken to transmit the rated electromagnetic torque from the HSR to the PPR was predicted. It is shown that for a fixed slot pole combination, the torque transmission delay is increased with the PPR outer diameter. Moreover, increasing the magnetic gear ratio for a fixed slot pole combination increases the torque transmission time delay. For a fixed PPR outer diameter, it was shown that increasing the number of HSR poles reduced the torque transmission delay of the magnetic gear element within the PDD.

The PDD actuator bandwidth was predicted for the sinusoidal actuator position and load profiles. It is shown that, for the selected designs with a PPR outer diameter of 45mm, the maximum achievable bandwidth at low displacements is reduced as the magnetic gear ratio is increased. This is due to the increase in inertia of the HSR and PPR with the magnetic gear ratio for the selected PDD designs. The maximum achievable bandwidth for all the selected PDD designs is substantially higher than the required specification.

Chapter 6: Fault-tolerant PDD design

The parametric scan was conducted on two different PDD slot pole combinations, 12s8p and 12s10p, each with four corresponding magnetic gear ratios. From the generated results presented in Chapter 5, Figure 5.8 and 5.9, for each slot-pole and gear ratio combination, PDD designs which have the lowest output PPR inertia with the 2D active mass and current density equal to or lower than 1.5kg and 10A/mm^2, respectively, have been selected. Figure 6.1 shows the comparison of PDD and PM mass as well as PDD efficiency for the selected 12s8p and 12s10p PDD designs. It can be observed that the variation in PDD active mass between the selected design is lower than 10% while the PM mass required to achieve the same output torque is increased as the gear ratio is increased for both slot-pole combinations. Moreover, since increasing the magnetic gear ratio reduces the HSR electromagnetic torque requirement together with the current demand for a fixed output torque and slot pole combination, the efficiency is increased with the gear ratio.

For each of the two selected slot pole combinations, Figure 6.2 shows that increasing the gear ratio generated an increase in the HSR and PPR rotor inertias. It can be observed that the 6.25:1 and 6.40:1 designs have the lowest inertias for the 12s8p and 12s10p slot-pole combinations. In comparison the 12s8p 7.75:1 design has HSR and PPR inertias increased by 9% and 7% respectively, but show a 4% higher efficiency with the copper loss being reduced by 53% when compared to the 12s8p 6.25:1 design. Although the 12s10p 6.40:1 design has the lowest inertia amongst the 12s10p designs, it is still 10% higher than the 12s8p 7.75:1 design while the efficiency is lower by 3%.

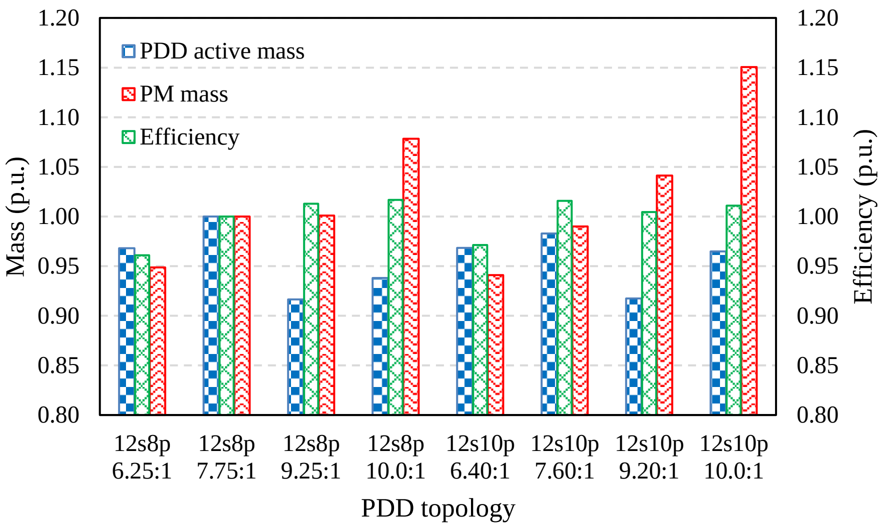

Figure 6.1. Comparison of PDD PM active mass and efficiency for 12s8p and 12s10p selected designs

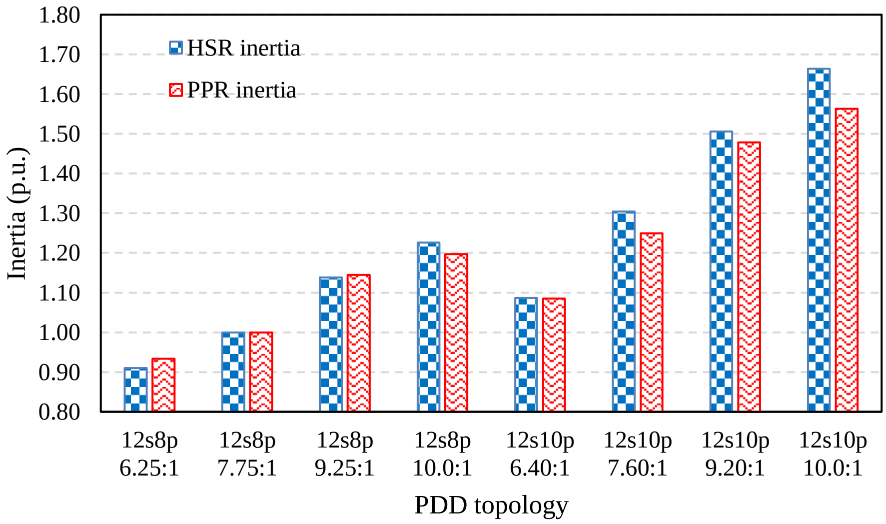

Figure 6.2. Comparison of HSR and PPR inertia for 12s8p and 12s10 selected designs

The magnetic gear rated torque transmission delay from the HSR to the PPR was analytically predicted for all the selected PDD designs as shown in Figure 6.3. It can be observed that the time delay is increased with the magnetic gear ratio. The 12s8p 7.75:1 design has a longer torque transmission time delay by 14-15% when compared to the 12s8p 6.25:1 and 12s10p 6.4:1 designs due to its higher HSR inertia and lower product of rated HSR torque and number of HSR poles.

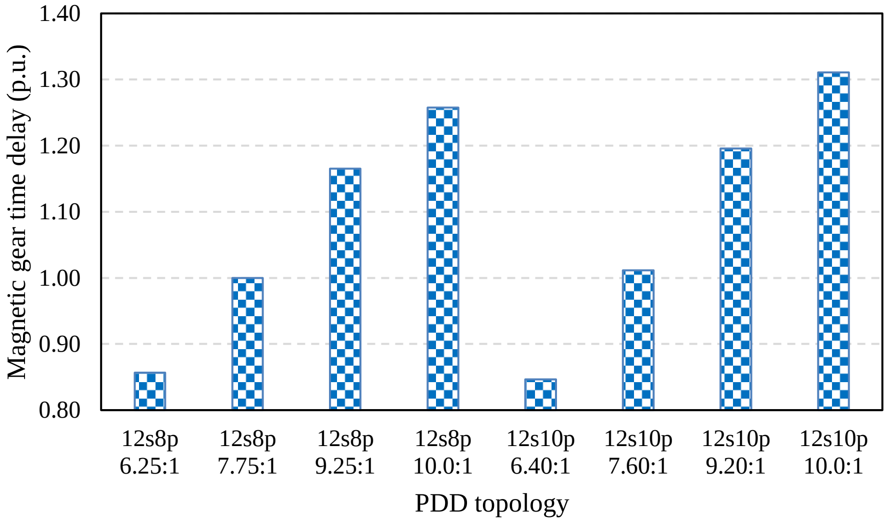

Figure 6.3. Comparison of magnetic gear element torque transmission delay time for 12s8p and 12s10p selected designs

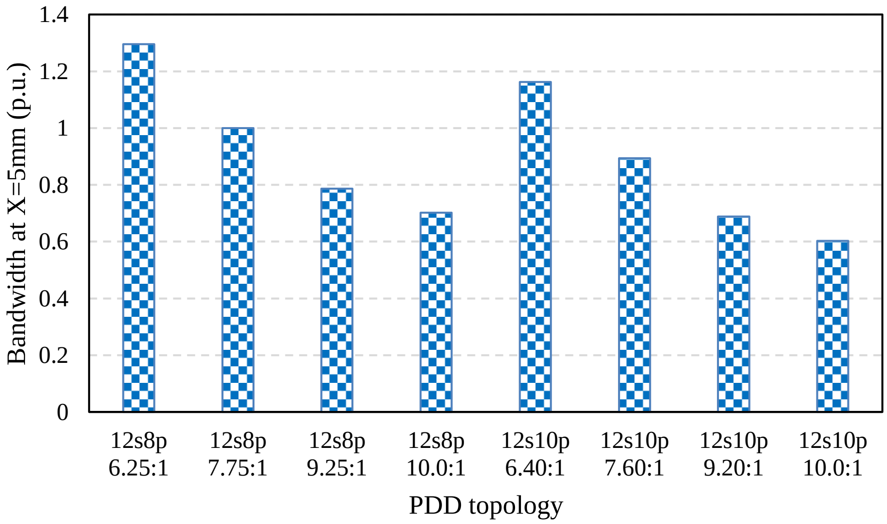

Figure 6.4. Comparison of PDD bandwidth at 5mm actuator displacement for 12s8p and 12s10p selected designs

The PDD bandwidth for the selected designs was analytically predicted in Chapter 5 based on the sinusoidal load and displacement actuator drive cycles discussed in Chapter 2. Figure 6.4 shows the comparison of maximum achievable PDD bandwidth under a 5mm displacement requirement for the selected PDD designs. For a fixed slot-pole combination, the achievable bandwidth is reduced as the gear ratio is increased. By comparing the 12s8p 6.25:1 and 7.75:1 designs which have the lowest rotor inertias as shown in Figure 6.2, it can be observed that the 7.75:1 designs have the lower bandwidth by 29.5%.

It is important to consider that all the selected PDD designs which resulted from the parametric scan satisfy both the active mass and bandwidth requirements, with the 12s8p 6.25:1 and 7.75:1 having the lowest HSR and PPR inertias. Thus, since the 12s8p 7.75:1 design has a substantially lower copper loss and 4% higher efficiency than the 6.25:1 design, it was selected for prototyping with a duplex 3-phase winding and integration in the actuator mechanical drive train.

6.1 PDD design for manufacture

The PDD 12s8p 7.75:1 which resulted from the parametric scans has an idealised cross-section which can substantially complicate the manufacturing process and affect the reliability of the prototype electrical machine. In order to produce a design which can be manufactured reliably and reduce the assembly complexity, certain modifications are required to the HSR, PPR, stator PMs and stator teeth.

A comparison between the ideal and detailed cross-section design of the HSR is shown in Figure 6.5. It can be observed that the ideal HSR design does not have any features on the HSR steel hub which can be used to locate the PMs on the surface of the hub. In order to enable accurate positioning of the radially and circumferentially magnetised PMs, steel notches were added to the HSR hub design which mark the landing area for the HSR PMs. To simplify the assembly process, the radially magnetised PM are designed as square blocks while the circumferentially magnetised PMs are designed to fill the spaces between the radial PMs. The circumferential PMs have the same nominal radial thickness as in the ideal HSR design while the radially magnetised PMs have the radial thickness increased by 0.3mm in order to engage with the notches of the HSR hub. The inter-magnet gap is kept at the same thickness for both designs.

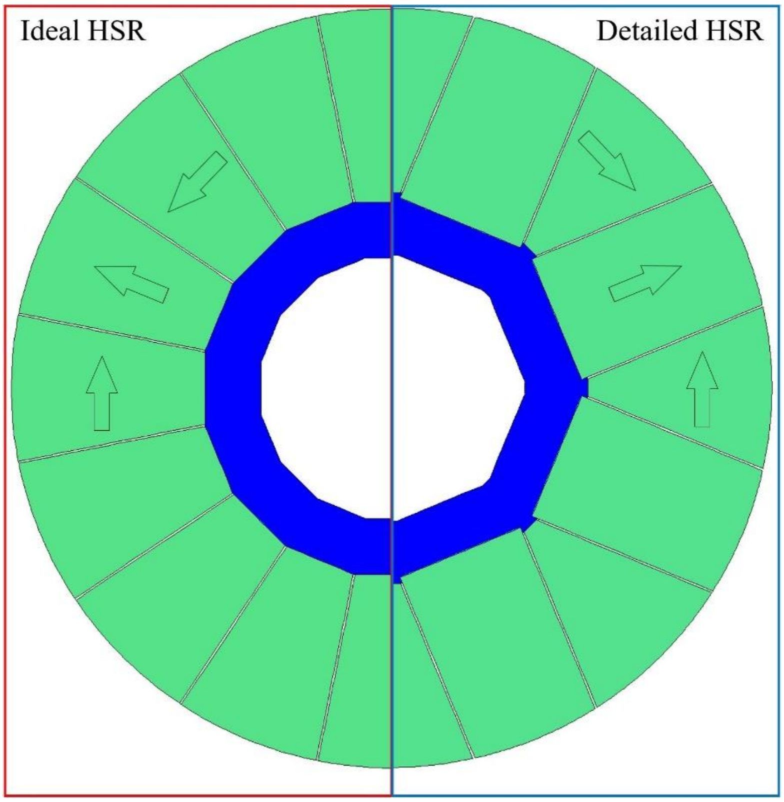

Figure 6.5.Cross-section comparison of ideal and detailed HSR design

Figure 6.6 shows the cross-section comparison of the ideal and detailed PPR designs for the same pole piece radial thickness, outer diameter and pole piece pitch ratio. The ideal PPR design would require an inner and outer composite wrap in order to secure the pole piece. This would increase both the inner and outer airgaps and reduce the PDD performance characteristics such as output pull-out torque and efficiency, increasing the active length, and rotor inertia. Alternative PPR designs where only one, inner or outer, wrap is required have been discussed in Chapter 4. The detailed PPR design allows for the pole pieces to be secured to the PPR support structure without increasing the thickness of the inner and outer airgaps. Thus, each pole piece has circular cut-outs on each side which allows for circular composite rods to secure the pole pieces without allowing any radial movement during machine operation.

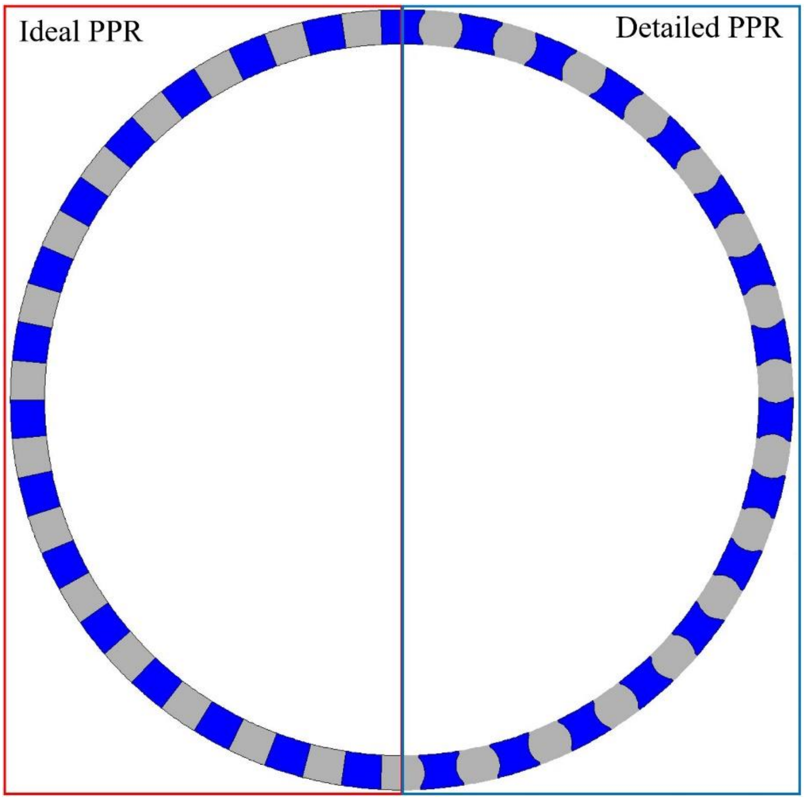

Figure 6.6. Cross-section comparison of ideal and detailed HSR design

Figure 6.7 shows the comparison between the ideal and detailed stator design. It can be observed that the stator teeth of the detailed design have castellations which create a flat landing area for the flat faced rectangular stator PMs. In contrast, the ideal stator design does not have any features on the stator bore to facilitate the assembly of the stator PM array. For the detailed stator design, the circumferentially magnetised PMs have the same thickness as the stator PMs of the ideal design while the radially magnetised PMs have the radial thickness increased by 0.3mm in order to engage with the castellations of the stator teeth. Thus, the detailed stator design allows for the radially and circumferential PMs to be easily fixed on the stator teeth during assembly without any additional tooling being required to pre-form the stator PM array before fixing it with adhesive to the stator bore. All the other geometric parameters of the stator assembly were left unchanged from the 12s8p 7.75:1 PDD design which resulted from the parametric scans

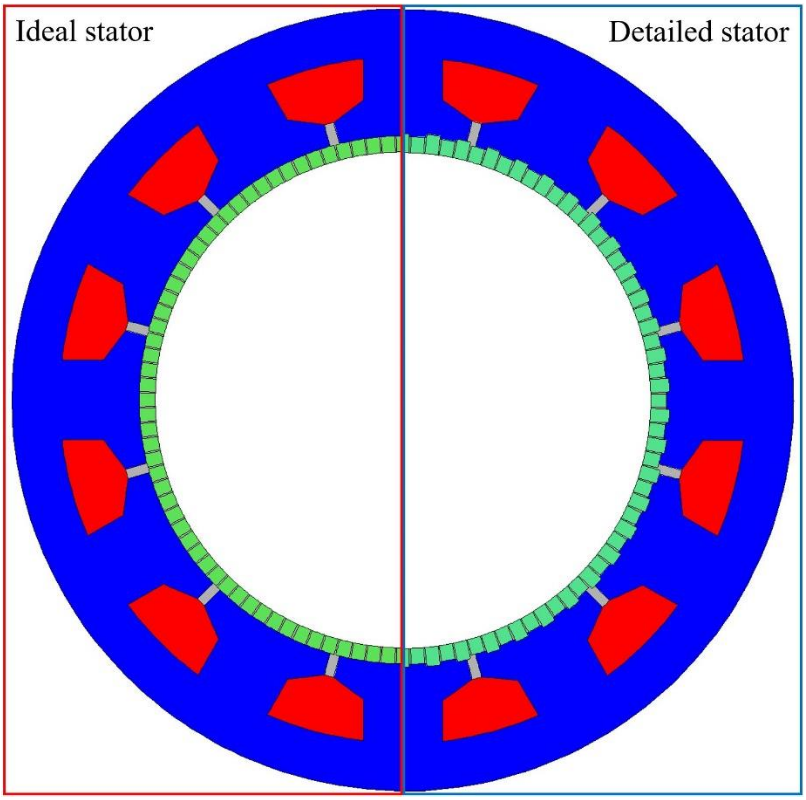

Figure 6.7. Cross-section comparison of ideal and detailed stator / stator PM design

Due to the substantial difference in the HSR PM Halbach array, an investigation was conducted on the HSR PM thickness and Halbach ratio for the cross section of the detailed design of the PDD actuator motor. The geometric parameters and FE results of the detailed PDD designs are compared with the selected 12s8p 7.75:1 idealised PDD cross-section in Table 6.1. It can be observed that for the same HSR PM radial thickness the Halbach ratio of the inner PM array was reduced to 0.75 in order to maximised the pull-out torque capability, reduce PPR inertia and PDD active mass for the limitations imposed by the HSR design. Due to the castellations of the HSR hub and stator teeth, the radial thickness of the radially magnetised HSR and stator PMs was increased by 0.3mm. Thus, the total PM mass is slightly increased, together with the outer airgap shear stress. Moreover, since the detailed PDD design achieved a 4% higher PPR pull out torque capability, the PPR and HSR inertias and PDD active mass are reduced. Due to the decrease in active length and slight increase in effective airgap between the HSR and stator bore caused by the extended stator PMs, the winding flux linkage is reduced by 3% while the rated copper loss is increased by 6%.

Table 6.1. Comparison of ideal and detailed 12s8p 7.75:1 PDD designs

Parameter	**Ideal design**	**Detailed design**
HSR pole pairs	4	
Stator pole pairs	27	
Gear ratio	7.75	
Active length (mm)	42.0	40.3
Stator outer diameter (mm)	73.8	
PPR outer diameter (mm)	45	
HSR outer diameter (mm)	39.6	
Inner/outer airgap (mm)	0.7	
Stator PM radial length (mm)	1.5	1.5 / 1.8
Stator PM width (mm)	1.27	
Pole piece radial length (mm)	2	
Pole piece pitch ratio	0.5	
HSR PM radial length (mm)	10	10 / 10.3
HSR Halbach ratio	1	0.75
Outer airgap shear stress (kPa)	77.1	80.3
HSR PM mass (kg)	7.84	7.95
Stator PM mass (kg)	1.72	1.89
PDD active mass (kg)	1.40	1.32
PPR inertia (gcm^2)	349	340
HSR inertia (gcm^2)	1058	1011
Flux linkage (mWb)	1.21	1.17
Copper loss (W)	80.8	85.5
Iron loss (W)	15.5	16.0
Efficiency (%)	91.6	91.2

6.2 Inductance limited short circuit current

The fault-tolerant PDD actuator motor employs a duplex 3-phase winding topology, which can be driven from two independent 3-phase inverters, with each lane capable of supplying rated power, enabling electrical isolation between lanes. Thus, redundancy is achieved, allowing the PDD machine to operate with one faulty lane. Furthermore, due to the single layer duplex 3-phase winding, each slot only contains the conductors of one phase, with any two adjacent phases being separated by a stator tooth. This ensures physical and thermal isolation between the different phases of the winding configuration. Magnetic isolation between phases is also implemented due to the reduced mutual coupling between adjacent phases, such that the fault current in one phase does not induce large voltages in the adjacent phases It is important to ensure that during a symmetrical 3-phase short circuit of one lane, the short circuit current does not exceed the value of the rated machine current. Thus, the copper loss associated with the faulty lane will not exceed the rated copper loss of the heathy lane, enabling the PDD to operate with a faulty lane without exceeding the thermal limits. Moreover, due to the inductive reactance limited short circuit current, the associated drag torque is also reduced. The independent inverter of the lane can be used to trigger a symmetrical 3-phase short circuit in order to supresses the large fault currents associated with phase to phase faults or inter-turn short circuit.

The phase inductance of the duplex 12s8p 7.75:1 PDD can be calculated by considering the proposed method in [172]–[175], where the d- and q-axis inductances, L_d and L_q are given by the ratios between the dq-axis currents, I_d and I_q and flux linkages, ψ_d and ψ_q, such that:

$$L_d\left(I_d, I_q\right) = \frac{\psi_d\left(I_d, I_q\right) - \psi_{PM}(I_q)}{I_d} \tag{6.1}$$

$$L_q\left(I_d, I_q\right) = \frac{\psi_q(I_d, I_q)}{I_q} \tag{6.2}$$

where the change of the no load PM flux linkage, ψ_{PM}, with I_q current is given by:

$$\psi_{PM}(I_q) = \psi_d(I_d = 0, I_q) \tag{6.3}$$

Since the fault tolerant PDD produces the electromagnetic torque on the HSR due to the synchronous coupling between the stator windings and the non-salient surface permanent magnet HSR, and for this actuator application the PDD is operated only in the constant torque region, where I_d is zero and I_q is the rated phase current, the phase inductance, L_{ph}, is given by:

$$L_{ph} = L_d = L_q = \frac{\psi_q(0, I_q)}{I_q} \tag{6.4}$$

Since the 2D cross-section of the PDD is fixed as a result of the parametric scan for reduced active mass and rotor inertia, the phase inductance can be adjusted to limit the short circuit current by adjusting the slot leakage inductance component. Thus, by increasing the leakage flux across the slot opening, the phase inductance is increased. In order to achieve this, the slot opening thickness and tooth tip thickness are changed as shown in Figure 6.8.

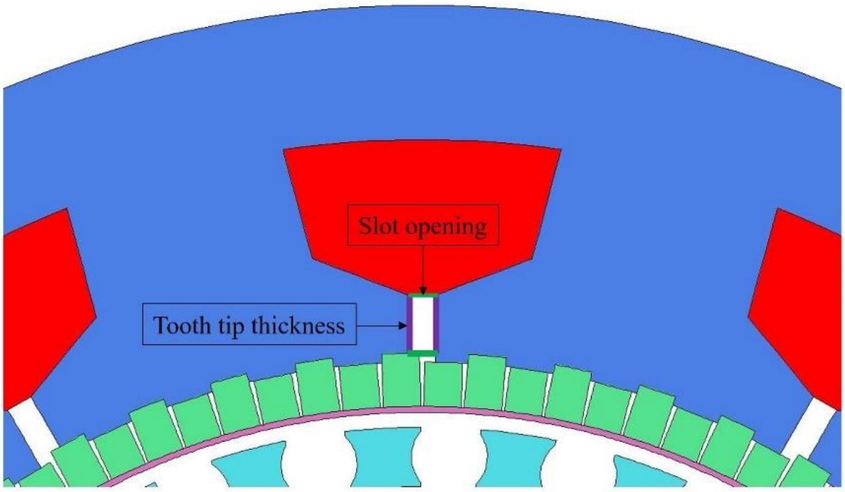

Figure 6.8. Slot opening geometry

For a range of tooth tip thicknesses, Figure 6.9 shows the variation of the phase inductance with the slot opening length. It can be observed that the phase inductance is reduced as the slot opening length is increased. This is due to the change in the slot leakage flux which is reduced as the separation between adjacent teeth is increased. Hence, the slot leakage component and implicitly the total phase inductance, are reduced when the slot opening is increased. For a fixed slot opening length, reducing the tooth tip length has the same effect of reducing the slot leakage flux and reducing the phase inductance. Figure 6.9 also shows that several slot opening/ tooth tip lengths are capable of producing a PDD cross-section with 1 p.u. phase inductance which would limit the short circuit current amplitude at maximum output speed to the value of the rated phase current.

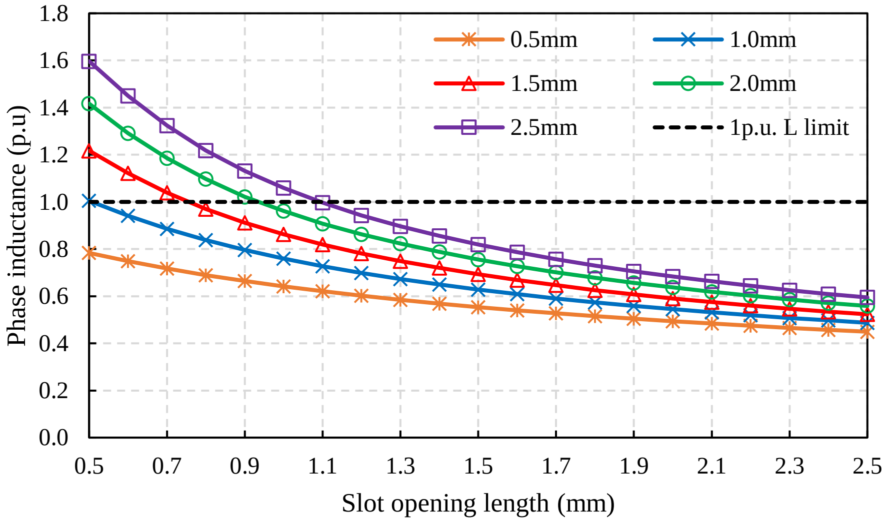

Figure 6.9. Variation of phase inductance with slot opening length for a range of tooth tip thicknesses

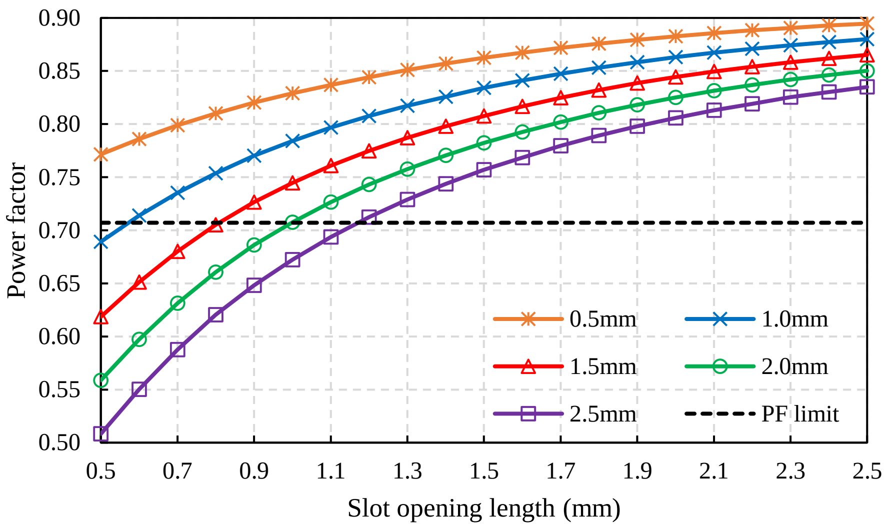

Figure 6.10. Variation of power factor during Active-Passive operation with slot opening length for a range of tooth tip thicknesses

Selecting a design with 1 p.u. inductance to limit the short circuit current to the rated current, translates to a power factor during Active-Passive operation of 0.707. Figure 6.10 shows that as the phase inductance is reduced by increasing the slot opening length, the power factor during Active-Passive operation is increased.

After using 2D FE to calculate the phase inductance, the 3-phase symmetric short-circuit model for non-salient pole PM electrical machines, presented in [176], was used to analytically predict the short circuit current. The short circuit current response when one of the two 3-phase lanes, of the duplex 3-phase PDD winding, is under 3-phase symmetrical short circuit is represented by the initial current response and EMF response.

The initial current response for a non-salient pole PDD is represented by $I_q(0) \neq 0$ and $EMF = 0$, such that:

$$I_d(t)_I = I_q(0)e^{-t\frac{R_{ph}}{L_{ph}}}\sin(\omega_e t) \tag{6.5}$$

$$I_q(t)_I = I_q(0)e^{-t\frac{R_{ph}}{L_{ph}}}\cos(\omega_e t) \tag{6.6}$$

$$I(t)_I = \sqrt{I_d^2(t)_I + I_q^2(t)_I} = \left|I_q(0)\right|e^{-t\frac{R_{ph}}{L_{ph}}} \tag{6.7}$$

where $I_d(t)_I, I_q(t)_I$ and $I(t)_I$ are the d-axis, q-axis and total currents during the initial current response while R_{ph} and ω_e are the phase resistance and HSR electrical frequency, respectively.

$$\omega_e = 2\pi f_{hsr} = \frac{\pi}{30}p_h\Omega_{PPR}G_r \tag{6.8}$$

where f_{hsr} is the electrical frequency of the HSR and Ω_{PPR} is the mechanical rotational velocity of the PPR in rpm.

It can be observed from equation (6.7) that the initial current response $I(t)_I$ is a damped current response which starts with a peak value given by the initial healthy operation current current $I_q(0)$ and decays towards zero.

The EMF response is represented by $I_q(0) = 0$ and $EMF = \omega_e\psi_{PM}$ and the dq-axis short circuit currents are given by:

$$I_d(\theta_e)_E = -\frac{\omega_e^2 L_{ph}\psi_{PM}}{\omega_e^2 L_{ph}^2 + R_{ph}^2}\left(1 - \frac{\sin(\theta_e + \gamma)}{\sin(\gamma)}e^{-\theta_e\frac{R_{ph}}{\omega_e L_{ph}}}\right) \tag{6.9}$$

$$I_q(\theta_e)_E = -\frac{\omega_e R_{ph}\psi_{PM}}{\omega_e^2 L_{ph}^2 + R_{ph}^2}\left(1 - \frac{\cos(\theta_e + \gamma)}{\cos(\gamma)}e^{-\theta_e\frac{R_{ph}}{\omega_e L_{ph}}}\right) \tag{6.10}$$

$$I(\theta_e)_E = \sqrt{I_d^2(\theta_e)_E + I_q^2(\theta_e)_E} \tag{6.11}$$

$$\gamma = \tan^{-1}\left(\omega_e L_{ph}/R_{ph}\right) \tag{6.12}$$

$$\theta_e = \omega_e t \tag{6.13}$$

where the steady state d-axis, q-axis and total steady state short circuit currents,$I_{d_{SS}}$, $I_{q_{ss}}$ and $I_{sc_{ss}}$ are given by:

$$I_{d_{ss}} = \frac{\omega_e^2 L_{ph} \psi_{PM}}{\omega_e^2 L_{ph}^2 + R_{ph}^2} \tag{6.14}$$

$$I_{q_{ss}} = \frac{\omega_e R_{ph} \psi_{PM}}{\omega_e^2 L_{ph}^2 + R_{ph}^2} \tag{6.15}$$

$$I_{sc_{ss}} = \frac{\omega_e \psi_{PM}}{\sqrt{\omega_e^2 L_{ph}^2 + R_{ph}^2}} \tag{6.16}$$

The peak d- and q-axis short circuit currents can be obtained by applying the $\frac{dI_d}{d\theta_e} = 0$ and $\frac{dI_q}{d\theta_e} = 0$ to (6.9) and (6.10), respectively. Thus, the peak short circuit d-axis current is achieved when $\theta_e = \pi$, while the peak short circuit q-axis current occurs when $\theta_e = \frac{\pi}{2}$, such that:

$$I_{d\,peak} = -\frac{\omega_e^2 L_{ph} \psi_{PM}}{\omega_e^2 L_{ph}^2 + R_{ph}^2}\left(1 + e^{-\frac{\pi R_{ph}}{\omega_e L_{ph}}}\right) \tag{6.17}$$

$$I_{q\,peak} = -\frac{\omega_e R_{ph} \psi_{PM}}{\omega_e^2 L_{ph}^2 + R_{ph}^2}\left(1 - \frac{\omega_e L_{ph}}{R_{ph}} e^{-\frac{\pi R_{ph}}{2\omega_e L_{ph}}}\right) \tag{6.18}$$

Designing the PDD with 1p.u. phase inductance means that the steady state current would equal the rated phase current. This ensures that during short circuit operation the PDD rated thermal limits are not exceeded. However, during the short circuit transient, the amplitude of the negative d-axis current is significantly higher than the rated current. Thus, this high negative d-axis current gives rise to a negative d-axis flux which is against the d-axis PM flux and contributes do the demagnetisation of the PM arrays. Thus, the risk of demagnetisation of the PDD PM arrays needs to be carefully considered during the short circuit transient.

The HSR and PPR drag torque during the symmetrical 3-phase short circuit can be analytically predicted by considering the steady state total short circuit current such that:

$$T_{HSR\ drag} = \frac{T_{PPR\ drag}}{G_r} = \frac{3I_{sc_{ss}}^2 R_{ph}}{\frac{\pi}{30}\Omega_{PPR} G_r} \tag{6.19}$$

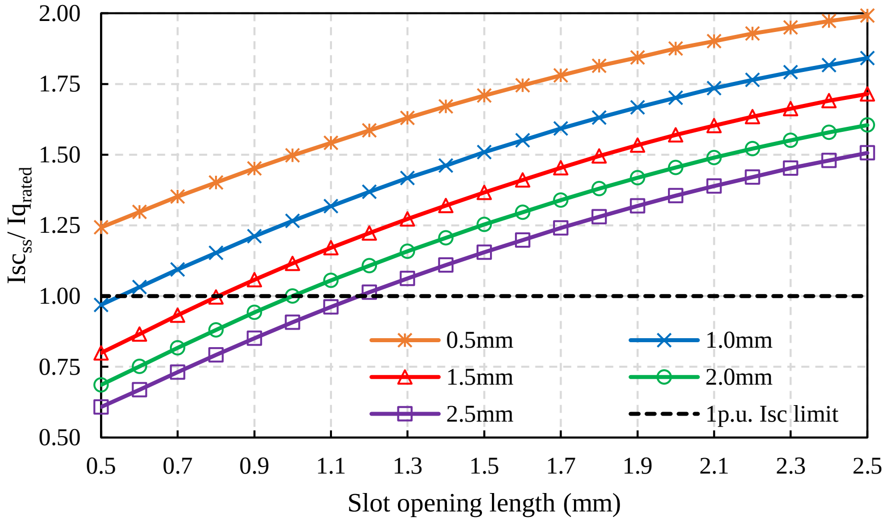

Figure 6.11. Variation of ratio of total steady state short circuit current to rated q-axis current, $I_{sc_{ss}}/I_{q\ rated}$, with slot opening length for a range of tooth tip thicknesses

The variation of the ratio between the steady state short circuit current and q-axis rated current with slot opening length and tooth tip thickness at the rated operating speed, is shown in Figure 6.11. For a fixed tooth tip thickness, as the slot opening is increased, the phase inductance is reduced which acts to increase the steady state short circuit current. Fixing the slot opening and increasing the tooth tip thickness has the opposite effect, as the phase inductance is increased and steady state short circuit current is reduced.

Figure 6.12 and 6.13 show the variation of the ratio between the peak short circuit d-axis and q-axis current and the steady state d-axis and q-axis short circuit current, respectively.

It can be observed that as the phase inductance is reduced, the peak dq-axis short circuit currents are reduced when compared to their steady state values.

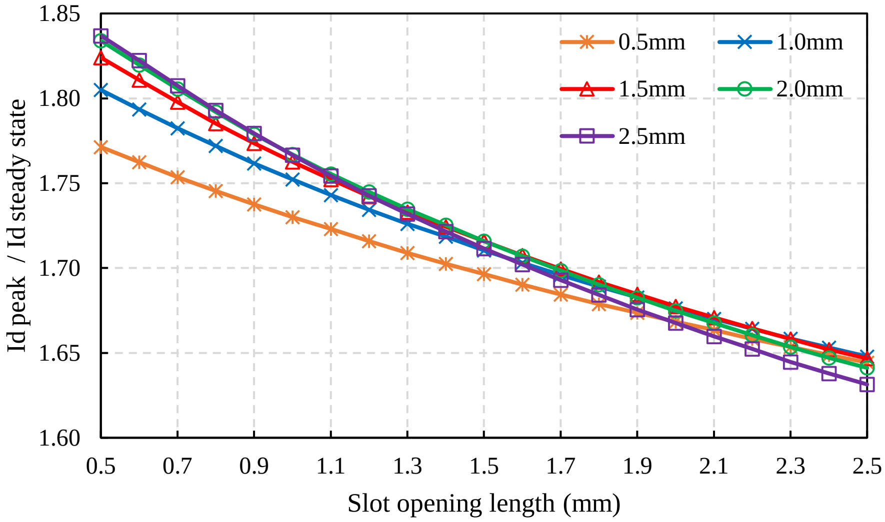

Figure 6.12. Variation of ratio of peak to steady state d-axis short circuit current, $I_{d\ peak}/I_{d\ ss}$, with slot opening length for a range of tooth tip thicknesses

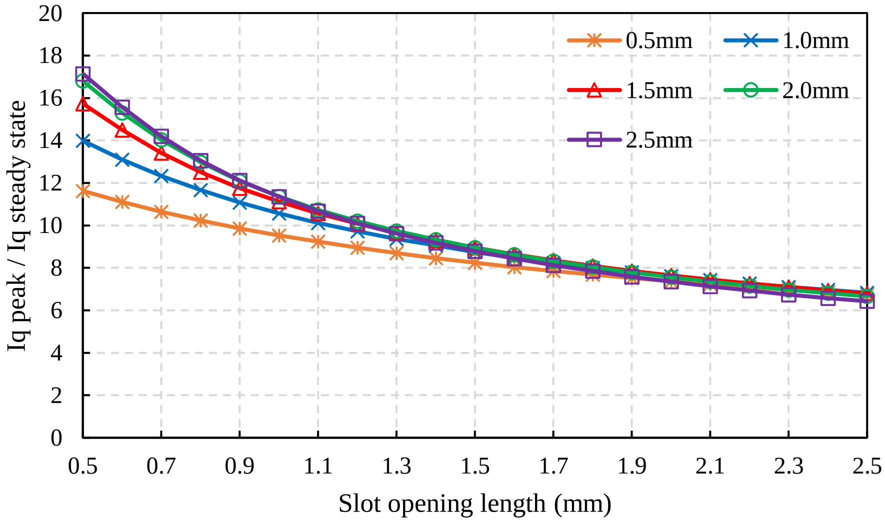

Figure 6.13. Variation of ratio of peak to steady state q-axis short circuit current, $I_{q\ peak}/I_{q\ ss}$, with slot opening length for a range of tooth tip thicknesses

Figure 6.14 shows the variation of the ratio of the total steady state short circuit current to the rated phase current with the PPR speed for a 2mm tooth tip thickness and a range of slot opening lengths. Thus, as the phase inductance is reduced by increasing the slot opening length, the steady state short circuit current is limited to a higher amplitude. It can be observed that at low output speeds, the short circuit current increases with speed as it is phase resistance limited. As the output speed is increased further, and the inductive reactance terms is dominant, the short circuit current is inductance limited. Thus, for a 1mm slot opening length and 2mm tooth tip thickness, the steady state short circuit current is limited by the high 1 p.u. inductance and its amplitude equal the rated q-axis current.

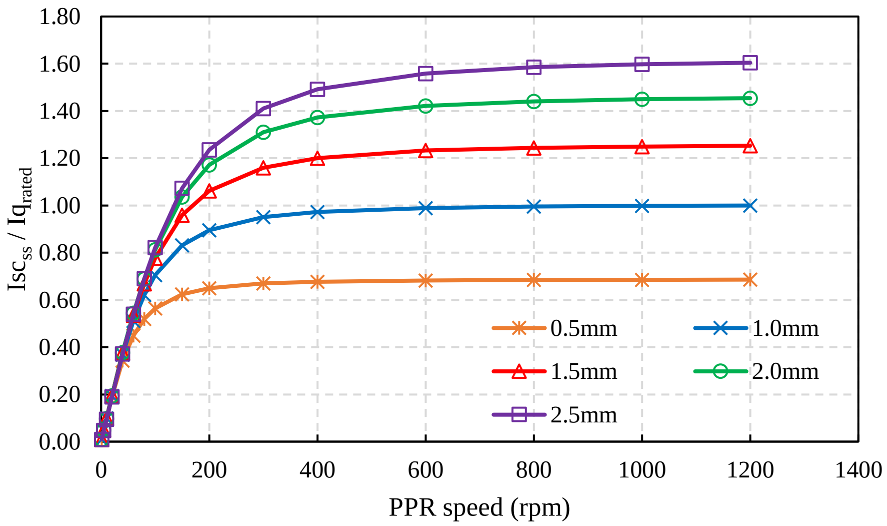

Figure 6.14. Variation of ratio of total steady state short circuit to rated q-axis current, $I_{sc\ ss}/I_{q\ rated}$,, with PPR speed for a fixed 2mm tooth tip thickness and a range of slot opening lengths

Figure 6.15 shows the variation of the ratio between the resultant short circuit drag torque and rated PPR torque with the PPR speed for a 2mm tooth tip thickness and a range of slot opening lengths. Similarly to the phase short circuit current, the drag torque initially increases with output speed as it is phase resistance limited. As the output speed is increased further, the short circuit current is inductance limited and the drag torque is reduced.

Since the drag torque is influenced by the q-axis short circuit current, the value of the electrical frequency, ω_e, for peak steady state q-axis current and drag torque can be obtained by applying ${dI_{q_{ss}}}/{d\omega_e} = 0$ to equation (6.15). Thus, when $\omega_e = \frac{R_{ph}}{L_{ph}}$, the q-axis steady state short circuit current and resultant drag torque have maximum amplitudes.

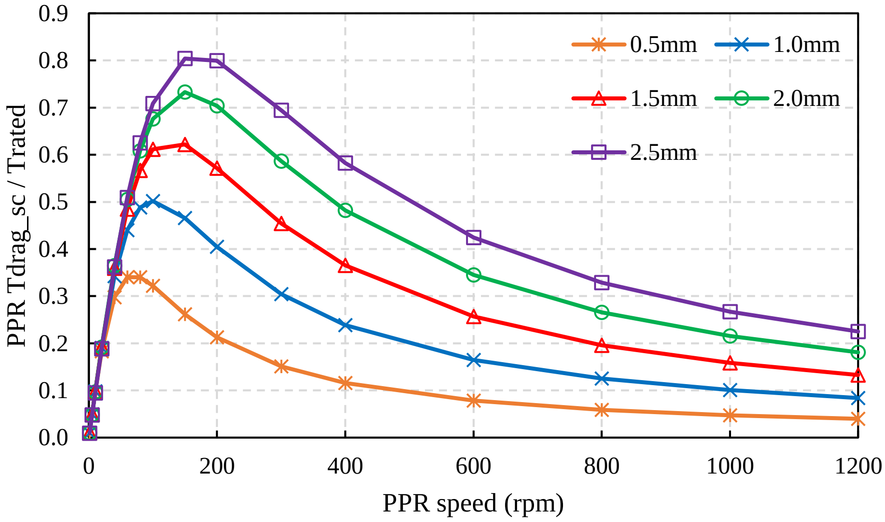

Figure 6.15. Variation of ratio of steady state PPR short circuit drag torque to rated PPR torque, $T_{PPR\ drag}/T_{PPR\ rated}$, with PPR speed for a fixed 2mm tooth tip thickness and a range of slot opening lengths

Figure 6.16 and 6.17 shows the analytically predicted variation of the d-axis and q-axis short circuit current for a 2mm tooth tip thickness and a range of slot opening lengths. It can be observed that during the short circuit transient, both the d-axis and q-axis current have the peak value substantially higher than the steady state value. The amplitude and steady state settling time of the dq-axis short circuit current are influenced by the ratio between the phase inductive reactance, $\omega_e L_{ph}$, and the phase resistance. The variation of this ratio with the slot opening length for a tooth tip thickness of 2mm is shown in Figure 6.18. Thus, it can be observed that at high $\frac{\omega_e L_{ph}}{R_{ph}}$ ratio, the amplitude of the dq-axis short circuit current oscillations is increased together with the settling time required to reach steady state. In contrast, as the slot opening is increased and the phase inductance is reduced, the $\frac{\omega_e L_{ph}}{R_{ph}}$ ratio is reduced and the amplitude and settling time of the short circuit current is reduced.

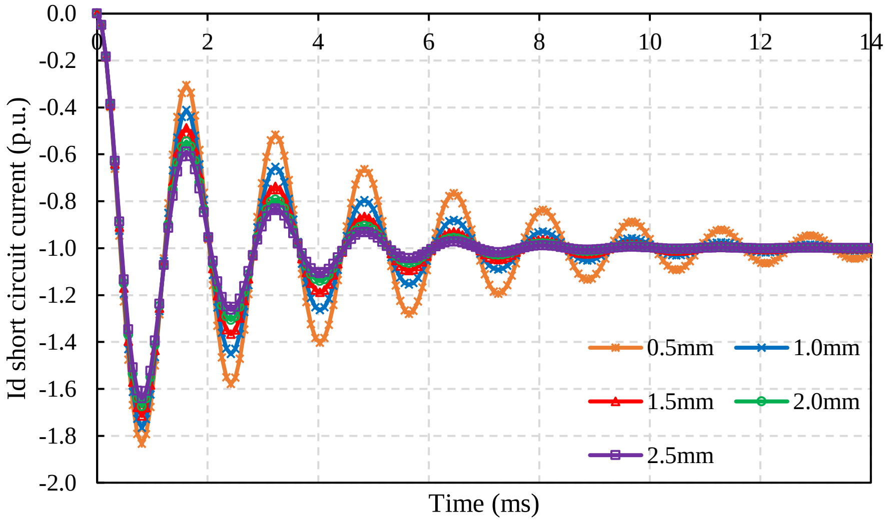

Figure 6.16. Variation of d-axis short circuit current for 2mm tooth tip thickness and a range of slot opening lengths

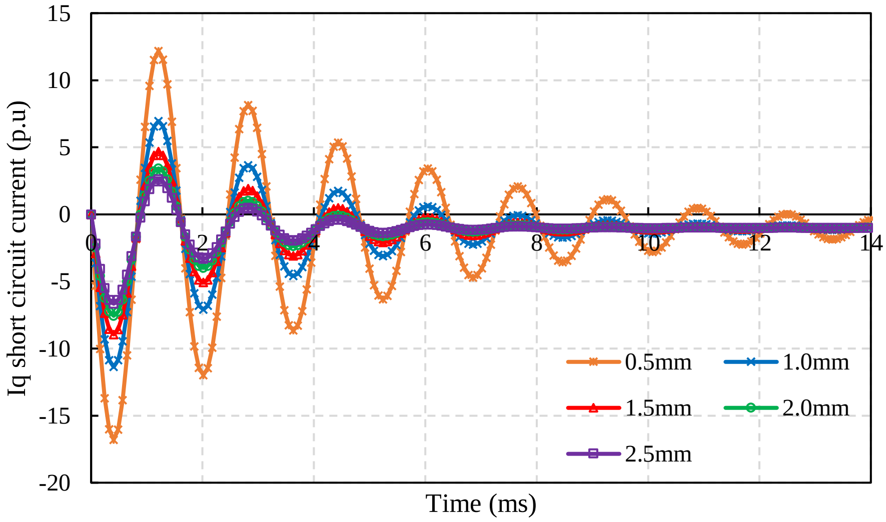

Figure 6.17. Variation of q-axis short circuit current for 2mm tooth tip thickness and a range of slot opening lengths

For the selected slot opening geometry, the tooth tip thickness was set to 1.95mm while the slot opening length was fixed at 0.9mm. This ensured that the stator PMs sitting next to the slot opening have a wide landing area on the tooth tip. This allows for the PMs to be glued against the notches of the tooth tips. The slot opening wedge which fills the slot opening was 3D printed from a high temperature polycarbonate material. Figure 6.19 shows the variation of the steady state short circuit current with PPR output speed for the selected slot opening/tooth tip geometry. It can be observed that a good agreement exists between the analytical and 2D FE steady state current, with the amplitude of the short circuit current at rated output speed being slightly lower than the rated q-axis current

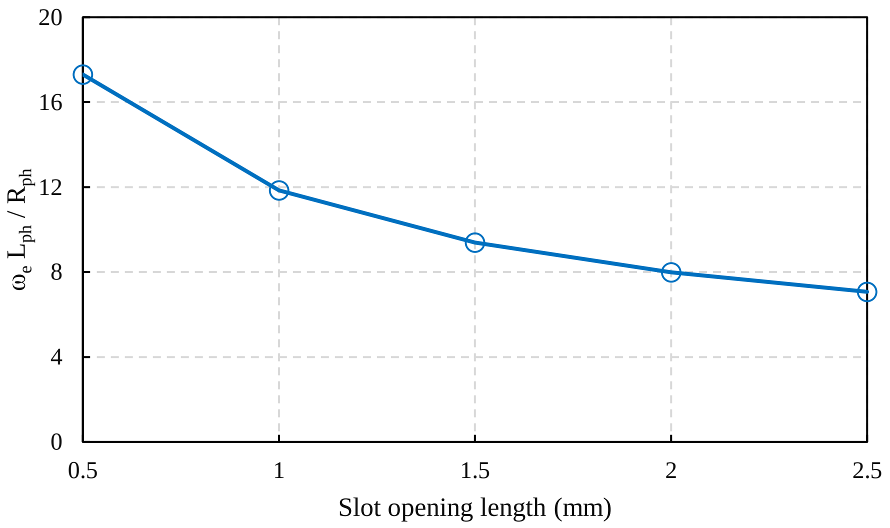

Figure 6.18. Variation of ratio of phase inductive reactance to phase resistance with slot opening length for a tooth tip thickness of 2mm at 620Hz (1200 rpm output speed)

The short circuit current transient response at the rated PPR speed of 1200rpm is shown in Figure 6.20. It can be observed that the d-axis current has the peak amplitude 80% higher than the steady state value. Due to this high negative d-axis current, the risk of demagnetisation of the HSR and stator PM arrays needs to be considered during the machine design process.

Figure 6.21 shows the variation of the steady state PPR drag torque with rotor speed. The peak value of the drag torque occurs at an output speed of 87 rpm based on the ratio between the phase resistance and inductance.

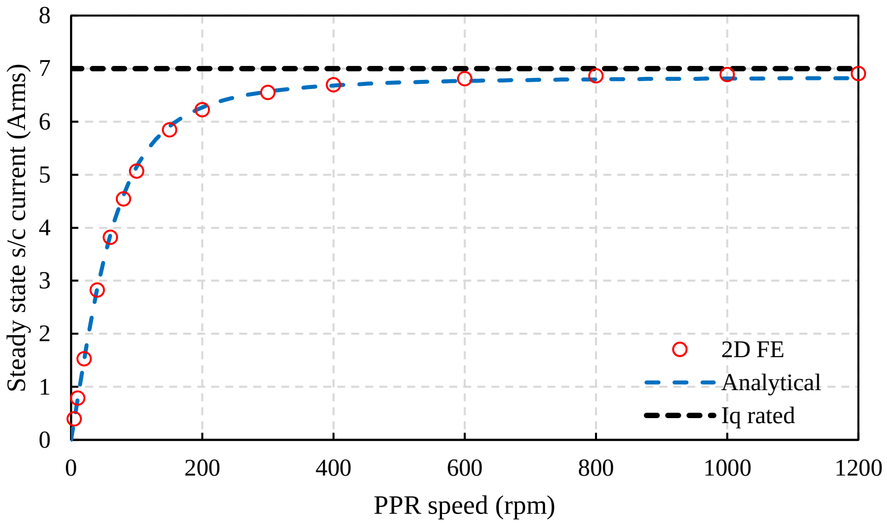

Figure 6.19. Variation of steady state short circuit current for selected PDD slot opening geometry

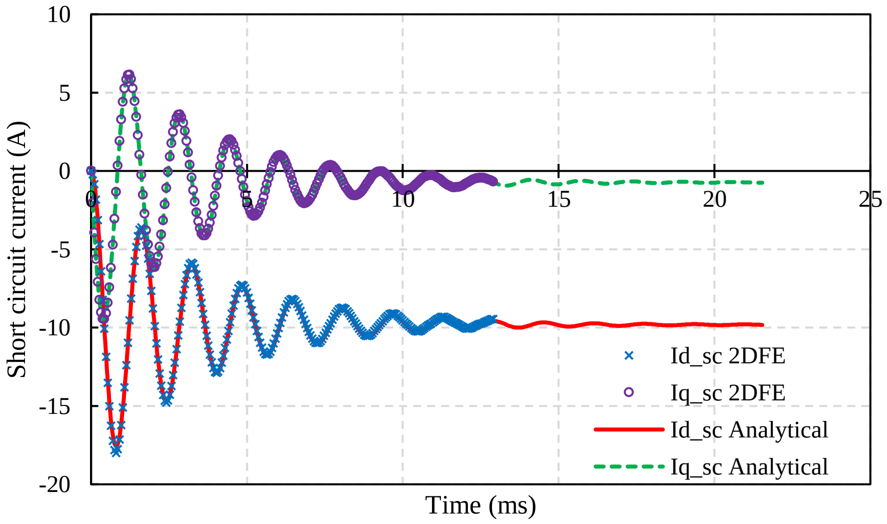

Figure 6.20. Comparison of analytic and 2D FE DQ-axis current for selected PDD slot opening geometry

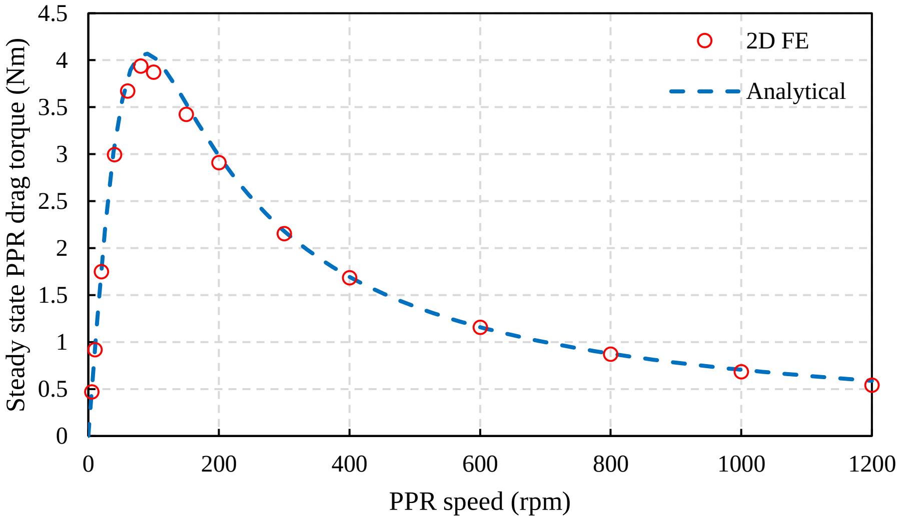

Figure 6.21. Variation of steady state drag torque for selected PDD slot opening geometry

6.3 Calculation of number of turns

The final PDD stator 2D cross-section was fixed based on the short circuit analysis such that a 1p.u phase inductance is obtained which limits the short circuit current to the rated phase current amplitude. Thus, since the phase inductance is now fixed, the number of turns required for a fixed DC bus voltage can be calculated.

For an Active-Passive operation, the phase voltage, V_{ph}, is given by:

$$V_{ph} = \sqrt{V_d^2 + V_q^2} \tag{6.20}$$

where V_d and V_q are the d-axis and q-axis voltages for 1 turn per coil, given by:

$$V_d = -\omega_e L_q I_q + R_{ph} I_d \tag{6.21}$$

$$V_q = \omega_e \left(\psi_{PM}(I_q) + L_d I_d\right) + R_{ph} I_q \tag{6.22}$$

where $I_d, I_q, L_d \; and \; L_q$ represent the d-axis and q-axis current and inductances, respectively. In order to consider the effect of magnetic saturation and the influence of dq axis cross coupling [172], [175], [177], [178], $\psi_{PM}(I_q)$ represents the PM flux linkage as a function of I_q current. Since the fault tolerant PDD is required to operate in the constant torque region, the effect of I_d on the PM flux linkage was ignored and I_d was set to zero.

For the 12s8p 3-phase duplex winding, the phase resistance, R_{ph}, is given by:

$$R_{ph} = \frac{L_{act}}{\gamma_{cu} A_{copper}} \tag{6.23}$$

where γ_{cu} and L_{act} are the copper conductivity and active length of the PDD. The copper area is proportional to the slot area, A_{slot}, and packing factor p_{fact}, such that:

$$A_{copper} = A_{slot} \cdot p_{fact} \tag{6.24}$$

Thus, by considering the phase voltage of the 12s8p 3-phase duplex PDD with one equivalent turn per coil, V'_{ph}, and the DC bus supply, V_{DC}, the number of turns, N_t, is given by:

$$N_t = \frac{V_{DC}/2}{V'_{ph}} \tag{6.25}$$

The DC supply voltage of the PDD actuator motor was fixed in the specification at a nominal value of 270 V_{DC} with the actuator being required to operate without any drop in performance on a minimum DC bus voltage of 235 V_{DC}. From this minimum DC supply, 5 volts were reserved for the voltage drop on the 3-phase inverter and due to additional wire length required for the connections between the inverter and PDD. The PDD actuator motor was also required to operate without loss of performance within an ambient temperature range of -55^{o}C to +75^{o}C. Thus, the effect of the wide ambient temperature range on PM flux linkage, phase current and resistance were considered during the calculation of the number of turns.

The variation of the d-axis PM flux linkage with stator MMF for a range of PM temperatures is shown in Figure 6.22, while the variation of the ratio of on load to no load d-axis PM flux linkage is shown in Figure 6.23. For an increasing PM temperature, it can be observed that the d-axis PM flux linkage is reduced since the remanence of the PMs is reduced as the temperature is increased. For a fixed PM temperature and reduced stator MMF, the saturation effect in the stator is negligible and the reduction in d-axis PM flux linkage due to magnetic saturation is not significant. As the stator MMF is increased by increasing the q-axis current, the on-load d-axis PM flux is slightly reduced due to high magnetic saturation in the stator.

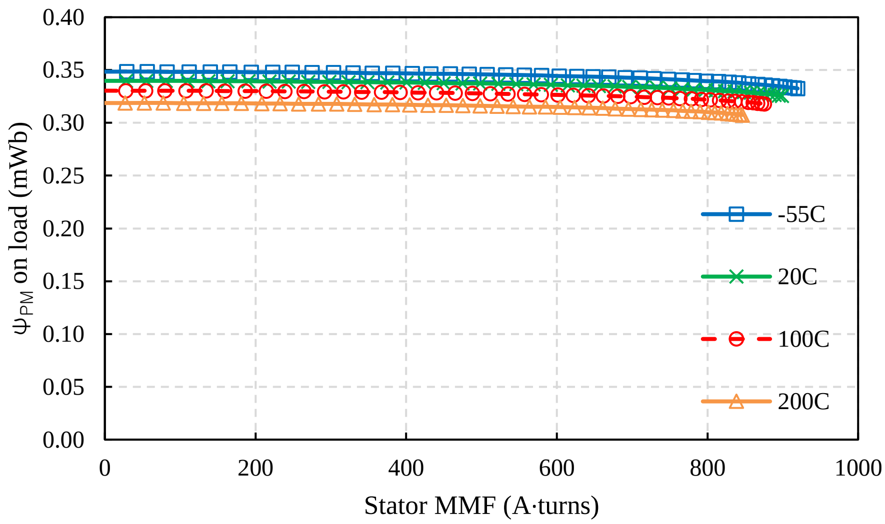

Figure 6.22. Variation of $\psi_{PM}(I_q)$ with stator MMF for a range of PM temperatures

The variation of the average PPR torque with stator MMF for a range of PM temperatures is shown in Figure 6.24. It can be observed that for the PPR rated torque of 8.6 Nm the stator MMF varies between 535 to 587 Amp·turns, depending on the PM temperature. Thus, for this stator MMF range, it can be observed that the d-axis on load PM flux linkage is not affected by the stator MMF due to reduced stator saturation.

For the 12s8p duplex 3-phase PDD with 1 turn per coil per phase, Figure 6.25 shows the variation of the q-axis inductance for one of the two 3-phase lanes with stator MMF for a range of PM operating temperatures.

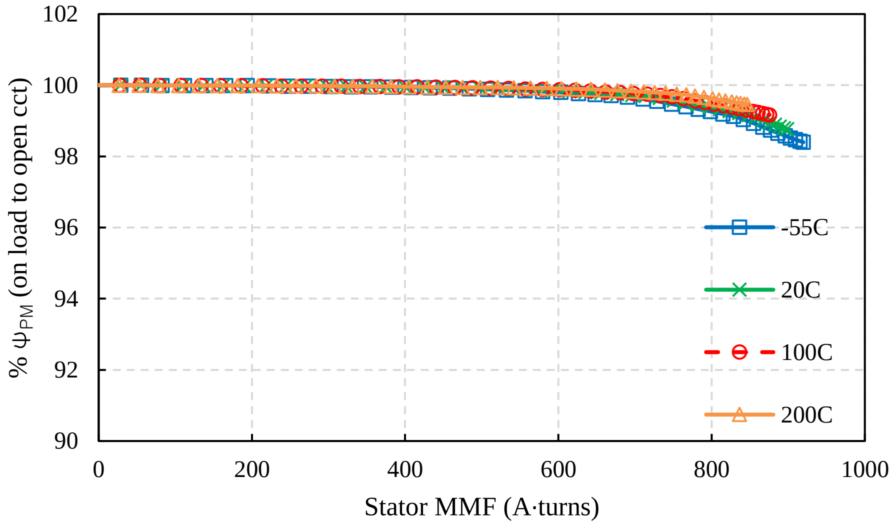

Figure 6.23. Variation of $\psi_{PM}(I_q)/\psi_{PM}(0)$ with stator MMF for a range of PM temperatures

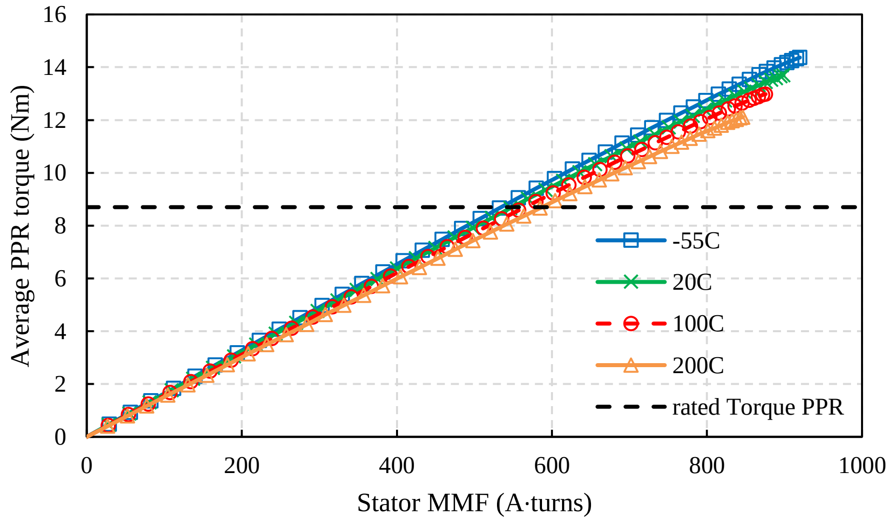

Figure 6.24. Variation of average PPR torque with stator MMF for a range of PM temperatures

Since the proposed PDD designs represent a non-salient pole electrical machine which will be operated only in the constant torque region where $I_d = 0A$, it was assumed that:

$$L_{ph} = L_d = L_q = \frac{\psi_q(0, I_q)}{I_q} \tag{6.26}$$

From Figure 6.25, it can be seen that the q-axis inductance of the PDD is constant at rated stator MMF, irrespective of PM temperature. At high values of MMF, the inductance is slightly reduced due to the increase in stator magnetic saturation.

Figure 6.26 shows the variation of the stator MMF and resultant on-load phase voltage with PM temperature for the 12s8p PDD in rated Active-Passive operation with 1 turn per coil per phase. The change in phase resistance with temperature was included when predicting the phase voltage. It can be observed that as the PM temperature is increased, the phase voltage per turn is increased and the resultant number of turns is reduced. Based on the on-load phase voltage at 200^{o}C PM and copper operating temperature, the number of turns was fixed at 54 turns per coil per phase. Selecting the number of turns based on a lower PM temperature would restrict the PDD from achieving peak power thought out the operational temperature range.

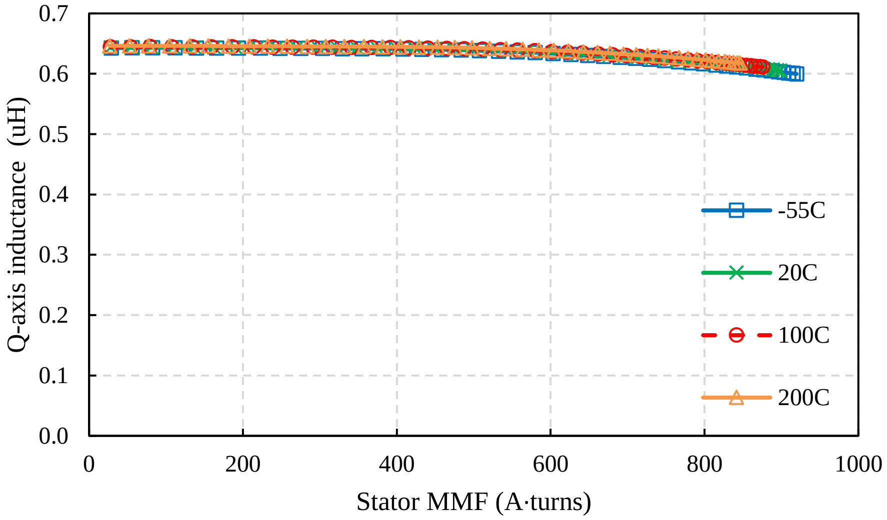

Figure 6.25. Variation of q-axis inductance with stator MMF for a range of PM temperature and for 1 turn per coil per phase PDD model

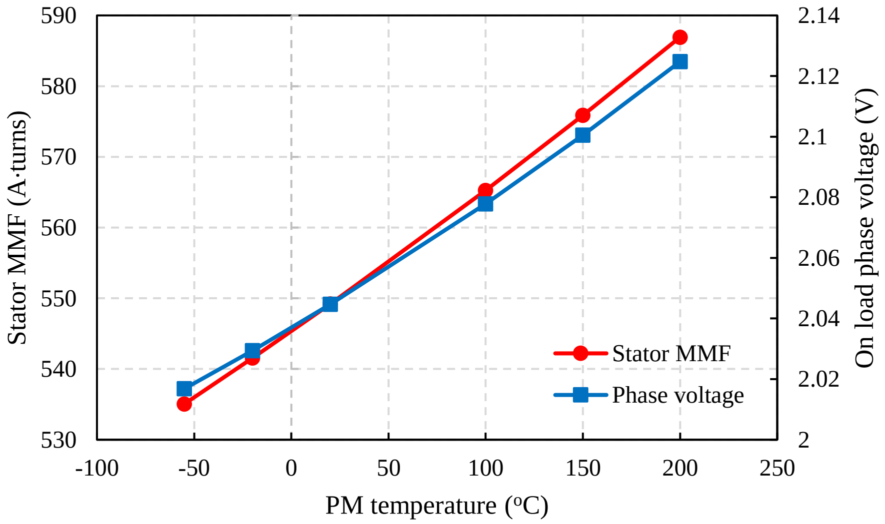

Figure 6.26. Variation of stator MMF and phase voltage of 1 turn per coil per phase at rated operation point

6.4 Inter-turn short circuit current

The inter-turn short circuit current of the proposed 12s8p duplex 3-phase fault tolerant PDD was predicted using analytical and 2D FE models. The total number of turns of the PDD winding is predicted based on the minimum DC supply voltage, with the effect of PM temperature on the PM flux linkage and rated phase current being considered. The entire process and assumptions used when calculating the number of turns is discussed in section 6.3.

The circuit model of the phase containing n_f turns under short circuit out of the total of N_t turns, is shown in Figure 6.27. For the healthy side of the coil, I_1represents the phase current, E_1 is the EMF, with R_1 and L_1being the heathy phase inductance and resistance. For the faulty side, I_2 is the short circuit current, E_2 is the EMF, while R_2 and L_2 are the resistance and inductance of the n_f faulty turns. The mutual inductance component between the healthy and faulty turns is represented by M_{12}

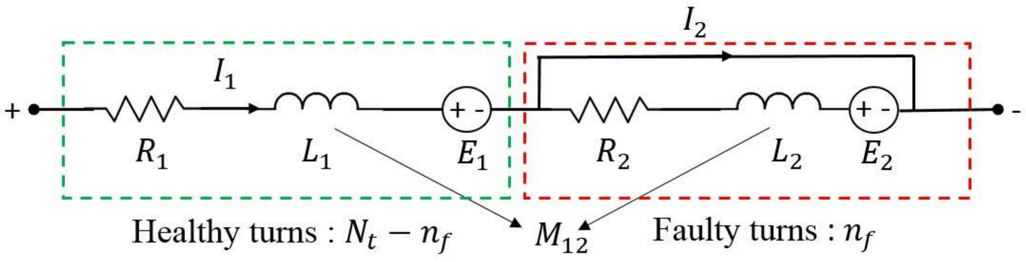

Figure 6.27. Phase model with n_f turns in short circuit

The electrical parameters of the phase circuit shown in Figure 6.27 can be calculated from the nominal phase values [179], such that:

$$R_1 = R_{ph}\frac{N_t - n_f}{N_t} \qquad R_2 = R_{ph}\frac{n_f}{N_t} \tag{6.27}$$

$$L_1 = L_{ph}\left(\frac{N_t - n_f}{N_t}\right)^2 \qquad L_2 = L_{ph}\left(\frac{n_f}{N_t}\right)^2 \tag{6.28}$$

$$E_1 = \omega_e\psi_{PM}\frac{N_t - n_f}{N_t} \qquad E_2 = \omega_e\psi_{PM}\frac{n_f}{N_t} \tag{6.29}$$

$$M_{12} = \sqrt{L_1L_2} \tag{6.30}$$

For the proposed 12s8p fault tolerant PDD, the equations describing the phase model containing the faulted turns are given by:

$$V_1(t) = R_1 I_1(t) + L_1 \frac{dI_1}{dt} + M_{12}\frac{dI_2}{dt} + E_1(t) \tag{6.31}$$

$$0 = R_2 I_2(t) + L_2 \frac{dI_2}{dt} + M_{12}\frac{dI_1}{dt} + E_2(t) \tag{6.32}$$

The analytical prediction of the short circuit current in the shorted turns has been conducted with zero and rated phase current in the healthy turns. The phasor diagrams for $I_1 = 0A$ and $I_1 = I_q$ are shown in Figure 6.28.

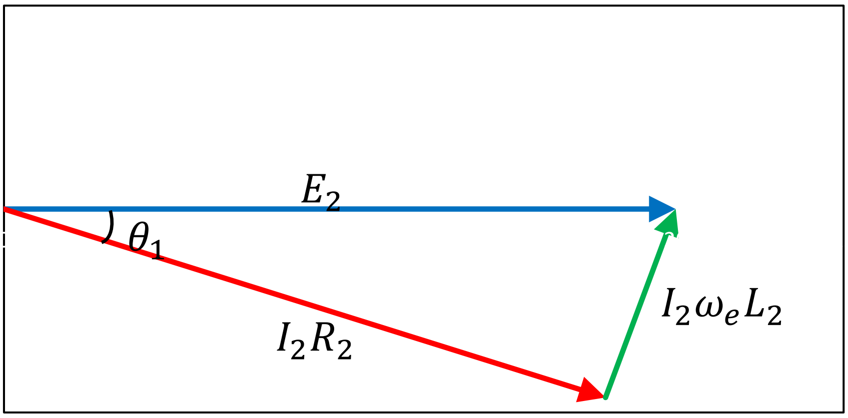

(a)

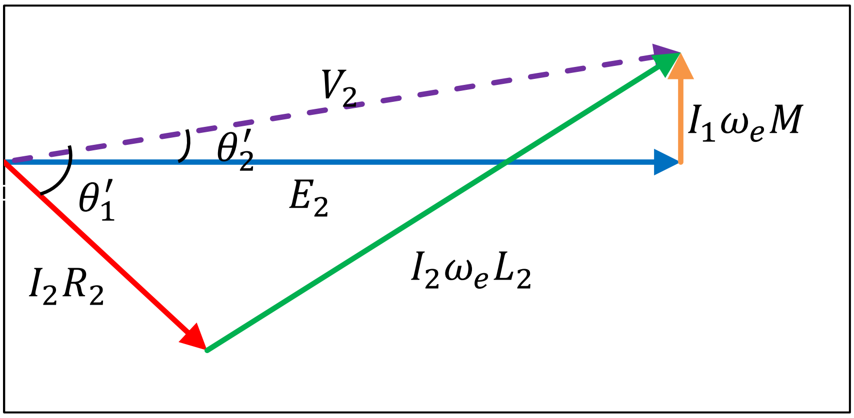

(b)

Figure 6.28. Phasor diagram for shorted turns (a)$I_1 = 0A$ (b) $I_1 = I_q$

The peak steady state short circuit current of the shorted turns, for $I_1 = 0A$, is given by:

$$I_2 = \frac{E_2}{\sqrt{R_2^2 + (\omega_e L_2)^2}} \tag{6.33}$$

The peak steady state short circuit current of the shorted turns when the remaining heathy turns are energised with rated I_q current, is given by:

$$I_2 = \frac{\sqrt{E_2^2 + (I_1 \omega_e M_{12})^2}}{\sqrt{R_2^2 + (\omega_e L_2)^2}} \tag{6.34}$$

For the analytical model, the change in the inductance of the shorted turn with the position in the slot was neglected.

Transient 2D FE analysis was used to predict the variation of the short circuit current with the number of shorted turns and position within the stator slot. The placement of the shorted turn was varied in the FE model, from near the slot opening to the inner diameter of the stator back-iron, as shown in Figure 6.29. Both the analytical and 2D FE models were used to predict the short circuit current of 1, 5 and 10 turns under short circuit.

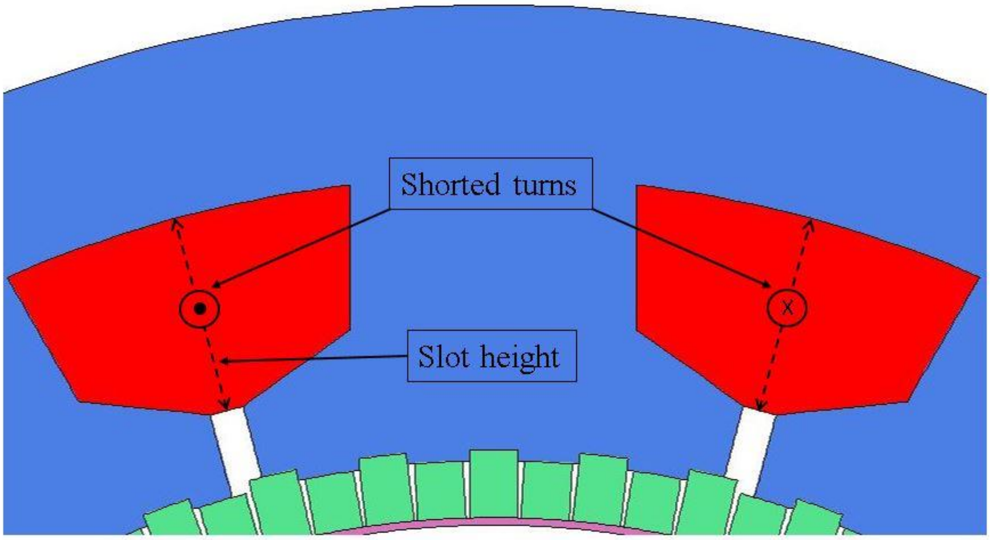

Figure 6.29. Position of shorted turns within the stator slot

The variation of the short circuit current, for 1, 5 and 10 turns in short circuit out of 54 turns, with the HSR position and for different slot positions of the shorted turns, with $I_1 = 0A$ and $I_1 = 10.2A$ (rated phase current) in the healthy turns, is shown in Figure 6.30 and Figure 6.31, respectively. As expected, the fault current amplitude, for both cases with $I_1 = 0A$ and $I_1 = 10.2A$, is reduced as the number of faulty turns is increased. This is due to the increase in resistance and inductive reactance of the faulted bundle as the number of turns is increased.

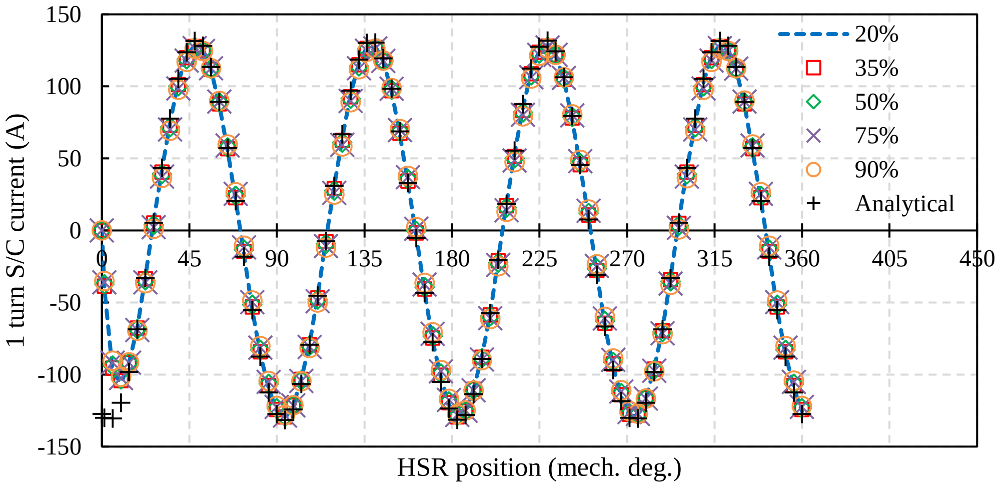

(a)

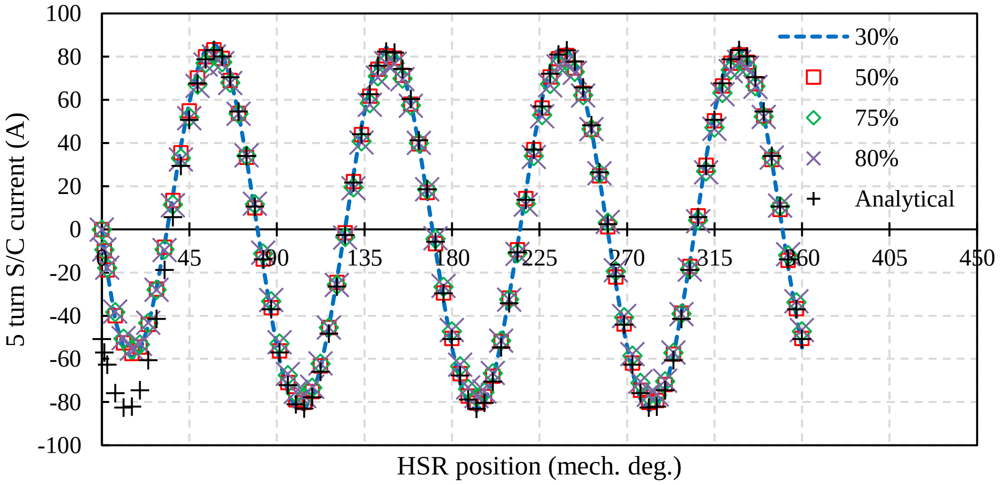

(b)

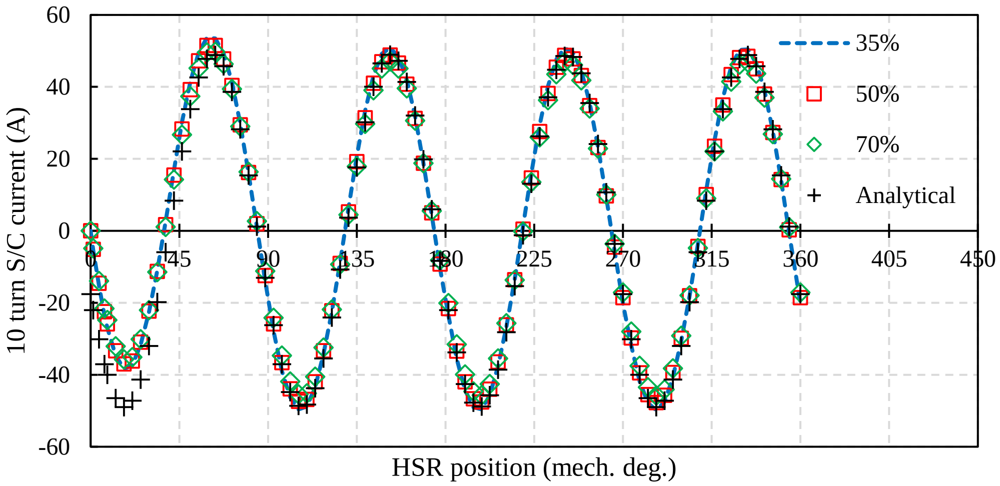

(c)

Figure 6.30. Variation of (a) 1 turn (b) 5 turns (c) 10 turns short circuit current with HSR position for different slot positions at 1200 rpm output speed for $I_1 = 0A$

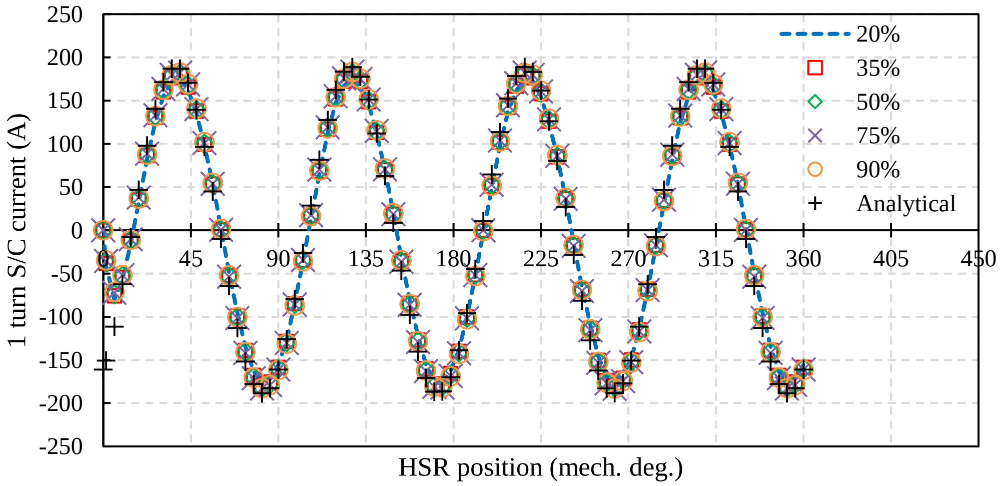

(a)

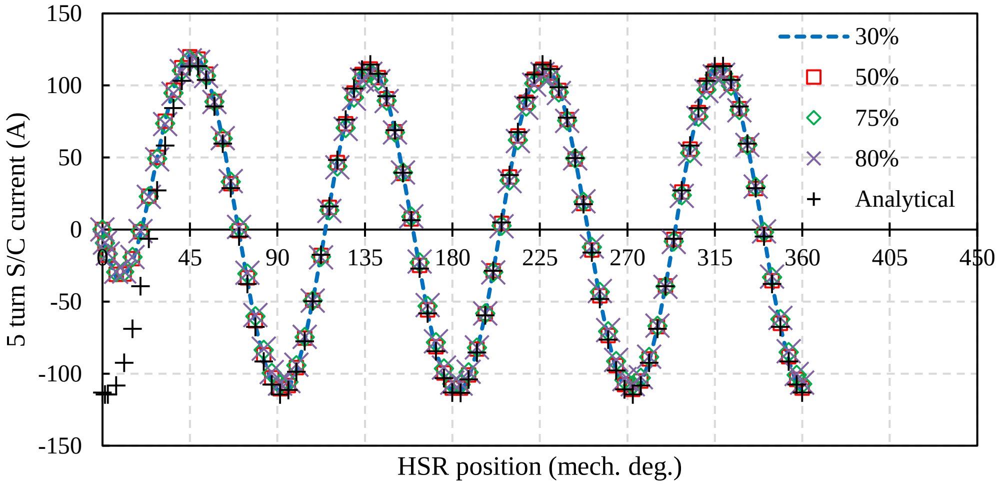

(b)

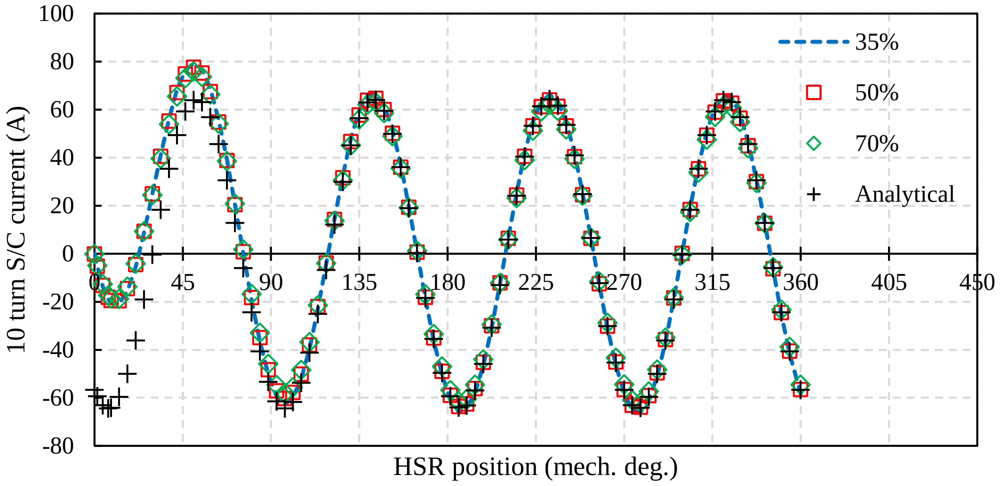

(c)

Figure 6.31. Variation of (a) 1 turn (b) 5 turns (c) 10 turns short circuit current with HSR position for different slot positions at 1200 rpm output speed for $I_1 = 10.2\ A$

Compared to the no load operation case, where $I_1 = 0A$, the fault current of the shorted turns is increased when the fault occurs during on load operation where $I_1 = 10.2A$. This is due to the mutual coupling between the healthy and faulty turns, which acts to increase the voltage that drives the short circuit current of the faulty turns, as shown in Figure 6.28 (b) and equation (6.34).

The variation of the peak short circuit current, for 1, 5 and 10 turns under short circuit out of the total of 54 turns, with the slot position of the faulty turns and for a range of output rotor speeds is shown in Figure 6.32. It can be observed that for all the numbers of turns in short circuit, the fault current is substantially higher than the rated current of the PDD. As the output speed is increased, the fault current is increased to 17 times the value of the rated phase current for 1 turn in short circuit at 1200 rpm, when the healthy turns are energised with the rated phase current. In this case, if no action is taken to reduce the fault current in the shorted turns by triggering a 3-phase symmetrical short circuit, a catastrophic winding failure can occur due to the high copper loss of the faulted turns. For comparison, for a 1 turn short circuit at 1200rpm, with rated current in the healthy turns, the copper loss of the shorted turn is 67% higher than the total rated copper loss of the PDD.

From Figure 6.32 it can be observed that, for a fixed number of turns in short circuit, the peak fault current amplitude is only mildly affected by the position of the faulty turns in the slot. This is due to the ratio between the resistance and inductive reactance of the shorted turns. Table 6.2 shows the variation of the resistance and reactance with the number of shorted turns at 1200 rpm PPR speed. It can be observed that for 1 faulty turn, the resistance of the turn is 3.86 times larger than its reactance. Thus, in this case the fault current is resistance limited and the change in inductance with slot position of the faulted turns has a minimal effect on the short circuit current amplitude. For example, for 1 turn under short circuit at 1200rpm with I_1 equal to the rated machine current, the peak value of the fault current is reduced by 2% when the faulted turn is moved from 20% to 90% slot height. If the number of turns in short circuit is increased, their inductive reactance becomes dominant, as shown in Table 6.2.Thus, for a 10 turn short circuit at 1200rpm with I_1 equal to the rated machine current, the peak value of the fault current is reduced by 6% when the position of the faulted turn is changed from 35% to 75% of the slot height. Furthermore, since this particular PDD motor was designed with a high slot leakage inductance component, the change in the slot inductance component of the faulted turns with their position in the slot has minimal effect on their total inductance.

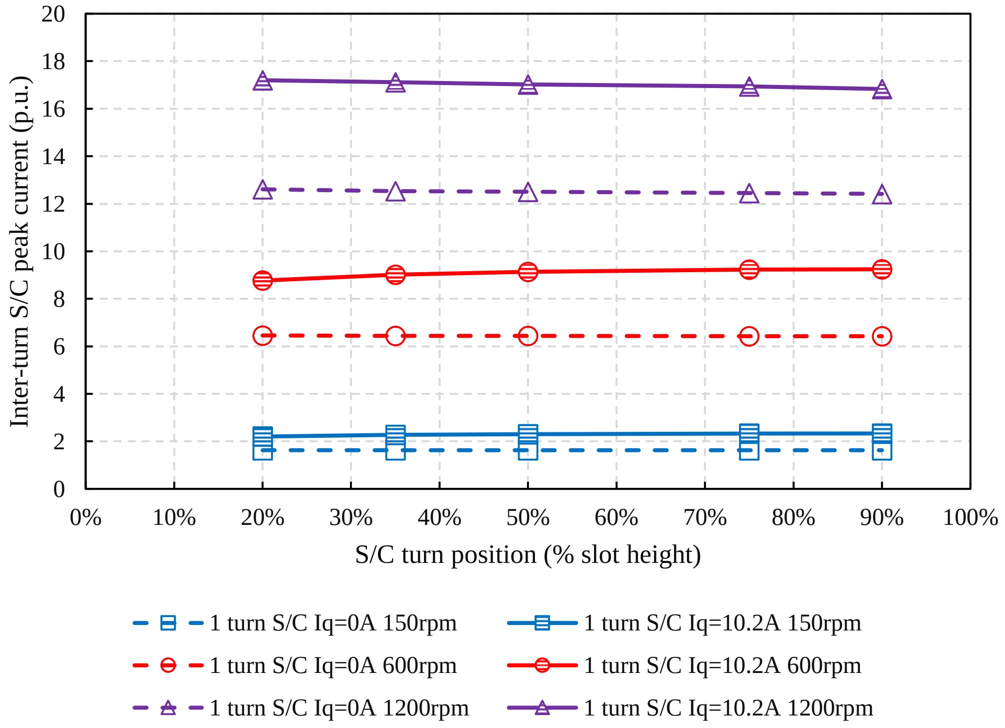

(a)

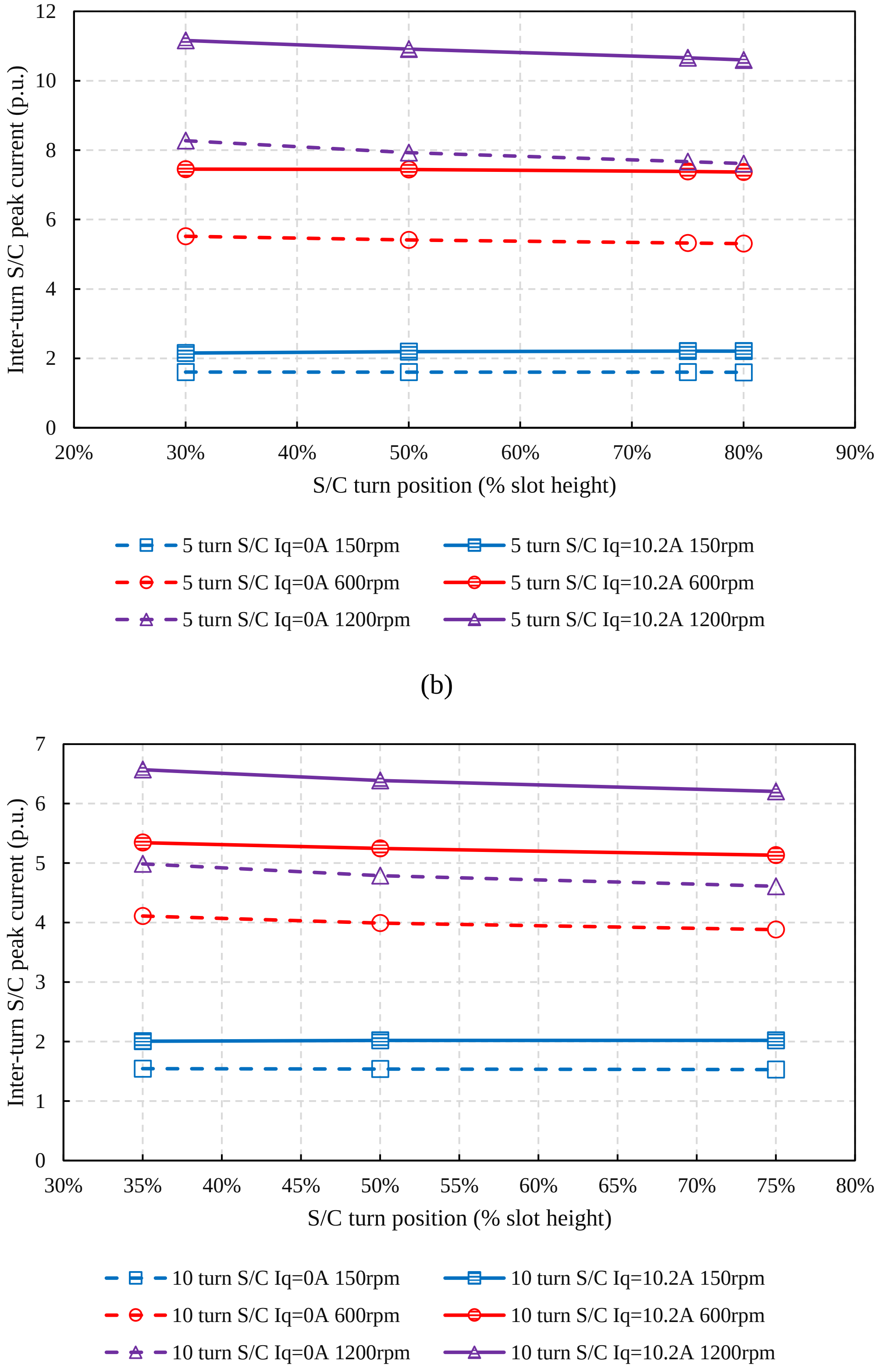

(b)

(c)

Figure 6.32. Variation of peak (a) 1 turn (b) 5 turns (c) 10 turns short circuit current with slot position of shorted turns. 1 p.u. = 10.2 A rated phase current

Table 6.2.Variation of resistance and inductive reactance of short turns at 1200rpm output speed

n_f	$R_2\ (m\Omega)$	$L_2\ (\mu H)$	$\omega_e L_2\ (m\Omega)$	$\frac{R_2}{\omega_e L_2}$
1	9.81	0.65	2.54	3.86
5	49.06	16.32	63.57	0.77
10	98.13	65.27	254.27	0.39

For the presented fault tolerant duplex 3-phase PDD design, assuming the stator turn fault of one of the 3-phase lanes can be detected quickly, the high fault current of the shorted turns can be reduced by triggering a symmetrical 3-phase short circuit of the affected lane. In this case, the PM field which drives the stator turn fault would be shared equally between the total number of turns of the shorted lane, and the stator turn to turn fault would be converted into a 3-phase symmetrical short circuit fault. Thus, the 1 p.u. inductance would limit the short circuit current in all the turns to the value of the rated machine current.

This fault mitigation method was investigated using 2D FE simulations for 1, 5 and 10 turns in short circuit out of the total of 54 turns. Figure 6.33 shows the coupled circuits used in the transient 2D FE simulation. The stator turn fault is modelled in lane 2, as shown in Figure 6.33 (b), with the stator turn short circuit being triggered by closing switch S_3. The symmetrical 3-phase short circuit is triggered by closing switched S_1 and S_2.

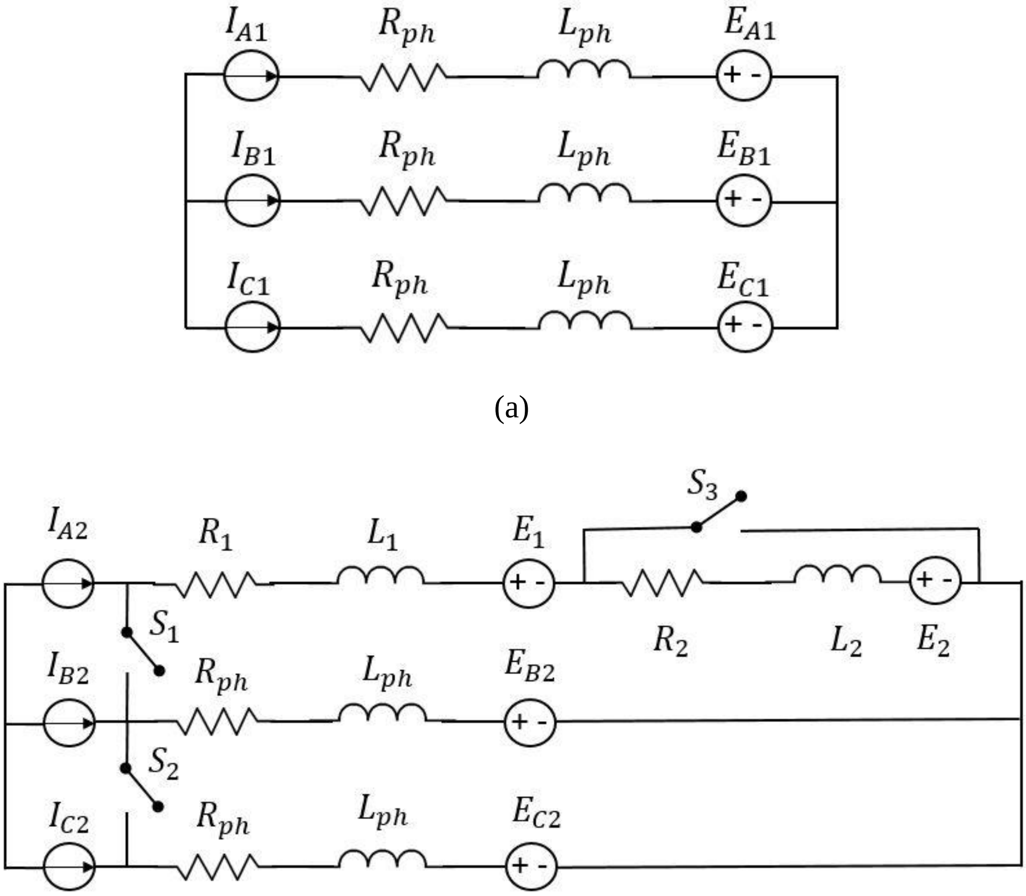

(b)

Figure 6.33. Coupled circuits used in 2D FE analysis (a) Lane 1 (b) Lane 2 with stator turn fault on phase A2

In order to show all the different operation stages of the PDD, such as normal operation, stator turn fault and stator fault current mitigation by triggering the 3-phase short circuit of the affected lane, the PDD electrical machine was simulated for 14 electrical cycles of the HSR. Table 6.3 shows the different operation states where τ_{HSR} represents one electrical cycle of the HSR.

Table 6.3. PDD operation states

State no.	Time	Description of operation state
1	$0 - \tau_{HSR}$	Lane 1 passive open circuit. Lane 2 normal healthy operation.
2	$2\tau_{HSR} - 5\tau_{HSR}$	Lane 1 passive open circuit. Lane 2 faulty operation. S_3 closed, stator turn fault triggered.
3	$6\tau_{HSR} - 14\tau_{HSR}$	Lane 1 normal healthy operation. S_1, S_2, S_3 closed, Lane 2 3-phase short circuit triggered.

During the first electrical cycle of the HSR, Lane 1 is not energised and Lane 2 is used to produce rated output power. From the start of the second electrical cycle until the end of the fifth electrical cycle, the stator turn fault is triggered by closing switch S_3. From the start of the sixth electrical cycle until the end of the FE simulation, switches S_1 and S_2 are closed, enabling the 3-phase symmetrical short circuit of Lane 2, while switch S_3 is kept closed. During the last operation stage, Lane 1 is energised to provide rated power.

During the first electrical cycle of the HSR, Lane 1 is not energised and Lane 2 is used to produce rated output power. Figure 6.34 shows the 3-phase currents and voltages of Lane 1. During this first cycle, the Lane 1 current is zero and the phase voltage represents the no-load back-EMF. In the first cycle, Lane 2 is energised with rated phase current and voltage as shown in Figure 6.35 and 6.36, respectively. During this state, switches S_1, S_2, S_3 are opened.

At the start of state 2, the stator turn fault is triggered on the phase A coil of Lane 2 by closing switch S_3. The current in the healthy turns of Lane 2 is kept unchanged during the second operation state. Figure 6.36 shows the fault current for 1, 5 and 10 turns under short circuit from a total of 54 turns. It can be observed that the amplitude of the fault current is reduced as the number of turns under fault is increased due to the increase in the inductance of the faulted bundle. Figure 6.37 shows the 3-phase voltages of Lane 2. It can be observed that during the stator fault state, the phase A2 voltage is reduced as the number of turns in short circuit is increased.

In order to reduce the amplitude of the fault current in the shorted turns of phase A2, a symmetrical 3-phase short circuit is created on Lane 2 at the start of the third operation state by closing switches S_1 and S_2. Figure 6.35 shows the 3-phase short circuit current of Lane 2, while the fault current of the shorted turns is shown in Figure 6.36. It can be observed that the fault current of the shorted turns is reduced to the value of the 3-phase short circuit current, since the PM field is equally distributed amongst the turns of phase A2. Thus, the resultant MMF of phase A2 is also equally shared between the total number of turns. Due to the 1p.u. phase inductance, the 3-phase short circuit current in all the turns of Lane 2 is limited to the rated current value. During the last state, Lane 1 is used to produce rated power.

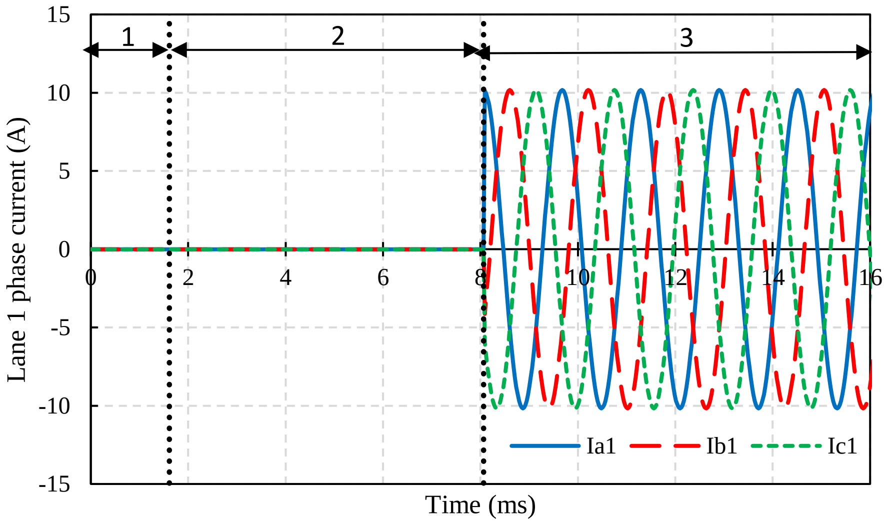

(a)

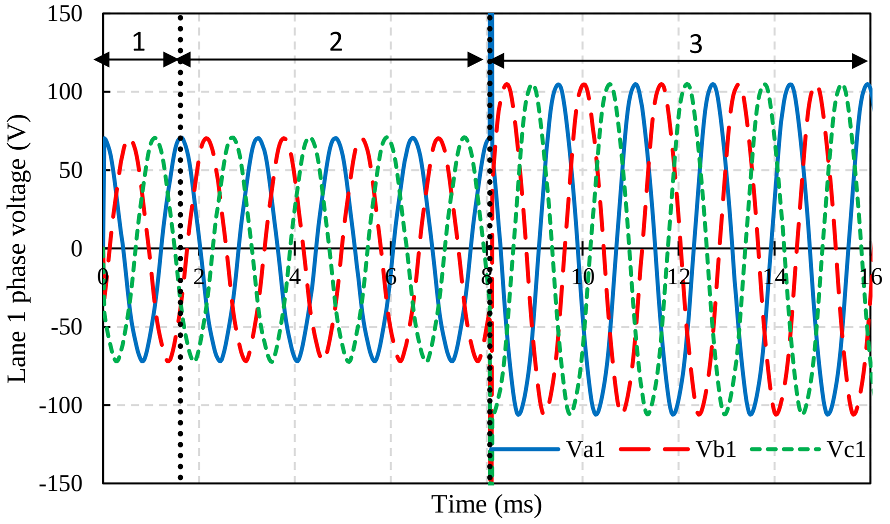

(b)

Figure 6.34. Lane 1 3-phase (a) currents (b)voltages

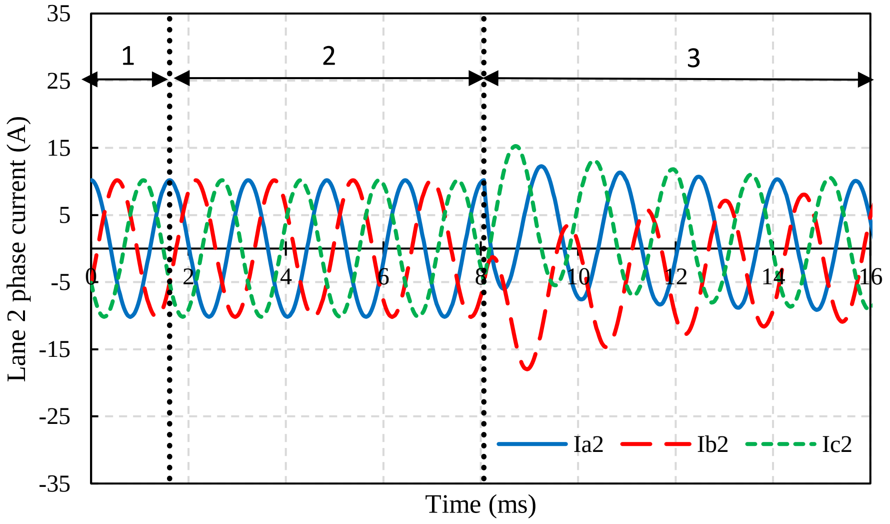

Figure 6.35. Lane 2 phase currents

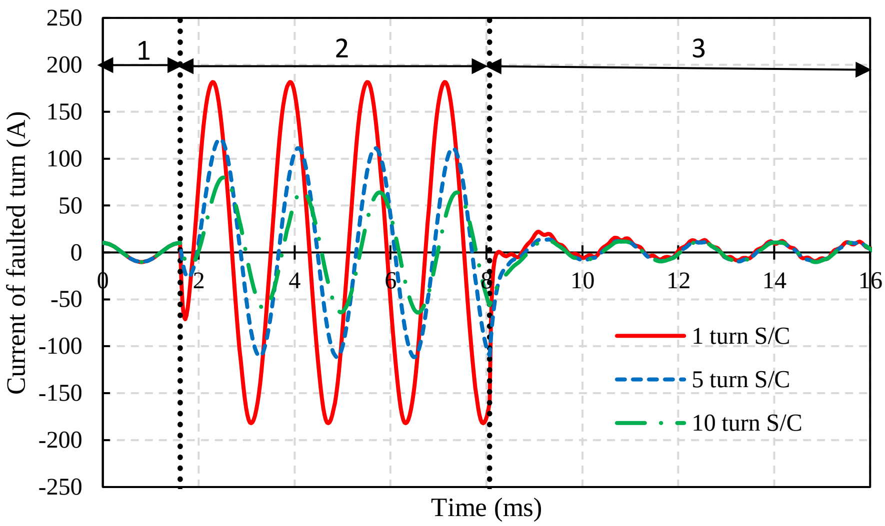

Figure 6.36. Current of faulted turns of Lane 2

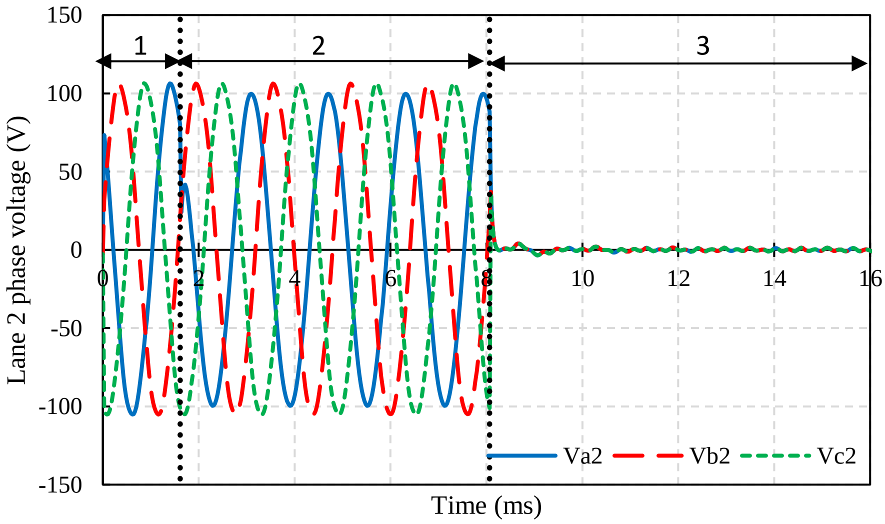

(a)

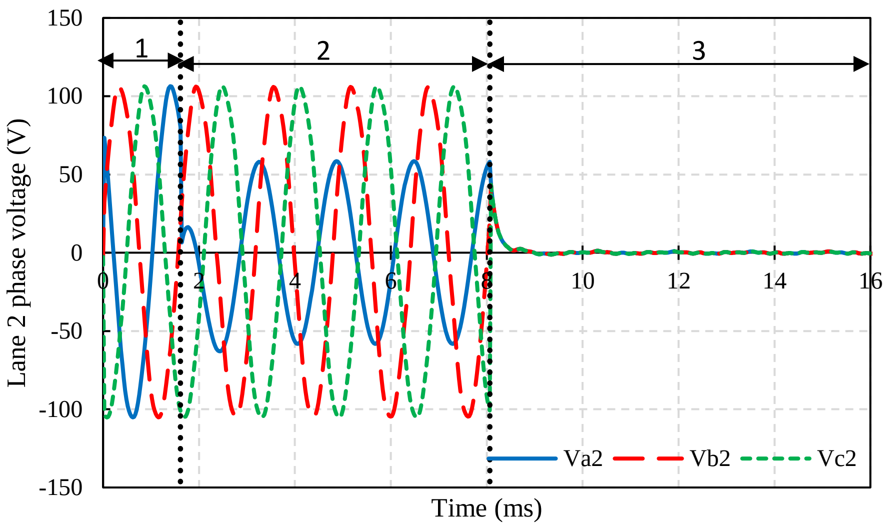

(b)

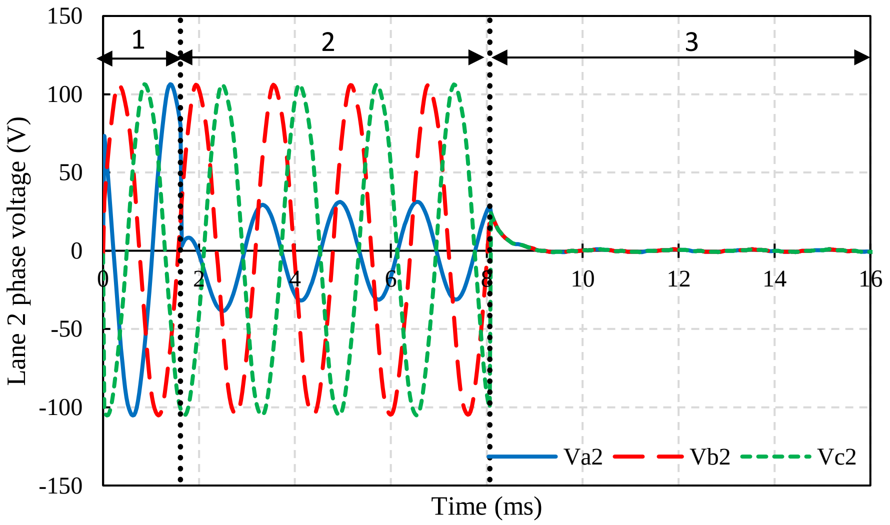

(c)

Figure 6.37. Lane 2 phase voltage (a) 1 turn s/c (b) 5 turn s/c (c) 10 turn s/c

6.5 Conclusions

The 12s8p 7.75:1 PDD design was modified to include castellations on the HSR hub and stator teeth in order to allow for the HSR and stator PM to be accurately positioned during manufacturing of the prototype. The pole piece cross-section was also modified to allow the pole piece to engage with the glass fibre support rods.

The fault-tolerant PDD was designed to have a 1.p.u phase inductance by modifying the slot opening, such that the slot leakage inductance component is increased. This was done in order to limit the 3-phase short circuit current to the value of the rated phase current. For each slot-opening geometry, the 3-phase short-circuit current was analytically evaluated and verified using 2D FEA. A slot opening geometry that provides a flat landing area for the stator PM, while achieving a limited short current, was selected.

For a 270V DC supply, the number of turns was predicted as a function of PM and copper temperature. A number of 54 turns was selected such that the fault-tolerant PDD can achieve rated power up to a PM and copper temperature of 200^{o}C.

The inter-turn fault current was predicted for 1, 5 and 10 turns under short circuit, from the total of 54 turns. It is shown that the highest fault current occurs for 1 turn under short circuit at rated speed. It was also established that, for the PDD, the fault current amplitude does not vary significantly with the location of the shorted turn. A viable inter-turn short circuit mitigation technique has been implemented in 2D FEA, showing that such a fault can be supressed by triggering a symmetrical 3-phase short circuit with the switches of the inverter.

Chapter 7: Permanent magnet demagnetisation in fault-tolerant PDD motor

In order to analyse the demagnetisation behaviour of the PM arrays in the proposed fault tolerant PDD design, the demagnetisation characteristics of the selected SmCo PM grade was investigated. Typically, in an electrical machine, the severity of PM demagnetisation is driven by the operating temperature of the PMs and the applied demagnetizing MMF which acts to reduce the operating point of the PMs below the knee point. Thus, in order to assess the demagnetisation of the PDD PM arrays the knee point has to be identified on the PM material demagnetisation curves. For the proposed design, Recoma 28 was selected as a permanent magnet material for the HSR and stator PM arrays. Due to the high specified operating ambient temperature of 75°C, this samarium-cobalt PM grade was preferred over the neodymium based grades, since it has a higher intrinsic coercivity and can withstand higher service temperatures.

The magnetic characteristics of several samarium-cobalt, SmCo, and neodymium-iron-boron, NdFeB, permanent magnet grades are shown in Table 7.1 and Table 7.2. It can be observed that the NdFeB PM grades have a higher energy product and magnetic remanence, B_r, than the SmCo grades. In comparison, the intrinsic coercivity, H_{ci}, of the SmCo grades is higher than that of the NdFeB PM grades. This represents an indication of the demagnetisation resistance of the PM grades. Generally, for any given rare-earth PM grade, the higher the intrinsic coercivity is, the lower the knee point is on the magnet demagnetisation BH curve. Thus, a higher demagnetisation magnetic field, H, can be applied without lowering the magnet working point below the knee point which marks the onset of irreversible demagnetisation.

The other important magnetic properties of PMs are represented by the reversible temperature coefficients for magnetic remanence and intrinsic coercivity. It can be observed that these coefficients are lower for the SmCo grades, which means that, as the temperature is increased, a smaller percentage of remanence and coercivity is lost in comparison to the NdFeB grades. Finally, the maximum operating temperature gives an indication of how suitable a given PM grade is for operation in the specific application. It can be observed that the SmCo PM grades have a much higher operating temperature than the NdFeB grades. The risk of demagnetisation should be evaluated by considering both the operating temperature, which would cause a reduction in the PM remanence and coercivity, as well as the applied magnetic field in the opposite direction to the direction of magnetisation of the PMs.

Table 7.1. Samarium-Cobalt magnet grade characteristics

PM grade	**BH energy product (MGOe)**	**B_r (T)**	**H_{ci} (kA/m)**	**B_r temp. coeff. (%/ºC)**	**H_{ci} temp. coeff. (%/ºC)**	**Max. operating temperature (ºC)**
Recoma 18	18.0	0.87	2400	-0.045	-0.19	250
Recoma 20	20.1	0.90	2400	-0.045	-0.19	250
Recoma 22	22.0	0.94	2400	-0.045	-0.25	250
Recoma 25	25.1	1.00	2400	-0.050	-0.24	250
Recoma 28	28.3	1.10	2000	-0.035	-0.24	350
Recoma 30	28.9	1.12	1600	-0.035	-0.25	250
Recoma 32	30.2	1.15	1350	-0.035	-0.25	250

Table 7.2. Neodymium-Iron-Boron magnet grade characteristics

PM grade	**BH energy product (MGOe)**	**B_r (T)**	**H_{ci} (kA/m)**	**B_r temp. coeff. (%/ºC)**	**H_{ci} temp. coeff. (%/ºC)**	**Max. operating temperature (ºC)**
N30	30	1.105	955	-0.12	-0.75	80
N35	35	1.210	955	-0.12	-0.75	80
N40	40	1.285	955	-0.12	-0.75	80
N45	44	1.350	955	-0.12	-0.75	80
N50	49	1.425	955	-0.12	-0.75	80
N30H	30	1.105	1353	-0.12	-0.605	120
N35H	35	1.210	1353	-0.12	-0.605	120
N40H	40	1.285	1353	-0.12	-0.605	120
N45H	44	1.350	1353	-0.12	-0.605	120
N50H	49	1.415	1274	-0.12	-0.605	120
N30UH	31	1.125	1990	-0.12	-0.465	180
N35UH	35	1.210	1990	-0.12	-0.465	180
N40UH	40	1.285	1990	-0.12	-0.465	180
N45UH	45	1.350	1910	-0.12	-0.465	180

For the selected Recoma 28 PM grade, Figure 7.1 shows the intrinsic JH magnetic polarisation and demagnetisation BH curves as a function of PM temperature. The intrinsic polarisation, J, represents only the magnetic field of the PM, while the magnetic induction, B, represents the magnetic field of the PM when the exterior magnetic field H is applied. The relation between J and B is given by:

$$B = \mu_0 H + J \tag{7.1}$$

where μ_0 is a constant representing the permeability of vacuum.

The slope of the magnetic induction curve represents the relative permeability of the PM grade, μ_r, and is given by:

$$\mu_r = \frac{B_r}{\mu_o H_c} \tag{7.2}$$

In order to understand the phenomenon of irreversible demagnetisation, Figure 7.1 (a) can be considered as an example. If an external magnetic field H, of an amplitude of 1200 kA/m, is applied in a direction which opposes the PM magnetisation direction, the PM will operate at working point WP1. When the external magnetic field is removed, the magnet working point will rise along the B curve to the initial remanence value, B_r. This represents the reversible demagnetisation effect since the PM is able to regain the initial remanence value after the external magnetic field is removed. The slope of the recoil curve is identical to the slope of the initial BH curve.

Assuming a higher opposing magnetic field is applied to the PM, the new working point, WP2 would be situated lower along the BH curve. In this case, for an $H = 1950\ kA/m$, WP2 is below the PM working point limit. It can be observed that the new recoil line, having the same slope as the original BH curve, would result in the PM obtaining a lower magnetic remanence when the exterior opposing magnetic field is removed. This represents the phenomenon of irreversible demagnetisation since the PM does not return to the initial remanence once the demagnetising field is removed.

For this safety critical application, the knee point, or working point limit was selected based on the remanence at which the PM would return to. Thus, it was deemed acceptable to have the PM return to a minimum value of remanence which is 5% lower than the initial B_r, for any PM temperature. Hence, if during healthy and faulty operation of the PDD, the value of H, and implicitly B, on the surface of each PM, and in the direction of the PM magnetisation, is above the working point limit, irreversible demagnetisation would be avoided. Recoil to a value of remanence which is lower by more than 5% of the initial Br would be classed as irreversible demagnetisation.

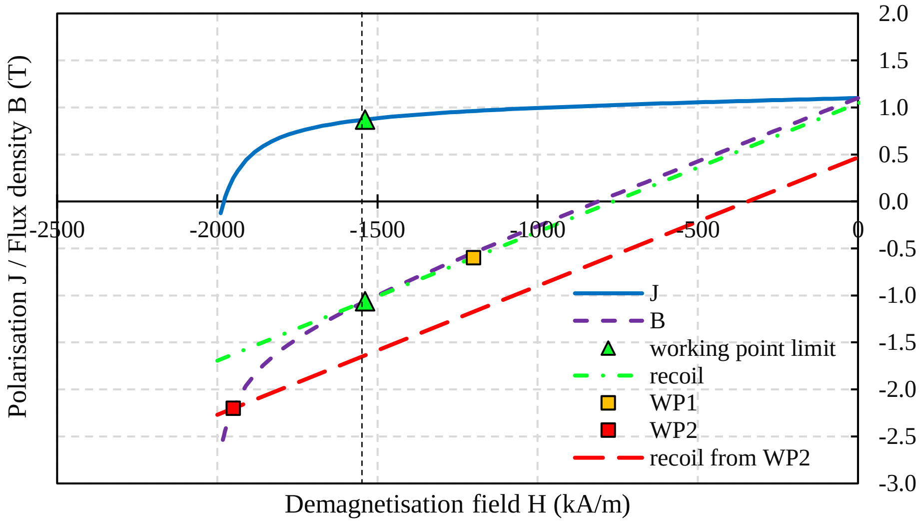
Polarisation J / Flux density B (T)
2.0
1.5
1.0
0.5
0.0
-0.5
-1.0
-1.5
-2.0
-2.5
-3.0
-2500
-2000
-1500
-1000
-500
0
J
B
working point limit
recoil
WP1
WP2
recoil from WP2
Demagnetisation field H (kA/m)

(a)

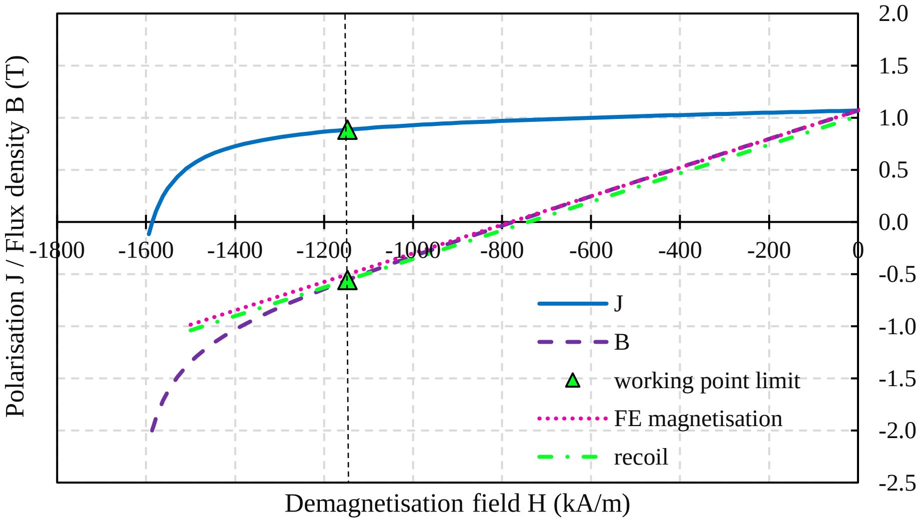
Polarisation J / Flux density B (T)
2.0
1.5
1.0
0.5
0.0
-0.5
-1.0
-1.5
-2.0
-2.5
-1800
-1600
-1400
-1200
-1000
-800
-600
-400
-200
0
J
B
working point limit
FE magnetisation
recoil
Demagnetisation field H (kA/m)

(b)

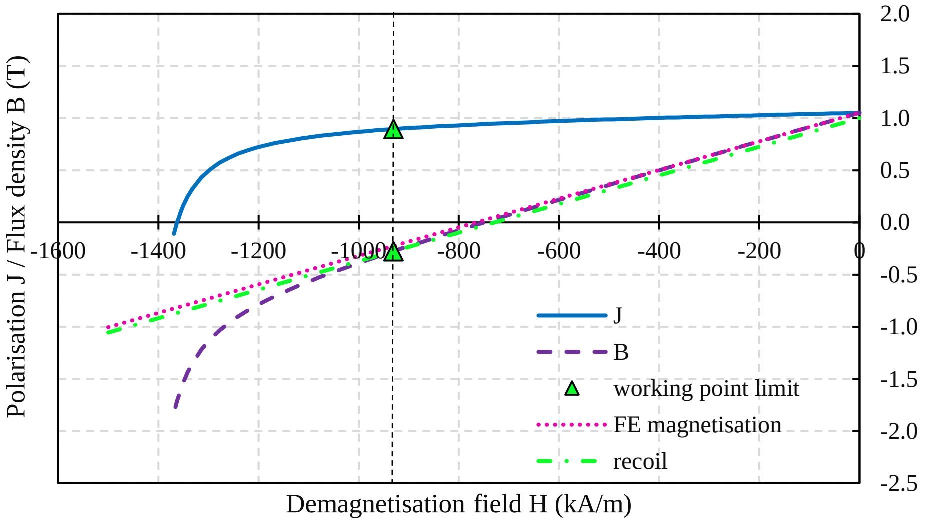

(c)

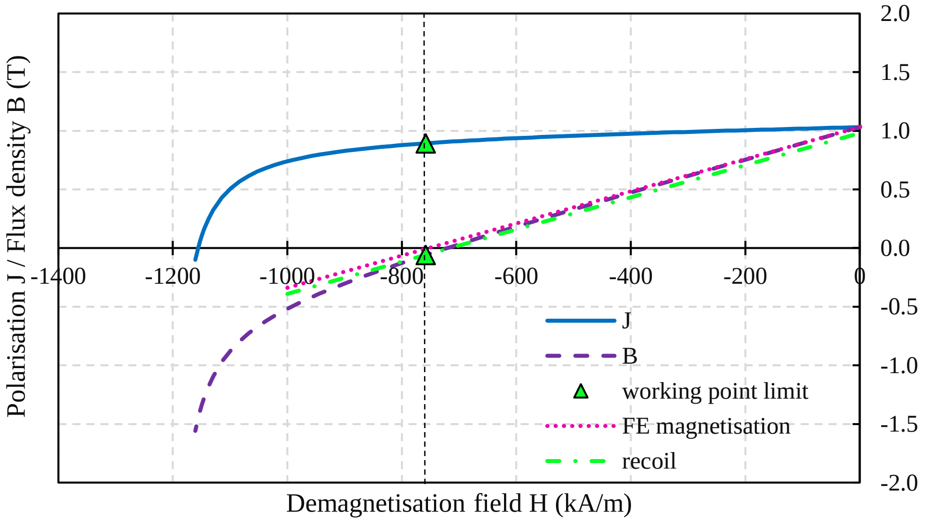

(d)

Figure 7.1. Recoma 28 B-H curves for (a) 20°C (b) 100°C (c) 150°C (d) 200°C

Several operation modes have been considered in order to investigate the demagnetisation behaviour of the PM arrays of the proposed fault tolerant PDD design. Table 7.3 shows the PDD operation modes investigated during the demagnetisation investigation.

Table 7.3. PDD operation modes used for demagnetisation investigation

Operation mode	**Lane 1**	**Lane 2**
Passive - Passive (OCOC)	Open circuit	Open circuit
Active – Passive (APOC)	Active	Open circuit
Passive – Short – circuit (OCSC)	Open circuit	Short circuit
Active – Short – circuit (ASC)	Active	Short circuit

In order to correctly assess the demagnetisation of the PM arrays within the PDD, the magnetic field strength, H, has to be assessed for each of the PM blocks along the direction of magnetisation. The Opera 2D FE electromagnetic simulation software was used to obtain the magnetic field strength vectors in the x and y directions, H_x, H_y, for each element of the mesh of each PM block. These vectors were then converted to obtain the magnetic field strength along the direction of magnetisation for each PM, H_{PM}, such that:

$$H_{PM} = H_x \cos(\alpha_{PM}) + H_y \sin(\alpha_{PM}) \tag{7.3}$$

where α_{PM} is an angle representing the direction of magnetisation of each PM block.

The same process can be applied for the magnetic flux density on the surface of each PM. However, it has to be considered that the demagnetisation phenomenon is due to the magnetic field strength, H, which results in a certain magnetic flux density, B. Thus, it can be said that the magnetic flux density within the magnet region is dependent on the applied magnetic field, and together, B and H represent the working point of the PM region. Thus, in this investigation, the magnetic field strength along the magnetisation direction was used to judge the demagnetisation of the PDD PM arrays.

In order to fully capture the extent of the PM demagnetisation within the proposed PDD design, the 2D FE electromagnetic software was used to transiently simulate all the operation modes from Table 7.3. For each time step of each simulation, the transient solution was interrogated in order to obtain the x and y components of the magnetic field strength, H_x and H_y, within each element of the mesh of each PM block on the HSR and stator. The value of the physical area of each element was also recorded.

A Matlab routine was developed in order to convert the magnetic field strength vectors, H_x and H_y, according to (7.3) and obtain the magnetic field strength along the PM magnetisation direction, for each mesh element of all the PMs. From all the considered time steps, the minimum value of H_{PM} was obtained for each element of the mesh of each PM block. If this minimum value of H_{PM}, of a given element, is lower than the working point limit, that certain element is deemed to have suffered irreversible demagnetisation. In this case the value of the area of that element is recorded. By post processing the working point data for all the PMs of the PDD, the percentage of the PM area that has suffered irreversible demagnetisation can be calculated for all the operation modes shown in Table 7.3. The demagnetisation analysis was conducted for operating PM temperatures of 20°C, 100 °C, 150 °C and 200 °C. The working point limits for the Recoma 28 SmCo PM grade are shown in Table 7.4.

Table 7.4. BH working point limit for Recoma 28 SmCo PM

PM temperature (°C)	**H limit (kA/m)**	**B limit (mT)**
20	-1538.52	-1062.13
100	-1147.60	-556.70
150	-930.80	-276.24
200	-758.42	-60.06

7.1 PDD PM demagnetisation

Due to the high temperature resistance and low working point limits of the Recoma 28 PM grade, irreversible demagnetisation of the PM arrays in the fault tolerant PDD is avoided at PM operating temperatures of 20°C and 100°C for all the operation modes presented in Table 7.3. Thus, in order to show the PM areas affected by irreversible demagnetisation, contour plots of the magnetic field strength, H, in the direction of magnetisation of each PM, are presented only for 150°C and 200°C PM operating temperatures.

During Passive-Passive (OCOC) operation, the duplex 3-phase winding is not energised. Thus, irreversible demagnetisation of the PDD PM arrays is only given by the increase in PM temperature and the magnetic field created by any one of the PM arrays which opposes the other PM array. Due to the large thickness difference between the HSR and stator PMs, the magnetic field produced by the thick HSR PMs can cause irreversible demagnetisation in the thinner stator PMs, at high operating temperatures. Figure 7.2 shows contour plots of the H-field, on the surface of the PMs, and in the direction of magnetisation of each PM, for Passive-Passive operation at 150°C and 200°C. The white regions on the surface of the PMs represent areas where the PM working point has dropped below the magnet working point limit. Thus, such PM regions have incurred irreversible demagnetisation. It can be observed that the working point of all the HSR PMs at 150°C and 200 °C is above the limit due to the relatively small opposing magnetic field created by stator PMs. Thus, for this operation mode, the HSR PMs do not suffer from irreversible demagnetisation. In comparison, at 150 °C, the stator PMs have regions were the operating point is close to the working point limits. These regions are situated in the corners of the circumferentially magnetised stator PMs, adjacent to the outer airgap. Such dark blue areas suggest that the working point is only slightly over the working point limit at 150 °C. As the temperature is increased to 200 °C, the small corner regions of the circumferentially magnetised stator PMs are irreversibly demagnetised. For these operating conditions, the working points of the radially magnetised stator PMs are higher than the working point limit. A small number of such magnets, which fall at the edges of the stator teeth, next to the slot opening, have lower working points. This is the case of PM7 in Figure 7.2 (b) which shows regions that have a working point only slightly above the irreversible demagnetisation limit.

The contour plots of the H-field on the surface of the PMs for Active-Passive operation (APOC), where Lane 1 (A1, B1, C1) are energised with rated phase current and Lane 2 is passive, are shown in Figure 7.3. In this operation mode, the HSR PMs can suffer irreversible demagnetisation due to the combined effect of the opposing PM field of the stator PMs and the stator MMF armature reaction. However, due to the increased PM thickness of the HSR PMs, irreversible demagnetisation during Active – Passive operation mode is avoided at 150 °C and 200 °C PM temperature.

The stator PM array is more susceptible to irreversible demagnetisation during Active – Passive (APOC) operation. This is due to the opposing magnetic field of the HSR PMs combined with the slot opening leakage flux given by the stator teeth which support the energised Lane 1 coils. Thus, the stator PMs, that are near the slot opening on the edges of the stator teeth with Lane 1 coils, are more susceptible to irreversible demagnetisation. This is shown in Figure 7.3 (b), where the radially magnetised PM7 and circumferentially magnetised PM106 have large areas with working points below the irreversible demagnetisation limit.

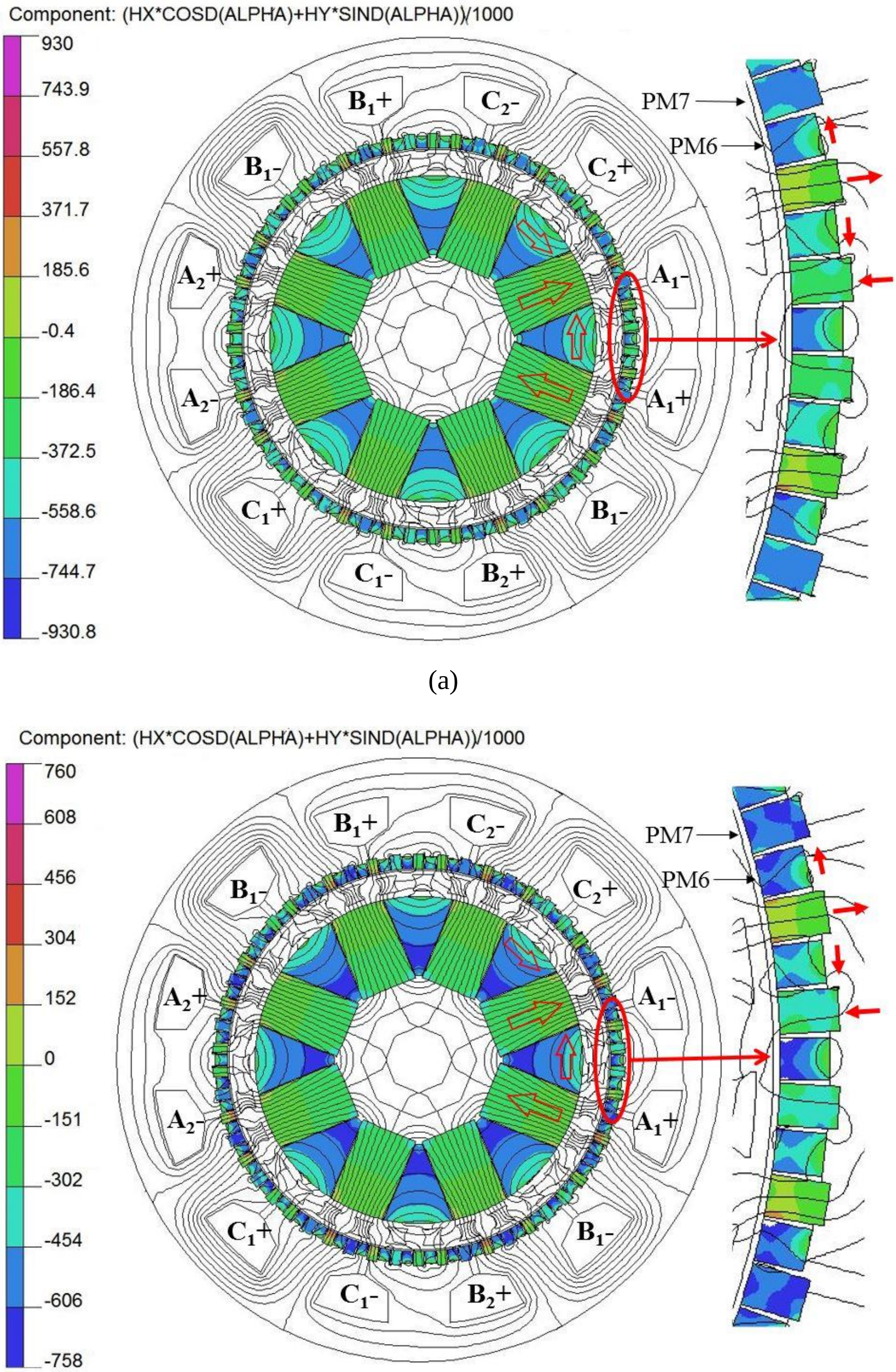

(a)

(b)

Figure 7.2. Passive - Passive H-field contour plot for (a) 150°C (b) 200°C PM temperature

For these specific PMs, which are near to the slot opening, the largest area affected by irreversible demagnetisation occurs when the sinusoidal current of phase A1 reaches peak positive amplitude and the slot opening flux leakage, flowing against the PM magnetisation direction, is maximised. This is the time step shown in Figure 7.3, with positive phase A1 current amplitude. It has to be considered that the magnetisation pattern of the PMs on the tooth that supports coil A1 is repeated every 4 teeth. Thus, this magnetisation pattern is also present on the teeth which hold coils B1 and C1. Hence, when the phase currents of coils B1 and C1 reach peak positive amplitude, the same demagnetisation pattern is seen on the stator PMs adjacent to phases B1 and C1. In contrast, when the phase currents of A1, B1 and C1 have peak negative amplitude, the slot leakage flux has a reversed direction and does not act against the magnetisation direction. Thus, in this case the working point of the stator PMs near the slot opening is not reduced below the limit.

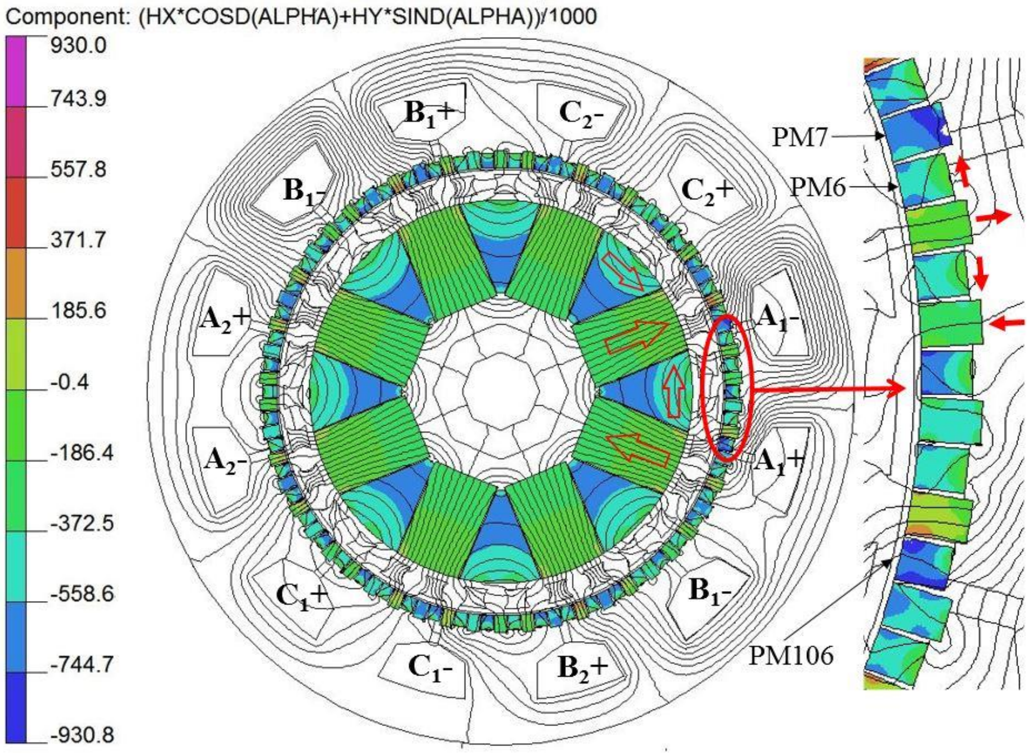

(a)

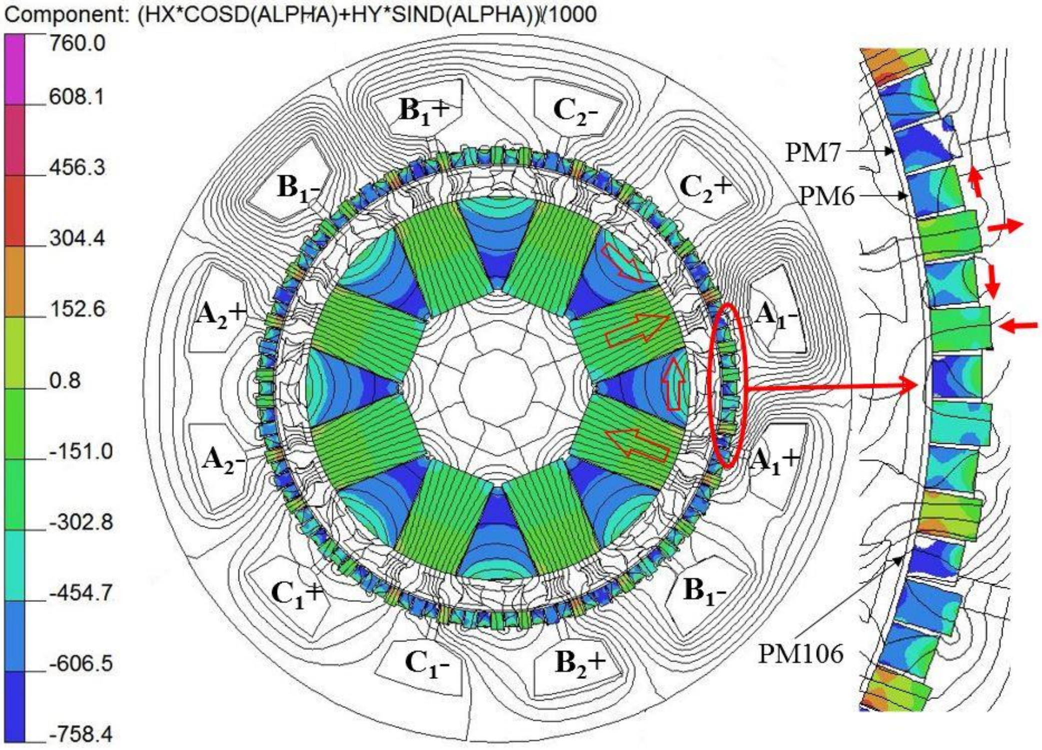

(b)

Figure 7.3. Active - Passive H-field contour plot for (a) 150 °C (b) 200 °C PM temperature

For the Passive – Short circuit (OCSC) operation, Lane 1 is in passive open circuit mode and Lane 2 is under symmetrical 3-phase short circuit. In this operation mode, the high negative d-axis short circuit transient, combined with the effect of the opposing field of the stator PMs, would reduce the working point of the HSR PMs. Figure 7.4 shows the DQ-axis short circuit current with the large negative d-axis transient current. Figure 7.6 shows the H-field contour plot with the HSR PMs being in the position of peak negative d-axis short circuit current. It can be observed that the HSR PMs do not show areas of irreversible demagnetisation at 150°C and 200°C.

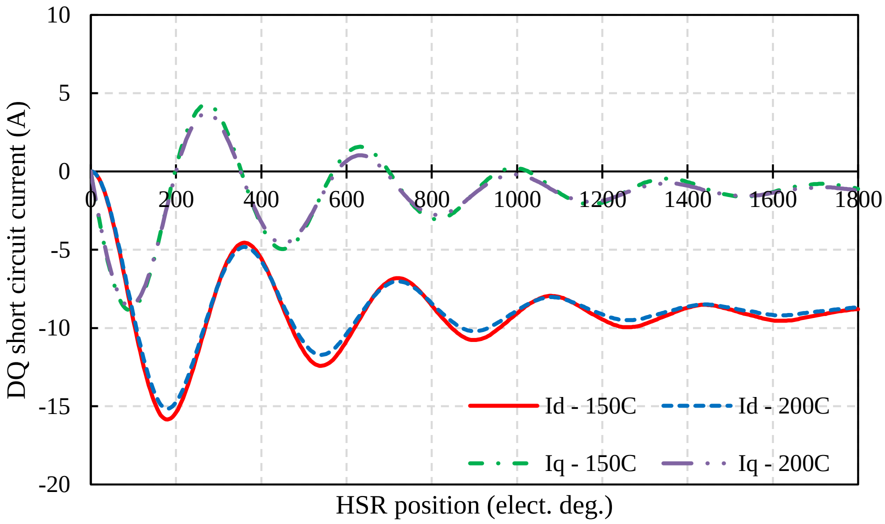

Figure 7.4. DQ axis short circuit current of Lane 2

In contrast, the irreversible demagnetisation of the stator PMs is caused by the opposing field of HSR PM array in combination with the slot opening leakage flux caused by the short circuit current. Since, the stator PMs are not in the same DQ reference frame as the HSR PMs, only the PMs which are supported by the stator teeth that hold the Lane 2 coils are affected by the short circuit condition. Thus, the PMs that are at the edges of the Lane 2 teeth, near the slot opening will be affected by the slot opening flux leakage. This effect is maximised for every phase of Lane 2 when the short circuit current in each phase reaches a peak positive value, as shown in Figure 7.5. The stator PM representations in Figure 7.6 show the H-field contour on the surface of the PMs adjacent to the phase C2 tooth when the short circuit current in phase C2 is at its peak transient value. It can be observed that during the peak transient short circuit current on phase C2, the stator PMs near the slot opening show a considerable degree of irreversible demagnetisation at 200°C.

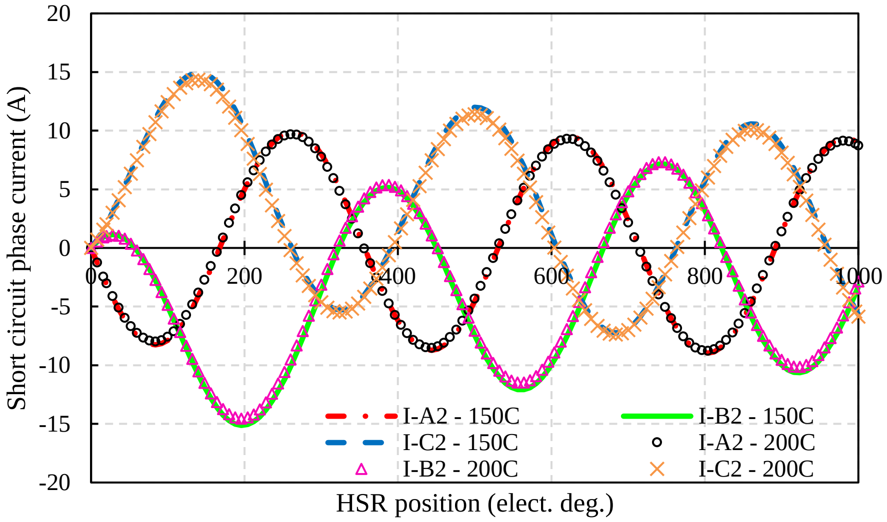

Figure 7.5. 3-phase short circuit current of Lane 2

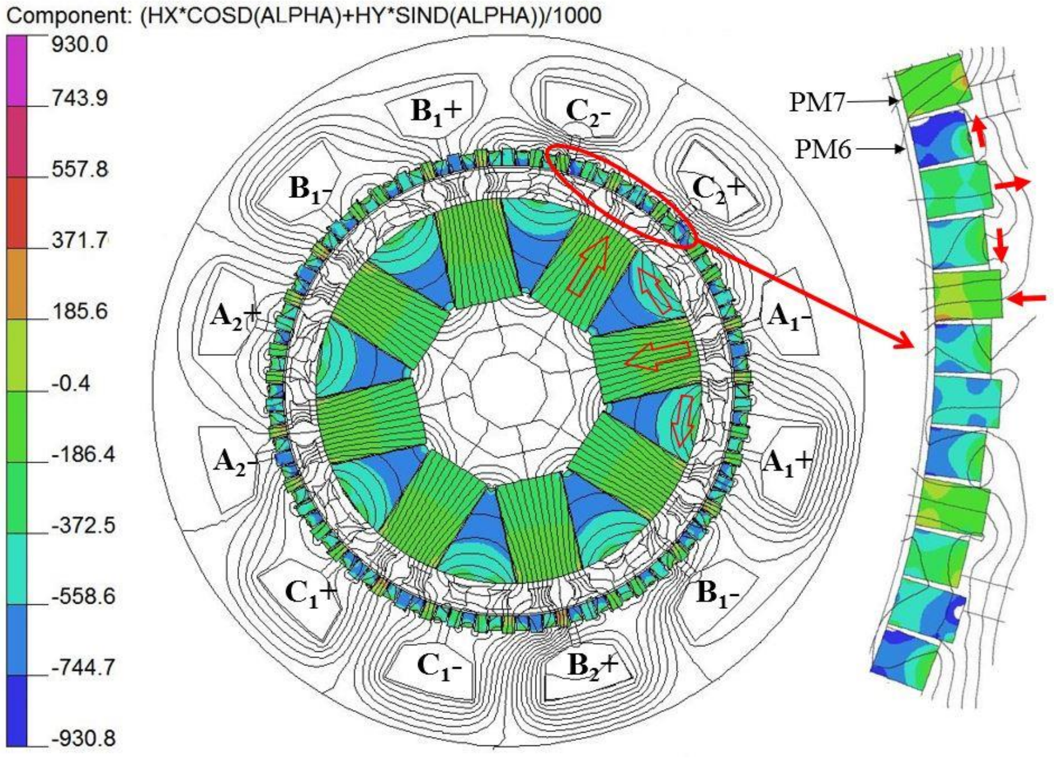

(a)

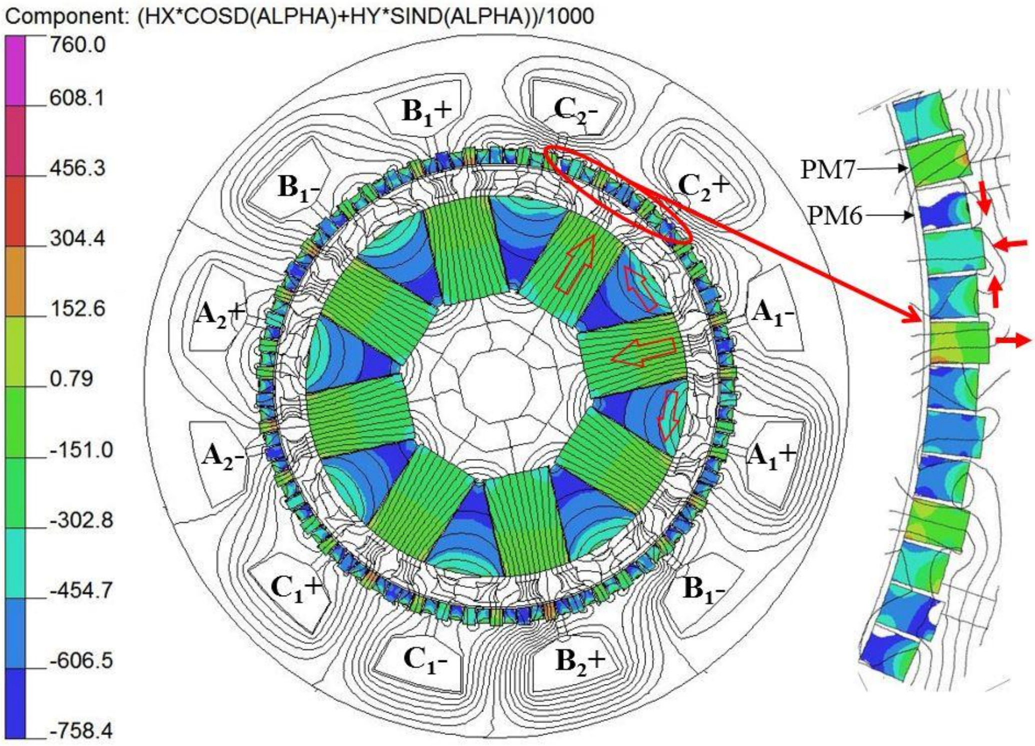

(b)

Figure 7.6. Passive – Short circuit H-field contour plot for (a) 150 ^{o}C (b) 200 ^{o}C PM temperature

During the Active – Short circuit (ASC) operation mode, Lane 1 is healthy and energised with rated q-axis current, while Lane 2 is under symmetrical 3-phase short circuit. Figure 7.7 shows the H-field contour plot for the Active – Short circuit operation. The HSR PMs have been captured at the position of peak negative d-axis short circuit transient current and do not show any regions of irreversible demagnetisation at 150^{o}C and 200^{o}C.

In comparison, the representation of the stator PMs, adjacent to the phase C2 coil, has been captured when the short circuit current in phase C2 is at its peak transient value. It can be observed that for these PMs, the degree of irreversible demagnetisation achieved is the same as for Passive – Short circuit operation. The representation of the stator PMs adjacent to the phase A1 coil has been captured at peak positive value of the healthy phase current. This captures the worst demagnetisation for these PMs, which is similar to the Active – Passive (APOC) case.

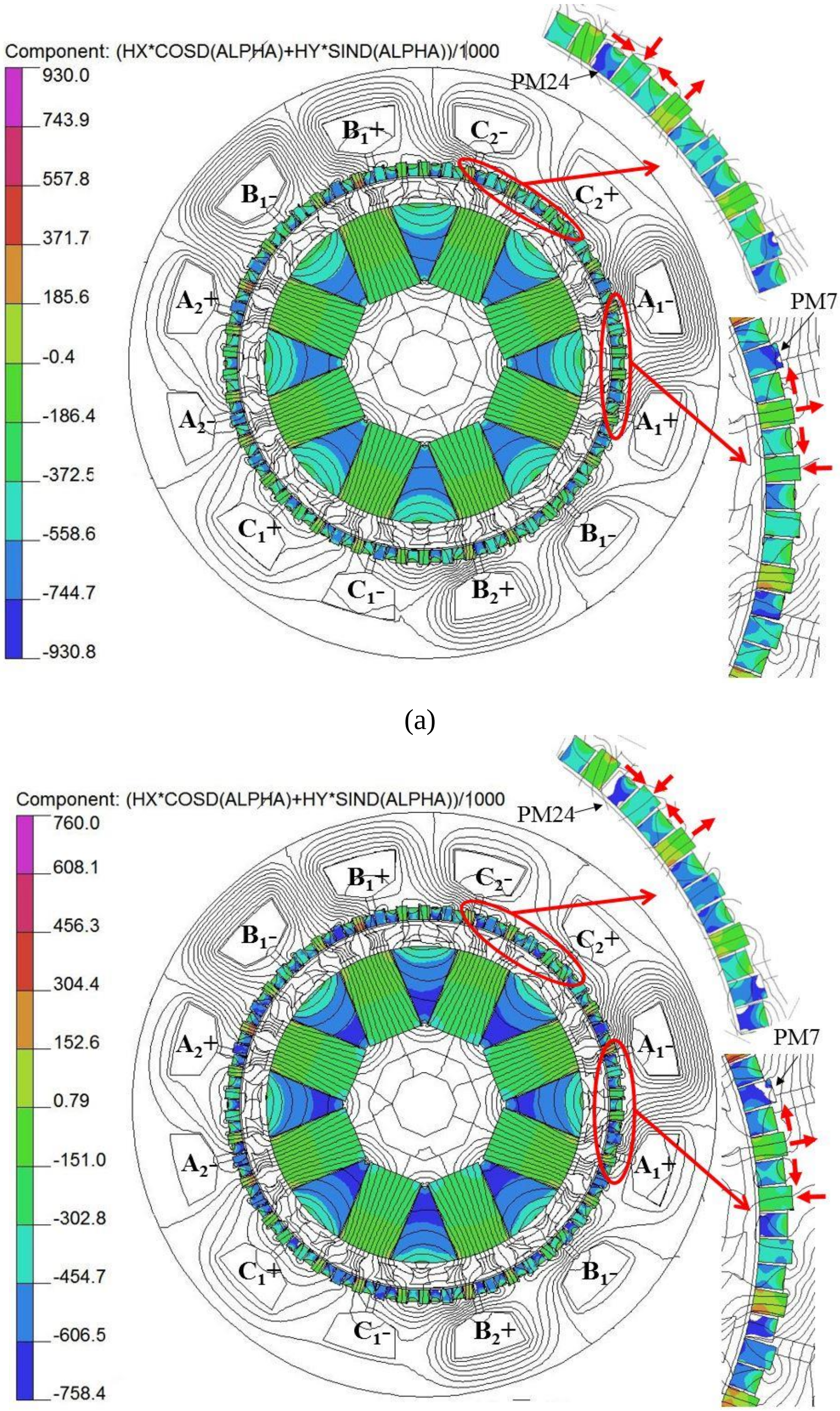

(a)

(b)

Figure 7.7. Active – Short circuit H-field contour plot for (a) 150 °C (b) 200 °C PM temperature

7.2 HSR PMs minimum working point

The variation of the maximum demagnetising H-field on the surface of the radially and circumferentially magnetised HSR PMs, for the different operation modes, is shown in Figure 7.8. It can be observed that, at a fixed PM temperature, for both types of HSR PMs, the lower magnet working point occurs in Active – Short circuit operation. Moreover, the circumferentially magnetised HSR PMs have a considerably lower working point than the radially magnetised PMs, for all the operating conditions. It can be observed from Figure 7.7 that the minimum working point for the circumferentially magnetised HSR PMs is in the bottom regions of each magnet where the thickness is at a minimum. By comparing the minimum PM working points from Figure 7.8 with the Recoma 28 working point limits from Table 7.4, it can be observed that the HSR PMs are not affected by irreversible demagnetisation.

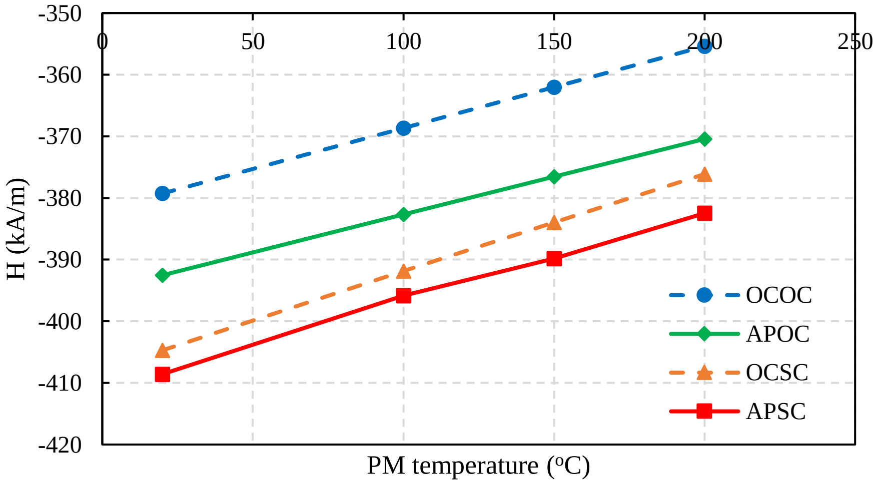

(a)

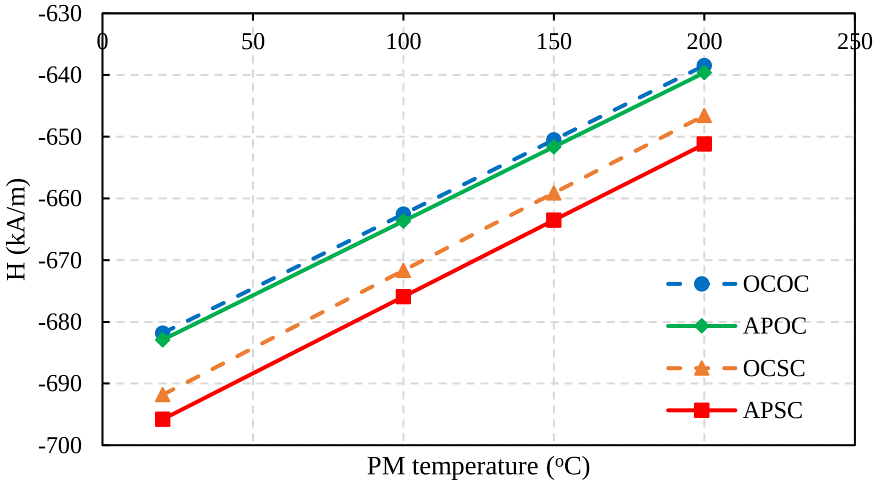

(b)

Figure 7.8. Variation of maximum demagnetising H-field with PM temperature on the surface of the HSR (a) radially magnetised PMs (b) circumf. magnetised PMs

7.3 Stator PMs minimum working point

For the radially and circumferentially magnetised stator PMs, which are near the slot opening and have the largest percentage of their area under irreversible demagnetisation, Figure 7.9 shows the maximum demagnetisation H-field on the surface of the stator PMs. It can be observed that the minimum working point of the circumferentially magnetised PMs is not changed for Passive-Passive and Active-Passive operation, Figure 7.9 (a), and for Passive-Short circuit and Active-Short circuit operation, Figure 7.9 (b). The minimum PM working point for the stator PMs, and for any of the considered PM temperatures, is reached during Active-Short circuit operation. By comparing with the working point limit, it can be observed that, for Active-Passive operation, irreversible demagnetisation occurs in regions of the stator radial PMs for a temperature slightly over 100°C. If fault operation is considered, with one lane under symmetrical 3-phase short circuit, Figure 7.9 shows that both types of stator PMs, with the area near the slot opening, undergo irreversible demagnetisation.

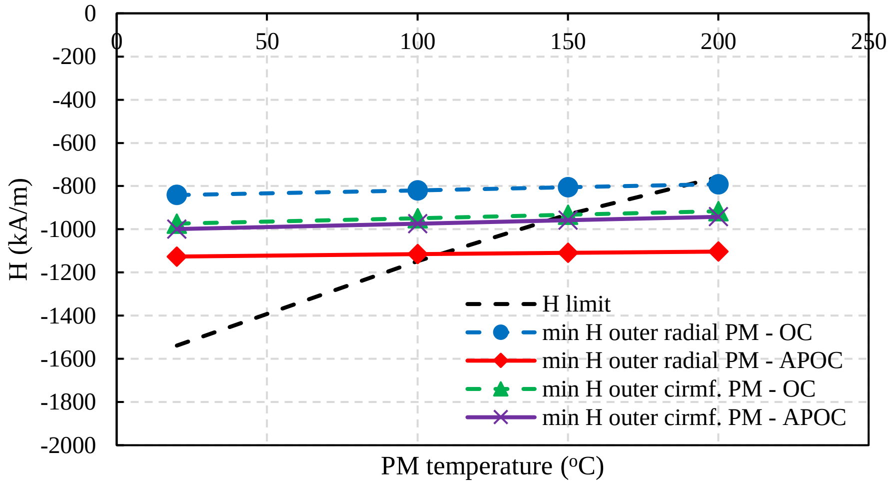

(a)

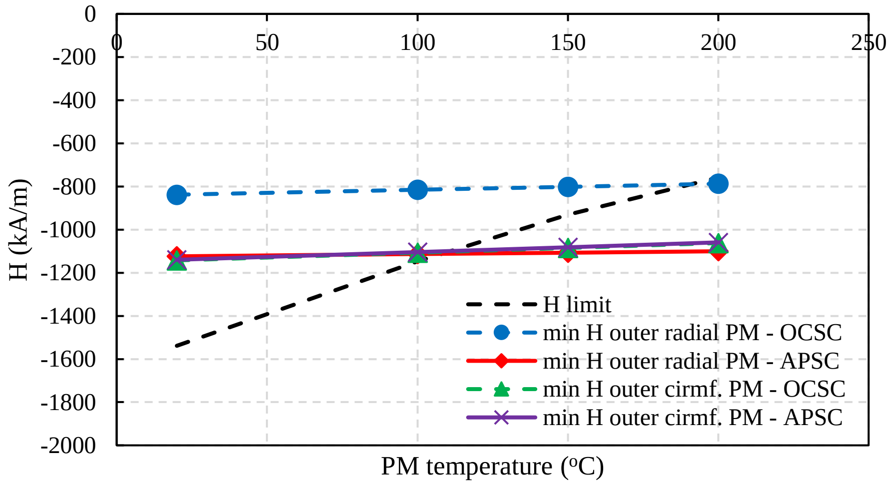

(b)

Figure 7.9. Variation of maximum demagnetising H-field with PM temperature on the surface of the stator (a) OC / APOC (b) OCSC / APSC

Due to the large total number of stator PMs, it is important to predict the percentage of stator PM area that has undergone irreversible demagnetisation during all the operation modes. Thus, by comparing the minimum PM working point per mesh element of the stator PMs, with the working point limit, at each time step and for all the operation modes from Table 7.4, a Matlab routine was implemented to calculate the total PM area that has been irreversibly demagnetised. Figure 7.10 shows the percentage stator PM area that has undergone irreversible demagnetisation for all the operation modes shown in Table 7.4.

For Passive-Passive operation, only an operating PM temperature of 200^{o}C causes 2.22% of the total area of the circumferentially magnetised stator PMs to be demagnetised. In comparison, for the same PM temperature, during Active-Passive operation, 3.43% of the total area of the circumferentially magnetised PMs and 1.32% for the radially magnetised PMs undergoes irreversible demagnetisation. A large majority of this total demagnetised PM area is contained within the stator PMs that are near the slot opening.

For the Passive-Short circuit (OCSC) operation, the percentage total area demagnetised is increased to 4.2% for the circumferentially magnetised PMs. The Active-Short circuit case represents the worst operation mode for total demagnetised area of the stator PM. At 200^{o}C, 5.34% of the total area of the circumferentially magnetised PMs and 2.44% for the radial PMs has undergone irreversible demagnetisation. This is due to the high slot opening flux leakage which is present for every tooth, affecting the PMs in the vicinity.

Thus, for an extreme operational PM temperature of 200^{o}C, irreversible demagnetisation of the stator PM is isolated, with a total affected area percentage under 10%. It can also be observed, that at lower PM temperatures the stator PM irreversible demagnetisation is negligible.

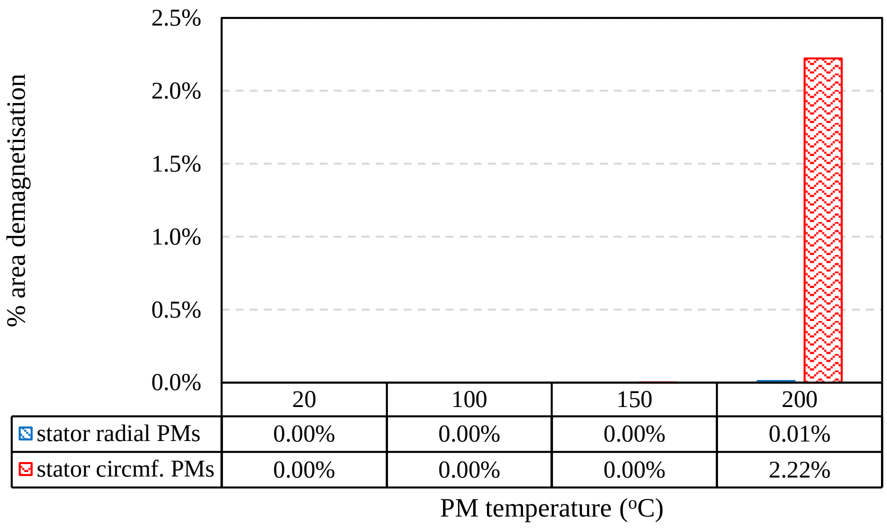

	20	100	150	200
▧ stator radial PMs	0.00%	0.00%	0.00%	0.01%
▨ stator circmf. PMs	0.00%	0.00%	0.00%	2.22%

(a)

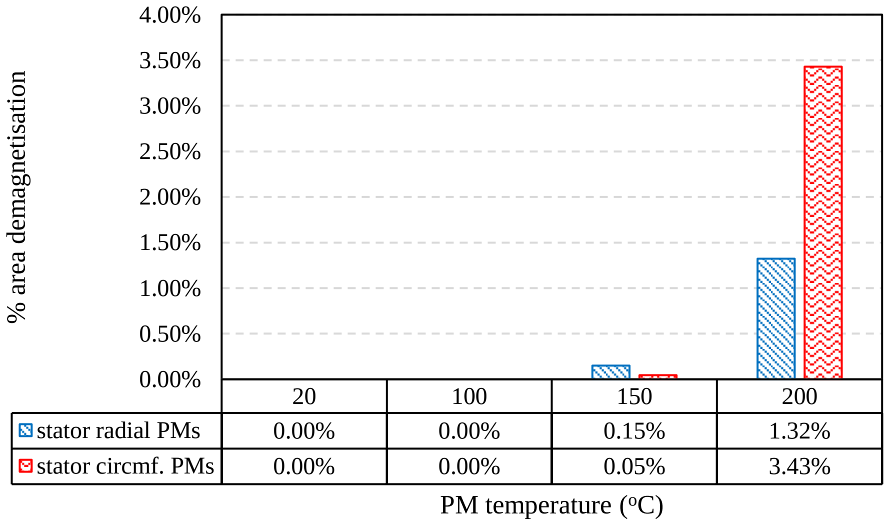

	20	100	150	200
▧ stator radial PMs	0.00%	0.00%	0.15%	1.32%
▨ stator circmf. PMs	0.00%	0.00%	0.05%	3.43%

(b)

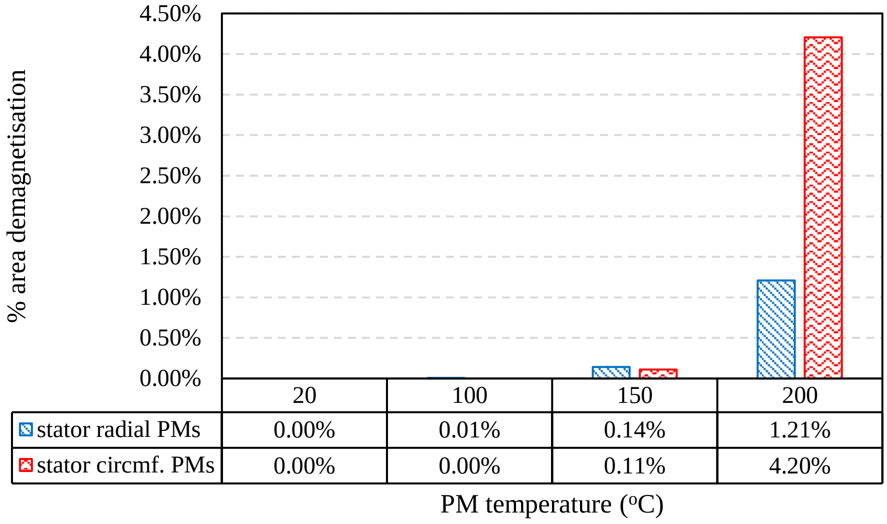

(c)

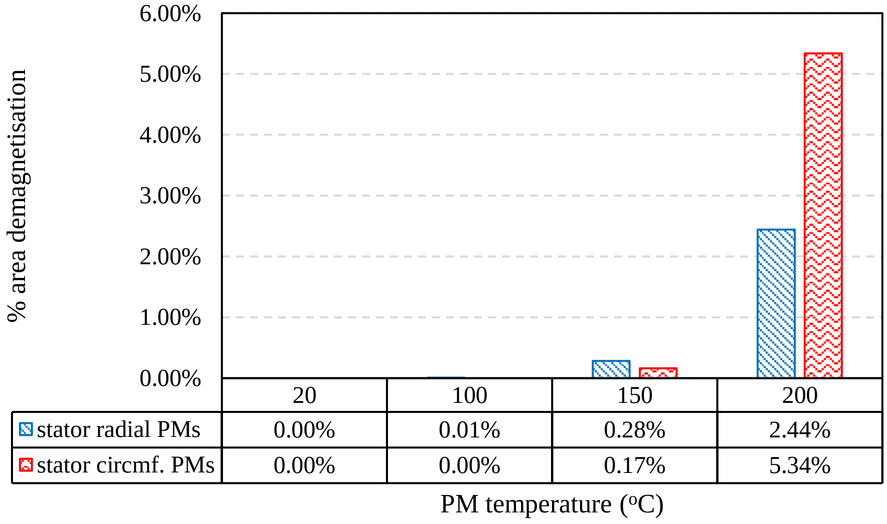

(d)

Figure 7.10. Variation of percentage stator PM area under irreversible demagnetisation with PM temperature for (a) Passive-Passive (b) Active-Passive (c) Passive-Short circuit (d)Active-Short circuit

7.4 Conclusions

The demagnetisation of the FT PDD PM arrays was investigated under healthy and faulty 3-phase short circuit operation. It is shown that, for a PDD design, the demagnetisation of the PM arrays is influenced by the operating temperature, opposing PM fields from the HSR and stator PM arrays, and amplitude of the stator armature reaction. Furthermore, the demagnetisation risk is increased during the transient d-axis current generated under symmetrical 3-phase short circuit.

The HSR PMs do not show any sign of irreversible demagnetisation at high operating temperatures or under symmetrical 3-phase short circuit operation. This is mainly related to the large thickness of the HSR PMs, combined with the increased overall airgap between the HSR and stator teeth.

In comparison, the stator PMs which are in the vicinity of the slot opening show small regions affected by irreversible demagnetisation only when the operating temperature is increased above 150^{o}C. At 200^{o}C, and under Active-Short circuit operation, the circumferentially and radially magnetised stator PMs have 5.34% and 2.44% of their total volume affected by irreversible demagnetisation, respectively. It has to be considered that the PM area affected by irreversible demangnetisation can be reduced by replacing the Halbach HSR PM array with a radial PM array. Thus, the PM field produced by the HSR PM array which opposes stator PM array magnetisation is reduced. This design option was explored in Chapter 4, where it was shown that a radial HSR PM array reduces the torque transmission capability of the magnetic gear element, resulting in increased weight.

Chapter 8: Electromagnetic losses of fault-tolerant PDD motor

The losses of the fault tolerant PDD prototype motor can be divided into copper and iron losses. The copper losses are torque dependent and influenced by the phase input current and phase resistance. The iron losses are dependent on the output speed and the flux density distribution. For the manufactured PDD prototype, the stator iron core is manufactured from M270-35A laminations with a thickness of 0.35mm. Due to the small size and light construction, the pole pieces are not laminated and made from the same material. The PM blocks on the stator, rotor, and the titanium retention sleeve of the outer PM array are divided in 2 segments along the z-axis. In such components the eddy current loss is dominant.

The losses were estimated using 2D FE time-varying simulations with the PM temperature of both arrays at 80°C and a copper temperature of 100°C. In such models the solid components are modelled as infinitely long eddy current conductors with the corresponding material conductivity. The eddy current flow in the z-axis is due to the time varying flux in the x-y simulation plane. In 2D simulations such loss components do not considered flux leakage end effects and the loss is scaled linearly with active length.

The eddy current loss of the non-laminated components was also estimated using 3D FE time-varying simulations where end effects are considered. The reduced level of segmentation of the PMs and titanium sleeve was also modelled. In order to limit the number of 3D simulations, the eddy current losses were predicted with 20°C PM temperature. Due to the thick HSR PMs, the iron losses in the solid HSR hub are negligible since the field in the hub is given by the HSR PMs and does not vary with time.

8.1 Copper losses

In order to estimate the copper losses, the fault tolerant PDD was simulated in 2D FE in several operational modes. For Active-Passive open circuit (APOC), only one of the duplex-3 phase lanes is energised to produce rated torque. In Active-Active (AA) operation, both 3-phase lanes are energised with half rated phase current, in order to produce rated output torque on the PPR. The phase current was calculated based on the output torque demand and average d-axis PM flux linkage for the constant torque operation region ($I_d = 0A$), such that:

$$\frac{T_L}{G_r} = \frac{3}{2} p_h \psi_{PM}(I_q) I_q \tag{8.1}$$

where T_L is the load torque of the PPR, p_h is the number of HSR pole pairs, and $\psi_{PM}(I_q)$ represents the variation of the d-axis PM flux linkage with q-axis current, I_q.

It has been shown in Chapter 6, Figure 6.23 that, for a fixed PM temperature, the PM flux linkage is not reduced by the armature reaction. Thus, in order to predict the phase current for a fixed load torque, the open circuit value of the d-axis flux linkage can be used in (8.1). Since the eddy current loss of the non-laminated components can be significant and is proportional to the square of the electrical HSR frequency, the effect of the resultant drag torque on the rated phase current is considered, such that the phase current is given by:

$$I_q = \frac{2}{3}\frac{\frac{T_L}{G_r} + \frac{P_{eddy}(\Omega_{HSR})}{\Omega_{HSR}\,\pi/30}}{p_h \psi_{PM}} \tag{8.2}$$

where P_{eddy} is the eddy current loss of the non-laminated components such as PM, pole pieces and stator PM retention sleeve.

In order to simulate the PDD with the correct load angle of the magnetic gear (MG) element, the variation of the average output PPR and HSR torque with the load angle of the MG is shown in Figure 8.1. It can be observed that, for an average peak torque of 8.6 Nm, the MG element operates in the linear region of the torque transmission capability curve.

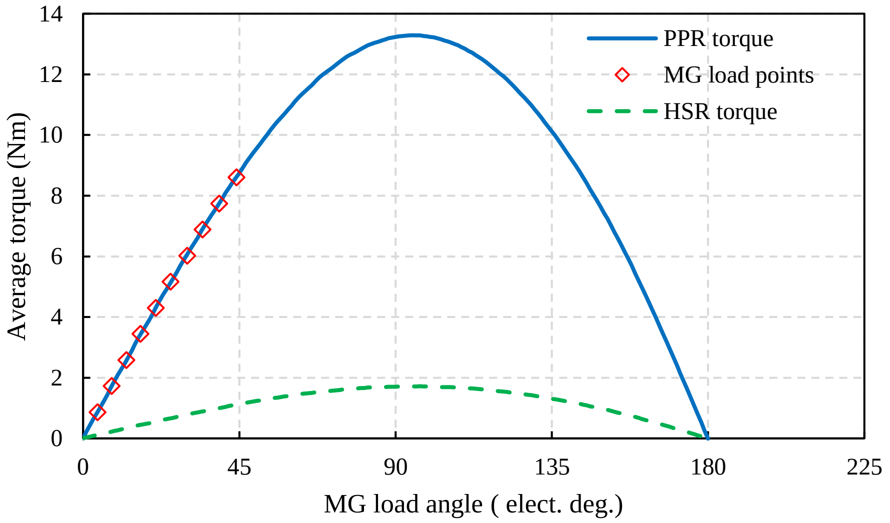

Figure 8.1. Variation of MG load angle with PPR and HSR average torque

The variation of the average output PPR torque with input phase current is shown in Figure 8.2. It can be seen that the phase current demand is increased with the output speed when the drag torque, caused by the eddy current losses of the solid components, is considered. For a 2D case, over 90% of the eddy current losses are concentrated in the pole pieces and outer sleeve. Thus, if the pole pieces were laminated, and titanium sleeve replaced with a composite variant, the phase current demand is reduced as shown in Figure 8.2.

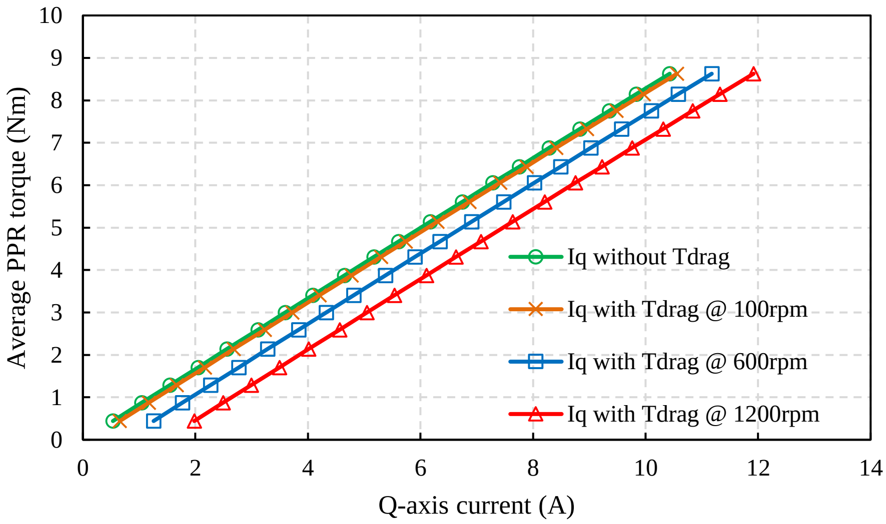

Figure 8.2. Variation of average PPR torque with input q-axis phase current

The copper loss, P_{cu}, of one lane of the duplex 3-phase topology is given by:

$$P_{cu} = 3I_{RMS}^2 R_{ph} \tag{8.3}$$

where R_{ph} is the phase resistance of one 3-phase lane and I_{RMS} is the RMS phase current.

For the 12s8p topology this is the same as the resistance of one coil. The variation of copper loss with PPR load torque for Active-Passive and Active-Active healthy operation with laminated pole pieces and composite PM retention sleeve is shown in Figure 8.3 (a). It can be observed during AA operation the copper losses at rated load are reduced by 50%.

In comparison, the copper losses are increased when the eddy current losses of the non-laminated pole pieces and titanium sleeve are considered, as shown in Figure 8.3 (b). For a fixed operation mode, the copper losses are increased by 30.6% due to the additional drag torque introduced by the considerable eddy current losses in the solid components.

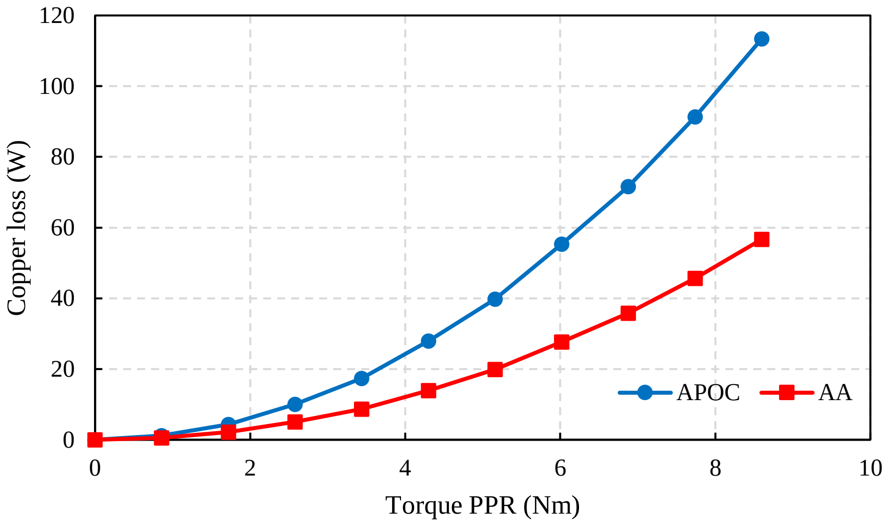

(a)

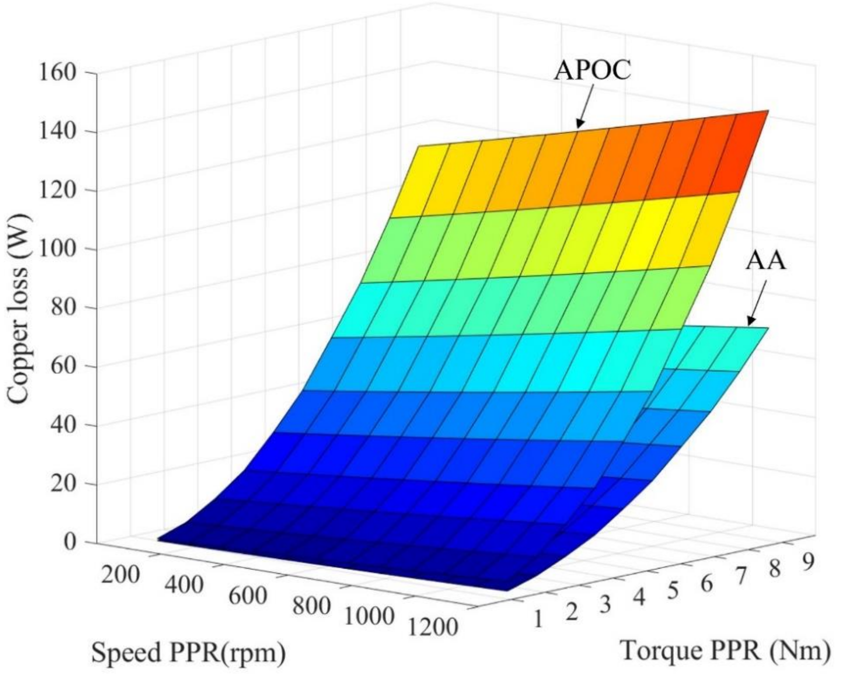

(b)

Figure 8.3. Variation of Active-Passive and Active-Active copper loss with (a) laminated (b) non-laminated pole pieces and sleeve

8.2 Iron losses

The laminated stator and pole piece iron losses were predicted from the flux density data of 2D time-varying FE simulations. The iron loss calculation is based on the Berttotti frequency domain model presented in [180] and [181]. The iron loss can be separated in hysteresis, eddy current and excess or anomalous loss. From the 2D FE simulations, the magnetic flux density data can be obtained at each time step. A Fourier harmonic analysis can be conducted to obtain the magnetic flux density amplitude of each harmonic. Thus, in frequency domain, the iron loss for each frequency component can be obtained from [182], [183]:

$$\text{Hysteresis loss: } P_{hyst} = k_h \hat{B}^{\alpha} f \quad \text{(W/kg)} \tag{8.4}$$

$$\text{Classical eddy current loss: } P_{cl} = k_e \hat{B}^{2} f^{2} \quad \text{(W/kg)} \tag{8.5}$$

$$\text{Excess eddy current loss: } P_{ex} = k_{ex} \hat{B}^{1.5} f^{1.5} \quad \text{(W/kg)} \tag{8.6}$$

where k_h, k_e, k_{ex}, α are material constant, while $\hat{B}$ represents the magnetic flux density harmonic amplitude for each component of frequency f.

The authors of [184], [185] have converted the frequency domain iron loss equations (8.4)-(8.6) in discrete time domain for used with time varying 2D simulations. Hence, the time varying magnetic flux density data can be used to calculate the three components of iron loss such that:

$$\text{Hysteresis loss: } P_{hyst} = k_h \frac{1}{\tau_e} B_{pk}^{\alpha} \quad \text{(W/kg)} \tag{8.7}$$

Classical eddy current loss: $P_{cl} = k_e \frac{1}{2\pi^2} \frac{1}{N} \sum_{i=1}^{i=N} \left| \frac{B_{i-1} - B_i}{t_{i-1} - t_i} \right|^2$ (W/kg) (8.8)

Excess eddy current loss: $P_{ex} = k_{ex} \frac{1}{8.76} \frac{1}{N} \sum_{i=1}^{i=N} \left| \frac{B_{i-1} - B_i}{t_{i-1} - t_i} \right|^{1.5}$ (W/kg) (8.9)

where B_{pk} represents the peak magnetic flux density, and N is the number of time steps over the electrical cycle, τ_e.

Since the magnetic flux density variation in the stator core is mainly given by the HSR PM flux and synchronous stator armature flux, the field electrical frequency is given by:

$$f_{hsr} = \frac{\pi \cdot p_h \Omega_{PPR} G_r}{60} \tag{8.10}$$

The magnetic flux variation in the pole pieces is given due to the HSR PM flux and synchronous stator armature flux, but also due to the outer PM array flux. Thus, the frequency of the magnetic flux density in the pole pieces is dependent on the magnetic gear ratio and is given by:

$$f_{ppr} = f_{hsr} \cdot \left(1 - \frac{1}{G_r}\right) \tag{8.11}$$

The eddy current loss constant, k_e, can be calculated from the M270-35A material constants such that:

$$k_e = \frac{\gamma_{fe} \pi^2 t_l^2}{6\rho_{fe}} \tag{8.12}$$

where $\gamma_{fe}$is the electrical steel conductivity, t_l is the lamination thickness and ρ_{fe} is the density of the iron laminations. The material constant of the M270-35A electrical steel are shown in Table 8.1.

The laminated PPR and stator core iron losses have been predicted for Active-Passive and Active-Active operation. Figure 8.4 shows the variation of the laminated pole pieces and stator core iron losses with output speed and torque.

Table 8.1. M270-35A material constants [186]

Parameter	**Value**
k_h	$11.745 \cdot 10^{-3}$
k_{ex}	$0.447 \cdot 10^{-3}$
α	1.992
γ_{fe} (S/m)	$1/(59 \cdot 10^{-8})$
t_l (mm)	0.35
ρ_{fe} (kg/m^3)	7650

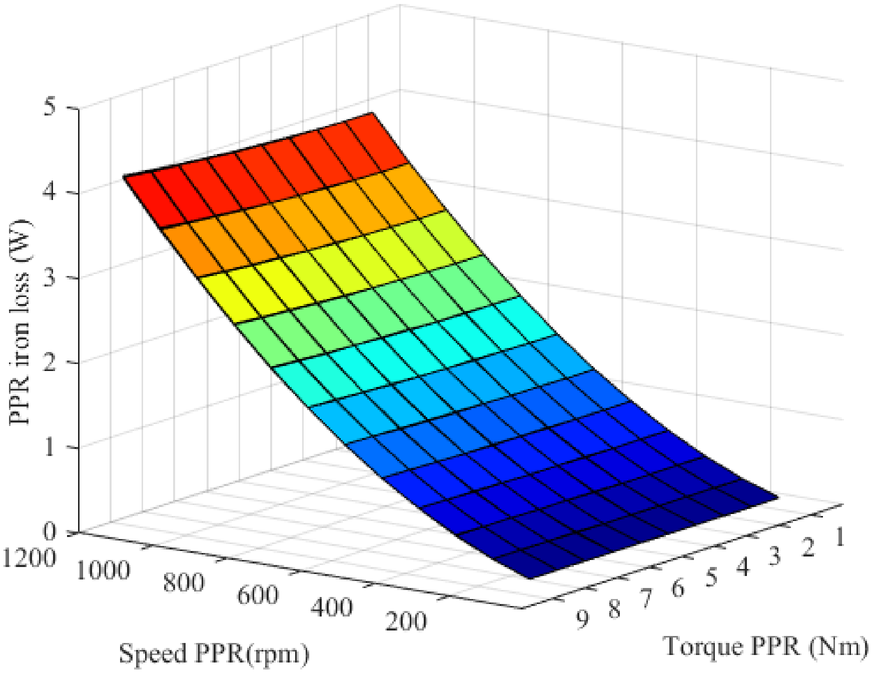

(a)

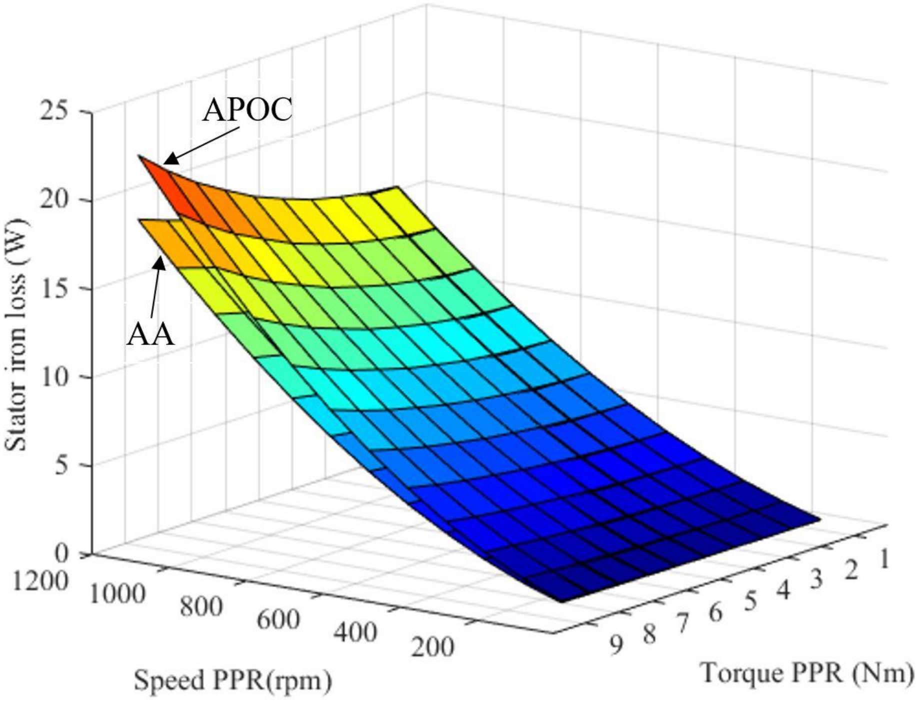

(b)

Figure 8.4. Variation of laminated(a) PPR and (b) stator core iron losses with output torque and speed

The change in iron loss of the laminated pole pieces, for the two PDD operation modes, is negligible. In contrast, due to localised higher stator tooth saturation, the APOC iron loss is increased by 20% when compared to the AA iron loss, at rated output speed and torque.

The variation of the stator iron loss with the increased phase current, due to the additional drag torque caused by the eddy current loss of the non-laminated PDD components, is shown in Figure 8.5. The APOC and AA stator iron loss are increased by 11.3% and 5.4%, respectively, when compared to the predictions from Figure 8.4 (b).

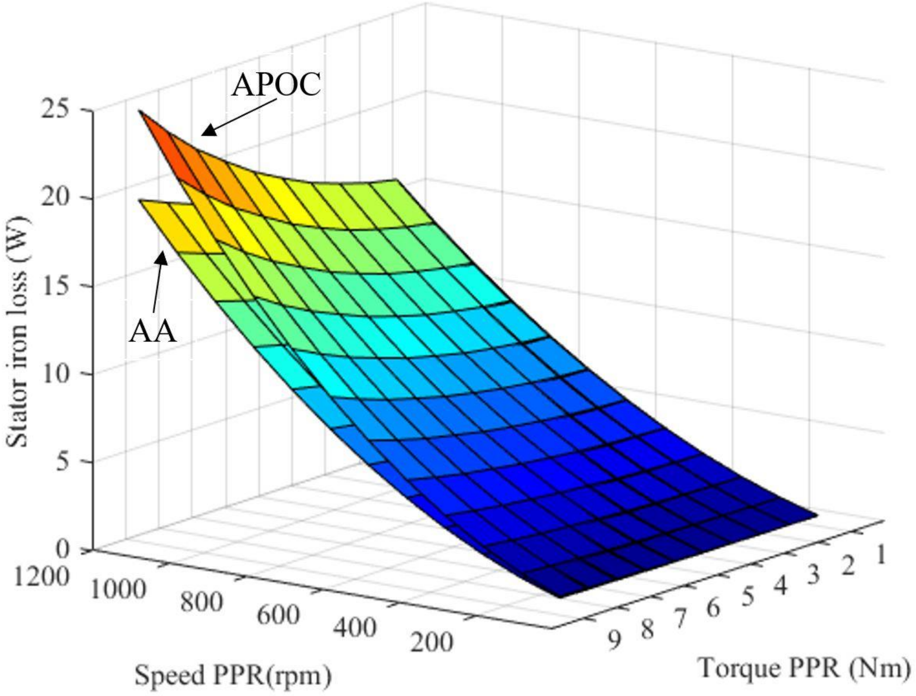

Figure 8.5. Variation of laminated stator core iron loss with output torque and speed and accounting for eddy current drag torque

8.3 Eddy current losses of non-laminated PDD components – 2D FEA

In order to simplify the mechanical design, reduce cost and obtain a light weight PDD prototype, certain active PDD components were not laminated. These are represented by the HSR and stator PMs, pole pieces and stator magnet retention sleeve. Thus, time-varying 2D electromagnetic FEA was used to predict the eddy current flow in the Z-axis due to the time-based variation of the magnetic fields in the XY simulation plane. By integrating the square of the eddy current density over the area of each PDD component, (8.13), the eddy current loss was predicted from 2D FE analysis.

$$P_{eddy} = \oint \frac{J_{eddy}^2 L_{act}}{\gamma} \tag{8.13}$$

where J_{eddy} is the eddy current density, L_{act} is the axial length of PDD and γ is the conductivity of the material.

It is well known that the eddy current loss varies with the square of the magnetic field density and frequency, such that:

$$P_{eddy} \propto B^2 f^2 \tag{8.14}$$

Thus, in order to accurately consider the saturation effects in the pole pieces, the PDD was simulated in Active-Passive open circuit and Active-Active operation modes, with the phase current being estimated based on the load and drag torque, for a range of output speed and torque values. The PM temperature on both arrays was fixed to 80^{o}C. The material conductivities for the non-laminated active components are shown in Table 8.2. It can be seen that the grade 5 titanium has three times the resistivity of electrical steel.

Table 8.2. Conductivities of M270-35A, Recoma 28 and Grade 5 Titanium

γ_{fe} (S/m)	$1/(59 \cdot 10^{-8})$
γ_{PM} (S/m)	$1/(90 \cdot 10^{-8})$
γ_{TTN} (S/m)	$1/(178 \cdot 10^{-8})$

The magnetic flux density contour plots for OCOC, AA and APOC operation are shown in Figure 8.6. It can be observed that the pole pieces have regions of high magnetic saturation. Thus, a considerable eddy current loss can be achieved with a non-laminated pole piece design.

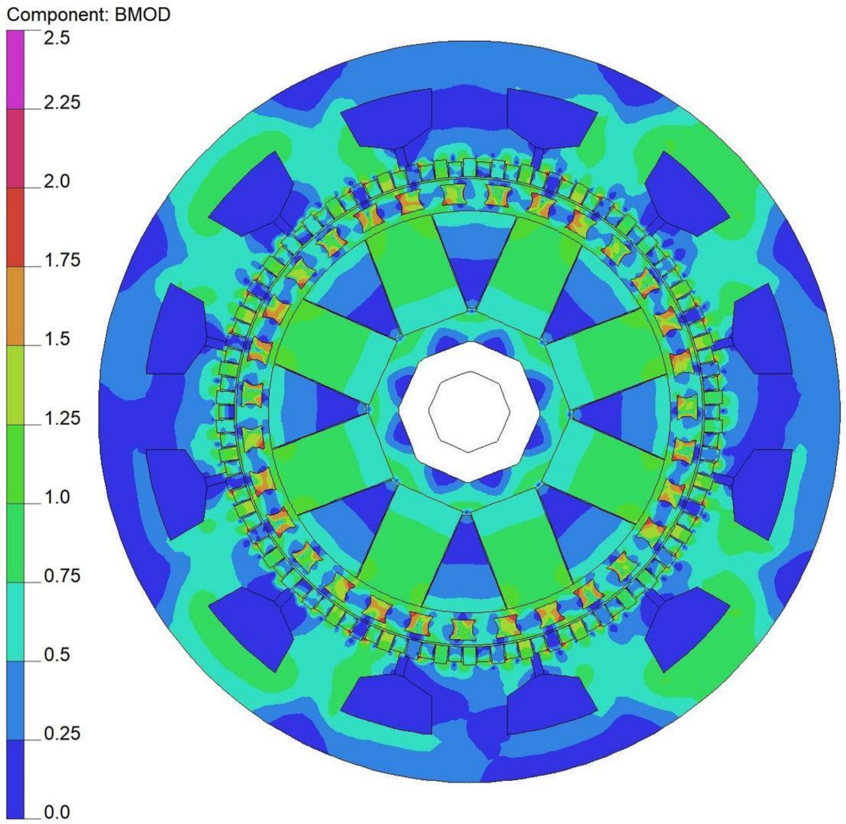
Component: BMOD
2.5
2.25
2.0
1.75
1.5
1.25
1.0
0.75
0.5
0.25
0.0

(a)

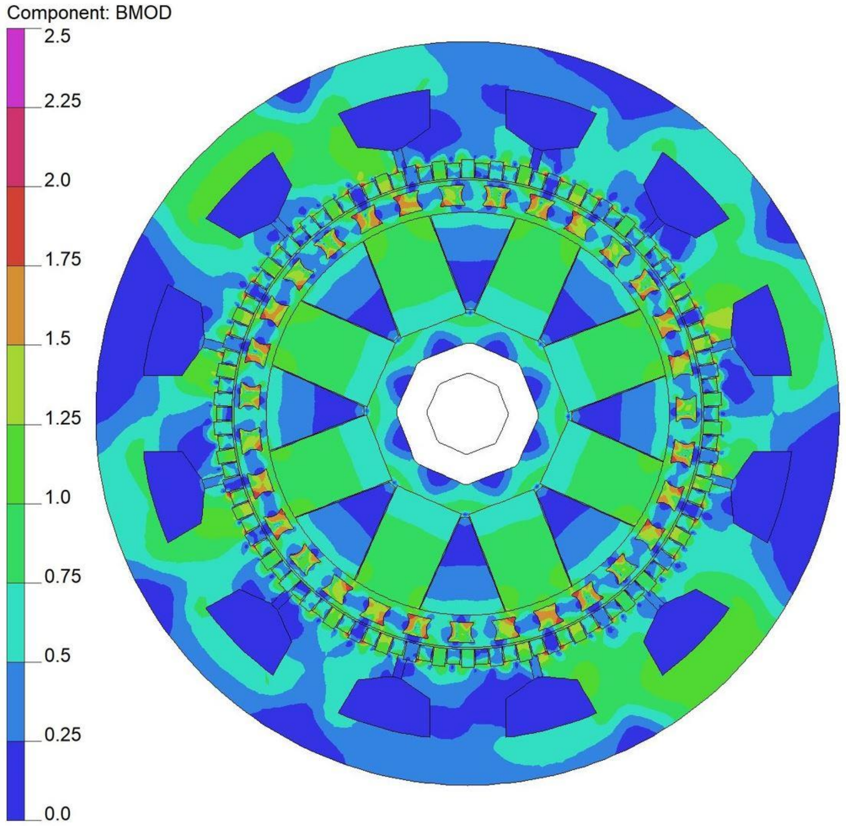
Component: BMOD
2.5
2.25
2.0
1.75
1.5
1.25
1.0
0.75
0.5
0.25
0.0

(b)

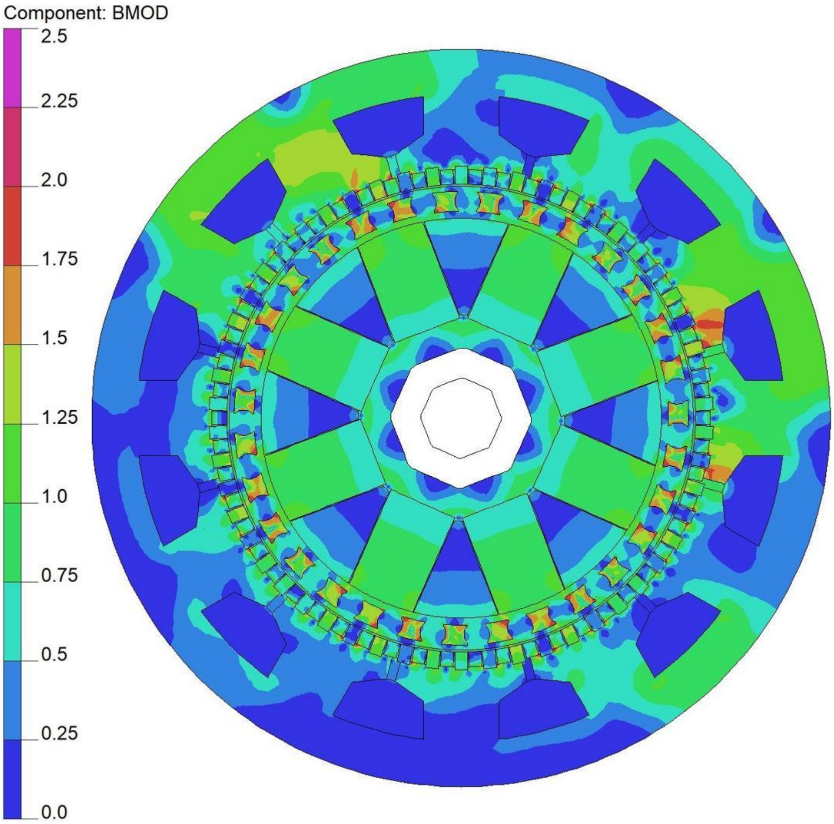

(c)

Figure 8.6. Magnetic flux density contour plot for (a) Open circuit (b) Active-Active (c) Active-Passive operation

The resultant eddy current plots due to the time-varying magnetic fields, for the different PDD operation modes are shown in Figure 8.7. It can be observed that the pole pieces together with the titanium sleeve, in the outer airgap, have regions with high eddy current densities. In comparison the HSR and stator PM regions are characterised by low eddy current densities. This shows that most of the eddy current loss is concentrated in the pole pieces and titanium sleeve. Depending on the loss of the sleeve, segmentation can be considered to reduce the eddy current loss and protect the stator magnets from high heating effects, which can reduce PM flux and implicitly, the pull-out torque of the PDD.

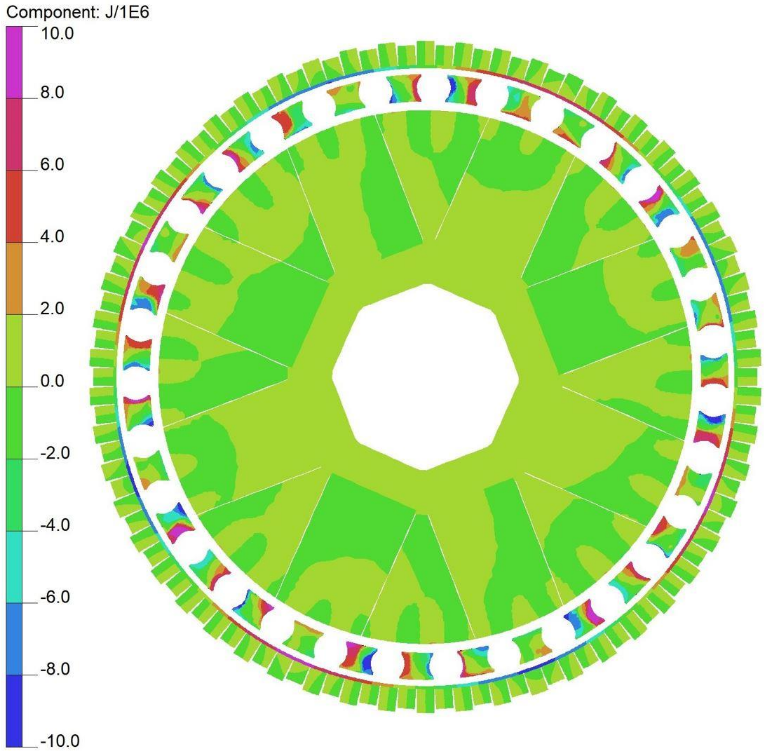
Component: J/1E6
10.0
8.0
6.0
4.0
2.0
0.0
-2.0
-4.0
-6.0
-8.0
-10.0

(a)

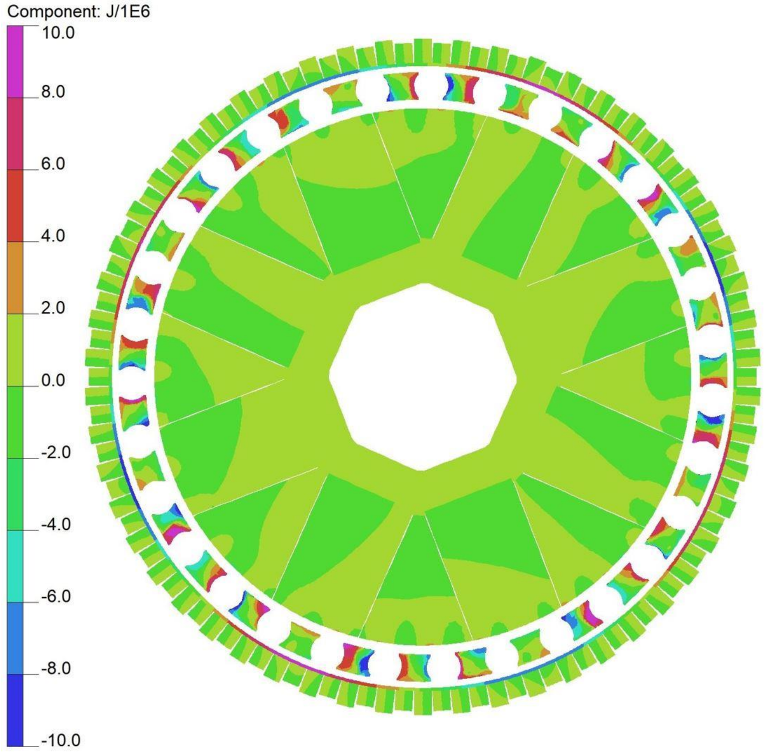
Component: J/1E6
10.0
8.0
6.0
4.0
2.0
0.0
-2.0
-4.0
-6.0
-8.0
-10.0

(b)

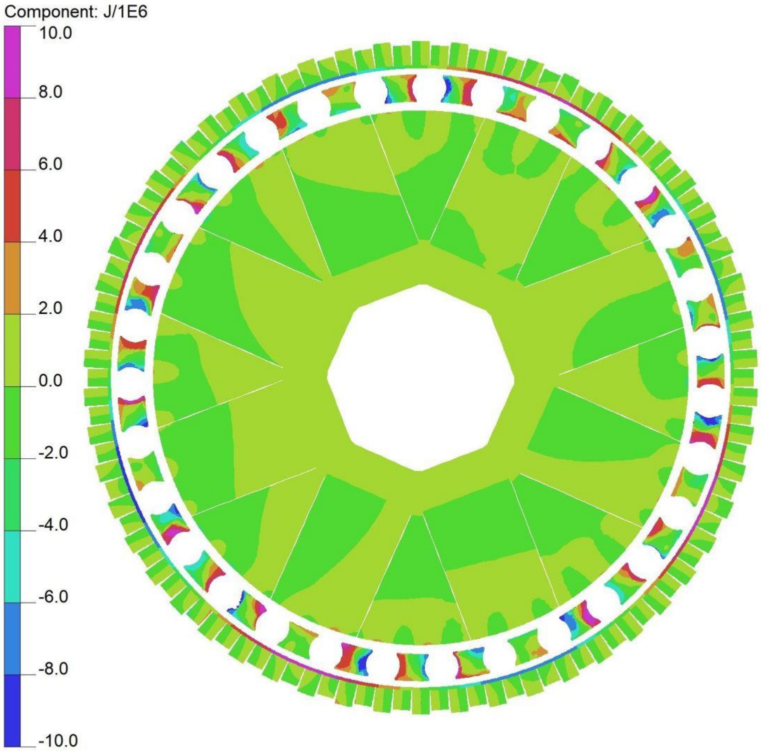

(c)

Figure 8.7. Eddy current density (A/mm^2) contour plot for (a) Open circuit (b) Active-Active (c) Active-Passive operation

The eddy current losses of the non-laminated PDD components were predicted for Active-Passive and Active-Active operation, for a range of output PPR torque and speed values. For the open circuit case, the load angle of the MG was changed to replicate the relative position of the PPR with respect to the PM arrays, for a given transmitted torque. Although this cannot occur in a PDD without phase excitation, this does represent the operation case of the embedded magnetic gear. Thus, this gives a good representation of the eddy current losses likely to exist in a stand-alone magnetic gear with the same cross-section.

Due to the fixed rotor hub magnetisation given by the thick HSR PMs, the eddy current loss of the solid steel hub is very small with 0.48W during APOC operation at rated torque and speed, as shown in Figure 8.8. Thus, the loss of this component was not considered in the 3D FE transient simulations. In comparison, the eddy current loss of the inner PM array, Figure 8.9, is an order of magnitude higher. The HSR PM loss in APOC and AA modes, at 1200rpm, is increased by 93% and 51% when compared to the open circuit case, respectively. It can be observed in Figure 8.9 (b), that for a fixed output torque level, and thus stator armature reaction, the HSR PM loss varies with the square of the electrical frequency.

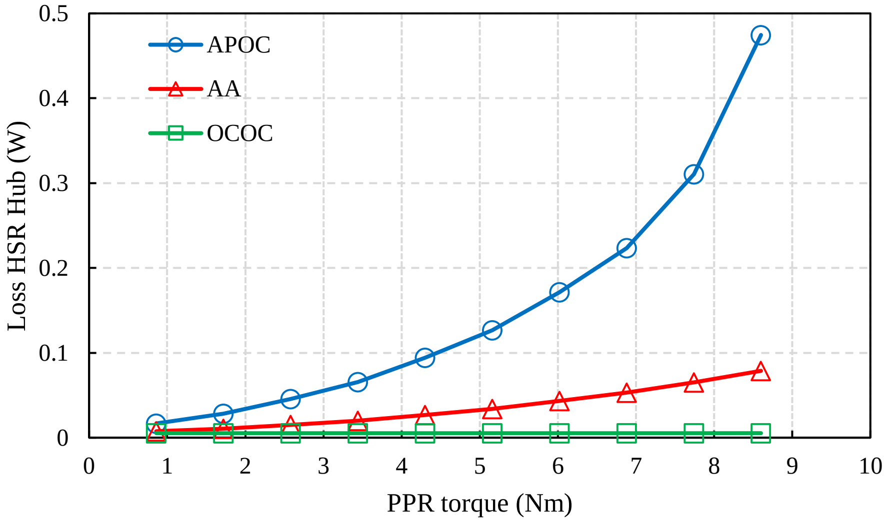

Figure 8.8. Variation of HSR hub eddy current loss with output torque at 1200rpm

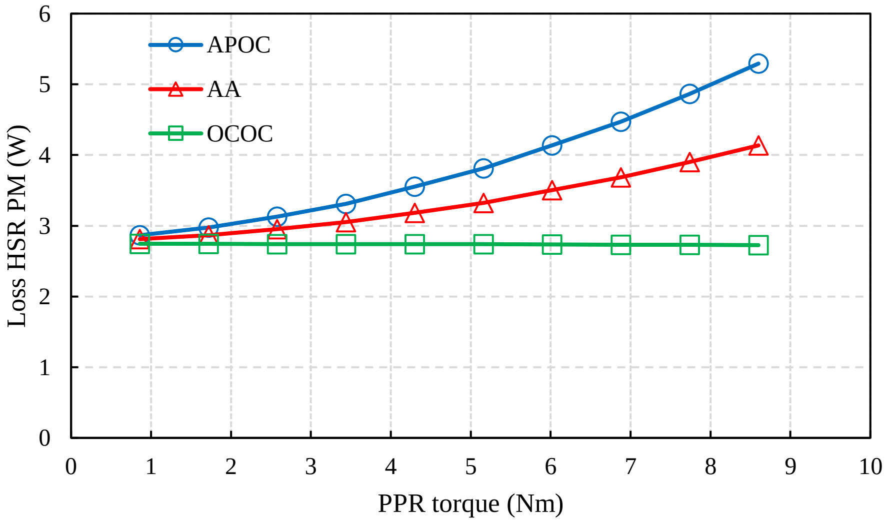

(a)

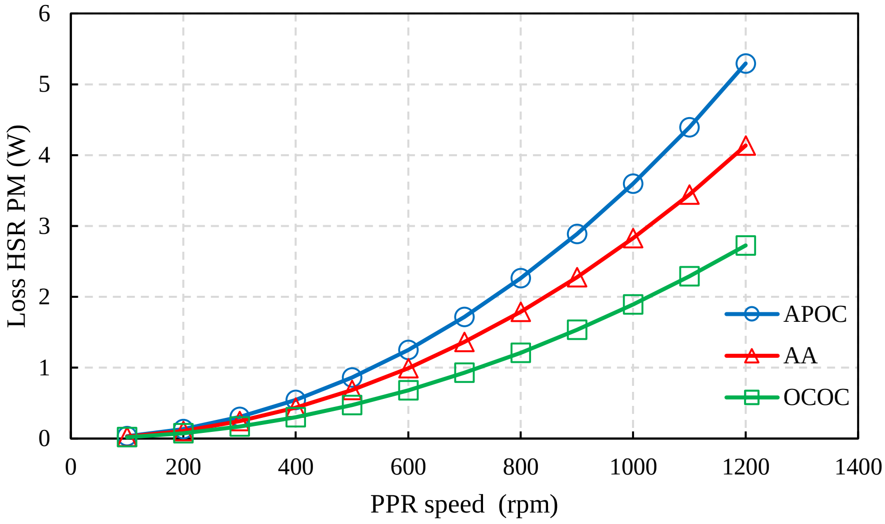

(b)

Figure 8.9. Variation of HSR PM eddy current loss with (a) output torque at 1200rpm and (b) PPR speed at rated output torque

The stator PM loss, shown in Figure 8.10, is fairly constant with load and operation mode. This shows that the eddy currents in the stator PMs are mainly influenced by the amplitude and frequency of the HSR PM field. For APOC operation, the stator PM loss is similar to the HSR PM loss. For these 2D simulation, electrical insulator boundaries were used between adjacent stator PM blocks and between all the stator PMs and the titanium retention sleeve. This ensures that the eddy current path is reduced, being limited to each PM block, while the total loss is reduced.

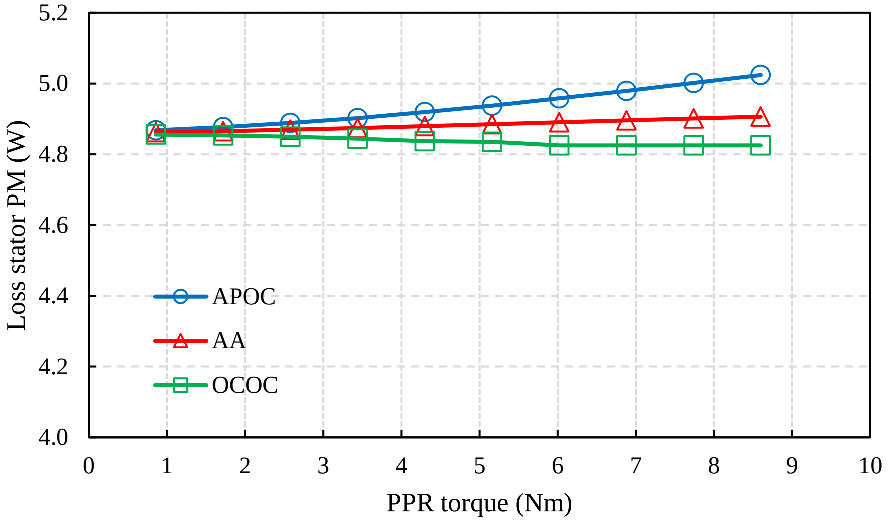

(a)

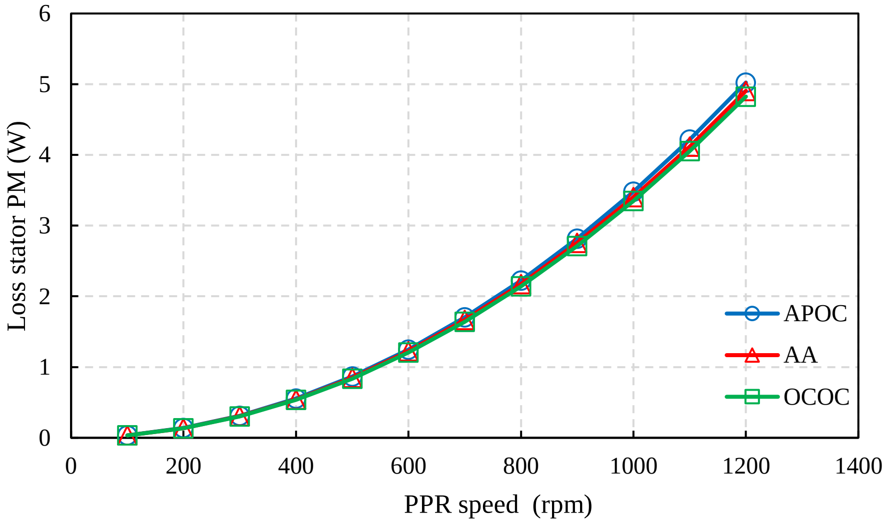

(b)

Figure 8.10. Variation of stator PM eddy current loss with (a) output torque at 1200rpm and (b) PPR speed at rated output torque

The eddy current loss of the non-laminated pole pieces is shown in Figure 8.11. For this prediction it was assumed that each pole piece is perfectly insulated from the adjacent pole pieces. Thus, insulator rings were introduced between the axial ends of each pole piece and the rotor endplates. It can be observed that the pole piece eddy current loss is not influenced by the stator armature reaction and is only dependent on the HSR and stator

PM field. Moreover, the pole piece loss is only slightly affected by the load angle of the MG element.

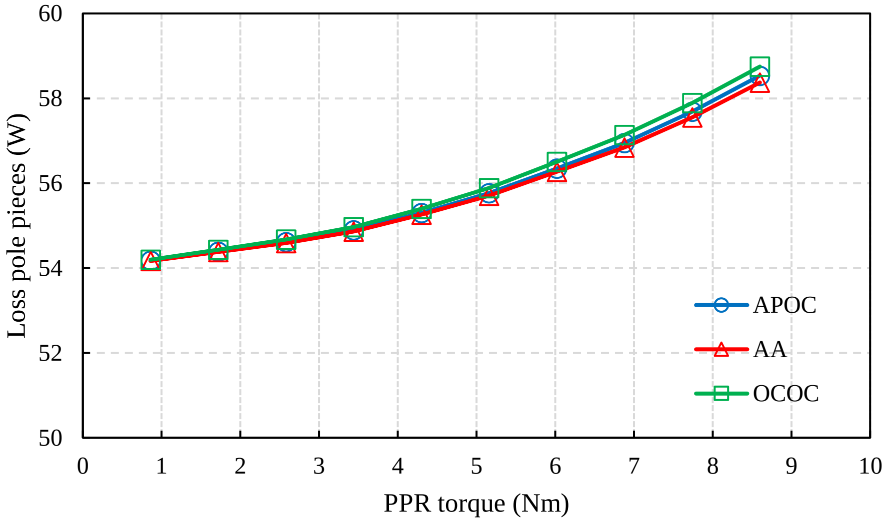

(a)

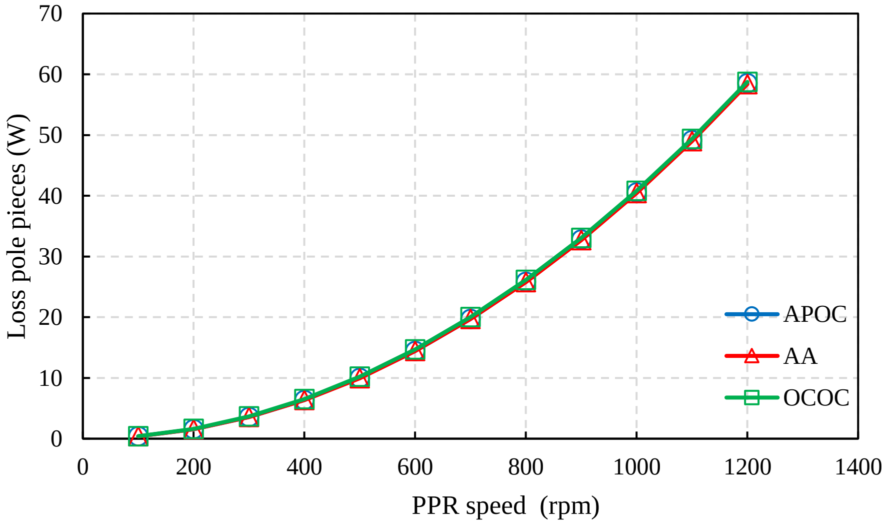

(b)

Figure 8.11. Variation of pole piece eddy current loss with (a) output torque at 1200rpm and (b) PPR speed at rated output torque

From the 2D FEA results, the highest eddy current loss is predicted in the titanium retention sleeve. It can be observed, from Figure 8.12 (a), that the sleeve loss is not largely affected by the increase in phase current with load output torque. At APOC rated operation point, the total eddy current loss of the solid components is predicted at 161 W based on 2D FEA. From this, 56.7% represents the sleeve loss and 36.5% is the eddy current pole piece loss. In order to reduce the sleeve eddy current loss axial segmentation is implemented and simulated in transient 3D FEA. A composite glass fibre sleeve can also be used to fully remove this loss component.

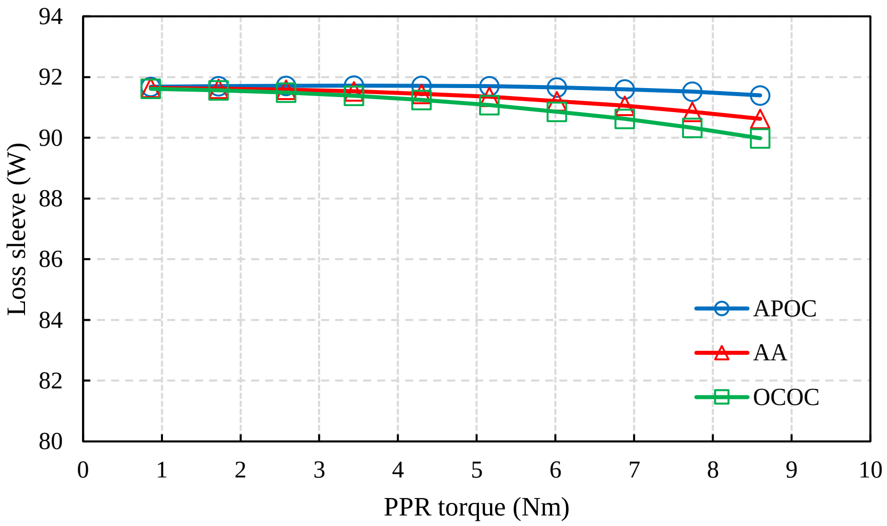

(a)

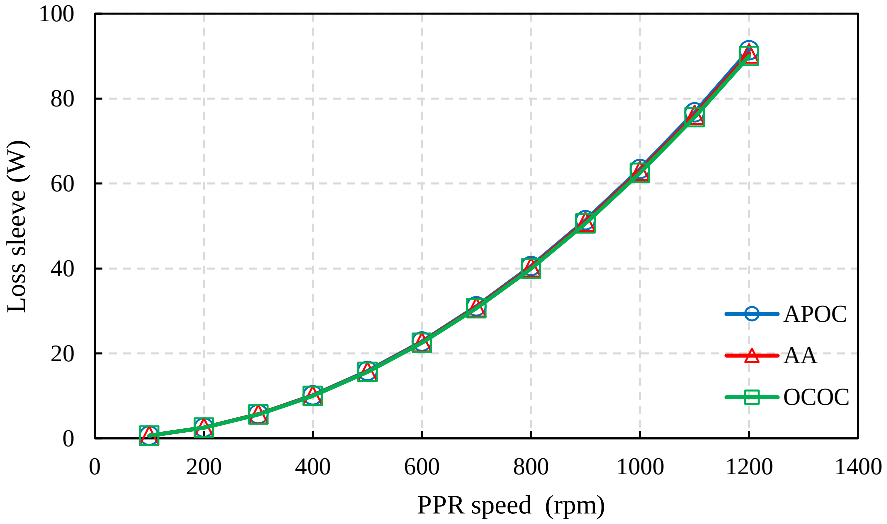

(b)

Figure 8.12. Variation of titanium sleeve eddy current loss with (a) output torque at 1200rpm and (b) PPR speed at rated output torque

8.4 Eddy current losses of non-laminated PDD components – 3D FEA

Due to the small size of the PDD prototype, several active component are not laminated, as in convectional machines, in order to reduce manufacturing complexity and cost while achieving a light weight and mechanically reliable design. To facilitate assembly, the PM blocks and titanium sleeve were only sectioned in half along the axial length, or Z-axis direction. In case of the PM blocks this enabled handling them during cleaning and rotor/stator assembly operations without substantial breakages. In contrast, the pole pieces were not laminated in order to increase the torsional stiffness of the PPR, given the small 2mm cross-section achieved without any composite overwrap or torque tube structures.

The PDD 3D magnetic flux density distribution due to the PM flux is shown in Figure 8.13. It can be observed, that the pole pieces are highly saturated by the PM flux. As this magnetic flux density in the pole pieces varies with time, the resultant high $\frac{dB}{dt}$ would cause high eddy current losses to be induced in each non-laminated pole piece.

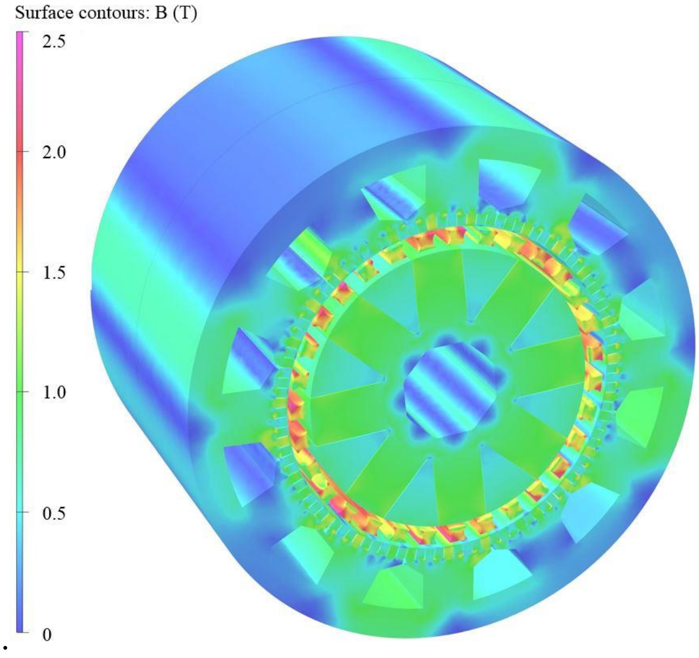

Figure 8.13. Magnetic flux density 3D contour plot at open circuit

The eddy current density plot and eddy current vectors for the HSR PMs are shown in Figure 8.14. These are mainly caused by the 27 pole pair asynchronous harmonic of the stator PM array. It can be observed that eddy currents do not penetrate deep in the HSR PMs. The eddy current flow is along the Z-axis, across the PM surface and is interrupted by the insulator boundary placed at the mid-point along the axial length of the machine. This models the mid-axial segmentation of the HSR PMs into two different blocks along the Z-axis.

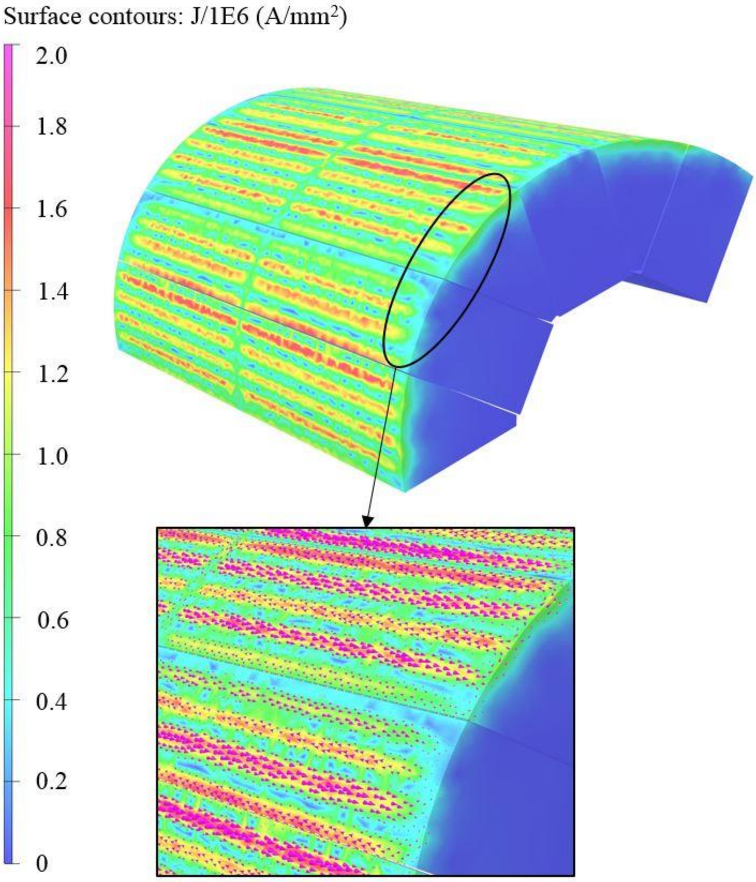

Figure 8.14. HSR PM eddy current density and vector plot

The eddy current density and vector plots of the stator PM array are shown in Figure 8.15. Similarly to the HSR PM array, the stator magnets have been segmented in half along the axial length. The eddy currents of the stator PMs are induced due to the HSR fundamental PM flux component. It can be observed that the HSR PM flux penetrates the entire stator

PM blocks, with the peak eddy current density in the stator PM blocks being similar to that of the HSR PMs.

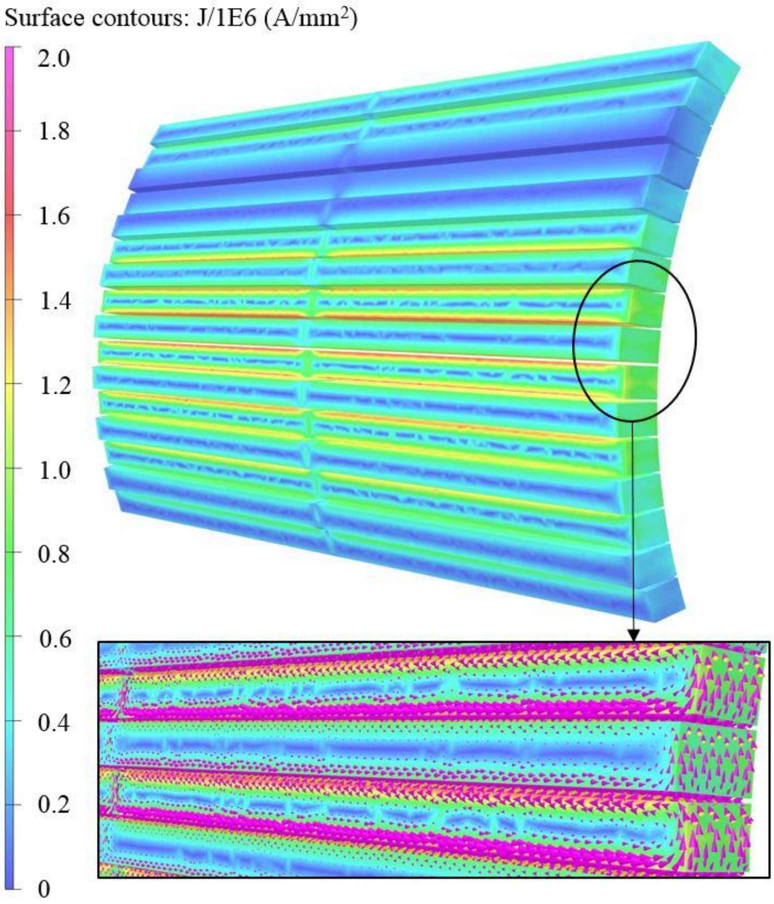

Figure 8.15. Stator PM eddy current density and vector plot

The eddy current density and vector plots of the non-laminated pole pieces are shown in Figure 8.16. Since the pole pieces are not connected to each other, and insulated from the rotor endplates by ceramic spacers, the eddy current flow is confined within each pole piece. The pole piece eddy currents are induced by both PM fields of the HSR and stator. It can be observed that peak eddy current density in the pole pieces is approximatively 5 times higher than that of the HSR and stator PMs. This can be highly reduced if a laminated pole piece structure is implemented.

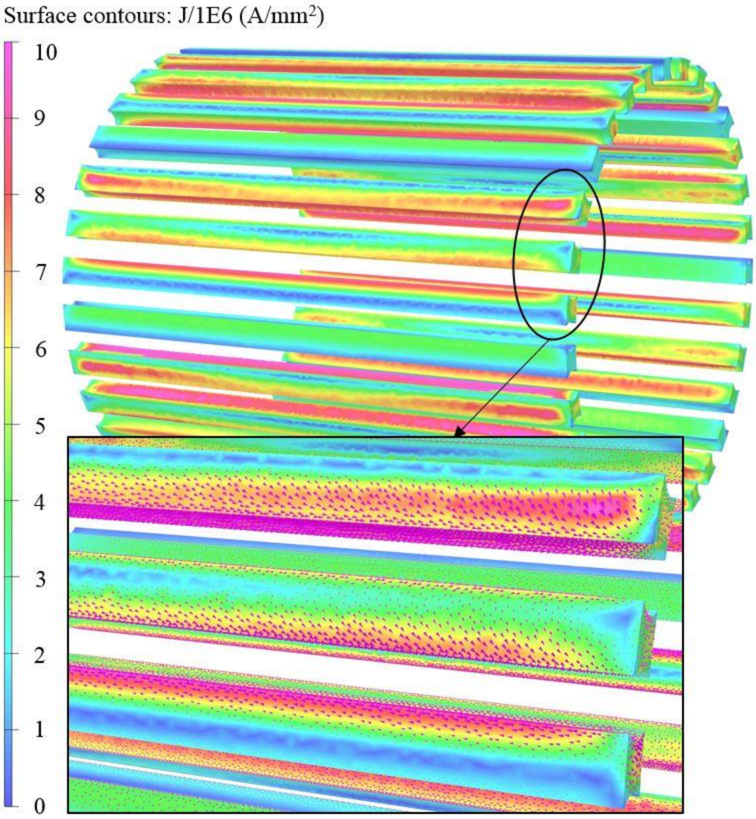

Figure 8.16. Pole piece eddy current density and vector plot

The eddy current density and vector plot of the grade 5 titanium sleeve is shown in Figure 8.17. The stator magnet retention sleeve was divided axially in two rings. Each ring has two axial layers of slits, machined on the circumference in order to break the eddy current path and reduce the eddy current loss. The slits are machined with an angle of 70^o and with a 20^o solid titanium bridge between consecutive slits. The next layer of slits for a given sleeve segment is rotated by 45^o. It can be observed that the eddy current density is fairly small, when compared to that of the non-laminated pole pieces, with an average value of 2.7 A/mm^2. From the vector plot, it can be seen that the eddy currents flow in circular pattern between the two layers of slits. The peak eddy current density was predicted at 9.8 A/mm^2 and is spread across very small areas, around the edges of the slits.

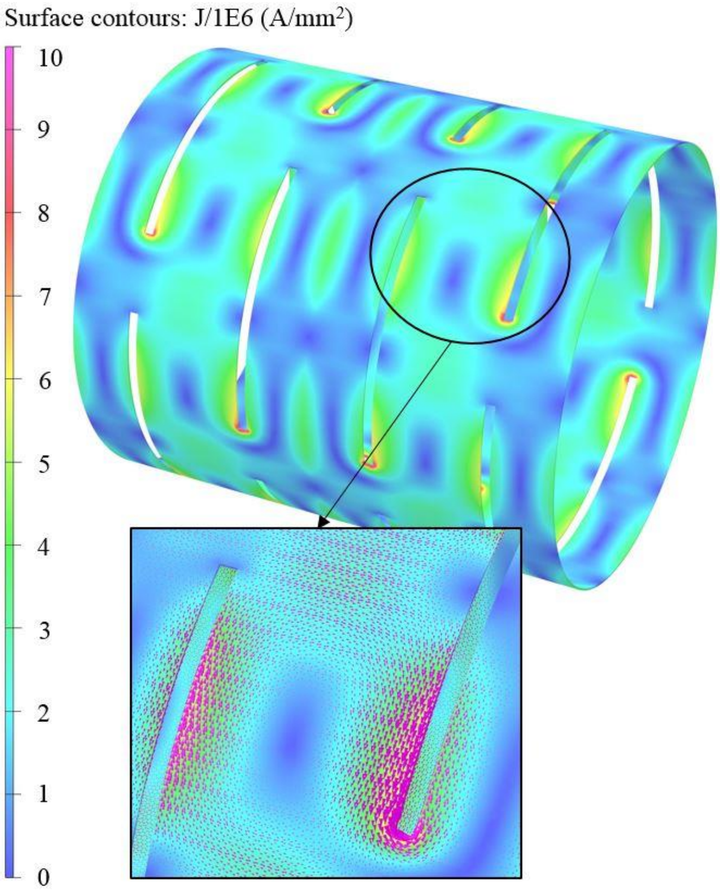

Figure 8.17. Titanium sleeve eddy current density and vector plot

The 3D and 2D FEA predicted eddy current loss of the non-laminated active PDD components are shown in Figure 8.18. It can be observed that the HSR and stator PM losses predicted from the 3D analysis agree well with the 2D case. Because, the PMs cross-sectional dimensions are significantly smaller that the axial length.

In comparison, the PPR eddy current loss predicted from 3D FEA is 30% higher than the 2D case. Upon further investigation, this increase in loss has been attributed to axial flux component caused by the large effective airgap of the PDD. This phenomenon is investigated and explained in section 8.4.2.

The PM retention sleeve eddy current loss predicted in 2D FEA is 6.5 times higher than the 3D result. This shows the significant loss reduction effect of the slits combined with the mid-axial segmentation. Thus, due to this substantial reduction in sleeve loss, the pole piece eddy current loss is now dominant, and represents 79% of the total eddy current loss of the non-laminated PDD component. The total 3D eddy current loss is approximated at 100W which represents a 38.6% reduction from the 2D case, for the same output speed of 1200rpm.

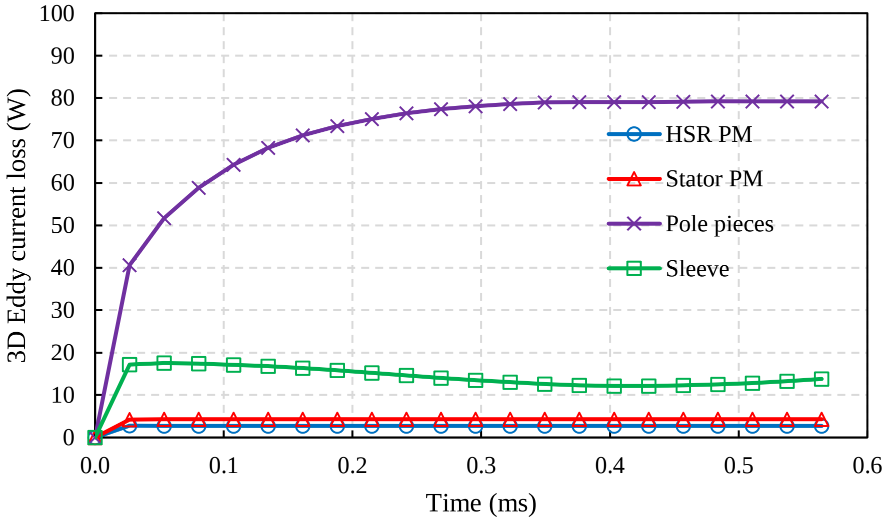

(a)

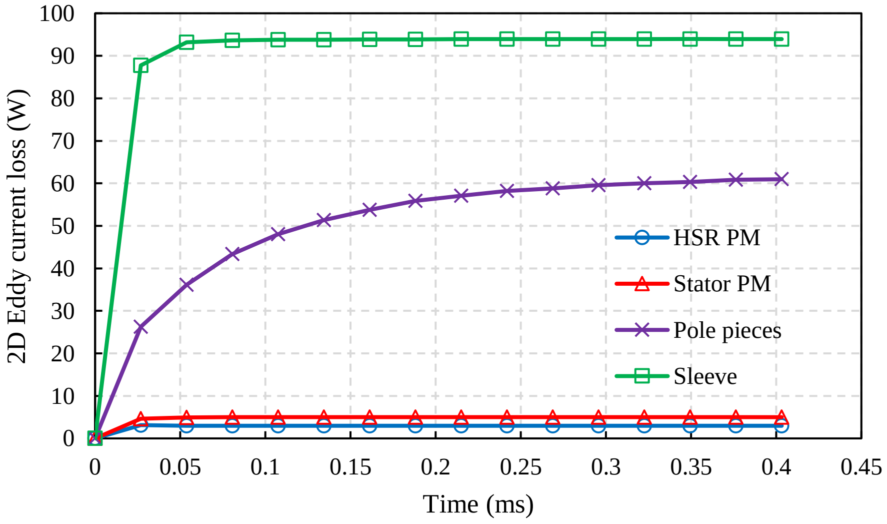

(b)

Figure 8.18. Eddy current loss of non-laminated active PDD components predicted from (a) 3D (b) 2D FEA

8.4.1 Titanium sleeve insulation and segmentation

In the 2D and 3D FE analysis presented previously, the stator PM array and titanium sleeve were separated by an electrical insulator boundary. In practice, if no physical insulator is placed between the two components, eddy currents would have a different path, flowing between the sleeve and the stator PM array. In the PDD prototype, the titanium sleeve has an electrically insulating coating applied to its surface in order to prevent electrical contact with the stator PMs. However, the sleeve is designed to have an interference fit with the inner diameter of the stator PM ring. Thus, this insulator coating can be scratched during prototype assembly, which can result in point contacts being developed between the sleeve and stator PMs. Since modelling such random contacts between the two parts in 3D FE can be very complex and time consuming, the worst have of a perfect electrical contact between the sleeve and stator PM array has been considered.

The eddy current density and vector plots for the stator PM and sleeve with slits and mid-axial segmentation, in perfect electrical contact, are shown in Figure 8.19 (a). It can be observed that, for these conditions, the eddy current density is substantially increased. The eddy current flow from magnet to magnet in a circumferential pattern across the titanium sleeve. Due to the substantial change in the eddy current path, the slits of the sleeve become completely ineffective in reducing the eddy current loss. This can be supported by Figure 8.19 (b), where the slits of the sleeve have been completely removed. It can be observed that the eddy current density induced in the sleeve and PMs together with the eddy current flow pattern are very similar to Figure 8.19 (a).

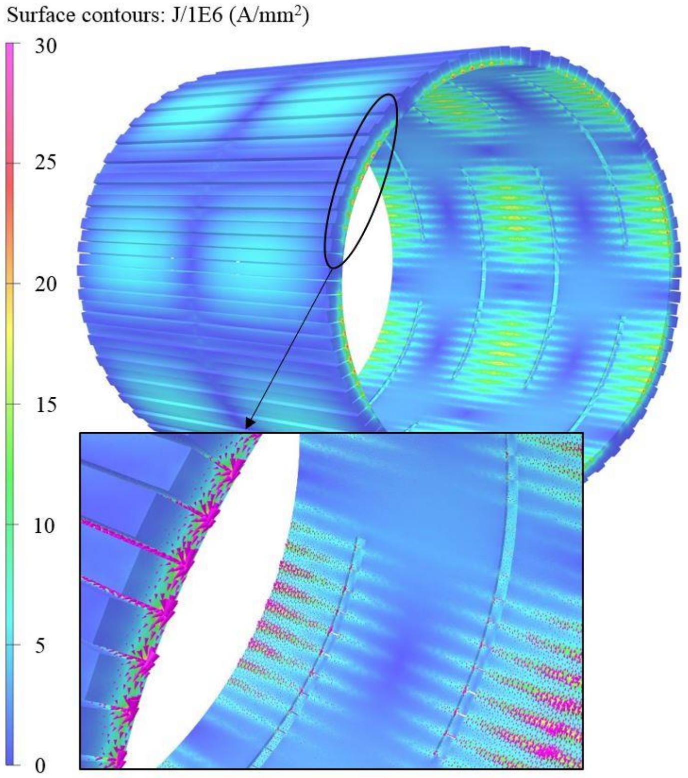

(a)

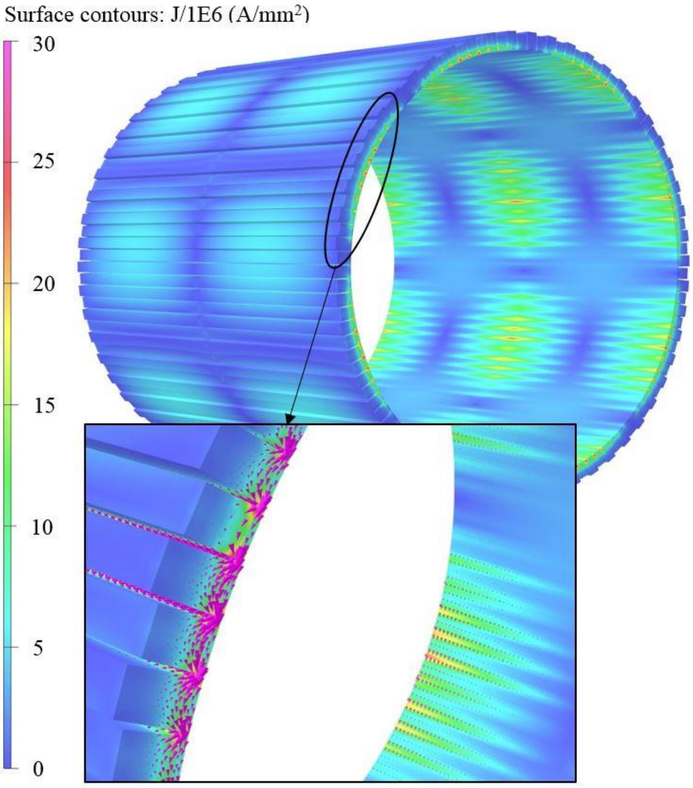

(b)

Figure 8.19. Eddy current density and vector plots without electrical insulator between stator PM and sleeve for (a) sleeve with slits (b) sleeve without slits

The 3D FEA loss prediction for the two cases is shown in Figure 8.20. It can be observed that the slits have no effect in reducing the induced high eddy current loss in the sleeve. Moreover, the eddy current loss of the sleeve and stator PM array is increased by a factor of 7.7 and 49.2, respectively, when compared to having an electrical insulator between the two parts.

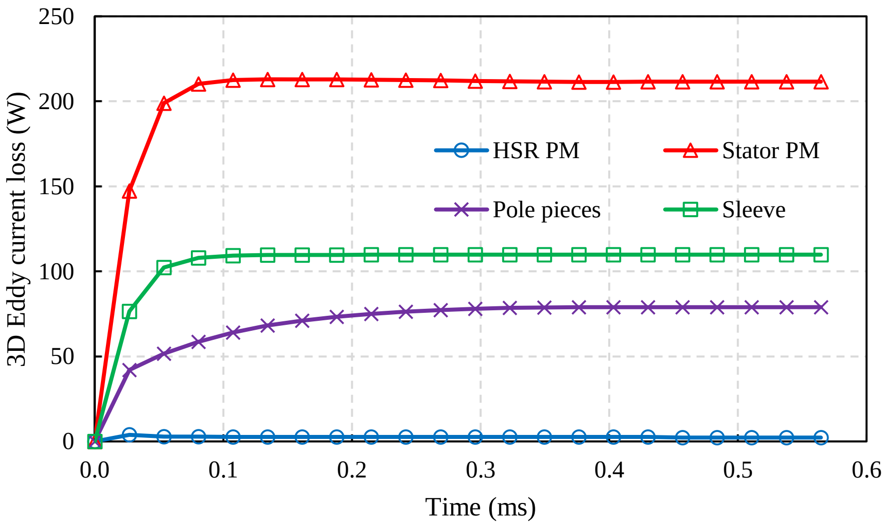

(a)

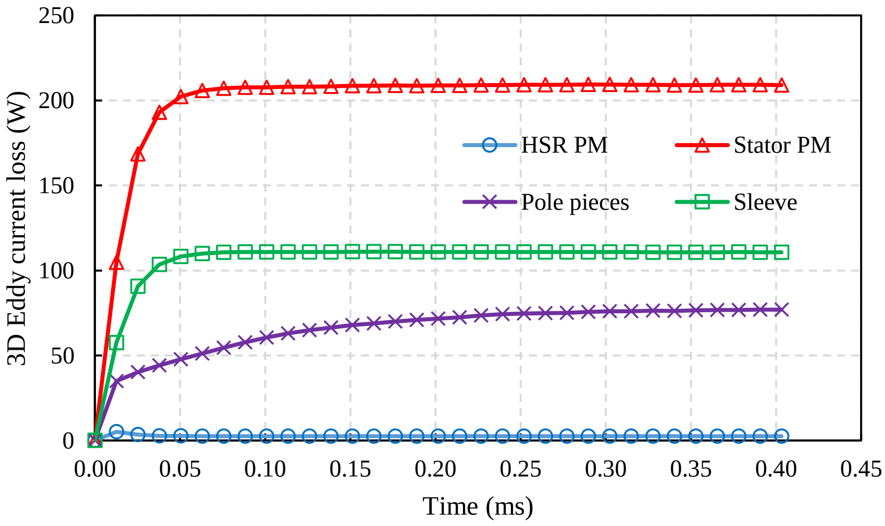

(b)

Figure 8.20. Eddy current loss for electrical contact between sleeve and stator PM, for (a) sleeve with slits (b) sleeve without slits

Due to the circumferential machined slits, the proposed PM retention sleeve design, although effective in reducing the eddy current loss, can be complex and expensive to manufacture. Thus, in order to reduce cost and lead times, conventional discrete sleeve segmentation has been considered in 3D FEA. In order to stop eddy current from flowing from one ring to the next, insulator boundary conditions were placed between the different segments of the sleeve. Figure 8.21 shows the eddy current density plots for different levels of axial segmentation of the titanium sleeve.

It can be observed that, as the number of segments is increased the eddy current path is shortened and the peak eddy current density is reduced. Moreover, the area affected by the peak eddy current density is substantially reduced as the number of segments is increased. The variation of the sleeve eddy current loss with level of segmentation is shown in Figure 8.22. It can be observed that the sleeve eddy current loss is reduced as the number of segments is increased. In comparison with the slit design, for one segment, the loss is increased by a factor of 4.4, while with four segments, this loss is only increased by 57%. Thus, if an electrically conductive sleeve is used, conventional discrete axial segmentation can be used to substantially reduce eddy current losses. Alternatively, by using a carbon or glass fibre composite sleeve, these losses can be completely removed.

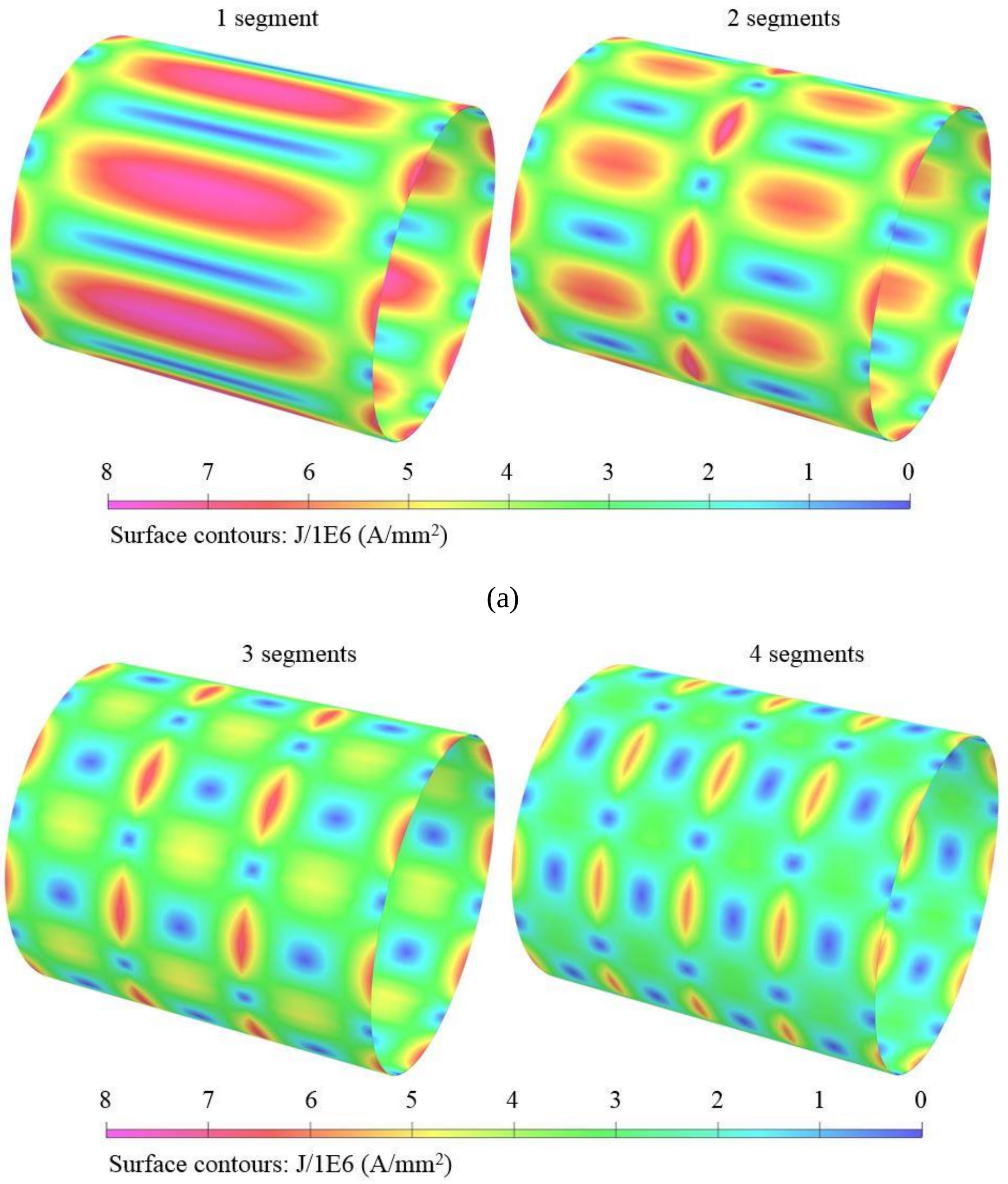

(a)

(b)

Figure 8.21. Titanium sleeve eddy current density plot for discrete axial segmentation with (a) 1 and 2 segments (b) 3 and 4 segments

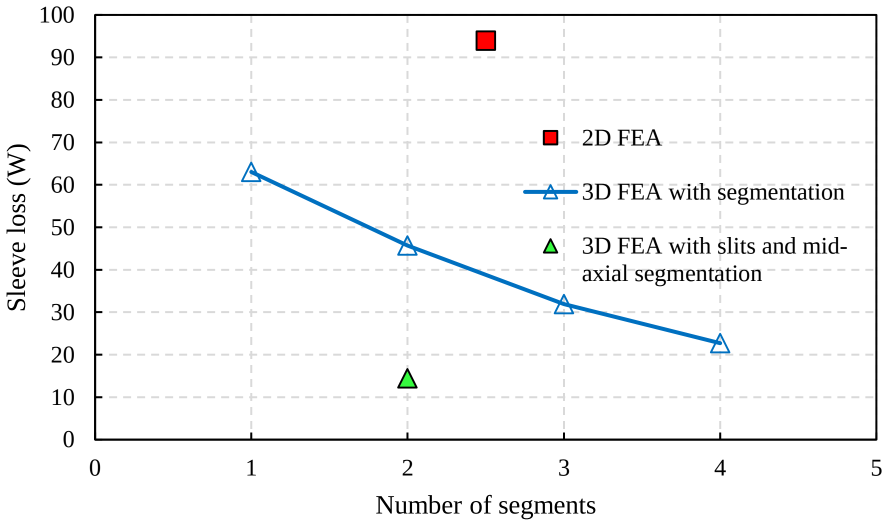

Figure 8.22. Variation of titanium sleeve eddy current loss with degree of segmentation

8.4.2 Pole piece rotor eddy current loss

The eddy current loss of the non-laminated pole pieces is mainly influenced by frequency and the PM field of the HSR and stator PM array. As discussed in section 8.3, for this prototype, this loss is not affected by stator current loading.

In Figure 8.18, it is shown that the 3D FEA PPR loss is 30% higher than the 2D case. This increase can be attributed to the flux leakage end effects. Due to the large effective airgap between the HSR PM and stator teeth, at the extremities of the PDD, the PM field flows axially through each pole piece and returns to the HSR without linking with the stator coils. The time variation of the Z-axis magnetic field density, induces eddy current flow in the XY – plane of each pole piece. Hence, since 2D FEA only models magnetic fields in the XY – plane, the eddy current loss due to the variation of the Z-axis flux is not considered. The Z-axis magnetic flux density, B_Z, in the pole pieces, at no load, is shown in Figure 8.23.

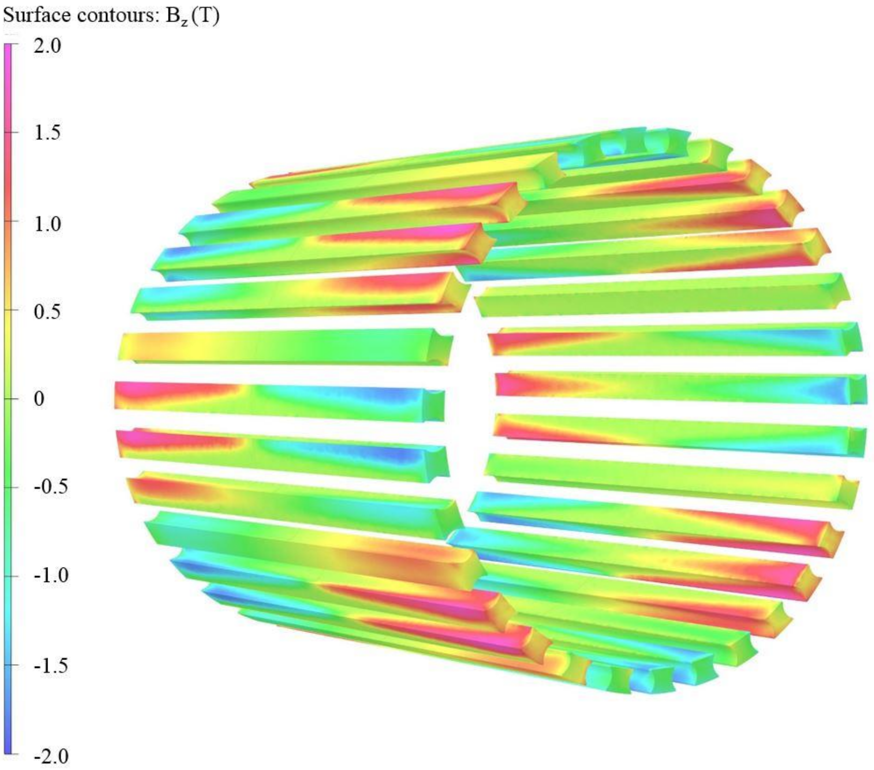

Figure 8.23. Pole piece rotor Z-axis magnetic flux density plot

It can be observed that, for a non-laminated PPR, a considerable degree of saturation occurs, in the Z-axis, towards the ends of the rotor. For a conventional PPR, with laminated pole pieces, the Z-axis saturation is reduced due to the lower Z-axis permeability.

Figure 8.24 (a) shows the variation of B_Z along a pole piece. It can be seen that, at the mid-point of each pole piece, the Z-axis magnetic flux density if zero. Thus, B_Z varies with both time and position within each pole piece. In contrast, Figure 8.24 (b) shows the normal component of the magnetic flux density.

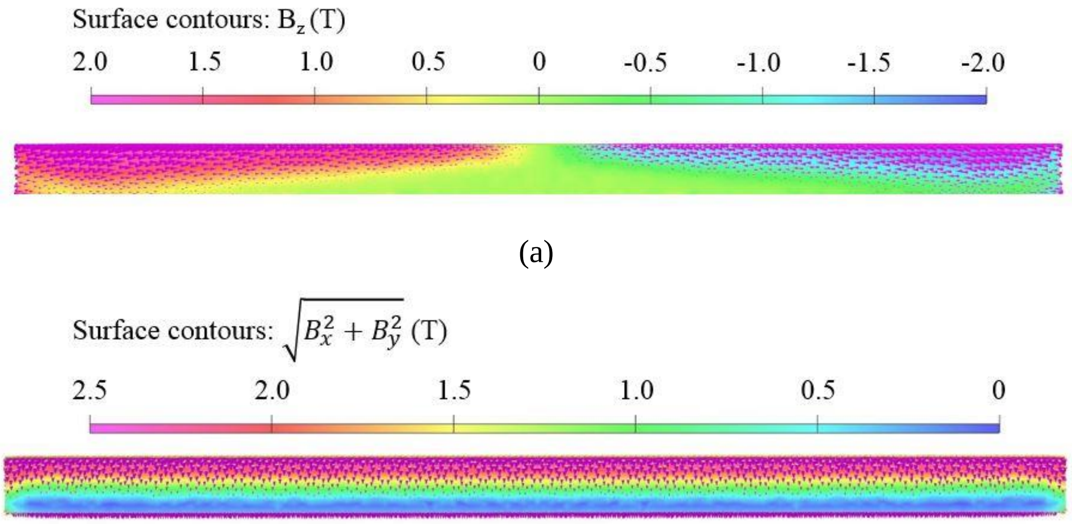

(a)

(b)

Figure 8.24. Magnetic flux density and vector plot of pole piece, along (a) Z-axis (b) XY-plane

The variation of the Z-axis magnetic flux density, with time and position along the pole piece, is shown in Figure 8.25. It can be observed that, at the pole piece axial mid-point, the axial magnetic flux density is zero. In contrast, at either axial end of the rotor, this value is substantially increased for a non-laminated pole piece. A peak value of 1.48 T was estimated for the pole piece mid-point, Figure 8.25 (a), while for the pole piece corner, adjacent to the outer airgap, this is increased to 1.75T, as shown in Figure 8.25 (b). Moreover, for a fixed Z-axis position, B_Z varies sinusoidally with time. The frequency of the Z-axis magnetic field is given by equation (8.11).

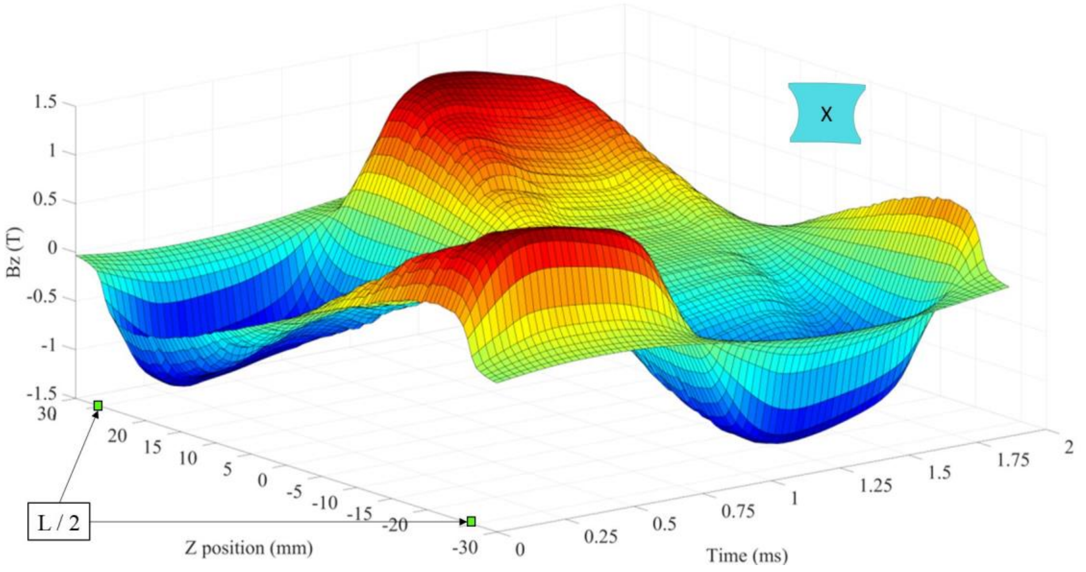

(a)

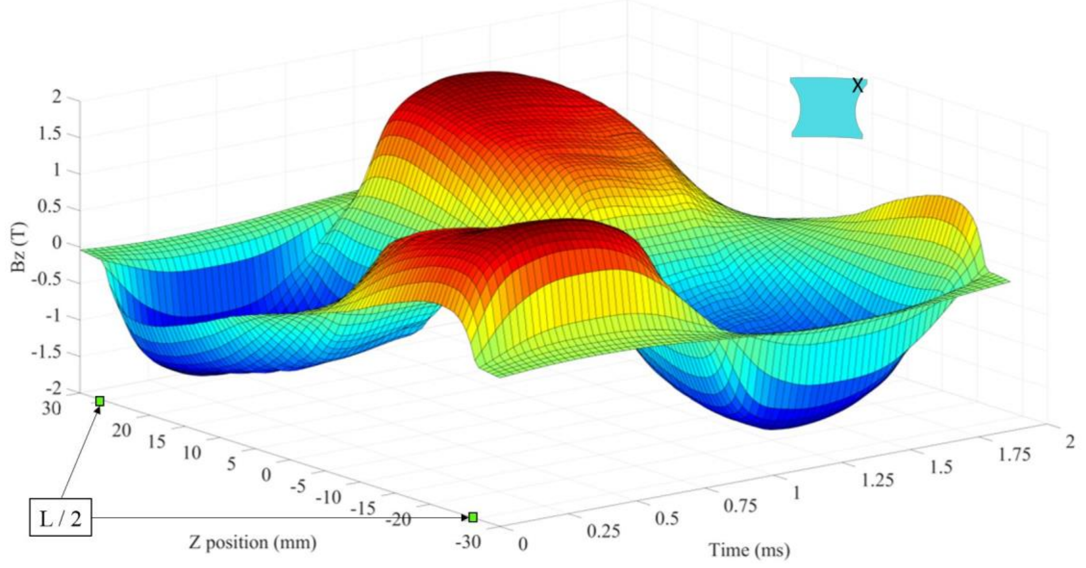

(b)

Figure 8.25. Variation of pole piece B_z with time and Z-axis position along a pole piece, for (a) middle (b) upper corner

The contour and vector plots, of the induced eddy current flowing in the XY – plane and along the Z-axis, are shown in Figure 8.26. It can be observed that the XY – plane eddy current density, shown in Figure 8.26 (a), varies with Z-axis position, along the pole piece, and is high towards the extremities of the rotor. The radial and circumferential components of the eddy current density have zero amplitude at the pole piece mid-point long the Z-axis. In contrast, the Z-axis eddy current density, shown in Figure 8.26 (b), does not vary significantly along the axial length of the pole piece.

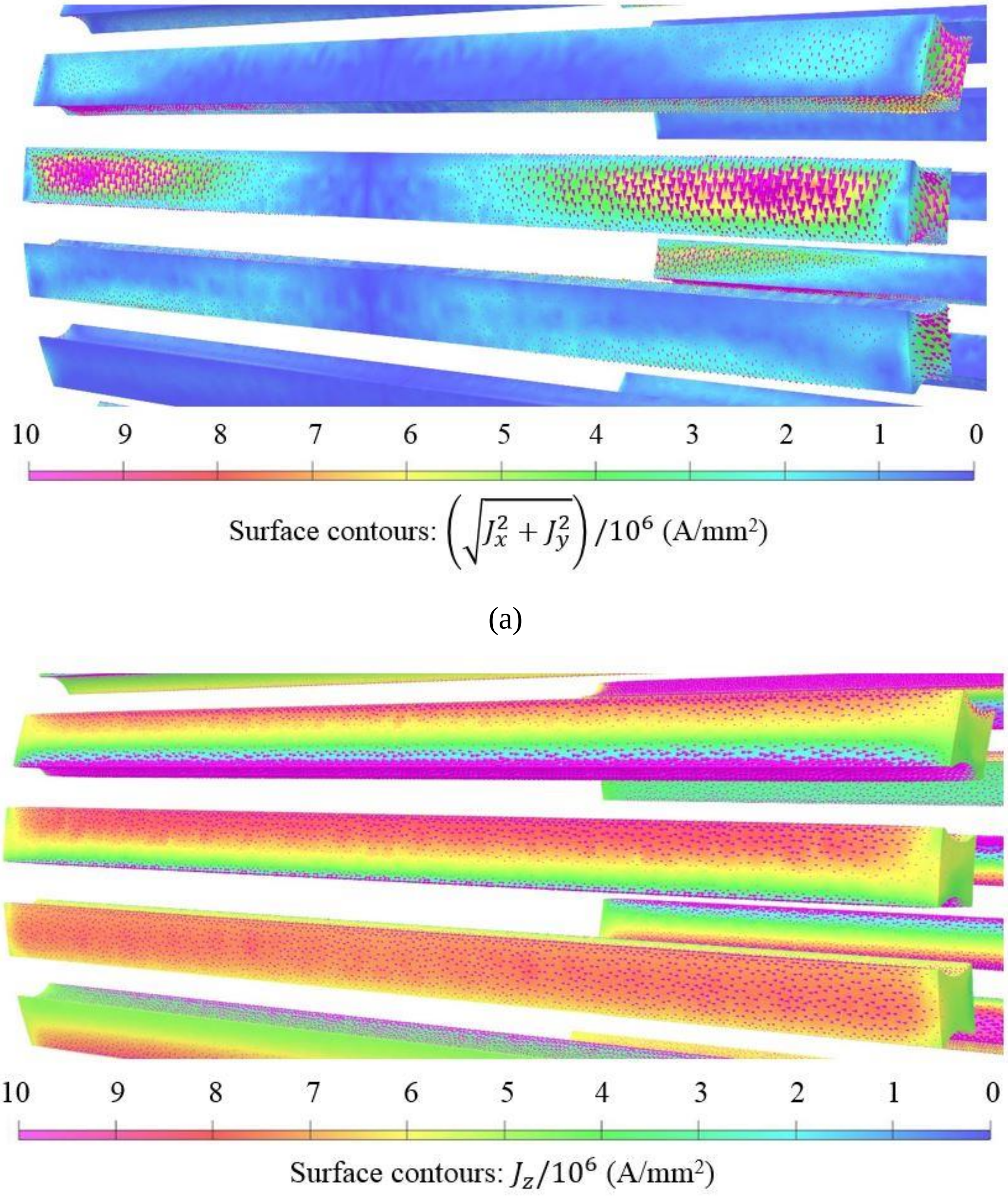

(a)

(b)

Figure 8.26. Pole piece eddy current density and vector plot of (a) XY-plane (b) Z-axis components

The comparison of the 2D and 3D FEA PPR eddy current losses is shown in Figure 8.27. It can be observed that the 2D and 3D loss predictions, due to Z-axis eddy current flow, are in good agreement. In contrast, the loss due to the XY-plane eddy current components represents 23% of the total 3D predicted PPR eddy current loss and 29% when compared to the 2D prediction. Thus, this shows that the pole piece loss is increased by the end leakage flux, with 3D FEA being required for an accurate and complete prediction.

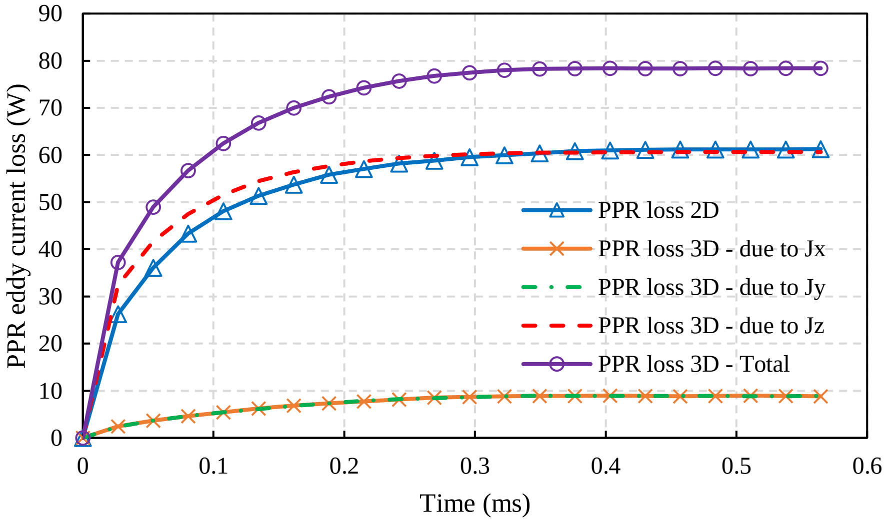

Figure 8.27. Comparison of 2D and 3D FEA PPR eddy current loss

8.5 Efficiency of fault-tolerant PDD motor

The efficiency of the fault tolerant PDD was predicted for the constant torque operating region by considering the winding copper losses, stator and PPR iron losses as well as the 3D predicted eddy current losses of the non-laminated components.

The prototype PDD efficiency for Active – Passive and Active – Active operation, while accounting for 3D eddy current losses and flux leakage end effects, is shown in Figure 8.28. During APOC operation, since only one lane of the duplex 3-phase winding is energised to produce rated torque, the copper loss doubled when compared to AA operation. This reduces the rated operation point efficiency to 79%.

If the PDD prototype is manufactured with laminated pole pieces and non-conductive stator PM sleeve, such that the eddy current losses are drastically minimised, the efficiency is substantially increased for both operation modes, as shown in Figure 8.29.

Thus, a maximum rated operating point efficiency of 93% can be obtained during Active-Active operation.

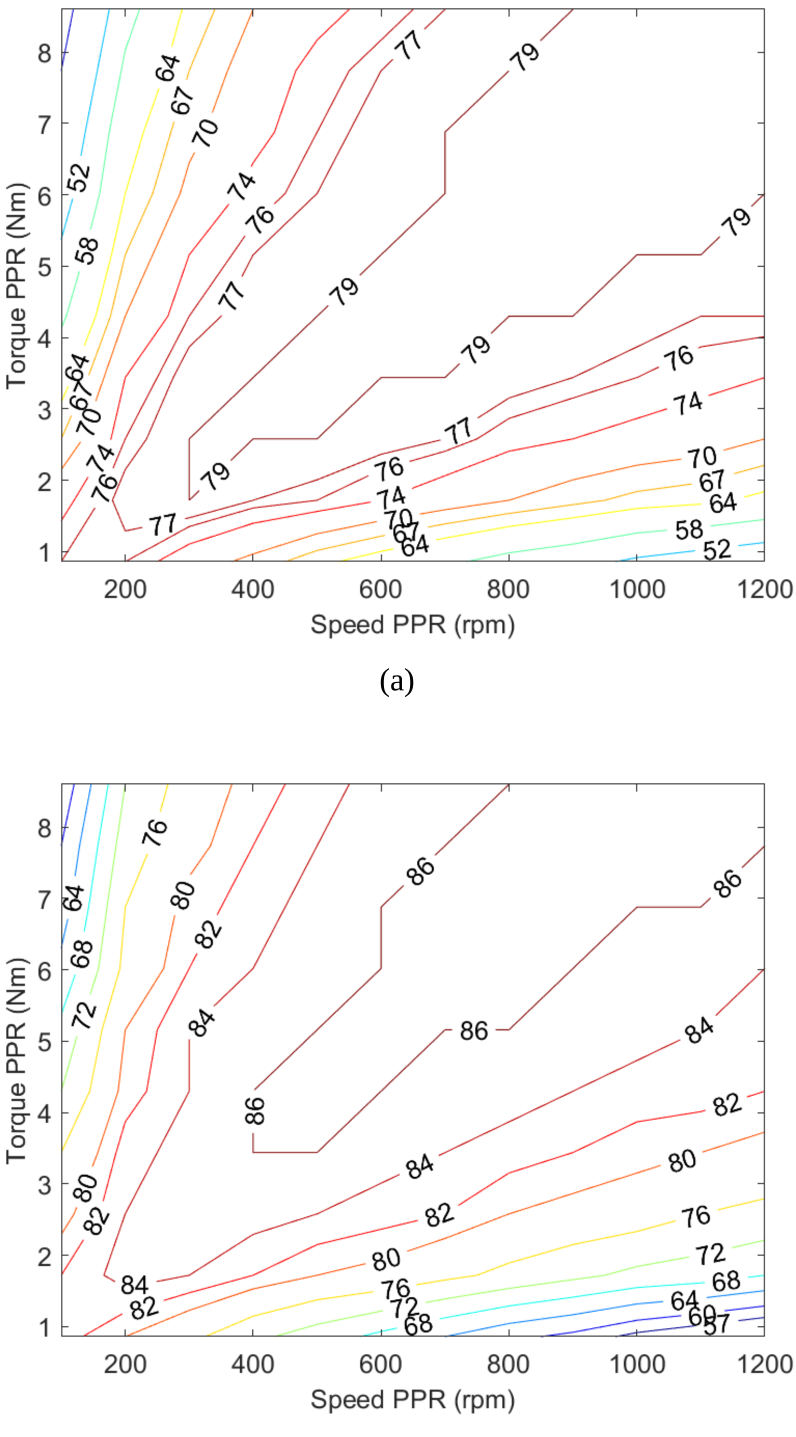

(a)

(b)

Figure 8.28. PDD efficiency in constant torque region with 3D FEA eddy current loss and PM flux linkage at (a) APOC (b) AA operation

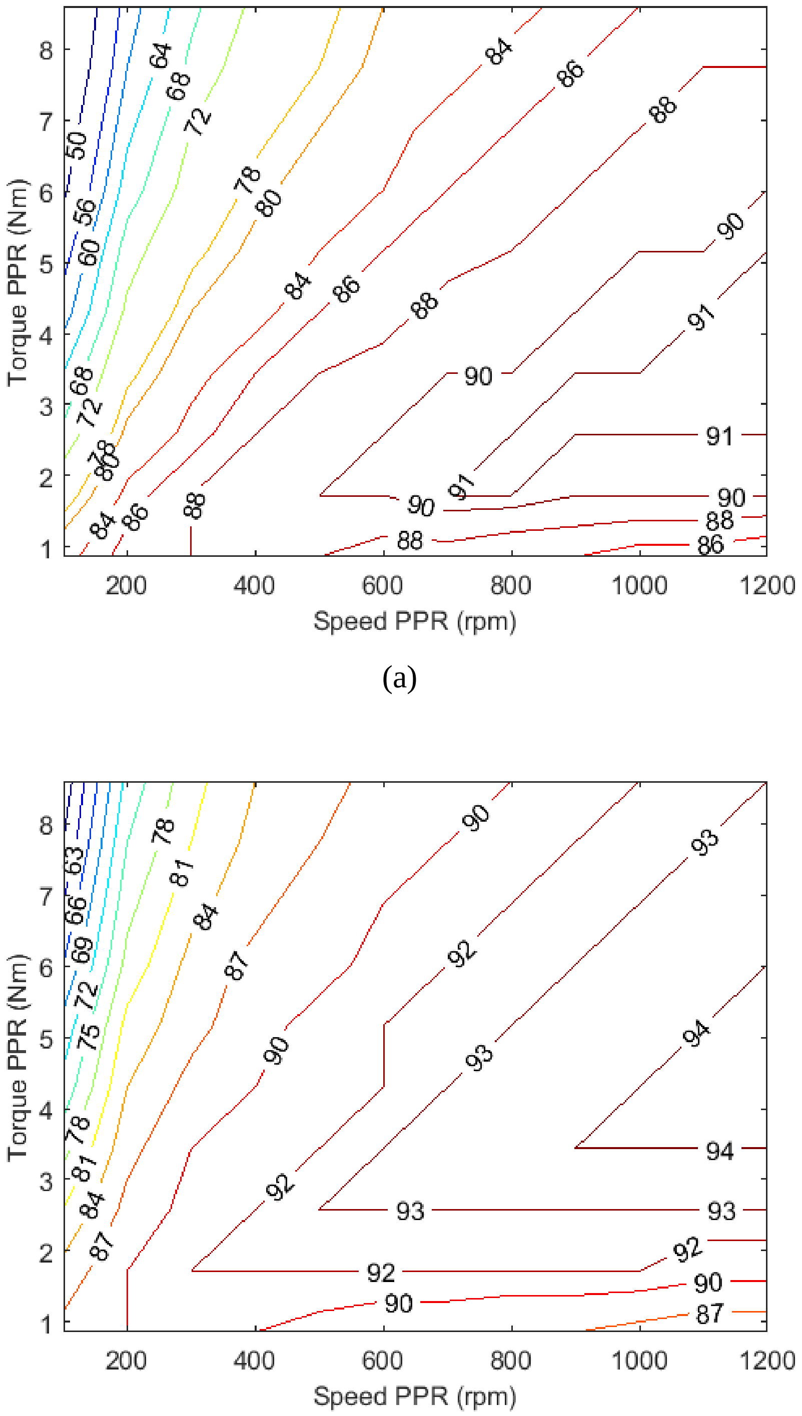

(a)

(b)

Figure 8.29. PDD efficiency in constant torque region with laminated components and non-conductive sleeve at (a) APOC (b) AA operation

8.6 Conclusions

The electromagnetic losses of the FT PDD, which include the copper loss, iron loss and eddy current loss of the non-laminated components, have been predicted from 2D and 3D FEA, for Active-Active and Active Passive operation.

The copper loss has been estimated for a PM temperature of 80^{o}C and copper temperature of 100^{o}C. The increase in phase current due to the drag torque generated by the eddy current losses of the non-laminated PDD components has been considered. It is shown that during Active-Active operation the copper losses are reduced by 50% when compared to Active-Passive operation, since both lanes require half the rated current to produce rated torque.

The iron losses of the stator and pole piece laminated stack have been predicted from 2D FEA during the two operating modes. It is shown that, when the non-laminated components are not considered, the stator iron losses in Active-Passive mode are increased by 20%, due to the localised stator tooth saturation, when compared to Active-Active operation. In contrast, when the phase current is increased to account for the drag torque generated by the losses in the PDD non-laminated components, the iron losses of the stator are increased by 11.3% and 5.4% for Active-Passive and Active-Active operation, respectively. The iron losses of the laminated pole pieces do not change significantly with the PDD operation mode.

The eddy current losses of the non-laminated components have been predicted from 2D and 3D FE simulations. It is shown that the eddy current losses are not substantially affected by the stator current loading, and only depend on the PM fields, from the HSR and stator arrays, and frequency.

It is shown that the eddy current losses in the steel hub of the HSR are negligible due to the fixed rotor hub magnetisation pattern given by the thick HSR PMs. The eddy current losses of the HSR and stator PMs show good agreement between the 2D and 3D FEA results. This is due to the PMs having cross-sectional dimensions which are significantly smaller than the active length of the electrical machine.

The eddy current losses of the non-laminated pole pieces, predicted in 3D FE, are 30% higher than the 2D FE estimation. It is shown that this increase in loss is due to the axial flux component, which flows through the pole pieces due to the large effective airgap of the PDD. Hence, the 2D FEA does not account for the pole piece eddy current loss in the XY-plane, generated by the time and position variant Z-axis magnetic field.

The eddy current loss of the Titanium sleeve was also investigated for several degrees of axial segmentation and with axially displaced slits. It is shown that, with conventional axial segmentation, the eddy current loss is reduced by 2.77 times when the number of segments is increased from one to four. For two axial segments, the introduction of axially and circumferentially displaced slits, resulted in the eddy current loss being reduced by a factor of 3.2. It was established that the eddy current loss, of the sleeve and stator PMs, is substantially increased when the two components are in electrical contact. In order to eliminate this loss component, the electrically conductive sleeve can be replaced with a composite variant, or an insulating layer can be placed between the sleeve and the stator PM array.

The efficiency of the manufactured FT PDD was predicted by considering the copper loss, stator and PPR iron losses and 3D predicted eddy current losses of the non-laminated components, for Active-Active and Active-Passive operation. It is shown that, for Active-Passive operation, the efficiency at the rated operation point is 79%, while for Active-

Active it is increased to 86%. The efficiency can be increased by laminating the pole pieces and replacing the Titanium sleeve with a composite variant. For this configuration the peak efficiency during Active-Passive operation was predicted at 91%, while for Active-Active this was increased to 94%.

Chapter 9: Manufacturing and experimental validation of MG prototype

The manufacturing and testing phase of the fault tolerant PDD actuator motor was divided in two stages. Due to small size of the proposed PDD design, much smaller than the previously manufactured PDDs from Magnomatics Ltd., it was decided to first manufacture and test a prototype of the magnetic gear element of the proposed fault tolerant PDD. Thus, the prototype magnetic gear is designed and manufactured to the same dimensions, with the same materials and using identical manufacturing processes to the fault tolerant PDD motor. This allowed for the active magnetic gear components of the PDD to be de-risked during no-load, on-load and pull-out torque tests. In particular, this includes de-risking of the Halbach PM HSR, PPR with non-laminated pole pieces and stator with the castellated Halbach PM array.

Based on the testing results of the magnetic gear prototype, the necessary adjustments can be made to the mechanical and electromagnetic design of the fault tolerant PDD design to ensure that the performance parameters are met.

The HSR de-risking investigated the manufacturing process, PM flux capability of the Halbach array, carbon fibre banding test at 10% overspeed (10230 rpm).

The PPR de-risking was concerned with the manufacturing process of two types of pole piece rotors, as shown in Figure 9.1. Both designs were based on the same 2x2 mm non-laminated pole piece cross-section. The PPR concept, shown in Figure 9.1 (a), is based on a carbon reinforced PEEK monocoque with slots machined for the ferromagnetic pole pieces. Two carbon fibre strips were wrapped on the outer circumference of the rotor in order to secure the pole pieces in the slots of the monocoque. Additionally, the pole pieces were bonded into the PEEK slots using DP760 adhesive.

In contrast, the G-11 truss PPR concept is based on glass fibre rods which engage with the pole pieces to transmit load. The G-11 rods are connected into the castellations of the endplates. Ceramic spacers are used at either end of each pole piece in order to isolate the pole pieces from the electrically conductive end-plates. DP760 adhesive was used to bond the G-11, pole pieces, ceramic spacers and end-plates.

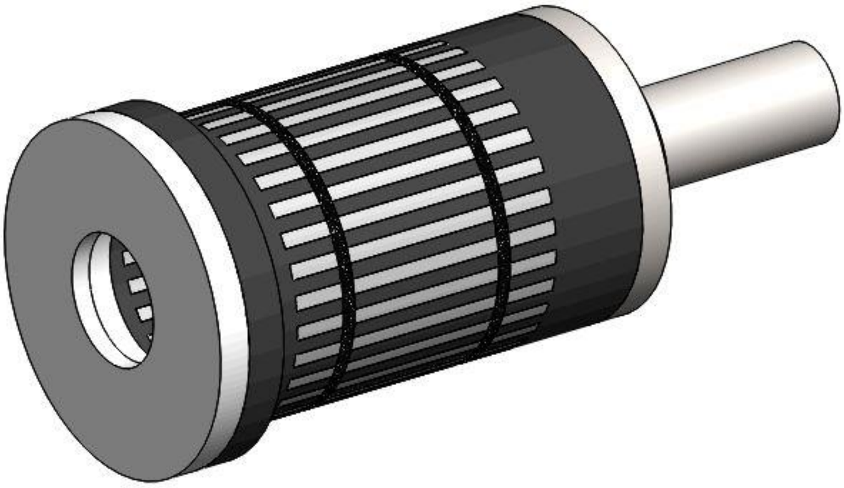

(a)

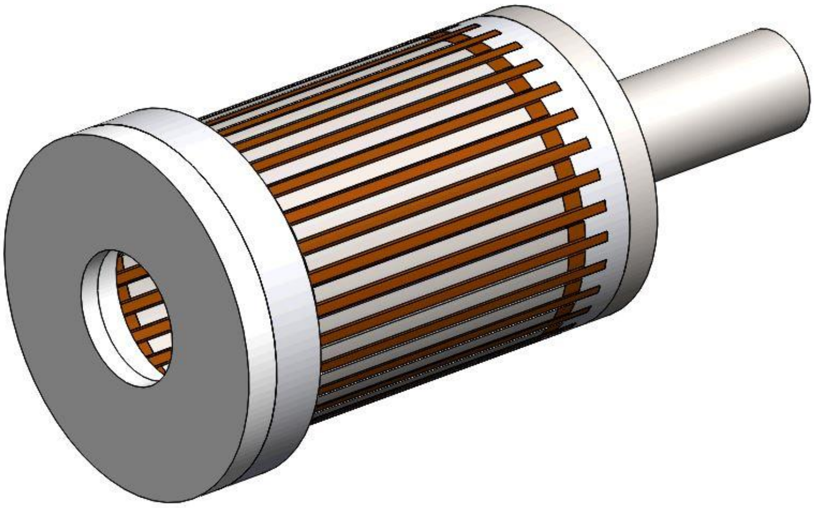

(b)

Figure 9.1. Pole piece rotor concepts (a) PEEK monocoque (b) G-11 glass fibre truss

The magnetic gear stator de-risking is mainly focused around the PM array manufactured from small individual PM blocks with different magnetisation directions. The stator stack represents an exact copy of the PDD stator bore with the castellations used for magnet positioning, as shown in Figure 9.2. The slot openings present in the PDD stator design were carried over in the magnetic gear demonstrator. This was done in order to check that the non-magnetic wedges can be inserter in the slot openings while providing a flat landing area for the stator PMs. The titanium sleeve was also fitted onto the inner diameter of the PM array.

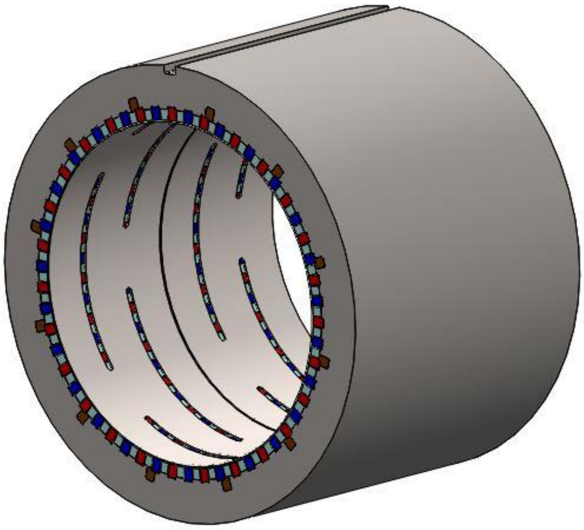

Figure 9.2. Magnetic gear laminated stator with Halbach PM array and titanium PM retention sleeve

9.1 Magnetic gear prototype design

The electromagnetic magnetic gear cross section is shown in Figure 9.3. This represents the cross-section from which the mechanical model and manufacturing drawings were produced.

The torque transmission capability of the magnetic gear is shown in Figure 9.4. This is based on 2D transient FE analysis for an active length of 39.4 mm required to achieve a pull-out torque of 10.3 Nm. For the magnetic gear de-risking studies, a PM temperature of 25^{o}C was assumed. 3D FEA was conducted in order to quantify the flux leakage end effects and adjust the gear active length. Thus, the analysis showed that the active length of the magnetic gear has to be increased to 45mm in order to obtain 10.3 Nm pull-out torque. This represents a 14.5% increase in length and mass from the 2D predictions.

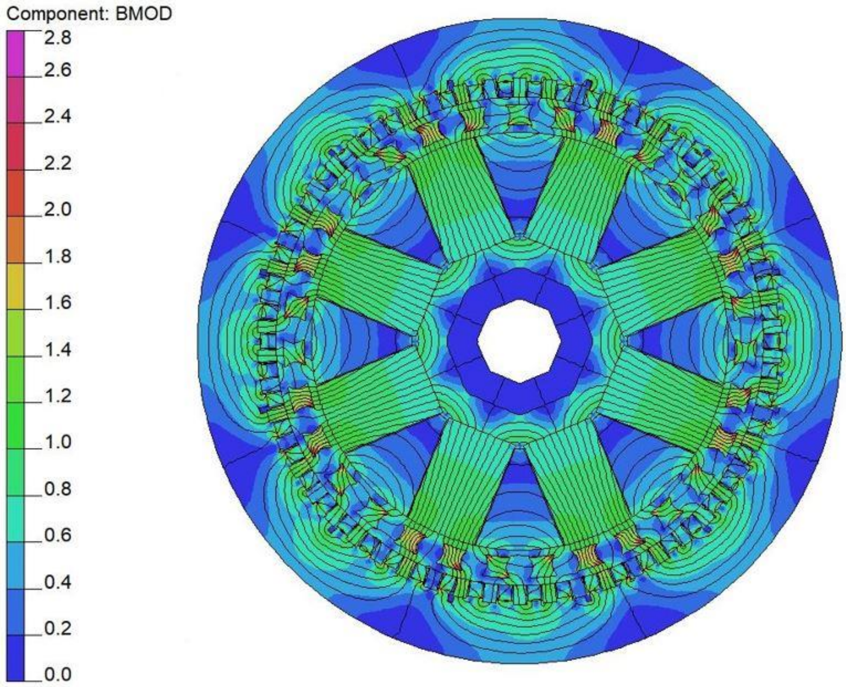

Figure 9.3. Magnetic gear magnetic flux density plot

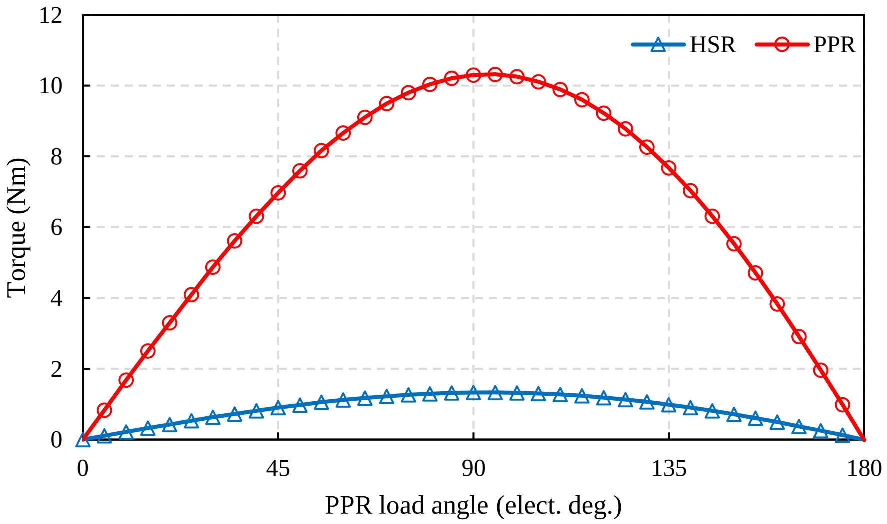

Figure 9.4. Magnetic gear torque transmission capability

The specification and performance parameters of the magnetic gear prototype is shown in Table 9.1. The rated torque and speed specification is identical to that of the fault tolerant PDD motor. The total weight represents the weight of the magnetic gear prototype which includes the outer case and endplate. The active weight is 62.2% of the total weight and represents the weight of the active components which includes the HSR, PPR, stator stack with PM, rotor endplates and bearings. The losses of the magnetic gear have been predicted with a PM temperature of 25^{o}C at the rated output speed of 1200 rpm with the gear simulated with a load angle of 90^{o}. The stator iron losses have been predicted from 2D FEA, while the PPR, PM and sleeve losses have been predicted in 3D FEA, where a perfect insulator was considered between the sleeve and outer PM array.

By utilising the magnetic gear 2D electromagnetic cross-section, a prototype model was built in SolidWorks, as shown in Figure 9.5. The input side of the gear is represented by the HSR shaft, while the PPR output shaft is connected to the load and represents the output low side. The HSR and PPR both require two bearings each such that the HSR can rotate freely inside the PPR, with a magnetic gear ratio of 7.75:1.

Table 9.1. Specification of magnetic gear prototype

Rated torque	8.6	Nm
Pull-out torque	10.3	Nm
Rated output speed	1200	rpm
Rated HSR speed	9300	rpm
HSR pole pairs	4	
Pole pieces	31	
Stator pole pairs	27	
Gear ratio	7.75 : 1	
Active length	45	mm

Total weight	1.88	kg
HSR PM weight	0.358	kg
Stator PM weight	0.085	kg
Active weight	1.17	kg
HSR outer diameter	39.6	mm
HSR PM thickness	10 / 10.3	mm
PPR outer diameter	45	mm
Pole piece thickness	2	mm
Stator PM thickness	1.5 / 1.8	mm
Back-iron thickness	6	mm
Stator outer diameter	62	mm
Inner airgap	0.7	mm
Outer airgap	0.7	mm
HSR carbon fibre wrap	0.2	mm
Stator PM sleeve	0.2	mm
Inertia HSR	379	gcm^2
Inertia PPR	1128	gcm^2
Case outer diameter	76	mm
Case total length	110	mm
Max. temperature	150	^{o}C
Stator iron loss	7.5	W
PPR iron loss	67.8	W
PM loss	5.9	W
Sleeve loss	6.3	W
PM material	Recoma 28	
Steel	M270-35A	
Sleeve	Titanium Grade 5	

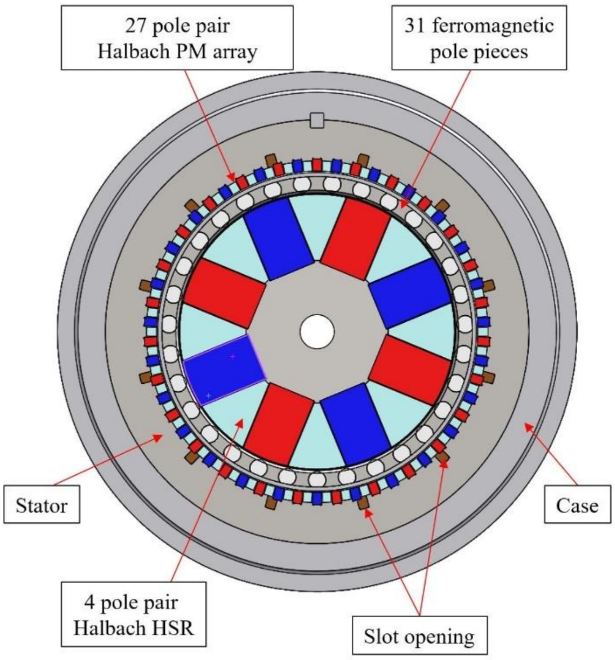

(a)

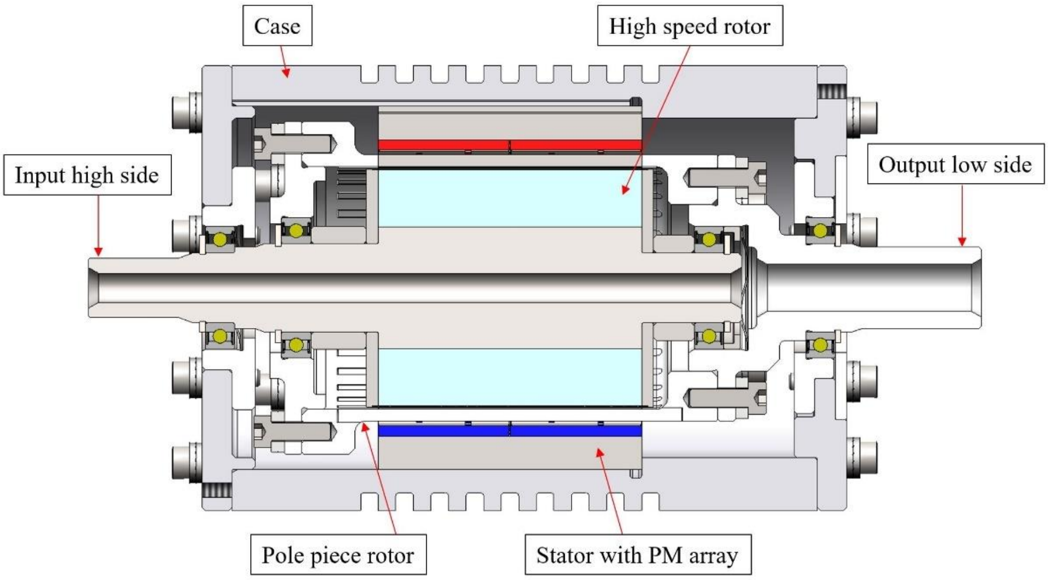

(b)

Figure 9.5. Magnetic gear prototype (a) cross-section (b) side-view

9.2 Manufacturing of magnetic gear prototype

The prototype model shown in Figure 9.5, was used to produce engineering drawings for all the parts required to assemble the magnetic gear demonstrator. The main components required to assemble the magnetic gear prototype are shown in Figure 9.6. The magnetic gear is designed such that the PEEK and G-11 glass fibre truss PPRs are interchangeable within the structure of the demonstrator unit. This allowed for the different PPRs to be tested with the same HSR and stator assemblies, in order to accurately assess their performance characteristics.

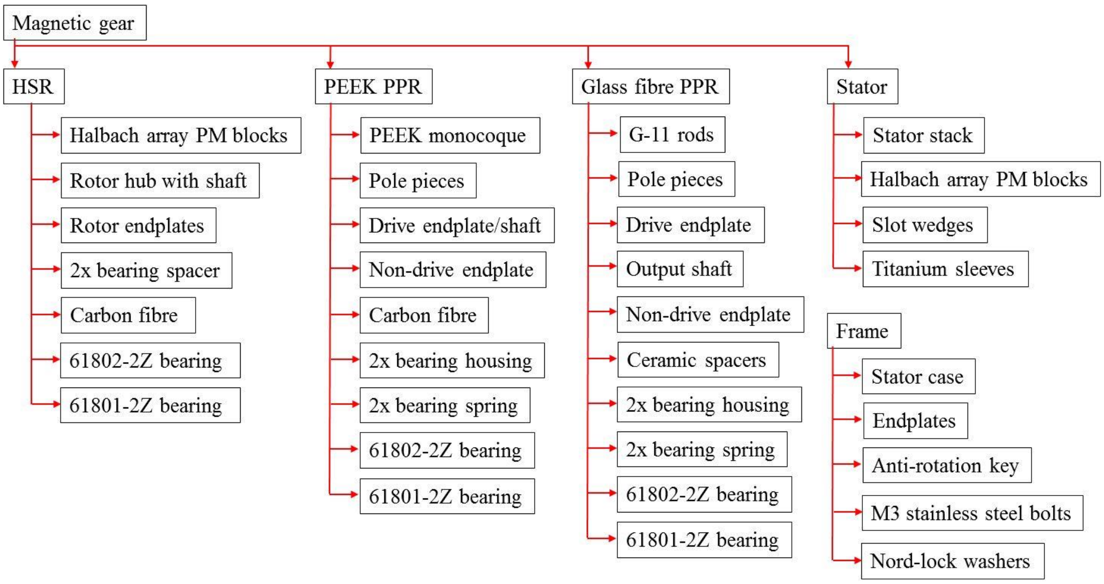

Figure 9.6. Main components of magnetic gear prototype

9.2.1 High speed rotor assembly

The high-speed rotor assembly, Figure 9.7, was manufactured by Arnold Magnetic Technologies in Sheffield, who also supplied the cut and magnetised Halbach PM blocks. The PM blocks have been glued to the surface of the HSR hub with Loctite 3342 adhesive which is activated using Loctite SF 7386 activator. A mixture of 20 parts adhesive and 1 part 0.1mm glass beads, by weight, was used to ensure uniform bond thickness. After the PM blocks are fixed onto the surface of the HSR hub and the glue has set, the Inconel 718 endplates are glued onto the sides of the HSR PM array. Once the endplates are fixed and the adhesive has set, the 0.5mm of carbon fibre overwrap is applied. Ultimeg 2220 varnish was applied to the surface of the carbon fibre tow during winding on the rotor surface. Once the overwrap is complete, the assembly is cured for 12 hours at 150^{o}C. When the resin curing process is complete, the excess carbon fibre is ground off and a 0.2mm carbon fibre sleeve is obtained on the outer diameter of the PM array. The bearing spacer is a loose fit on the surface of the HSR shaft, its only purpose being to space the rotating bearing from the endplate of the HSR. The HSR was balanced up to a speed of 10700 rpm by removing material from the endplate.

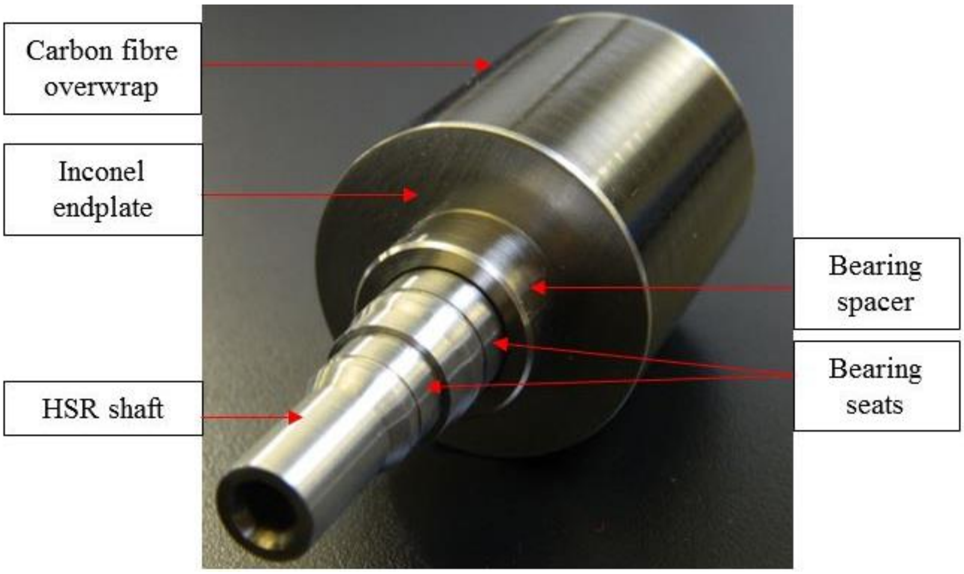

Figure 9.7. High-speed rotor assembly

9.2.2 PEEK pole piece rotor assembly

The PEEK PPR is based on a monocoque pole piece support structured manufactured from 30% carbon fibre reinforced polyether ether ketone. The datasheet of this material is shown in Appendix 1. The monocoque structure, shown in Figure 9.8, was machined from a solid block of PEEK. This material proved to be very difficult to machine due to the hollow cylinder structure and thin cross-section, with one out of four support structures being damaged during machining. Figure 9.9 shows the PEEK rotor which was damaged during manufacturing, due to material failure.

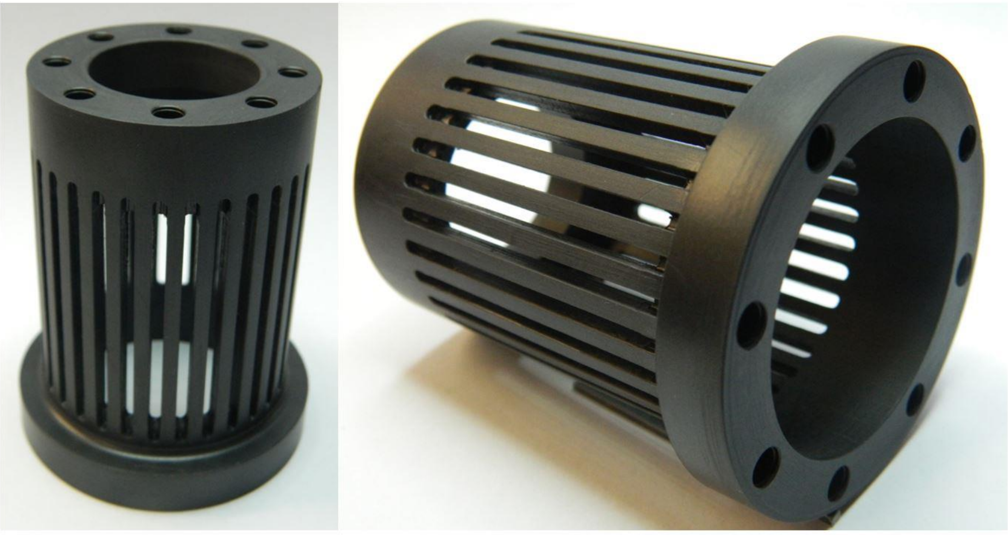

Figure 9.8. PEEK pole piece rotor support structure

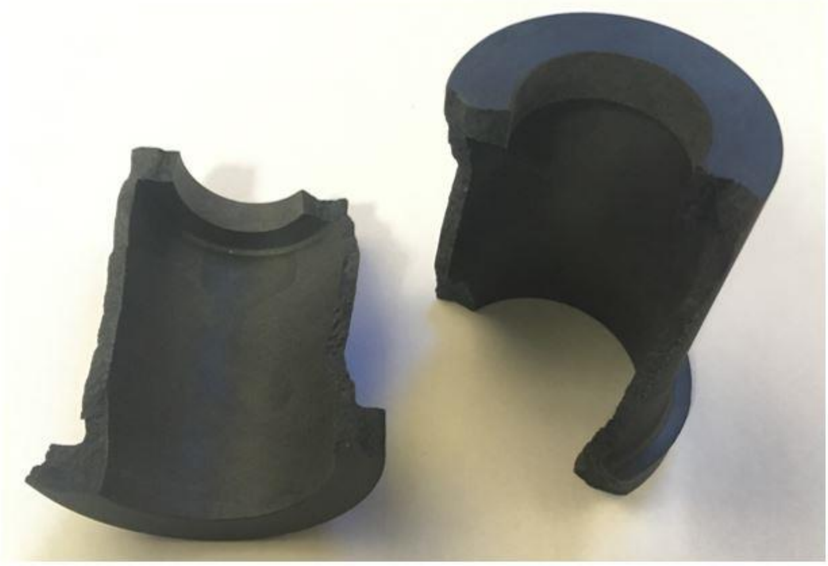

Figure 9.9. PEEK material failure during machining

The non-laminated ferromagnetic M270-35A pole pieces used for the manufacture of the PEEK PPR are shown in Figure 9.10. Before bonding, the pole pieces were grit-blasted with Guyson Saftigrit Brown in order to create a rough surface finish and increases the available bonding surface. After grit blasting, both the pole pieces and monocoque support structure were cleaned with acetone in order to remove any contaminants, such as oil, grease or grit residue, which would affect the quality of the bond.

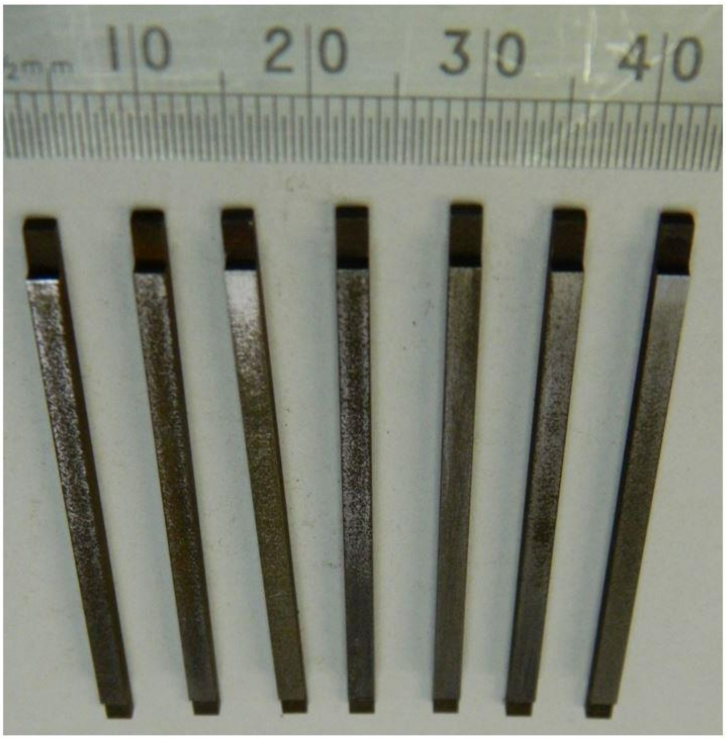

Figure 9.10. Pole pieces used in PEEK PPR assembly

The drive endplate with the PPR output shaft and non-drive endplate are shown in Figure 9.11. Both parts were machined from EN24T alloy steel and are connected to the PPR support structure using M3x8mm stainless steel socket head bolts with nord-lock wedge locking washers. Such washers help secure the bolts by tension rather than friction, which makes this type of washer ideal for applications characterised by dynamic loads.

Figure 9.11. PPR output shaft with drive end plate and non-drive end plate

The assembled PEEK PPRs, prior to surface grinding, are shown in Figure 9.12. The steel pole pieces have been glued into the machined slots using 3M Scotch-Weld DP760 adhesive. A mixture of 20 parts adhesive and 1 part 0.1mm glass beads, by weight, was used to ensure uniform bond thickness. The adhesive was cured for 120 minutes at 65^{o}C.

Figure 9.12. Assembled PEEK PPR with pole pieces

The PEEK PPR was then ground on the inner and outer diameter to remove the excess adhesive and achieve a smooth surface finish. Two channels were machined along the outer diameter of the rotors in order to accommodate the carbon fibre over-wrap rings, as shown in Figure 9.13 (a). Non-magnetic threaded brass inserts were glued in the holes at the drive and non-drive ends of the PEEK PPR. These were used to secure the endplate of the PPR to the PEEK support structure. Figure 9.13 (b) shows the assembled HSR - PPR assembly. The PPR has been overwrapped with two carbon fibre rings in order to provide a secondary retention method for the pole pieces in the event of adhesive failure. The PEEK PPR was balanced up to speed of 1300 rpm by taking material off from the PEEK support structure.

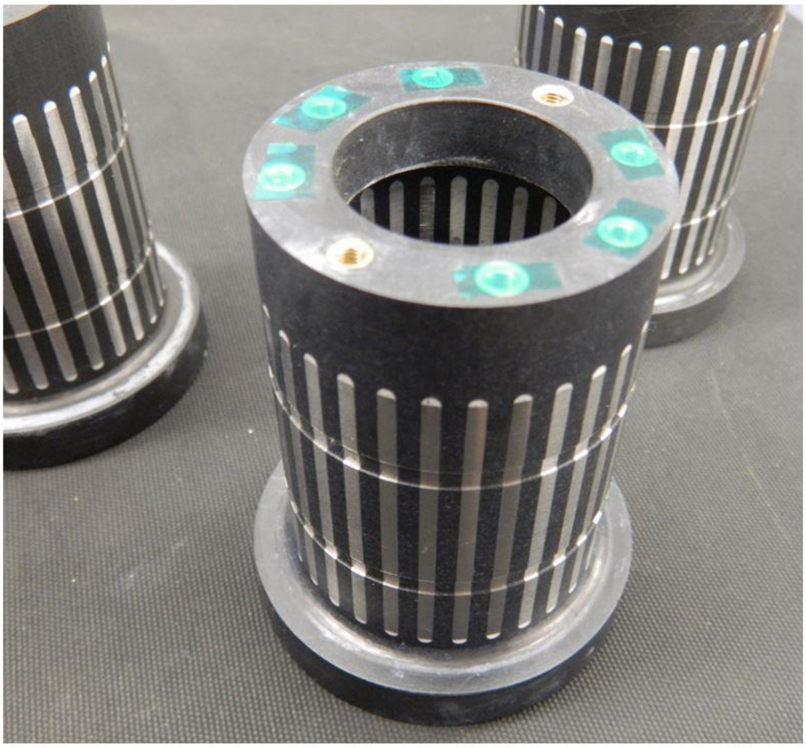

(a)

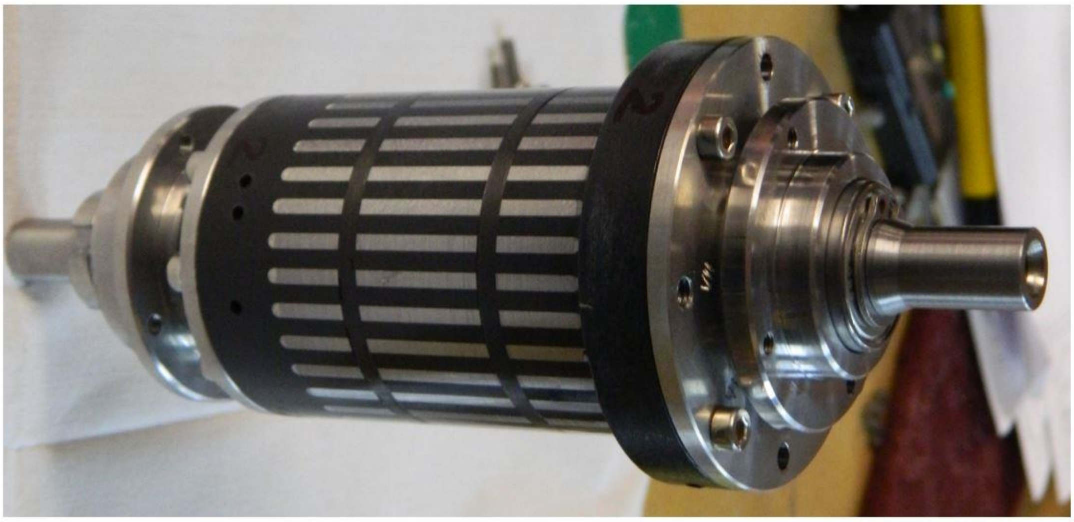

(b)

Figure 9.13. PEEK PPR (a) post grinding (b) assembled PPR with carbon fibre overwrap

9.2.3 Glass fibre truss pole piece rotor assembly

The glass fibre truss PPR design is based on G-11 pultruded rods with a diameter of 2.5 mm, that engage with the PPR endplates and pole pieces to transmit torque to the load. The drive and non-drive endplates of the truss PPR are shown in Figure 9.14. The machined slots are used to fix the glass fibre rods and bond them to each endplate. The endplates were machined from Inconel 718 with a relative permeability of 1.0013. Due to their relative vicinity to the HSR and stator PM arrays, the eddy current losses were predicted at rated speed operation using the 3D FE software. Figure 9.15 shows that the losses are negligible at 10 mW for both endplates.

The pole pieces used for this PPR design are shown in Figure 9.16. The side cut-outs are designed to allow the G-11 rods to engage with each pole piece and transmit load. Similarly to the PEEK PPR, these pole pieces have been grit-blasted and cleaned with acetone before bonding.

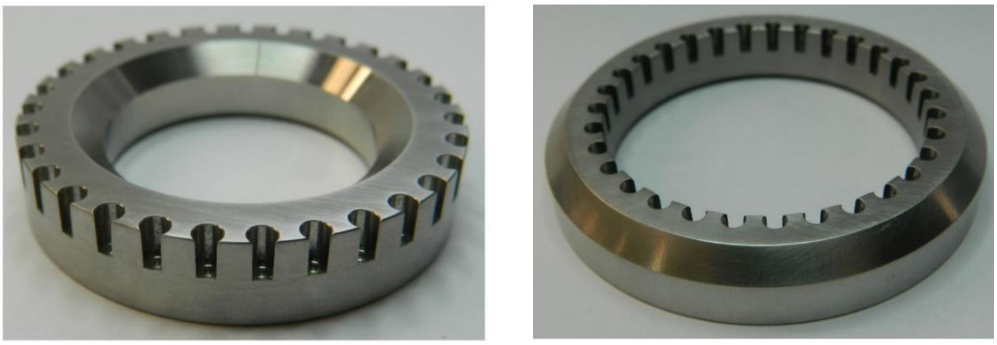

(a) (b)

Figure 9.14. (a) Drive (b) Non-drive endplates of glass fibre truss PPR

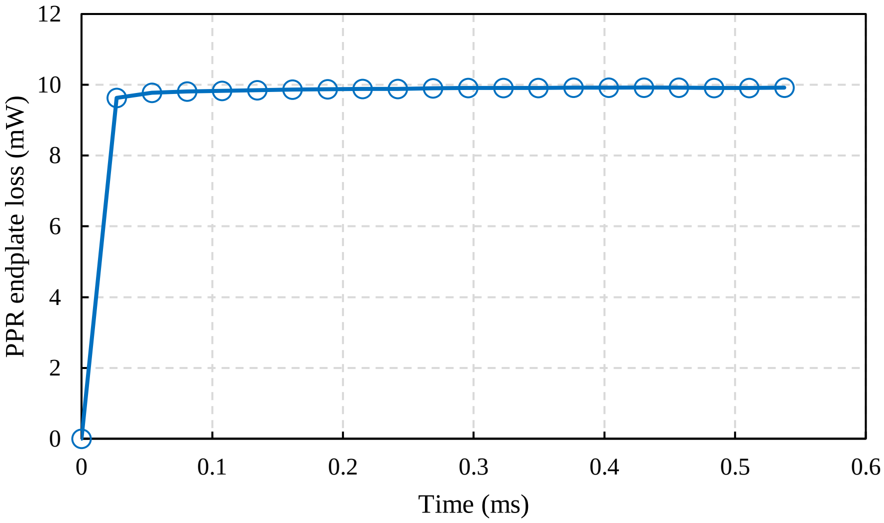

Figure 9.15. PPR Inconel 718 endplate loss

Figure 9.17 shows the ceramic spacers used to separate the ferromagnetic pole pieces from the electrically conductive Inconel endplates of the PPR. This ensures that a squirrel cage rotor is not created, and the eddy currents are confined in each pole piece without flowing through the endplate and into the adjacent pole pieces.

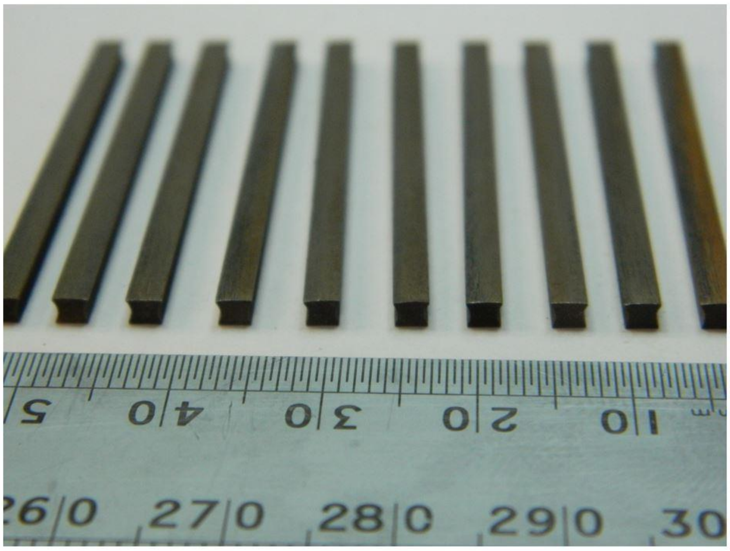

Figure 9.16. Pole pieces used for glass fibre truss PPR

Figure 9.17. Ceramic insulator end rings for glass fibre truss PPR

Figure 9.18 shows the dry-fit between the Inconel endplate, G-11 rods and pole pieces. The ceramic spacers have been omitted for this trial. The diameter of the endplate castellation was designed to allow for a 0.1mm bond line between the glass fibre rods and endplate. The truss PPR was assembled by inserting the G-11 rods in the drive endplate, around the PPR tooling shown in Figure 9.19. The channels machined in the aluminium tooling cylinder act as guides for the glass fibre rods. After each G-11 rods was inserted in the drive endplate, a pole piece would follow. Throughout the assembly operation, all the parts were covered in DP 760 adhesive with the same amount of glass beads as the PEEK PPR. In order to be able to separate the tooling from the completed PPR, a layer of conformal coating was applied to the tooling cylinder prior to bonding. This ensured that the completed PPR assembly can cure without bonding to the tooling cylinder.

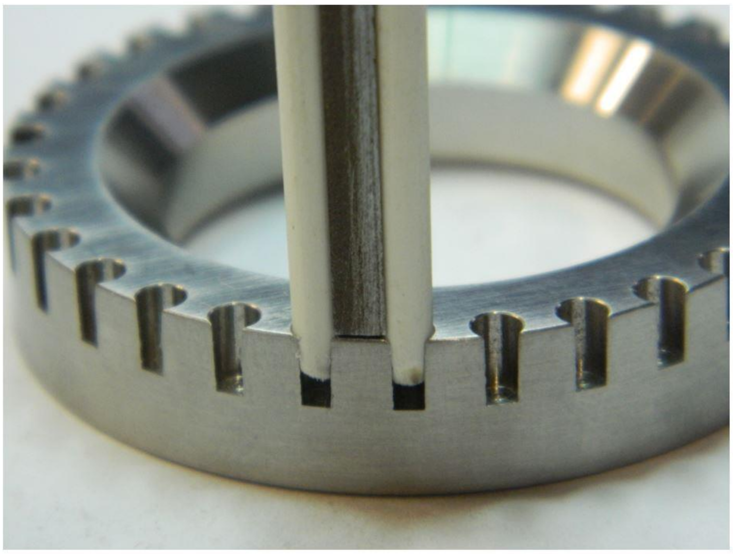

Figure 9.18. Dry fit of glass fibre rods and pole piece in PPR drive endplate

Figure 9.19. PPR tooling

After the curing cycle was complete, the tooling was removed with the help of a hydraulic press. Figure 9.20 shows the completed glass fibre PPR assembly before grinding. It can be observed that the glue layer on the inner diameter is intact, showing that the conformal coating did not allow the tooling to stick to the PPR while the adhesive was curing.

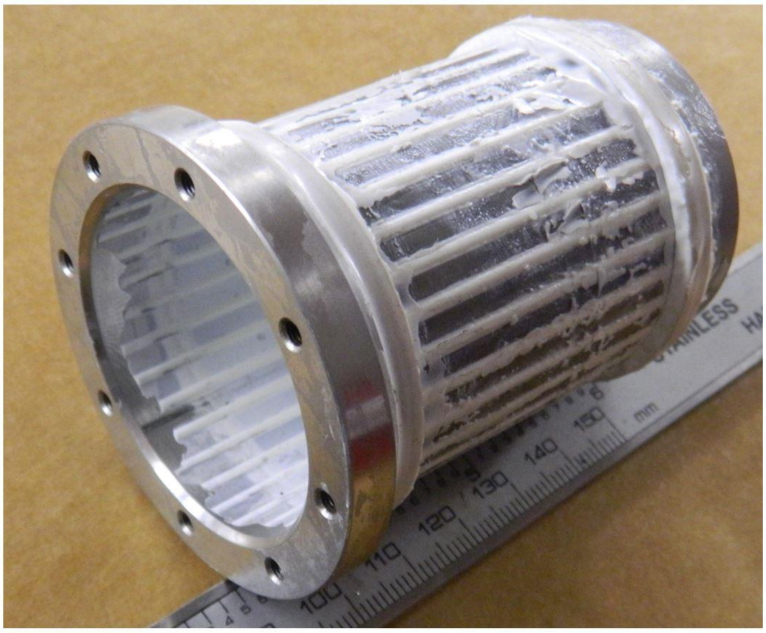

Figure 9.20. Assembled glass fibre PPR prior to grinding

After the tooling was removed, the PPR was sent for grinding along the inner and outer diameters. This removed the excess adhesive, together with the excess material of the glass fibre rods, as shown in Figure 9.21 (a). The PPR was balanced to a maximum speed of 1300 rpm by removing material from the Inconel endplate.

(a) (b)

Figure 9.21. Glass fibre truss PPR (a) post grinding (b) assembled PPR

9.2.4 Stator assembly

The magnetic gear stator assembly consists of a laminated stator stack, Halbach PM array, non-magnetic 3D printed slot wedges and grade 5 Titanium sleeve. The bonded stator stack was manufactured from M270-35A 0.35mm thick lamination steel. Figure 9.22 (a) shows the stator stack and non-magnetic slot wedges. The laminations for the stator stack were laser cut, with the inner bore of the stator having small castellations which allow for the stator magnets to be correctly positioned, as shown in Figure 9.22 (b). The stator stack also features the slot openings present in the PDD stator design. This allowed for a trial fit of the non-magnetic wedges in order to ensure that the created landing area is flat and allows correct positioning of the stator PMs.

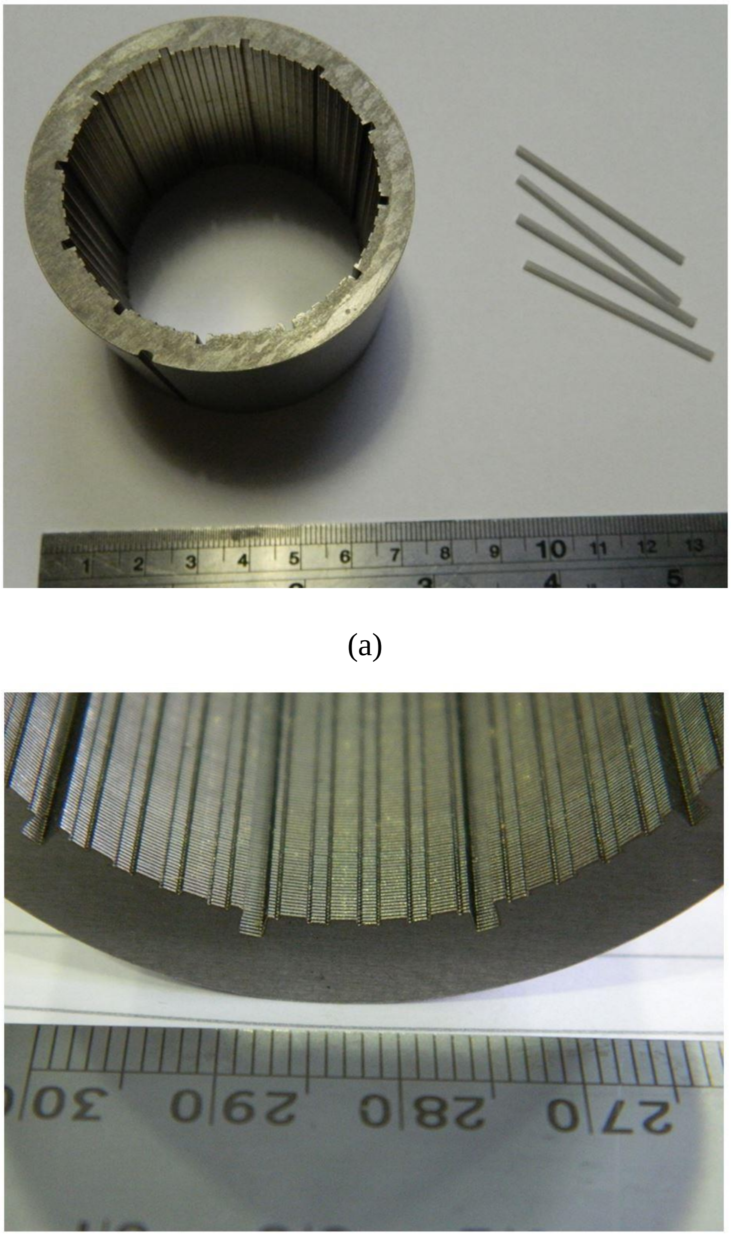

(a)

(b)

Figure 9.22. Magnetic gear (a) stator stack and slot wedges (b) castellations of laminated stator stack

Unfortunately, the 3D printed slot wedges were out of tolerance and did not allow the stator PMs to sit correctly within the castellations, as shown in Figure 9.23 (a). Each slot wedge was manually adjusted using hand files, until the correct fit was obtained. The adjusted slot wedge with the PM block sitting correctly within the castellation is shown in Figure 9.23 (b).

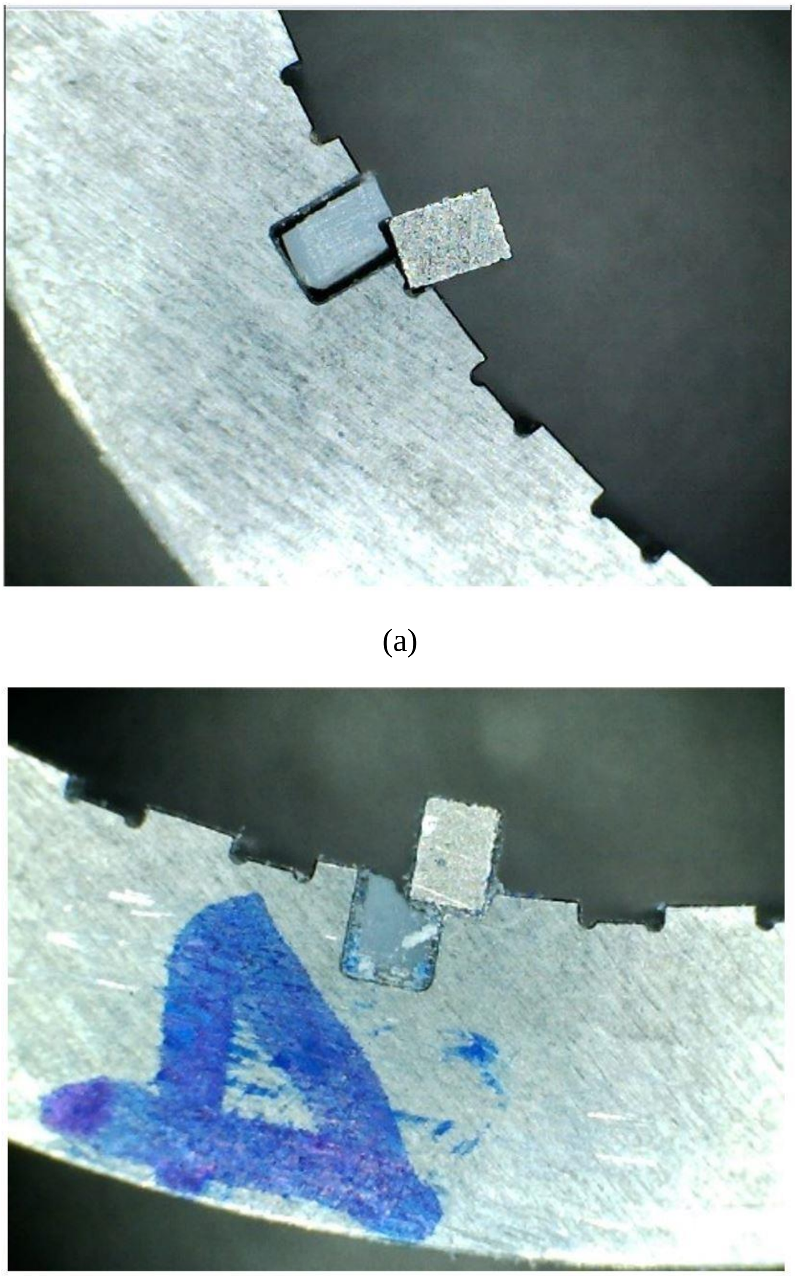

(a)

(b)

Figure 9.23. Slot wedge and stator PM trial fit (a) with original parts (b) post grinding of slot wedge

After all the wedges were adjusted and marked to a corresponding slot-opening, the stator stack and slot wedges were sent to Arnold Magnetic Technologies for magnet bonding. Figure 9.24 (a) shows the completed stator Halbach PM array prior to titanium sleeve insertion. In order to simplify the PM bonding process, the radially magnetised PMs which sit in the deep castellations were fitted first. After the radial array was complete, the circumferential PMs were bonded to the stator stack. Moreover, the Halbach PM array was segmented in half along the axial length in order facilitate assembly and reduce the number of breakages.

Due to the tolerance stack-up and tendency of the circumferentially magnetised PMs to be attracted to the radially magnetised PMs, there is a slight mismatch with respect to the two axial PM arrays, on the finished stator PM array. Figure 9.24 (a) shows that the two axially displaced Halbach PM arrays are not exactly aligned along the axial length of the machine. Figure 9.24 (b) shows the two segments of the titanium sleeve inserted in the stator assembly, prior to grinding. Due to the interference fit between the inner bore of the PM array and the outer diameter of the sleeve, the stator was heated to 80^{o}C and the titanium rings were cooled in liquid nitrogen. Once the parts have reached thermal equilibrium, the titanium rings were inserted into the stator assembly. The last operation was grinding the inner bore of the titanium sleeve to obtain a wall thickness of 0.2mm.

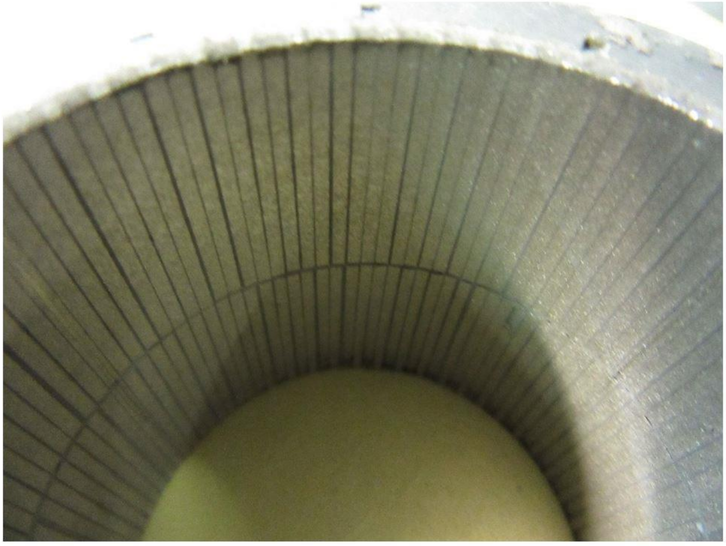

(a)

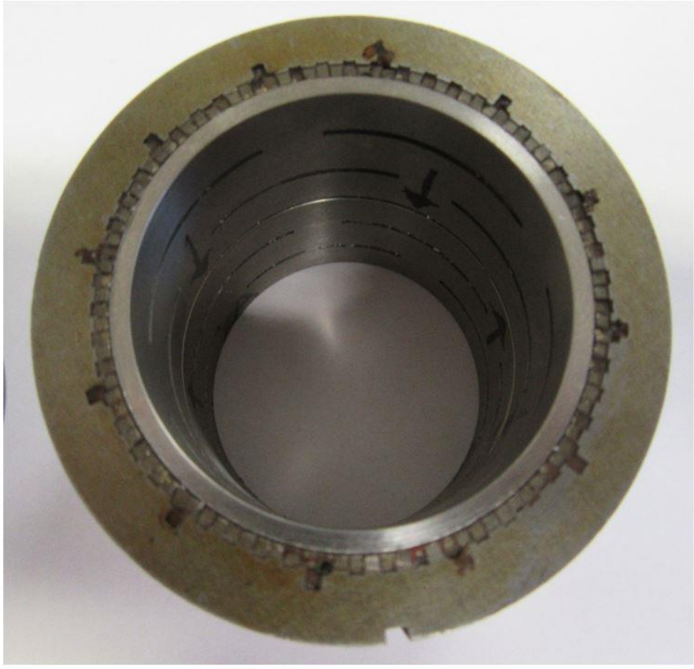

(b)

Figure 9.24. Magnetic gear stator (a) post Halbach PM assembly (b) post Titanium sleeve insertion

The finished magnetic stator assembly, with the ground sleeve, is shown in Figure 9.25. The Titanium sleeve used in this prototype was not insulated from the stator PM array. Thus, the power loss will vary based on the degree of electrical contact between the two parts.The final operation, in manufacturing the stator assembly, was fitting the stator into the case, as shown in Figure 9.26. A key was fitted to the stator stack which would engage with the slot on the case and act as an anti-rotation feature. Although the two parts are designed with an interference fit, during prolonged operation, the increase in temperature can cause the case to expand more than the stator stack, reducing the effectiveness of the interference fit. This is due to the high radial thermal expansion coefficient of aluminium which is twice as high as that of iron. Thus, purpose of the key is to provide a reliable connection between the two parts and prevent relative rotation while torque is being transmitted to the load.

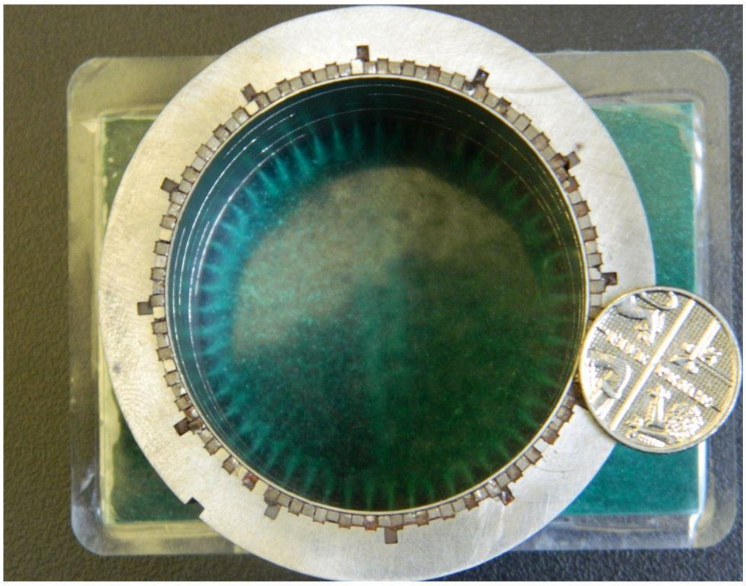

Figure 9.25. Completed magnetic gear stator assembly with 5p coin for size reference

Due to the interface fit between the two parts, the case was heated to a temperature of 140°C, while the stator assembly was left in the freezer at -18°C, for approximatively 18 hours. After thermal equilibrium was reached, the cooled stator with the key were inserted into the hot case.

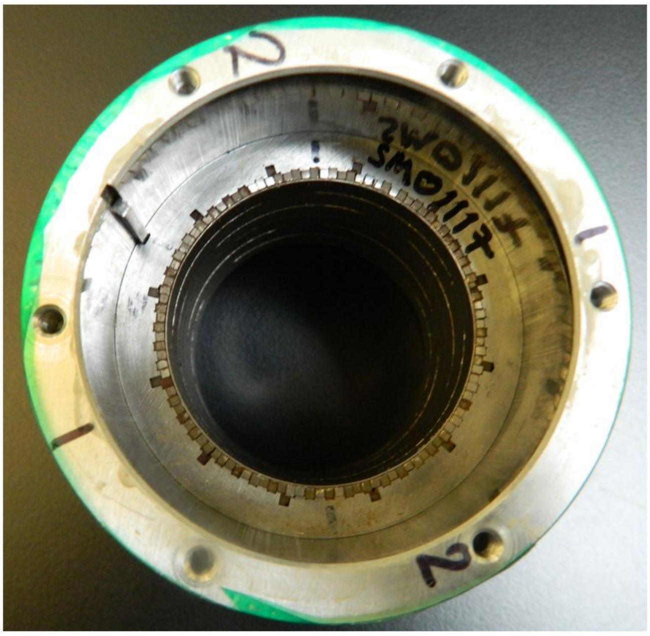

Figure 9.26. Stator heat fitted to case

9.2.5 Magnetic gear final assembly

After inserting the HSR into the PPR and securing the PPR endplates to the support structure, the HSR-PPR assembly can be inserted into the stator-case assembly, as shown in Figure 9.27. Guide pins, which screw into the PPR endplate and pass through the case drive endplate, are used to guide the HSR-PPR assembly into the case. Once the HSR-PPR assembly is in the stator-case assembly, M3x10mm stainless steel bolts with nord-lock washers are used to clamp the bearing housings on the PPR drive end and HSR non-drive end to the case drive endplate and non-drive endplate, respectively. The case endplates are then bolted to the case of the magnetic gear. The completed magnetic gear prototype is shown in Figure 9.28.

Figure 9.27. Final assembly of magnetic gear prototype

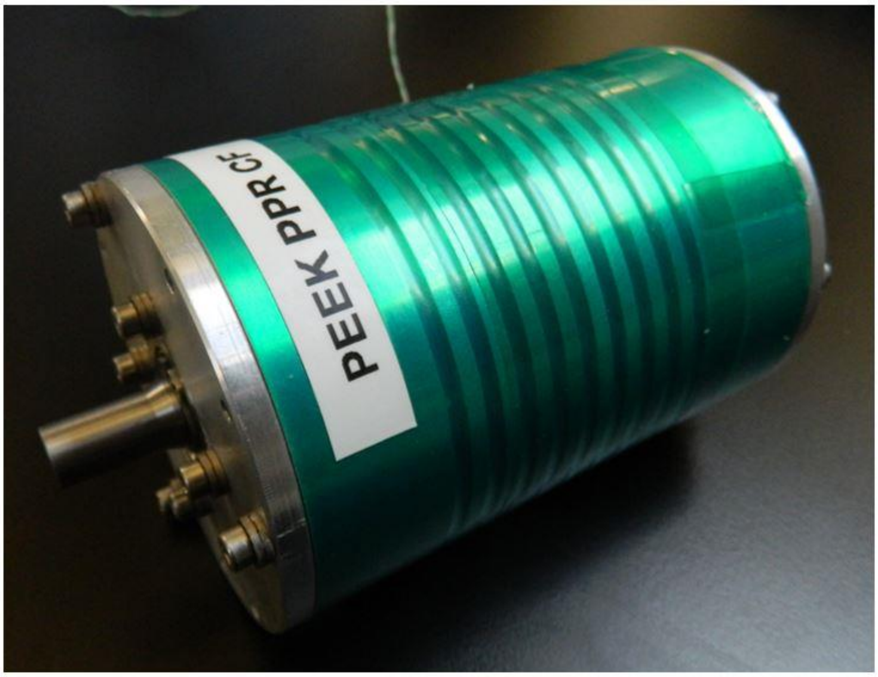

Figure 9.28. Completed magnetic gear prototype

9.3 Magnetic gear test dynamometer

The magnetic gear prototype testing was conducted at Magnomatics Ltd., on a bespoke KEB dynamometer. The magnetic gear dynamometer test setup is shown in Figure 9.29. A KEB TA41-V40-ER-TW PM servo drive was connected to the input or high-speed side of the magnetic gear through a 2:1 belt drive. This was required since the maximum speed of the input machine is limited to 5000 rpm, while the gear maximum input speed is 9300 rpm. A 5 Nm Sensor Technology RWT 410 series torque transducer was used to measure the input torque and speed of the magnetic gear input shaft. The output side of the magnetic gear was connected to a KEB TA61-V30-ER-TW load machine via a 30Nm Sensor Technology RWT 410 series torque transducer. Temperature sensors were mounted on the magnetic gear stator next to the PMs, and on the outside of the case, in order to ensure that the safe operating temperature is not exceeded. Each electrical machine on the test rig was aligned to its mating machine shaft by using the TKSA20 SKF laser shaft alignment tool.

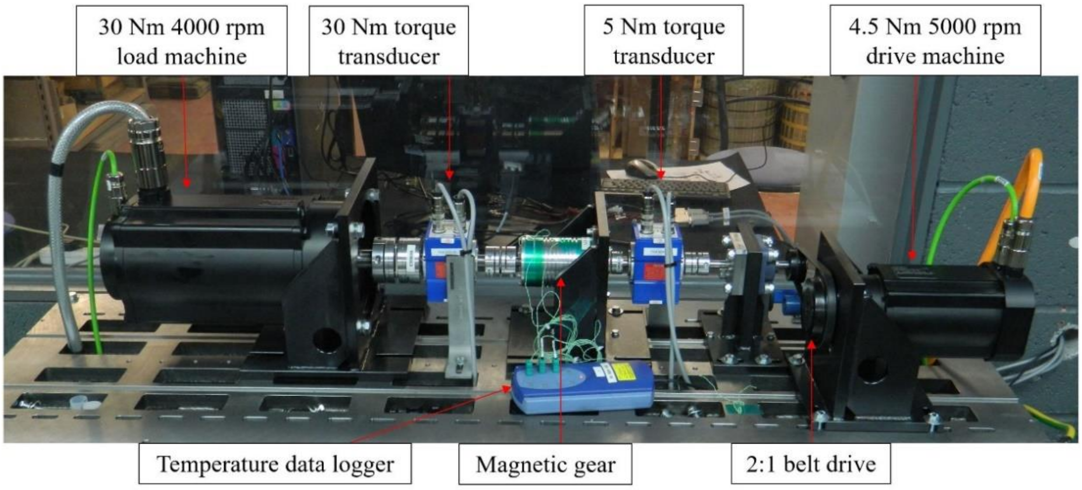

Figure 9.29. Magnetic gear dynamometer test setup

The PM servo motors were controlled by two H6-AAS-11B0 KEB 15kW DC input inverters with a maximum output frequency of 400Hz and capable of speed or torque mode operation under field orientated control. Figure 9.30 shows the schematic of the power inverter cabinet based on KEB H6 power inverters. A 3-phase variable auto-transformer and diode rectifier are used to provide a DC bus voltage between 240-600 VDC for the H6 inverters. Since both the drive and load power inverters share the DC link, with power being recirculated between the drive and load motors, the auto-transformer is only used to supply the system losses. The brake resistor connected to the H6 inverters and is used to dissipate the energy during ramp down events, such that the DC link does not increase past the rated level of the inverter. This function is automatically controlled by the inverter, with the connected of the brake resistor over the DC link being enabled when the DC link voltage exceeds 700V. The hardware components described in the schematic are shown in Figure 9.31 (a). The basic cabinet controls are shown in Figure 9.31 (b). The PLC control interface can be used to control basic drive functions such as setting the speed demand and current limits for the drive and load machines.

As an alternative, the H6 power inverters are controlled by the user using a desktop PC with the KEB Combivis 6 software. This can be used to autotune the PM motors, set ramp rates, current and speed limits, speed and torque demands as well as monitoring all the inverter parameters.

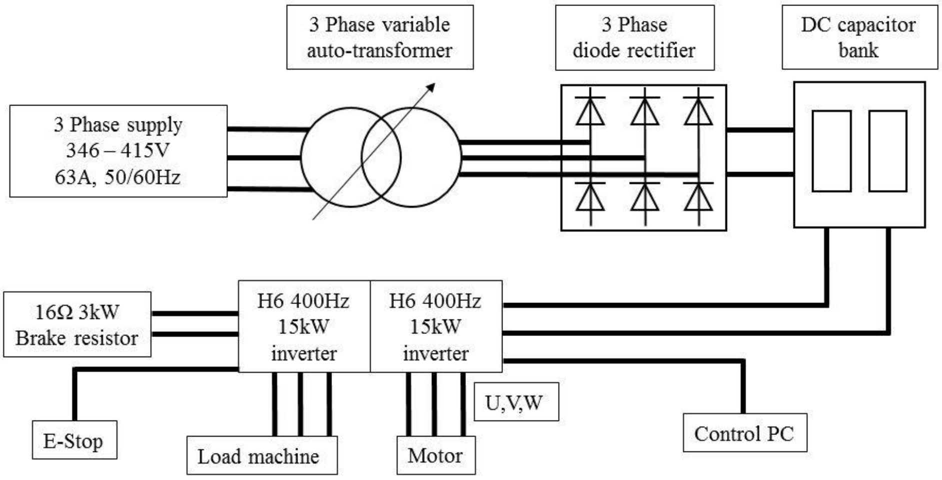

Figure 9.30. Schematic of KEB power inverter control cabinet

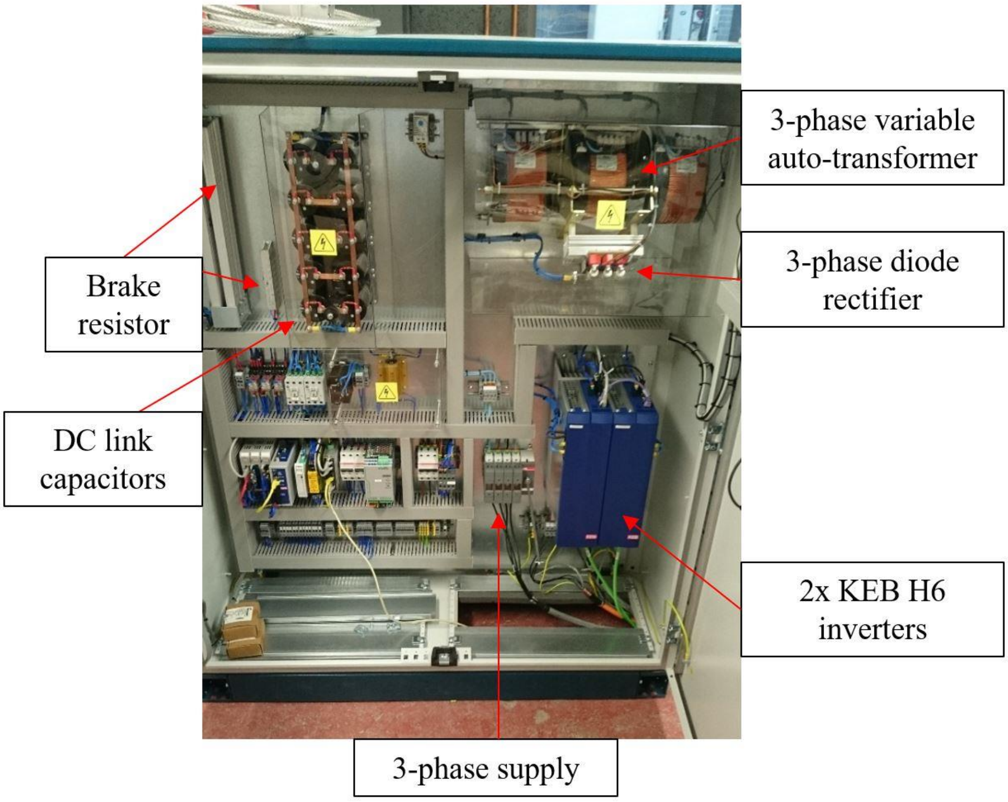

(a)

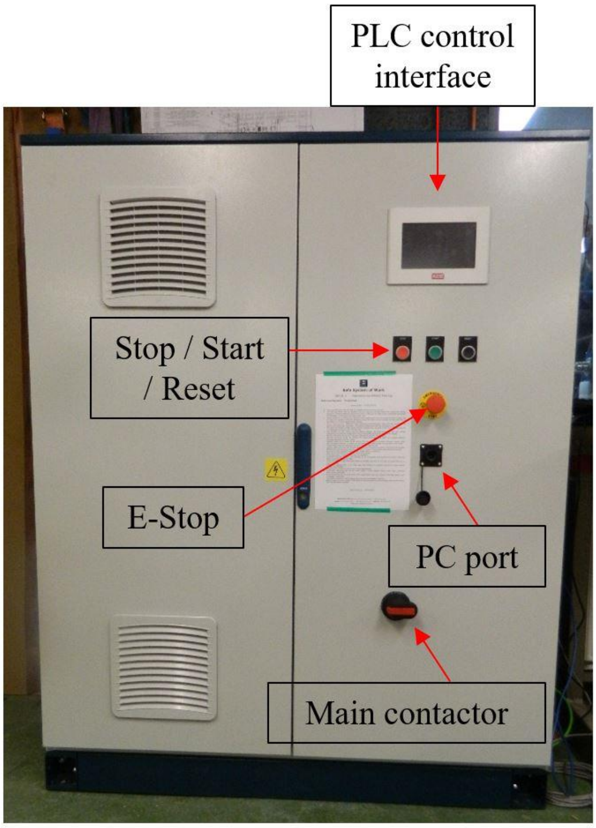

(b)

Figure 9.31. Motor / Load inverter control cabinet (a) variable frequency inverters and auxiliary hardware (b) front panel controls

9.4 Experimental validation of magnetic gear prototype

The experimental validation of the magnetic gear prototype consisted of measuring the PM HSR magnetic flux, power loss during no-load and on-load operation, and static and dynamic pull-out torque.

9.4.1 High speed rotor magnetic flux density

Before assembly, the PM flux density of the high-speed rotor was measured using a Hirst Magnetics GM07 Gauss meter capable of measuring DC magnetic fields, in order to check the magnetic performance of the supplied PM material. This meter was used with a TP002 probe, which is 1mm thick and 4mm wide. The relatively large size of the probe, when compared with the individual stator PM blocks, made it difficult to measure the stator PM field with a good accuracy. Thus, the test was limited to the HSR PM field, without and with the pole piece rotor. The magnetic field of the HSR was measured along the circumference of the rotor, at three different positions along the axial length, with the probe being pressed on the surface of the rotor. The measuring setup used for this test is shown in Figure 9.32.

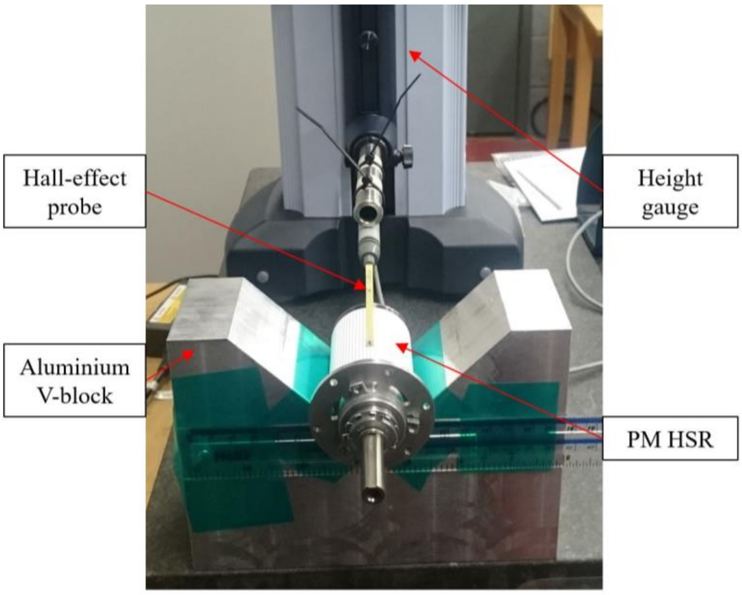

(a)

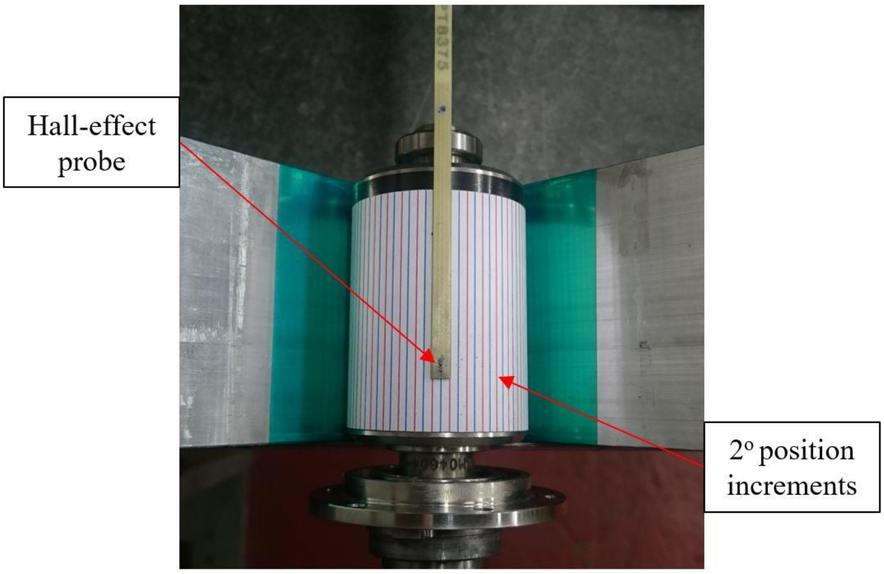

(b)

Figure 9.32. High speed rotor magnetic field measuring setup

Since each pole of the HSR is composed out of two magnet blocks displaced axially, the magnetic field was measured along the circumference, in the middle of each block, and at the mid-axial point of the rotor. Figure 9.33 (a) shows the comparison between the measured HSR magnetic field and 2D FEA prediction. Since the Hall-effect sensor is inserted in the glass fibre end of the GM07 probe, the FE prediction was obtained by interrogating the field at a distance of 0.5 mm from the outer diameter of the rotor. This assumes that the Hall-effect sensor is centred around the middle of the glass fibre probe. Figure 9.33 (b) shows the magnetic field of the HSR and PPR assembly measured around the outer circumference of the PPR. For both test configurations, with and without PPR, the measured data agrees well with the FE predictions. It is worth considering that the stator PMs were cut from the same PM block as the HSR magnets, and magnetised within the same specifications. Thus, although the B-field could not be accurately measured due to the large dimensions of the probe, the field amplitude is expected to be within predicted FE values.

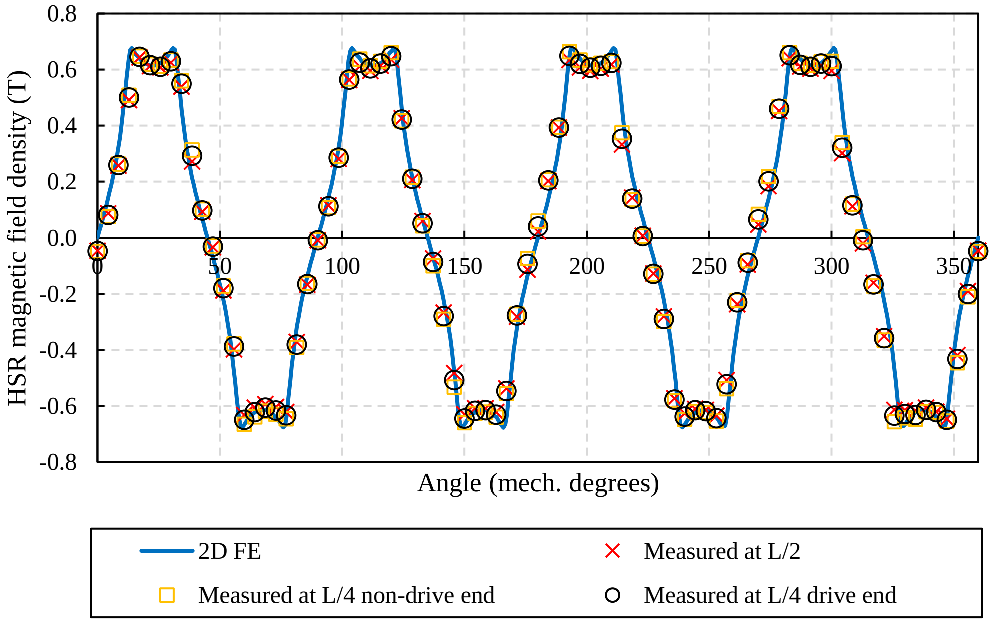

(a)

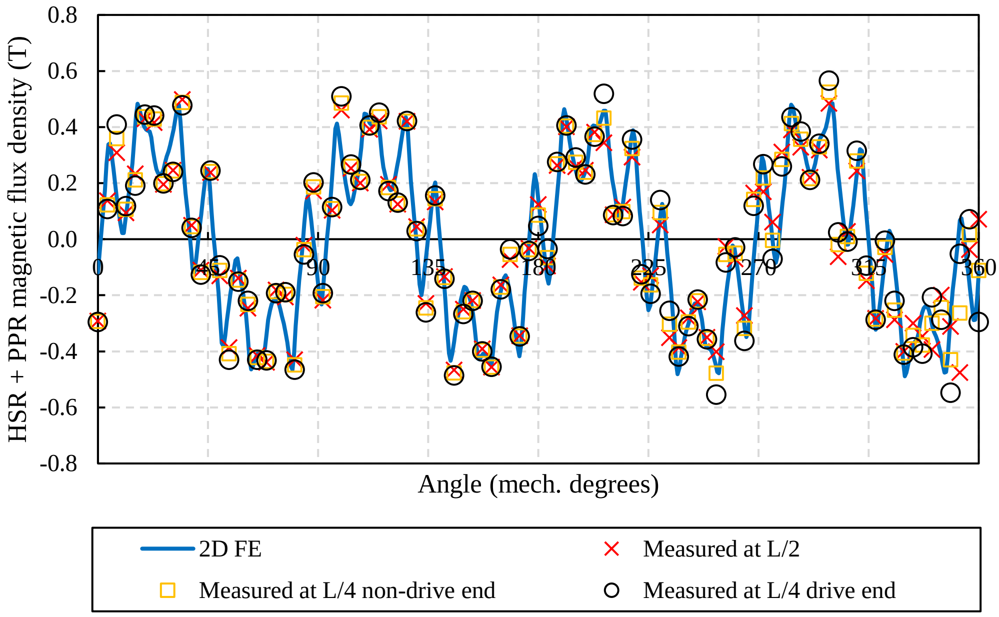

(b)

Figure 9.33. Variation of PM flux density with position on the outer circumference of (a) HSR (b) HSR-PPR assembly

9.4.2 Power loss

The no-load power loss of the magnetic gear was measured from the input side, while the output side was disconnected. The 5Nm torque transducer from the input side was used to measure the drag torque and speed of the HSR. For this test, the PM motor on the input side was set to speed mode, with the magnetic gear utilising the glass fibre G11 PPR. Figure 9.34 shows the variation of the magnetic gear no-load power with output rotor speed. The 7.75:1 ratio between input and output speed is given by the gear ratio of the magnetic gear. The loss of the sealed bearings was estimated based on the speed and mechanical pre-load conditions using the SKF calculator [187].

The power loss was also measured with the 30Nm torque transducer by driving the output side, while the input side was disconnected. Figure 9.35 shows good agreement between the measurements of the two torque transducers. The predicted bearing loss was subtracted from the measured loss in order to compare the loss from the input and output side.

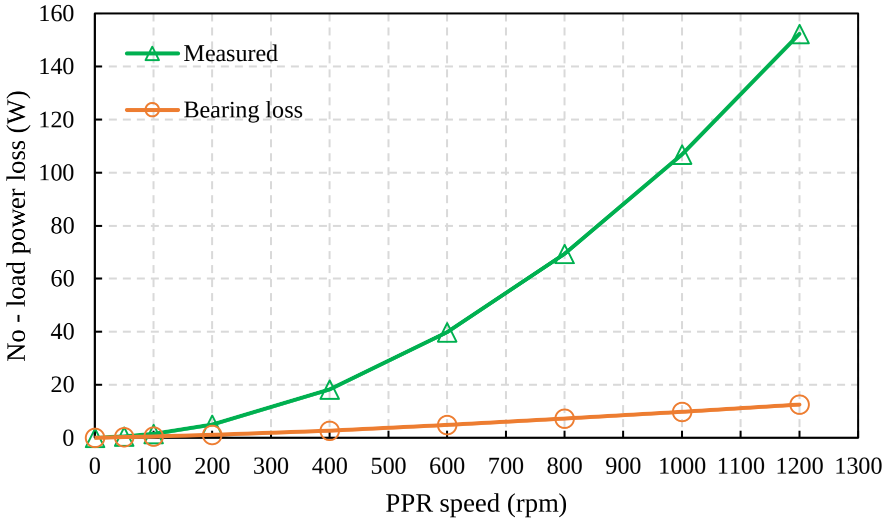

Figure 9.34. Variation of magnetic gear power loss (with glass fibre PPR) and bearing loss with output rotor speed

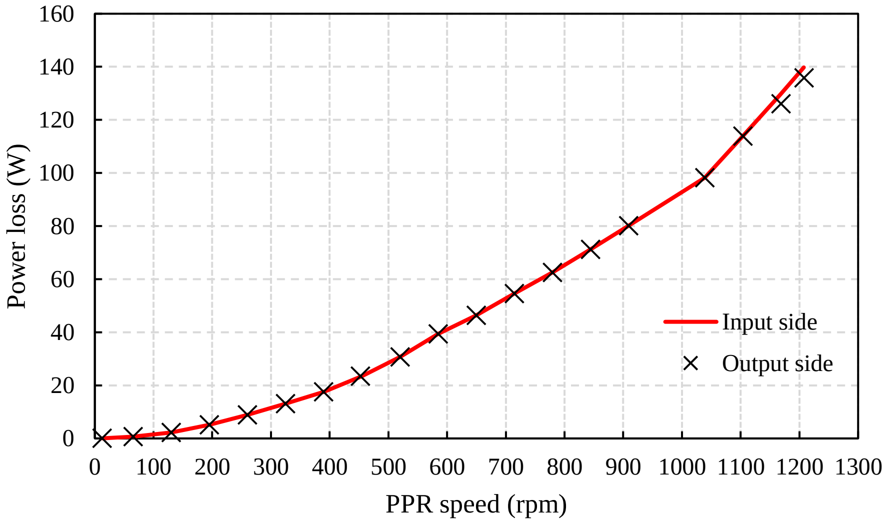

Figure 9.35. Comparison of magnetic gear power loss measured from input and output side

The comparison between the predicted and measured power loss of the magnetic gear with a G11 PPR is shown in Figure 9.36. The FE predicted loss considered the stator and pole piece iron loss, PM loss and sleeve loss. The eddy current in the pole pieces, PMs and sleeve were predicted from 3D FEA. Each PM block and sleeve were divided in two axial segments, with the titanium sleeve being modelled with slits. In 3D FEA, the sleeve was modelled as both in perfect contact and electrically insulated from the stator PM array. In Figure 9.36, it can be observed that the measured power loss is 60% higher than the predicted loss with an insulated sleeve, while being only 48% of the predicted loss with a non-insulated titanium sleeve. This shows that there is a highly imperfect contact between the sleeve and the stator PM array. This can be due machining tolerances of all the parts, causing some of the PMs to sit slightly higher than the others, while being in better contact with the sleeve. Moreover, certain impurities such as adhesive residue, could exist between the sleeve and PM array, causing the net electrical conductivity between the two components to be decreased.

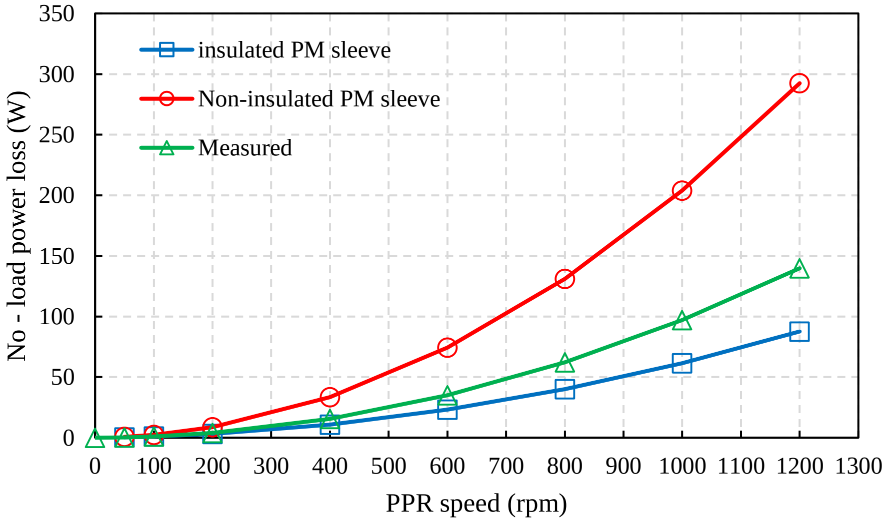

Figure 9.36. Variation of magnetic gear (with glass fibre PPR) power loss with rotor output speed

The variation of the magnetic gear power loss and corresponding HSR drag torque with the output PPR speed for PEEK and G11 glass fibre based PPRs is shown in Figure 9.37. It can be observed that a good match exists between the losses measured for the two types of PPRs. It can be concluded, that since the PEEK support structure does not have an endplate, the losses in the Inconel endplates of the G11 PPR are negligible and can be ignored in the FE analysis.

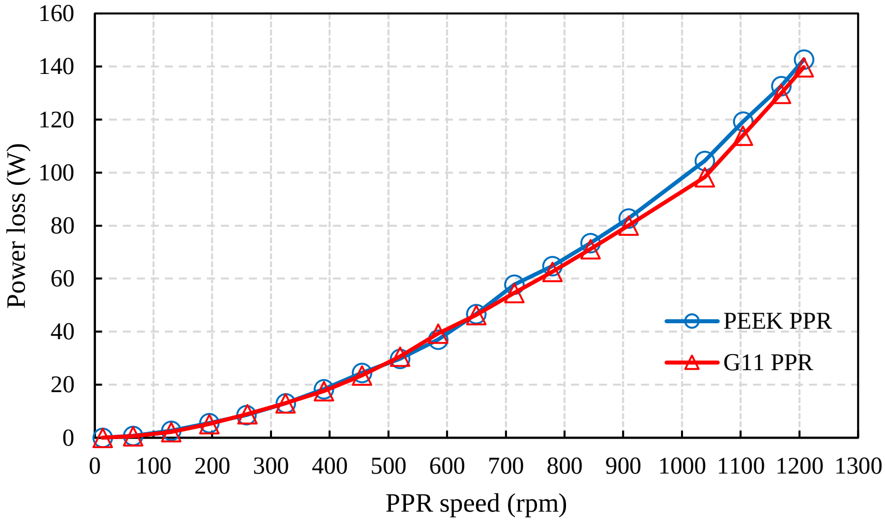

(a)

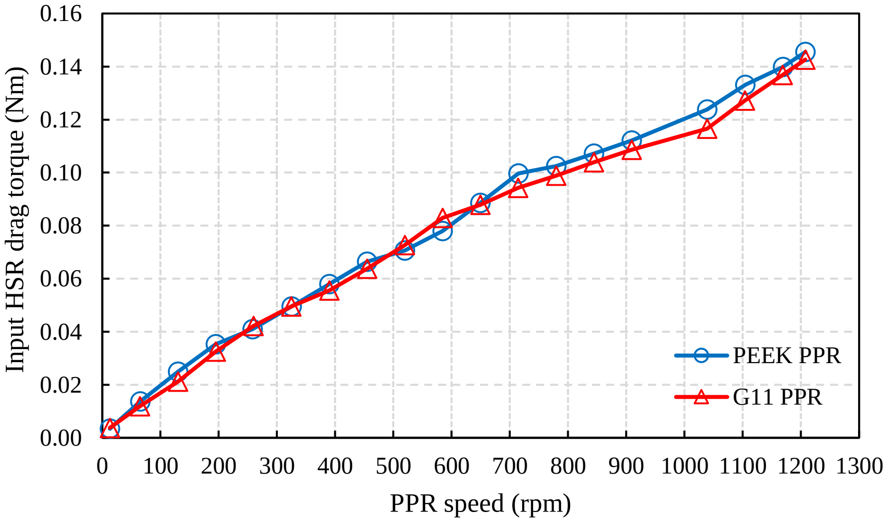

(b)

Figure 9.37. Variation of magnetic gear (a) power (b) HSR drag torque loss with output rotor speed for PEEK and glass fibre G11 PPRs

In order to measure the magnetic gear power loss while mechanical power is being transmitted from the input to the output shaft, both the input and load PM machines were connected to the magnetic gear. Since it was found that at load, vibrations were created by the belt pulley assembly causing the torque transducer reading to fluctuate, the input machine was connected only with the torque transducer to the high side of the magnetic gear. Due to the speed rating of the PM motor, the input speed was limited to 4650 rpm for this test. For this test the input motor was set to speed control while the load machine was in torque mode, with the torque of the load machine being applied in the opposite direction to the input motor. Thus, the speed of the system was fixed by the input machine, which was also reacting the torque of the load motor through the magnetic gear. A speed limit was imposed on the load machine in order to ensure that, in the event of loss of control of the input side, the system is not accelerated past its rated speed. Figure 9.38 shows the variation of the magnetic gear power loss for no-load and on-load operation, at different levels of output torque. This loss was calculated as the difference between the input and output power, with the torque transducers being used to measure both shaft speed and torque. It can be observed that the measured power loss does not change with the increase in transmitted torque to the load. This is explained by the fact that the losses in a magnetic gear are only affected by the strength of the magnetic fields of the two PM arrays and the operational speed. More importantly, this shows that the measured no-load loss can be used to accurately predict the efficiency of the magnetic gear. For example, at 7.8Nm of load at 600 rpm the efficiency of the magnetic gear is 92.5%, while at the rated operation point of 8.6 Nm and 1200 rpm the efficiency is reduced to 87.6%.

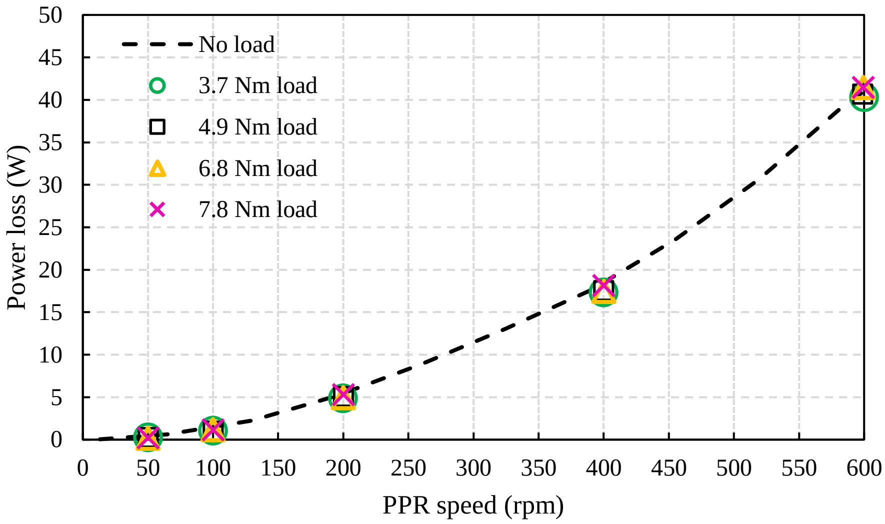

Figure 9.38. Variation of magnetic gear power loss with output speed for different levels of output transmitted load torque

9.4.3 Dynamic and static pull-out torque

The magnetic gear was designed to operate at a rated torque of 8.6 Nm. However, if the load torque is continuously increased, the magnetic gear will pole slip, with the load being isolated from the input. The torque at which this occur represents the pull-out torque of the magnetic gear. This inherent capability is the overload protection mechanism of the magnetic gear element and can be beneficial in protecting the mechanical drive train from sudden shock loads [84], [88].

A. Dynamic pull-out torque

The pull-out torque of the magnetic gear prototype was measured in an overload test triggered during normal operation. The input PM machine, connected to the HSR, was set in speed mode with a constant speed demand of 1550 rpm, as shown in Figure 9.40 (b), while the current limit was set to the value of the rated machine phase current. The load PM machine, connected to the LSR, was set to achieve a zero speed with a variable current/torque limit. The measured HSR and PPR torque and speed, during initial normal operation, are shown in Figure 9.39 and Figure 9.40, respectively. Initially, the test is started and the speed of the input machine is increased to 1550 rpm, which corresponds to 200 rpm output speed. The load torque on the PPR was then increased from 0Nm to 6.4Nm by adjusting the current limit of the load machine with a zero-speed demand.

In order to achieve overload, the load machine current limit was increased until the load torque exceeded the pull-out torque of the magnetic gear. At this point, the output rotor was locked in a fixed position by the load machine and the PPR speed was reduced to 0 rpm, as shown in Figure 9.40 (a). During this overload condition the HSR rotor connected to the input PM motor continues to rotate freely from the stationary output rotor, as shown in Figure 9.40 (b). The PPR torque during overload oscillates between the maximum and minimum pull-out torque values, as the magnetic gear is unable to reach a load angle capable of sustaining continuous power transmission. Figure 9.39 shows the PPR and HSR measured torque during normal and overload operation. The ratio between the maximum PPR and HSR torque is given by the gear ratio of 7.75:1. As the excess load is removed, normal operation is passively resumed by the magnetic gear with mechanical power being transmitted from input to output. The PPR load torque is reduced to 6.4 Nm and speed is increased to 200 rpm, as shown in Figure 9.39 and Figure 9.40, respectively.

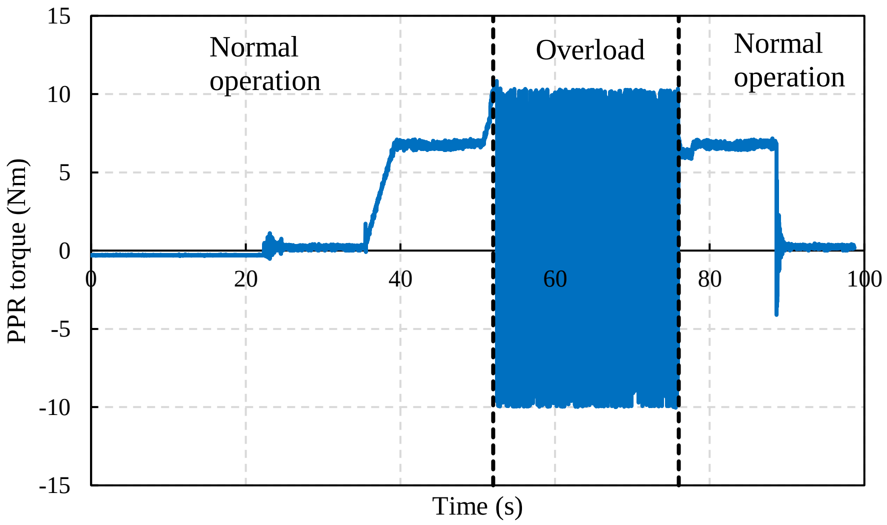

(a)

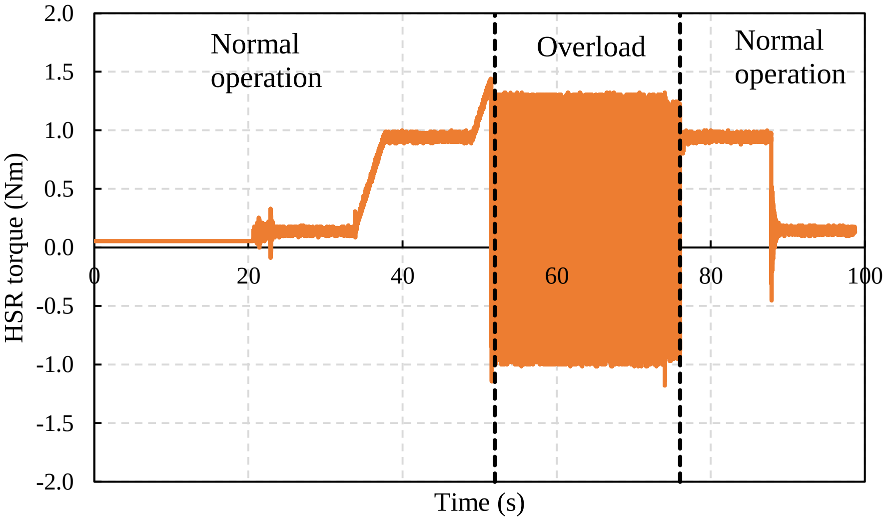

(b)

Figure 9.39. Torque during dynamic pull-out torque test (a) PPR (b) HSR

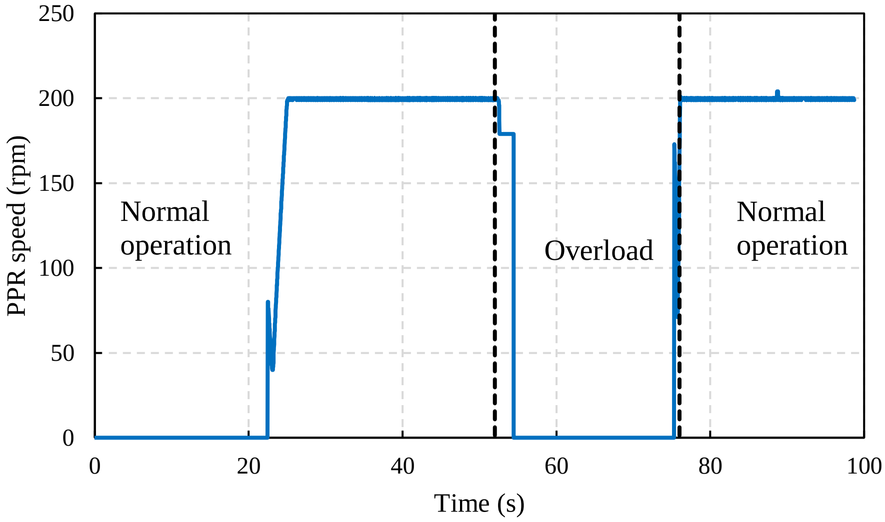

(a)

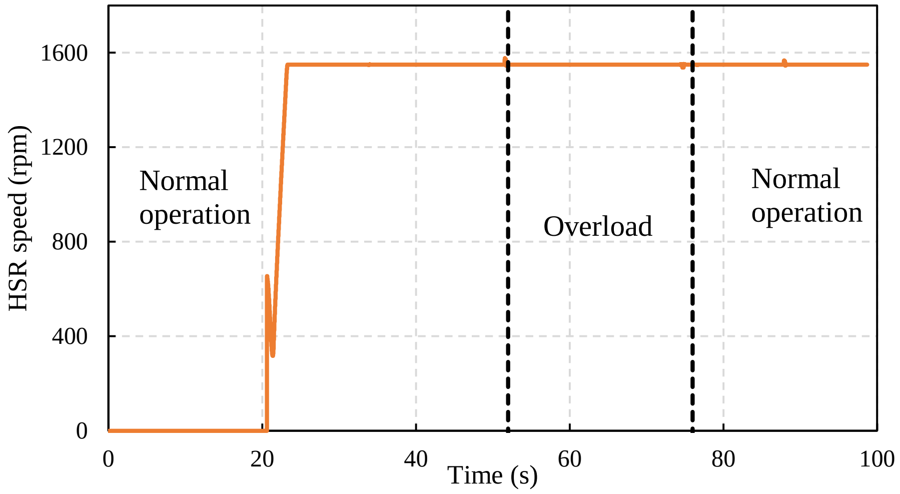

(b)

Figure 9.40. Speed during dynamic pull-out torque test (a) PPR (b) HSR

The measured amplitude of the dynamic pull-out torque for the manufactured PPRs, is shown in Table 9.2. The measurements were conducted at 20^{o}C and 80^{o}C, at 1550 rpm input speed. It can be observed that the pull-out torque of the PEEK PPRs is smaller than the values measured on the G11 glass fibre PPRs. The PEEK PPR measured pull-out torque is 8.4% lower than the 3D FE predicted value of 10.3 Nm at 20^{o}C. In comparison, the G11 PPR achieves a pull-out torque which is only 1% below the expected value

Table 9.2. Dynamic pull-out torque

MG PPR type	**Pull-out torque (Nm) @ 25^{o}C**	**Pull-out torque (Nm) @ 80^{o}C**
PEEK CF 1	9.82	9.48
PEEK CF 2	9.18	9.01
PEEK CF 3	9.29	9.1
Glass fibre 1	10.16	10.04
Glass fibre 2	10.23	10.09
Glass fibre 3	10.21	9.97

The material selection for the PPR support structure is important when considering twist under load of the output rotor. Figure 9.41 shows the displacement of the PPR non-drive end, with respect to the drive-end under rated load torque, for the PEEK and G11 glass fibre PPRs. The tangential forces acting of each pole piece are predicted from 2D FE electromagnetic analysis. Ansys Workbench Mechanical FEA is then utilised in order to predict the deformation of the output rotor. By considering the displacement at the outer radius of the non-drive endplate, the twist of each PPR concept can be evaluated. For the same output torque, the angular displacement of the PEEK PPR was approximated at 0.145 mechanical degrees, which is 13.6 times higher than the G11 PPR variant. It has to be considered that the Ansys mechanical model represents an approximation of the final prototype rotors, since it does not consider the adhesive bonds between the PPR support structure and pole pieces.

Thus, the different PPR twist angles can contribute towards the change of pull-out torque with the type of PPR support structure. The difference in angular twist between the two PPR designs can be related to the overall torsional stiffness of the two rotors. For the G11 PPR, the Inconel endplates are analogous to the PEEK end regions, but have a much larger stiffness. The G11 pultruded rods which are good in tension and shear perpendicular to the fibre, show better torsional capability than the PEEK beams of the monocoque PPR.

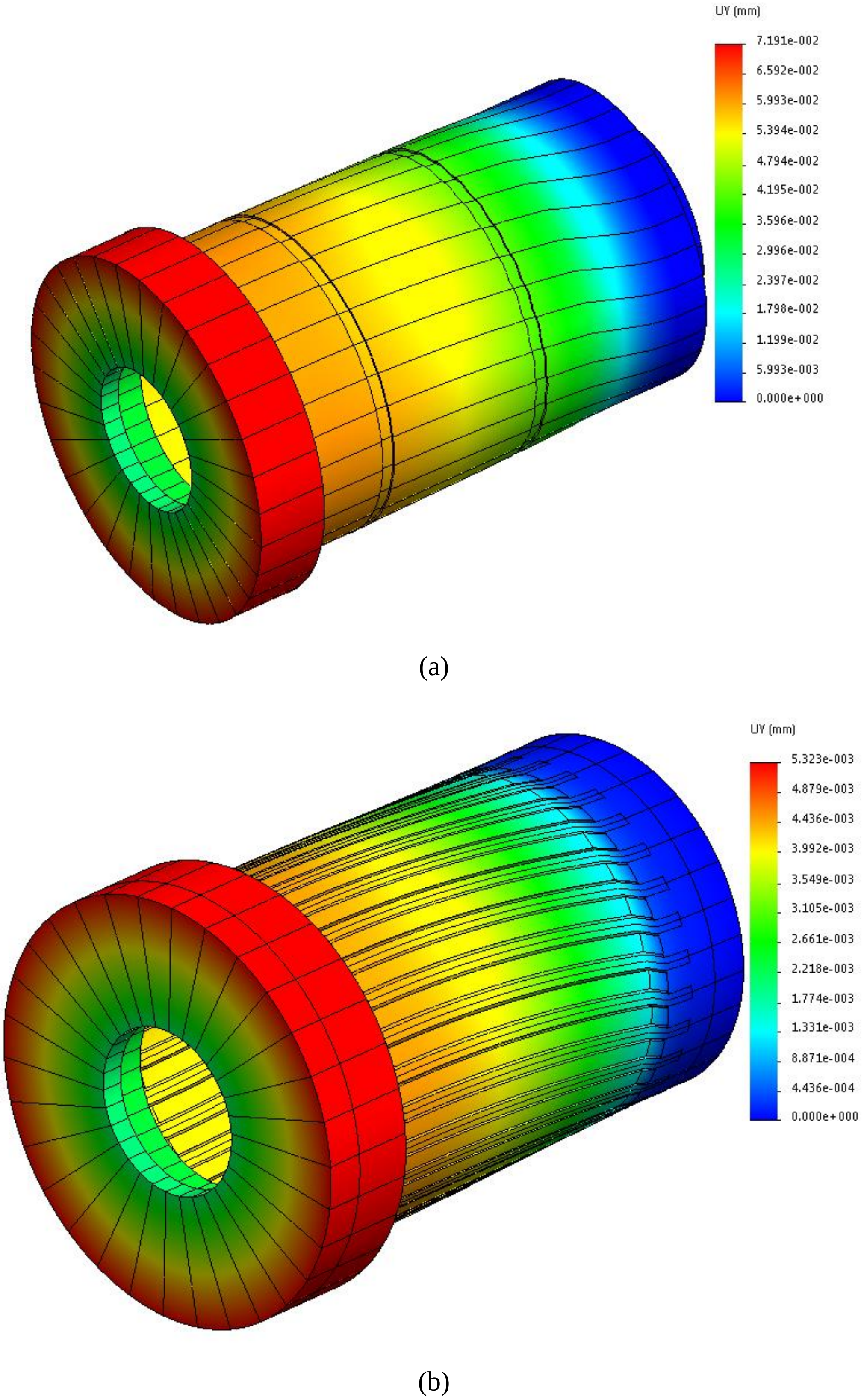

Figure 9.41. PPR twist under rated load (a) PEEK (b) G11 fibre glass

B. Static pull-out torque

In order to further investigate the pull-out torque capability of the G11 glass fibre PPR, a static torque test setup was implemented, as shown in Figure 9.42. The input shaft was bolted to the locking plate, which allowed for the HSR to be locked into different positions with respect to the stator. As the HSR position was changed, the output shaft would rotate to reach the no-load position.

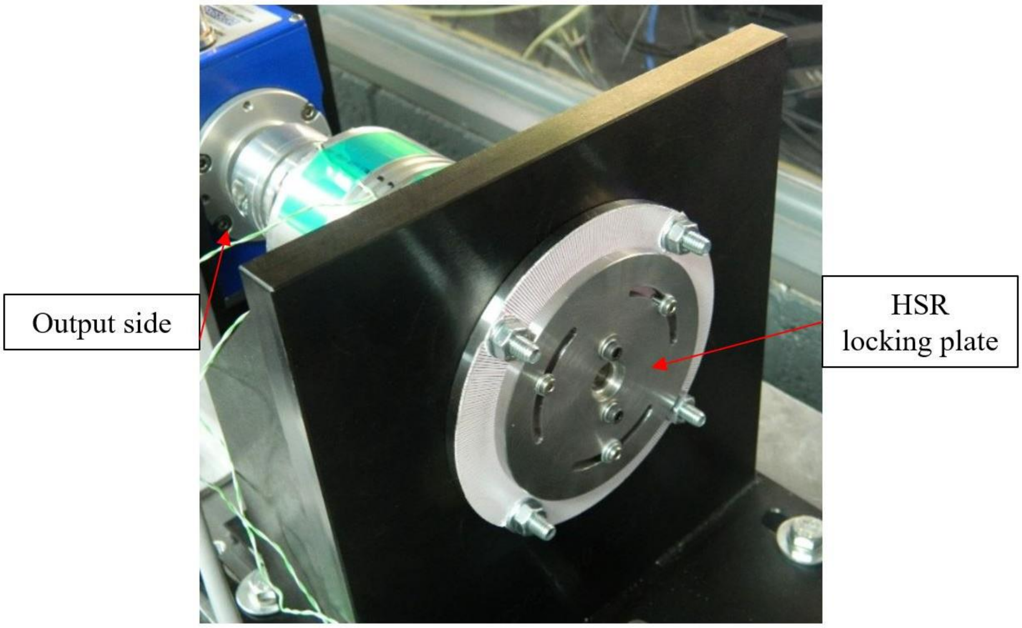

Figure 9.42. Static magnetic gear pull-out torque test setup

The load torque was applied manually to the coupling on the load motor side by using an Allen key engaged with coupling hex-head bolt. The load torque was measured by the 30Nm torque transducer. Figure 9.43 shows the change in the position of the PPR after one pole slip event. The measured pull-out torque at different HSR angles, for the G11 PPR, are shown in Table 9.3. It can be observed that the results show a good match to the dynamic pull-out torque test results. The PDD active length required to obtain a pull-out torque value of 10.3 Nm at 150°C PM temperature was predicted based on the lowest measured static pull-out torque value of the magnetic gear and PM flux drop of with temperature from 2D FEA, which accounted for 8.65% increase in active length.

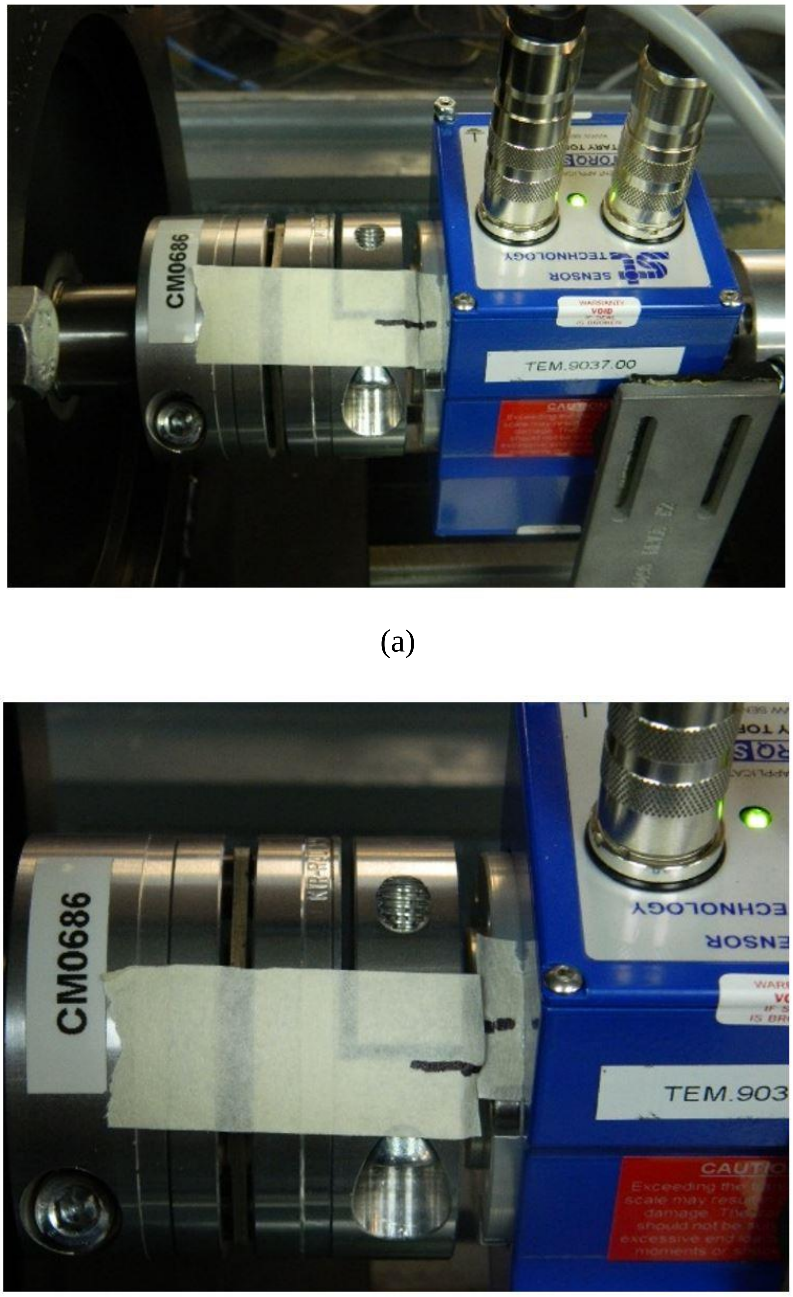

(a)

(b)

Figure 9.43. Position of output side coupling (a) before (b) after pull-out

Table 9.3. Static pull-out torque of magnetic gear with G11 glass fibre PPR

HSR position (mech. deg.)	Pull-out torque (Nm) @ 20ºC
0	9.968
22.5	9.991
45	9.988
67.5	9.969
90	9.972

9.5 Conclusions

The magnetic gear demonstrator was designed to the same cross-section and specifications as the magnetic gear element of FT PDD design, in order to validate the electromagnetic and mechanical models. The active and structural parts of the MG and PDD were de-risked from basic component level, to sub-assembly and final prototype assembly. The HSR and stator-PM assemblies were manufactured to specification by the permanent magnet supplier. Discussions prior to manufacturing lead to the adoption of castellations in the HSR hub and stator stack. This allowed for the small stator and HSR PMs to be easily located in the correct position, while minimising the assembly time and number of breakages. The PPR assemblies were manufactured at Magnomatics. Certain features on the PPR endplates and bearing seats were modified in order to facilitate assembly of the final FT PDD prototype. In order to reduce the PPR shaft run-out due to the PPR end-plates not being perpendicular to the pole piece support structure, clamping plates were used to keep pressure on the PPR endplates during adhesive curing. During final assembly, the HSR-PPR assembly was lowered into the stator-case assembly.

A bespoke test dynamometer was commissioned to experimentally validate the magnetic gear and FT PDD prototypes. The dynamometer used two PM machines connected via torque transducers to the input and output shafts of the magnetic gear. The control of the test rig was done by two 15kW KEB power inverters, with power being recirculated and the losses supplied from the DC link.

The experimental validation of the magnetic gear prototype includes no-load tests to measure the no-load power loss from the input and output sides, on-load tests to measure losses and dynamic and static pull-out tests. The measurement of the HSR PM flux without and with the PPR shows good agreement to the FE predictions. Due to the small size of the stator PMs in relation to the Gauss probe, the stator PM field could not be accurately measured.

The no-loan power loss measurements show a good match between the losses measured from the input and output side, with the power loss being 60% higher than the 3D FE prediction. This increase can be attributed to the eddy current loss related to the imperfect contact of the titanium sleeve and stator PM array. In order to reduce this loss mechanism, the titanium sleeve of the FT PDD was coated with an electrical insulator prior to insertion in the PM-stator assembly. The power losses of the two PPR design shows similar values. It was also validated that the power loss of the magnetic gear does not vary with the transmitted power. This enables the rapid calculation of magnetic gear efficiency from no-load losses, both in FEA and experiments.

The pull-out torque of the magnetic gear prototype was measured in dynamic and static tests. The dynamic test results show that the G11 PPRs have an 8% higher pull-out torque than the PEEK topologies, and 1% below the 3D FEA prediction. In comparison the static pull-out torque of the G11 PPR is 3% below the predicted value. The final active length of the PDD, of 53mm, was set based on the magnetic gear tests and drop in PM flux with temperature obtained from 2D FEA.

Chapter 10: Manufacturing and experimental validation of fault-tolerant PDD motor prototype

The fault tolerant Pseudo Direct Drive motor was manufactured according to the specification presented in Chapter 6, section 6.1, Table 6.1.

The lessons learnt from the magnetic gear demonstrator were applied to the manufacture of the PDD motor. These include utilising the G11 glass fibre PPR due to its higher torsional rigidity, lack of banding and ease of manufacture when compared to the PEEK variant. Furthermore, the time and cost required to produce a G11 PPR are substantially lower than that of the PEEK support structure, which was prone to machining errors and material imperfections, resulting in expensive additional delays.

The small slot wedges were removed due to high inaccuracies in manufacture which were extremely time and resource consuming to correct. Furthermore, the slot opening is shielded by the stator PM array and Titanium sleeve.

In order to reduce the eddy current losses due to the imperfect electrical contact between the titanium sleeve the stator PM array, the sleeve was coated with Tribobond 42 electric insulator. The material properties of this coating are presented in Appendix 1.

The active length of the PDD was increased from 45mm to 53mm in order to account for drop in pull-out torque due to manufacturing tolerances and PM temperature increase to 150^{o}C. The FT PDD prototype was tested on a modified configuration of the magnetic gear dynamometer, with the input motor and torque transducer being removed.

10.1 Manufacturing of fault-tolerant PDD motor prototype

The main components of the fault tolerant duplex 3-phase PDD are shown in Figure 10.1. The cross-section and side views of the PDD model are shown in Figure 10.2. The majority of the components of the magnetic gear element have been left unchanged, with the outer back-iron being replaced with a stator with duplex 3-phase single layer winding. The PDD case was modified to interface with the actuator housing and accommodate exit ports for the 3-phase power connections and thermal and position sensors.

For increased redundancy, a dual resolver configuration was selected, based on the Smartsyn 15 brushless resolvers. It can be observed in Figure 10.2 (b), that the HSR shaft has been extended in order to attach the resolver rotors, with the resolver stators being secured in a housing bolted to the end of the PDD case. In this configuration the position feedback reports the position of the PM HSR.

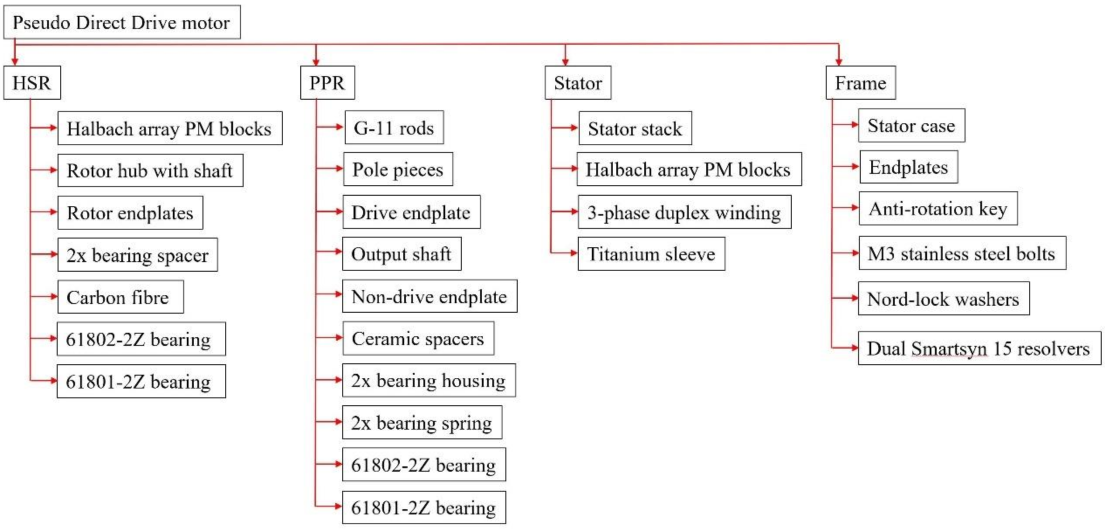

Figure 10.1. Main components of FT PDD prototype

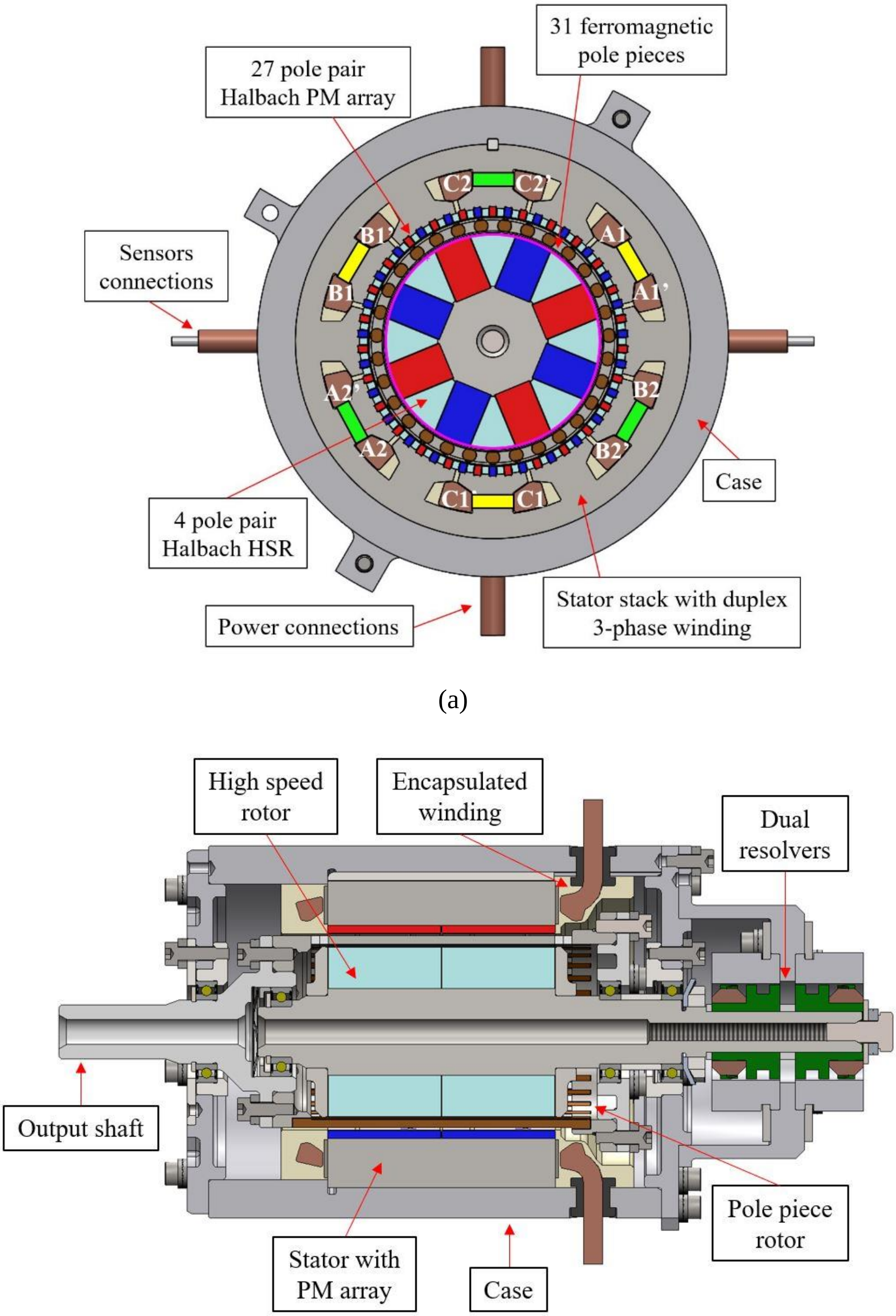

(a)

(b)

Figure 10.2. FT PDD motor prototype (a) cross-section (b) side-view

10.1.1 High speed rotor assembly

The high-speed rotor assembly, shown in Figure 10.3, was manufactured by Arnold Magnetic Technologies, who also supplied and magnetised the PM blocks of the Halbach array. The PM bonding and rotor assembly procedure utilised was identical to the process described in Chapter 9, section 9.2.1. The HSR was balanced to 10700 rpm by machining material off the endplates, as seen in Figure 10.3.

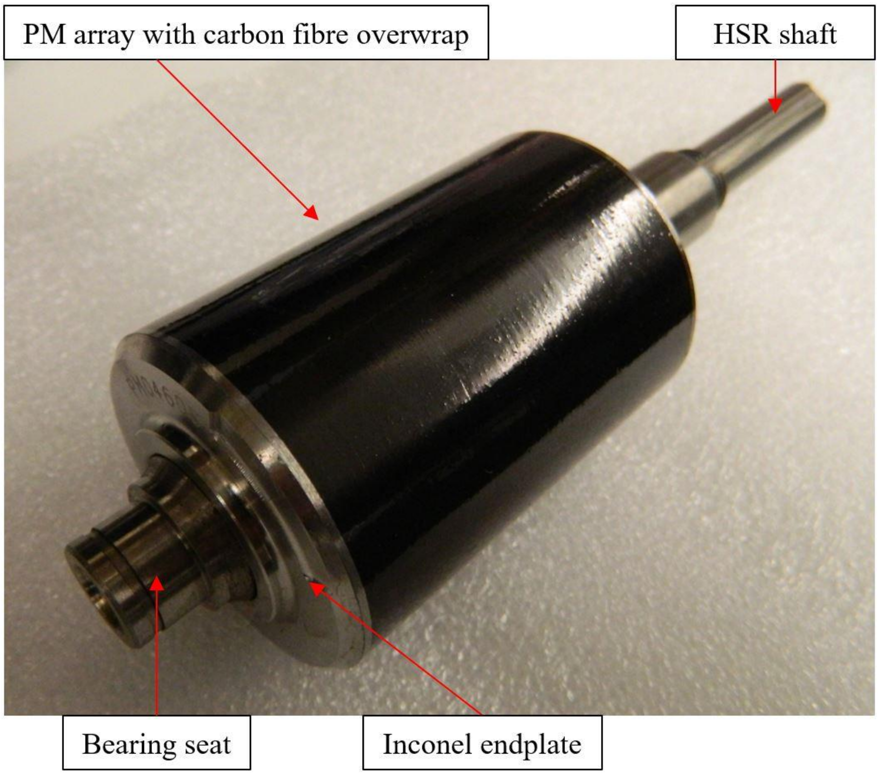

Figure 10.3. High-speed rotor assembly

10.1.2 Pole piece rotor assembly

The PDD PPR was based on the design of the G11 glass fibre magnetic gear output rotor, due to reduced twist angle under load and less expensive manufacturing process than the PEEK variant. Figure 10.4 shows the main components required to assemble the PPR. The assembly procedure and adhesive utilised are similar to the process described in Chapter 9, section 9.2.3.

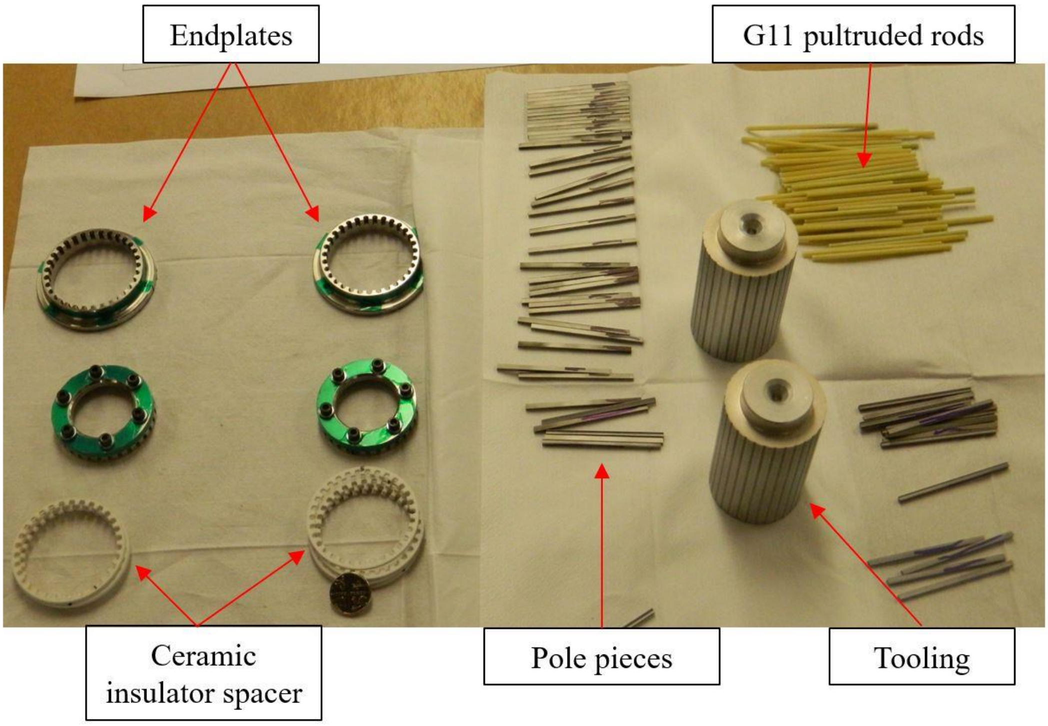

Figure 10.4. PPR components prepared for assembly

The PPR wet assembly was done around an aluminium tooling cylinder inserted in the rotor drive endplate, as shown in Figure 10.5 (a). The ceramic pole piece spacer rings were stacked on top of the endplate, using the tooling as a guide. The G11 glass fibre pultruded rods and pole pieces where then placed around the tooling cylinder. After the rod-pole piece array was complete, the non-drive endplate was positioned on top of the PPR assembly, such that the rods would interlock with the castellations of the endplate.

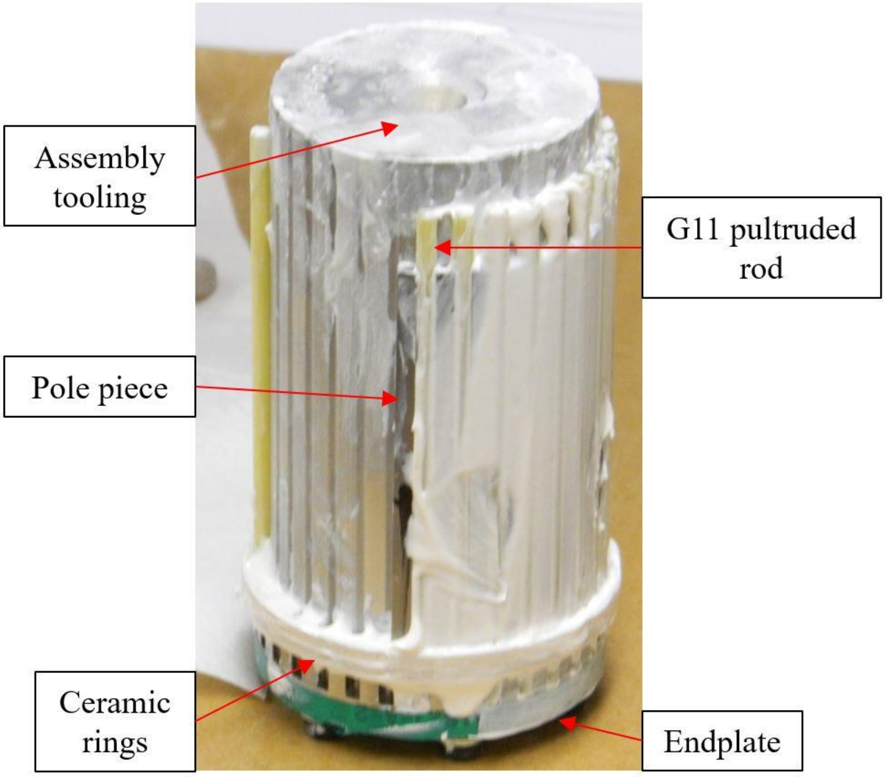

(a)

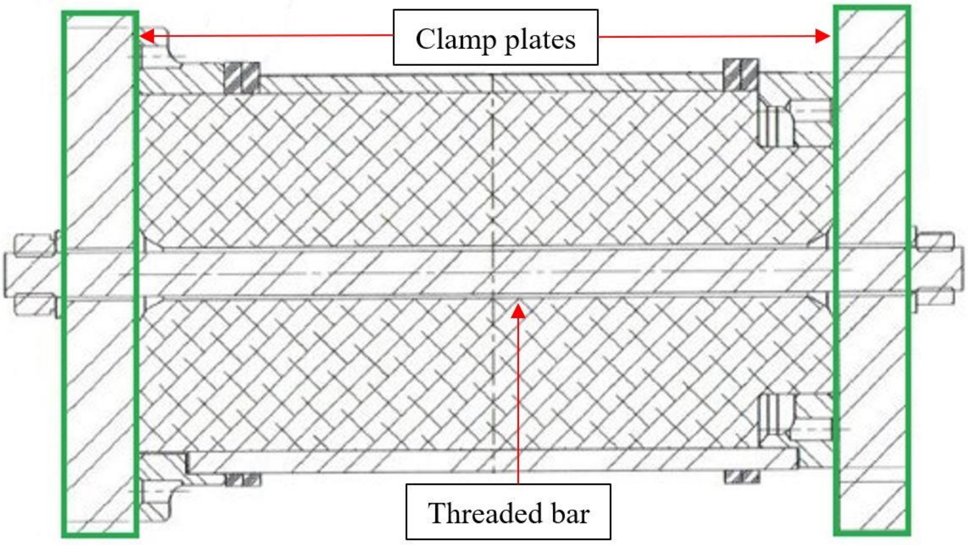

(b)

Figure 10.5. Pole piece rotor (a) during assembly (b) adhesive curing assembly

10.1.3 Stator assembly

The PDD stator assembly was manufactured in several stages. These include the bonding of PM arrays, Titanium sleeve insertion, winding of phase coils, case insertion and varnishing or encapsulation of stator winding. The wire-eroded stator lamination stack and grade 5 Titanium sleeve are shown in Figure 10.6. The stator castellations were utilised to position the stator PM blocks similarly to the magnetic gear stator. The Titanium sleeve was coated with Tribobond 42 in order to reduce the electrical conductivity between the sleeve and stator PM array. The stator PMs were delivered and glued to the stator bore by Arnold Magnetic Technologies using the same adhesive and procedure as for the magnetic gear stator.

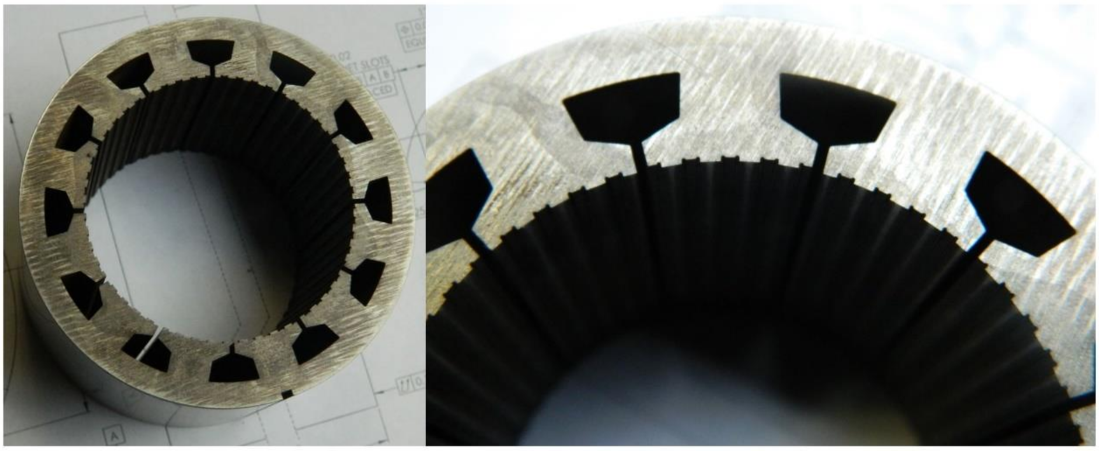

(a)

(b)

Figure 10.6. PDD stator (a) laminated stack (b) coated Titanium 5 sleeve

The stator with the Halbach PM array and Titanium sleeve is shown in Figure 10.7. The sleeve was ground to a final wall thickness of 0.2mm. Figure 10.8 shows the PDD stator with one copper coil. Glass fibre G11 stator end-cheeks and 0.1 mm Nomex sheets were used to protect the copper insulation from the sharp edges of the stator stack. Figure 10.9 shows the PDD stator phase coil placement together with the interconnections of the star points and hook-up wire, for the duplex 3-phase winding. The wiring and labelling conventions are shown in Figure 10.10. The winding specification is shown in Table 10.1. The termination wires of each 3-phase lane were displaced by 180°, towards the exit holes in the case. All the winding interconnections were done with high temperature solder and heat-shrink. Six T-type thermocouples and six RTD temperature sensors were fitted to the end winding, on the non-drive end of the stator.

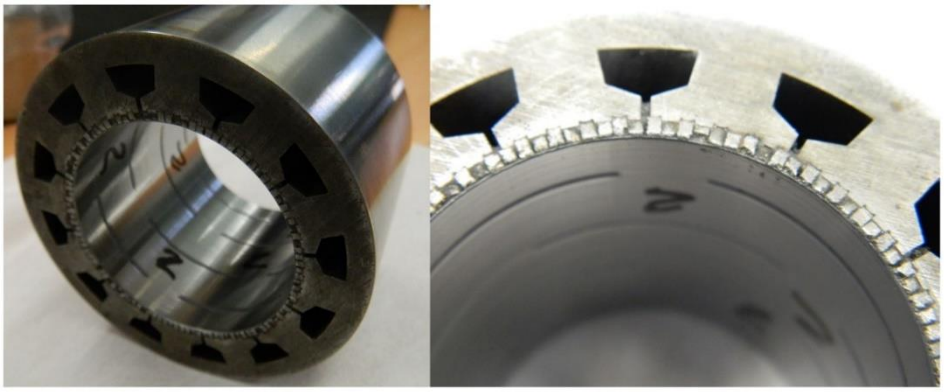

Figure 10.7. PDD stator with Halbach PM array and Titanium 5 sleeve

Figure 10.8. PDD single layer phase coil winding

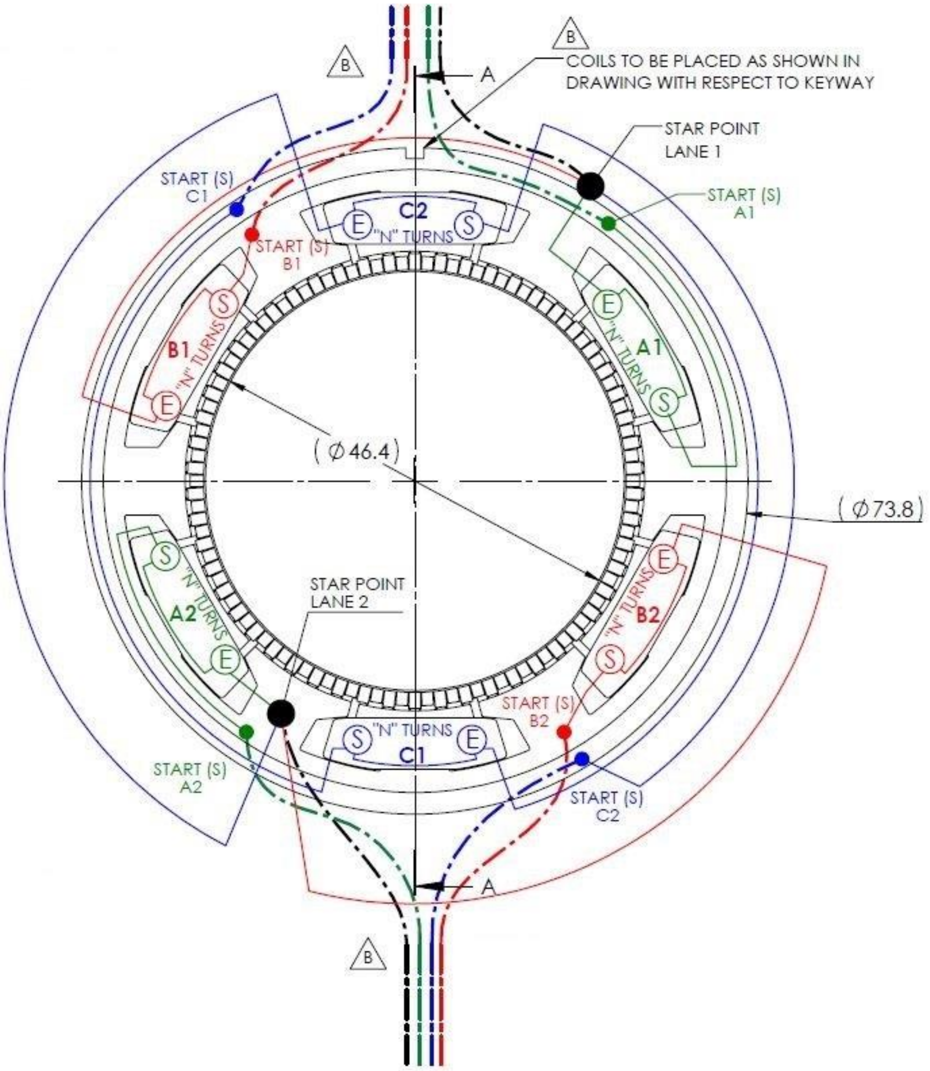

Figure 10.9. Position of FT PDD phase coils and winding terminations

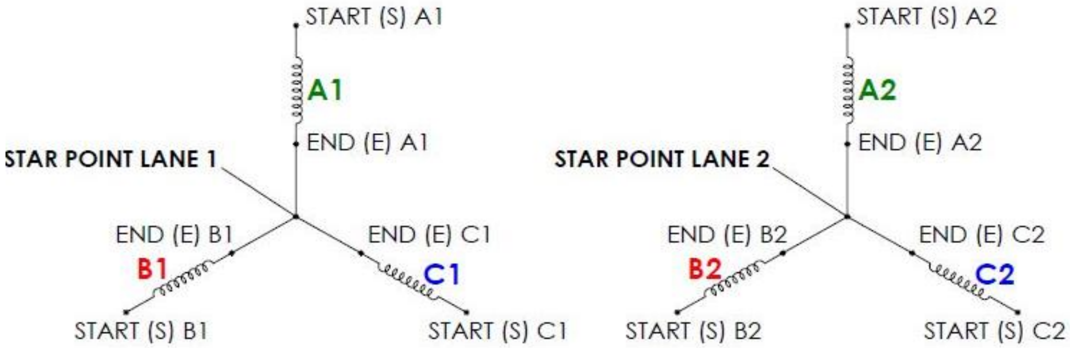

Figure 10.10. FT PDD winding wiring diagram

Table 10.1. FT PDD duplex 3-phase stator winding specification

Total slot area	$3.80\cdot10^{-5}$	m^2
Slot area (excluding slit liner)	$3.56\cdot10^{-5}$	m^2
Slot liner thickness	0.1	mm
Number of turns	54	
Packing factor	0.4	
Diameter copper wire with insulation	0.53	mm
Predicted phase resistance	0.57	Ω
Voltage DC	270	VDC
Voltage AC	135	VAC
Maximum operating temperature	200	°C
Copper wire type	ML wire – 240°C	-
Hook-up wire	AWG 18 TFE Teflon	-

The completed stator assembly with the winding and interconnections is shown in Figure 10.11. The stator assembly was inserted into the aluminium PDD case by cooling the stator and heating the case to the same temperatures as for the magnetic gear demonstrator. The stator is fixed to the case due to the interference fit and rectangular key. Figure 10.12 shows the completed PDD case-stator assembly prior to varnishing or encapsulation of the winding.

For three prototype FT PDDs, the stator winding was varnished with Ultimeg 2220. The resin was degassed before it was poured over the end windings and left cure for 12 hours at 150°C. Four varnishing runs were conducted per stator, with the varnished being poured from both the drive and non-drive ends. Figure 10.13 shows the PDD stator – case assembly during varnishing.

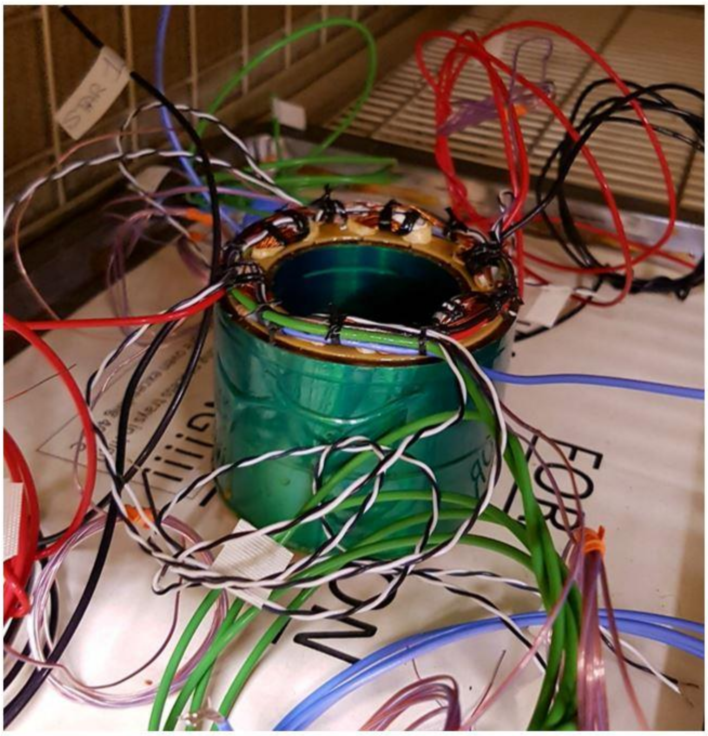

Figure 10.11. Completed stator assembly

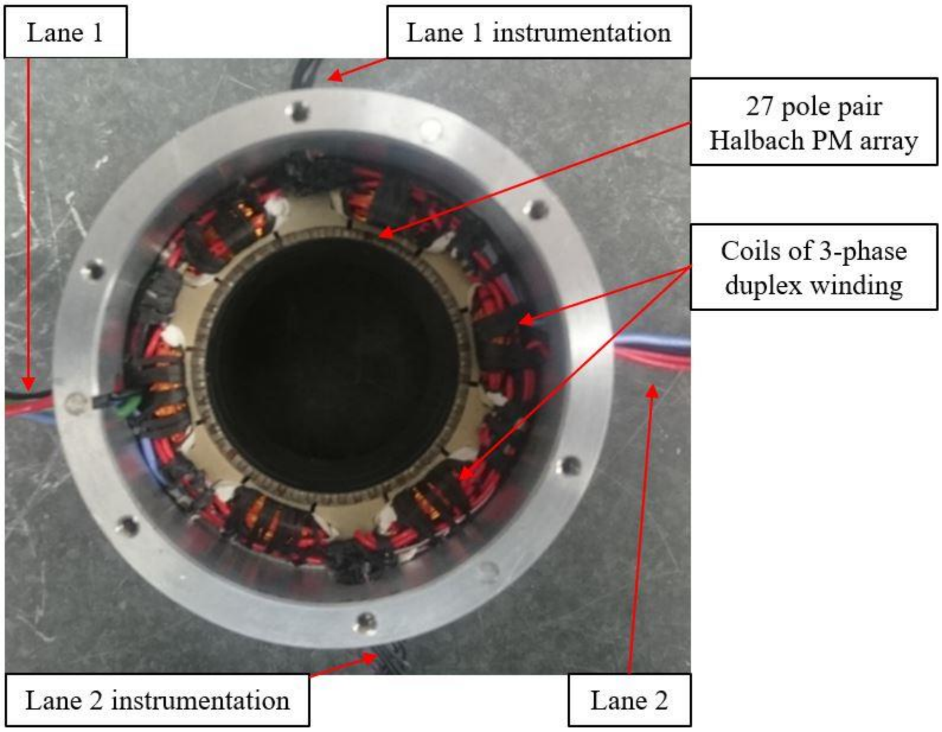

Figure 10.12. Stator inserted in PDD aluminium case

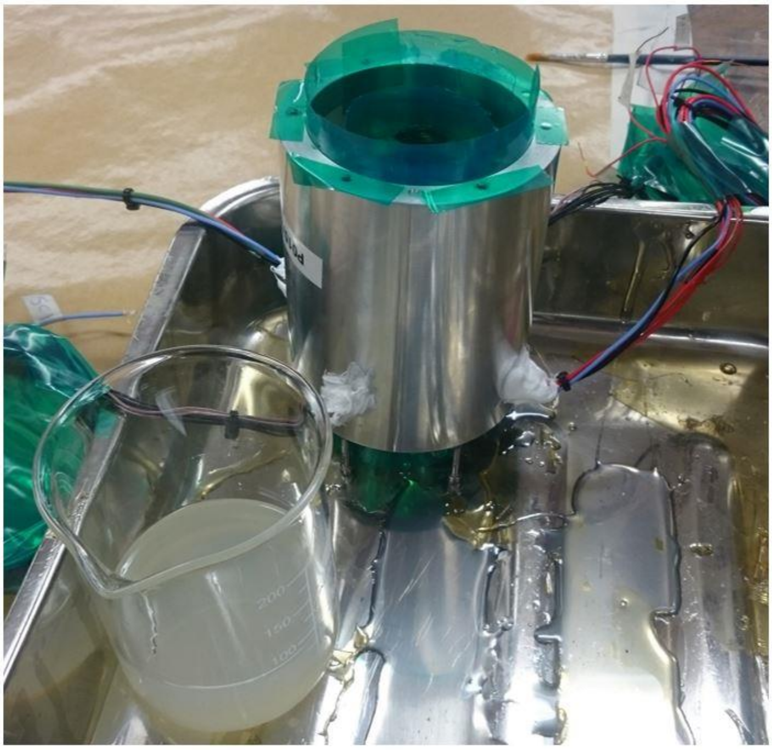

Figure 10.13. PDD stator in case during winding varnishing

For two prototype FT PDDs, the stator winding was encapsulated with Duralco 4538 from Cotronics. Encapsulating the wound FT PDD stator was done with the view of securing the copper bundles in the stator slots, reducing possible vibrations and movement of the copper wires. Moreover, the potting material added thermal mass to the winding end-regions and improves the thermal conductivity between the copper wires and stator laminations, reducing the temperature rise and improving the thermal response during transient actuation cycles.

The encapsulant was selected due to its wide operational temperature range of -75^{o}C to +230^{o}C. The solution comes in two parts, with a mixture of 1-part resin and 1.2-parts hardener being used to obtain a flexible potting structure around the stator windings. The resultant resin has good adhesion to the surrounding parts and resistance to vibrations. The thermal conductivity of the cured resin is 1.01 W/(m·K). The datasheet of the material is shown in Appendix 1.

In order to encapsulate the wound PDD stators, a potting rig, shown in Figure 10.14, was designed and manufactured such that the resultant stators do not have voids in the cured resin, with the encapsulant region being moulded around the pole piece rotor. The rig is based on an ECVP 4300 vacuum pump, utilised to drop the pressure inside the vacuum chamber. The resin was stored in a container outside the vacuum chamber. The unpotted stator was fixed in a tool that interfaced with the PDD case and stator bore. This acted to route the resin in the winding copper bundles and mould it in the required shape, such that there is no interference with the HSR-PPR assembly and case endplates. All the stators which required potting were not varnished in order to allow the encapsulant to flow through the copper bundle. Prior to assembly, the potting tooling was fully covered with 3 layers of conformal coating, allowing for 5 minutes intervals between the application of each layer. This ensured that the encapsulant does not stick to the tooling during curing, and the cured potting body is not damaged during tooling disassembly. Pneumatic fittings were used to connect the exterior resin container to the vacuum chamber and the PDD potting tolling.

Prior to potting the resin and hardener were heated to 65^{o}C in order to reduce viscosity and allow increased flow. Due to the fact that the resin cures at room temperature, a working window of only 20 minutes, from preparing the mixture, was available. Once ready to commence potting, the resin and hardener were mixed according to the data sheet specifications for a flexible finish.

As air was removed from the chamber by the compressor, the pressure difference, between the inside of the chamber and exterior, forced the mixed resin from the exterior container to flow through the PDD stator copper bundles, and exit the tooling through the drain tubes. During potting the resin in the exterior container was continuously mixed and heated to a temperature between 40-50^{o}C using a heat gun. A PID controlled adhesive heat blanket wrapped around the exterior container would have been a better choice due to the accurate temperature control.

Until the resin started continuously flow through the drains, the pressure was regulated to 0.7 bar of vacuum pressure by adjusting the bleed valve of the chamber. This is because the resin takes a certain time to flow through the circuit, and if the vacuum pressure is increased towards 1 bar of vaccum pressure, the resin will boil at room temperature. This will cause voids to form inside the resin, reducing the fill factor in the stator, and impacting thermal performance.

Once constant flow of resin is achieved, the pressure is set to 0.9 bar of vacuum pressure for 10x5 second intervals with 10 second between consecutive runs. This ensured that all the air is removed from the chamber, and the resin is allowed to flow into all the gaps within the bundle, without boiling the mixture. Once the process is complete the vacuum pump is switched off, the chamber bleed valve is released, and the encapsulated stator is cooled in this position, at room temperature for 24 hours. Jacking bolts are used to remove the potting tooling post-curing.

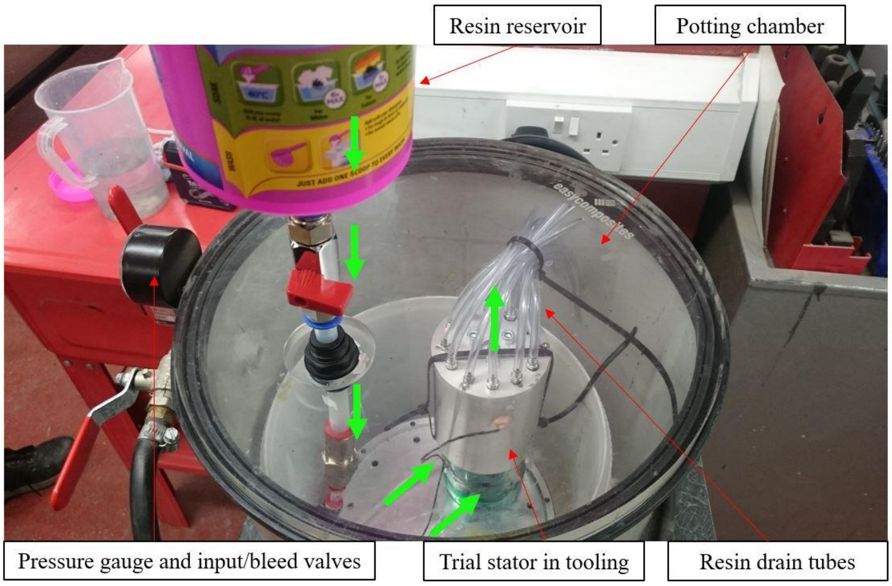

Figure 10.14. PDD potting rig

The results of the first potting trial run conducted on a wound dummy stator is shown in Figure 10.15. The drive end shows a very good fill factor with the potting resin being well moulded around the end windings, in the available volume. The non-drive end, shown in Figure 10.15 (b), has irregularities in the end winding region which are caused by boiling of the resin. During this run, the resin was kept at 1 bar of vacuum pressure for 15 second intervals. Nonetheless, the resin slot fill factor within the copper wires, shown in Figure 10.15 (c), is good.

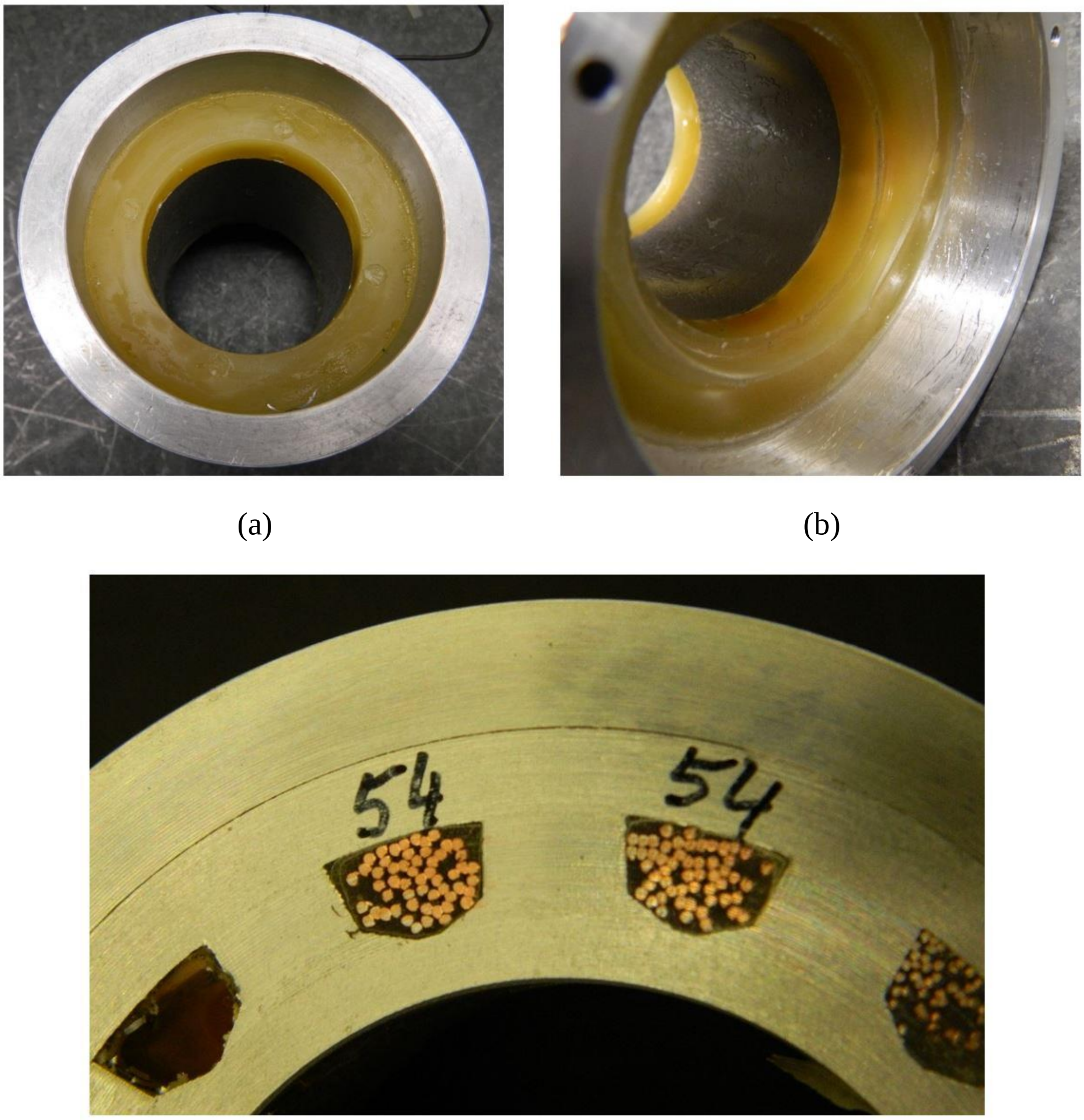

(a) (b)

(c)

Figure 10.15. Potting trial 1 (a) drive end (b) non-drive end (c) slot fill

The results of the second potting run are shown in Figure 10.16. The drive end shows a good fill, while the non-drive end was affected by severe boiling of the resin. The pressure was kept at 1 bar of vacuum pressure for 10 seconds between pulls. Despite this, all the copper wires were completely encapsulated, with an unchanged slot fill factor, as shown in Figure 10.16 (c).

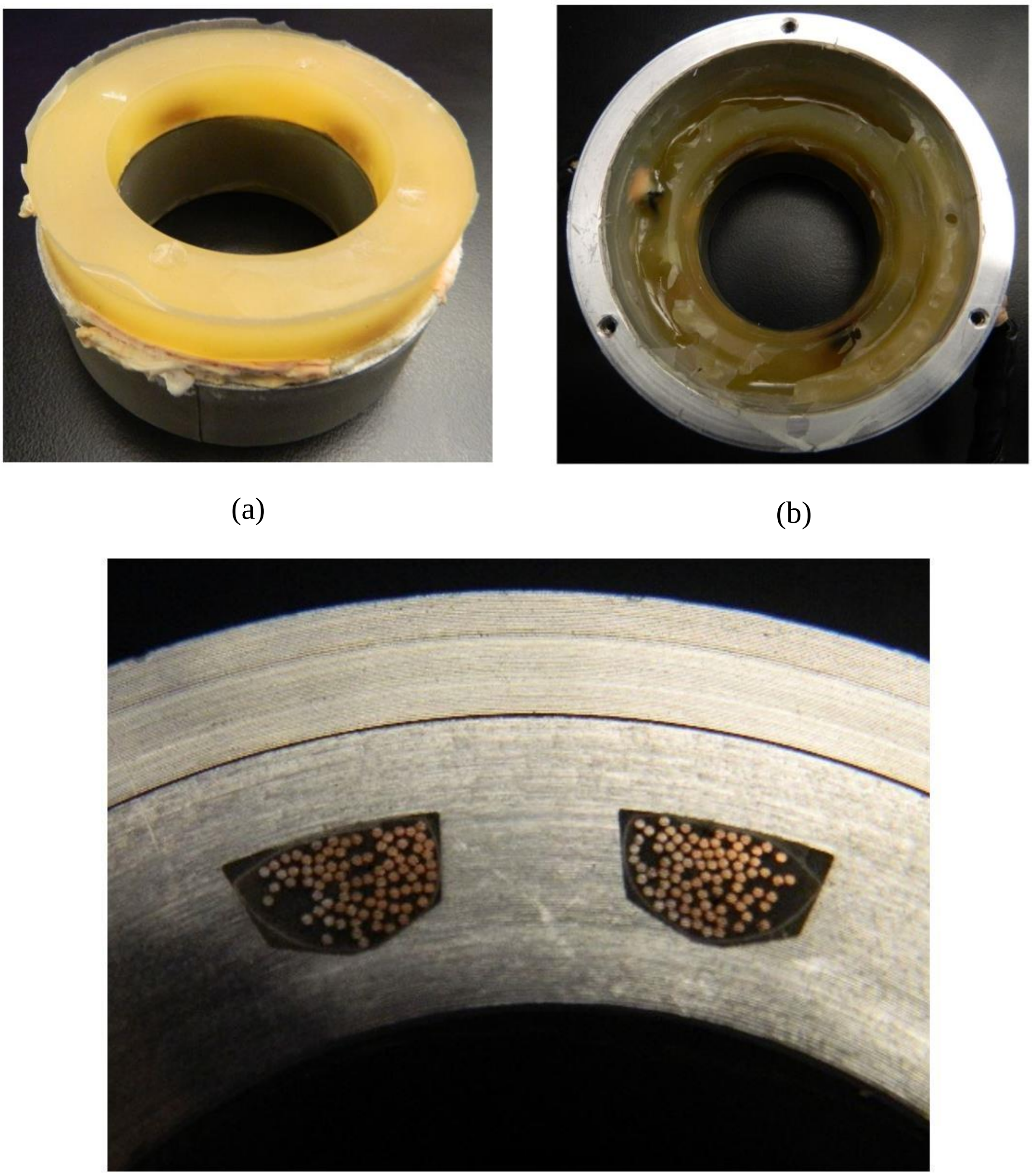

(a)

(b)

(c)

Figure 10.16. Potting trial 2 (a) drive end (b) non-drive end (c) slot fill

The final encapsulation trial run, Figure 10.17, shows the best results. The pressure in the chamber was set at 0.9 bar of vacuum pressure for 10x5 second intervals with 10 second between consecutive runs. This produced by far the best results, with both stator end winding regions being completely encapsulated, with clear potting compound, while having the correct shape. The stator slot fill was not affected, with the resin completely filling all the available volume.

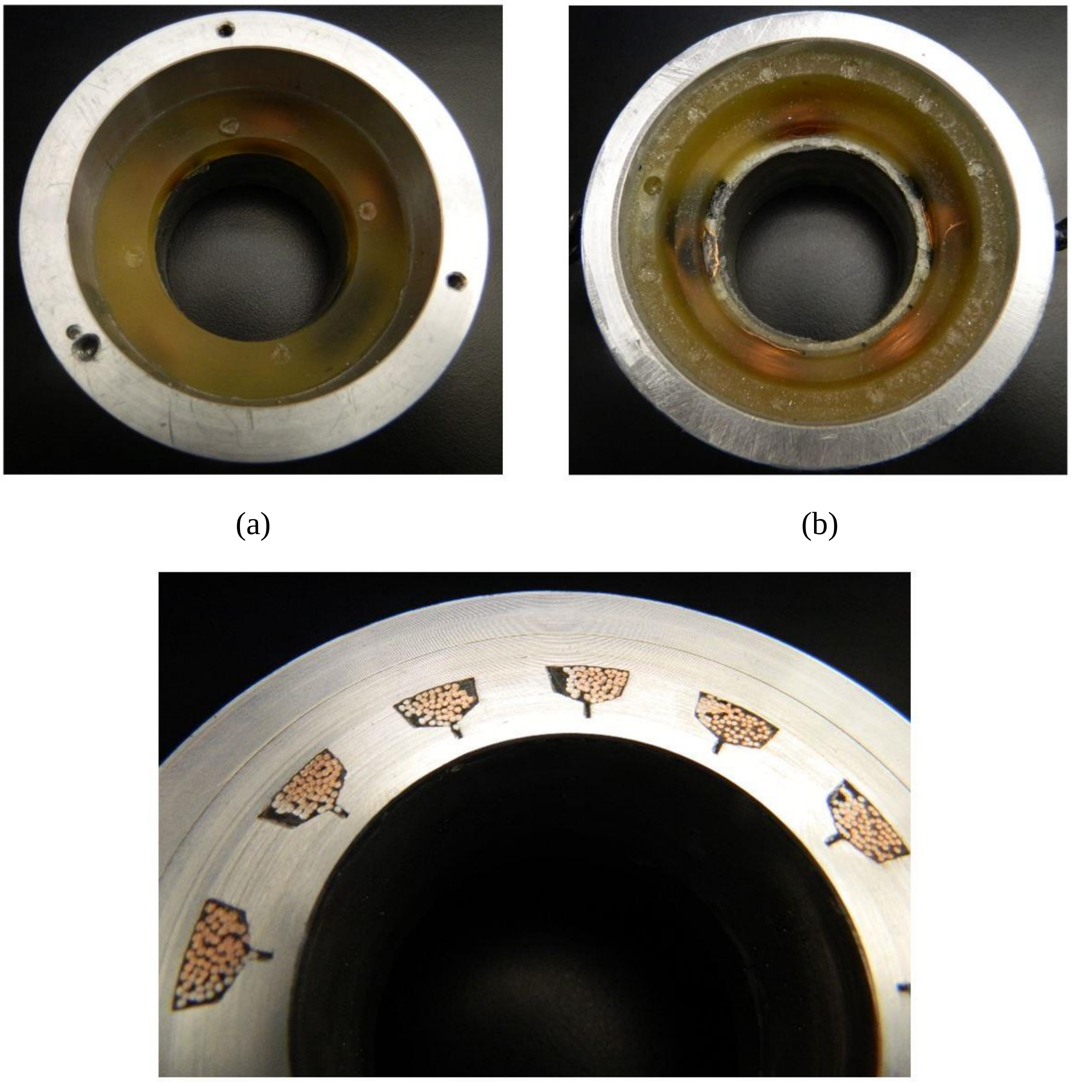

(a) (b)

(c)

Figure 10.17. Potting trial 3 (a) drive end (b) non-drive end (c) slot fill

The final encapsulated FT PDD stator assembly is shown in Figure 10.18. The wire exit holes were sealed, prior to potting, with silicone sealant. The drive and non-drive ends show excellent resin fill and are within the dimensional limits. The stator bore was cleaned of resin residue, in order to ensure no interference with the airgap of the machine.

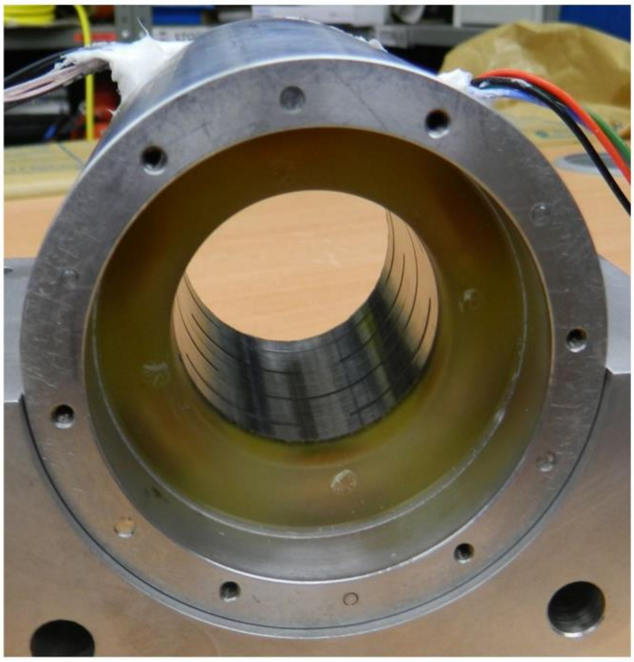

(a)

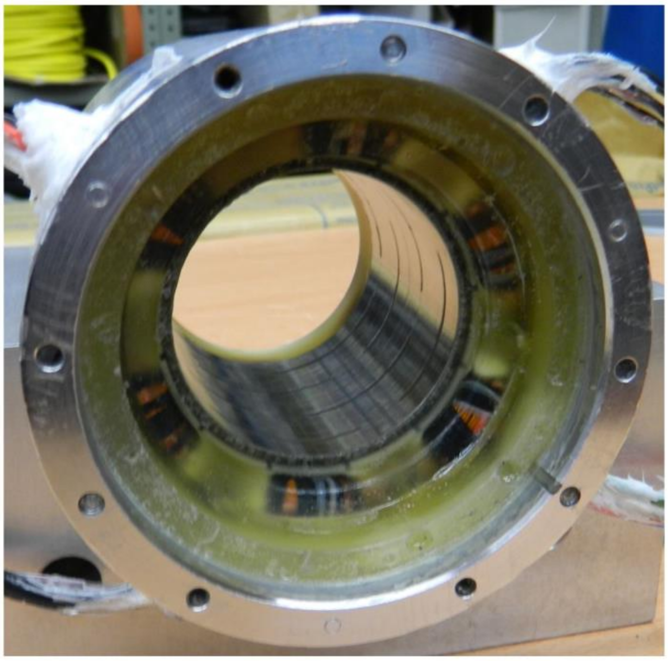

(b)

Figure 10.18. FT PDD stator winding encapsulation

10.1.4 Fault-tolerant PDD final assembly

For the final PDD assembly, shown in Figure 10.19, tooling was used to guide the PPR assembly into the case-stator assembly. The guide shaft passed through the hollow HSR and PPR shafts in order to align the two rotors with respect to the centre of the case-stator assembly. The PPR guide rods, are threaded bars with engage with the case drive endplate to locate the drive end bearing holder into the endplate. The HSR-PPR assembly slides into position on the main guide shaft. Figure 10.19 (b) shows the completed FT PDD motor prototype.

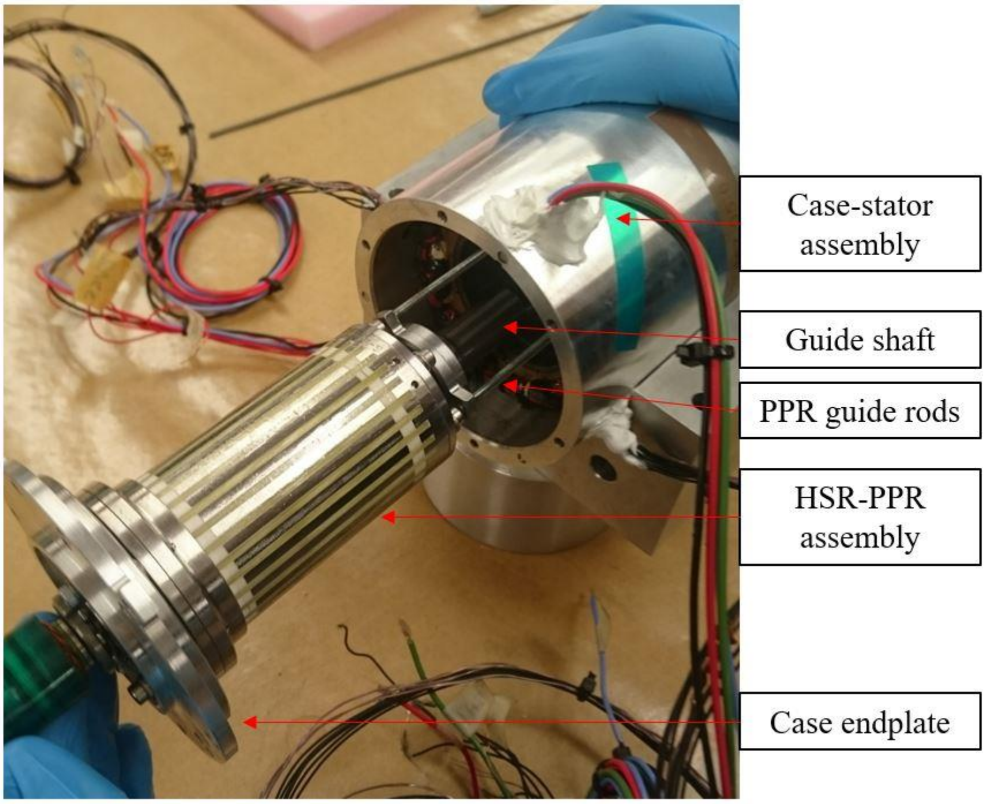

(a)

(b)

Figure 10.19. FT PDD (a) final assembly setup (b) completed motor

10.2 Fault-tolerant PDD test dynamometer

The dynamometer developed for the magnetic gear testing was modified to accommodate the FT PDD prototype, as shown in Figure 10.20. The input side PM motor and belt assembly were removed. The FT PDD was attached to the test bracket and connected to the load PM machine using torsionally-rigid couplings. The torque between the two electrical machines was measured by the 30 Nm torque transducer. Each electrical machine on the test rig was aligned to its mating machine shaft by using the TKSA20 SKF laser shaft alignment tool.

The FT PDD was operated during testing in Active-Passive configuration, with one lane being connected to an H6 KEB power inverter. The commutation of the inverter switches was based on the HSR position feedback given by one of the duplex resolvers.

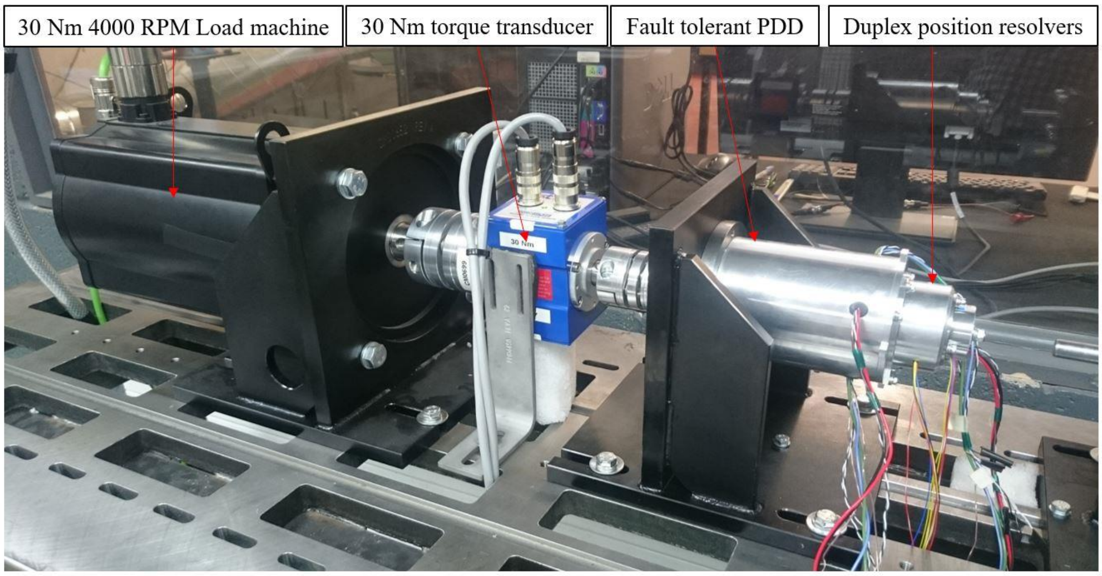

Figure 10.20. FT PDD mounted on dynamometer

10.3 Experimental validation of fault-tolerant PDD motor

The experimental validation of the fault tolerant PDD actuator motor consisted of no-load, on-load and short circuit operation. The pull-out of the magnetic gear element was measured in static and dynamic tests. The thermal performance and bandwidth capability were assessed according to the actuator drive cycles presented in Chapter 2, section 2.5.

The phase resistance and inductance were measured with the FT PDD motor fully assembled. The phase resistance of each phase was measured using the Cropico D07 micro-ohm-meter connected between the end tails of each phase and corresponding star point of each 3-phase lane. The measured phase resistance values shown in Table 10.2 include the hook-up wire connected to the copper coils inside the machine. The AWG 18 TFE Teflon hook-up wire was specified with a length of 1.5m per end connections. This represents 56 mΩ of additional resistance. The predicted value in Table 10.2 includes the resistance of the hook-up wires.

Table 10.2. FT PDD phase resistance measurement

Resistance	**Value (Ω)**
A1 - Star 1	0.662
B1 - Star 1	0.661
C1 - Star 1	0.669
A2 - Star 2	0.662
B2 - Star 2	0.660
C2 - Star 2	0.682
Predicted	0.626

The phase and mutual inductance were measured using a Hioki 3522 LCR meter. The phase-inductance was measured by connecting the meter between the end connection wire of each phase and the corresponding star point of each lane. The mutual inductance was calculated from the phase and line inductance measurements. Table 10.3 shows a good agreement between the measured and predicted values of the self and mutual inductance.

Table 10.3. FT PDD phase inductance measurement

Inductance	**Value (mH)**	**Inductance**	**Value (mH)**
L A1	1.83	L A2	1.84
L B1	1.83	L B2	1.83
L C1	1.84	L C2	1.83
Predicted	1.82	Predicted	1.82
M A1B1	1.20E-02	M A2B2	7.00E-03
M A1C1	1.40E-02	M A2C2	7.00E-03
M B1C1	1.10E-02	M B2C2	7.00E-03
Predicted A1B1	1.13E-02	Predicted A2B2	1.12E-02
Predicted A1C1	1.13E-02	Predicted A2C2	1.13E-02
Predicted B1C1	1.12E-02	Predicted B2C2	1.12E-02

10.3.1 Open circuit EMF

The phase open circuit EMF of the FT PDD was measured by connecting the TPS2000B oscilloscope between each phase and corresponding star point of each lane. The FT PDD was back driven at a fixed speed by the load PM electrical machine. Figure 10.21 shows the measured open circuit phase EMF at a PPR speed of 1200 rpm and HSR speed of 9300rpm, for both 3-phase lanes of the duplex winding. Figure 10.22 shows the harmonic components of predicted and measured open circuit EMF waveforms at 1200 rpm PPR speed. The frequency of the fundamental component is 620Hz. It can be observed that a good agreement exists between the 3D FE prediction and measured values. The 2D FE value is 12% higher than measured, while the 3D FE prediction is only 4% higher than the measured EMF fundamental component. The substantial difference between 2D FEA and measured is due to the inability of the 2D model to consider flux end leakage effects. Unlike conventional SPM electrical machines, due to the large effective airgap between the HSR and stator teeth, it is important to model the PDD cross-section in 3D FE in order to obtain an accurate representation of the flux linkage and voltage.

The variation of the measured peak open circuit EMF with PPR speed for both lanes is shown in Figure 10.23. It can be observed that the EMF variation with output rotor speed for the two lanes is identical, with a good match to the 3D FE prediction.

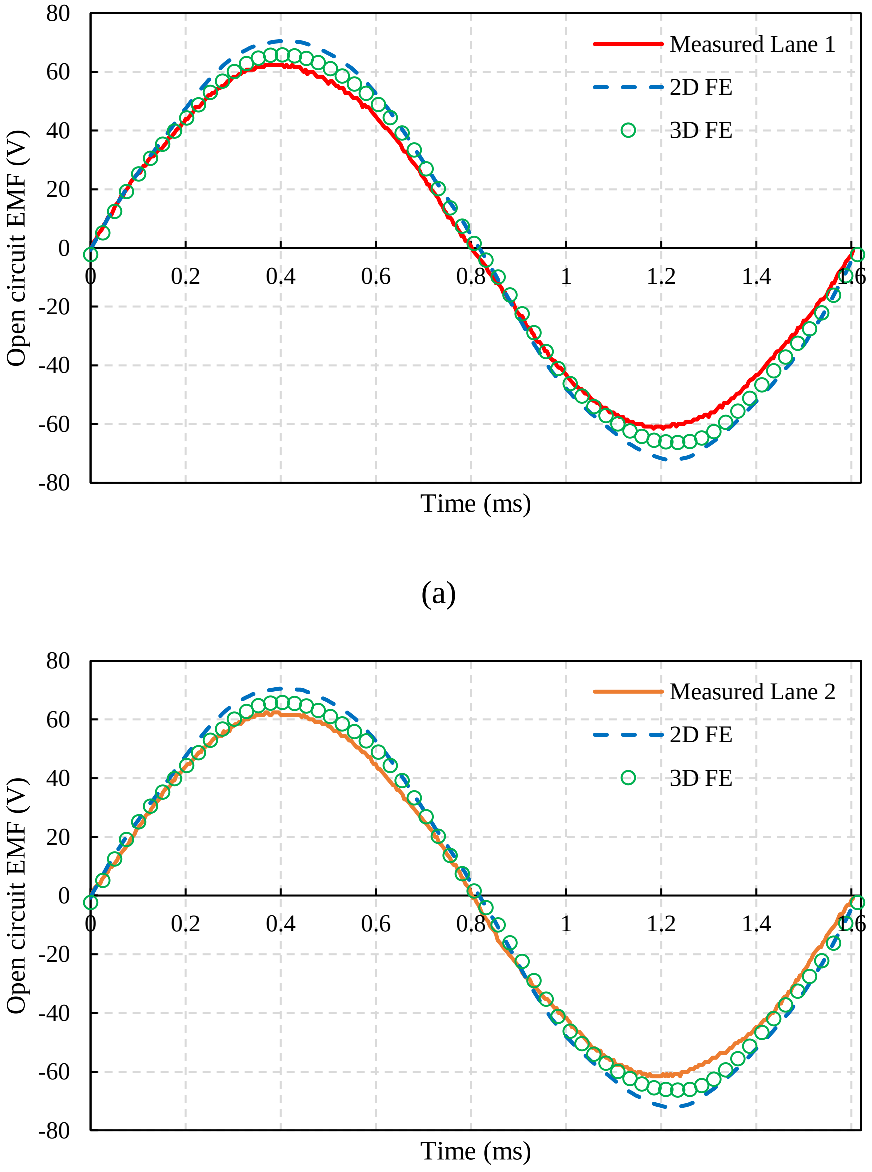

(a)

(b)

Figure 10.21. Measured open circuit EMF at 1200rpm PPR speed for (a) Lane 1 (b) Lane 2

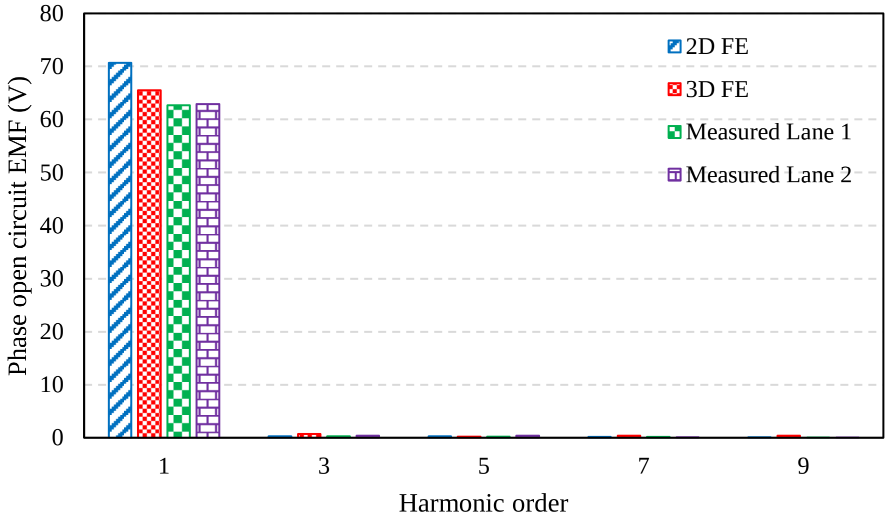

Figure 10.22. Harmonic content of measured open circuit EMF

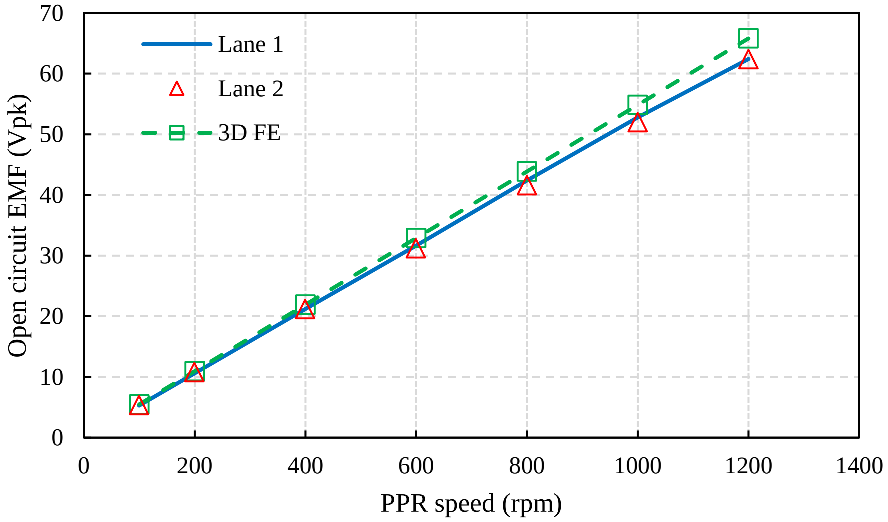

Figure 10.23. Variation of measured peak open circuit EMF with PPR speed

10.3.2 Open circuit power loss

The open circuit power loss was measured from the output side of the FT PDD while it was back-driven by the load machine. The torque transducer between the PDD and load motor was used to record the drag torque of the PDD and speed of the output rotor. Figure 10.24 shows the variation of the FT PDD power loss and PPR drag torque with output rotor speed. The FT PDD and magnetic gear prototypes have been designed with the same bearings and bearing preloads. Thus, the bearing loss of the FT PDD is identical to that of the magnetic gear prototype. The corresponding bearing loss, shown in Figure 9.34, has been subtracted from the total no-load measured loss of the FT PDD. Due to the insulator coating of the Titanium sleeve, which acts to reduce the electrical contact and eddy current flow between the sleeve and stator PMs, the measured loss and resultant PPR drag torque are only 16.8% higher than the predicted value at 1200rpm output rotor speed. Moreover, although the FT PDD is 8mm longer than the magnetic gear prototype, the no-load power losses of the two prototypes are similar. This shows that the coating applied to the sleeve is effective at insulating the stator PMs from the retention sleeve and reduced the eddy current losses between the two parts.

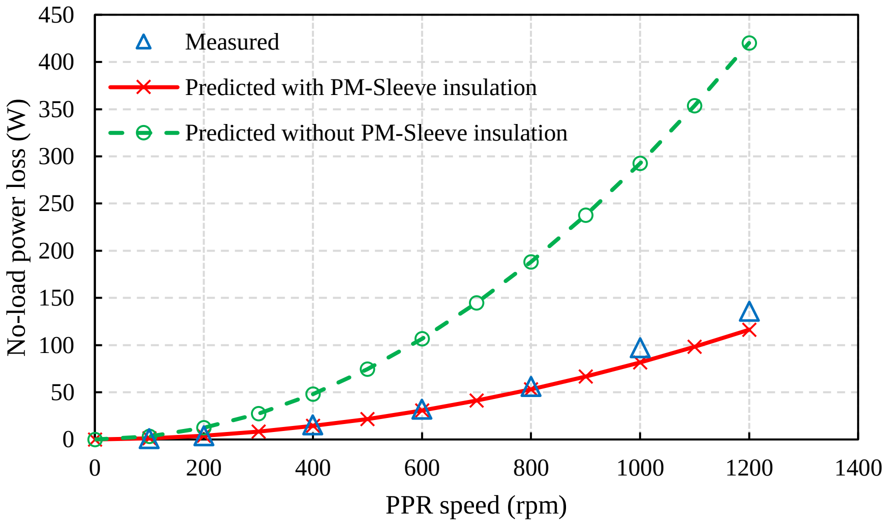

(a)

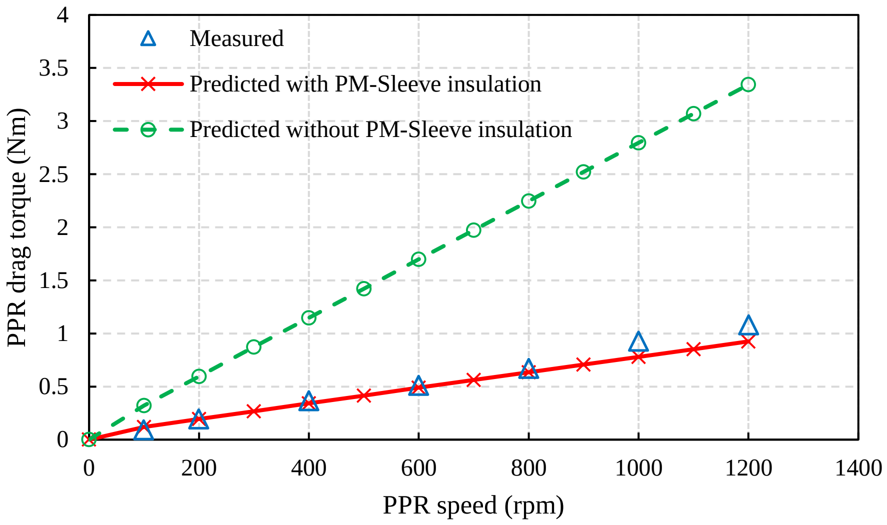

(b)

Figure 10.24. Variation of FT PDD (a) no-load power loss (b) average PPR drag torque with PPR speed

10.3.3 On-load healthy operation

On-load tests were conducted in order to measure the FT PDD phase current input in response to a torque demand, at constant speed, from the PM load machine. During on-load operation, the FT PDD was set in speed mode with a constant speed demand and a current limit which equals the rated current. The PM load machine was controlled in torque mode by varying the current demand, and with a safety speed limit. This would ensure that when PDD control is lost, the load machine does not accelerate past the rated speed of the PDD. The load machine was applying torque in the opposite direction to the PDD shaft rotation, and was enabled once the FT PDD reached steady state speed.

The shaft torque and speed were measured using the 30Nm torque transducer. The phase current of the FT PDD was measured using a Tektronix TCP312A 30A 100MHz current probe coupled to a Tektronix TCPA300 current probe amplifier. The analog outputs of the torque transducer and current probe amplifier were recorded using a 4-channel 20MHz PicoScope 4424 oscilloscope.

The variation of the average PPR torque with input phase current, for a range of speeds during Active-Passive operation, is shown in Figure 10.25. The 3D FE prediction was obtained from magneto-static simulations where the effect of eddy currents was not considered. It can be observed that due to the drag torque generated by the induced eddy currents in the non-laminated components, i.e. Titanium sleeve, permanent magnets and pole-pieces, the difference between the predicted and measured torque is increased with speed. The slope of the torque-current characteristic is fairly constant as the input phase current is increased. The phase current and torque measured waveforms at 1200 rpm and 8.5 Nm average torque are shown in Figure 10.26.

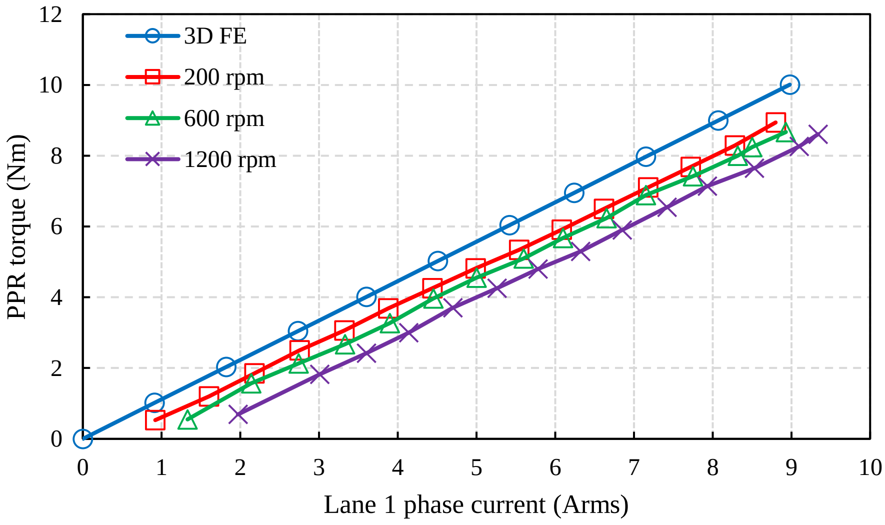

(a)

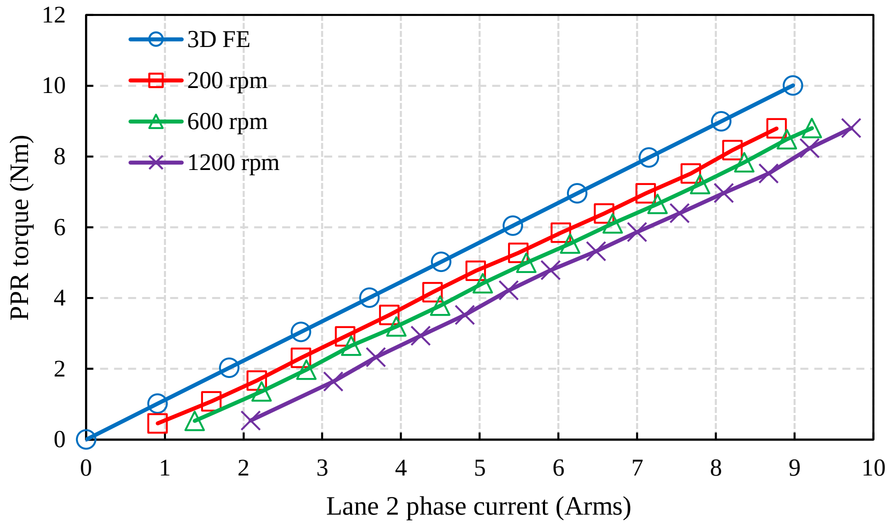

(b)

Figure 10.25. Variation of average output torque with phase current for (a) Lane 1 (b) Lane 2

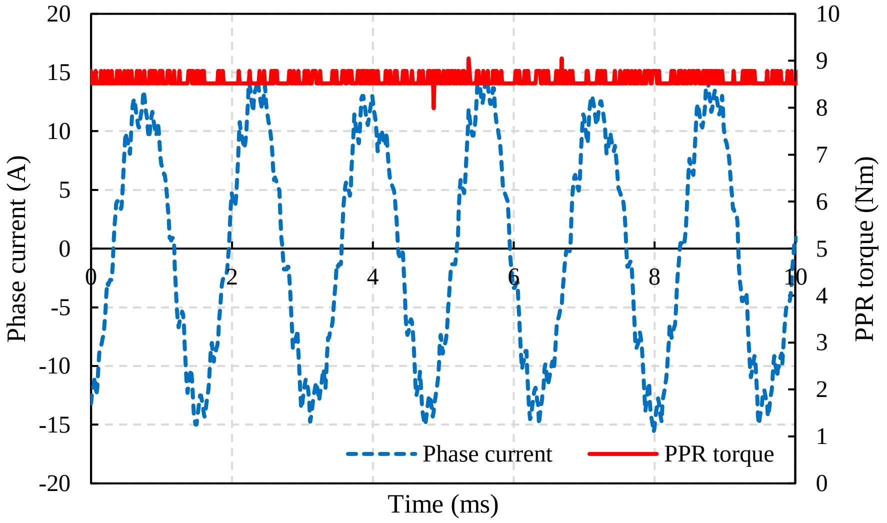

Figure 10.26. Measured PDD input phase current and output torque at 1200 rpm and 8.5 Nm demand

10.3.4 Terminal 3-phase short circuit operation

The FT PDD actuator motor is designed with a 1 p.u. phase inductance such that the symmetrical 3-phase short circuit current does not exceed the rated phase current. This combined with the duplex 3-phase winding enables motor operation during the 3-phase short circuit of one lane, without demagnetising the PMs or exceeding the thermal limit of the electrical machine.

During testing, the 3-phase short circuit was created at the lane terminals, while the healthy lane was connected to the 3-phase power inverter. The short circuit current was measured using a Tektronix TCP312A 30A 100MHz current probe coupled to a Tektronix TCPA300 current probe amplifier. The induced 3-phase short circuit current was measured with the healthy lane switched off, by back-driving the FT PDD to a constant speed with the load machine controlled in speed mode. Figure 10.27 shows the measured short circuit current and PPR drag torque at 1200 rpm. The PPR drag torque measured by the torque transducer accounts for the PDD electromagnetic losses, bearing losses and copper losses of the faulty lane.

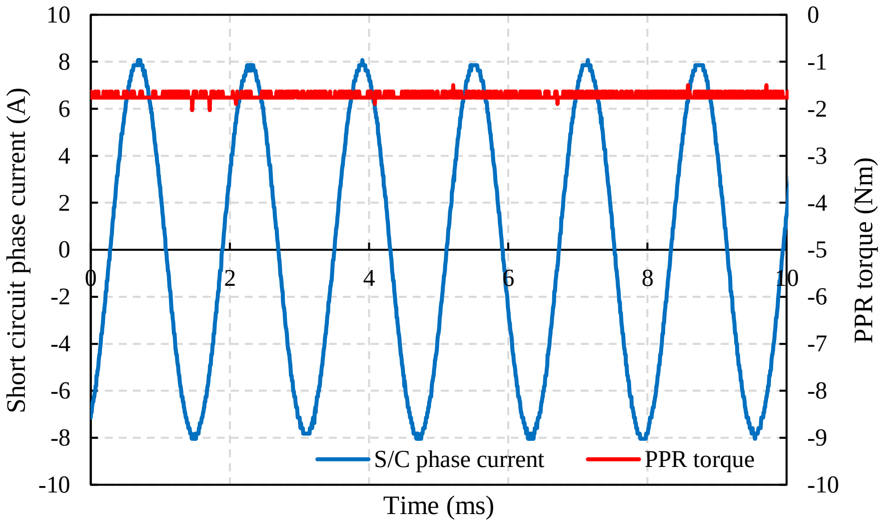

Figure 10.27. Measured phase current and PPR drag torque during symmetrical 3-phase short circuit at 1200rpm

The variation of the short circuit current with PPR speed, with one lane under symmetrical 3-phase short circuit, is shown in Figure 10.28 (a). As the rotor speed is increased, the short circuit current is inductance limited. The 3D FE prediction of the short circuit current includes the flux leakage end effects and end-winding inductance, while the 2D FE results do not consider end-winding inductance or flux leakage-end effects

At rated speed, the measured short circuit current is 4% lower than the 3D FE prediction. In comparison the 2D FE prediction, which does not consider end leakage effects, it is 21.8% higher than measured.

The measured PPR torque with one lane under 3-phase short circuit is shown in Figure 10.28 (b). The drag torque due to the short circuit current was estimated from the short circuit phase current and phase resistance measurements, by calculating the copper loss associated with the short-circuited lane. The torque transducer measurement accounts for the PDD electromagnetic losses, bearing losses and copper losses of the faulty lane. It can be observed that initially, at low speed, the drag torque increases with output rotor speed and is phase resistance limited. The peak drag torque is produced at ~90rpm. As the speed is increased further, the short-circuit phase current is inductance limited and the drag torque is reduced. It can be observed that, as the speed is increased and the eddy current losses become significant, the torque measured by the transducer is higher than the approximated drag torque, which is due to the copper losses of the induced 3-phase short circuit current.

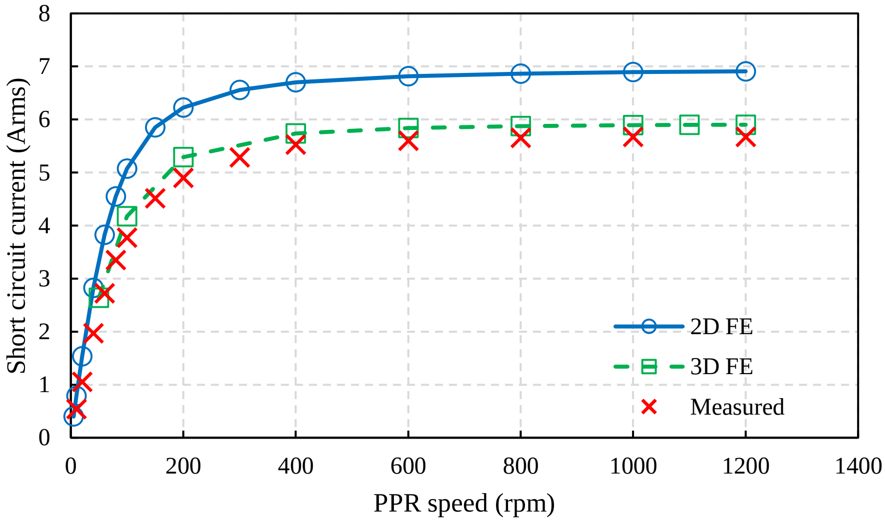

(a)

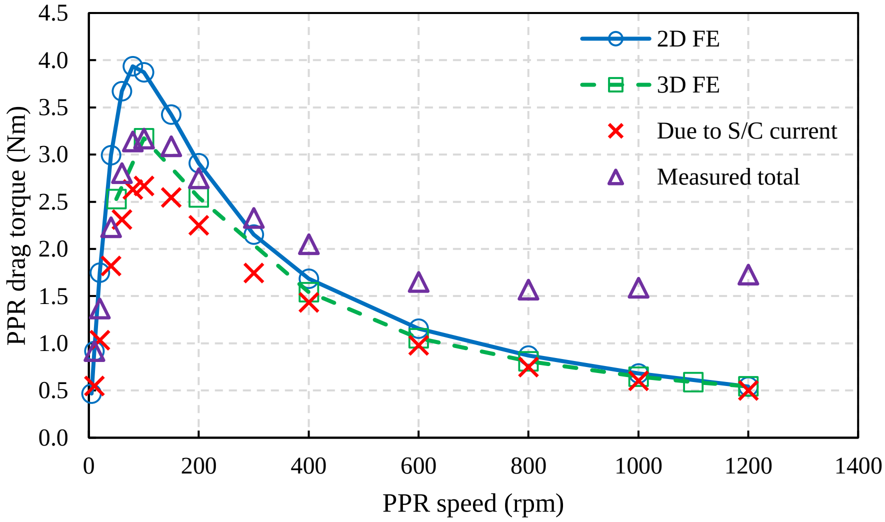

(b)

Figure 10.28. Variation of symmetrical 3-phase short circuit (a) current (b) average PPR drag torque with PPR speed

The comparison of the short circuit current and resultant total drag torque of the two 3-phase lanes is shown in Figure 10.29. It can be observed that a good match exists between the electromagnetic performance of the two lanes both under healthy and faulty operation.

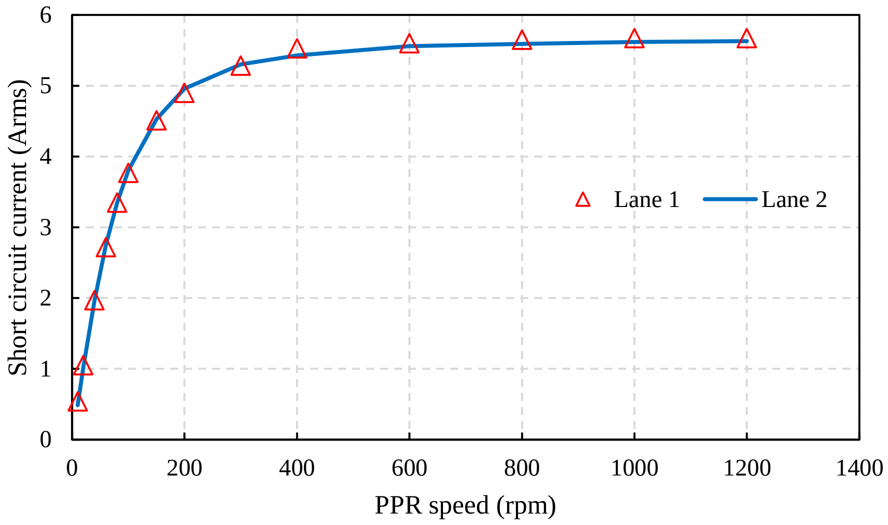

(a)

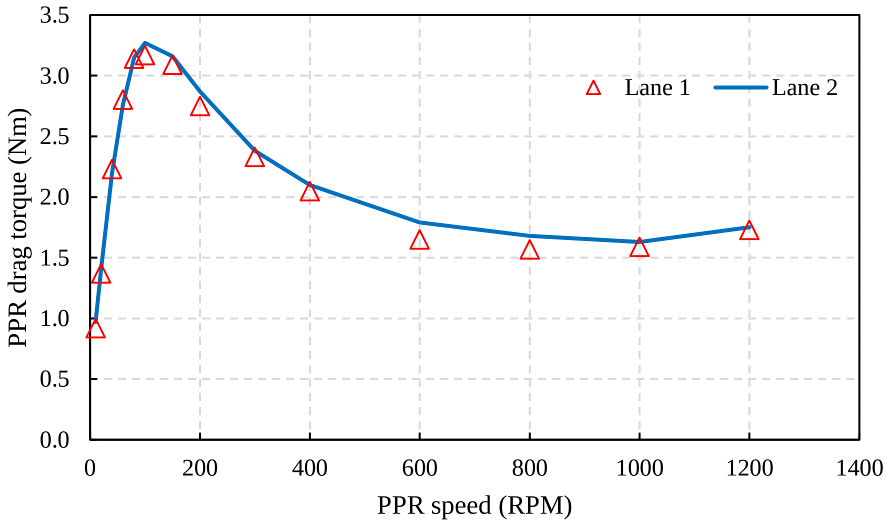

(b)

Figure 10.29. Comparison of symmetrical 3-phase short circuit (a) current (b) average PPR drag torque with PPR speed for Lane 1 and 2

The FT PDD was tested under speed mode control, in Active-Passive operation with Lane 2 under 3-phase short circuit. The load PM machine was set in torque mode with the torque being applied in the opposite direction to the PPR rotation. The phase input current of the healthy Lane 1 was measured with the current probe. Figure 10.30 shows the variation of the average PPR output torque with input phase current for Active-Passive

S/C operation. It can be observed that, for a fixed output torque, the current demand is increased based on the drag torque caused by the faulty lane, which is dependent on the output speed and amplitude of the phase short circuit current. Since the induced PPR drag torque is high at 200rpm, the torque per ampere characteristic is reduced when compared to faulty operation at higher speeds.

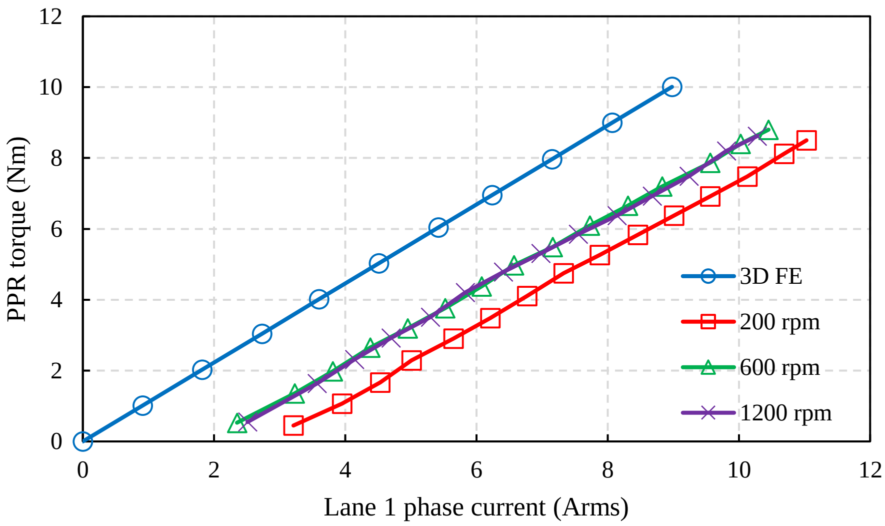

Figure 10.30. Variation of average PPR output torque with input phase current of healthy Lane 1, with Lane 2 under 3-phase short circuit – Active Passive S/C operation

10.3.5 Dynamic and static pull-out torque

The pull-out torque of the FT PDD represents the maximum torque transmission capability of the embedded magnetic gear element. Similar to the magnetic gear prototype, increasing the PDD load torque past the pull-out torque value would will cause the PPR to slip. Thus, the output shaft and connected load are magnetically isolated from the HSR, until the excess load is removed. The pull-out torque of the FT PDD was measured in an overload test triggered during normal operation. The FT PDD was used under speed mode control while the load machine was set in torque mode with a zero speed demand. During normal operation the current limit and load torque applied by the

PM load machine are increased, as shown in Figure 10.31 (a). As the load torque is increased past the torque transmission capability of the embedded magnetic gear element, the PDD slips, with the PPR shaft being held in place by the load machine, as shown in Figure 10.31 (b). Normal operation is resumed once the excess load torque is removed.

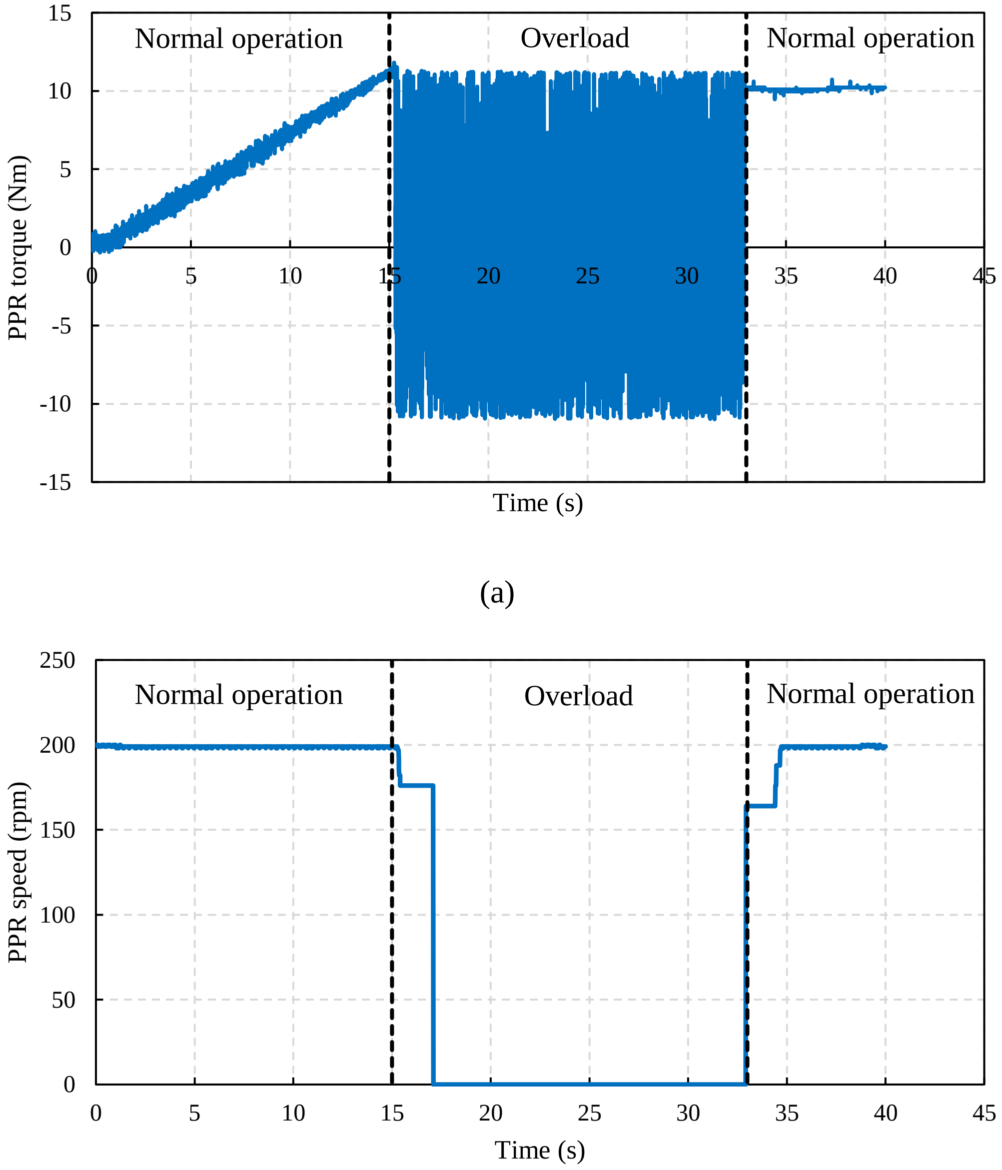

(a)

(b)

Figure 10.31. PPR (a) torque (b) speed during dynamic pull-out torque test

Figure 10.32 (a) shows the output PPR torque and input phase current during steady state Active-Passive operation for a constant transmitted load torque with an average value of

10.53Nm. During pull-out of the magnetic gear element, the average transmitted torque to the load is zero, with a reduced PDD phase current demand, as shown in Figure 10.32 (b). Here the HSR speed is kept at 1550rpm while the PPR is held stationary by the load PM machine. The average dynamic pull-out torque was measured at 11.81Nm which is less by 18% and 3% when compared to the predicted 2D and 3D FE values at 20°C PM temperature, respectively.

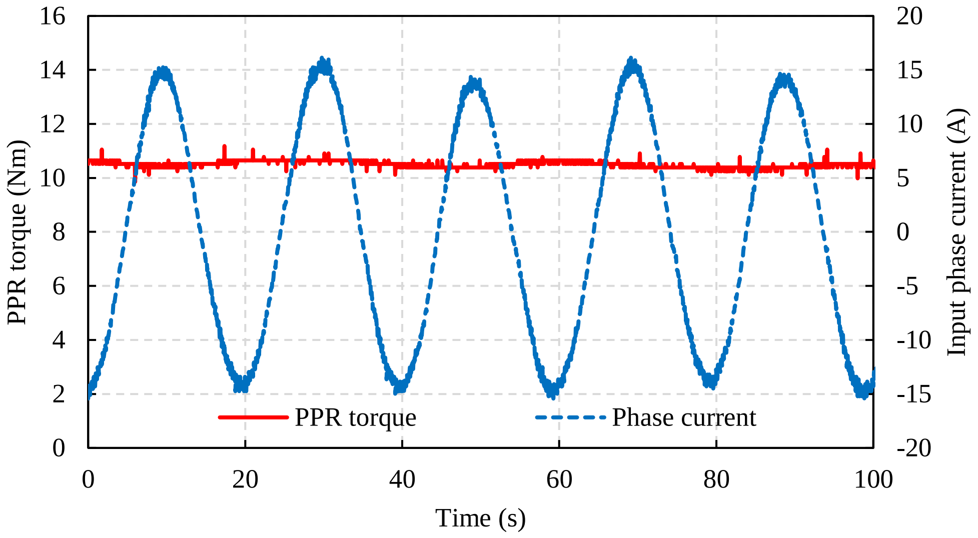

(a)

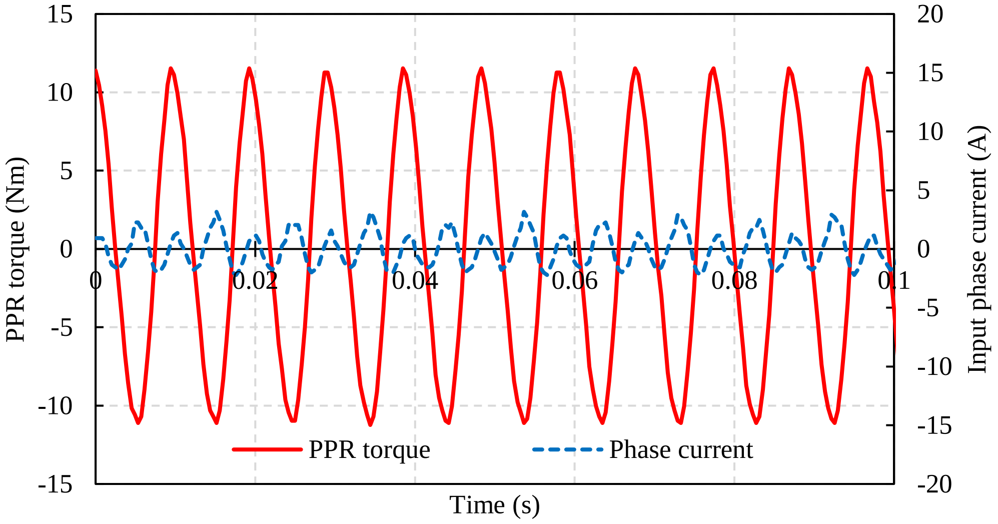

(b)

Figure 10.32. Measurement of input phase current and PPR torque (a) before (b) during pull-out event of FT PDD magnetic gear element

The pull-out torque of the FT PDD was also measured during static torque tests. For this, the load machine was first enabled with a zero-speed demand and torque limit fixed at 20Nm, substantially higher than the PDD torque capability. A torque on the HSR was manually applied using an Allen key connected to the HSR resolver shaft. The peak transmitted PPR torque is measured by the torque transducer between the load machine and FT PDD. Table 10.4 shows the measured average pull-out torque from three FT PDDs. Each value was obtained from five individual measurements per machine. The measured average static pull-out torque is reduced by 14% and 0.2% when compared to the 2D and 3D FEA predictions.

Table 10.4. FT PDD average static pull-out torque

PDD no.	**Average static pull-out torque (Nm)**
1	12.228
2	12.204
3	12.212

10.3.6 Thermal performance during actuation cycles

The thermal performance of the FT PDD prototype was assessed using FE transient analysis and experimentally on the varnished FT PDD. This variant of the FT PDD can be regarded as the having inferior thermal performance, due to the absence of the potting compound which adds thermal mass and improves the thermal conductivity between the copper wires in the slot and stator laminations.

Ansys 3D transient thermal analysis was used to initially evaluate the thermal response of the FT PDD under the actuator operation cycles presented in Chapter 2, section 2.5. Since the sinusoidal drive cycles have a large number of points, the PDD torque and speed demands were approximated to their rms values which changed with time. This was used to greatly reduce the FEA simulation time. The model geometry used in Solidworks for the mechanical design was simplified and used in the thermal analysis. This included the removal of fasteners and spacers, while details as the slot liner, copper slot fill and endplates have been kept. This helped to greatly reduce the mesh complexity and solve time. The thermal material properties, such as density, thermal conductivity and specific heat capacity, used in the transient thermal simulation, are shown in Appendix 1. Heat convection coefficients of 5 and 10 W/m^{2}K were applied to the case endplates and cylindrical body, respectively [188]–[191]. These coefficients represent a conservative approximation, since the case of the FT PDD motor is designed to be a slide fit in the actuator housing. Assuming a good thermal contact is obtained between the two assemblies, the actuator housing can increase the thermal mass of the PDD, improving the thermal response during transient operation cycles.

The airgap heat convection coefficients have been calculated from PDD geometrical dimensions and operating speed of the two rotors, by utilising the method described in [192]. This is based on Nusselt number which is a dimensionless representation of convective heat transfer coefficient, and the Taylor number. If the latter is higher than the critical Taylor number, the fluid flow in the airgap, between two rotating cylinders, is not laminar, with secondary Taylor vortices being formed. The Nusselt number and airgap heat convection coefficient are calculated based on the Taylor number, PDD geometrical factors and operating speeds. The Ansys Workbench V16 thermal software did not allow for a feedback of the winding temperature to recalculate the copper loss. This limitation was overcome by studying the sensitivity of this parameter and selecting an average copper temperature. Figure 10.33 shows the variation of winding temperature during take-off actuator cycle, for a range of assumed average copper temperatures. It can be observed that by increasing the winding average temperature by a factor of 2.8, the peak temperature of the winding is increased by 18%. For the simulation of all the actuator cycles, an average copper temperature of 50^{o}C was assumed for predicting the copper loss.

The thermal performance of the FT PDD was also evaluated experimentally, during simulated actuator cycles on the test dynamometer, developed at the University of Sheffield as part of the EMMAS project. A PM Unidrive 3-phase 2.2kW servo motor, powered by a Unidrive SP3402 3-phase inverter, was used as a load. The FT PDD was powered by a duplex 3-phase drive based on Texas Instruments HVMotorCtrl power inverter development kit. The FT PDD and load PM machine were controlled through dSpace, which set the sinusoidal torque demand from the load machine and position demand of the FT PDD. The temperature was measured using K-type thermocouples connected to the end-winding region and case of the FT PDD having.

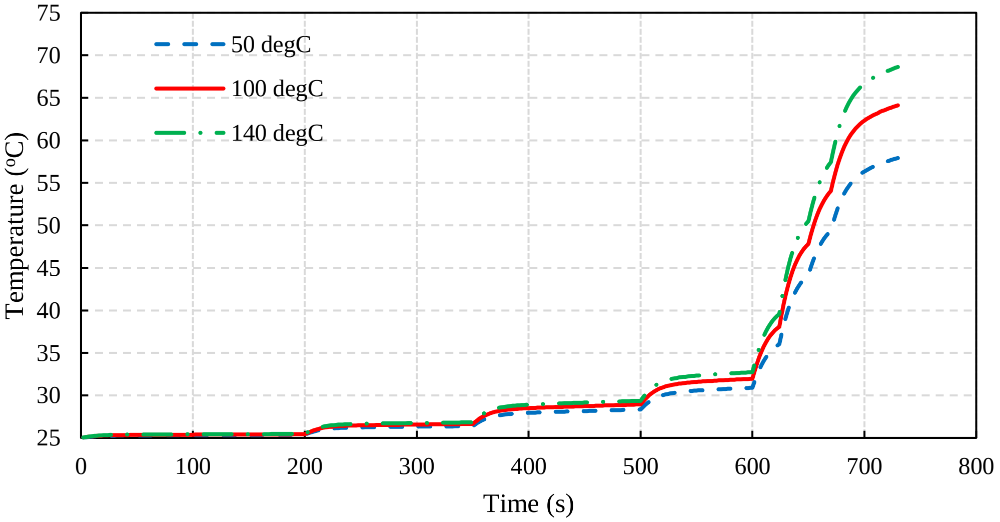

Figure 10.33. Variation of winding temperature during take-off actuator cycle for a range of assumed copper temperatures

Figure 10.34 (a) shows the peak winding and case temperature variation with time during the take-off actuator cycles. It can be observed that the measured case temperature agrees well with the FE prediction. In comparison, the peak winding temperature is overestimated by the FE model by 11.7°C or 27%. The temperature response of the machine during the emergency cruise actuator cycle is shown in Figure 10.34 (b), with the peak winding temperature being slightly overestimated by 10°C or 22%. During the landing cycle, this difference is reduced to 4°C or 7.7%. It has to be considered that the load during the landing cycle, shown in Chapter 2, section 2.5, Figure 2.33, is generally low, and the time spent at high torque and speed is reduced when compared to the take-off and emergency cruise cycles. This indicates that the Ansys thermal model overestimates the temperature during high loss conditions, most likely due to the conservative estimation of the heat convection coefficients.

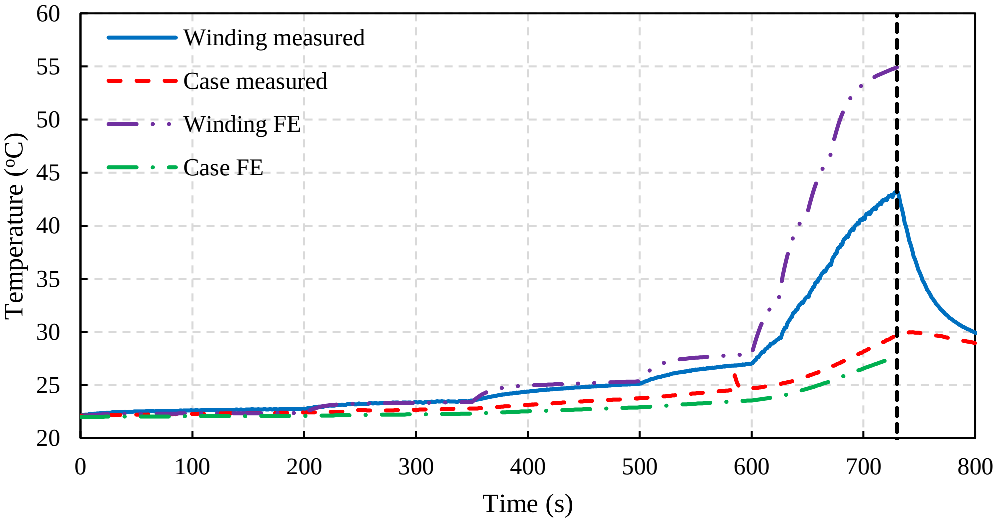

(a)

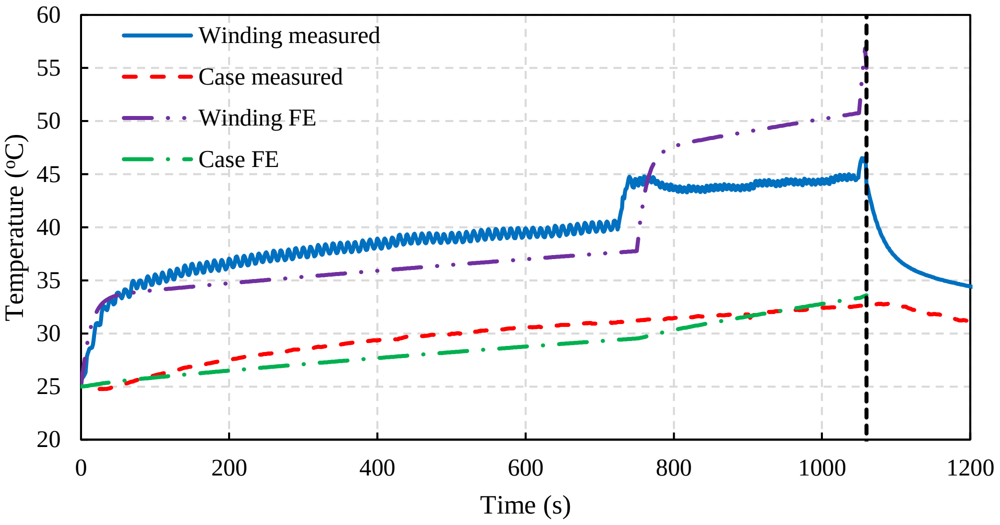

(b)

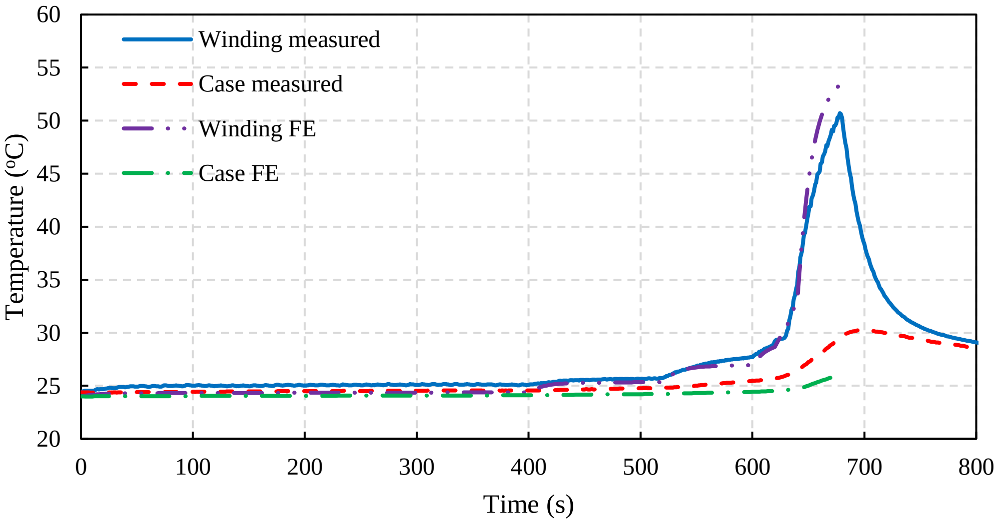

(c)

Figure 10.34. Variation of measured and predicted winding and case temperature during (a) take-off (b) emergency cruise (c) landing rudder actuator operation cycles

The thermal performance of the FT PDD was further investigated using Ansys transient thermal FEA, during the actuator cycles, with the FT PDD operating in Active-Passive short circuit mode, with Lane 1 being healthy and Lane 2 being under symmetrical 3-phase short-circuit. The healthy phase current of Lane 1 was scaled to account for the drag torque of the faulty lane. Figure 10.35 shows the peak temperature rise of various

FT PDD components during the Active-Passive short-circuit operation for the take-off, emergency cruise and landing actuator cycles. It can be observed that the highest temperature is reached at the faulty winding in the end region. This is due to the short-circuit current which reaches the value of the rated phase current at approximatively 90rpm PPR speed. The maximum winding temperature seen during the Active-Passive short-circuit operation was approximated at 102.5^{o}C which is below the 200^{o}C rating of the ML wire. In comparison, the highest temperature seen by the HSR and stator PM arrays is 50^{o}C, which is relatively low for the samarium PM grade.

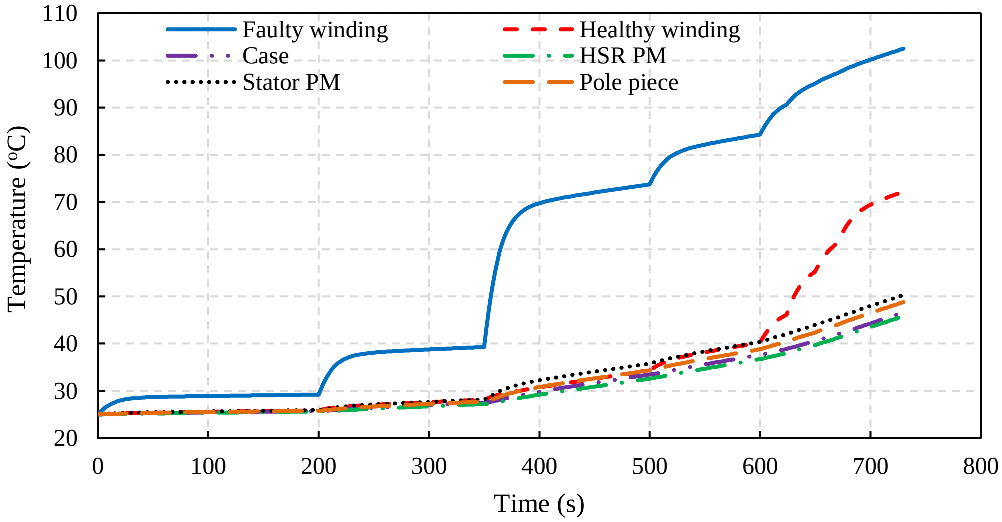

(a)

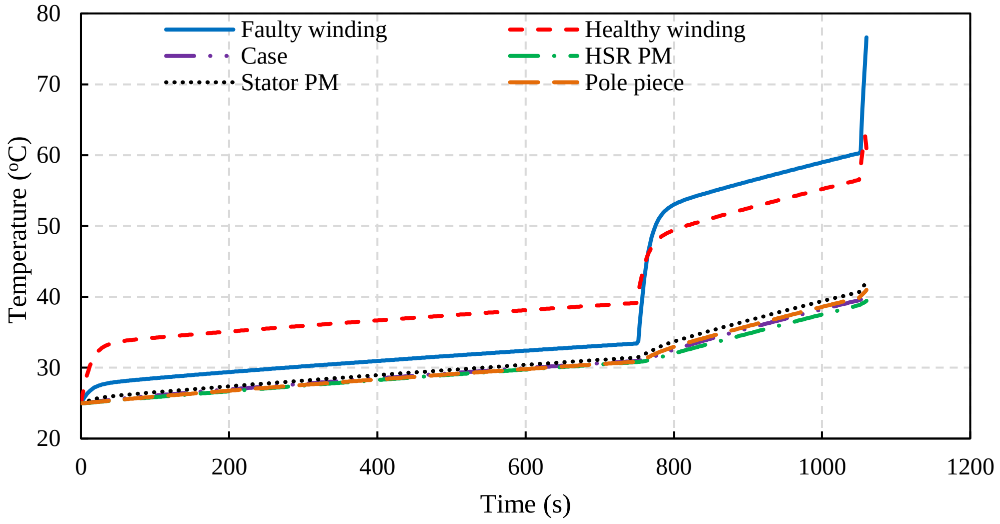

(b)

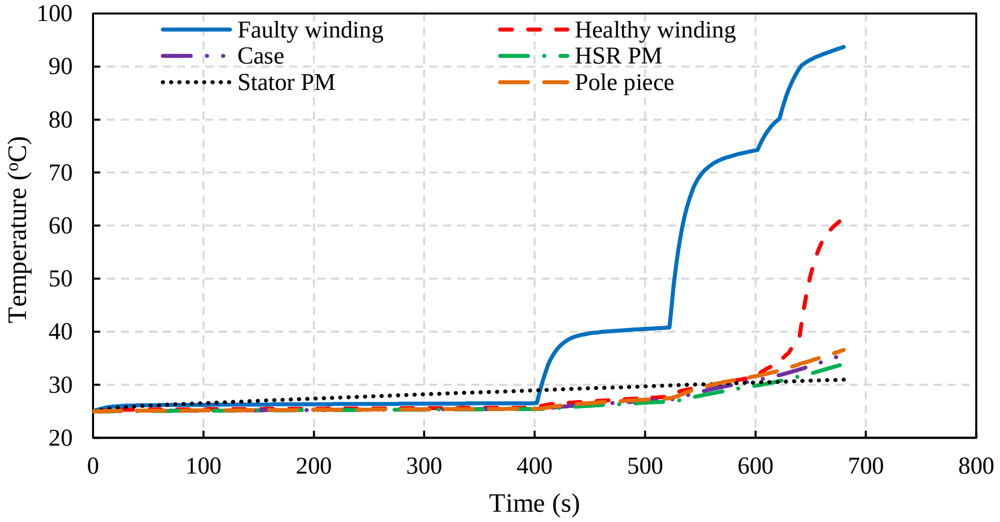

(c)

Figure 10.35. Variation of predicted temperature (a) take-off (b) emergency cruise (c) landing rudder actuator operation cycles for Active-Passive short circuit operation

The thermal performance of the FT PDD was also predicted for the take-off rudder actuator cycle, with an ambient temperature of 70°C, as a worst-case scenario. For this investigation the copper loss was predicted with the copper temperature at 140°C. Figure 10.36 shows the temperature rise of the FT PDD active components during Active – Passive and Active – Passive short circuit operation. It can be observed that, for the healthy operation, the winding reaches a peak temperature of approximatively 115°C. For this operation mode, the temperature of the HSR and stator PM arrays is at 80°C and 76°C, respectively. In comparison, during faulty short-circuit operation of one lane, the maximum temperature is seen by the faulty end-windings at 165°C. The healthy winding is substantially lower at 125°C, while the HSR and stator PMs operate at 90°C and 95°C, respectively. Thus, under this worst-case scenario, all the active components of the FT PDD do not exceed their rated thermal limit.

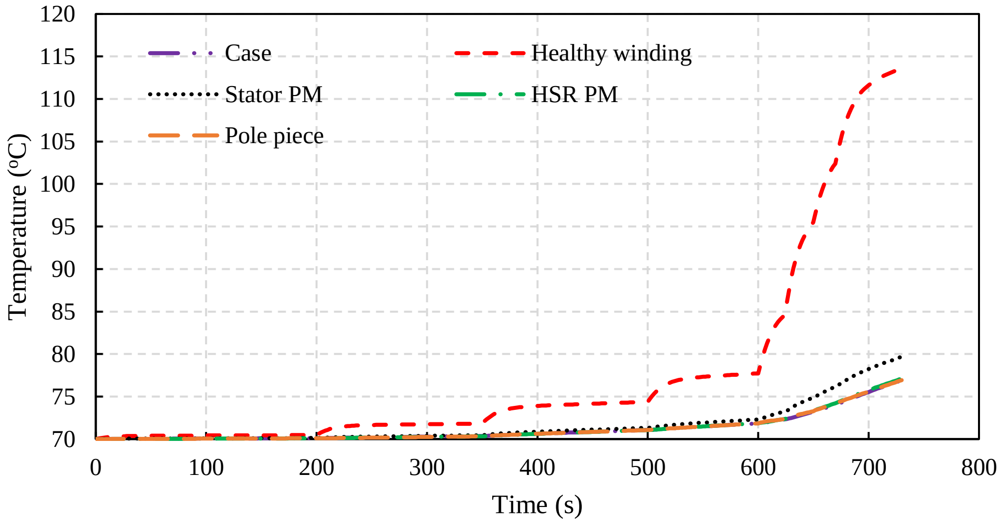

(a)

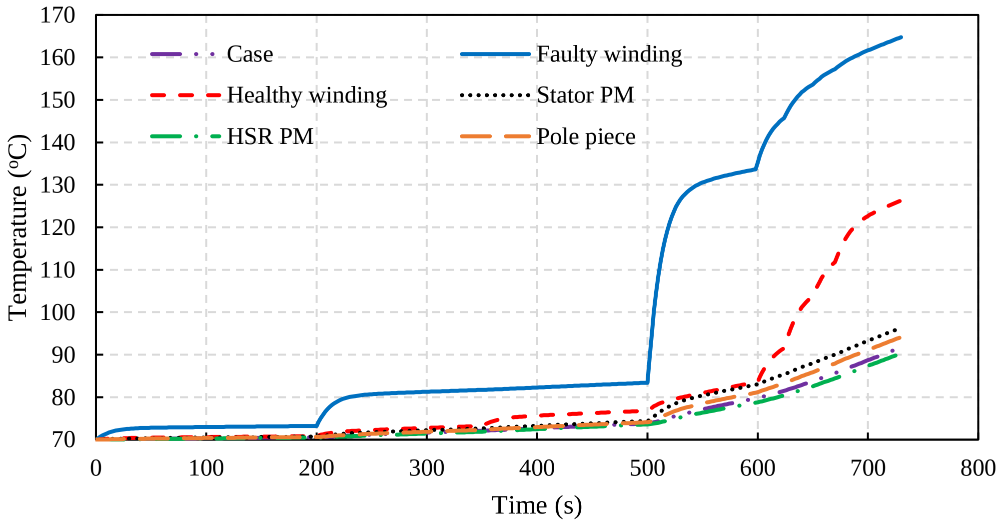

(b)

Figure 10.36. Variation of predicted temperature (a) Active-Passive (b)Active-Passive short circuit operation for 70°C ambient temperature

10.3.7 Bandwidth capability

The bandwidth capability of the FT PDD was experimentally validated on the test dynamometer and control system designed at the University of Sheffield. The load servo machine having the total inertia comparable to that of the rudder surface and the mechanical drive train, referred to the output of the PDD, was used to assess the bandwidth of the prototype actuator. The high-level control of the FT PDD and load motor was done through dSpace, which sent the speed and torque demand commands to the TI HVMotorCtrl and Unidrive SP3402 power inverter, respectively, based on the position feedback of the load machine. The speed and current control loops were implemented on the TI HVMotorCtrl kit, while the load machine was controlled in torque mode by the Unidrive SP3402 power inverter. The torque and speed were measured using a 20Nm Sensor technology torque transducer.

The bandwidth of the FT PDD was experimentally validated by measuring the PPR position from the PM load machine position sensor during sinusoidal load and displacement cycles. Figure 10.37 shows the measured 5Hz sinusoidal angular displacement of the output rotor of the FT PDD, and corresponding linear slide displacement of 1 mm, while Figure 10.38 shows the measured load torque. Figure 10.39 compares the required, analytically predicted and measured bandwidth. It can be observed that the prototype FT PDD achieved a bandwidth that exceeds the requirement, with a good agreement existing between the measurements and analytical predictions.

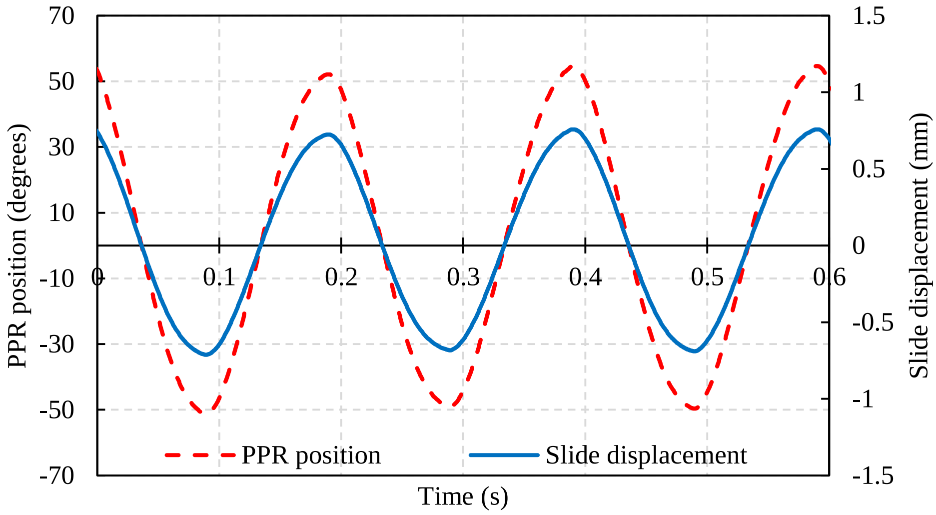

Figure 10.37. Variation of PPR position and slide displacement

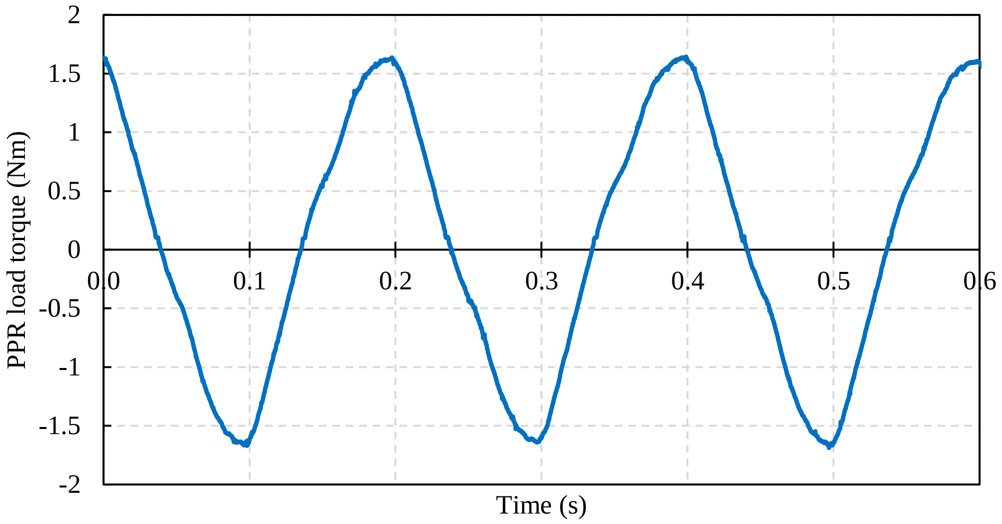

Figure 10.38. Variation of FT PDD output torque

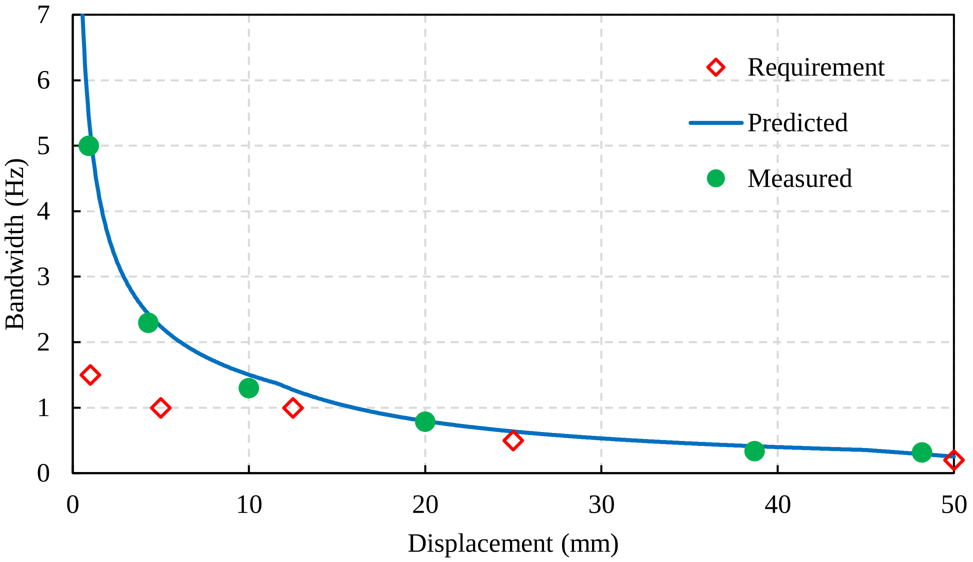

Figure 10.39. Bandwidth capability of emulated FT PDD actuator

10.4 Conclusions

The fault tolerant PDD prototype was manufactured according to the proposed cross-section and lessons learnt from the magnetic gear demonstrator.

The FT PDD motor featured the G11 PPR due to its higher pull-out capability, ease of manufacture and cost. The manufacturing procedure of the PPR was modified to include a compression tool to secure the rotor assembly during adhesive curing. This was done to ensure that the endplates are perpendicular to the cylindrical plane of the support structure and well engaged with the G11 rods.

The slot wedges were removed from the FT PDD stator since they were highly out off tolerance when tested on the magnetic gear demonstrator. For a PDD design, it is important to ensure that the slot wedges fit the stator without interfering with the PM array. In larger design this problem might not occur, since the machining tolerances are much smaller when compared to the slot opening. Different non-magnetic materials, easier to machine, could also be used to ensure an accurate fit.

In order to reduce the eddy current losses between the stator PM array and Titanium sleeve, the latter was coated with an electric insulator coating prior to fixing it around the stator PM array.

A potting procedure was devised for two of the five FT PDD stators. Due to the prototype nature of the machine, the stator potting was mainly adopted in order to minimise the likelihood of encountering a failure in the winding during testing. Stator potting can reduce vibrations in the copper strands during operation, reduce winding temperature and protect from insulation burn-out.

The FT PDD results shown in this thesis were measured on a varnished machine tested on a KEB dynamometer, under no-load and on-load operation. The open circuit EMF measurements showed a good agreement to the FEA predictions, being 4% below 3D FEA and 12% lower than the 2D prediction. This is due to the large flux leakage end effects which characterise the PDD topology, due to the large effective airgap between the HSR PM and stator teeth. This shows that 3D FEA is a necessity when designing a PDD for manufacture, to a certain specification. The open circuit power loss of the PDD was measured to be 16.8% higher than predicted. The electric insulator coating applied to the Titanium sleeve was effective at reducing the no-load loss of the FT PDD prototype slightly below the loss measured on the magnetic gear prototype, despite the increase in active length of the FT PDD by 17% over the magnetic gear demonstrator.

The FT PDD was tested on-load under Active-Passive operation, with only one lane energised. The measurements showed that the input current demand for a fixed load torque is increased with speed, due to the additional drag torque generated by the iron losses of the machine. A good agreement was established between the operation characteristics of the two lanes of the duplex 3-phase winding configuration.

The operation of the FT PDD under symmetrical 3-phase short circuit of one lane showed its capability of limiting the fault current to the rated value. The short circuit current was measured within 4% of the 3D FEA prediction. The measured drag torque during 3-phase short circuit operation accounted for the PDD electromagnetic losses, bearing losses and copper losses of the faulted lane.

The FT PDD pull-out torque measured under static and dynamic tests shows good agreement to the 3D FEA prediction. During the design and manufacturing stages, it is important to select a pole piece support structure material with high torsional stiffness, in order to reduce the twist on load of the output rotor. Moreover, a design that produces a stiff connection between the support structure and PPR endplates is highly recommended to reduce twist during load transmission. For the G11 PPR design, ensuring that a good bond is achieved between the rods and PPR endplates is beneficial to achieve good reliability under high load conditions. The adhesive of the PPR should also be selected based on the operating temperature of the PPR.

The thermal performance of the FT PDD was investigated for normal and faulty operation cycles. It was shown that the critical temperature of the active materials, such as PMs and copper winding, is not exceeded.

The bandwidth capability of the simulated actuator drive train was measured on a dynamometer capable of position and load control. The rotor inertia of the load machine was similar to the total inertia of the actuator drive train and rudder. It was shown that, for the sinusoidal load and position motion profiles, the FT PDD is capable of exceeding the bandwidth requirement, at low values of displacement.

Chapter 11: Conclusions and future work

The fault-tolerant Pseudo-Direct Drive actuator motor was designed and manufactured in line with the rudder linear actuator specifications, for a light to medium aircraft platform, obtained from a Tier 1 aerospace equipment manufacturer. Due to the PDD embedded magnetically geared transmission, the mechanical gear stages, typically present in an EMA can be removed, with the HSR of the PDD being connected through the magnetic gear element to the linear screw. This can increase the overall reliability of the actuator by removing a large number of mechanical components associated with the mechanical gearbox, while reducing the probability of jamming of the actuator mechanical drive train. The inherent passive non-contact torque fuse capability can protect the mechanical drive train of the actuator from shock loads on the control surface, such as sudden gusts of wind or object strikes. The mechanical actuator drive train is also isolated from the high stored kinetic energy of the HSR and is only connected to the low inertia output rotor. Certain jam-tolerant EMAs which implement mechanical disconnect devices have been presented in literature. Several of them are characterised by the ability to re-engage normal operation, but all of them use a complex mechanical disconnect device which includes a large number of components. In contrast, the proposed PDD design introduces passive overload protection through a contactless magnetic transmission, capable of re-engaging normal operation, with low component count and reduced complexity.

- **Enabling reduced rotor inertia**

A large percentage of linear EMA topologies are based on a PM machine which is connected to the screw of the actuator via a reduction gearbox, in order to reduce the motor torque requirement and overall mass. This results in a complex geared drive train topology with high stored kinetic energy in the rotor of the electrical machine. It was shown that the kinetic energy stored in a geared SPM actuator drive train is higher than in a PDD based system by 70%. It can be concluded that the significant reduction in kinetic energy enabled by the PDD is due to the high achievable airgap shear stress and the inherent low inertia of the pole piece output rotor.

- **Power screws for linear actuation**

An important component in the actuator drive train is represented by the linear power screw, which transforms the rotational motion of the motor into linear motion of the slide connected to the control surface. The analytical prediction of screw efficiency shows that the lead screws are the least efficient, while ball and planetary roller screws achieve an increased efficiency, by a factor of 2, at 80% to 90%, depending on screw lead and diameter.

- **Fault-tolerant Pseudo direct drive topology**

The fault tolerant winding topology for the PDD was selected based on the failure rates of the windings and power converter components. In order to achieve a fault tolerant design, it was established that the lanes which form the FT PDD winding need to be physically, magnetically, electrically and thermally isolated, in order to reduce the likelihood of fault propagation. From the investigated winding topologies, the 3-phase duplex and independent 3-phase topologies have the lowest hazard rate. Several fractional and integer slot-pole combinations, compatible with the duplex 3-phase winding configuration, have been identified.

Due to the reduced load torque requirement, and implicitly reduced stator outer diameter, the slot-pole combination selection is focused around 12 stator slots. It was shown that several magnetic gear ratios can be achieved based on the number of HSR poles required for the fractional and integer slot-pole combinations. The cogging torque factor was analytically predicted for the PM machine and magnetic gear element embedded in the

PDD. Initial sizing of the FT PDD was conducted based on a range of values for the outer airgap shear stress. This allowed for the active length and output rotor inertia to be estimated. It is shown that a trade-off exists between increasing the output rotor diameter to reduce active length and mass, at the cost of a higher output rotor inertia. Furthermore, it is important to consider that high magnetic gear ratios, which require high numbers of outer PM poles and pole pieces, can complicate manufacturing and increase cost due to the small size of the individual PM blocks and pole pieces.

- **Electromagnetic design for reduced mass and output rotor inertia**

The PDD electromagnetic performance for different PM array topologies, on the HSR and stator bore, was investigated for a fixed PPR outer diameter and pole piece radial thickness. Four PM topology combinations were implemented on four different slot-pole combinations, with similar gear ratios. It is shown that the 12s8p and 12s10p topologies, with Halbach PMs, achieved reduced active mass and lower copper losses when compared to the 12s14p and 12s16p topologies, which are characterised by high flux leakage from the HSR and poor pull-out torque capability. It is also concluded that the non-integer gear ratios have a lower torque ripple than the integer gear ratio, which can be improved by implementing a Halbach PM array to reduce torque ripple by approximatively 50%.

An investigation into the pole piece rotor design was conducted for the 12s8p and 12s10p combinations, with a fixed PPR outer diameter and constant total PM mass per unit length. Apart from the proposed PPR design, the investigation included trapezoidal and circular pole pieces. It is shown that for the trapezoidal pole piece cross-section, the PPR pull-out torque amplitude, active mass of the PDD, inertia of the PPR and copper loss can be reduced by minimising the pole piece radial thickness. It was shown that the optimum values of inner and outer pole piece pitch change based on the pole piece thickness, with a square aspect ratio being desirable. The proposed pole piece cross-section is based on a glass fibre rod design which interlocks with the side cut-out of the pole pieces. The pole piece cross-section is similar to the trapezoidal design and does not require an inner or outer torque tube to retain the pole pieces and transmit load. The comparison of the three pole piece shapes showed that the circular pole piece design achieved an inferior pull-out torque capability, resulting in a PDD with an increased mass and output rotor inertia. The trapezoidal and proposed pole piece cross-sections showed similar results, with the PPR inertia being slightly reduced for the proposed design due to the lower rotor active mass. In comparison, the circular pole piece design achieved slightly lower copper loss designs, but at the expense of active length and mass. For the fixed PPR outer diameter of 45mm it is shown that, irrespective of pole piece topology or slot-pole combination, increasing the magnetic gear ratio results in a decrease of PPR pull-out torque and increase in output rotor inertia and PDD active mass. In contrast, increasing the gear ratio can reduce the copper loss of the PDD, as the electromagnetic torque requirement is reduced for a fixed output torque. It was established that selecting a gear ratio with a cogging torque factor of 1, results in low HSR and PPR torque ripple irrespective of pole piece topology. For integer gear ratios, the adoption of circular pole piece further increases the torque ripple. The unbalanced magnetic pull was also investigated, showing that fractional gear ratios with an odd number of pole pieces have high HSR and PPR UMP. In contrast, the 12s10p topology with fractional gear ratios achieved from an even number of pole pieces have both low torque ripple and UMP.

The 2D FE electromagnetic parametric scans have been conducted for the 12s8p and 12s10p topologies with Halbach PM arrays on the HSR and stator, and for a range of magnetic gear ratio between 6-10:1. It is shown that by increasing the PPR outer diameter, the PDD active mass is reduced and PPR inertia increased. As the PPR outer diameter is increased beyond 45mm, the inertia of the output rotor is substantially increased while the PDD active mass is only moderately reduced. This is due to the increase in HSR PM mass required in order to increase the PPR pull-out torque capability and reduce the active length and mass of the PDD. It is important to acknowledge that, during an overload condition, due to the torque fuse characteristic of the magnetic gear transmission, the kinetic energy stored in the HSR is isolated from the actuator mechanical drive train. In this case, the PDD will pole slip and the HSR will rotate independently from the PPR, with zero average power being transmitted from the HSR to the PPR. Thus, additional weight can be removed from the actuator drive train as it is only rigidly connected to the low inertia PPR.

The 12s8p and 12s10p PDD designs have been selected based on the criteria of lowest mass and PPR inertia for each PPR outer diameter design family. It is shown that the 12s8p designs achieve the maximum allowable active mass requirement of 1.5 kg at lower PPR outer diameters than the 12s10p variants. Thus, it can be concluded that the PPR inertia of the 12s8p designs is reduced when compared to the 12s10p topologies.

The magnetic gear torque response time which represents the time taken to transmit the rated electromagnetic torque from the HSR to the PPR was predicted for the selected PDD designs. It is shown that for a fixed slot pole combination, the torque transmission delay is increased with PPR outer diameter and gear ratio. For a fixed PRR outer diameter, it was shown that increasing the number of HSR poles reduces the torque transmission delay of the PDD magnetic gear element, since the HSR needs to rotate by a smaller angle to transmit rated torque.

The PDD actuator bandwidth was analytically predicted for the sinusoidal actuator position and load profiles. It is shown that, for the selected designs with a PPR outer diameter of 45mm, increasing the magnetic gear ratio results in an increased HSR and PPR inertia, which reduces the maximum achievable bandwidth at low displacements. Despite this, it is shown that for all the selected PDD designs, the maximum achievable bandwidth is substantially higher than the required specification.

- **Fault tolerant Pseudo direct drive design**

In order to achieve a fault-tolerant PDD design, where the fault current under symmetrical 3-phase short-circuit is limited to the value of the rated phase current, the phase inductance was increased to 1.p.u. by adjusting the slot leakage inductance component. For a fixed PDD cross-section optimised for reduced active mass and output rotor inertia, this was realised by adjusting the slot opening geometry, such that the slot leakage inductance component is increased. The symmetrical 3-phase short-circuit current estimation was obtained from a well-known analytical method previously applied on conventional SPM electrical machines. The findings show good agreement with 2D FEA predictions. It is shown that a PDD design capable of limited 3-phase short current can be achieved, while ensuring that the slot opening design allows for a landing area for the stator PMs. The inter-turn short circuit current was predicted for 1,5 and 10 turns in short-circuit, out of 54 total turns, with zero and rated phase current in the remaining healthy turns. It is shown that the fault current amplitude is reduced as the number of turns is increased, due to increase of resistance and inductive reactance of the faulty bundle. It is important to consider that for an inter-turn short circuit fault, the fault current is substantially higher than the rated current value. The worst case occurs when a 1-turn short-circuit is triggered, with the fault current reaching 17 times the rated current value. In this case, the high fault current can be limited by triggering a 3-phase short circuit of the affected lane, such that the faulted current is reduced to the value of the 3-phase short-circuit current. The output power can then be delivered by the second healthy lane of the duplex 3-phase winding configuration.

- **Demagnetisation analysis of fault-tolerant Pseudo direct drive motor**

The demagnetisation of the FT PDD PM arrays was investigated under healthy and faulty operation. It was established the demagnetisation of the PMs is mainly influenced by operating temperature, opposing PM fields from the HSR and stator PM arrays and amplitude of the stator armature reaction. The worst demagnetisation field occurs during symmetrical 3-phase operation, since the negative peak of the d-axis current transient is substantially higher than the steady state value. Due to the considerable thickness of the HSR PM array, combined with the low knee point of the Recoma 28 material, irreversible demagnetisation of the HSR PMs is completely avoided for all healthy and faulty operation modes, up to a magnet temperature of 200°C. In contrast, the stator PMs witness the highest percentage total area affected by irreversible demagnetisation, at 7.78%, under Active-Passive short-circuit operation at 200°C. It has to be considered that this is an extremely high operating temperature and at 150°C, for the same operating case, the total stator PM area affected by irreversible demagnetisation is negligible, at under 1%.

- **Loss analysis of fault-tolerant Pseudo direct drive motor**

The electromagnetic losses of the fault tolerant PDD, which included copper, iron and eddy current losses in the non-laminated components, were predicted from 2D and 3D FEA. The copper loss was predicted during Active-Active and Active-Passive operation, with and without the effect of the additional drag torque generated by the eddy current losses on the solid PDD components. It was established that the copper loss can be reduced by 50% if the PDD is operated in Active-Active mode, with both lanes providing rated power. For any of the two operation modes, the copper losses are increased by 30.6% when the drag torque associated with the eddy current loss of the non-laminated

PDD components is considered. The iron losses in the stator and pole piece laminations were predicted from 2D FEA simulations for the two FT PDD operation modes. It is shown that during Active-Passive operation, due to localised saturation, the iron loss of the stator stack is increased by 20% when compared to Active-Active operation. Moreover, when the phase current is increased to account for the drag torque in the non-laminated PDD components, the stator iron losses are increased by 11.3% and 5.4% for the Active-Passive and Active-Active operation modes, respectively. The eddy current losses of the PMs, non-laminated pole pieces and Titanium sleeve have been predicted using 2D and 3D FEA. It is shown that for the PM loss prediction, good agreement exists between the 2D and 3D FEA predictions. This is due to the PMs having cross-sectional dimensions which are significantly smaller than the axial length. In comparison, the 3D FEA predicted PPR eddy current loss for the non-laminated pole pieces is 30% higher than the 2D case. This increase in loss is due to the axial flux component caused by the large effective airgap of the PDD. Thus, the 2D FEA does not account for the pole piece loss due to the XY-plane eddy current component, which is induced by the time and position variant Z-axis magnetic field within each pole piece. The eddy current loss of the Titanium sleeve was also investigated, showing that axial segmentation and axially displaced slits can substantially reduce this loss component. Furthermore, it was established that the eddy current losses of the sleeve and stator PM array are substantially increased if the two components are in electrical contact. Thus, in order to eliminate this loss component, the electrically conductive sleeve can be replaced with a composite variant, or an insulating layer can be placed between the sleeve and stator PM array.

The efficiency of the FT PDD motor was predicted for Active-Passive and Active-Active operation, by accounting for the winding copper loss, stator and PPR iron losses, and 3D predicted eddy current losses of the non-laminated components. The manufactured FT

PDD was predicted to be most efficient in Active-Active operation, while in Active-Passive the efficiency is reduced by 7%, to 79%, due to the higher copper loss of the single energised 3-phase lane. The efficiency can be substantially improved by reducing the eddy current loss component of the non-laminated PDD components. Thus, the pole pieces can be laminated, while the Titanium sleeve can be replaced with a composite variant. The highest efficiency at the rated operation point was predicted at 93%.

- **Manufacturing and experimental validation MG and FT PDD**

The magnetic gear demonstrator was designed to the same cross-section as the magnetic gear element of the FT PDD, in order to validate the electromagnetic and mechanical modes. From this de-risking exercise, certain modifications were implemented to the mechanical design and manufacturing stages of the FT PDD. The assembly process and alignment on the dynamometer of the MG demonstrator showed the need to ensure that the run-out of the PPR shaft is minimised. As a result, clamping plates, designed to constrain the PPR to a fixed position during adhesive curing, were implemented for the output rotor of the FT PDD. This ensured for the PPR endplates, to which the output shaft connects, to be perpendicular to the plane of the pole pieces as the adhesive sets. Two PPR topologies were produced, based on the PEEK and G11 rod support structure. During manufacturing of the output rotors, it is shown that the PEEK material can be problematic to machine when compared to the G11 variant.

The MG stator manufacturing showed that the 3D printed slot wedges were substantially out of tolerance, making them difficult and time consuming to position accurately. It the FT PDD prototype, the slot wedges were removed, with the tips of the stator teeth providing enough of a landing area for the stator PMs. On larger electrical machines of this type, the slot wedge would need to be included due to the large slot opening. It is advisable to select a different manufacturing process for the slot wedges, such as water-jetting or wire eroding composite slot wedges to a much better tolerance.

The experimental validation of the MG demonstrator investigated the no-load and on-load operation of the prototype. The measurements of the HSR PM flux density showed good agreement to the predicted 2D FE values. The power losses were measured during no-load and on-load operation. It is shown that the losses of the prototype are 60% higher than the 3D FEA prediction. This was attributed to the imperfect electrical contact between the Titanium sleeve and stator PM array, which allowed for eddy currents to flow between the two parts. Furthermore, the sleeve can be replaced with a composite variant in order to eliminate the losses of the sleeve and risk of electrical contact with the stator PM array. A good match was established between the no-load and on-load losses, showing that the efficiency of the MG can be approximated from no-load loss values. The pull-out torque for the two PPR designs was measured in dynamic and static tests. It is shown that the PEEK PPR achieved a slightly lower torque transmission capability then the G11 truss PPR. This is attributed to the lower stiffness and higher twist under load associated with the PEEK support structure. From these findings, the G11 PPR design was selected as the output rotor of the FT PDD.

The fault tolerant PDD prototype was manufactured from the proposed electromagnetic cross-section and lessons learnt from the magnetic gear demonstrator. The manufacturing processes for the HSR and PPR were slightly modified based on the findings of the MG de-risking exercise. The FT PDD stator was successfully manufactured prior to winding and encapsulation trials. Two of the five FT PDD prototypes were fitted with an encapsulated stator winding in order to secure the copper bundles in the stator slots, reduce vibrations within the bundle and improve the thermal conductivity between the copper strands and stator laminations. The rest of the machines were assembled with a varnished stator.

The FT PDD experimental evaluation consisted of open circuit and on load tests. The open circuit EMF and loss shows good agreement to the 3D FEA predictions. Furthermore, it is shown that the insulator coating on the Titanium sleeve is effective at reducing the no-load power loss of the FT PDD motor. The on-load tests considered the effects of machine drag torque and measured the variation of output torque with input phase current for a range of speeds. The operation of the FT PDD under symmetrical 3-phase short circuit of one lane showed the fault current limiting characteristics given by the 1 p.u inductance. A higher input current is required for the healthy lane in Active-Passive faulty operation in order to supply the rated output torque.

The pull-out torque of the FT PDD was measured in dynamic and static tests showing the torque fuse capability of the proposed actuator motor topology. The thermal response during actuator cycles was verified through FE analysis and experimental tests. It was shown that under Active-Passive faulty operation, the peak temperature does not exceed the temperature limit of the active components, even for an ambient temperature of 70^{o}C.

The bandwidth capability was experimentally evaluated, under actuator cycles, on a bespoke dynamometer, capable of position and load control, which was designed and implemented at the University of Sheffield. The rotor inertia of the load machine was similar to the total inertia of the actuator drive train and rudder. A good agreement is established between the predicted and measured bandwidth, with the FT PDD exceeding the requirements at reduced slide displacements.

- **Comparison with conventional PM electrical machine**

The FT PDD prototype can be compared with an off-the-shelf aerospace approved frameless non-fault tolerant Kollmorgen PM motor [193], with a similar output torque capability. Furthermore, the FT PDD was converted to a non-fault-tolerant (NFT) configuration, with a double layer 3-phase winding topology, and with the same magnetic gear element. The stator radial thickness was reduced to further reduce mass and obtain a similar slot current density. The copper loss of the NFT PDD was reduced by 30% when compared to the FT variant. In comparison, the ratio between copper loss at rated torque output, and outer case area of the FT design was 20% higher than that of the NFT variant. This can indicate that the thermal response of the NFT PDD should not exceed the temperature rating of the active machine components. Furthermore, the thermal mass of the NFT stator can be increased by encapsulating the stator. The total loss can be further reduced by laminating the pole pieces and utilising a composite sleeve.

The comparison of the KBM 25, FT and NFT PDDs is shown in Table 11.1. It can be observed that the PDD designs enable a significant reduction in mass, while the inertia of the PPR connected to the mechanical drivetrain is only 6.2% of the inertia of the conventional PM machine. The low inertia of the output rotor combined with the torque limiting characteristic of the magnetic gear element can be beneficial in reducing the mass and size of the end stops, which are typically used in an actuator to absorb the kinetic energy associated with runaway conditions due to loss of control.

Table 11.1. Comparison of PM and PDD electrical machines

Parameter	**KBM 25** [193]	**FT PDD**	**NFT PDD**
Rated torque (Nm)	8.7	8.6	8.6
Rated power (W)	1765	1080	1080
Rated output speed (rpm)	2300	1200	1200
Inertia output rotor ($kg.cm^2$)	6.78	0.42	0.42
Stator outer diameter (mm)	110.0	73.8	62.8
Active length (mm)	93.7	53.0	53.0
Active mass (kg)	3.50	1.78	1.05
Torque per active vol. (Nm/l)	9.80	37.90	53.40
Torque per active mass (Nm/kg)	2.50	4.83	8.20

The fault tolerant PDD prototype, presented in this thesis, has subsequently been integrated within the rudder actuator shown in Figure 11.1. The PDD actuator integration and actuator drive train design was conducted by Triumph Group – Integrated Systems – Actuation & Control. The actuator was showcased at Farnborough Airshow 2018, on the Aerospace Technology Institute stand.

Figure 11.1. Magnetically geared fault tolerant PDD rudder actuator

The future research work that can be undertaken is represented by:

- Explore the scalability of the FT PDD for larger magnetically geared EMA systems representative of the actuation requirements of commercial aircraft with a MTOW between 50 – 150 tonnes.
- Research the bandwidth requirements for military primary flight control surfaces such as ailerons, elevators etc.
- Investigate novel construction methods for the pole piece rotor such injection moulding high performance ceramics around the ferromagnetic pole pieces.
- Investigate the trade-off of implementing aluminium windings to further reduce PDD weight.
- Explore the use of high performance soft magnetic materials, such as cobalt iron, for stator and pole piece laminations, in order to further increase the power density of the PDD.
- Investigate different electromagnetic designs capable of reducing the PDD end flux leakage and pole piece Z-axis magnetic flux. This has the potential of increasing the torque density of the PDD as well as reducing the losses of the pole piece rotor.

References

[1] R. I. Jones, “The More Electric Aircraft: the past and the future?,” in *IEE Colloquium. Electrical Machines and Systems for the More Electric Aircraft*, 1999, vol. 1999, pp. 1–1.

[2] W. Pearson, “The More Electric/All Electric aircraft - a military fast jet perspective,” in *IEE Colloquium on All Electric Aircraft*, 1998, vol. 1998, pp. 5–5.

[3] D. van den Bossche, “`More Electric’ Control Surface Actuation - A Standard for the Next Generation of Transport Aircraft,” in *Conference: More Electric Aircraft*, 2004, pp. 1–8.

[4] S. J. Cutts, “A collaborative approach to the More Electric Aircraft,” in *International Conference on Power Electronics Machines and Drives*, 2002, vol. 2002, pp. 223–228.

[5] P. Wheeler and S. Bozhko, “The More Electric Aircraft: Technology and challenges.,” *IEEE Electrif. Mag.*, vol. 2, no. 4, pp. 6–12, Dec. 2014.

[6] R. T. Naayagi, “A review of more electric aircraft technology,” in *2013 International Conference on Energy Efficient Technologies for Sustainability*, 2013, pp. 750–753.

[7] Charlotte Adams, “A380: ‘More Electric’ Aircraft,” *Avionics International*, Oct-2001.

[8] J. A. Weimer, “Electrical power technology for the more electric aircraft,” in *[1993 Proceedings] AIAA/IEEE Digital Avionics Systems Conference*, pp. 445–450.

[9] L. Faleiro, “Beyond the more electric aircraft,” *Aerospace America*, pp. 35–40, Sep-2005.

[10] S. D. Soban and E. Upton, “Beyond the more electric aircraft,” in *Society of Aerospace Engineers Conference*, 2006, pp. 1–16.

[11] C. Anghel and M. Xu, “Study on main engine start for more electric architecture aircraft,” in *Society of Aerospace Engineers Conference*, pp. 1–4.

[12] B. Sarlioglu and C. T. Morris, “More Electric Aircraft: Review, Challenges, and Opportunities for Commercial Transport Aircraft,” *IEEE Trans. Transp. Electrif.*, vol. 1, no. 1, pp. 54–64, 2015.

[13] W.R. Schley, “The State of the art and remaining challenges in electric actuation for flight and propulsion control,” in *Society of Aerospace Engineers Conference*, p. 14.1-14.11.

[14] M. E. Roth, L. M. Taylor, and I. G. Hansen, “Status of electrical actuator applications,” in *IECEC 96. Proceedings of the 31st Intersociety Energy Conversion Engineering Conference*, vol. 1, pp. 191–196.

[15] J. W. Bennett *et al.*, “A prototype electrical actuator for aircraft flaps and slats,” in *IEEE International Conference on Electric Machines and Drives, 2005.*, 2005, pp. 41–47.

[16] G. M. Raimondi, T. Sawata, and P. Green, “Fan Shaft Driven Generator,” in *Aerospace Engineers Conference*, p. 9.1-9.7.

[17] D. R. Trainer and C. R. Whitley, “Electric actuation - power quality management of aerospace flight control systems,” *IET Int. Conf. Power Electron. Mach. Drives*, no. 487, pp. 229–234, 2002.

[18] P. W. Wheeler, “An electro-hydrostatic aircraft actuator using a matrix converter permanent magnet motor drive,” in *Second IEE International Conference on Power Electronics, Machines and Drives*, 2004, vol. 2004, pp. v2-464-v2-464.

[19] S. L. Botten, C. R. Whitley, and A. D. King, “Flight Control Actuation Technology

for Next-Generation All-Electric Aircraft," *Technol. Rev. J.*, no. Millennium Issue, pp. 55–67.

[20] A. Boglietti, A. Cavagnino, A. Tenconi, S. Vaschetto, and P. di Torino, "The safety critical electric machines and drives in the more electric aircraft: A survey," in *2009 35th Annual Conference of IEEE Industrial Electronics*, 2009, pp. 2587–2594.

[21] R. Sebastian and A. Alexander, "Rotary Actuator for Retractable Landing Gear Systems," *Recent Adv. Aerosp. Actuation Syst. Components*, pp. 133–139, 2016.

[22] Todeschi, "Airbus - EMAs for Flight Control Actuation System," in *SAE International Journal of Aerospace*, 2011, pp. 1–16.

[23] Wagner-et-al, "Challenges for Health Monitoring of Electromechanical Flight Control Actuation Systems," *SAE Int. J. Aerosp.*, vol. 4, no. 2, pp. 1316–1323, Oct. 2011.

[24] P. Chouinard, M. Denninger, and J. S. Plante, "Reliable and lightweight primary flight control actuation using magneto-rheological clutches in slippage," in *Proceedings - IEEE International Conference on Robotics and Automation*, 2015, vol. 2015–June, no. June, pp. 213–219.

[25] F. L. J. Linden, N. Dreyer, and A. Dorkel, "EMA Health Monitoring: An overview.," *Recent Adv. Aerosp. Actuation Syst. Components*, pp. 21–26, 2016.

[26] M. A. A. Ismail, E. Balaban, and H. Spangenberg, "Fault detection and classification for flight control electromechanical actuators," *IEEE Aerosp. Conf. Proc.*, vol. 2016–June, pp. 1–10, 2016.

[27] NSK Europe, "Ballscrew flaking," *Ballscrew troubleshooting*. [Online]. Available: http://www.nskeurope.com/flaking-ball-screws-204.htm.

[28] NSK Europe, "Ballscrew wear," *Ballscrew troubleshooting*. [Online]. Available: http://www.nskeurope.com/wear-ball-screws-205.htm.

[29] NSK Europe, "Ballscrew indentations," *Ballscrew troubleshooting*. [Online]. Available: http://www.nskeurope.com/indentations-ball-screws-207.htm.

[30] NTN Global, "Care and Maintenance of Bearings," *Care and Maintenance of Bearings*. [Online]. Available: http://www.ntnglobal.com/en/products/care/index.html.

[31] M. Mazzoleni *et al.*, "Development of a reliable electro-mechanical actuator for primary control surfaces in small aircrafts," *IEEE/ASME Int. Conf. Adv. Intell. Mechatronics, AIM*, pp. 1142–1147, 2017.

[32] A. Jiménez, E. Novilo, F. Aguado, and E. Mrante, "Electromechanical Actuator with Anti-Jamming System for Safety critical aircraft applications," *Proc. 6th Int. Conf. Recent Adv. Aerosp. Actuation Syst. Components*, pp. 116–120, 2014.

[33] B. M., "A Built-In Testable Jam Release Device for Electromechanical Actuators in Flight Control Application," in *Proceedings of the 6th International Conference on Recent Advances in Aerospace Actuation Systems and Components (R3ASC'14)*, 2014, pp. 105–108.

[34] A. Naubert, M. Bachmann, M. Christmann, and U. C. S. A, "Disconnect device design options for jam-tolerant electromechanical actuators," pp. 187–192, 2016.

[35] N. Elliott and A. Didey, "Jam-tolerant actuator." Google Patents, 2011.

[36] J. E. Flatt, "Jam tolerant electromechanical actuation systems and methods of operation." Google Patents, 2005.

[37] J. Corney, "Apparatus for releasing a jam in a lead screw actuator." Google Patents, 2005.

[38] E. Richter, "Switched reluctance machines for high performance operations in a harsh environment-A review paper," in *ICEM conference*, 1990.

[39] E. Richter, A. V. E. Radun, C. Ferreira, and E. Ruckstader, “An integrated electrical starter/generator system for gas turbine application, design and test results,” in *ICEM conference Paris,* 1994.

[40] L. Castellini, S. Lucidi, and M. Villani, “Design optimization of switched reluctance motor for aerospace application,” in *2015 IEEE International Electric Machines & Drives Conference (IEMDC),* 2015, pp. 1678–1682.

[41] Xiaoyuan Chen, Zhiquan Deng, and Jingjing Peng, “Fault tolerant switched reluctance machine for fuel pump drive in aircraft,” in *2009 4th IEEE Conference on Industrial Electronics and Applications,* 2009, pp. 2340–2344.

[42] B. C. Mecrow, A. G. Jack, J. A. Haylock, and J. Coles, “Fault-tolerant permanent magnet machine drives,” *IEE Proc. - Electr. Power Appl.,* vol. 143, no. 6, p. 437, 1996.

[43] A. Schramm and D. Gerling, “Researches on the suitability of switched reluctance machines and permanent magnet machines for specific aerospace applications demanding fault tolerance,” in *International Symposium on Power Electronics, Electrical Drives, Automation and Motion, 2006. SPEEDAM 2006.,* pp. 56–60.

[44] S. Shoujun, L. Weiguo, D. Peitsch, and U. Schaefer, “Detailed Design of a High Speed Switched Reluctance Starter/Generator for More/All Electric Aircraft,” *Chinese J. Aeronaut.,* vol. 23, no. 2, pp. 216–226.

[45] D. J. Powell, G. W. Jewell, S. D. Calverley, and D. Howe, “Iron loss in a modular rotor switched reluctance machine for the "More-Electric" aero-engine,” *IEEE Trans. Magn.,* vol. 41, no. 10, pp. 3934–3936, Oct. 2005.

[46] C. Cossar, “The design of a switched reluctance drive for aircraft flight control surface actuation,” in *IEE Colloquium. Electrical Machines and Systems for the More Electric Aircraft*, 1999, vol. 1999, pp. 2–2.

[47] K. Atallah *et al.*, “Comparison of electrical drive technologies for aircraft flight control surface actuation,” in *1999. Ninth International Conference on Electrical Machines and Drives (Conf. Publ. No. 468),* 1999, pp. 159–163.

[48] A. J. Mitcham, G. Antonopoulos, and J. J. A. Cullen, “Favourable slot and pole number combinations for fault-tolerant PM machines,” *IEE Proc. - Electr. Power Appl.,* vol. 151, no. 5, p. 520, 2004.

[49] M. Rottach, C. Gerada, and P. W. Wheeler, “Design optimisation of a fault-tolerant PM motor drive for an aerospace actuation application,” in *7th IET International Conference on Power Electronics, Machines and Drives (PEMD 2014)*, 2014, pp. 1–6.

[50] P. S. Sangha and T. Sawata, “Design and test results for dual-lane fault-tolerant PM motor for safety critical aircraft actuator,” in *2015 IEEE Energy Conversion Congress and Exposition (ECCE)*, 2015, pp. 4055–4060.

[51] J. W. Bennett, G. J. Atkinson, B. C. Mecrow, and D. J. Atkinson, “Fault-Tolerant Design Considerations and Control Strategies for Aerospace Drives,” *IEEE Trans. Ind. Electron.*, vol. 59, no. 5, pp. 2049–2058, May 2012.

[52] M. Galea, Z. Xu, C. Tighe, T. Hamiti, C. Gerada, and S. Pickering, “Development of an aircraft wheel actuator for green taxiing,” in *2014 International Conference on Electrical Machines (ICEM)*, 2014, pp. 2492–2498.

[53] T. Raminosoa, T. Hamiti, M. Galea, and C. Gerada, “Feasibility and electromagnetic design of direct drive wheel actuator for green taxiing,” in *2011 IEEE Energy Conversion Congress and Exposition*, 2011, pp. 2798–2804.

[54] A. M. EL-Refaie, M. R. Shah, and K. Huh, “High-Power-Density Fault-Tolerant PM Generator for Safety-Critical Applications,” *IEEE Trans. Ind. Appl.*, vol. 50, no. 3, pp. 1717–1728, 2014.

[55] J. D. Ede, K. Atallah, J. B. Wang, and D. Howe, “Modular fault-tolerant permanent magnet brushless machines,” in *2002 International Conference on Power Electronics, Machines and Drives (Conf. Publ. No. 487)*, 2002, pp. 415–420.

[56] N. Bianchi, M. D. Pre, and S. Bolognani, “Design of a Fault-Tolerant IPM Motor for Electric Power Steering,” *IEEE Trans. Veh. Technol.*, vol. 55, no. 4, pp. 1102–1111, Jul. 2006.

[57] B. C. Mecrow *et al.*, “Design and testing of a four-phase fault-tolerant permanent-magnet machine for an engine fuel pump,” *IEEE Trans. Energy Convers.*, vol. 19, no. 4, pp. 671–678, 2004.

[58] J. A. Haylock, B. C. Mecrow, A. G. Jack, and D. J. Atkinson, “Operation of a fault tolerant PM drive for an aerospace fuel pump application,” in *1997 Eighth International Conference on Electrical Machines and Drives (Conf. Publ. No. 444)*, 1997, pp. 133–137.

[59] P. M. Tlali, R. J. Wang, and S. Gerber, “Magnetic gear technologies: A review,” in *2014 International Conference on Electrical Machines (ICEM)*, 2014, pp. 544–550.

[60] C. G. Armstrong, “Power-transmitting device.” Google Patents, 1901.

[61] H. T. Faus, “Magnet gearing.” Google Patents, 1941.

[62] S. H. P, “Magnetic gears.” Google Patents, 1968.

[63] M. J. T. B, “Magnetic transmission.” Google Patents, 1968.

[64] L. Nikolaus, “Magnetic transmission.” Google Patents, 1972.

[65] K. Tsurumoto and S. Kikuchi, “A new magnetic gear using permanent magnet,” *IEEE Trans. Magn.*, vol. 23, no. 5, pp. 3622–3624, 1987.

[66] M. Venturini and F. Leonardi, “High torque, low speed joint actuator based on PM brushless motor and magnetic gearing,” in *Conference Record of the 1993 IEEE Industry Applications Conference Twenty-Eighth IAS Annual Meeting*, 1993, pp. 37–42 vol.1.

[67] B. Ackermann and L. Honds, “Magnetic drive arrangement comprising a plurality of magnetically cooperating parts which are movable relative to one another.” Google Patents, 1997.

[68] J. F. Charpentier and G. Lemarquand, “Mechanical behavior of axially magnetized permanent-magnet gears,” *IEEE Trans. Magn.*, vol. 37, no. 3, pp. 1110–1117, 2001.

[69] K. Atallah and D. Howe, “A novel high-performance magnetic gear,” *IEEE Trans. Magn.*, vol. 37, no. 4, pp. 2844–2846, 2001.

[70] K. Atallah, S. D. Calverley, and D. Howe, “Design, analysis and realisation of a high-performance magnetic gear,” *IEE Proc. - Electr. Power Appl.*, vol. 151, no. 2, pp. 135–143, 2004.

[71] P. O. Rasmussen, T. O. Andersen, F. T. Jorgensen, and O. Nielsen, “Development of a high-performance magnetic gear,” *IEEE Trans. Ind. Appl.*, vol. 41, no. 3, pp. 764–770, 2005.

[72] L. Shah, A. Cruden, and B. W. Williams, “A Magnetic Gear Box for application with a Contra-rotating Tidal Turbine,” in *2007 7th International Conference on Power Electronics and Drive Systems*, 2007, pp. 989–993.

[73] L. Jian, K. T. Chau, Y. Gong, J. Z. Jiang, C. Yu, and W. Li, “Comparison of Coaxial Magnetic Gears With Different Topologies,” *IEEE Trans. Magn.*, vol. 45, no. 10, pp. 4526–4529, 2009.

[74] N. W. Frank and H. A. Toliyat, “Gearing ratios of a magnetic gear for wind turbines,” in *2009 IEEE International Electric Machines and Drives Conference*, 2009, pp. 1224–1230.

[75] N. W. Frank and H. A. Toliyat, “Analysis of the concentric planetary magnetic gear with strengthened stator and interior permanent magnet (IPM) inner rotor,” in *2010 IEEE Energy Conversion Congress and Exposition*, 2010, pp. 2977–2984.

[76] Y. Man, Y. Zhao, C. Bian, S. Wang, and H. Zhao, “A kind of magnetic gear with high speed ratio,” in *The 3rd International Conference on Information Sciences and Interaction Sciences*, 2010, pp. 632–634.

[77] L. Yong, X. Jingwei, P. Kerong, and L. Yongping, “Principle and simulation analysis of a novel structure magnetic gear,” in *2008 International Conference on Electrical Machines and Systems*, 2008, pp. 3845–3849.

[78] K. K. Uppalapati, J. Z. Bird, D. Jia, J. Garner, and A. Zhou, “Performance of a magnetic gear using ferrite magnets for low speed ocean power generation,” in *2012 IEEE Energy Conversion Congress and Exposition (ECCE)*, 2012, pp. 3348–3355.

[79] K. K. Uppalapati, W. Bomela, J. Z. Bird, M. Calvin, and J. Wright, “Construction of a low speed flux focusing magnetic gear,” in *2013 IEEE Energy Conversion Congress and Exposition*, 2013, pp. 2178–2184.

[80] K. K. Uppalapati, M. Calvin, J. Wright, J. Pitchard, W. Williams, and J. Z. Bird, “A Magnetic Gearbox with an Active Region Torque Density of 239Nm/L,” *IEEE Trans. Ind. Appl.*, vol. PP, no. 99, p. 1, 2017.

[81] J. Rens, R. Clark, S. Calverley, K. Atallah, and D. Howe, “Design, analysis and realization of a novel magnetic harmonic gear,” in *2008 18th International Conference on Electrical Machines*, 2008, pp. 1–4.

[82] J. Rens, K. Atallah, S. D. Calverley, and D. Howe, “A Novel Magnetic Harmonic Gear,” *IEEE Trans. Ind. Appl.*, vol. 46, no. 1, pp. 206–212, 2010.

[83] K. Atallah, J. Rens, S. Mezani, and D. Howe, “A Novel ‘Pseudo’ Direct-Drive Brushless Permanent Magnet Machine,” *IEEE Trans. Magn.*, vol. 44, no. 11, pp. 4349–4352, Nov. 2008.

[84] K. Atallah, J. Rens, S. Mezani, and D. Howe, “A Novel ‘Pseudo’ Direct-Drive Brushless Permanent Magnet Machine,” *IEEE Trans. Magn.*, vol. 44, no. 11, pp. 4349–4352, 2008.

[85] Jiabin Wang and Kais Atallah, “Modeling and control of ‘pseudo’ direct-drive brushless permanent magnet machines,” in *2009 IEEE International Electric Machines and Drives Conference*, 2009, pp. 870–875.

[86] M. Bouheraoua, Jiabin Wang, and K. Atallah, “Observer based state feedback controller design for pseudo direct drive,” in *6th IET International Conference on Power Electronics, Machines and Drives (PEMD 2012)*, 2012, pp. B51–B51.

[87] M. Bouheraoua, J. Wang, and K. Atallah, “A complex frequency domain analysis of a closed loop controlled pseudo direct drive,” in *2012 XXth International Conference on Electrical Machines*, 2012, pp. 2428–2434.

[88] M. Bouheraoua, J. Wang, and K. Atallah, “Slip Recovery and Prevention in Pseudo Direct Drive Permanent-Magnet Machines,” *IEEE Trans. Ind. Appl.*, vol. 51, no. 3, pp. 2291–2299, 2015.

[89] M. Bouheraoua, J. Wang, and K. Atallah, “Speed control for a Pseudo Direct Drive permanent magnet machine with one position sensor on low-speed rotor,” in *2013 International Electric Machines & Drives Conference*, 2013, pp. 986–992.

[90] M. Bouheraoua, J. Wang, and K. Atallah, “Rotor position estimation of a Pseudo Direct Drive PM machine using extended Kalman filter,” in *2015 IEEE Energy Conversion Congress and Exposition (ECCE)*, 2015, pp. 292–299.

[91] S. D. Calverley, D. J. Powell, K. Daffey, and F. de Wildt, “Design and analysis of a pseudo direct-drive propulsion motor,” in *5th IET International Conference on*

Power Electronics, Machines and Drives (PEMD 2010), 2010, pp. 253–253.

[92] A. Penzkofer and K. Atallah, “Analytical Modeling and Optimization of Pseudo-Direct Drive Permanent Magnet Machines for Large Wind Turbines,” *IEEE Trans. Magn.*, vol. 51, no. 12, pp. 1–14, Dec. 2015.

[93] C. G. C. Neves, A. F. Flores Filho, and D. G. Dorrel, “Design of a Pseudo Direct Drive for Wind Power Applications,” in *2016 International Conference of Asian Union of Magnetics Societies (ICAUMS)*, 2016, pp. 1–5.

[94] A. Penzkofer and K. Atallah, “Scaling of Pseudo Direct Drives for Wind Turbine Application,” *IEEE Trans. Magn.*, vol. 52, no. 7, pp. 1–5, Jul. 2016.

[95] G. Cooke and K. Atallah, “‘Pseudo’ Direct Drive Electrical Machines With Alternative Winding Configurations,” *IEEE Trans. Magn.*, vol. 53, no. 11, pp. 1–8, Nov. 2017.

[96] X. Yin, Y. Fang, and P.-D. Pfister, “High-torque-density pseudo-direct-drive permanent-magnet machine with less magnet,” *IET Electr. Power Appl.*, vol. 12, no. 1, pp. 37–44, Jan. 2018.

[97] A. Penzkofer, G. Cooke, M. Odavic, and K. Atallah, “Coil Excited Pseudo Direct Drive Electrical Machines,” *IEEE Trans. Magn.*, vol. 53, no. 1, pp. 1–11, Jan. 2017.

[98] L. Castellini, S. Lucidi, and M. Villani, “Design optimization of switched reluctance motor for aerospace application,” in *2015 IEEE International Electric Machines & Drives Conference (IEMDC)*, 2015, pp. 1678–1682.

[99] M. Villani, M. Tursini, G. Fabri, and L. Di Leonardo, “A switched-reluctance motor for aerospace application,” in *2014 International Conference on Electrical Machines (ICEM)*, 2014, pp. 2073–2079.

[100] M. Villani, M. Tursini, G. Fabri, and L. Castellini, “Fault-tolerant PM brushless DC drive for aerospace application,” in *The XIX International Conference on Electrical Machines - ICEM 2010*, 2010, pp. 1–7.

[101] X. Jiang, W. Huang, R. Cao, Z. Hao, C. Li, and W. Jiang, “Analysis of a dual-winding fault-tolerant permanent magnet machine drive for aerospace applications,” in *2015 IEEE Magnetics Conference (INTERMAG)*, 2015, p. 1.

[102] J. Zhu, N. Ertugrul, and W. L. Soong, “Performance Investigation of a Fault-Tolerant Brushless Permanent Magnet AC Motor Drive,” in *2006 CES/IEEE 5th International Power Electronics and Motion Control Conference*, 2006, vol. 2, pp. 1–5.

[103] T. Raminosoa and C. Gerada, “Novel fault tolerant design of flux switching machines,” in *5th IET International Conference on Power Electronics, Machines and Drives (PEMD 2010)*, 2010, pp. 1–6.

[104] T. Raminosoa and C. Gerada, “A comparative study of permanent magnet - synchronous and permanent magnet - flux switching machines for fault tolerant drive systems,” in *2010 IEEE Energy Conversion Congress and Exposition*, 2010, pp. 2471–2478.

[105] N. Takorabet, J. P. Caron, B. Vaseghi, B. Nahid-Mobarakeh, F. Meibody-Tabar, and G. Humbert, “Study of Different Architectures of Fault Tolerant Actuator Using a Double-Star PM Motor,” in *2008 IEEE Industry Applications Society Annual Meeting*, 2008, pp. 1–6.

[106] J. Chai, J. Wang, Z. Sun, and D. Howe, “Analytical prediction of inter-turn short-circuit current in fault-tolerant permanent magnet brushless machines,” in *2008 4th IET Conference on Power Electronics, Machines and Drives*, 2008, pp. 1–5.

[107] S. Nandi, H. A. Toliyat, and X. Li, “Condition Monitoring and Fault Diagnosis of Electrical Motors—A Review,” *IEEE Trans. Energy Convers.*, vol. 20, no. 4, pp.

719–729, 2005.

[108] S. M. A. Cruz and A. J. M. Cardoso, “Stator winding fault diagnosis in three-phase synchronous and asynchronous motors, by the extended Park’s vector approach,” in *Conference Record of the 2000 IEEE Industry Applications Conference. Thirty-Fifth IAS Annual Meeting and World Conference on Industrial Applications of Electrical Energy (Cat. No.00CH37129)*, 2000, vol. 1, pp. 395–401 vol.1.

[109] A. J. M. Cardoso, S. M. A. Cruz, and D. S. B. Fonseca, “Inter-turn stator winding fault diagnosis in three-phase induction motors, by Park’s vector approach,” *IEEE Trans. Energy Convers.*, vol. 14, no. 3, pp. 595–598, 1999.

[110] M. Wolkiewicz, G. Tarchała, T. Orłowska-Kowalska, and C. T. Kowalski, “Online Stator Interturn Short Circuits Monitoring in the DFOC Induction-Motor Drive,” *IEEE Trans. Ind. Electron.*, vol. 63, no. 4, pp. 2517–2528, 2016.

[111] T. Boileau, N. Leboeuf, B. Nahid-Mobarakeh, and F. Meibody-Tabar, “Synchronous Demodulation of Control Voltages for Stator Interturn Fault Detection in PMSM,” *IEEE Trans. Power Electron.*, vol. 28, no. 12, pp. 5647–5654, 2013.

[112] M. B. Abadi *et al.*, “Detection of stator and rotor faults in a DFIG based on the stator reactive power analysis,” in *IECON 2014 - 40th Annual Conference of the IEEE Industrial Electronics Society*, 2014, pp. 2037–2043.

[113] B. Wang, J. Wang, A. Griffo, and B. Sen, “Stator Turn Fault Detection by Second Harmonic in Instantaneous Power for a Triple-Redundant Fault-Tolerant PM Drive,” *IEEE Trans. Ind. Electron.*, vol. 65, no. 9, pp. 7279–7289, 2018.

[114] P. Arumugam, T. Hamiti, and C. Gerada, “Turn–turn short circuit fault management in permanent magnet machines,” *IET Electr. Power Appl.*, vol. 9, no. 9, pp. 634–641, 2015.

[115] P. Arumugam, C. Gerada, T. Hamiti, C. Hill, and S. Bozhko, “A review on turn-turn short circuit fault management,” in *2015 International Conference on Electrical Systems for Aircraft, Railway, Ship Propulsion and Road Vehicles (ESARS)*, 2015, pp. 1–5.

[116] P. Arumugam, T. Hamiti, and C. Gerada, “Modeling of Different Winding Configurations for Fault-Tolerant Permanent Magnet Machines to Restrain Interturn Short-Circuit Current,” *IEEE Trans. Energy Convers.*, vol. 27, no. 2, pp. 351–361, 2012.

[117] A. J. Mitcham, G. Antonopoulos, and J. J. A. Cullen, “Implications of shorted turn faults in bar wound PM machines,” *IEE Proc. - Electr. Power Appl.*, vol. 151, no. 6, pp. 651–657, 2004.

[118] M. D. K. Dooley, “Method and apparatus for controlling an electric machine,” 2008.

[119] L. G. R. F.J. Gieras, “Permanent magnet electric generator with variable magnet flux excitation,” US Parent 7859231, 2010.

[120] S. Sjökvist and S. Eriksson, “Experimental Verification of a Simulation Model for Partial Demagnetization of Permanent Magnets,” *IEEE Trans. Magn.*, vol. 50, no. 12, pp. 1–5, 2014.

[121] H. Xiong, J. Zhang, M. W. Degner, C. Rong, F. Liang, and W. Li, “Permanet magnet demagnetization test fixture design and validation,” in *2015 IEEE Energy Conversion Congress and Exposition (ECCE)*, 2015, pp. 3914–3921.

[122] S. Ruoho, J. Kolehmainen, J. Ikaheimo, and A. Arkkio, “Demagnetization Testing for a Mixed-Grade Dovetail Permanent-Magnet Machine,” *IEEE Trans. Magn.*, vol. 45, no. 9, pp. 3284–3289, 2009.

[123] H. V. Xuan, H. Polinder, D. Lahaye, and J. A. Ferreira, “Modeling for the design

of fractional slot PM machines with concentrated windings protected from demagnetization during three-phase short circuit,” in *2012 IEEE Energy Conversion Congress and Exposition (ECCE)*, 2012, pp. 1276–1283.
[124] G. Choi and T. M. Jahns, “Interior permanent magnet synchronous machine rotor demagnetization characteristics under fault conditions,” in *2013 IEEE Energy Conversion Congress and Exposition*, 2013, pp. 2500–2507.
[125] J. D. McFarland and T. M. Jahns, “Investigation of the Rotor Demagnetization Characteristics of Interior PM Synchronous Machines During Fault Conditions,” *IEEE Trans. Ind. Appl.*, vol. 50, no. 4, pp. 2768–2775, 2014.
[126] J. D. McFarland and T. M. Jahns, “Influence of d- and q-axis currents on demagnetization in PM synchronous machines,” in *2013 IEEE Energy Conversion Congress and Exposition*, 2013, pp. 4380–4387.
[127] V. I. Patel, J. Wang, and S. S. Nair, “Demagnetization Assessment of Fractional-Slot and Distributed Wound 6-Phase Permanent Magnet Machines,” *IEEE Trans. Magn.*, vol. 51, no. 6, pp. 1–11, 2015.
[128] G. Choi and T. M. Jahns, “Investigation of Key Factors Influencing the Response of Permanent Magnet Synchronous Machines to Three-Phase Symmetrical Short-Circuit Faults,” *IEEE Trans. Energy Convers.*, vol. 31, no. 4, pp. 1488–1497, 2016.
[129] G. Choi and T. M. Jahns, “PM Synchronous Machine Drive Response to Asymmetrical Short-Circuit Faults,” *IEEE Trans. Ind. Appl.*, vol. 52, no. 3, pp. 2176–2185, 2016.
[130] G. Choi, Y. Zhang, and T. M. Jahns, “Experimental Verification of Rotor Demagnetization in a Fractional-Slot Concentrated-Winding PM Synchronous Machine Under Drive Fault Conditions,” *IEEE Trans. Ind. Appl.*, vol. 53, no. 4, pp. 3467–3475, 2017.
[131] D. J. Evans and Z. Q. Zhu, “Influence of design parameters on magnetic gear’s torque capability,” in *2011 IEEE International Electric Machines & Drives Conference (IEMDC)*, 2011, pp. 1403–1408.
[132] M. Filippini and P. Alotto, “Coaxial Magnetic Gear Design and Optimization,” *IEEE Trans. Ind. Electron.*, vol. 64, no. 12, pp. 9934–9942, 2017.
[133] S. Pakdelian, N. W. Frank, and H. A. Toliyat, “Magnetic Design Aspects of the Trans-Rotary Magnetic Gear,” *IEEE Trans. Energy Convers.*, vol. 30, no. 1, pp. 41–50, 2015.
[134] C. T. Services, “Opera FEA.” 2018.
[135] T. A. Systems, “EMA actuator weight breakdown study,” 2015.
[136] SDP/SI, “Stock Drive Products Sterling Instrument,” *ACME Lead Screws & Ball Screws - Technical section*, 2017. [Online]. Available: http://www.sdp-si.com/PDFS/ACME-LEAD Screws.pdf#page=15.
[137] MOOG, “Ball screws and planetary roller screws,” *Catalogue-ball screws and planetary roller screws*, 2014. [Online]. Available: http://www.moog.com/content/dam/moog/literature/ICD/ballplanetaryrollerscrews_en_it.pdf.
[138] SKF, “Roller screws,” *Catalogue - Roller screw*, 2014. [Online]. Available: http://www.skf.com/binary/82-153959/14489-EN---Roller-screw-catalogue.pdf.
[139] Gary Shelton, “Roller Screw Actuators: Benefits, Selection and Maintenance,” *Design World*, 2018. [Online]. Available: https://www.designworldonline.com/roller-screw-actuators-benefits-selection-and-maintenance/.
[140] J. K. N. Richard G. Budynas, *Shigley’s Mechanical Engineering Design*, 9th ed. 2011.

[141] S. Gerber and R. J. Wang, "Analysis of the end-effects in magnetic gears and magnetically geared machines," in *2014 International Conference on Electrical Machines (ICEM)*, 2014, pp. 396–402.

[142] G. Cooke and K. Atallah, "“Pseudo” Direct Drive Electrical Machines With Alternative Winding Configurations," *IEEE Trans. Magn.*, vol. 53, no. 11, pp. 1–8, 2017.

[143] E. K. Hussain, K. Atallah, M. Odavic, R. S. Dragan, and R. E. Clark, "Pseudo Direct Drive electrical machines for flight control surface actuation," in *8th IET International Conference on Power Electronics, Machines and Drives (PEMD 2016)*, 2016, pp. 1–6.

[144] M. Boettcher, J. Reese, and F. W. Fuchs, "Reliability comparison of fault-tolerant 3L-NPC based converter topologies for application in wind turbine systems," in *IECON 2013 - 39th Annual Conference of the IEEE Industrial Electronics Society*, 2013, pp. 1223–1229.

[145] United States of America - Department of Defense, *Military Handbook - Reliability Prediction of Electronic Equipment*. 1991.

[146] Triumph Actuation & Motion Control Systems - UK, "Reliability of power electronic devices," Deeside, 2015.

[147] N. Bianchi and M. D. Pre, "Use of the star of slots in designing fractional-slot single-layer synchronous motors," *IEE Proc. - Electr. Power Appl.*, vol. 153, no. 3, pp. 459–466, 2006.

[148] Z. Q. Zhu and D. Howe, "Influence of design parameters on cogging torque in permanent magnet machines," in *1997 IEEE International Electric Machines and Drives Conference Record*, p. MA1/3.1-MA1/3.3.

[149] Sam Pashneh-Tala, A. Malins, R. Lewis, G. Heppell, and E. Rodriguez-Falcon, *The Little Book of Design 1st Edition*. 2011.

[150] K. Halbach, "Design of permanent magnet multipole magnets with oriented rare earth cobalt material," *Nucl. Instrum. Methods*, vol. 169, pp. 1–10, 1980.

[151] Z. Q. Zhu and D. Howe, "Halbach permanent magnet machines and applications: a review," *IEE Proc. - Electr. Power Appl.*, vol. 148, no. 4, pp. 299–308, 2001.

[152] K. Atallah, D. Howe, and P. H. Mellor, "Design and analysis of multi-pole Halbach (self-shielding) cylinder brushless permanent magnet machines," in *1997 Eighth International Conference on Electrical Machines and Drives (Conf. Publ. No. 444)*, 1997, pp. 376–380.

[153] Z. Q. Zhu, Z. P. Xia, K. Atallah, G. W. Jewell, and D. Howe, "Novel permanent magnet machines using Halbach cylinders," in *Proceedings IPEMC 2000. Third International Power Electronics and Motion Control Conference (IEEE Cat. No.00EX435)*, 2000, vol. 2, pp. 903–908 vol.2.

[154] T. M. Jahns and W. L. Soong, "Pulsating torque minimization techniques for permanent magnet AC motor drives-a review," *IEEE Trans. Ind. Electron.*, vol. 43, no. 2, pp. 321–330, 1996.

[155] J. Ofori-Tenkorrang and J. H. Lang, "A comparative analysis of torque production in Halbach and conventional surface-mounted permanent-magnet synchronous motors," in *Industry Applications Conference, 1995. Thirtieth IAS Annual Meeting, IAS '95., Conference Record of the 1995 IEEE*, 1995, vol. 1, pp. 657–663 vol.1.

[156] J. Bird, K. Li, J. Kadel, J. Wright, D. Som, and W. Williams, "Analysis and testing of a hybrid Halbach magnetic gearbox," in *2017 IEEE International Magnetics Conference (INTERMAG)*, 2017, pp. 1–2.

[157] L. B. Jing and Y. J. Zhang, "Exact analytical method for magnetic field

computation in the concentric magnetic gear with Halbach permanent-magnet arrays," in *2013 IEEE International Conference on Applied Superconductivity and Electromagnetic Devices*, 2013, pp. 343–346.

[158] S. L. Ho, Q. Wang, S. Niu, and W. Fu, "A novel magnetic-geared tubular linear machine with halbach permanent-magnet arrays for tidal energy conversion," in *2015 IEEE Magnetics Conference (INTERMAG)*, 2015, p. 1.

[159] K. Min, J. Choi, H. Cho, and H. Shin, "Torque analysis of magnetic spur gear with halbach magnetized permanent magnets using an analytical method," in *2015 IEEE Magnetics Conference (INTERMAG)*, 2015, p. 1.

[160] W. N. Fu and L. Li, "Optimal Design of Magnetic Gears With a General Pattern of Permanent Magnet Arrangement," *IEEE Trans. Appl. Supercond.*, vol. 26, no. 7, pp. 1–5, 2016.

[161] L. Jian and K. T. Chau, "A Coaxial Magnetic Gear With Halbach Permanent-Magnet Arrays," *IEEE Trans. Energy Convers.*, vol. 25, no. 2, pp. 319–328, 2010.

[162] H. W. Jun, H. S. Seol, and J. Lee, "Design of High Power Density TVC Driving Motor for Space Launch Vehicle Using Halbach Magnet Array Structure," *IEEE Trans. Appl. Supercond.*, vol. 28, no. 3, pp. 1–5, 2018.

[163] H. Huang, L. Jing, R. Qu, and D. Li, "Analysis and Application of Discrete Halbach Magnet Array With Unequal Arc Lengths and Unequally Changed Magnetization Directions," *IEEE Trans. Appl. Supercond.*, vol. 28, no. 3, pp. 1–5, 2018.

[164] D. G. Dorrell, M. F. Hsieh, M. Popescu, L. Evans, D. A. Staton, and V. Grout, "A Review of the Design Issues and Techniques for Radial-Flux Brushless Surface and Internal Rare-Earth Permanent-Magnet Motors," *IEEE Trans. Ind. Electron.*, vol. 58, no. 9, pp. 3741–3757, 2011.

[165] Z. Q. Zhu, Z. P. Xia, and D. Howe, "Comparison of Halbach magnetized brushless machines based on discrete magnet segments or a single ring magnet," *IEEE Trans. Magn.*, vol. 38, no. 5, pp. 2997–2999, 2002.

[166] P. H. Mellor and R. Wrobel, "Optimization of a Multipolar Permanent-Magnet Rotor Comprising Two Arc Segments per Pole," *IEEE Trans. Ind. Appl.*, vol. 43, no. 4, pp. 942–951, 2007.

[167] Y. Shen, G. Y. Liu, Z. P. Xia, and Z. Q. Zhu, "Determination of Maximum Electromagnetic Torque in PM Brushless Machines Having Two-Segment Halbach Array," *IEEE Trans. Ind. Electron.*, vol. 61, no. 2, pp. 718–729, 2014.

[168] J. H. Lee, D. W. Kim, Y. J. Kim, and S. Y. Jung, "Study on topology of magnetic gear considering shape of pole piece," in *2017 20th International Conference on Electrical Machines and Systems (ICEMS)*, 2017, pp. 1–4.

[169] P. O. Rasmussen, H. H. Mortensen, T. N. Matzen, T. M. Jahns, and H. A. Toliyat, "Motor integrated permanent magnet gear with a wide torque-speed range," in *2009 IEEE Energy Conversion Congress and Exposition*, 2009, pp. 1510–1518.

[170] T. V Frandsen, P. O. Rasmussen, and K. K. Jensen, "Improved motor intergrated permanent magnet gear for traction applications," in *2012 IEEE Energy Conversion Congress and Exposition (ECCE)*, 2012, pp. 3332–3339.

[171] P. O. Rasmussen, T. V Frandsen, K. K. Jensen, and K. Jessen, "Experimental Evaluation of a Motor-Integrated Permanent-Magnet Gear," *IEEE Trans. Ind. Appl.*, vol. 49, no. 2, pp. 850–859, 2013.

[172] G. Qi, J. T. Chen, Z. Q. Zhu, D. Howe, L. B. Zhou, and C. L. Gu, "Influence of Skew and Cross-Coupling on Flux-Weakening Performance of Permanent-Magnet Brushless AC Machines," *IEEE Trans. Magn.*, vol. 45, no. 5, pp. 2110–2117, 2009.

[173] L. Chang, "An improved FE inductance calculation for electrical machines," *IEEE*

Trans. Magn., vol. 32, no. 4, pp. 3237–3245, 1996.

[174] G. Qi, J. T. Chen, Z. Q. Zhu, D. Howe, L. B. Zhou, and C. L. Gu, "Influence of skew and cross-coupling on d- and q-axis inductances and flux-weakening performance of PM brushless AC machines," in *2008 International Conference on Electrical Machines and Systems*, 2008, pp. 2854–2859.

[175] H. Jianhui, Z. Jibin, and L. Weiyan, "Finite element calculation of the saturation DQ-axes inductance for a direct drive PM synchronous motor considering cross-magnetization," in *The Fifth International Conference on Power Electronics and Drive Systems, 2003. PEDS 2003.*, 2003, vol. 1, p. 677–681 Vol.1.

[176] W. Q. Chu and Z. Q. Zhu, "Analytical modeling and investigation of transient response of PM machines with 3-phase short-circuit fault," in *2011 IEEE International Electric Machines & Drives Conference (IEMDC)*, 2011, pp. 125–130.

[177] A. M. El-Serafi and J. Wu, "Determination of the parameters representing the cross-magnetizing effect in saturated synchronous machines," *IEEE Trans. Energy Convers.*, vol. 8, no. 3, pp. 333–342, 1993.

[178] A. M. El-Serafi, A. S. Abdallah, M. K. El-Sherbiny, and E. H. Badawy, "Experimental study of the saturation and the cross-magnetizing phenomenon in saturated synchronous machines," *IEEE Trans. Energy Convers.*, vol. 3, no. 4, pp. 815–823, 1988.

[179] C. Bianchini, E. Fornasiero, T. N. Matzen, N. Bianchi, and A. Bellini, "Fault detection of a five-phase Permanent-Magnet machine," in *2008 34th Annual Conference of IEEE Industrial Electronics*, 2008, pp. 1200–1205.

[180] G. Bertotti, "General properties of power losses in soft ferromagnetic materials," *IEEE Trans. Magn.*, vol. 24, no. 1, pp. 621–630, 1988.

[181] G. Bertotti, A. Boglietti, M. Chiampi, D. Chiarabaglio, F. Fiorillo, and M. Lazzari, "An improved estimation of iron losses in rotating electrical machines," *IEEE Trans. Magn.*, vol. 27, no. 6, pp. 5007–5009, 1991.

[182] H. Nam, K.-H. Ha, J.-J. Lee, J.-P. Hong, and G.-H. Kang, "A study on iron loss analysis method considering the harmonics of the flux density waveform using iron loss curves tested on Epstein samples," *IEEE Trans. Magn.*, vol. 39, no. 3, pp. 1472–1475, 2003.

[183] K. Atallah, Z. Q. Zhu, and D. Howe, "An improved method for predicting iron losses in brushless permanent magnet DC drives," *IEEE Trans. Magn.*, vol. 28, no. 5, pp. 2997–2999, 1992.

[184] P. A. Hargreaves, B. C. Mecrow, and R. Hall, "Calculation of iron loss in electrical generators using finite element analysis," in *2011 IEEE International Electric Machines & Drives Conference (IEMDC)*, 2011, pp. 1368–1373.

[185] M. A. Mueller *et al.*, "CALCULATION OF IRON LOSSES FROM TIME-STEPPED FINITE-ELEMENT MODELS OF CAGE INDUCTION MACHINES," in *1995 Seventh International Conference on Electrical Machines and Drives (Conf. Publ. No. 412)*, 1995, p. 88.

[186] D. Eggers, S. Steentjes, and K. Hameyer, "Advanced Iron-Loss Estimation for Nonlinear Material Behavior," *IEEE Trans. Magn.*, vol. 48, no. 11, pp. 3021–3024, Nov. 2012.

[187] SKF, "SKF bearing calculator." [Online]. Available: http://www.skf.com/uk/knowledge-centre/engineering-tools/skfbearingcalculator.html.

[188] P. H. Mellor, D. Roberts, and D. R. Turner, "Lumped parameter thermal model for electrical machines of TEFC design," *IEE Proc. B - Electr. Power Appl.*, vol. 138,

no. 5, pp. 205–218, 1991.

[189] D. Staton, A. Boglietti, and A. Cavagnino, “Solving the more difficult aspects of electric motor thermal analysis,” in *IEEE International Electric Machines and Drives Conference, 2003. IEMDC’03.*, 2003, vol. 2, pp. 747–755 vol.2.

[190] A. Boglietti, A. Cavagnino, and D. Staton, “Determination of Critical Parameters in Electrical Machine Thermal Models,” *IEEE Trans. Ind. Appl.*, vol. 44, no. 4, pp. 1150–1159, 2008.

[191] D. Kuehbacher, A. Kelleter, and D. Gerling, “An improved approach for transient thermal modeling using lumped parameter networks,” in *2013 International Electric Machines & Drives Conference*, 2013, pp. 824–831.

[192] D. A. Howey, P. R. N. Childs, and A. S. Holmes, “Air-gap convection in rotating electrical machines,” *IEEE Trans. Ind. Electron.*, vol. 59, no. 3, pp. 1367–1375, 2012.

[193] Kollmorgen, “Kollmorgen Frameless Motor Series.” [Online]. Available: https://www.maccon.de/fileadmin/redaktion/downloads/Produkte/Bausatzmotoren/hohe_leistung/KBM_25_data.pdf.

Appendix 1:Material Properties

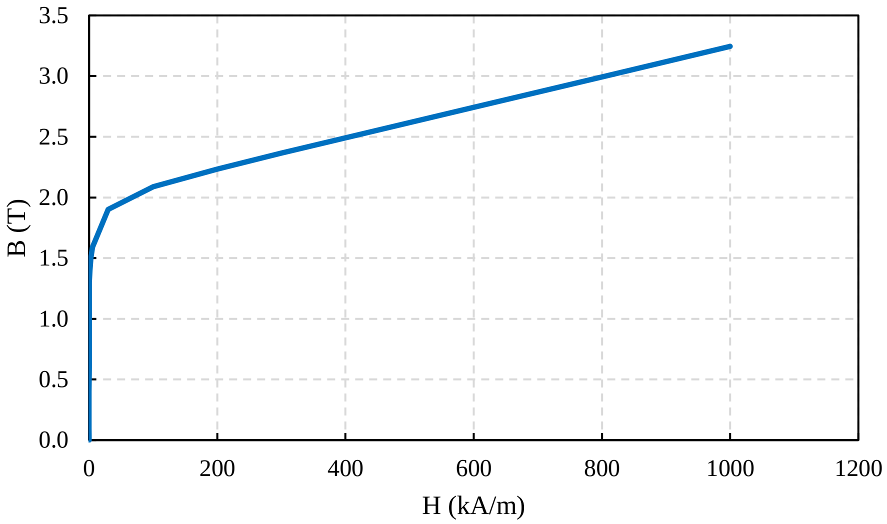

Appendix Figure 1. M270-35A BH curve

Appendix Table 1. Recoma 28 material properties

Property	Value	Units
Residual induction, B_r	1.10	T
Coercivity, H_{cB}	800	kA/m
Intrinsic coercivity, H_{ci}	2000	kA/m
Energy product, BH_{max}	225	kJ/m^3
Induction temp. coef.	-0.035	%/^{o}C
Coercivity temp. coef.	-0.24	%/^{o}C
Thermal conductivity	10	W/(m·K)
Specific heat	350	J/(kg·K)
Max. temperature	350	^{o}C
Flexural strength	120	MPa
Compressive strength	800	MPa
Young's Modulus	140	GPa
Density	8300	Kg/m^3
Electrical resistivity	90	µΩ·cm

Appendix Table 2. PEEK C30 material properties

Property	**Value**	**Units**
Density	1.40	g/cm^3
Melting temp.	340	oC
Thermal conductivity	0.92	W/(m·K)
Coef. thermal expansion	$25\cdot10^{-6}$	K^{-1}
Max. temp (short periods)	310	^{o}C
Max. temp (continuously)	250	^{o}C
Min. service temp	-20	^{o}C
Tensile stress at break	144	MPa
Tensile strain at break	3.5	%
Modulus of elasticity	9200	MPa
Electric resistivity	$<10^5$	Ω·cm

Appendix Table 3. G11 fibre glass material properties

Property	**Value**	**Units**
Tensile strength	550	MPa
Tensile modulus	30	GPa
Density	1.9	g/cm^3
Electrical strength	10	kV/mm
Thermal conductivity	0.35	W/mK
Water absorption	0.2%	% wt/wt
Max. temp	180	^{o}C

Appendix Table 4. Tribobond 42 material properties

Property	**Values**	**Units**
Thickness	4 to 6 µm	µm
Surface Roughness	0.03	Ra
Friction coefficient	0.04 - 0.06	-
	< 0.1	-
Hardness ($HV_{0.025}$)	4 - 6000	kg/mm^2
Nano hardness	10 - 40	GPa
Young’s Modulus	250 - 180	GPa
Stress	0.5 - 2	GPa
Chemical stability	Very good	-
Thermal stability	300	°C
Electrical resistance	> 10^{10}	Ω·cm
Thermal conductivity	~ 400 W/m^{2}K	W/(m·K)
Thermal expansion	~9 x 10^{-6}	/°C
Dielectrical constant	10.9 - 4.0	-
Colour	black	

Appendix Table 5. Duralco 4538 material properties

Property	**Value**	**Units**
Mixed viscosity	17200	cps
Tensile strength	6000	psi
Thermal conductivity	1.01	W/(m·K)
Dielectric strength	450	V/mm
Volume resistivity	10^{14}	Ω·cm
Max. temperature	232	^{o}C

Appendix Table 6. Thermal properties of different PDD materials

Material	**Density (kg/m^3)**	**Thermal Conductivity (W/(m·K))**	**Specific heat (J/(kg·K))**
EN24T	7830	37.8	470.5
Al 7075-T6	2800	134	946
Inconel 718	8220	12.1	449
AISI 4040C	7800	25	475
AISI 316L	7970	15	510
Alumina Spacers (ADS-96R)	3750	26	880
G11 Rods	1800	0.288	1000
Bearings (EN10025 ST52)	7850	50.5	480
Recoma 28	8300	10	350
Copper	3584	2 / 2 /154 (x/y/z)	380
M270-35A	7600	29.6	430
Nomex	800	0.14	1300
Ultimeg 2220	1150	0.2	1500